

MASS SPECTROMETRY: AN APPROACH TO CHARACTERIZING POLYURETHANE
POLYMERS

By

Tiffany M. Crescentini

Dissertation

Submitted to the Faculty of the
Graduate School of Vanderbilt University

in partial fulfillment of the requirements

for the degree of

DOCTOR OF PHILOSOPHY

in

Chemistry

March, 2019

Nashville, Tennessee

Approved:

Date:

Professor John A. McLean _____

Professor David M. Hercules _____

Professor Ned A. Porter _____

Professor M. Shane Hutson _____

This work is dedicated to all those who believed in me.

ACKNOWLEDGEMENTS

Firstly, I would like to thank my God and Savior for the opportunity to be at Vanderbilt and pursue a Ph.D. in Chemistry. Secondly, I would like to thank my husband for being so patient and steadfast through this journey. Kodiak, you have been a rock and incredible champion, thank you for your love and so many great memories.

I would also like to thank my dissertation advisor Dr. John A. McLean for the last 6 + years in his lab. Thank you for letting me start my career early on during the SyBBURE days as an undergraduate. You have been incredibly helpful through this journey. I value the experiences that I've gained working in your lab. Next, I would like to thank the one who brought me to Vanderbilt University, Professor. David M. Hercules. Prof. Hercules, you made it possible for me to come to Vanderbilt, all the way from Waynesburg, PA back in the spring of 2013. Who would have thought a rendezvous at PITTCON would lead to this incredible experience. I have thoroughly enjoyed working along side of you, characterizing many polymer samples within your box of many.

Next, I would like to thank Ian Tomlinson, Keri Tallman, and Robby Woods for all of their help learning the fundamentals of synthesis. Special thanks to Ian for his patience teaching me the art of organic chemistry. I would also like to thank my dissertation committee members Prof. Ned A. Porter and Prof. Shane M. Hutson for their valuable input along the way. I would also like to thank my colleagues, past and present in the McLean lab for being good co-workers and good friends.

Many thanks to all my friends and family for their love and support. I would not have made it to this point without all of you! Special thanks to Ron, Gina, and Casey Crescentini you all have been incredibly supportive throughout this journey. Thank you mom (Cindy Onifer) and Jake Onifer for all of your love and support! Special thanks to some of my best friends: Heather

Drummond, Alisha Hooker, and Danielle Young. You are all beautiful people doing incredible things here in Nashville.

Lastly, I would like to acknowledge the entities, which provided financial support for this work: the Vanderbilt University of Arts and Sciences, Center for Innovative Technology (CIT) at Vanderbilt University. Financial support for this research was provided by the National Institutes of Health (NIH NIGMS R01GM092218 and NIH NCI 1R03CA222452-01).

TABLE OF CONTENTS

| | |
|----------------------------|------|
| ACKNOWLEDGEMENTS..... | iii |
| LIST OF TABLES..... | vii |
| LIST OF SCHEMES..... | viii |
| LIST OF FIGURES..... | xi |
| LIST OF ABBREVIATIONS..... | x |

CHAPTERS

| | |
|---|-----|
| I. MASS SPECTROMETRY OF POLYURETHANES..... | 1 |
| 1.1. Introduction..... | 1 |
| 1.2. Polyurethane Hard Segment Characterization..... | 6 |
| 1.3. Polyurethane Soft Segment Characterization..... | 13 |
| 1.4. Polyurethane Material Characterization..... | 18 |
| 1.5. Other MS-Based Techniques for PU Characterization..... | 29 |
| 1.6. Concluding Remarks..... | 30 |
| 1.7. Acknowledgements..... | 30 |
| 1.8. References..... | 31 |
| II. STRUCTURAL CHARACTERIZATION OF METHYLENEDIANILINE REGIOISOMERS BY ION MOBILITY-MASS SPECTROMETRY AND TANDEM MASS SPECTROMETRY: II. ELECTROSPRAY SPECTRA OF 3-RING AND 4-RING ISOMERS..... | 50 |
| 2.1. Introduction..... | 50 |
| 2.2. Experimental..... | 52 |
| 2.3. Results and Discussion..... | 56 |
| 2.4. Conclusions..... | 69 |
| 2.5. Acknowledgements..... | 70 |
| 2.6. References..... | 71 |
| III. STRUCTURAL CHARACTERIZATION OF METHYLENEDIANILINE REGIOISOMERS BY ION MOBILITY-MASS SPECTROMETRY, TANDEM MASS SPECTROMETRY, AND COMPUTATIONAL STRATEGIES: III. MALDI SPECTRA OF 2-RING ISOMERS..... | 74 |
| 3.1. Introduction..... | 74 |
| 3.2. Experimental..... | 76 |
| 3.3. Results and Discussion..... | 78 |
| 3.4. Conclusions..... | 98 |
| 3.5. Acknowledgements..... | 100 |
| 3.6. References..... | 102 |

| | | |
|-----|--|-----|
| IV. | STRUCTURAL CHARACTERIZATION OF METHYLENEDIANILINE REGIOISOMERS BY ION MOBILITY-MASS SPECTROMETRY AND TANDEM MASS SPECTROMETRY: IV. MALDI SPECTRA OF 3-RING AND 4-RING ISOMERS | 106 |
| | 4.1. Introduction..... | 106 |
| | 4.2. Experimental..... | 108 |
| | 4.3. Results and Discussion | 109 |
| | 4.4 Conclusions..... | 127 |
| | 4.5. Acknowledgements..... | 128 |
| | 4.6. References..... | 129 |
| V. | ALKALI METAL CATION ADDUCT EFFECT ON POLYBUTYLENE ADIPATE OLIGOMERS: ION MOBILITY-MASS SPECTROMETRY..... | 131 |
| | 5.1. Introduction..... | 131 |
| | 5.2. Experimental..... | 134 |
| | 5.3. Results and Discussion | 135 |
| | 5.4 Conclusions..... | 149 |
| | 5.5 Future Directions | 150 |
| | 5.6. Acknowledgements..... | 152 |
| | 5.7. References..... | 153 |
| VI. | STEPWISE ADDITION AND CHARACTERIZATION OF POLYURETHANE BLOCK COPOLYMERS | 158 |
| | 6.1. Introduction..... | 158 |
| | 6.2. Experimental..... | 162 |
| | 6.3. Results and Discussion | 164 |
| | 6.4 Conclusions..... | 217 |
| | 6.5. Synthetic Procedures..... | 218 |
| | 6.6. Future Directions | 229 |
| | 6.7. Acknowledgements..... | 230 |
| | 6.8. References..... | 232 |
| | APPENDICES | 235 |
| | A. Reprint Permission for Chapters..... | 235 |
| | B. Supporting Information for Chapter II..... | 236 |
| | C. Supporting Information for Chapter III | 268 |
| | D. Supporting Information for Chapter IV | 303 |
| | E. Supporting Information for Chapter V | 325 |
| | F. Curriculum Vitae | 347 |

LIST OF TABLES

| | | |
|-------------|---|-----|
| Table 3.1. | Percent relative ion current data for 2-Ring MDA | 85 |
| Table 5.1. | Region of structural transition and tipping point | 141 |
| Table 5.2. | Summary of ANOVA results for charge states +1, +2, and +3 CCS..... | 145 |
| Table 6.1. | Percent relative ion current for PBA n = 1 [M+Li] ⁺ , [M+Na] ⁺ , and [M+Ag] ⁺ .. | 171 |
| Table 6.2. | Percent relative ion current for PBA n = 2 [M+Li] ⁺ | 179 |
| Table 6.3. | Percent relative ion current for PBA n = 2 [M+Na] ⁺ | 180 |
| Table 6.4. | Percent relative ion current for PBA n = 2 [M+Ag] ⁺ | 181 |
| Table 6.5. | Mass lists and fragmentation pathways for P(1,2) precursor | 188 |
| Table 6.6. | Percent relative ion current for P(1,2) [M+Li] ⁺ | 189 |
| Table 6.7. | Percent relative ion current for P(1,2) [M+Na] ⁺ | 192 |
| Table 6.8. | Percent relative ion current for P(1,2) [M+Ag] ⁺ | 196 |
| Table 6.9. | Mass lists and fragmentation pathways for P(1,4) precursor..... | 204 |
| Table 6.10. | Percent relative ion current for P(1,4) [M+Li] ⁺ | 205 |
| Table 6.11. | Percent relative ion current for P(1,4) [M+Na] ⁺ | 208 |
| Table 6.12. | Percent relative ion current for P(1,4) [M+Ag] ⁺ | 213 |

LIST OF SCHEMES

| | | |
|-------------|---|-----|
| Scheme 2.1. | Proposed Fragmentation Pathways for 3-Ring and 4-Ring MDA | 66 |
| Scheme 3.1. | Fragmentation mechanisms for M-1 MDA isomer mass loss..... | 93 |
| Scheme 3.2. | Fragmentation mechanisms for M-16 MDA isomer mass loss..... | 95 |
| Scheme 3.3. | Fragmentation mechanisms for M-17 MDA isomer mass loss..... | 97 |
| Scheme 3.4. | Fragmentation mechanisms for M-15 MDA isomer mass loss..... | 99 |
| Scheme 4.1. | 3-Ring MDA fragmentation pathways..... | 124 |
| Scheme 4.2. | 4-Ring MDA fragmentation pathways..... | 126 |

LIST OF FIGURES

| | | |
|-------------|---|-----|
| Figure 1.1. | Polyurethane reaction scheme | 2 |
| Figure 1.2. | Polyurethane precursors and their applications | 5 |
| Figure 1.3. | MALDI-TOF mass spectrum of TDI-MDI sample | 8 |
| Figure 1.4. | Liquid chromatography separation of derivatized isocyanates..... | 10 |
| Figure 1.5. | IM-MS and MD simulation of charged PEG derivatives | 15 |
| Figure 1.6. | MALDI-TOF MS spectra of reaction monitoring | 20 |
| | | |
| Figure 2.1. | Structures of 3-Ring and 4-Ring MDA..... | 51 |
| Figure 2.2. | ESI-MS of 3-Ring and 4-Ring MDA..... | 55 |
| Figure 2.3. | 3-Ring and 4-Ring MDA CID CCS profiles..... | 57 |
| Figure 2.4. | CCS profiles for 3-ring and 4-ring MDA against theoretical conformations | 61 |
| Figure 2.5. | RMSD clustering for the 3-ring and 4-ring MDA | 63 |
| | | |
| Figure 3.1. | Structures of MDA 2-Ring isomers and 2,7-DAF | 75 |
| Figure 3.2. | ESI and MALDI MS/MS spectra for $[M+H]^+$ | 79 |
| Figure 3.3. | MALDI MS/MS spectra for 197 Da 2-Ring MDA precursors | 81 |
| Figure 3.4. | Collision induced dissociation curves for $[M+H]^+$, $[M]^+$, and $[M-H]^+$ | 83 |
| Figure 3.5. | Ion mobility traces and computational modeling comparison | 89 |
| | | |
| Figure 4.1. | Structures of 3-Ring and 4-Ring MDA precursors | 107 |
| Figure 4.2. | 3-Ring and 4-Ring MDA ESI-MS and MALDI-MS comparison..... | 111 |
| Figure 4.3. | 3-Ring and 4-Ring MDA MALDI MS/MS spectra | 113 |
| Figure 4.4. | 3-Ring and 4-Ring MDA MALDI-IM-MS spectra | 115 |
| Figure 4.5. | Collision-induced dissociation curves for 3-Ring MDA precursors..... | 118 |

| | | |
|--------------|--|-----|
| Figure 4.6. | Collision-induced dissociation curves for 4-Ring MDA precursors..... | 122 |
| Figure 5.1. | Structure of telechelic polybutylene adipate..... | 133 |
| Figure 5.2. | IM-MS mobility plot of CCS versus degree of polymerization..... | 137 |
| Figure 5.3. | Plots of Δ CCS vs DP monitoring gas-phase structural trends | 139 |
| Figure 5.4. | IM plots of PBA-cations having charge state +1 | 142 |
| Figure 5.5. | Fragmentation reaction mechanisms for singly charged PBA..... | 148 |
| Figure 5.6. | Divalent PBA-cations | 151 |
| Figure 6.1. | PBA PUs to synthesized using stepwise addition..... | 160 |
| Figure 6.2. | ESI MS/MS spectra for n = 1 PBA $[M+Li]^+$, $[M+Na]^+$, and $[M+Ag]^+$ | 165 |
| Figure 6.3. | Collision-induced dissociation curves for PBA n = 1 PBA..... | 167 |
| Figure 6.4. | Fragmentation ion pathway for PBA n = 1 PBA | 168 |
| Figure 6.5. | ESI MS/MS spectra for n = 2 PBA $[M+Li]^+$, $[M+Na]^+$, $[M+Ag]^+$ | 172 |
| Figure 6.6. | Collision-induced dissociation curves for PBA n = 2 | 173 |
| Figure 6.7. | Fragmentation ion pathway for PBA n = 2 PBA | 175 |
| Figure 6.8. | Collision-induced dissociation curves for PBA n = 2 with %RSD..... | 177 |
| Figure 6.9. | Collision-induced dissociation curves for P(1,2) | 184 |
| Figure 6.10. | ESI MS/MS spectra of the P(1,2) $[M+Li]^+$ | 185 |
| Figure 6.11. | Collision-induced dissociation curves for P(1,2) minor ions..... | 186 |
| Figure 6.12. | Zoomed ESI MS/MS spectra of the P(1,2) $[M+Li]^+$ | 187 |
| Figure 6.13. | ESI MS/MS spectra of the P(1,2) $[M+Na]^+$ | 191 |
| Figure 6.14. | ESI MS/MS spectra of the P(1,2) $[M+Ag]^+$ | 195 |
| Figure 6.15. | Collision-induced dissociation curves for P(1,2) with %RSD. | 197 |

| | | |
|--------------|---|-----|
| Figure 6.16. | Collision-induced dissociation curves monitoring for P(1,4) | 199 |
| Figure 6.17. | ESI MS/MS spectra of the P(1,4) [M+Li] ⁺ | 200 |
| Figure 6.18. | Collision-induced dissociation curves for P(1,4) minor ions. | 202 |
| Figure 6.19. | Zoomed ESI MS/MS spectra of the P(1,4) [M+Li] ⁺ | 203 |
| Figure 6.20. | ESI MS/MS spectra of the P(1,4) [M+Na] ⁺ | 207 |
| Figure 6.21. | ESI MS/MS spectra of the P(1,4) [M+Ag] ⁺ | 210 |
| Figure 6.22. | Collision-induced dissociation curves for P(1,4) with %RSD. | 214 |
| Figure 6.23. | IM-MS profiles for PBA n = 1, n = 2, P(1,2), and P(1,4) | 216 |
| Figure 6.24. | Symmetrical and asymmetrical P(1,2) and P(1,4) oligomers | 231 |

LIST OF ABBREVIATIONS/NOMENCLATURE/SYMBOLS

| | |
|--------|---|
| -NCO | Isocyanate |
| -OH | Polyol |
| 1,2MP | 1-(2-Methoxyphenyl) Piperazine |
| APCI | Atmospheric Pressure Chemical Ionization |
| APPI | Atmospheric Pressure Photoionization |
| ASAP | Atmospheric Solid Analysis Probe |
| BD | 1,4-Butanediol |
| BPA | Bisphenol A |
| CDI | Carbodiimides |
| CID | Collision Induced Dissociation |
| CI-MS | Chemical Ionization Mass Spectrometry |
| DBA | Dibutylamine |
| DESI | Desorption Electrospray Ionization |
| EG | Ethylene Glycol |
| EI-MS | Electron Ionization-Mass Spectrometry |
| ESI | Electrospray Ionization |
| ESSI | Electrosonic Spray Ionization |
| GC | Gas Chromatography |
| H12MDI | Hydrogenated MDI |
| HDI | Hexamethylene Diisocyanate |
| HILIC | Hydrophilic Interaction Liquid Chromatography |
| HPLC | High Performance Liquid Chromatography |
| HRMS | High Resolution Mass Spectrometry |
| IM-MS | Ion Mobility-Mass Spectrometry |

| | |
|------------|---|
| IPDA | Isophorone Diamine |
| IPDI | Isophorone Diisocyanate |
| LC | Liquid Chromatography |
| <i>m/z</i> | Mass-to-Charge |
| MALDI | Matrix Assisted Laser Desorption/Ionization |
| MDA | Methylene Dianiline |
| MDI | Methylene Bisphenyl Diisocyanate |
| MS | Mass Spectrometry |
| MS/MS | Tandem Mass Spectrometry |
| MWD | Molecular Weight Distribution |
| NBMA | <i>N</i> -Benzylmethylamine |
| NIPU | Non-Isocyanate Polyurethanes |
| PAA | Primary Aromatic Amines |
| PBA | Polybutylene Adipate |
| PBG | Polybutylene Gluarate |
| PCLD | Poly(ϵ -Caprolactone)-Diol |
| PEG | polyethylene glycol |
| PEO | Polyethylene Oxide |
| PEPU | Polyester-Polyurethane |
| PET | Polyethylene Terephthalate |
| PFPA | Pentafluoropropionic Anhydride |
| PLA | Polylactic Acid |
| pMDI | Polymeric Methylene Bisphenyl Diisocyanate |
| PPG | Polypropylene Glycol |
| PPG_GL | Polypropylene Glycol Glycerol Triether |
| PPO | Polypropylene Oxide |

| | |
|-------|----------------------------------|
| pTHF | Polytetrahydrofuran |
| PTMO | Polytetramethylene Oxide |
| PU | Polyurethane |
| Py-MS | Pyrolysis-MS |
| SEC | Size-Exclusion Chromatography |
| SFC | Super Critical Fluid |
| TDA | Toluene Dianiline |
| TDI | Toluene Diisocyanate |
| TETA | Triethylenetetramine |
| TMP | Trifunctional Trimethylolpropane |
| TPU | Thermoplastic Polyurethane |
| TRI | Trimer pMDI Isomers |

CHAPTER I

MASS SPECTROMETRY OF POLYURETHANES

1.1. Introduction

Polyurethane (PU) di-block copolymers are one of the most versatile polymeric materials, commonly manufactured in the form of flexible and ridged foams, thermoplastics, thermosets, coatings, adhesives, sealants, and elastomers.¹ In the 1930s, Otto Bayer and his co-workers at I.G. Farbenindustrie in Leverkusen, Germany developed PUs that were later used as a rubber alternative during World War II.² Since PU's creation, the resourcefulness of this material has increased due to its ability to undergo synthetic alteration, which enhances PUs societal footprint. PUs are commonly used for biomedical applications, construction, automotives, and textiles. In a PU network, the polymer backbone is comprised of hard and soft segments. PU hard segments include aromatic or aliphatic diisocyanates (-NCO) and soft segments consist of aliphatic polyols (-OH). Hard segments contain isocyanates, which are formed by reaction between toluene diamine (TDA) or methylene dianiline (MDA) with phosgene to produce toluene diisocyanate (TDI) or methylene diphenyl diisocyanate (MDI), respectively.³ Polyesters and polyethers are regularly used soft segment polyols which contribute to the polymer's elasticity. The urethane (carbamate) moiety is the major repeat unit formed by random and/or block polyaddition between diisocyanates and polyols,⁴ as depicted in **Figure 1.1**. PUs can also have customizable applications, where they contain other groups such as aromatic compounds, esters, ethers, and ureas.^{5,6} They can also include additives such as flame retardants, pigments, cross-linkers, fillers, blowing agents, and surfactants which can enhance certain polymer properties.⁷ By increasing the structural and architectural complexity of this copolymer system, the demands for thorough characterization methods become necessary.

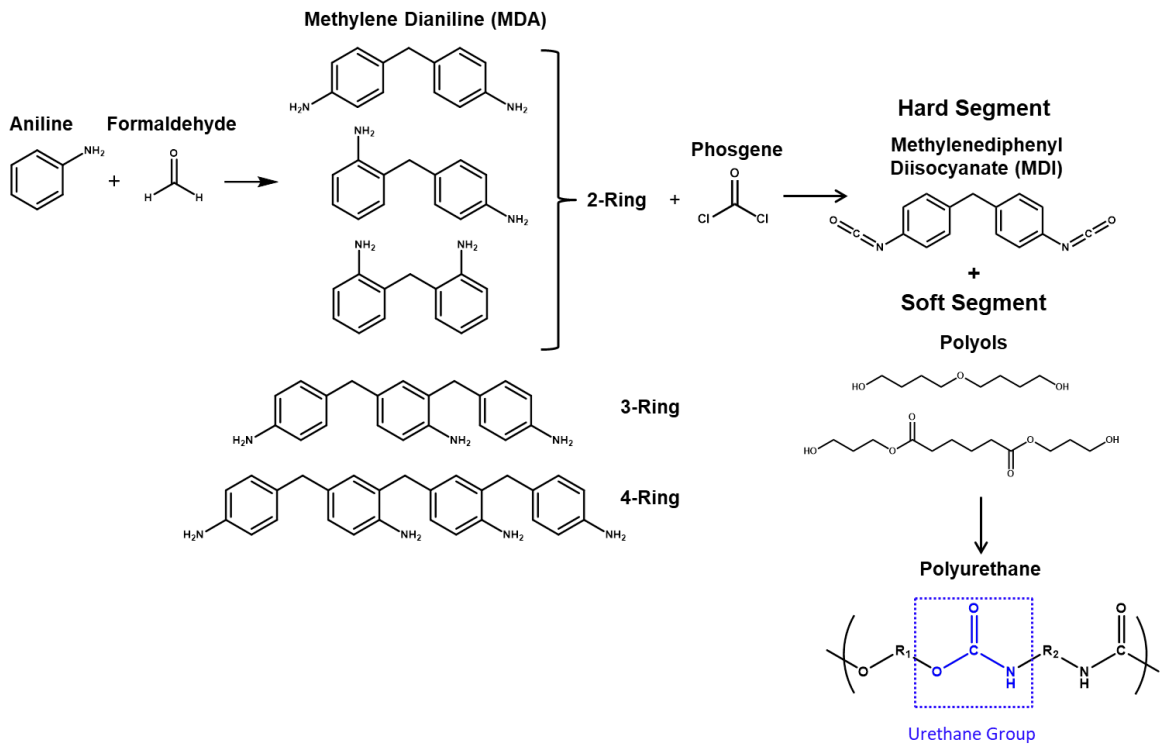


Figure 1.1. Polyurethane reaction scheme between polyol and diisocyanates to form a urethane group, highlighted in blue.

Mass spectrometry is a powerful technique for identification and characterization of many biopolymers (e.g. proteins, oligonucleotides, carbohydrates, etc.), aiding in the sequential identification and chemical analysis of ionized molecules based on their mass to charge (m/z) ratio.^{8,9} Similar to biopolymer characterization, MS based strategies have been developed to investigate synthetic polymers complexity.¹⁰ In recent years, MS has become an indispensable tool for polymer analysis and often complements characterization data obtained through classical methods such as NMR, vibrational spectroscopy, size-exclusion chromatography (SEC), and liquid chromatography (LC).¹⁰ Although these classical methods have aided in the characterization of polymer systems, advanced analytical strategies such as MS-based techniques are needed to further elucidate polymer molecular structures. MS can be used for polymeric end-group analysis, direct mass measurement, molecular weight distribution (MWD), sequential identification, and detection of impurities or additives.¹¹

Soft ionization techniques such as electrospray ionization (ESI) and matrix-assisted laser desorption/ionization (MALDI) are frequently used for polymer characterization.^{11,12} MALDI is used for direct desorption of ions, generating mostly singly charged species, which attenuates complexity observed when there are overlapping charge states.^{12,13} MALDI is relatively tolerant of contamination and salts, making high sensitivity and MS analysis accessible. ESI is typically considered a softer ionization technique compared to MALDI. For labile substances, ESI may be more appropriate for samples containing fragile end-groups, or supramolecular assemblies which are held together by noncovalent interactions. ESI is known for producing multiply charged species, therefore this ionization technique is useful for characterizing high mass species although the mass spectra may become more difficult for interpretation owing to complex spectra.^{14,15} Another way to improve the characterization of complex polymer samples is through additional dimensions of separation combined with MS, such as LC-MS. LC-MS provides chromatographic separations prior to MS analysis that can aid in separating heterogeneous samples prior to MS characterization.^{16,17}

Another multidimensional technique is tandem mass spectrometry (MS/MS), which can be performed in combination with MALDI or ESI ionization. When conducting MS/MS experiments, collision-induced dissociation (CID) fragmentation studies provide structural information about a precursor ion, a precursor's fragment ions, and fragmentation pathways at low and high activation energy.¹⁸⁻²⁰ Although, MS and MS/MS techniques are useful for structural characterization, they are still limited when characterizing isomeric or isobaric species within a heterogeneous or polydisperse sample.

Ion mobility-mass spectrometry (IM-MS) is a gas-phase separation technique, comparable to gas chromatography (GC) or LC separation. While GC and LC methods separate molecules based on their volatility or polarity differences, IM-MS separates ions based on their size, shape, and charge.^{21,22} In IM, ions are subject to many low energy collisions with a neutral buffer gas providing a drag force proportional to surface area. Thus these ions are then separated by their effective gas-phase size and shape, and can be described by their collisional cross section (CCS).^{23,24} For example, IM-MS has been used to differentiate between linear and cyclic polymer topologies.^{10,25-28} IM-MS data are often supplemented with computational studies to gain further insight about a molecule's gas-phase conformation.²⁹ These studies are generally conducted in two steps: (1) computational sampling of conformational space and (2) theoretical determination of CCS values for the generated conformations. IM-MS and computational methods are useful for characterizing PU precursors; however when it comes to fragmentation studies of complex polymers, computational methods are essential for chemical and structural interpretation.³⁰⁻³⁴

This review primarily focuses on literature pertaining to the characterization of PU polymers using MS techniques, mainly MALDI, ESI, IM-MS, and computational strategies. More specifically, this review will highlight literature that has characterized either intact synthetic PU polymers or hard and soft segments used to make PUs. As illustrated in **Figure 1.2**, intact PUs to be reviewed include flexible and ridged foams, thermoplastics, thermosets, coatings, adhesives, sealants, and elastomers. Hard segments to be reviewed include aromatic isocyanates, methylene

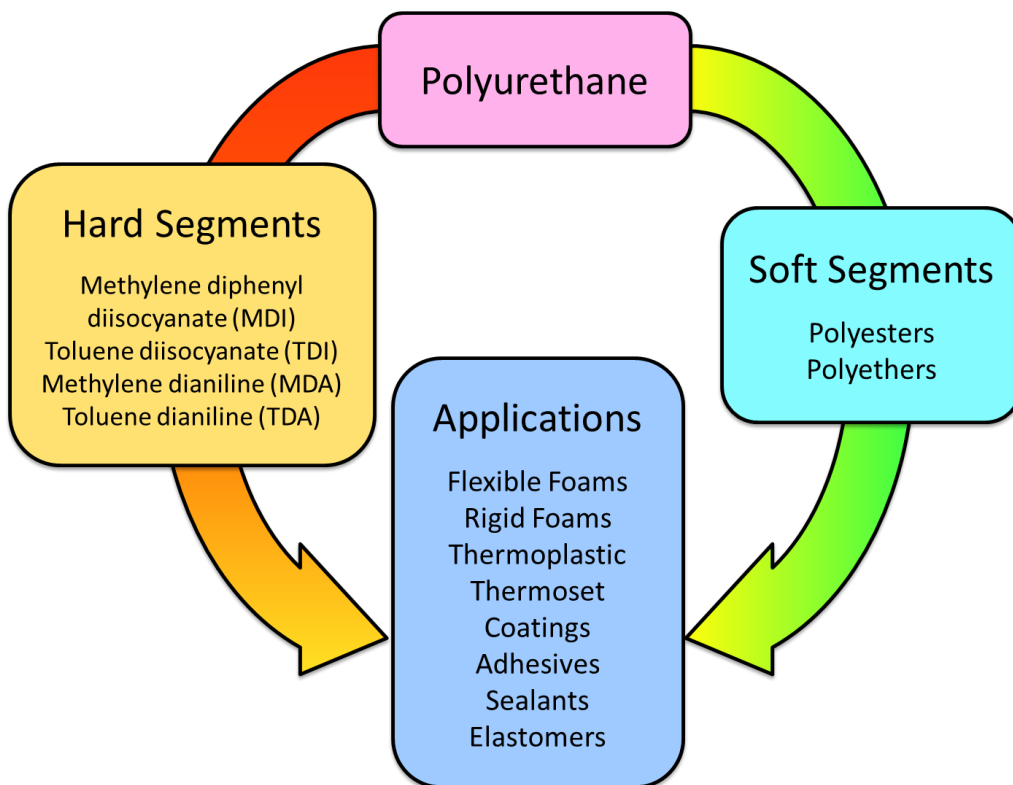


Figure 1.2. Example of important PU types and their common hard and soft segments to be reviewed.

diphenyl diisocyanate ((MDI) 4,4'-MDI, and 2,4'-MDI) and toluene diisocyanate ((TDI) 2,4'-TDI and 2,6'-TDI). Hard segment precursors, such as methylene dianiline (MDA) and toluene dianiline (TDA) will also be considered. Soft segments that will be reviewed include polyesters and polyethers. Our goal is to focus on recent literature characterizing intact PU networks and their precursors using MS. This review will emphasize PUs and their precursors that are of large scale industrial importance.

1.2. Polyurethane Hard Segment Characterization

1.2.1. Urethanes and Isocyanates

Given the urethane sequence -NH-C(O)- , isocyanates (-NCO) are essential for PU synthesis. Isocyanates can be di- or polyfunctional where two or more -NCO groups are represented per molecule. Isocyanates are electrophiles that react towards a variety of nucleophiles such as polyols (forming urethanes), amines (forming ureas), and water (producing CO_2).³ Commonly used aromatic diisocyanates are TDI and MDI. TDI exists in the form of two isomers 2,4- and 2,6-TDI.³⁵ MDI can exist as 2,4'- and 4,4'-MDI, or short chain polymeric MDI (pMDI). While still important, aliphatic diisocyanates are not as commonly used. These include hexamethylene diisocyanate (HDI), hydrogenated MDI (H12MDI), and isophorone diisocyanate (IPDI).³ In this review, aliphatic isocyanates will be mentioned in the context of a specific case study.

1.2.2. MDI and TDI

MDI and TDI are used for various applications: MDI is used to make rigid foams, insulation, and automobiles and TDI is used to make flexible PU foams, coatings, adhesives, sealants, and elastomers. MDI is formed through the reaction between aniline and formaldehyde, using hydrochloric acid as a catalyst to produce a mixture of methylenedianiline (MDA) and multimeric MDA precursors.³ When MDA is treated with phosgene, the isocyanate is formed

making pMDI and mixtures of MDI isomers. To make TDI, toluene is reacted with nitric acid to produce diaminotoluene (TDA) isomers. Upon treatment with phosgene, the TDA isomers form into TDI isomers and multimers.¹ Aromatic isocyanate derivatives such as 2,4'- and 4,4'-MDI, and 2,4- and 2,6-TDI that have been characterized using MS-based techniques will be discussed below.

For investigating the urethane bond of a hard segment, Pasch and Maujana used MALDI-MS to probe the PU urethane backbone. They highlighted how MS can be used to identify a polymer and its copolymer sequence, determine the end group functionality, determine MWD, and predict urethane fragmentation mechanisms.^{36,37} Mass et al. later investigated the urethane backbone and studied isocyanate fragment ions and their respective fragmentation pathways using CID experiments.³⁸ The hard segments characterized were multimeric MDI-TDI copolymers, and multimer MDI and TDI homopolymers. These results indicated MDI-TDI copolymer fragmentation occurred at the single bonds near the carbonyl group, making it possible to determine fragmentation pathways. **Figure 1.3** shows the MALDI-TOF mass spectrum of an MDI-TDI copolymer. The intense peaks alternating at mass increments of 148 (TDI) and 224 (MDI) Da, were observed up to masses of about 1000 m/z . The peak at 609 m/z was assigned to an oligomer with two MDI and one TDI repeat units, the peak at 682 m/z was assigned to an oligomer with one MDI and three TDI repeat units and so on.³⁸

Carr et al. also investigated MDIs using MALDI-MS.³⁹ In this study, MALDI was used to monitor pMDI and MDI isomers treated with methanol, which produced stable urethanes. Warbuton et al. then investigated ways to characterize the derivatized PU isocyanate monomeric and prepolymeric species: MDI, HDI, 2,4-TDI and 2,6-TDI⁴⁰. Warbuton discovered that immediate derivatization prevented the decomposition of the isocyanates. Therefore, derivatization enhanced the detection and structural information gained about each precursor during MS/MS studies. Derivatizing agent 1-(2-methoxyphenyl) piperazine (1,2MP) was found to stabilize the monomeric and prepolymeric isocyanate mixtures.⁴⁰ Vangronsveld and Mandel also

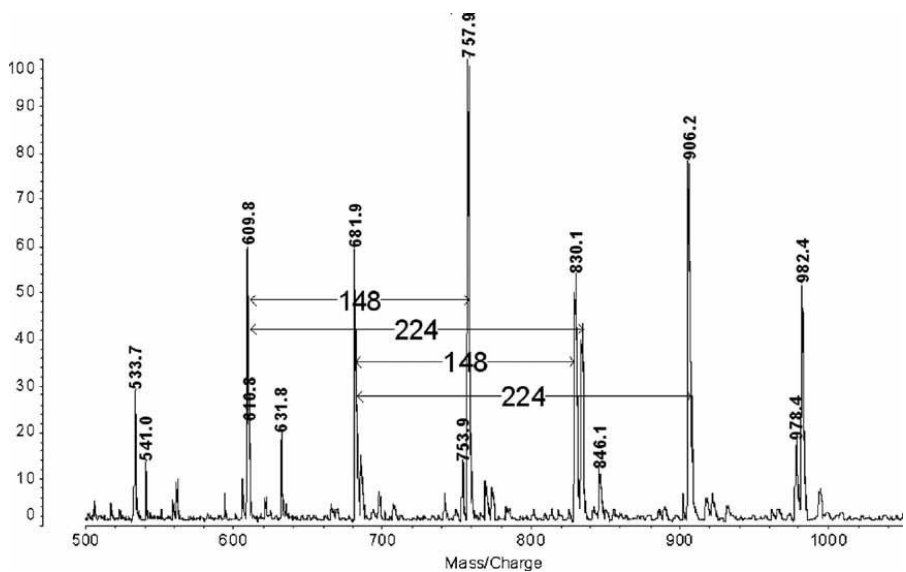


Figure 1.3. MALDI-TOF mass spectrum of the TDI-MDI sample. Mass distributions of 148 m/z and 224 m/z represent the addition of TDI and MDI respectively. Copyright 2009 Wiley. Used with permission from V. Mass, W. Schrepp, B. Von Vacano, H. Pasch, *Sequence analysis of an isocyanate oligomer by MALDI-TOF mass spectrometry using collision induced dissociation, Macromolecular Chemistry and Physics.*

investigated a LC-UV-MS/MS method to chromatographically separate, detect, and identify the derivatized isocyanate species. In **Figure 1.4**, LC was used for separations and MS/MS was used to characterize derivatized isocyanates: phenyl isocyanate (PI), 2,4'- and 4,4'-MDI, 2,4- and 2,6-TDI, trimer pMDI isomers (TRI).⁴¹ Their chromatographic method showed separation between all targeted isocyanate compounds.

1.2.3. MDA and TDA

MDA is a precursor used to synthesize MDI. Most formulations of industrial grade MDI are comprised of 2,4'-MDI and 4,4'-MDI isomers, or pMDI. This level of heterogeneity arises from structural isomers and multimeric species present within the MDA sample. In an in depth study, Hercules and coworkers structurally characterized pure MDA regioisomers and multimers using a variety of MS techniques (ESI, MALDI, MS/MS, IM-MS, and MS/MS) and interpreted the data with computational models.^{32-34,42} The MDA species investigated include 2-ring MDA: 2,2'-MDA, 2,4'-MDA, and 4,4'-MDA, 3-ring MDA, and 4-ring MDA. For each precursor species, the preferred protonation site was determined both experimentally and computationally. This helped elucidate fragmentation pathways for each MDA species during the CID experiments. IM-MS data was interpreted using computational models to provide structural information regarding each MDA precursor and their protonation sites.³²⁻³⁴ ESI and MALDI ionization techniques were both investigated in the MDA study. In ESI, the $[M+H]^+$ precursor was the only type observed for all MDA species.^{32,33} However, when each MDA species was characterized using MALDI, three unique precursors were formed: $[M+H]^+$, $[M]^+$, and $[M-H]^+$. When comparing ESI MS, MALDI MS, and MS/MS spectra from both ionization techniques, each precursor was found to have a unique fragmentation pathway.^{34,42}

Fewer studies have characterized TDA isomers in great detail. Wang et al. are among those to study TDA's degradation pathway using a biodegradable polyester urea-urethane.⁴³ In that study, the degradation of TDA from TDI-derived polyester urea-urethanes was investigated using a

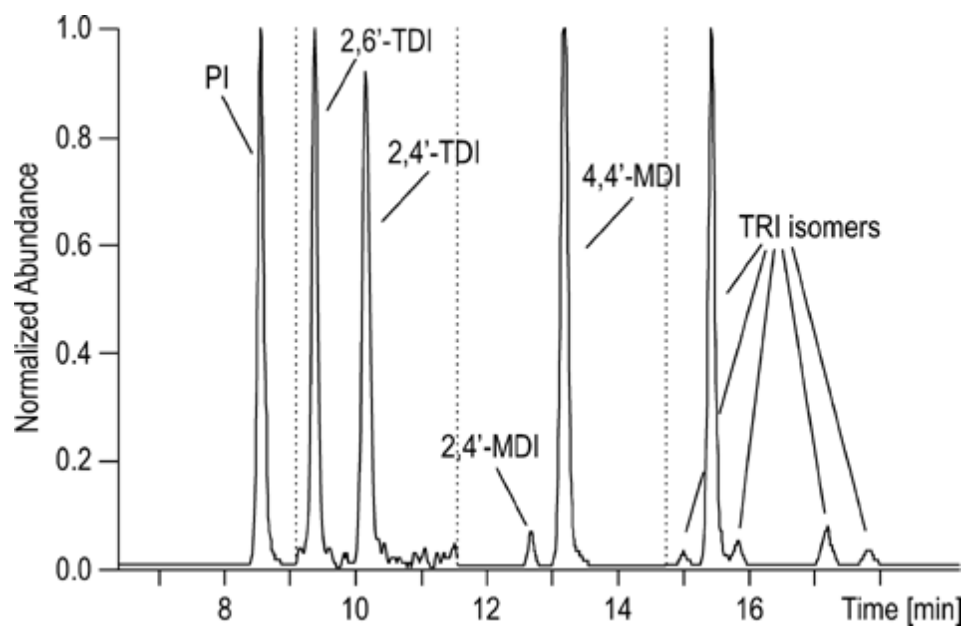


Figure 1.4. Extracted ion chromatograms for the m/z 193 fragment ion for all 1-2MP derivatives of isocyanates. LC separations showed good base peak resolution of derivatized isocyanates. Copyright 2003 Wiley. Used with permission from *E. Vangronsveld, F. Mandel, Workplace monitoring of isocyanates using ion trap liquid chromatography/tandem mass spectrometry, Rapid Communications in Mass Spectrometry.*

radioactive ^{14}C label to enhance the TDA degradation pathway. The degradation products formed were separated using high performance liquid chromatography (HPLC) and structurally characterized by MS/MS fragmentation studies.⁴³ In another study, TDA was determined to originate from unpolymerized TDI, or in the presence of water.⁴⁴ When moisture was present, TDI was found to convert back into TDA.

1.2.4. Carbodiimides and Polymeric MDI

During PU production, the formation of side products from isomeric MDI and pMDI can be of great hindrance to a polymeric material. These side products can occur at any step when making PUs and lead to viscosity buildup or the formation of solids which can alter the manufacturing process.³ One modification to making MDI is the condensation reaction between isocyanate groups, which forms carbodiimides (CDI) and reversible uretonimines. The formation of CDI and uretonimines effectively breaks up the crystallinity and reduces the polymer viscosity. Using CDI-MDI materials is of increasing interest industrially, due to its ability to form into soft high resilient elastomers.⁴⁵ In a recent study, the formation of CDI-TDI side products was characterized using MALDI TOF/TOF and CID experiments.⁴⁶ To prepare the MALDI sample, a non-conventional evaporation-grinding method was utilized. The side products observed in CDI-TDI sample were identified as urethane links, branched species, uretone imine branched CDIs, and urea allophanates. In another study, evaporation-grinding was also used to prepare a pMDI sample for MALDI ionization.⁴⁷ In this study, side products were determined to form in the presence of catalysts, iron (II), and iron (III) chlorides. In the mass spectra, small quantities of CDIs were observed which indicated the presence of viscosity buildup. This results in catalyzed side reactions between iron catalysts and CDIs causing extensive branching to occur within the sample.

1.2.5. *Hard Segment Reaction Monitoring*

Reaction monitoring between polyols and isocyanates are important to understand polymerization reaction rates. There have been several studies which have monitored the reactivity of isocyanates with primary and secondary polyol hydroxyl groups. For example, studies discern that secondary hydroxyl groups have a lower reactivity compared to primary hydroxyl groups.⁴⁸⁻⁵⁰ In other studies, tri-functional polyol reactivity was studied, which found that hydroxyl reactivity decreases as the degree of substitution increases along the polyol soft segment.^{51,52} In a study by He et al., the step growth polymerization reaction between TDI and trifunctional trimethylolpropane (TMP) was monitored at various temperatures using ESI-MS.⁵³ They determined the optimal -NCO/-OH reaction ratios, temperature conditions, and stoichiometry of each isocyanate/polyol component within the TDI-TMP product. The steric hindrance of TMP's chemical structure was observed to reduce side reactions during the step growth process, which yielded a more desirable urethane product. Ahn et al. investigated two different PU polyaddition reactions: TDI and water 54, and TDI and ethylene glycol (EG) 55, using MALDI TOF-MS. The quantitative changes in the mass composition of each polymer during the polymerization reaction were determined. Uncatalyzed reaction monitoring between 2,4'-TDI and 4,4'-MDI with 1-butanol, 1,4-butanediol (BD), and diethylene glycol monomethylether was later performed by Nagy et al. using an HPLC-ESI-MS method 56. Nagy monitored the urethane reaction rate at different temperatures, to determine the rate constants for each alcohol and diisocyanate. First-order rate constants were determined between the polyol-MDI reaction, (polypropylene glycol (PPG), polytetrahydrofuran (pTHF), poly(3-caprolactone)-diol (PCLD), and polypropylene glycol glycerol triether (PPG-GL)) 57. Beldi et al. later monitored the changes within a polymer's topology, the formation of linear and cyclic PU species using MALDI-MS 58. Krol and Pilch-Pitera used computational simulations with MS strategies to determine the step-by-step polyaddition reaction between 2,4- and 2,6-TDI with BD, polyethers, and polyesters 59. Computational modeling helped to interpret proposed structures

and provided an understanding of reaction compositions formed during different polymerization stages.

1.3. Polyurethane Soft Segment Characterization

1.3.1. Polyols

There are two main types of polyurethane polyols: polyethers and polyesters. Both classes of polyols have elastic properties which relate to their unique range of industrial importance. Polyols used for PU synthesis typically consist of two or more -OH groups. Polyether urethanes are considered to be a harder urethane, having superior dynamic properties. Polyester urethanes are typically softer and known for their tensile strength. Types of polyether polyols used in PU production include polypropylene oxide (PPO) also called PPG, polytetramethylene oxide (PTMO) also known as polytetrahydrofuran (pTHF), and polyethylene glycol (PEG).³ Types of polyester polyols can be made from adipic acid and EGs (polyethylene adipate), or from butanediols and adipic acid known as polybutylene adipate (PBA). Additionally, copolyesters are often prepared from a mixture of glycols, adipic acid, and anhydrides.⁶⁰

1.3.2. Polyethers

There are many studies which have characterized polyethers using MS-based techniques,⁶¹ however a few studies will be highlighted in this section. Chattopadhyay et al. structurally investigated PPG and IPDI based PU prepolymers using MALDI-MS.⁶² In this study, they monitored the reaction between PPG and IPDI at different time intervals, to investigate mono-urethane transition into the di-urethane species. In another study led by Mehl et al., the degradation reaction between PU polyether (pTHF) and polyester (PBA) were also monitored by MALDI-MS.⁵ To selectively degrade pTHF they used ethanolamine, and to degrade PBA they used phenyl isocyanate due to the high reactivity of the ester. In this study, SEC was coupled to

MALDI to enhance accurate MW determination of each degraded ether-urethane and ester-urethane species.

IM is an emerging tool for separation and identification of synthetic polymers (linear, cyclic, star-shaped, etc.). Recently, IM-MS has been used to investigate polydisperse samples, allowing for the identification and characterization of unique CCS trends, charge-dependent conformations, and different polymer topology.^{63,64} IM-MS has been used to characterize the experimental and theoretical conformation of multicharged linear-chain PEGs,⁶⁵⁻⁶⁸ polylactic acid (PLA),⁶⁹ polyethylene terephthalate (PET),⁷⁰ PPG,⁷¹ polyethylene oxide (PEO),⁷² and polycaprolactone (PCL).^{72,73} Sodium cationized PLA was investigated using IM-MS to experimentally determine the three-dimensional structure of the multiply charged PLA adducts. Experimental and theoretical observations were recorded to investigate how the polymer size and number of charged adducts effect the folding of the PLA through cation coordination.⁶⁹ Duez et al. used PLA and PEG polymers as reference calibrants for a home-made traveling wave IM-MS drift-tube. These polyethers were good calibrants due to the polymer ions covering a large mass range and a large CCS window.⁷⁴ Previous studies have shown low-energy CID of PEG ionized with alkali metal cations to yield small fragment ions from hydrogen-rearrangement reactions. At high CID energies, 1,4-H₂ elimination can be observed producing two types of unsaturated fragment ions along with a homolytic cleavage reaction at both ends of the polymer.⁷⁵ Hilton et al. used IM-MS and IM-MS/MS to separate and differentiate between polyether oligomers with the same nominal molecular weights.⁷⁶ For instance, isobaric mixtures of PEGs with the same nominal m/z ratio were structurally characterized and separated using IM-MS/MS. Larriba et al. in **Figure 1.5**, characterized the gas-phase structure of coulombically stretched PEG ions.⁶⁷ Higher charge state PEG ions were observed to form a “beads on a string” motif. In this study, structural transitions for the ionized singly charged PEG species were interpreted through molecular dynamic simulations. Cody and Fouquet, in a recent study, used paper spray ionization

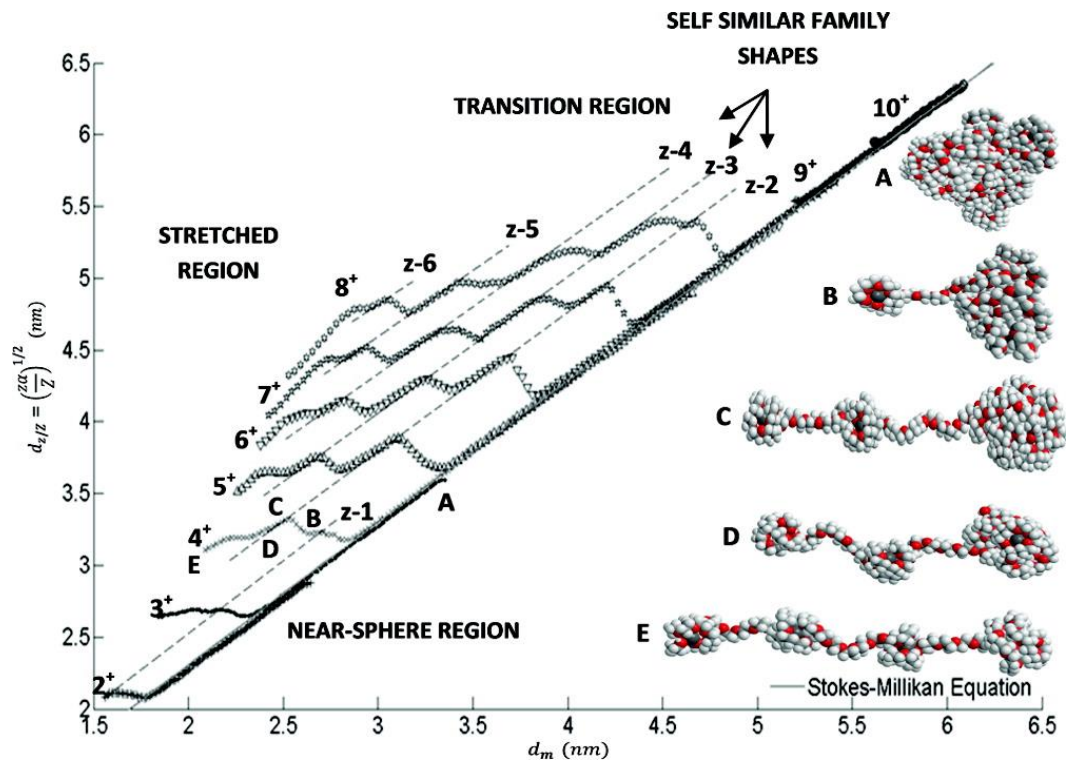


Figure 1.5. Representation of transitional region of sphere equivalent diameters based on Z/z and m , respectively. MD simulations comparable to experimental values are included for several lengths of $z = 4$ ions. Not all the data points correspond to exact oligomer masses. Charge state trends and proposed structural molecular dynamic simulations are represented (A-E). Reprinted (adapted) with permission from C. Larriba, J. Fernandez De La Mora, *The gas phase structure of coulombically stretched polyethylene glycol ions*, *J. Phys. Chem. B.* 116 (2011) 593–598. Copyright 2012 American Chemical Society.

MALDI/TOF system to characterize 13 block and 2 random ethylene oxide and PPO copolymers and homopolymers using Kendrick mass defect.⁷⁷ The Kendrick mass defect plots were used to estimate the percentage of the ethylene oxide and PPO in the copolymer materials. Girod et al. used MS/MS to characterize doubly charged PEO oligomers formed using ESI.⁷⁸ Similarly, Tintaru et al. experimentally and theoretically studied PEO-poly(amidoamine) polymer using H⁺ and Li⁺ cations.⁷⁹ IM-MS and MS/MS were employed to elucidate unique charge state trends (+2 and +4) of the adducted species. The experimental findings were coupled to molecular dynamics simulations to investigate conformational changes within different charge states. Other PEG studies probed low energy CID pathways using an assortment of monovalent cations (Li, Na, K, Rb, Cs)⁸⁰⁻⁸² and transition metal cations (Ag).⁸³ In addition to gas-phase PEG folding, Ude et al. studied charge-induced unfolding of PEG species.⁶⁶ Kokudo et al. performed IM-MS on PEGs as model polymers to obtain the dielectric constant of their doubly charged species.⁸⁴ Proposed mechanistic pathways were used to determine the fragmentation reactions of radical cationic species.

Over the years, there have been environmental concerns with producing polyethers for PU synthesis from petroleum sources. Therefore, researchers have investigated bio-renewable feedstocks to be used in place of petroleum based polyols. Li et al. performed LC-ESI-MS and MS/MS fragmentation experiments to detail an approach to the characterization of novel bio renewable polyols 85.

1.3.3. Polyesters

Polyesters, known as polycondensation polymers, can be used for a variety of applications. In a study by Williams et al., MALDI-MS was used to characterize a series of aliphatic polyesters and their derivatives.⁸⁶ The oligomeric peaks observed in the MS allowed for determination of each polymer repeat unit and the presence of cyclic species. Both the M_n and M_w values were determined by MS, and compared to consecutive NMR and GPC findings. GPC MW estimations

were found to be larger than those determined by MALDI. In another study by Williams et al., MALDI-MS was used to study discrete mass polybutylene glutarate (PBG) oligomers having 8, 16, 32, and 64 degrees of polymerization.⁸⁷ These PBG derivatives were used to optimize MALDI and GPC analysis of PU-PBA species due to structural similarities between PBG and PBA. In this study, they investigated the effect of the MALDI matrix, laser intensity, and detector saturation. Rizzarelli et al. later probed the fragmentation pathways of four PBA isomers at relatively high collision energies using MALDI-TOF/TOF CID.⁸⁸ High collision energies were found not as useful as low collision energies for studying native chemical alterations. Gies et al. later demonstrated a method for characterizing PBA species at low fragmentation energies using MALDI-TOF/TOF CID.⁸⁹ They were able to identify PBA fragment ions and unexpected side products from a complex mixture of melt polymerized PBA. Low energy fragmentation pathways were interpreted by computational models to verify the structure of the fragment ions. PBA oligomers were observed to undergo a number of low energy degradation pathways such as 1,5 H-shift (preferred), 1,3 H-shift, remote hydrogen abstraction, and multiple combinations of these reactions.

To study polyester reaction kinetics, Pretorius et al. developed a model system to study the reaction between phthalic acid and PEG based polyesters.⁹⁰ They monitored the reaction under different conditions to investigate the stages of polyesterification, MW, chemical composition, and end group analysis of these synthesized species using HPLC separations coupled to MALDI-TOFMS analysis. In related studies, Pretorius et al. investigated the same phthalic acid and PEG based polyesters using a combination of SEC, supercritical fluid chromatography (SFC), ESI-MS⁹¹ and MALDI-MS.⁹² The polyester samples in these studies were fractionated by SEC, analyzed by SFC (to determine degree of polymerization), then characterized by MS to determine the presence of linear or cyclic species. For a polyvinyl acetate (PVA) system, Gigurere and Mayer modeled the fragmentation pathways of ionized PVA using

ESI-MS and MS/MS techniques to determine mechanistic dissociation reactions that could occur when PVA is used for PU adhesives or sealants in the textile industry.⁹³

Polyester polyols are typically formed from diacids and glycols. Usually polyester polyols are more viscous, as well as more expensive, compared to polyether polyols. Biodegradable and biocompatible urethane-macromolecules are a growing field even within PU polyester production. The biodegradation of PLA urethane copolymers are investigated to determine the rate of biodegradation as PLA content increases.⁹⁴ Borda et al. explored novel methods towards synthesizing biodegradable thermoplastic multiblock copolymers and characterizing this copolymer system using MALDI-TOFMS. In one study, linear-chain PUs were synthesized using PLA and 4,4'-MDI and TDI.⁹⁵ In another study, Borda et al. synthesized PLA, PCL (poly(ϵ -caprolactone)), and PCL-PA copolymers using TDI as chain extender and PEG as the intrinsic plasticizer.⁹⁶ They determined the chemical structure of each biodegradable PU polymer and the relative Mn using MALDI-TOFMS. In a study by Tang, telechelic hydroxyl-terminated polyesters were synthesized using biodegradable monomers in the MW range of 700 – 1,300 Da.⁹⁷ Other biodegradable PU routes have been explored by Baez et al.,⁹⁸ where the reaction between PCL diols was monitored using MALDI-MS to determine formation of the ring opening ester-urethanes-ureas. Osaka et al. showed a detailed ESI and MALDI method for characterizing linear and cyclic PLAs and their solvolysis products.⁹⁹ Polyester urea-urethanes were synthesized with ¹⁴C labeled TDI and ¹⁴C labeled ethylene diamine chain extender to study cholesterol esterase.⁴³ The PU degradation products were characterized to determine the presence of unreacted TDI.

1.4. Polyurethane Material Characterization

1.4.1. Diisocyanate and Polyol Characterization

PU complexity arises from the addition reaction between isomeric diisocyanates and heterogeneous mixtures of varying polyol lengths. These synthetic complications lead to the

formation of random, alternating, block, and graft copolymers. PU properties are greatly influenced by their structure, monomer functionality, hydroxyl group reactivity, polymerization temperature, and -NCO/-OH reaction ratio. Addressing PU complexity requires advanced analytical techniques such as MS to characterize the complexity of PU intact materials.^{100,101}

The reaction between diisocyanates and polyols (polyesters and polyethers) is a key process for making various PU products. Nagy et al. used HPLC-MS to determine reaction kinetics between diisocyanates (MDI and 2,4-TDI) and polyols: 1-butanol, 1,4-butanediol (BD), and diethylene glycol monomethylether (DEGME).⁵⁶ These results indicated that the first isocyanate group on MDI reacted 1.5 times faster with the polyols compared to the second isocyanate, however the para isocyanate on 2,4-TDI was determined to react with the polyols faster than the first isocyanate on MDI. Both MDI and 2,4-TDI isocyanates reacted in a similar manner. Ferrerira et al. also used HPLC-UV and HPLC-ESI-MS/MS techniques to extensively characterize free monomeric MDI found in PU foams.¹⁰² Ferrerira outlined the use of a new isocyanate derivatizing agent, N-benzylmethylamine (NBMA), which enhanced monomeric MDI solubility in the solvents routinely used for HPLC.

Diisocyanates and polyols are also known to react in the presence or absence of a catalyst; optimal reaction conditions have been previously studied.¹⁰³⁻¹⁰⁵ However, Nagy et al. extensively studied the reaction between MDI and several polyols: pTHF, PCLD and PPG glycerol triether (PPG_GL) to determine intermediates, reaction products, and the reactivity of the polyols hydroxyl groups.⁵⁷ When, monitoring MDI and PPG_GL reaction using MALDI-MS, the formation of B_n, C_n, and D_n series appear, as shown in **Figure 1.6**. Series A_n in **Figure 1.6** represents the start of the reaction and series D_n represents the distribution at the end point of the reaction. As the reaction progresses, the appearance of additional series labelled B_n and C_n are noted, which correspond to mass shifts of 282 Da indicating the addition of MDI to the PPG_GL hydroxyl groups. In this study, rate constants of the forming intermediates and final products were determined. MALDI-MS was also useful for monitoring the formation of cyclics and other

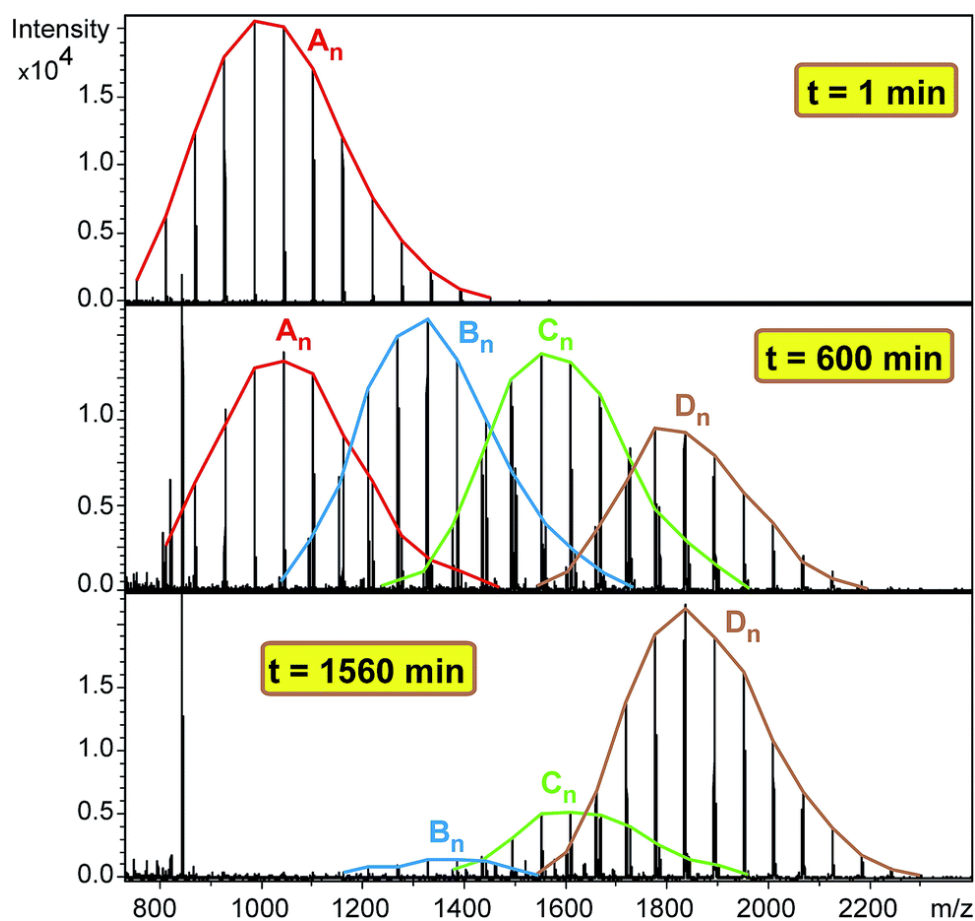


Figure 1.6. MALDI-TOF MS spectra of the quenched reaction mixture obtained in the reaction of PPG_GL with MDI at 1, 600 and 1560 minutes. Experimental conditions: $[\text{MDI}]_0 = 0.32 \text{ M}$, $[\text{PPG_GL}]_0 = 0.01 \text{ M}$ and $T = 80 \text{ }^\circ\text{C}$. By monitoring the MDI and PPG_GL reaction using MALDI-MS, the formation of B_n , C_n , and D_n series appeared, series A_n represents the start of the reaction. Reprinted (adapted) with permission from *T. Nagy, B. Antal, A. Dekany-Adamoczky, J. Karger-Kocsis, M. Zsuga, S. Kéki, Uncatalyzed reactions of 4,4'-diphenylmethane-diisocyanate with polymer polyols as revealed by matrix-assisted laser desorption/ionization mass spectrometry, RSC Adv. 6 (2016) 47023–47032. Copyright 2016 Journal of Physics and Chemistry.*

side products formed during the reaction.⁵⁸ In a study led by Gies et al., a combination of MALDI, CID, and IM-MS experiments was used to study a polyester-based PU ($M_n \sim 13,000$ by GPC) prepared by melt polymerization; reactants were PBA and MDI, with BD as an extender.¹⁰⁶ Fragmentation studies were performed at relatively low collision energies to model pyrolysis reactions. Bond energy calculations were used to help to elucidate possible fragmentation pathways. The major species observed by MALDI were cyclic polyesters and PUs, linear polyesters (diol and acid terminated) and linear polyurethanes up to $n \sim 20$. PUs containing up to 10 hard blocks were observed. CID for linear PUs identified two major fragmentation pathways, 1,3 and 1,5 H-shift, the latter involving carbonyls both in the urethane group and in the polyester chain. Fragmentation of cyclics is a two-step process: (1) initial ring opening and (2) subsequent fragmentation. Both steps primarily involve 1,3 and 1,5 H-shift. IM-MS studies were performed to show the utility of this technique when characterizing complex polymeric mixtures. For example, it was shown that PU hard blocks capable of forming H-bonding were found to have a shorter drift times than hard blocks not capable of H-bonding.¹⁰⁶

1.4.2.1. Flexible and Rigid Foams: Biodegradable Importance

PU foams are classified as flexible or rigid foams depending on their flexibility and density. PU foams are complex engineered materials which can have customizable temperature or humidity control and visco-elastic behavior. The flexibility, morphology, and microstructure of PU foams are based on the degree of cross-linking and the -NCO/-OH ratio.^{3,107} Flexible PU foams are known for their application as cushion materials, and rigid foams are known for their thermal stability and flame resistant properties. These foams are commonly made with PPO, however renewable alternatives for petrochemical polymer materials is a growing field.¹⁰⁸ Bio-based polyols, such as natural oils chemically modified to contain hydroxyl groups, are a new technique for integrating bio-based polyols in PU foam materials.¹⁰⁹ For example, Basso et al. studied renewable polyol alternatives in flexible-elastic copolymerized PU tannin foams using

MALDI-MS.¹¹⁰ The fatty amines were reacted with pMDI and tannins to make PU foams with highly flexible and elastic properties. MS based techniques were used to characterize the chemical and sequential arrangement of the amines, isocyanates, and tannins integrated within the PU foam matrix. Another method for monitoring the coreaction between amines, isocyanates, and tannins was to monitor the MW_{av} . Gaussian distributions of the coreacted species obtained by MALDI. The Gaussian distributions, can help determine which coreaction and reaction conditions are preferred (amine-pMDI or tannin-pMDI), to form the urethane bridge and detect unreacted starting material.¹¹¹

1.4.2.2. Flexible Foams

When characterizing intact flexible foams, selective extraction processes are needed to investigate the chemical composition. During foaming, hard segments undergo chain-growth, whereas in hydrolysis a step-growth process occurs which contributes to the formation of cyclic species.¹⁰⁷ MALDI-MS is a common technique for PU foam reaction monitoring, hard segment distribution characterization, and detection of cyclic or hydrolysis products. In one study, the hydrolysis products of viscoelastic and conventional flexible foams were characterized using MALDI-MS.¹¹² MALDI characterization revealed the presence of cyclic species, hard segment chains with urea repeat units, and PPO based polyols.¹¹³ The experimental hard segment length distributions were compared to theoretical Monte Carlo simulations. The simulations in this study agreed with the number-average degree of polymerization experimentally.¹¹² In a study by Yontz et al., MALDI-MS was also used to investigate water-blown PU foams by monitoring the addition of water in the poly(urea-urethane) formulation.¹¹⁴ The water-blown PU foams were prepared with different hard segment lengths and at various temperatures. By using MS, they were able to determine the unique features related to each foams unique sample preparation method, the number of hard segment repeat units, and the formation of side products.

Chromatographic techniques integrated with MS, such as LC-MS can increase the level of dimensional analysis for the characterization of aromatic amines (TDA/MDA). Marand, was among the first to develop an LC-MS method for foam hydrolysis extracts containing TDI/TDA compounds and other oligomeric species.¹¹³ Marand tested extraction solvents to observe hydrolysis products. He found that organic solutions altered the physical properties of the foams and alcohol solutions caused free isocyanates to react and form urethane side products. Mild acid solutions were found to stabilize extracted aromatic amines from intact flexible foams.¹¹³ More recently, Johnson et al. compared Marand's LC-MS method to their hydrophilic interaction liquid chromatography (HILIC-MS) and MS/MS technique. In Johnson's study, they focused on developing a separation method for HILIC-MS to distinguish TDA and MDA aromatic amines found in foam extracts. The free diamines required a derivatizing agent to prevent oxidation and both HILIC-MS/MS and Marand's LC-MS method showed agreement for free amines detection in PU foams.⁶

1.4.2.3. Rigid Foams

Rigid PU foams have not been extensively characterized using MS-based techniques. As such, there are only a few studies characterizing bio-based polyols that can be used to make rigid PU foams. In a recent study, MALDI-MS was used to monitor the cross linking between highly functional polyols that underwent epoxy ring opening reactions with glycerols to make a bio-based polyester.¹⁰⁹ In a related study, MALDI-MS was used to characterize unique resins derived from natural products (polyflavonoid tannins-furfuryl alcohols). The urethane formation between flavonoid monomers, glyoxals, and isocyanate was monitored to determine the functionality of this PU natural product starting material.¹¹¹

1.4.3. *Thermoplastic Polyurethanes*

Thermoplastic PUs (TPUs) have numerous applications due to their diverse physical properties and processability. TPUs are known to be flexible, elastic, have resistance to impact, abrasion, weather, and become melt-processable. TPU materials are suitable for applications in the automotive, clothing, sports equipment, furniture, biomedical, and construction industries.¹¹⁵ Conventionally, TPUs are synthesized from polymeric isocyanates and polyols with or without chain extenders. Common polyols used in TPUs include polyesters and polyethers; however specialty polyols such as polycarbonate, polysiloxane and polyolefin diols can also be used.¹¹⁶ Recently, non-conventional PUs such as non-isocyanate polyurethanes (NIPUs) have been developed. This novel type of PU can be prepared by ring opening reactions between bis-cyclic carbonates and diamines which enable the replacement of hazardous phosgene and isocyanates which are used in the conventional PU synthesis.^{117,118} NIPUs can also be made through a fully bio- and CO₂-sourced synthesis. In a recent study, Poussard monitored the formation of NIPUs under supercritical conditions using ESI-MS.¹¹⁹ In another study, biodegradable TPU synthesis was monitored using MALDI-MS between TDI, PEG, and polylactic acid caprolactone to make a type of TPU multiblock polymer.⁹⁶ Oleochemicals are a type of vegetable oil that can be used as a TPU building block. To model the use of oleochemical, oleic acid and undecylenic acid derivatives were used to synthesize PUs through a polycondensation reaction. The formation of linear TPUs was monitored using MS-based techniques and further characterized to test for thermal stability.¹²⁰ Due to environmental concerns, TPU chemical interaction with water is of interest. To study the water diffusion rate in TPUs, LC-MS was used to monitor water diffusion, and MS strategies can help elucidate structural cross-linking within the polymer back-bone.¹²¹

Due to the increasing application for TPU materials, studying decomposition reactions with respect to time and temperature can enhance synthetic strategies allowing for tailored polymeric design to match desired degradation patterns. One method used to study decomposition reactions and reaction products is pyrolysis.³ Pyrolyzate products are formed during the

decomposition process and can help to determine decomposition mechanisms and covalent/noncovalent chemical bond arrangement throughout a material. Lattimer was among the first to study TPU pyrolysis using MALDI-MS, to determine the structural properties pertaining to TPU and the pyrolysis conditions. Pyrolysis MS (Py-MS) is a method which heats PUs in a solid probe.¹²² This method allows for slow pyrolysis to be monitored with respect to time or temperature, forming various pyrolyzate products. Py-MS has shown that segmented TPUs decompose at different stages. Ravey and Pearce previously studied the decomposition of TDI and complex polyether (glycerol, PPO, and polypropylene ethylene oxide) based PU foams, to better understand decomposition reactions.¹²³ Later, Lattimer et al. characterized segmented PU pyrolyzate products (MDI, BD, and PBA) using MALDI-MS. In their MALDI studies, higher mass pyrolyzate products were detected (800 – 10,000 Da species), elucidating pyrolysis mechanisms.¹²⁴ More generally, MALDI-MS indicates that the degradation products followed two primary pathways: (1) dissociation of the urethane linkage to form isocyanato and hydroxyl end groups and (2) an ester exchange where cyclic pyrolyzate oligomers were produced.^{122,124,125} In 2002, Lattimer further characterized PEG pyrolysis products at different temperatures using MALDI-MS. At low temperatures, pyrolyzate products were detected to undergo C-O bond cleavage, forming hydroxyl and ethyl ether end groups. When temperatures were increased, methyl ether and vinyl ether end groups became more abundant.¹²⁶ They also studied thermal decomposition of pTHF pyrolyzates at low temperatures.¹²⁷ Although MALDI-MS has been widely used to analyze pyrolyzate products from PPG, PEG, pTHF, PBA, and bisphenol A (BPA) polycarbonate, the disadvantage of this technique lies within the insolubility of some pyrolyzates which increase characterization complications.^{126,128}

1.4.4. Thermoset Polyurethanes

Thermoset PUs are materials that undergo a curing chemical reaction and transform from a liquid to a solid. During the reaction, the PU forms a cross-linked network causing the material

to solidify, which is irreversible. For example, shape memory foam is a type of thermoset PU that is manufactured for its desirable physical properties: amorphous, high crosslinking, and ultra-low density. Weems et al. performed an in-depth study on the degradation of porous shape memory foams. LC-MS techniques were used for absolute quantification and determination of degradation rate in biological materials.¹²⁹ In another study, Dopico-García aimed to develop a robust HPLC-UV-MS method for separation of curing agent polyamines (isophorone diamine (IPDA), TCD-diamine, and triethylenetetramine (TETA)). The chromatographic separations were coupled to UV detection of the aromatic compounds, and MS strategies aided in the determination of the exact chemical structures of the curing agents.¹³⁰

1.4.5. Polyurethane Coatings

PU coatings have many consumer uses such as: inner surface coatings for metallic food or beverage containers, steel hydraulic structures to prevent corrosion, and automotive clear coats, primers, and sealers.^{3,131} The most common coatings are epoxy-resins which are based on BPA. Due to safety concerns related to BPA exposure, alternative coatings have been sought.¹³² Polyester and thermoset polyester-polyurethane (PEPU) coatings are an alternative to epoxy-based resins for metallic food containers. In PEPU coatings, polyisocyanates are used to facilitate the cross-linking of polymer networks. The high reactivity of the isocyanate moiety results in urethane linkages upon curing. Therefore the three-dimensional polymer network can reduce small molecule migration. Many studies have explored a variety of analytical MS-based techniques (ESI-MS, LC-MS, and MS/MS) to monitor small molecule migration in PU coated food containers. Driffield et al. released an LC-MS/MS method for testing residual IPDI trimers in experimental formulations of thermoset PEPU coatings in food containers. This method involved extraction of IPDI trimers from the coated panels, and derivatization of the extracted IPDI trimer with dibutylamine (DBA).¹³³ The curing kinetics of the PEPU coating and unreactive analytes were monitored using chromatography based MS techniques. Bradley et al. identified

small molecule contaminants related to starting materials used in the formulation of coatings, reaction byproducts, and degradation products resulting from prolonged storage of the can. They used a variety of analytical techniques to detect volatile (GC-MS) and non-volatile substances (LC-MS).^{134,135}

Recently, Omer et al. developed a method to predict non-intentionally added substances (NIAS) migrating from PEPU coatings.¹³⁶ They constructed a database which predicted a combination of known monomers based on their exact monoisotopic masses. They used a global untargeted approach, coupling LC to a high resolution MS (LC-HRMS) to elucidate lacquer extract fingerprints. Both positive and negative ionization modes were tested where more intense signals related to NIAS were found in the positive mode compared to the negative mode, and the findings were consistent with other research groups.^{135,137,138} Omer's confidence in peak identification was based on fragmentation patterns and chromatographic behavior of the lacquer samples tested.¹³⁶

1.4.6. Polyurethane Adhesives

PU adhesives are known for their high performance and range of applications. PU adhesives have been characterized using MS-based techniques, for example, adhesive tape for immobilized inorganic materials¹³⁹ and wood adhesives for particleboard.¹⁴⁰ PU adhesives are also used for preparing multilayered laminates to coat the inner lining of food containers. When the adhesive is not properly cured, the polymerization reaction can yield unpolymerized aromatic isocyanates, causing primary aromatic amines (PAA) when reacted with water. There are several methods to isolate and chemically analyze the degradation products of PAAs from PU adhesives, for example TDA isomers can undergo derivatization with pentafluoropropionic anhydride (PFPA) prior to LC-MS characterization.¹⁴⁰ Marand et al. were among the first to implement this method of derivatization, showing the sensitivity for aromatic amines increased in TDI-based PU foams when derivatized prior to LC-MS analysis.¹¹³

Adhesives are used to bond films together to form a laminate, for food storage. Lawson et al. investigated the migrants from a range of PU adhesives using MALDI-MS.¹⁴¹ Due to rising concern for PAAs in manufactured plastic laminates; these PU adhesives were tested to determine if the adhesive was fully cured prior to use. Mortensen et al. developed an LC-MS/MS method to determine traces of 20 PAAs associated with PU adhesives.¹⁴² In another study, Aznar et al. quantitatively determined 22 PAAs using cation-exchange solid-phase extraction and LC-MS methods for characterization.¹⁴³ Due to the relatively low detection limit of LC-MS, this method was advantageous for PAA detection in PU materials. Pezo et al. used a Q-TOFMS method for the identification and pattern recognition of PAAs in PU food packaging.¹⁴⁴ In a recent study, a non-targeted MS approach was used for the characterization of unexpected chemicals and NIAS found in food packaging materials.¹⁴⁵ They identified 26 potential migrants from the two packaging materials studied. Cyclic ester oligomers were found to migrate from the multilayer high barrier food contact material. Zhang et al. later completed an extensive study, performing a migration test on 537 commercial and/or developmental laminate samples.¹⁴⁶ MS techniques such as electron ionization (EI-MS), chemical ionization (CI-MS), and LC-MS were used to identify 56 short-chain cyclic oligoesters at both high and low concentration levels within the packaging material.

1.4.7. *Encoded Polyurethanes*

A new generation of high precision polymers is promising for a wide range of applications due to the synthetic ability to control radical polymerizations, stepwise syntheses, molecular structure and morphology. Development of polymeric material containing discrete encoded information and then recovering information by an MS sequencing technique is a growing field of research.¹⁴⁷⁻¹⁴⁹ Applying the encoding technique to PU materials will likely be increasingly utilized for the identification of counterfeit goods. In a recent study by Gunay et al., uniform sequence-coded PUs were synthesized by a chemoselective multistep-growth process

and sequenced using negative-mode MS/MS. The sequence-coded PUs are easily sequenced by MS due to their carboxylic acid deprotonation and predictable C-O carbamate fragmentation pathway.¹⁵⁰ In a complementary study, sequence-coded PUs, that contain digitally encoded oligourethanes with two monomers defined by arbitrarily binary units, 0 and 1 bits, can be used as molecular barcodes and blended in low amounts with other polymeric materials. These sequence-coded PUs were tested as anticounterfeiting tags for the labeling of methacrylate-based intraocular implants and were determined to be viable coding and labeling methods due to the ease of MS/MS identification by sequencing.¹⁵¹

1.5. Other MS-Based Techniques for PU Characterization

PUs are produced through a wide range of diisocyanates and polyols to make flexible and rigid foams, TPUs, thermosets, coatings, adhesives, sealants, elastomers, and many commercial products. However, in this review mainly soft ionization sources such as ESI and MALDI have been reviewed. There are many useful MS ionization sources that are appropriate in PU characterization. Ion sources specific for liquid sample introduction include atmospheric pressure chemical ionization (APCI), atmospheric pressure photoionization (APPI), desorption electrospray ionization (DESI), and electrosonic spray ionization (ESSI).¹⁵²⁻¹⁵⁸ For solid analysis, atmospheric solid analysis probe (ASAP) is used, and for volatile samples GC is useful. A few studies have used alternative ionization sources to characterize PU samples. DESI and ESSI have previously been proven to provide accurate average MW and MWD of industrial polymers, both as solids and in solution.¹⁵⁶ In a study by Bonnaire et al., PU films were analyzed on two instrumentation platforms: DESI-MS and ESI-MS. DESI-MS was found to generate mass spectral profiles of irradiated PU films with no sample preparation; when compared to conventional ESI-MS methods, the same species were observed confirming DESI-MS as a valid technique for PU film characterization.¹⁵⁴ Lebeau et al. used ASAP-MS applications for the characterization of PU copolymer material. ASAP-MS was found to require no sample pretreatment. ASAP-MS was

able to differentiate between chemical structures within the PU, polyester and polyether monomers. ASAP-MS was easy for direct analysis of crude polymer samples.¹⁵⁵

1.6. Concluding Remarks

PUs are versatile materials contributing to a wide variety of societal and consumer applications. In this study, MS-based techniques used to characterize PU hard and soft segments, precursors, and intact PU materials have been extensively reviewed. The literature reviewed highlights a variety of techniques such as soft ionization sources ESI and MALDI, IM-MS, MS/MS, and computational methods for data interpretation. Additionally, this review highlights areas of PU research that are in need of further MS-based characterization studies.

1.7. Acknowledgements

This work was funded and supported in part by the resources of the Center for Innovative Technology (CIT) at Vanderbilt University. Financial support for this research was provided by the National Institutes of Health (NIH NIGMS R01GM092218 and NIH NCI 1R03CA222452-01).

1.8. References

1. Szycher, M. Szycher's Handbook of Polyurethanes; CRC press, 1999.
2. Bayer, O. Das Di-Isocyanat-Poluadditionsverfahren (Polyurethane). *Angew. Chemie* 1947, 59 (9), 257–272.
3. Oertel, G. Polyurethane Handbook; Carl Hanser Verlag, 1985.
4. Hepburn, C. Polyurethane Elastomers; Springer Science & Business Media, 2012.
5. Mehl, J. T.; Murgasova, R.; Dong, X.; Hercules, D. M.; Neftzger, H. Characterization of Polyether and Polyester Polyurethane Soft Blocks Using MALDI Mass Spectrometry. *Anal. Chem.* 2000, 72 (11), 2490–2498.
6. Johnson, J. R.; Karlsson, D.; Dalene, M.; Skarping, G. Determination of Aromatic Amines in Aqueous Extracts of Polyurethane Foam Using Hydrophilic Interaction Liquid Chromatography and Mass Spectrometry. *Anal. Chim. Acta* 2010, 678 (1), 117–123.
7. Chattopadhyay, D. K.; Webster, D. C. Thermal Stability and Flame Retardancy of Polyurethanes. *Prog. Polym. Sci.* 2009, 34 (10), 1068–1133.
8. McLean, J. A.; Ruotolo, B. T.; Gillig, K. J.; Russell, D. H. Ion Mobility-Mass Spectrometry: A New Paradigm for Proteomics. *Int. J. Mass Spectrom.* 2005, 240 (3 SPEC. ISS.), 301–315.
9. Fenn, L. S.; Kliman, M.; Mahsut, A.; Zhao, S. R.; McLean, J. A. Characterizing Ion Mobility-Mass Spectrometry Conformation Space for the Analysis of Complex Biological Samples. *Anal. Bioanal. Chem.* 2009, 394 (1), 235–244.
10. Altuntaş, E.; Schubert, U. S. “Polymeromics”: Mass Spectrometry Based Strategies in Polymer Science toward Complete Sequencing Approaches: A Review. *Anal. Chim. Acta* 2014, 808, 56–69.
11. Montaudo, G.; Robert P. Lattimer. *Mass Spectrometry of Polymers*; CRC press, 2001.
12. Montaudo, G.; Samperi, F.; Montaudo, M. S. Characterization of Synthetic Polymers by MALDI-MS. *Prog. Polym. Sci.* 2006, 31 (3), 277–357.

13. Dey, M.; Castoro, J. A.; Wilkins, C. L. Determination of Molecular Weight Distributions of Polymers by MALDI-FTMS. *Anal. Chem.* 1995, 67 (9), 1575–1579.
14. Hart-Smith, G.; Lammens, M.; Du Prez, F. E.; Guilhaus, M.; Barner-Kowollik, C. ATRP Poly(Acrylate) Star Formation: A Comparative Study between MALDI and ESI Mass Spectrometry. *Polymer (Guildf)*. 2009, 50 (9), 1986–2000.
15. McLafferty, F. W. High-Resolution Tandem FT Mass Spectrometry above 10 KDa. *Acc. Chem. Res.* 1994, 27 (11), 379–386.
16. Baumgaertel, A.; Altuntaş, E.; Schubert, U. S. Recent Developments in the Detailed Characterization of Polymers by Multidimensional Chromatography. *J. Chromatogr. A* 2012, 1240, 1–20. <https://doi.org/10.1016/j.chroma.2012.03.038>.
17. Gruending, T.; Guilhaus, M.; Barner-Kowollik, C. Quantitative LC-MS of Polymers: Determining Accurate Molecular Weight Distributions by Combined Size Exclusion Chromatography and Electrospray Mass Spectrometry with Maximum Entropy Data Processing. *Anal. Chem.* 2008, 80 (18), 6915–6927.
18. Hanton, S. D. Mass Spectrometry of Polymers and Polymer Surfaces. *Chem. Rev.* 2001, 101 (2), 527–570.
19. Barner-Kowollik, C.; Gruending, T.; Falkenhagen, J.; Weidner, S. *Mass Spectrometry in Polymer Chemistry*; John Wiley & Sons, 2012.
20. Pasch, H.; Schrepp, W. *MALDI-TOF Mass Spectrometry of Synthetic Polymers*; Springer Science & Business Media, 2013.
21. May, J. C.; Goodwin, C. R.; Lareau, N. M.; Leaptrot, K. L.; Morris, C. B.; Kurulugama, R. T.; Mordehai, A.; Klein, C.; Barry, W.; Darland, E.; et al. Conformational Ordering of Biomolecules in the Gas Phase: Nitrogen Collision Cross Sections Measured on a Prototype High Resolution Drift Tube Ion Mobility-Mass Spectrometer. *Anal. Chem.* 2014, 86 (4), 2107–2116.

22. May, J. C.; McLean, J. A. Ion Mobility-Mass Spectrometry: Time-Dispersive Instrumentation. *Anal. Chem.* 2015, 87 (3), 1422–1436.
23. Eiceman, G. A.; Karpas, Z.; Jr., H. H. H. *Ion Mobility Spectrometry*; CRC press, 2013.
24. Wilkins, C. L.; Trimpin, S. *Ion Mobility Spectrometry-Mass Spectrometry: Theory and Applications*; CRC press, 2010.
25. Weidner, S. M.; Trimpin, S. *Mass Spectrometry of Synthetic Polymers.* 2010, 82 (12), 4811–4829.
26. Hoskins, J. N.; Trimpin, S.; Grayson, S. M. Architectural Differentiation of Linear and Cyclic Polymeric Isomers by Ion Mobility Spectrometry-Mass Spectrometry. *Macromolecules* 2011, 44 (17), 6915–6918.
27. Montenegro-Burke, J. R.; Bennett, J. M.; McLean, J. A.; Hercules, D. M. Novel Behavior of the Chromatographic Separation of Linear and Cyclic Polymers. *Anal. Bioanal. Chem.* 2016, 408 (3), 677–681.
28. Trimpin, S.; Clemmer, D. E. Ion Mobility Spectrometry / Mass Spectrometry Snapshots for Assessing the Molecular Compositions of Complex Polymeric Systems. *Anal. Chem.* 2008, 80 (23), 9073–9083.
29. Stow, S. M.; Goodwin, C. R.; Kliman, M.; Bachmann, B. O.; McLean, J. A.; Lybrand, T. P. Distance Geometry Protocol to Generate Conformations of Natural Products to Structurally Interpret Ion Mobility-Mass Spectrometry Collision Cross Sections. *J. Phys. Chem. B* **2014**, 118 (48), 13812–13820.
30. Wesdemiotis, C. Multidimensional Mass Spectrometry of Synthetic Polymers and Advanced Materials. *Angew. Chemie Int. Ed.* 2017, 56 (6), 1452–1464.
31. Crotty, S.; Gerişlioğlu, S.; Endres, K. J.; Wesdemiotis, C.; Schubert, U. S. Polymer Architectures via Mass Spectrometry and Hyphenated Techniques: A Review. *Anal. Chim. Acta* 2016, 932, 1–21.

32. Forsythe, J. G.; Stow, S. M.; Nefzger, H.; Kwiecien, N. W.; May, J. C.; McLean, J. A.; Hercules, D. M. Structural Characterization of Methylenedianiline Regioisomers by Ion Mobility-Mass Spectrometry, Tandem Mass Spectrometry, and Computational Strategies: I. Electrospray Spectra of 2-Ring Isomers. *Anal. Chem.* 2014, 86 (9), 4362–4370.
33. Stow, S. M.; Onifer, T. M.; Forsythe, J. G.; Nefzger, H.; Kwiecien, N. W.; May, J. C.; McLean, J. A.; Hercules, D. M. Structural Characterization of Methylenedianiline Regioisomers by Ion Mobility-Mass Spectrometry, Tandem Mass Spectrometry, and Computational Strategies. 2. Electrospray Spectra of 3-Ring and 4-Ring Isomers. *Anal. Chem.* 2015, 87 (12), 6288–6296.
34. Stow, S. M.; Crescentini, T. M.; Forsythe, J. G.; May, J. C.; McLean, J. A.; Hercules, D. M. Structural Characterization of Methylenedianiline Regioisomers by Ion Mobility-Mass Spectrometry, Tandem Mass Spectrometry, and Computational Strategies. 3. MALDI Spectra of 2-Ring Isomers. *Anal. Chem.* 2017, 89 (18).
35. Vandenplas, O.; Malo, J. L.; Saetta, M.; Mapp, C. E.; Fabbri, L. M. Occupational Asthma and Extrinsic Alveolitis Due to Isocyanates: Current Status and Perspectives. *Br. J. Ind. Med.* 1993, 50 (3), 213–228.
36. Pasch, H.; Mautjana, N. A. Matrix-assisted Laser Desorption/Ionization Mass Spectrometry of Polymers. *Encyclopedia of Analytical Chemistry: Applications, Theory and Instrumentation*; 2006.
37. Mautjana, N. A.; Pasch, H. Matrix-Assisted Laser Desorption Ionization Mass Spectrometry of Synthetic Polymers. *Macromol. Symp.* 2012, 313 (1), 157–161.
38. Mass, V.; Schrepp, W.; Von Vacano, B.; Pasch, H. Sequence Analysis of an Isocyanate Oligomer by MALDI-TOF Mass Spectrometry Using Collision Induced Dissociation. *Macromol. Chem. Phys.* 2009, 210 (22), 1957–1965.
39. Carr, R. H.; Jackson, A. T. Preliminary Matrix-assisted Laser Desorption Ionization Time-of-flight and Field Desorption Mass Spectrometric Analyses of Polymeric

- Methylene Diphenylene Diisocyanate, Its Amine Precursor and a Model Polyether Prepolymer. *Rapid Commun. Mass Spectrom.* 1998, 12 (24), 2047–2050.
40. Warburton, K. E.; Clench, M. R.; Ford, M. J.; White, J.; Rimmer, D. A.; Carolan, V. A. Characterization of Derivatized Monomeric and Prepolymeric Isocyanates by Matrix-Assisted Laser Desorption/Ionization Time-of-Flight Mass Spectrometry and Structural Elucidation by Tandem Mass Spectrometry. *Eur. J. Mass Spectrom.* 2005, 11 (6), 565–574.
41. Vangronsveld, E.; Mandel, F. Workplace Monitoring of Isocyanates Using Ion Trap Liquid Chromatography/Tandem Mass Spectrometry. *Rapid Commun. Mass Spectrom.* 2003, 17 (15), 1685–1690.
42. Crescentini, T. M.; Stow, S. M.; Forsythe, J. G.; May, J. C.; McLean, J. A.; Hercules, D. M. Structural Characterization of Methylenedianiline Regioisomers by Ion Mobility-Mass Spectrometry and Tandem Mass Spectrometry. 4. 3-Ring and 4-Ring Isomers. *Anal. Chem.* 2018, 90 (24).
43. Wang, G. B.; Labow, R. S.; Santerre, J. P. Biodegradation of a Poly(Ester)Urea-urethane by Cholesterol Esterase: Isolation and Identification of Principal Biodegradation Products. *J. Biomed. Mater. Res.* 1998, 36 (3), 407–417.
44. Lelah, M. D.; Cooper, S. L. *Polyurethanes in Medicine*; CRC press, 1986.
45. Ulrich, H. *Chemistry and Technology of Carbodiimides*; John Wiley & Sons: West Sussex, England, 2008.
46. Gies, A. P.; Heath, W. H.; Keaton, R. J.; Jimenez, J. J.; Zupancic, J. J. MALDI-TOF/TOF CID Study of Polycarbodiimide Branching Reactions. *Macromolecules* 2013, 46 (19), 7616–7637.
47. Gies, A. P.; Stefanov, Z.; Rau, N. J.; Chakraborty, D.; Boopalachandran, P.; Chauvel, J. P. Iron(III)-Catalyzed Chain Growth Reactions of Polymeric Methylene Diphenyl Diisocyanate. *Macromolecules* 2016, 49 (4), 1201–1221.

48. Frisch, K. C.; Reegen, S. L.; Thir, B. Kinetics of Alcohol and Polyether Polyol-Isocyanate Reactions Using Metal Catalysts. *J. Polym. Sci. Part C* 1967, 16 (4), 2191–2201.
49. Willeboordse, F. The Use of Differential Reaction Kinetics in Determining Rate Constants of Hydroxyl-Isocyanate Reactions. *J. Phys. Chem.* 1970, 74 (3), 601–606.
50. Krol, P.; Galina, H.; Kaczmarek, K. A Three Parameter Kinetic Model of Formation of Linear Polyurethane from 2,4-Toluenediisocyanate and Butane-1,4-Diol. *Macromol. Theory Simulations* 1999, 8 (2), 129–136.
51. Krol, P. Experimental Verification of the Kinetic Model for the Reaction Yielding Linear Polyurethanes, Claiming Dependence of Oligomer Reactivities on Molecular Weights. III. *J. Appl. Polym. Sci.* 1996, 61 (12), 2207–2219.
52. Krol, P. Kinetic Model for the Process Giving Linear Polyurethanes, with Consideration of Substitution Effects and Different Chemical Reactivities of Functional Groups in Toluene 2,4-Diisocyanate. *J. Appl. Polym. Sci.* 1998, 69 (1), 169–181.
53. He, Y.; Zhang, X.; Zhang, X.; Huang, H.; Chang, J.; Chen, H. Structural Investigations of Toluene Diisocyanate (TDI) and Trimethylolpropane (TMP)-Based Polyurethane Prepolymer. *J. Ind. Eng. Chem.* 2012, 18 (5), 1620–1627.
54. Ahn, Y. H.; Kim, J. S.; Kim, S. H. Reaction Monitoring of Toluenediisocyanate (TDI) Polymerization on a Non-Mixable Aqueous Surface by MALDI Mass Spectrometry. *Anal. Sci.* 2013, 29 (7), 703–708.
55. Ahn, Y. H.; Lee, Y. J.; Kim, S. H. MALDI MS-Based Composition Analysis of the Polymerization Reaction of Toluene Diisocyanate (TDI) and Ethylene Glycol (EG). *Anal. Sci.* 2015, 31 (6), 513–520.
56. Nagy, T.; Antal, B.; Czifrak, K.; Papp, I.; Karger-Kocsis, J.; Zsuga, M.; Keki, S. New Insight into the Kinetics of Diisocyanate-Alcohol Reactions by Highperformance Liquid

- Chromatography and Mass Spectrometry. *J. Appl. Polym. Sci.* 2015, 132 (25), 42127–42136.
57. Nagy, T.; Antal, B.; Dékány-Adamoczky, A.; Karger-Kocsis, J.; Zsuga, M.; Kéki, S. Uncatalyzed Reactions of 4,4'-Diphenylmethane-Diisocyanate with Polymer Polyols as Revealed by Matrix-Assisted Laser Desorption/Ionization Mass Spectrometry. *RSC Adv.* 2016, 6 (52), 47023–47032.
58. Beldi, M.; Medimagh, R.; Chatti, S.; Marque, S.; Prim, D.; Loupy, A.; Delolme, F. Characterization of Cyclic and Non-Cyclic Poly-(Ether-Urethane)s Bio-Based Sugar Diols by a Combination of MALDI-TOF and NMR. *Eur. Polym. J.* 2007, 43 (8), 3415–3433.
59. Krol, P.; Pilch-Pitera, B. Urethane Oligomers as Raw Materials and Intermediates for Polyurethane Elastomers. *Methods for Synthesis, Structural Studies and Analysis of Chemical Composition. Polymer (Guildf).* 2003, 44 (18), 5075–5101.
60. Akindoyo, J. O.; Beg, M. D. H.; Ghazali, S.; Islam, M. R.; Jeyaratnam, N.; Yuvaraj, A. R. Polyurethane Types, Synthesis and Applications-a Review. *RSC Adv.* 2016, 6 (115), 114453–114482.
61. Wesdemiotis, C.; Solak, N.; Polce, M. J.; Dabney, D. E.; Chaicharoen, K.; Katzenmeyer, B. C. Fragmentation Pathways of Polymer Ions. *Mass Spectrom. Rev.* 2011, 30 (4), 523–559.
62. Chattopadhyay, D. K.; Raju, N. P.; Vairamani, M.; Raju, K. V. S. N. Structural Investigations of Polypropylene Glycol (PPG) and Isophorone Diisocyanate (IPDI) Based Polyurethane Prepolymer by Matrix-Assisted Laser Desorption/Ionization Time-of-Flight (MALDI-TOF)-Mass Spectrometry. *Prog. Org. Coatings* 2008, 62 (2), 117–122.
63. Helden, G. Von; Bowers, M. T.; Wyttenbach, T. Inclusion of a MALDI Ion Source in the Ion Chromatography Technique: Conformational Information on Polymer and Biomolecular Ions. *Int. J. Mass Spectrom. Ion Process.* 1995, 147, 349–364.

64. Haler, J. R. N.; Far, J.; Aqil, A.; Claereboudt, J.; Tomczyk, N.; Giles, K.; Jérôme, C.; De Pauw, E. Multiple Gas-Phase Conformations of a Synthetic Linear Poly(Acrylamide) Polymer Observed Using Ion Mobility-Mass Spectrometry. *J. Am. Soc. Mass Spectrom.* 2017, 28 (11), 2492–2499.
65. Trimpin, S.; Plasencia, M.; Isailovic, D.; Clemmer, D. E. Resolving Oligomers from Fully Grown Polymers with IMS-MS. *Anal. Chem.* 2007, 79 (21), 7965–7974.
66. Ude, S.; Fernández De La Mora, J.; Thomson, B. A. Charge-Induced Unfolding of Multiply Charged Polyethylene Glycol Ions. *J. Am. Chem. Soc.* 2004, 126 (38), 12184–12190.
67. Larriba, C.; Fernandez De La Mora, J. The Gas Phase Structure of Coulombically Stretched Polyethylene Glycol Ions. *J. Phys. Chem. B* 2011, 116 (1), 593–598.
68. Gidden, J.; Wytttenbach, T.; Jackson, A. T.; Scrivens, J. H.; Bowers, M. T.; Ts, C. V.; August, R. V.; Re, V.; Recci, M.; March, V. Gas-Phase Conformations of Synthetic Polymers: Poly(Ethylene Glycol), Poly(Propylene Glycol), and Poly(Tetramethylene Glycol). *J. Am. Chem. Soc.* 2000, 122 (19), 4692–4699.
69. De Winter, J.; Lemaury, V.; Ballivian, R.; Chiro, F.; Coulembier, O.; Antoine, R.; Lemoine, J.; Cornil, J.; Dubois, P.; Dugourd, P.; et al. Size Dependence of the Folding of Multiply Charged Sodium Cationized Polylactides Revealed by Ion Mobility Mass Spectrometry and Molecular Modelling. *Chem. - A Eur. J.* 2011, 17 (35), 9738–9745.
70. Gidden, J.; Wytttenbach, T.; Batka, J. J.; Weis, P.; Bowers, M. T.; Jackson, A. T.; Scrivens, J. H. Poly(Ethylene Terephthalate) Oligomers Cationized by Alkali Ions: Structures, Energetics, and Their Effect on Mass Spectra and the Matrix-Assisted Laser Desorption/Ionization Process. *J. Am. Soc. Mass Spectrom.* 1999, 10 (9), 883–895.
71. Wytttenbach, T.; von Helden, G.; Bowers, M. T. Conformations of Alkali Ion Cationized Polyethers in the Gas Phase: Polyethylene Glycol and Bis[(Benzo-15-Crown-5)-15-Ylmethyl] Pimelate. *Int. J. Mass Spectrom. Ion Process.* 1997, 165, 377–390.

72. Haler, J. R. N.; Morsa, D.; Lecomte, P.; Jérôme, C.; Far, J.; De Pauw, E. Predicting Ion Mobility-Mass Spectrometry Trends of Polymers Using the Concept of Apparent Densities. *Elsevier Methods* 2018, 144, 125–133.
73. Morsa, D.; Defize, T.; Dehareng, D.; Jérôme, C.; De Pauw, E. Polymer Topology Revealed by Ion Mobility Coupled with Mass Spectrometry. *Anal. Chem.* 2014, 86 (19), 9693–9700.
74. Duez, Q.; Chirot, F.; Liénard, R.; Josse, T.; Choi, C. M.; Coulembier, O.; Dugourd, P.; Cornil, J.; Gerbaux, P.; De Winter, J. Polymers for Traveling Wave Ion Mobility Spectrometry Calibration. *J. Am. Soc. Mass Spectrom.* 2017, 28 (11), 2483–2491.
75. Selby, T. L.; Wesdemiotis, C.; Lattimer, R. P. Dissociation Characteristics of $[M+ X]^+$ Ions ($X= H, Li, Na, K$) from Linear and Cyclic Polyglycols. *J. Am. Soc. Mass Spectrom.* 1994, 5 (12), 1081–1092.
76. Hilton, G. R.; Jackson, A. T.; Thalassinos, K.; Scrivens, J. H. Structural Analysis of Synthetic Polymer Mixtures Using Ion Mobility and Tandem Mass Spectrometry. *Anal. Chem.* 2008, 80 (24), 9720–9725.
77. Cody, R. B.; Fouquet, T. Paper Spray and Kendrick Mass Defect Analysis of Block and Random Ethylene Oxide/Propylene Oxide Copolymers. *Anal. Chim. Acta* 2017, 989, 38–44.
78. Girod, M.; Carissan, Y.; Humbel, S.; Charles, L. Tandem Mass Spectrometry of Doubly Charged Poly(Ethylene Oxide) Oligomers Produced by Electrospray Ionization. *Int. J. Mass Spectrom.* 2008, 272, 1–11.
79. Tintaru, A.; Chendo, C.; Wang, Q.; Viel, S.; Quéléver, G.; Peng, L.; Posocco, P.; Pricl, S.; Charles, L. Conformational Sensitivity of Conjugated Poly(Ethylene Oxide)-Poly(Amidoamine) Molecules to Cations Adducted upon Electrospray Ionization - A Mass Spectrometry, Ion Mobility and Molecular Modeling Study. *Anal. Chim. Acta* 2014, 808, 163–174.

80. Lattimer, R. P. Tandem Mass Spectrometry of Lithium-Attachment Ions from Polyglycols. *J. Am. Soc. Mass Spectrom.* 1992, 3 (3), 225–234.
81. Memboeuf, A.; Vékey, K.; Lendvai, G. Structure and Energetics of Poly (Ethylene Glycol) Cationized by Li⁺, Na⁺, K⁺ and Cs⁺: A First-Principles Study. *J. Mass Spectrom.* 2011, 17 (1), 33–46.
82. Shimada, K.; Nagahata, R.; Kawabata, S. I.; Matsuyama, S.; Saito, T.; Kinugasa, S. Evaluation of the Quantitativeness of Matrix-Assisted Laser Desorption/Ionization Time-of-Flight Mass Spectrometry Using an Equimolar Mixture of Uniform poly(Ethylene Glycol) Oligomers. *J. Mass Spectrom.* 2003, 38 (9), 948–954.
83. Chen, R.; Li, L. Lithium and Transition Metal Ions Enable Low Energy Collision-Induced Dissociation of Polyglycols in Electrospray Ionization Mass Spectrometry. *J. Am. Soc. Mass Spectrom.* 2001, 12 (7), 832–839.
84. Kokubo, S.; Vana, P. Obtaining the Dielectric Constant of Polymers from Doubly Charged Species in Ion-Mobility Mass Spectrometry. *Macromol. Chem. Phys.* 2017, 218 (17), 1–8.
85. Li, J.; Zhu, M. Structural Characterization of a Vegetable Oil-Based Polyol through Liquid Chromatography Multistage Mass Spectrometry. *J. Polym. Sci. Part A Polym. Chem.* 2017, 55 (2), 255–262.
86. Williams, J. B.; Gueev, A. L.; Hercules, D. M. Characterization of Polyesters by Matrix-Assisted Laser Desorption Ionization Mass Spectrometry. *Macromolecules* 1997, 30 (13), 3781–3787.
87. Williams, J. B.; Chapman, T. M.; Hercules, D. M. Matrix-Assisted Laser Desorption/Ionization Mass Spectrometry of Discrete Mass Poly(Butylene Glutarate) Oligomers. *Anal. Chem.* 2003, 75 (13), 3092–3100.

88. Rizzarelli, P.; Puglisi, C.; Montaudo, G. Matrix-assisted Laser Desorption/Ionization Time-of-flight/Time-of-flight Tandem Mass Spectra of Poly(Butylene Adipate). *Rapid Commun. Mass Spectrom.* 2006, 20 (11), 1683–1694.
89. Gies, A. P.; Ellison, S. T.; Chakraborty, A. K.; Kwiecien, N. W.; Hercules, D. M. MALDI-TOF/TOF CID Study of Poly(Butylene Adipate) Fragmentation Reactions. *RSC Adv.* 2012, 2 (10), 4135–4151.
90. Pretorius, N. O.; Rhode, K.; Simpson, J. M.; Pasch, H. Characterization of Complex Phthalic Acid/Propylene Glycol Based Polyesters by the Combination of 2D Chromatography and MALDI-TOF Mass Spectrometry. *Anal. Bioanal. Chem.* 2015, 407 (1), 217–230.
91. Pretorius, N. O.; Willemse, C. M.; de Villiers, A.; Pasch, H. Combined Size Exclusion Chromatography, Supercritical Fluid Chromatography and Electrospray Ionization Mass Spectrometry for the Analysis of Complex Aliphatic Polyesters. *J. Chromatogr. A* 2014, 1330, 74–81.
92. Pretorius, N. O.; Rode, K.; Simpson, J. M.; Pasch, H. Analysis of Complex Phthalic Acid Based Polyesters by the Combination of Size Exclusion Chromatography and Matrix-Assisted Laser Desorption/Ionization Mass Spectrometry. *Anal. Chim. Acta* 2014, 808, 94–103.
93. Giguère, M. S.; Mayer, P. M. Climbing the Internal Energy Ladder: The Unimolecular Decomposition of Ionized Poly(Vinyl Acetate). *Int. J. Mass Spectrom.* 2004, 231 (1), 59–68.
94. Owen, S.; Masaoka, M.; Kawamura, R.; Sakota, N. Biodegradation of Poly-D, L-Lactic Acid Polyurethanes. *J. Macromol. Sci. Part A Pure Appl. Chem.* 1995, 32 (4), 843–850.
95. Borda, J.; Bodnár, I.; Kéki, S.; Sipos, L.; Zsuga, M. Optimum Conditions for the Synthesis of Linear Polylactic Acid-Based Urethanes. *J. Polym. Sci. Part A Polym. Chem.* 2000, 38 (16), 2925–2933.

96. Borda, J.; Keki, S.; Bodnar, I.; Nemeth, N.; Zsuga, M. New Potentially Biodegradable Polyurethanes. *Polym. Adv. Technol.* 2006, 17 (11), 945–953.
97. Tang, D.; Noordover, B. A.; Sablong, R. J.; Koning, C. E. Metal-Free Synthesis of Novel Biobased Dihydroxyl-Terminated Aliphatic Polyesters as Building Blocks for Thermoplastic Polyurethanes. *J. Polym. Sci. Part A Polym. Chem.* 2011, 49 (13), 2959–2968.
98. Báez, J. E.; Marcos-Fernández, Á.; Martínez-Richa, A.; Galindo-Iranzo, P. Poly(ϵ -Caprolactone) Diols (HOPCLOH) and Their Poly(Ester-Urethanes) (PEUs): The Effect of Linear Aliphatic Diols [HO-(CH₂)_M-OH] as Initiators. *Polym. - Plast. Technol. Eng.* 2017, 56 (8), 889–898.
99. Osaka, I.; Watanabe, M.; Takama, M.; Murakami, M.; Arakawa, R. Characterization of Linear and Cyclic Polylactic Acids and Their Solvolysis Products by Electrospray Ionization Mass Spectrometry. *J. Mass Spectrom.* 2006, 41 (10), 1369–1377.
100. Soares, B. P.; Wood-Adams, P. M. Chemical Composition Distribution of Multicomponent Copolymers. *Macromol. theory simulations* 2003, 12 (4), 229–236.
101. Montaudo, G.; Lattimer, R. P. *Mass Spectrometry of Polymers*; CRC press, 2001.
102. Ferreira, H. E.; Condeço, J. A. D.; Fernandes, I. O.; Duarte, D. E.; Bordado, J. C. M. HPLC-UV and HPLC-ESI+-MS/MS Analysis of Free Monomeric Methylene Diphenyl Diisocyanate in Polyurethane Foams and Prepolymers after Stabilization with NBMA a New Derivatizing Agent. *Anal. Methods* 2014, 6 (23), 9242–9257.
103. Brock, F. H. Kinetics of the 2,4-Tolylene Diisocyanate-Alcohol Reaction. *J. Phys. Chem.* 1961, 65 (9), 1638–1639.
104. Dyer, E.; Taylor, H. A.; Mason, S. J.; Samson, J. The Rates of Reaction of Isocyanates with Alcohols. I. Phenyl Issocyanate with 1- and 2-Butanol. *J. Am. Chem. Soc.* 1949, 71 (12), 4106–4109.

105. Burkus, J.; Eckert, C. F. The Kinetics of the Triethylamine-Catalyzed Reaction of Diisocyanates with 1-Butanol in Toluene. *J. Am. Chem. Soc.* 1958, 80 (22), 5948–5950.
106. Gies, A. P.; Hercules, D. M. Collision Induced Dissociation Study of Ester-Based Polyurethane Fragmentation Reactions. *Anal. Chim. Acta* 2014, 808, 199–219.
107. Saunders, J. H.; Klemmner, D. *Handbook of Polymeric Foams and Foam Technology*; Munich: Hanser, 1991.
108. Guo, A.; Javni, I.; Petrovic, Z. Rigid Polyurethane Foams Based on Soybean Oil. *J. Appl. Polym. Sci.* 2000, 77 (2), 467–473.
109. Kirpluks, M.; Kalnbunde, D.; Benes, H.; Cabulis, U. Natural Oil Based Highly Functional Polyols as Feedstock for Rigid Polyurethane Foam Thermal Insulation. *Ind. Crops Prod.* 2018, 122, 627–636.
110. Basso, M. C.; Giovando, S.; Pizzi, A.; Pasch, H.; Pretorius, N.; Delmotte, L.; Celzard, A. Flexible-Elastic Copolymerized Polyurethane-Tannin Foams. *J. Appl. Polym. Sci.* 2014, 131 (13), 2–7.
111. Basso, M. C.; Pizzi, A.; Lacoste, C.; Delmotte, L.; Al-Marzouki, F. M.; Abdalla, S.; Celzard, A. MALDI-TOF and ¹³C NMR Analysis of Tannin-Furanic-Polyurethane Foams Adapted for Industrial Continuous Lines Application. *Polymers (Basel)*. 2014, 6 (12), 2985–3004.
112. Aou, K.; Schrock, A. K.; Ginzburg, V. V.; Price, P. C. Characterization of Polyurethane Hard Segment Length Distribution Using Soft Hydrolysis/MALDI and Monte Carlo Simulation. *Polymer (Guildf)*. 2013, 54 (18), 5005–5015.
113. Marand, A.; Karlsson, D.; Dalene, M.; Skarping, G. Extractable Organic Compounds in Polyurethane Foam with Special Reference to Aromatic Amines and Derivatives Thereof. *Anal. Chim. Acta* 2004, 510 (1), 109–119.
114. Yontz, D. J.; Hsu, S. L. A Mass Spectrometry Analysis of Hard Segment Length Distribution in Polyurethanes. *Macromolecules* 2000, 33 (22), 8415–8420.

115. Tang, D.; Macosko, C. W.; Hillmyer, M. A. Thermoplastic Polyurethane Elastomers from Bio-Based Poly(δ - Decalactone) Diols. *Polym. Chem.* 2014, 5 (9), 3231–3237.
116. Holden, G.; Kricheldorf, H. R.; Quirk, R. P. *Thermoplastic Elastomers*; Munich: Hanser, 2004.
117. Guan, J.; Song, Y.; Lin, Y.; Yin, X.; Zuo, M.; Zhao, Y.; Tao, X.; Zheng, Q. Progress in Study of Non-Isocyanate Polyurethane. *Ind. Eng. Chem. Res.* 2011, 50 (11), 6517–6527.
118. Lamarzelle, O.; Durand, P. L.; Wirotius, A. L.; Chollet, G.; Grau, E.; Cramail, H. Activated Lipidic Cyclic Carbonates for Non-Isocyanate Polyurethane Synthesis. *Polym. Chem.* 2016, 7 (7), 1439–1451.
119. Poussard, L.; Mariage, J.; Grignard, B.; Detrembleur, C.; Jérôme, C.; Calberg, C.; Heinrichs, B.; De Winter, J.; Gerbaux, P.; Raquez, J. M.; et al. Non-Isocyanate Polyurethanes from Carbonated Soybean Oil Using Monomeric or Oligomeric Diamines to Achieve Thermosets or Thermoplastics. *Macromolecules* 2016, 49 (6), 2162–2171.
120. More, A. S.; Gadenne, B.; Alfos, C.; Cramail, H. AB Type Polyaddition Route to Thermoplastic Polyurethanes from Fatty Acid Derivatives. *Polym. Chem.* 2012, 3 (6), 1594–1605.
121. Prasad, A.; Xiang, H.; Wang, J.; Remsen, E. E. Analysis of Pre- and Post-Conditioned Polyurethane CMP Pad Surfaces as a Function of Conditioning Temperature. *ECS Trans.* 2007, 3 (41), 31–44.
122. Lattimer, R. P.; Muenster, H.; Budzikiewicz, H. Pyrolysis Tandem Mass Spectrometry (Py-MS/MS) of a Segmented Polyurethane. *J. Anal. Appl. Pyrolysis* 1990, 17 (3), 237–249.
123. Ravey, M.; Pearce, E. M. Flexible Polyurethane Foam. I. Thermal Decomposition of a Polyether-Based, Water-Blown Commercial Type of Flexible Polyurethane Foam. *J. Appl. Polym. Sci.* 1997, 63 (1), 47–74.

124. Lattimer, R. P.; Polce, M. J.; Wesdemiotis, C. MALDI-MS Analysis of Pyrolysis Products from a Segmented Polyurethane. *J. Anal. Appl. Pyrolysis* 1998, 48 (1), 1–15.
125. Lattimer, R. P. Mass Spectral Analysis of Low-Temperature Pyrolysis Products from Poly(Ethylene Glycol). *J. Anal. Appl. Pyrolysis* 2000, 56 (1), 61–78.
126. Lattimer, R. P. Mass Spectral Analysis of Low-Temperature Pyrolysis Products from Poly(Tetrahydrofuran). *J. Anal. Appl. Pyrolysis* 2001, 57 (1), 57–76.
127. Lattimer, R. P.; Williams, R. C. Low-Temperature Pyrolysis Products from a Polyether-Based Urethane. *J. Anal. Appl. Pyrolysis* 2002, 63 (1), 85–104.
128. Ketata, N.; Sanglar, C.; Waton, H.; Alamercery, S.; Delolme, F.; Raffin, G.; Grenier-Loustalot, M. F. Thermal Degradation of Polyurethane Bicomponent Systems in Controlled Atmospheres. *Polym. Polym. Compos.* 2005, 13 (1), 1–26.
129. Weems, A. C.; Wacker, K. T.; Carrow, J. K.; Boyle, A. J.; Maitland, D. J. Shape Memory Polyurethanes with Oxidation-Induced Degradation: In Vivo and in Vitro Correlations for Endovascular Material Applications. *Acta Biomater.* 2017, 59, 33–44.
130. Dopico-García, M. S.; López-Vilariño, J. M.; Fernández-Martínez, G.; González-Rodríguez, M. V. Liquid Chromatography Method to Determine Polyamines in Thermosetting Polymers. *Anal. Chim. Acta* 2010, 667 (1), 123–129.
131. Simonsick, W. J.; Aaserud, D. J. Modern Mass Spectrometry For Coatings. *Prog. Org. Coatings* 1998, 34 (1), 206–213.
132. European Food Safety Authority (EFSA). Opinion of the Scientific Panel on Food Additives, Flavourings, Processing Aids and Materials in Contact with Food on a Request from the Commission Related to Para Hydroxybenzoates (E 214-219). *EFSA J.* 2006, 965 (October 2000), 1–7.
133. Driffield, M.; Bradley, E. L.; Castle, L. Identification of Unknown Reaction By-Products and Contaminants in Epoxyphenolic-Based Food Can Coatings by LC/TOF-MS; Wilmington, 2006.

134. Driffield, M.; Bradley, E. L.; Castle, L. A Method of Test for Residual Isophorone Diisocyanate Trimer in New Polyester-Polyurethane Coatings on Light Metal Packaging Using Liquid Chromatography with Tandem Mass Spectrometric Detection. *J. Chromatogr. A* 2007, 1141 (1), 61–66.
135. Bradley, E. L.; Driffield, M.; Guthrie, J.; Harmer, N.; Thomas Oldring, P. K.; Castle, L. Analytical Approaches to Identify Potential Migrants in Polyester–polyurethane Can Coatings. *Food Addit. Contam.* 2009, 26 (12), 1602–1610.
136. Omer, E.; Cariou, R.; Remaud, G.; Guitton, Y.; Germon, H.; Hill, P.; Dervilly-Pinel, G.; Le Bizec, B. Elucidation of Non-Intentionally Added Substances Migrating from Polyester-Polyurethane Lacquers Using Automated LC-HRMS Data Processing. *Anal. Bioanal. Chem.* 2018, 410 (22), 5391–5403.
137. Schaefer, A. Identification and Quantification of Migrants from Can Coatings, University of Hamburg, 2004.
138. Schaefer, A.; Ohm, V. A.; Simat, T. J. Migration from Can Coatings: Part 2. Identification and Quantification of Migrating Cyclic Oligoesters below 1000 Da. *Food Addit. Contam. Part A* 2004, 21 (4), 377–389.
139. Ren, S. F.; Zhang, L.; Cheng, Z. H.; Guo, Y. L. Immobilized Carbon Nanotubes as Matrix for MALDI-TOF-MS Analysis: Applications to Neutral Small Carbohydrates. *J. Am. Soc. Mass Spectrom.* 2005, 16 (3), 333–339.
140. Wang, G. B.; Santerre, J. P.; Labow, R. S. High-Performance Liquid Chromatographic Separation and Tandem Mass Spectrometric Identification of Breakdown Products Associated with the Biological Hydrolysis of a Biomedical Polyurethane. *J. Chromatogr. B Biomed. Appl.* 1997, 698 (1), 69–80.
141. Lawson, G.; Bartram, S.; Fitchner, S.; Woodland, E. D. MALDI-MS and Colorimetric Analysis of Diisocyanate and Polyol Migrants from Model Polyurethane Adhesives Used in Food Packaging. *Analyst* 2000, 125 (1), 115–118.

142. Mortensen, S. K.; Trier, X. T.; Foverskov, A.; Petersen, J. H. Specific Determination of 20 Primary Aromatic Amines in Aqueous Food Simulants by Liquid Chromatography-Electrospray Ionization-Tandem Mass Spectrometry. *J. Chromatogr. A* 2005, 1091 (1), 40–50.
143. Aznar, M.; Canellas, E.; Nerín, C. Quantitative Determination of 22 Primary Aromatic Amines by Cation-Exchange Solid-Phase Extraction and Liquid Chromatography-Mass Spectrometry. *J. Chromatogr. A* 2009, 1216 (27), 5176–5181.
144. Pezo, D.; Fedelib, M.; Bosetti, O.; Nerína, C. Aromatic Amines from Polyurethane Adhesives in Food Packaging: The Challenge of Identification and Pattern Recognition Using Quadrupole-Time of Flight-Mass Spectrometry. *Anal. Chim. Acta* 2012, 756, 49–59.
145. Ramos, M. J. G.; Lozano, A.; Fernández-Alba, A. R. High-Resolution Mass Spectrometry with Data Independent Acquisition for the Comprehensive Non-Targeted Analysis of Migrating Chemicals Coming from Multilayer Plastic Packaging Materials Used for Fruit Purée and Juice. *Elsevier Talanta* 2019, 191, 180–192.
146. Zhang, N.; Kenion, G.; Bankmann, D.; Mezouari, S.; Hartman, T. G. Migration Studies and Chemical Characterization of Low Molecular Weight Cyclic Polyester Oligomers from Food Packaging Lamination Adhesives. *Packag. Technol. Sci.* 2018, 31 (4), 197–211.
147. Lutz, J. F.; Lehn, J. M.; Meijer, E. W.; Matyjaszewski, K. From Precision Polymers to Complex Materials and Systems. *Nat. Rev. Mater.* 2016, 1 (5), 16024.
148. Mutlu, H.; Lutz, J. F. Reading Polymers: Sequencing of Natural and Synthetic Macromolecules. *Angew. Chemie Int. Ed.* 2014, 53 (48).
149. Lutz, J. F. Coding Macromolecules: Inputting Information in Polymers Using Monomer-Based Alphabets. *Macromolecules* 2015, 48 (14), 4759–4767.

150. Gunay, U. S.; Petit, B. E.; Karamessini, D.; Al Ouahabi, A.; Amalian, J. A.; Chendo, C.; Bouquey, M.; Gigmes, D.; Charles, L.; Lutz, J. F. Chemoselective Synthesis of Uniform Sequence-Coded Polyurethanes and Their Use as Molecular Tags. *Chem* 2016, 1 (1), 114–126.
151. Karamessini, D.; Petit, B. E.; Bouquey, M.; Charles, L.; Lutz, J. F. Identification-Tagging of Methacrylate-Based Intraocular Implants Using Sequence Defined Polyurethane Barcodes. *Adv. Funct. Mater.* 2017, 27 (3).
152. Takáts, Z.; Wiseman, J. M.; Gologan, B.; Cooks, R. G. Electrosonic Spray Ionization. A Gentle Technique for Generating Folded Proteins and Protein Complexes in the Gas Phase and for Studying Ion-Molecule Reactions at Atmospheric Pressure. *Anal. Chem.* 2004, 76 (14), 4050–4058.
153. Takáts, Z.; Wiseman, J. M.; Gologan, B.; Graham Cooks, R. Mass Spectrometry Sampling under Ambient Conditions with Desorption Electrospray Ionization. *Science.* 2004, 306 (5695), 471–473.
154. Bonnaire, N.; Dannoux, A.; Pernelle, C.; Amekraz, B.; Moulin, C. On the Use of Electrospray Ionization and Desorption Electrospray Ionization Mass Spectrometry for Bulk and Surface Polymer Analysis. *Appl. Spectrosc.* 2010, 64 (7), 810–818.
155. Lebeau, D.; Ferry, M. Direct Characterization of Polyurethanes and Additives by Atmospheric Solid Analysis Probe with Time-of-Flight Mass Spectrometry (ASAP-TOF-MS). *Anal. Bioanal. Chem.* 2015, 407 (23), 7175–7187.
156. Nefliu, M.; Venter, A.; Cooks, R. G. Desorption Electrospray Ionization and Electrosonic Spray Ionization for Solid- and Solution-Phase Analysis of Industrial Polymers. *Chem. Commun.* 2006, 888–890.
157. Terrier, P.; Desmazieres, B.; Tortajada, J.; Buchmann, W. APCI/APPI for Synthetic Polymer Analysis. *Mass Spectrom. Rev.* 2011, 30 (5), 854–874.

158. Whitson, S. E.; Erdodi, G.; Kennedy, J. P.; Lattimer, R. P.; Wesdemiotis, C. Direct Probe-Atmospheric Pressure Chemical Ionization Mass Spectrometry of Cross-Linked Copolymers and Copolymer Blends. *Anal. Chem.* 2008, 80 (20), 7778–7785.

CHAPTER II

STRUCTURAL CHARACTERIZATION OF METHYLENEDIANILINE REGIOISOMERS BY ION MOBILITY-MASS SPECTROMETRY, TANDEM MASS SPECTROMETRY, AND COMPUTATIONAL STRATEGIES

II. ELECTROSPRAY SPECTRA OF 3 RING AND 4 RING ISOMERS

2.1. Introduction

Methylenedianiline (MDA) is commonly used as the starting material in the production of methylene diphenylene diisocyanate (MDI), which is a major hard block component in polyurethanes. Industrial grade MDA is composed of 2-ring MDA and larger multimeric species which are formed by the reaction of aniline and formaldehyde and named according to the number of aniline rings present.^{1,2} Structural isomers reflecting attachment of additional anilines at different sites can exist in industrial grade MDA which contributes to heterogeneity in many polyurethane systems.³ Determining preferred protonation sites and location of aniline attachments for larger MDA multimers is of great interest in polymer chemistry, because isomeric characterization can contribute to an enhanced understanding of structure–property relationships of many commercially relevant MDI-based polyurethane (PU) systems.⁴

In our previous work, purified 2-ring MDA regioisomers (4,4'-MDA, 2,4'-MDA, and 2,2'-MDA) were structurally characterized using tandem mass spectrometry (MS/MS), ion mobility-mass spectrometry (IM-MS), and computational modeling.⁵ We observed that protonation can occur both on amine groups and on the aniline ring, which is consistent with previous findings.⁶ Depending on the location of the amine group in the 2-ring MDA species, gas-phase protonation on the amine can lead to low energy fragmentation pathways via a charge-directed process.⁷ In the present study, we aim to characterize purified 3-ring and 4-ring MDA

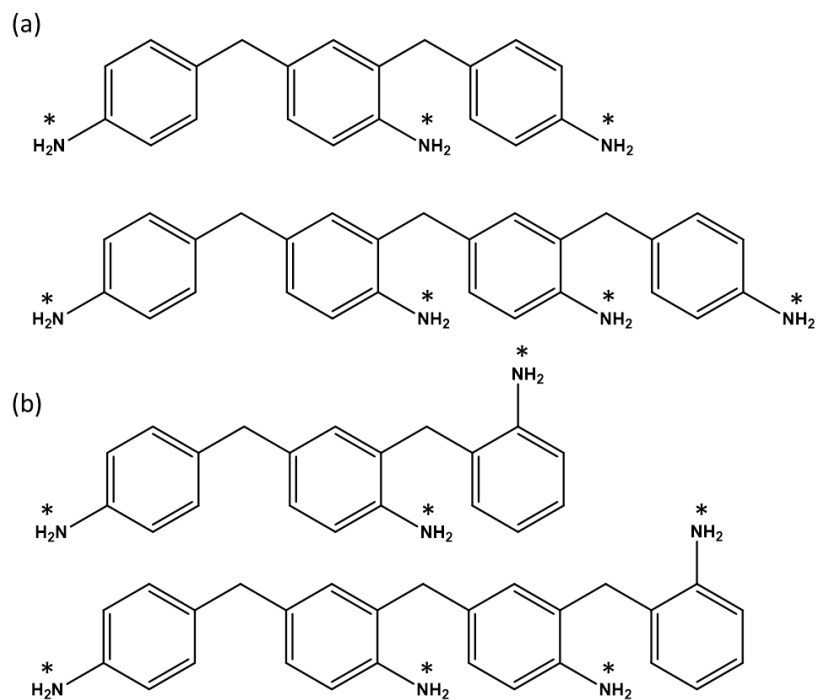


Figure 2.1. Structures of 3-ring and 4-ring MDA (theoretical neutral molecule monoisotopic masses = 303.17 and 408.23 Da, respectively). **(a)** All *para* substitution; **(b)** one *ortho* substitution. Potential protonation sites are labeled with an asterisk.

multimeric regioisomers. Possible protonation sites on the 3-ring and 4-ring MDA species are illustrated in **Figure 2.1**. In **Figure 2.1a**, each aniline ring is attached with its amine group in the *para* position which represents the primary solution-phase conformation based on NMR studies (**Supporting Information, Figure B.1 and B.2**). Due to the location of the amine groups and bridging carbons, protonation in **Figure 2.1a** is possible only on the amine group and not the aniline ring. The structures shown in **Figure 2.1b** have one terminal aniline ring with its amine group attached in the *ortho* position (this structure is only representative of <5% of the NMR signals for both the 3-ring and 4-ring MDA). Thus, while it is possible for both 3-ring and 4-ring MDA species to have the last aniline ring attached with an amine group in the *ortho* position (**Figure 1b**), this isomer is not preferred. As a result, this manuscript will focus on the structures and protonation sites shown in **Figure 1a**.

A series of MS techniques are utilized in this study to structurally characterize these larger MDA multimers. MS/MS is used to map fragmentation pathways of the MDA multimers, while IM-MS provides broad insight into the gas-phase conformations of ionized MDA species.⁸⁻

¹¹ Two IM-MS instruments are utilized in this study: a commercial traveling wave instrument which supports multiple stages of fragmentation and a commercial drift tube instrument which supports direct collisional cross section (CCS) measurements in a variety of drift gases. Computational strategies can then supplement these experimental approaches to provide enhanced structural interpretation. These combined techniques facilitate the separation and characterization of isomeric species that exist for 3-ring and 4-ring MDA. The structural characterization of these multimeric MDA species and their fragments provides a basis for characterization of industrial MDA and MDI mixtures.

2.2. Experimental Methods

2.2.1. Materials

3-ring MDA and 4-ring MDA samples were provided by Dr. Stefan Wershofen, Bayer MaterialScience AG, 47812 Uerdingen, Germany. The authenticity of each sample was determined by ^1H NMR, as provided in the **Supporting Information (Figures B.1 and B.2)**. Tetralkylammonium salts and solvents were purchased from Sigma-Aldrich (St. Louis, MO). These included tetraalkylammonium bromides (TAA 1-8) and HPLC grade methanol. Water blended with 0.1% formic acid (optima grade) was obtained from Fisher Scientific.

2.2.2. Instrumentation

Traveling Wave ESI-IM-TOF/MS

Synapt G2 and G2-S (Waters Corporation, Milford, MA) mass spectrometers were used for acquiring MS, traveling wave (TW) IM-MS, and tandem MS/MS data. The MS/MS capabilities of these instruments enable fragmentation experiments to be conducted both before and after the IM region. Although collision cross section (CCS) values cannot be obtained directly from the kinetic theory of gases using TW IM-MS experimental drift time values, a relative CCS method that uses quaternary ammonium salts as CCS calibration standards was utilized to obtain CCS data from these instruments.¹²

Further experimental details can be found from our earlier study,⁵ but, briefly, the TWIM drift cell settings were as follows: TWIM pressure 3 mbar (2.25 Torr), electrodynamic wave height 35 V, wave velocity of 700 m/s, TOF resolution ca. 20,000 ($m/\Delta m$), 3.00 kV ESI capillary voltage, 80 °C source temperature, 150 °C desolvation temperature, 10 V sampling cone, 2 V (source offset) extraction cone, 20 L/h cone gas flow, 1 mL/min trap gas flow, and 90 mL/min IMS gas flow. Sodium formate clusters were used for TOFMS calibration. Collision-induced dissociation (CID) experiments were performed either prior to or following TWIM mobility separation (MS/IM-MS, and MS-IM/MS, respectively). Lab frame energies were converted to center-of-mass (COM) collision energies for MS/MS experiments to better represent the energy available for rearrangement and fragmentation.¹³ All samples were analyzed as positive ions

generated by ESI. MDA 3-ring and 4-ring polymer samples were dissolved at a concentration of 0.1 mg/mL in 9:1 methanol:water, the latter containing 0.1% formic acid (*v/v*). A direct infusion flow rate of 6.00 $\mu\text{L}/\text{min}$ was used for all samples.

Drift-Tube ESI-IM-TOFMS

Drift tube ion mobility (DTIM) measurements using both N_2 and He buffer gases were performed on a commercial ESI-IM-QTOF mass spectrometer (6560, Agilent Technologies, Santa Clara, CA) which was modified to support various drift gases. Details of this instrumentation are provided elsewhere.¹⁴ Briefly, the IM-MS consists of a 78 cm uniform-field drift tube coupled to a QTOF mass spectrometer ($m/\Delta m$ ca. 40,000). The buffer gas was maintained at a pressure of ca. 4 Torr, and drift voltages were varied in order to correct for the non-IM flight time of ions through the interfacing ion optics. CCS values were calculated from drift times using the Mason-Schamp equation. Nitrogen-based CCS measurements were obtained for direct comparison with TWIM CCS measurements, while helium-based CCS values were measured for comparison with computational CCS calculations. MDA samples were analyzed at a concentration of 0.095 mg/mL in 9:1 methanol:water, the latter containing 0.1% formic acid (*v/v*). A direct infusion flow rate of 6.00 $\mu\text{L}/\text{min}$ was used.

2.2.3. Computational Methods

As IM provides a general picture of ion structure in the form of an orientationally averaged surface area (CCS), IM-MS results are often supplemented with computational studies to gain further insight into the gas phase conformations of the ion of interest. A more detailed description of the computational methods used here is included in our previous paper in this series.⁵ A simulated annealing protocol implemented in AMBER¹⁵ was used for conformational sampling with a separate simulation for each of the possible protonation sites on both the 3-ring (3 sites) and 4-ring (4 sites) MDA species. A combination of the projection approximation (He)

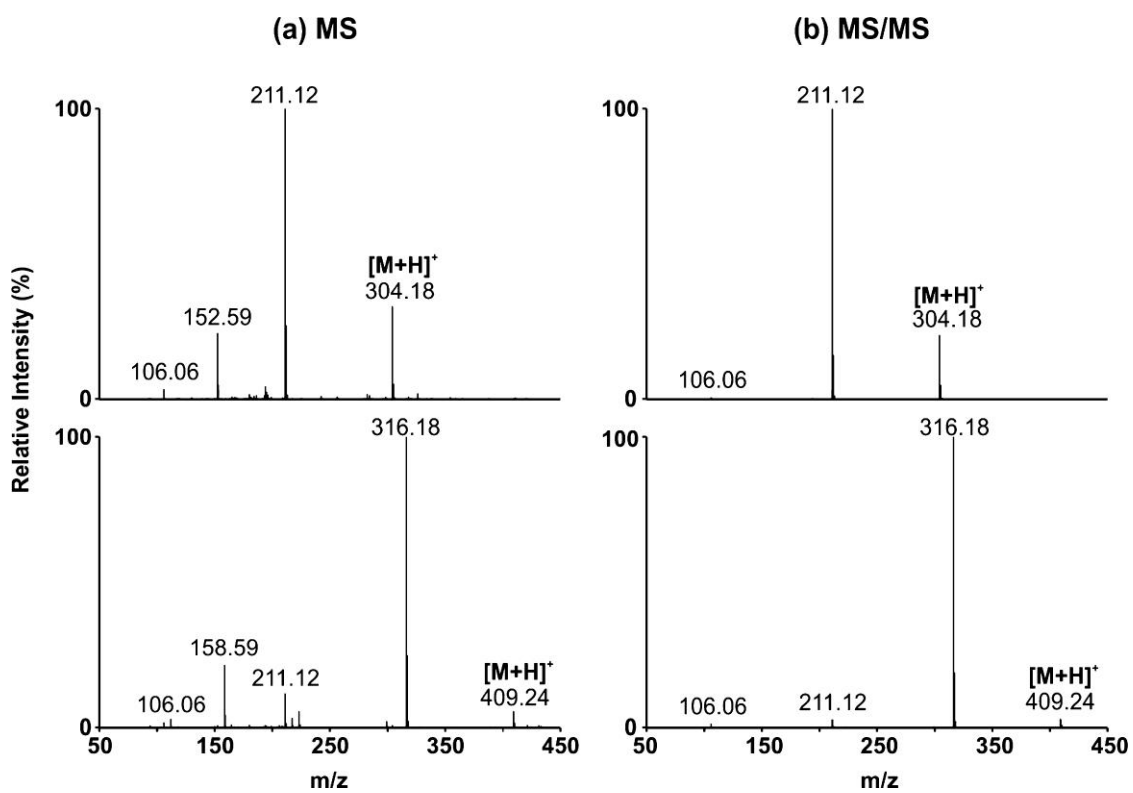


Figure 2.2. (a) Mass spectra of 3-ring and 4-ring MDA using direct infusion ESI-TOFMS. (b) Tandem mass spectra for 3-ring and 4-ring MDA parent ions ($[M + H]^+ = 304.18$ Da and $[M + H]^+ = 409.24$ Da, respectively).

and the trajectory method (N_2) utilizing MOBCAL¹⁶⁻¹⁸ was then used to calculate theoretical CCS values for the generated conformations. The theoretical conformations were then aligned with the experimental CCS values to provide structural insight into the 3-ring and 4-ring MDA isomers. Alignment of theoretically generated conformations with experimental CCS values is shown in the **Supporting Information, Figures B.3 and B.4**.

2.3. Results and Discussion

2.3.1. Characterization by MS and Tandem MS

ESI spectra were obtained for the protonated 3-ring ($[M + H^+] = 304$ Da) and 4-ring ($[M + H^+] = 409$ Da) MDA species and are shown in **Figure 2.2a**. In addition to the protonated precursor ions, significant peaks are observed at 211 and 106 Da for the 3-ring MDA species and peaks at 316, 211, and 106 Da are observed for the 4-ring MDA. These peaks correspond to fragments of the precursor ion and become more intense in the tandem mass spectra as shown in **Figure 2.2b**. Even before collision energy is applied to induce fragmentation, the peak at 211 Da for the 3-ring and 316 Da for the 4-ring MDA correspond to the base peaks of the spectra, signifying that the corresponding precursor ions are readily dissociated. It is also interesting to note that the mass difference of 93 Da between the precursor ion and its most abundant fragment present in the spectra is the same mass difference that was observed for the 2-ring MDA species between the 199 Da precursor ion and its major fragment at 106 Da, corresponding to the loss of a terminal neutral aniline.

In addition to the fragment peaks, additional signals are observed at m/z 152.6 and m/z 158.6, respectively, for both the 3-ring and 4-ring spectra. These masses correspond to doubly charged ions for the 3-ring and the 4-ring isomers based on isotope spacing. When these ions were mass selected and fragmented via an MS/MS experiment, singly charged ions at higher m/z values were produced further indicating that these peaks correspond to doubly charged species (**Supporting Information, Figures B.5 and B.6**).

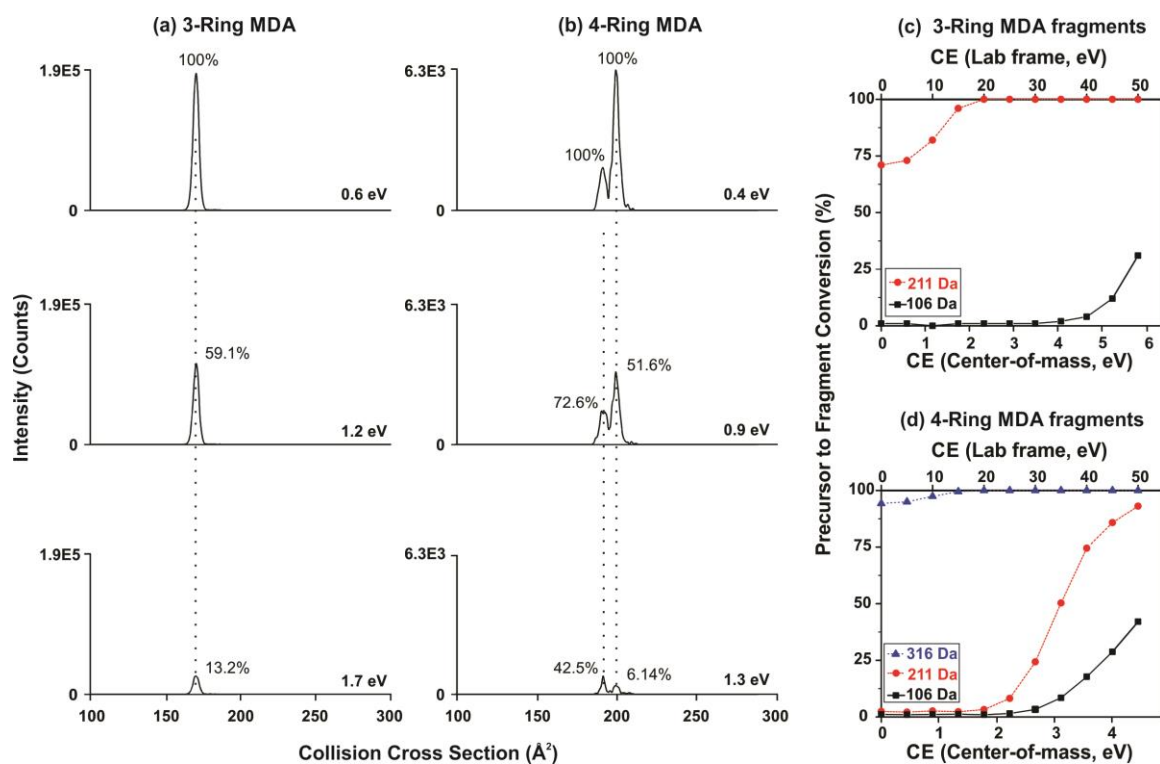


Figure 2.3. Collisionally activated CCS profiles of $[M + H]^+$ ions for (a) 3-ring MDA and (b) 4-ring MDA. Center of mass energies are shown. The inset relative percentages represent signal intensities compared to those without collisional activation. Vertical lines are added for visual alignment. Collision-induced dissociation curves monitoring the transition of precursor ions to fragment ions for (c) 3-ring MDA and for (d) 4-ring MDA. Center of mass collision energies (CE) are shown on the lower axis. (See text for details.)

The conversion from precursor ion to fragment ions was monitored as a function of applied collision energy for both the 3-ring and 4-ring MDA as shown in **Figure 2.3**. The IM-MS/MS structural depletion of the precursor ion is shown in **Figure 2.3a,b**, and the breakdown curves for the fragment ions are shown in **Figure 2.3c,d**. These breakdown curves show the percentage of precursor ion to fragment conversion observed in the spectra at various collision energies and were obtained by taking the intensity of the indicated fragment ion and dividing by the intensity of its corresponding precursor ion. In **Figure 2.3c**, 3-ring MDA has two breakdown curves, representative of the 106 and 211 fragments. The precursor ion breaks down into the 211 fragment at a significantly lower energy threshold than the 106 fragment. **Figure 2.3d** corresponds to 4-ring MDA, which has three curves, representative of the 106, 211, and 316 fragments. Again the 316 and 211 fragments form at lower collision energies than the 106 fragment. This observation is further discussed later in the manuscript in the context of IM and computational results.

In our previous study involving 2-ring MDA, the 106 fragment formed readily when external amines were located *ortho* to the bridging carbon (2,2'-MDA and 2,4'-MDA) but not readily for the 4,4'-MDA. The observation that the 106 fragment requires higher collision energy than the other isomers to form from both the 3-ring and 4-ring MDA species suggests that the external amines are located in *para* positions to the bridging carbon in a similar manner as the 2-ring 4,4'-MDA. The observation of the 106 fragment ion forming at higher collision energies further indicates that the structures shown in **Figure 2.1a** are accurate structural depictions of the 3-ring and 4-ring isomers. However, when comparing **Figure 2.3c,d** with the 2-ring MDA breakdown curves from our previous study there is a notable difference between the 3-ring and 4-ring isomers, relative to the 2-ring isomers. Specifically, the 2-ring isomers showed ~30% fragmentation at a center-of-mass (COM) of 4.0 eV, and the 4-ring isomer in this work shows essentially the same behavior in **Figure 2.3d**. On the other hand, the 3-ring isomer requires a collision energy of 5.8 eV to reach a similar 30% fragmentation yield. This indicates that there

must be a significant structural difference between the 3-ring and 4-ring isomers, making production of 106 Da ions a higher energy pathway in the 3-ring isomer system, *vide infra*.

2.3.2. Structural Analysis Using IM-MS and Computational Methods

Collision cross section (CCS) values were measured for the $[M + H]^+$ ions using both TWIM and DTIM instrumentation and are provided in **Table 2.1**. The number of measurements for each CCS value is shown in parentheses. Slight differences were observed for the N_2 CCS values between the two instrument platforms most likely reflecting the chemical mismatch of the TAA calibration standards used for TWIM CCS measurements. As discussed in our previous study, these differences likely reflect the exposure of the proton charge on the MDA molecules, which would result in stronger inelastic interactions with the N_2 buffer gas, as compared to the charge-shielded tetraalkylammonium salts used for calibration. Of particular note is the second conformation observed in the mobility spectrum for 4-ring MDA using the TWIM (199.5 \AA^2) but not observed in the DTIM analysis. This is reflective of the gas phase stability of these ions; the temperature of the DTIM ion source ($225 \text{ }^\circ\text{C}$) probably causes thermal depletion of the more labile species, which is not depleted in the lower temperature TWIM ion source ($80 \text{ }^\circ\text{C}$). CCS values were also obtained in helium in order to provide better comparison with the theoretical CCS values calculated for the computationally generated conformations. Alignment of theoretical and experimental data in both helium and nitrogen drift gases is available in the **Supporting Information, Figures B.3 and B.4**.

The TWIM, IM traces obtained in nitrogen shown in **Figure 2.4a** indicate two conformations for both the 3-ring and 4-ring MDA species. The larger CCS conformation observed for the 3-ring MDA species is much less abundant than the smaller CCS conformation, accounting for ~2%. For the 4-ring MDA, the larger CCS conformation is more abundant than the smaller CCS conformation, the latter accounting for ~8% of the intensity. The IM-MS/MS structural depletion study in **Figure 2.3** shows the stability of these conformations at varying

collision energies. The mobility profiles were obtained at increasing collision energies to compare the depletion rates of the precursor ions. Only the smaller CCS 3-ring MDA conformation appears once collision energy is applied (**Figure 2.3a**) compared to the IM trace with no collision energy (**Figure 2.4a**). The two conformations for the 4-ring MDA are visible for all collision energies used. **Figure 2.3b** also shows that the larger CCS conformation of the 4-ring MDA decreases at a much faster rate (100% to 52% to 6%) than the smaller CCS conformation (100% to 73% to 43%) indicating that the species having the larger CCS conformation is less stable than species represented by the smaller CCS. Although we ascribe the rate of fragmentation to directly depend on the conformational state of the precursor, or directed thermodynamically, we cannot rule out minor influence arising from proton mobility.

In order to facilitate direct comparison between the 3-ring and 4-ring MDA structures, the COM collision energies are considered. Using COM energies, the 1.2 eV in the middle panel for the 3-ring MDA can be compared with the 1.3 eV in the bottom panel for the 4-ring MDA, showing that the 3-ring and smaller 4-ring MDA CCS conformations decrease at similar percentages (~50%) which suggests that the two have similar structural conformations. It is also worth noting that the depletion rates do not mimic those observed for the 4,4', 2,2', or 2,4' 2-ring MDA isomers from our previous paper. This observation suggests two differences between the 2-ring MDA isomers and 3-ring and 4-ring MDA. First, from our earlier paper, the 4,4'-MDA 2-ring isomer has the same $[M + H]^+$ intensity at 0.0 and 1.7 eV and decreased only to 46.2% at 4.2 eV. In this work the 3-ring isomer $[M + H]^+$ intensity in **Figure 2.3a** is reduced to 13.2% at 1.7 eV, while the major 4-ring isomer peak shows only 6.1% at 1.3 eV in **Figure 2.3b**. This suggests that, although the 4,4'-MDA 2-ring, the 3-ring, and the 4-ring isomers all have terminal para-amino groups, different processes dominate fragmentation for the higher order multimers which are characterized by the m/z 211 and 106 fragments. Second, the behavior of the lower abundance peak in **Figure 2.3b** extrapolates to a value of about 25% intensity for the energy of 1.7 eV, a behavior comparable to that of the 2,2'- and 2,4'-MDA 2-ring isomers from our earlier study.

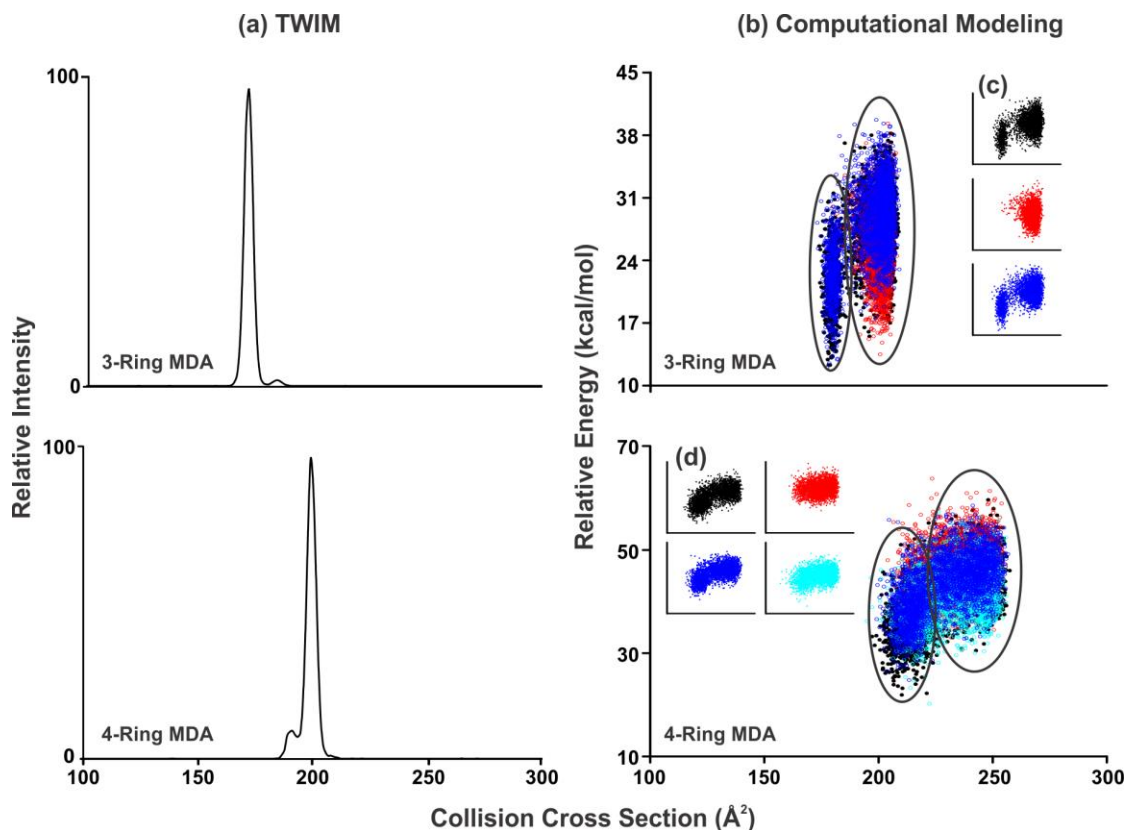


Figure 2.4. (a) CCS profiles for 3-ring MDA (top) and 4-ring MDA (bottom) extracted from TWIM data. (b) Conformational space plots for the possible protonation sites of 3-ring MDA (top) and 4-ring MDA (bottom) generated using computational conformational search methods. The theoretical nitrogen CCS is plotted against the relative energy for each conformation. Theoretical conformations for each protonation site are black, red, and blue, respectively, across the structure depicted in **Figure 2.1** for the 3-ring MDA and black, red, cyan, and blue, respectively, across the structure for the 4-ring MDA. Insets of the conformations resulting from individual protonation species are shown in (c) and (d) to clarify the conformational clusters present on each plot.

These observations indicate that fragmentation of the 3-ring and 4-ring isomers must be dominated by the internal amine group(s), leading to lower energy pathways, *vide infra*.

Computational modeling generates theoretical structures that can be aligned with the experimental data according to their CCS values. This gives insight into the conformations that were observed experimentally and why a difference in stability is observed. For both 3-ring and 4-ring MDA, the structures shown in **Figure 2.1a** were modeled separately with an additional proton for each possible protonation site. This resulted in 3 unique starting structures for the 3-ring MDA and 4 unique starting structures for the 4-ring MDA. The conformational space plots based on the molecular dynamics conformational space sampling simulations are shown in **Figure 2.4b**. The overlaid colors on the conformational space plots represent independently modeled protonation sites, with the color scheme following protonation on the amine nitrogen from left to right across the structures shown in **Figure 2.1a**. For the 3-ring MDA, the protonation sites are indicated in black, red, and blue, respectively, across the structure, and for the 4-ring MDA the protonation sites are indicated in black, red, cyan, and blue, respectively, across the structure. **Figure 2.4c,d** show the results from each independently modeled protonation site that are combined in **Figure 2.4b**. Conformation space plots for each protonation site for both helium and nitrogen exhibit similar distributions as seen in the **Supporting Information, Figures B.3** and **B.4**. The plots in **Figure 2.4b** show two distinct conformational clouds indicated with the black circles for both the 3-ring and 4-ring MDA, which agrees with the experimental bimodal IM traces in **Figure 2.4a**.

Figure 2.5 shows selected conformations based on root mean squared deviation (RMSD) clustering and alignment with experimental CCS values. Each conformation is labeled with its theoretical CCS value along with the percentage of conformations that the structure represents based on RMSD clustering analysis. Each conformation shown represents a different protonation site and thus a separately modeled set of conformations. The percentage indicates how representative the conformation shown is of the independently modeled protonation sites and

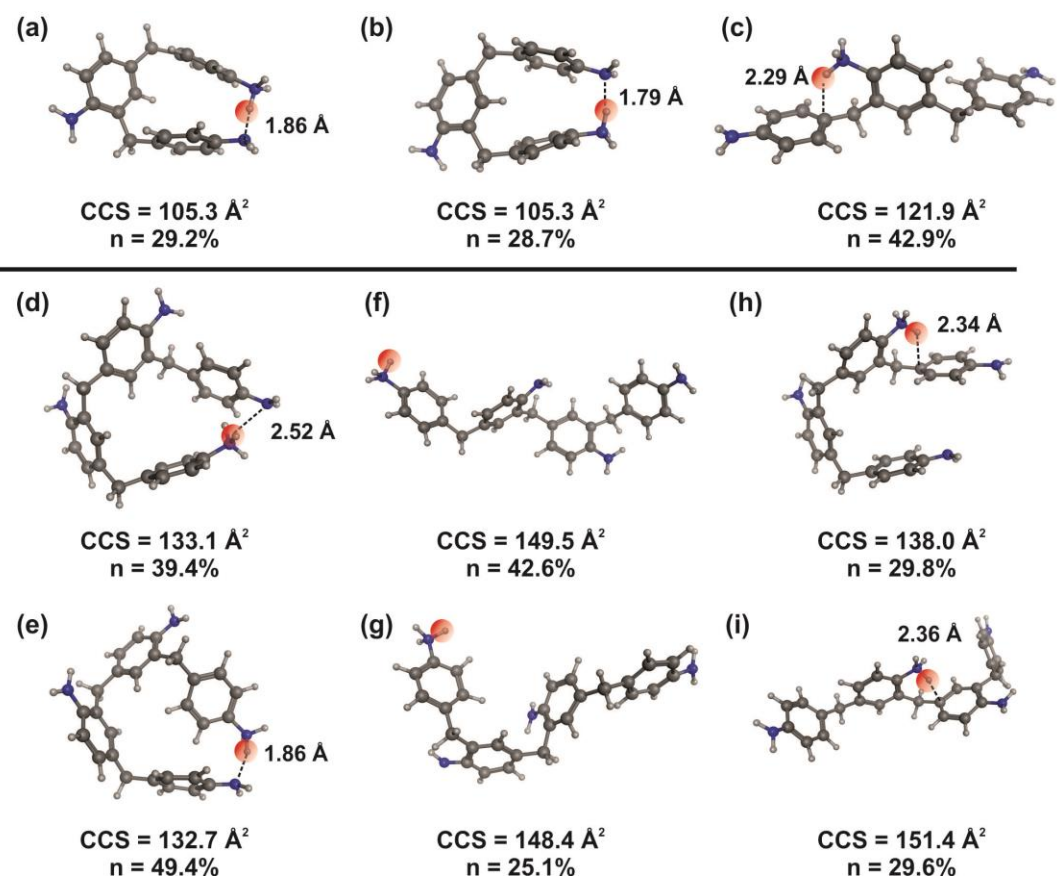


Figure 2.5. RMSD clustering representatives from computational conformational sampling are shown for each of the protonation sites for the 3-ring MDA (**a–c**) and for the 4-ring MDA (**d–i**). Labeled bond distances are used to show the proximity of the additional proton to the terminal nitrogen or bridging carbon that would lead to a 1,5-hydrogen shift fragmentation.

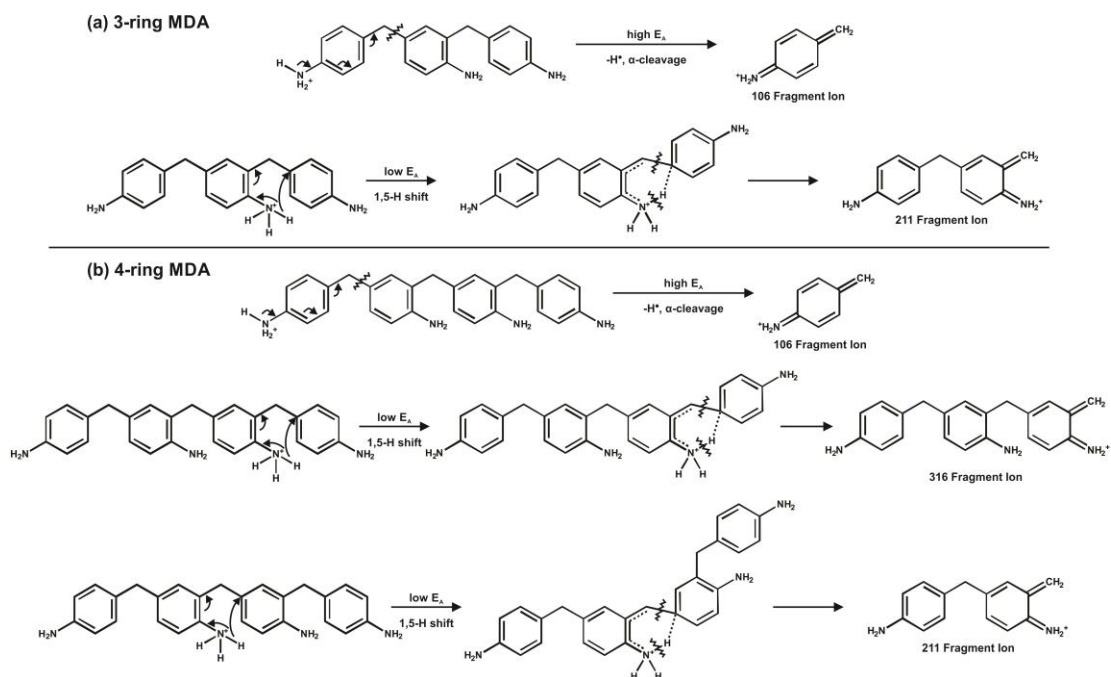
therefore does not show relations between the conformations in **Figure 2.5** since each of these protonated species was modeled separately. A comprehensive set of representative conformations that were generated for each protonation site can be found in the **Supporting Information, Figures B.7–B.31**.

Conformations for the 3-ring MDA are shown in **Figure 2.5a–c**. The conformations in **Figure 2.5a,b** represent the smaller CCS conformational space cluster and are the result obtained when protonation occurs at the amines on the terminal rings. These conformations agree with experimental CCS helium values obtained on the DTIM instrument (**Table 2.1**) and are the most representative structures based on RMSD clustering analysis. The smaller CCS, and more stable conformation of the 3-ring MDA, reflects the structure in which the two external amine groups share the additional proton. Likewise, the conformation in **Figure 2.5c** is representative of protonation on the internal amine and aligns with the larger CCS conformational space cluster for the 3-ring MDA (**Figure 2.4b**). This conformation is a cluster representative structure but due to gas-phase stability does not have a corresponding experimental CCS value from the DTIM instrument. Given that the CCS value we observe experimentally for the 3-ring MDA aligns with the smaller CCS conformational cluster, we surmise that the larger experimental CCS value corresponds to the larger CCS conformational space cloud. The position of the proton on the internal amine is very similar to that of protonation on both the 2,2' and 2,4' 2-ring MDA species when protonation occurs on the *ortho* amine. It is also important to note that this additional proton on the amine is aligned in an energetically favorable position with the most basic region of the adjacent aniline ring.

For the 4-ring MDA, two conformational clusters exist in **Figure 2.4b** with representative structures shown in **Figure 2.5d–i**. The conformations in **Figure 2.5d,e** are representative of the smaller CCS cluster, in agreement with **Table 2.1**, and represent conformations that are protonated on the external amines. Protonation at the periphery of the molecule form smaller CCS conformations, similar to the 3-ring MDA, that wrap around and share the proton between the

two external amine groups. The conformations in **Figure 2.5f–i** are representative of the larger CCS cluster, for which there are two possibilities. The first is shown in **Figure 2.5f,g** where protonation occurs on the external amines, similar to the conformations in **Figure 2.5d,e**, but here the conformation remains in an extended form rather than forming a cyclic species to share the proton. **Figure 2.5h,i** shows the other possibility where protonation occurs on one of the two internal amines. Again, this position of the proton on the internal amine is very similar to that of protonation on both the 2,2' and 2,4' 2-ring MDA species when protonated on the *ortho* amine. This similarity suggests the 3-ring and 4-ring MDA should fragment via a similar mechanism to that of the 2-ring MDA.

There is an interesting difference in the IM intensities shown in **Figure 2.3a,b** for both the 3-ring and 4-ring MDA. As indicated above, the 3-ring MDA peak corresponding to the lower CCS structures (**Figure 2.5a,b**) is intense, whereas the lower CCS peak for the 4-ring MDA spectra (**Figure 2.5d,e**) is much lower in abundance. Also, the onset of the 106 Da fragment peak is accessed at higher collision energies for the 3-ring isomer, as seen in **Figure 2.3c**. These observations correlate well with the known behavior of macrocyclic structures. Specifically, there is an optimum size for the formation of large cyclic structures, the most stable in the range of 15 atoms in the ring.¹⁹ The cyclic 3-ring MDA structures in **Figure 2.5a,b** have 16 atoms, while the cyclic 4-ring MDA structures in **Figure 2.5d,e** are composed of 20 atoms; and thus the former should be the more stable. Compatible with this, the noncyclic structures in **Figure 2.5f,g** are prominent for the 4-ring MDA but not for the 3-ring isomer. Because of the shared hydrogen in **Figure 2.5a,b** this stability is reflected in the higher fragmentation energy required for dissociation of the 3-ring MDA. A similar effect has been noted previously for hydrogen transfer reactions in the MS/MS fragmentation of aramids.²⁰



Scheme 2.1. Proposed fragmentation pathways for 3-ring and 4-ring MDA structures.

2.3.3. Mechanism for Protonation and Fragmentation of MDA Isomers

Based on the conformational observations from both IM and theoretical simulations and the results from tandem MS studies, fragmentation mechanisms can be suggested for both the 3-ring and 4-ring MDA species. These mechanisms are shown in **Scheme 2.1**. For the 3-ring MDA, there are two fragments in the MS/MS spectra in **Figure 2.2b** at 106 and 211 Da compared to the 2-ring MDA isomers in our previous manuscript which only yielded a single fragment at 106 Da. **Scheme 2.1a** shows how both of these fragments are formed from the 304 Da precursor ion. Here, the 106 Da fragment forms via an α -cleavage reaction of the 304 Da ion that also results in the loss of a neutral 198 Da fragment that mimics the 2,4' 2-ring MDA. The conformation of the 304 Da precursor ion for this reaction is shown in **Figure 2.5a,b** and has a theoretical He CCS of 105.3 Å² which is very similar to the He experimental value in **Table 2.1** of 105.5 Å². As previously mentioned, the 15-member ring present in these conformations is energetically favorable and must therefore be opened before the α -cleavage reaction can occur. This explains why there is not significant formation of the 106 Da fragment in **Figure 2.3c** until ca. 4 eV. **Figure 2.3c** also shows that at 0 eV the 304 Da fragment is already converted to the 211 Da fragment over 70%, suggesting that this fragmentation pathway is readily accessible. This low energy 1,5 hydrogen shift mechanism was previously observed for the 2,2' and 2,4' 2-ring MDA isomers but not with protonation on an internal amine as shown here in **Scheme 2.1a** with the 3-ring MDA. Although the larger 3-ring conformation shown in **Figure 2.5c** does not have a corresponding experimental He CCS value, this conformation is assigned to the 304 Da precursor ion for the 1,5 hydrogen shift fragmentation pathway due to the location of the additional proton near the most basic site on the adjacent aniline ring. This 1,5 hydrogen shift fragmentation results in loss of neutral aniline as well as the 211 Da fragment.

For the 4-ring MDA there are three fragments present in the MS/MS spectra in **Figure 2.2b** at 106, 211, and 316 Da. **Scheme 2.1b** shows how these three fragment ions are formed from the 409 Da precursor ion. Similar to the 3-ring MDA, the 106 Da fragment forms

via a high-energy α -cleavage reaction. Also similar to the 3-ring MDA, the 4-ring MDA forms a cyclic conformation as seen in **Figure 2.5d,e** with theoretical He CCS values of 133.1 and 132.7 \AA^2 , respectively. These conformations exhibit the best agreement with the experimental He CCS value of 132.7 \AA^2 in **Table 2.1**. At 20 atoms though, these cyclic structures are no longer as energetically favored as the 3-ring MDA, and therefore the extended conformations shown in **Figure 2.5f,g** are also possible. The proposed favorability of this extended conformation is further validated by the observation that significant production of the 106 Da fragment occurs at 2.75 eV in **Figure 2.3d** compared to the 4 eV for the 3-ring MDA. Additionally, the larger CCS conformation for the 4-ring MDA is more abundant than the smaller CCS conformation in **Figure 2.4a**. **Figure 2.3d** also shows that the 409 Da precursor ion has converted to the 316 Da fragment at 94% at 0 eV. Similar to the 3-ring MDA, the low energy 1,5 hydrogen shift fragmentation mechanism is initiated by protonation on an internal amine, which is represented by the conformation in **Figure 2.5h**. This fragmentation reaction results in loss of neutral aniline as well as the 316 Da ion fragment. The 211 Da fragment of the 4-ring MDA also occurs via a 1,5 hydrogen shift initiated by protonation on an internal amine, but instead of the protonated amine being located adjacent to an external aniline this internal amine is located directly in the middle of the 4-ring MDA structure with two 2-ring MDA units on each side as shown in the conformation in **Figure 2.5i**. In order for the fragmentation mechanism to occur, a larger portion of the structure must be orientated such that the additional proton is in proximity to the most basic site on the adjacent aniline ring. This explains why significant formation of the 211 Da fragment does not occur until 2.25 eV in **Figure 2.3d**. These fragmentation mechanisms observed for the 3-ring and 4-ring MDA, which mimic the α -cleavage and 1,5 hydrogen shift observed for the 2-ring MDA isomers, will serve as the basis for characterizing larger MDA sample mixtures possessing additional internal amines which can serve as possible protonation sites.

2.4. Conclusions

In this study, 3-ring and 4-ring MDA species have been characterized using an MS-based analytical approach. We conclude that the protonation sites for the 3-ring and 4-ring MDA regioisomers are only at the amine group. Additionally we determined that protonation on either external or internal amine groups greatly influences the gas-phase stability of these species. The use of MS/MS, IM-MS, and computational modeling allowed for the structural characterization of these gas-phase ions and further promotes the benefit of combining several different MS-based technologies for comprehensive characterization studies.

These larger MDA units are composed primarily of linking anilines with the amine group in the para position to the bridging carbon but do not maintain the gas-phase stability of the 4,4'-MDA due to possible protonation on internal amine groups, leading to charge-directed fragmentation of the 3-ring and 4-ring MDA. A thorough understanding of the fragmentation mechanisms initiated by internally protonated amines for both the 3-ring and 4-ring MDA will greatly facilitate the interpretation of fragmentation spectra of the larger MDA units which are expected to dissociate via similar mechanisms. Further studies on larger MDA units will allow us to observe if this trend continues as chain length increases or if other, more stable attachment patterns form. Understanding that these chains fragment easily when protonated on internal amines will prove helpful when identifying the structures of precursor and fragment ions with MS. Tandem MS studies will provide fragmentation titration curves that can be compared to those for the 2-, 3-, and 4-ring MDA to determine if ions formed from the larger MDA units fragment via similar pathways. IM and theoretical simulations have been demonstrated to separate different protonation sites for the 2-, 3-, and 4-ring isomers and should help to identify different conformers in mixtures of larger MDA species, where the structural heterogeneity is more diverse.

2.5. Acknowledgment

The authors thank Dr. Stefan Wershofen for providing 3-ring and 4-ring MDA samples. We also acknowledge the characterization support of Dr. Don Stec and the Vanderbilt NMR facilities, which is supported by the National Institutes of Health (NIH, grant award number S10 RR019022). Additionally, we acknowledge the Vanderbilt Center for Structural Biology and Dr. Terry Lybrand for computational support and the Searle Systems Biology and Bioengineering Undergraduate Research Experience (SyBBURE) Program for summer support for N.W.K. and T.M.O. This research was funded by the Defense Threat Reduction Agency under Grants HDTRA1-09-1-00-13 and the National Institutes of Health UH2RT000491.

2.6. References

1. Wang, C.Y.; Li, H.Q.; Wang, L.G.; Cao, Y.; Liu, H.T.; Zhang, Y. Insights on the mechanism for synthesis of methylenedianiline from aniline and formaldehyde through HPLC–MS and isotope tracer studies. *Chin. Chem. Lett.*, 2012, 23 (11), 1254-1258.
2. Eifler, W.; Ick, J. U.S. Patent 4,189,443, February 19, 1980.
3. Chattopadhyay, D.K.; Raju, K.; Structural engineering of polyurethane coatings for high performance applications. *Prog. Polym. Sci.*, 2007, 32 (3), 352-418.
4. Perego, C.; Angelis, A. U.S. Patent 20,030,171,619, September 11, 2003.
5. Forsythe, J.G.; Stow, S.M.; Nefzger, H.; Kwiecien, N.W.; May, J.C.; McLean, J.A.; Hercules, D.M. Structural characterization of methylenedianiline regioisomers by ion mobility-mass spectrometry, tandem mass spectrometry, and computational strategies: I. Electrospray spectra of 2-ring isomers. *Anal. Chem.*, 2014, 86 (9), 4362-4370.
6. Rappoport, Z. *The Chemistry of Anilines*; John Wiley & Sons: Chichester, UK, 2007.
7. Tsaprailis, G.; Nair, H.; Somogyi, Á.; Wysocki, V.H.; Zhong, W.; Futrell, J.H.; Summerfield, S.G.; Gaskell, S.J. Influence of secondary structure on the fragmentation of protonated peptides. *J. Am. Chem. Soc.*, 1999, 121 (22), 5142-5154.
8. Wesdemiotis, C.; Solak, N.; Polce, M.J.; Dabney, D.E.; Chaicharoen, K.; Katzenmeyer, B.C. Fragmentation pathways of polymer ions. *Mass Spectrom. Rev.*, 2011, 30 (4), 523-559.
9. Li, X.; Guo, L.; Casiano-Maldonado, M.; Zhang, D.; Wesdemiotis, C. Top-down multidimensional mass spectrometry methods for synthetic polymer analysis. *Macromolecules*, 2011, 44 (12), 4555-4564.
10. Laphorn, C.; Dines, T.J.; Chowdhry, B.Z.; Perkins, G.L.; Pullen, F.S. Can ion mobility mass spectrometry and density functional theory help elucidate protonation sites in 'small' molecules?. *Rapid Commun. Mass Spectrom.*, 2013, 27 (21), 2399-2410.

11. Tintaru, A.; Chendo, C.; Wang, Q.; Viel, S.; Quéléver, G.; Peng, L.; Posocco, P.; Priel, S.; Charles, L.; Conformational sensitivity of conjugated poly (ethylene oxide)-poly (amidoamine) molecules to cations adducted upon electrospray ionization—A mass spectrometry, ion mobility and molecular modeling study. *Anal. Chim. Acta*, 2014, 808, 163-174.
12. Ruotolo, B.T.; Benesch, J.L.; Sandercock, A.M.; Hyung, S.J.; Robinson, C.V.; Ion mobility–mass spectrometry analysis of large protein complexes. *Nat. Protoc.*, 2008, 3 (7), 1139-1152.
13. Sleno, L.; Volmer, D.A. Ion activation methods for tandem mass spectrometry. *J. Mass Spectrom.*, 2004, 39 (10), 1091-1112.
14. May, J.C.; Goodwin, C.R.; Lareau, N.M.; Leaprot, K.L.; Morris, C.B.; Kurulugama, R.T.; Mordehai, A.; Klein, C.; Barry, W.; Darland, E.; Overney, G.; Conformational ordering of biomolecules in the gas phase: nitrogen collision cross sections measured on a prototype high resolution drift tube ion mobility-mass spectrometer. *Anal. Chem.*, 2014, 86 (4), 2107-2116.
15. Case, D. A.; Babin, V.; Berryman, J.; Betz, R. M.; Cai, Q.; Cerutti, D. S.; Cheatham, T. E., III; Darden, T. A.; Duke, R. E.; Gohlke, H. et al. *AMBER 14*; University of California: San Francisco, CA, **2014**.
16. Mesleh, M.F.; Hunter, J.M.; Shvartsburg, A.A.; Schatz, G.C.; Jarrold, M.F. Structural information from ion mobility measurements: effects of the long-range potential. *J. Phys. Chem.*, 1996, 100 (40), 16082-16086.
17. Shvartsburg, A.A.; Jarrold, M.F. An exact hard-spheres scattering model for the mobilities of polyatomic ions. *Chem. Phys. Lett.*, 1996, 261 (1), 86-91.
18. Campuzano, I.; Bush, M.F.; Robinson, C.V.; Beaumont, C.; Richardson, K.; Kim, H.; Kim, H.I. Structural characterization of drug-like compounds by ion mobility mass

spectrometry: comparison of theoretical and experimentally derived nitrogen collision cross sections. *Anal. Chem.*, 2011, 84 (2), 1026-1033.

19. Wilen, S. H.; Mander, L. N.; Eliel, E. L. *Stereochemistry of Organic Compounds*; *John Wiley & Sons*: New York, **1994**.
20. Gies, A.P.; Ellison, S.T.; Stow, S.M.; Hercules, D.M. Matrix-assisted laser desorption/ionization-time-of-flight/time-of-flight collision-induced dissociation study of poly (p-phenylenediamine terephthalamide) fragmentation reactions. *Anal. Chim. Acta*, 2014, 808, 124-143.

CHAPTER III

STRUCTURAL CHARACTERIZATION OF METHYLENEDIANILINE REGIOISOMERS BY ION MOBILITY AND MASS SPECTROMETRY: III. MALDI SPECTRA OF 2-RING ISOMERS

3.1 Introduction

Previously, electrospray ionization-ion mobility-mass spectrometry (ESI-IM-MS) was used to characterize the MDA 2-ring regioisomers (i.e., 2,2'-MDA, 2,4'-MDA, and 4,4'-MDA) and larger multimeric species.^{1,2} These 2-ring MDA isomeric structures and their probable protonation sites are denoted with asterisks in **Figure 3.1**. The available protonation sites that played a critical role in our earlier manuscripts deserve repeating because they are critical for describing the gas-phase behavior of MDA. The 4,4'-MDA species can protonate only on *para*-amino groups (*p*-NH₂), whereas 2,2'-MDA can protonate at two locations: on *ortho*-amino groups (*o*-NH₂) or on the ring *para* to the *ortho*-amino group. The 2,4'-MDA species has all three types of protonation sites. The stability of these ions was monitored in ESI by measuring the degree of fragmentation of the parent ion ($[M+H]^+ = 199$ Da) to form the characteristic 106 Da fragment ion. 4,4'-MDA (double *para*-substituted) proved to be much more stable than either 2,2'-MDA (double *ortho*-substituted) or 2,4'-MDA (combined *ortho*- and *para*-substituted) isomers. These findings were supported experimentally by MS, MS/MS, IM-MS, and computational modeling.

In the present study, 2-ring MDA isomers were characterized using matrix assisted laser desorption/ionization (MALDI), a technique commonly used in MS analysis of polymers³⁻⁶ including polyurethanes.^{7,8} The differences between ESI and MALDI are widely understood in the MS and analytical communities.^{9,10} Both are soft ionization sources (i.e., generally retaining structural integrity of the ion of interest), and frequently form the same parent ions. However, the laser-induced MALDI process can be more energetic, thus generating different precursor ions

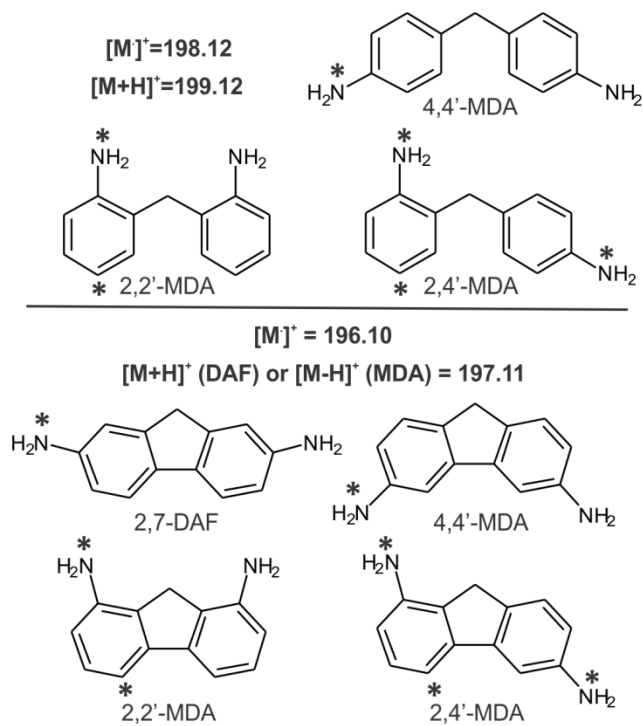


Figure 3.1. MDA 2-ring isomers and 2,7-DAF. Neutral molecular masses (M) are shown along with those for $[M+H]^+$ (2,7-DAF) and $[M-H]^+$ (MDA) ions. Possible protonation sites are noted with an asterisk (*).

than those produced by ESI. We have observed the formation of two unique precursor ions $[M-H]^+$ = 197 Da and $[M]^+$ = 198 Da, and suggest that they result from the MALDI process in addition to the $[M+H]^+$ = 199 Da species observed alone in ESI. MS/MS, IM-MS, and computational strategies were utilized to characterize these new precursor ion species.

3.2 Experimental Section

Materials

Sample preparation and experimental parameters have been previously described in detail for ESI studies, but a few details will be mentioned here¹. Methylenedianiline (MDA) 2-ring isomers (2,2'-MDA, 2,4'-MDA, and 4,4'-MDA) were provided by Dr. Stefan Wershofen (Bayer MaterialScience AG, 47812 Krefeld, Germany). Methanol and water with 0.1% formic acid were obtained from Fisher Scientific (Waltham, MA). Tetralkylammonium salts, α -cyano-4-hydroxycinnamic acid (CHCA), alkali salts, and 2,7-diaminofluorene (2,7-DAF) were obtained from Sigma-Aldrich (St. Louis, MO). Samples were dissolved at a concentration of 1 mg/mL in 9:1 methanol/water containing 0.1% formic acid (v/v). Each MDA isomer was combined in a 10:1 matrix-to-analyte ratio and 2 to 3 layers of 0.5 μ L of sample were spotted on a 100-well MALDI plate.

Traveling Wave MALDI-IM-TOF/MS

A traveling wave IM-MS (TWIM-MS, Synapt G2-S, Waters Corporation, Milford, MA) with interchangeable MALDI and ESI sources was used to acquire MS, IM-MS, and MS/MS data either before or after the IM region.¹¹ Although collision cross section (CCS) values cannot be obtained directly from TWIM experimental drift time values, a relative CCS method that uses quaternary ammonium salts as CCS calibration standards was utilized to obtain CCS data from TWIM.¹²⁻¹⁴

The MALDI source for the Synapt G2-S mass spectrometer features a frequency-tripled Nd:YAG laser which emits 355 nm at a 1 kHz pulse repetition rate. Laser attenuation ranged from 190 to 300 (arbitrary units), with 270 selected for all experiments unless otherwise noted. TOF calibration was performed using CHCA matrix cluster peaks. The TWIM drift cell settings were as follows: TWIM pressure 3 mbar nitrogen (2.25 Torr), electrodynamic wave height 35 V, wave velocity 700 m/s, TOF resolving power ca. 18,000 $m/\Delta m$ at 200 m/z . Collision-induced dissociation (CID) experiments were performed using argon as the target gas. The mass resolving quadrupole was set to 18 resolving power for the MS/MS experiments. This provided the best separation of the three precursor ion species without significant signal loss. Experiments were conducted to evaluate the influence of the MALDI laser fluence and the resolving power of the MS/MS resolving quadrupole on the resulting intensities of the precursor ions and these results have been included in the **Supplemental Information, Figure C.10**. The results of these experiments demonstrate that the resolving quadrupole can efficiently separate the three precursor ions and that laser fluence does not affect the relative intensities of the three different ion forms.

Computational Methods

To gain more insight into the experimental results, both a molecular dynamics conformational sampling calculation and quantum mechanical bond energy calculations were performed. A detailed description of the methods used can be found in the **Supporting Information** as well as in previous manuscripts, but briefly, a simulated annealing calculation implemented in AMBER¹⁵ was used to sample the conformational space of the $[M-H]^+$, and $[M+H]^+$ cations for the 2-ring MDA isomers. Corresponding theoretical CCS values were then obtained from MOBCAL¹⁶⁻¹⁸ and PSA¹⁹⁻²² to align the computationally generated structures with the experimental CCS measurements. Bond energy calculations were performed with Gaussian09²³ using density functional theory (DFT) to calculate the energy of the geometry optimized precursor and each of the two fragment structures resulting from breaking the bond of

interest. The energies of the two fragments were summed and subtracted from the energy of the precursor structure resulting in the energy change of the reaction or relative bond energy of the broken bond. DFT/B3LYP/6-31G* level of theory was used for all calculations, which were performed *in vacuo* and in the ground state.

3.3 Results and Discussion

Differences Between ESI and MALDI Spectra for $[M+H]^+$

MS/MS spectra acquired at a fixed collision energy of 25 eV laboratory frame for $[M+H]^+$ MDA regioisomers are compared in **Figure 3.2** for ESI and MALDI. The MS/MS spectra are shown for ESI on the left panels (**Figure 3.2a-c**) and for MALDI on the right panels (**Figure 3.2d-f**). The ESI and MALDI spectra for 4,4'-MDA (**Figure 3.2a,d**) are qualitatively identical in that 106 Da is the prominent fragment ion and additional low abundance peaks are observed at 182 and 165 Da in both spectra. In contrast, the ESI and MALDI spectra for 2,2'- and 2,4'-MDA exhibit significant differences in the fragment ions observed. For 2,2'- and 2,4'-MDA, the ESI MS/MS spectra (**Figure 3.2b,c**) exhibit a single major fragment ion peak at 106 Da and, unlike 4,4'-MDA, no ion signals are observed at 199 Da. The 2,2'- and 2,4'-MDA MALDI spectra (**Figure 3.2e,f**) are significantly more complex than ESI, with fragment ions observed at 198, 182, 181, 180, and 106 Da. These differences observed for the $[M+H]^+$ ion along with additional precursor ions indicate that these MDA regioisomers behave significantly differently when ionized by MALDI than with ESI.

Characterization of 2-Ring MDA by MS and MS/MS

Figure 3.3 shows the MALDI MS/MS spectra for the two additional precursor ions species ($[M-H]^+$ and $[M]^+$) for the MDA isomers and corresponding MS/MS spectra for a standard 2,7-diaminofluorene (2,7-DAF). Results for 2,7-DAF are shown in parallel with the MDA regioisomers due to its known fluorene backbone structure which we hypothesize to be the

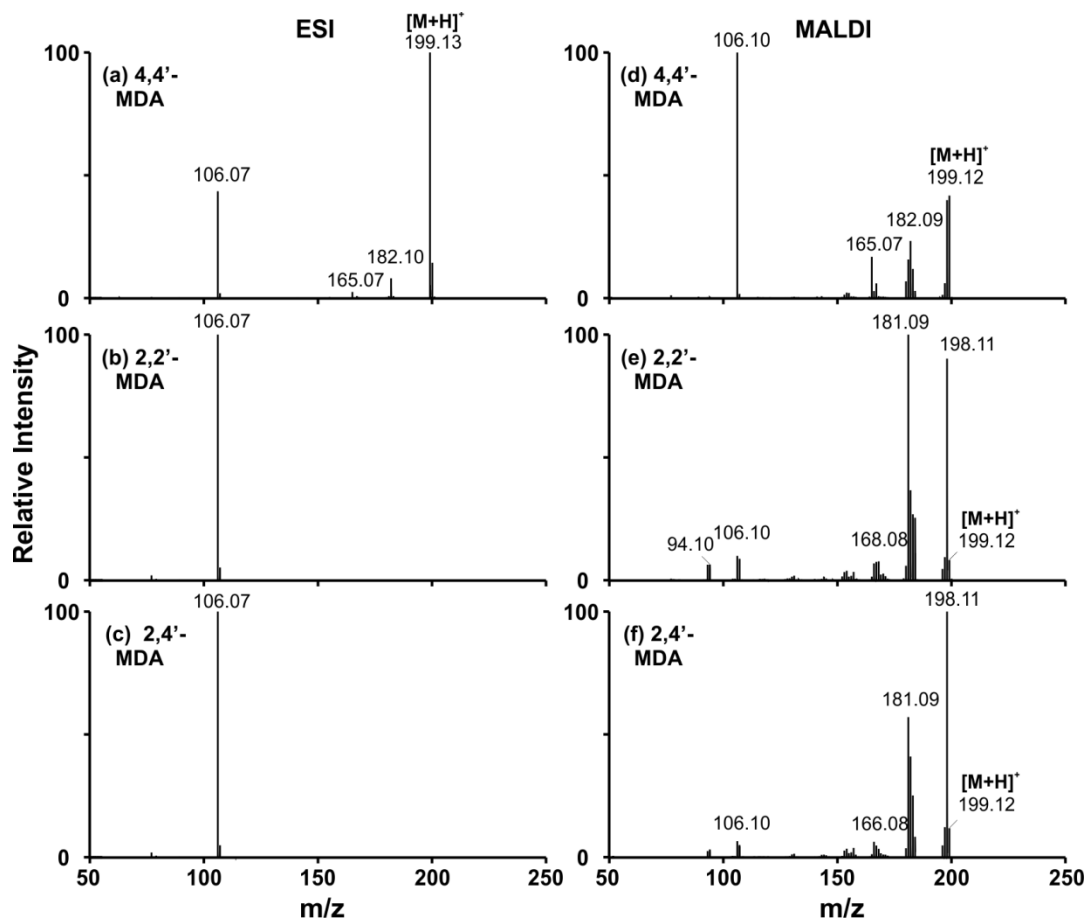


Figure 3.2. MS/MS spectra for the $[M+H]^+$ isomer species for both (left) ESI and (right) MALDI. Results for 4,4'-MDA are shown in (a) and (d), for 2,2'-MDA in (b) and (e) and for 2,4'-MDA in (c) and (f). These spectra were obtained at 25 eV lab frame energy.

structure of the $[M-H]^+$ species (**Figure 3.1**). It is important to note that the 2,7-DAF species shown in **Figure 3.3a** is the $[M+H]^+$ species while the spectra shown in **Figure 3.3b-d** are the $[M-H]^+$ species. All species shown in **Figure 3.3e-h** correspond to the $[M]^+$ species, but the 2,7-DAF precursor in **Figure 3.3e** is 196 Da, whereas the MDA precursors in **Figure 3.3f-h** are 198 Da. Additional MS and MS/MS spectra can be found in the **Supporting Information (Figures C.1-C.9)** including MS/MS of fragments that result from operating with high (350 arbitrary units) laser fluence. The MS/MS spectra in **Figure 3.3** were acquired at 25 eV and show fragments in many of the same regions that were observed in **Figure 3.1** for the $[M+H]^+$ species. These fragment ions fall into four groups: 196-198 Da, 180-183 Da, 152-153 Da and 106 Da. The first group corresponds to a loss of one H-atom (1 Da) from the parent ion. The second fragment ion group represents nominal losses involving the loss of NH (15), NH₂ (16), NH₃, (17) or NH₄ (18). The third group involves nominal losses of both amino groups and an additional carbon atom. The fourth group of fragment ions corresponds to formation of a 106 Da fragment that has been previously discussed in earlier manuscripts. These four fragment ion groups are observed for the $[M+H]^+$, $[M-H]^+$, and the $[M]^+$ isomer species, but at very different intensities.

The MS/MS spectrum for 2,7-DAF in **Figure 3.3a** shows major fragment peaks at 196 Da, 180 Da and 181 Da. The $[M-H]^+$ MDA regioisomers all primarily form a 180 Da fragment in substantial amounts, but again the 4,4'-MDA is more stable in **Figure 3.3b** as significant depletion of the precursor ion occurs in **Figure 3.3c,d** at 25 eV for both the 2,2'-MDA and 2,4'-MDA. Both 2,2'-MDA and 2,4'-MDA $[M-H]^+$ ions exhibit far less of the 181 Da ion than that of 4,4'-MDA. The $[M]^+$ species form a combination of all the fragments previously mentioned for $[M+H]^+$ and $[M-H]^+$. The MS/MS spectra of the 196 Da peak for 2,7-DAF in **Figure 3.3e** has fragment peaks at 195 and 180 Da. The MS/MS spectra for the MDA isomers (**Figure 3.3f-h**) show an additional peak at 106 Da, along with some minor peaks. This suggests that while the $[M-H]^+$ MDA ion behaves similarly to the 2,7-DAF $[M+H]^+$ ion, the $[M]^+$ species does not. As observed with the other ion forms, the $[M]^+$ of 4,4'-MDA exhibits greater stability than either

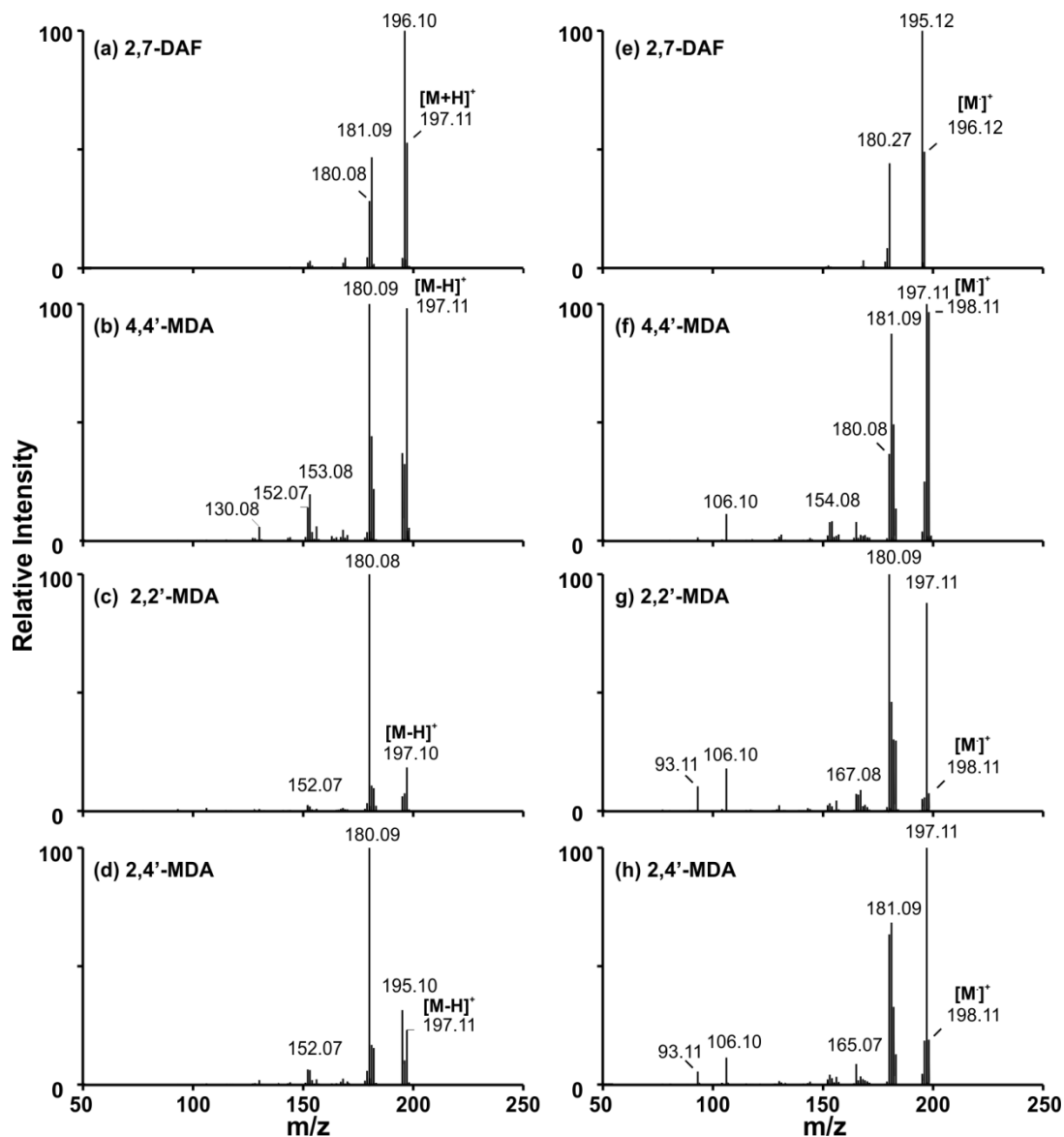


Figure 3.3. MALDI MS/MS spectra for the (left) 197 Da precursor and (right) $[M]^+$ isomer species for MALDI. Results for 2,7-DAF are shown in (a) and (e), for 4,4'-MDA in (b) and (f), for 2,2'-MDA in (c) and (g) and for 2,4'-MDA in (d) and (h). These spectra were obtained at 25 eV lab frame energy.

2,2'-MDA or 2,4'-MDA isomers as evidenced by a more prominent 198 Da precursor peak (**Figure 3.3f**). 2,2'-MDA forms a majority of a 180 Da fragment in **Figure 3.3g** and 2,4'-MDA forms primarily a 197 Da fragment and similar amounts of both the 180 and 181 Da fragments in **Figure 3.3h**. 4,4'-MDA produces significantly more of the 181 Da fragment than the other isomers, which suggests that preference for the 181 Da fragment arises from *para* amino substitution, and that the 180 Da fragment correlates predominantly with the *ortho*-amino group. The 106 Da fragment is also present in the $[M]^+$ MS/MS spectra, but not in the $[M-H]^+$ MS/MS spectra. Because there are numerous fragment ions which originate from three different precursor ions for each of the three different MDA regioisomers, the methods used to interpret and organize the data will be introduced briefly before detailed discussions of relative fragment ion intensities and fragmentation pathways resume.

While MS/MS spectra highlight the major fragment ions for each of these species, they offer only a snapshot of the numerous fragmentation experiments performed to better understand these different precursor ion species. MS/MS experiments were ramped from 0-50 eV for the three precursor ions for each of the MDA regioisomers in 5 eV increments and this energy correlation experiment (99 spectra) was performed in triplicate. Ion collision-energy curves corresponding to the change in percent relative ion current (%RIC) for the $[M+H]^+$, $[M-H]^+$, and $[M]^+$ ion forms of the MDA isomers are shown in **Figures 3.4a-c** for fragment ions exhibiting a %RIC of 20% or more along the 0-50 eV ramp. For clarity, the average %RIC of the three different isomers are shown here as solid traces, except the $[M+H]^+$ ion of 4,4'-MDA which exhibits different behavior (discussed later) and is represented by a dashed line in **Figure 3.4a**. Individual curves for each isomer, along with error bars, are provided as **Supporting Information (Figure C.10)**. Note that the percentage values projected on the y-axes of **Figure 3.4** are relative to other ions which appear in the plot. Collision curves for all fragment ions present at %RIC values of 5% or more along the 0-50 eV ramp are included as **Supporting Information (Figures C.11-C.15)**.

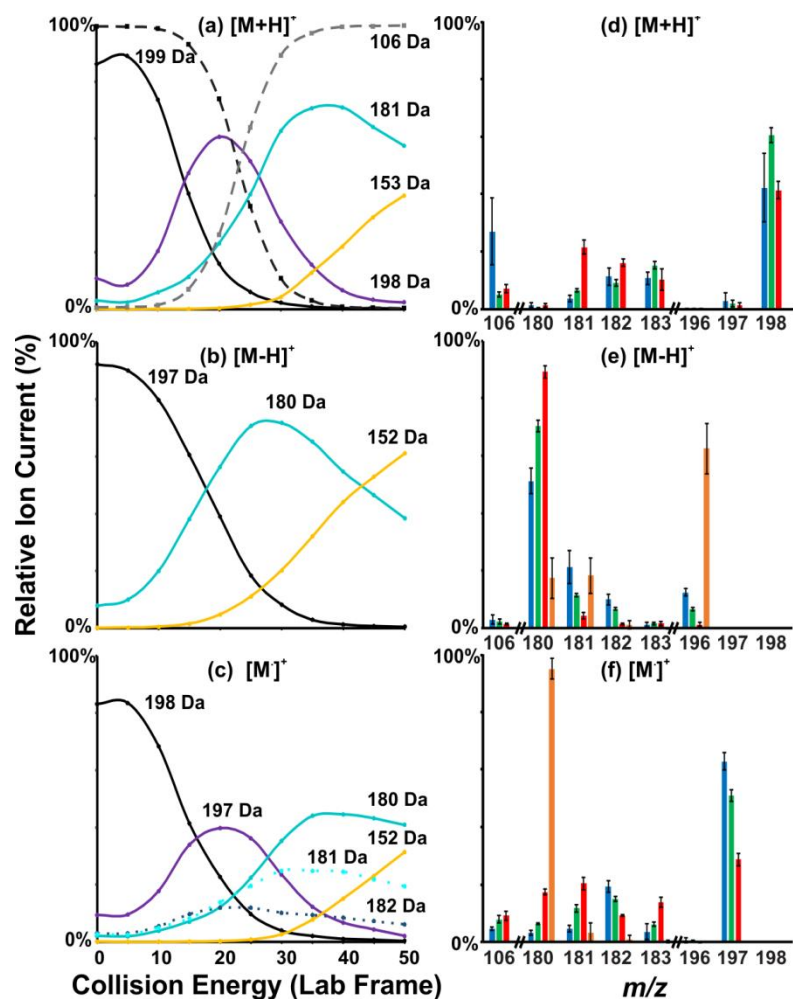


Figure 3.4. Collision induced dissociation curves monitoring the transition of precursor to fragment ions for (a) $[M+H]^+$ ions, (b) $[M-H]^+$ ions, and (c) $[M]^+$ ions. The different line weights represent the average of all three isomers (solid); the 4,4'-MDA isomer for the protonated species (dashed); and secondary fragments for the radical cation species (dotted). Color coding is for precursor ions (black); the M-1 species (purple); the M-17 and M-18 species (teal); the M-45 and M-46 species (yellow); the M-93 species (gray); and the M-15 and M-16 species (cyan and navy). Bar graphs of %RIC at low collision energies are shown for (d) $[M+H]^+$, (e) $[M-H]^+$, and (f) $[M]^+$ ion species. The bar colors correspond to 4,4'-MDA (blue); 2,2'-MDA (red); 2,4'-MDA (green); and 2,7-DAF (orange).

Figure 3.4d-f and **Table 3.1** provide detailed %RIC data for the three precursor species, 4,4'-MDA (blue), 2,4'-MDA (green), and 2,2'-MDA (red), averaged over 0, 5, and 10 eV. At these low collision energies, the six fragment ions of interest are: 198 Da ($[M-1]^+$), 180-183 Da ($[M-18]^+$, $[M-17]^+$, $[M-16]^+$, and $[M-15]^+$) and 106 Da ($[M-93]^+$). These eight ions constitute greater than 95% of the total ion currents observed across all low energy spectra and thus participate in the primary fragmentation pathways for the MDA isomer system. A complete list of all fragment ions observed is provided as **Supporting Information (Tables C.7-C.10)**, however, the fragment ions listed here will be the main focus of discussion. Statistical significance of each of these low energy measurements across the regioisomers was determined using an analysis of variance (ANOVA) and a t-test. Briefly, ANOVA allowed for comparison across the three regioisomers for each fragment to highlight when one regioisomer had a percent relative intensity that was significantly different from the other two. A detailed summary of the ANOVA and t-test analysis is provided as **Supporting Information (Tables C.1-C.6)**.

When ANOVA testing indicates that the most abundant isomer in **Table 3.1** behaves significantly differently than the other two isomers, yellow highlighting is used. Pink highlighting in **Table 3.1** indicates that there is also a significant difference in fragment abundance between the other two isomers. For example, the mass 198 peak for $[M+H]^+$ is significantly more intense for 2,4'-MDA than for the other two isomers (which were not statistically different from one another), and 2,2'-MDA exhibits the most intense peak at 181 Da, but the other two isomers are significantly different.

$[M+H]^+$ Species

As observed in **Figure 3.2**, the MALDI MS/MS spectra are significantly more complex than the ESI MS/MS spectra for the $[M+H]^+$ ion of 2,2'-MDA and 2,4'-MDA. In contrast, the 4,4'-MDA isomer exhibits qualitatively similar spectra from both ion sources, which is due in

| Fragment Ions for [M+H] ⁺ | | | | | | | | |
|--------------------------------------|-----------------|----------------|----------------|----------------|----------------|----------------|-----------------|-----------------|
| Isomer | 106 | 180 | 181 M-18 | 182 M-17 | 183 M-16 | 196 | 197 | 198 M-1 |
| 2,2'-MDA | 7.1 ± 1.5% | 1.4 ± 0.6% | 21.7 ± 1.4% | 16.2 ± 1.4% | 10.4 ± 3.7% | 0.2 ± 0.1% | 1.4 ± 1.0% | 41.5 ± 3.1% |
| 2,4'-MDA | 5.3 ± 0.9% | 0.5 ± 0.3% | 6.7 ± 0.6% | 9.3 ± 1.2% | 15.4 ± 1.2% | 0.2 ± 0.1% | 2.0 ± 1.1% | 60.7 ± 2.6% |
| 4,4'-MDA | 27.1 ± 11.6% | 1.4 ± 0.9% | 3.9 ± 1.1% | 11.4 ± 3.1% | 10.9 ± 2.2% | 0.2 ± 0.2% | 2.8 ± 2.9% | 42.3 ± 11.9% |
| Fragment Ions for [M-H] ⁺ | | | | | | | | |
| Isomer | 106 | 180 M-17 | 181 M-16 | 182 M-15 | 183 | 196 M-1 | 197 | 198 |
| 2,2'-MDA | 1.6 ± 0.3% | 89.3 ± 2.2% | 4.3 ± 1.2% | 1.6 ± 0.2% | 1.8 ± 0.7% | 1.4 ± 0.7% | | |
| 2,4'-MDA | 2.5 ± 0.8% | 70.6 ± 2.1% | 11.5 ± 0.6% | 6.8 ± 0.5% | 1.7 ± 0.4% | 6.8 ± 0.6% | | |
| 4,4'-MDA | 3.1 ± 1.7% | 51.4 ± 4.5% | 21.5 ± 5.8% | 10.1 ± 1.8% | 1.3 ± 0.8% | 12.6 ± 1.3% | | |
| Fragment Ions for [M] ⁺ | | | | | | | | |
| Isomer | 106 | 180 M-18 | 181 M-17 | 182 M-16 | 183 M-15 | 196 | 197 M-1 | 198 |
| 2,2'-MDA | 9.4 ± 1.6% | 17.5 ± 1.0% | 20.5 ± 2.3% | 9.5 ± 0.4% | 14.0 ± 1.7% | 0.2 ± 0.1% | 28.9 ± 2.1% | |
| 2,4'-MDA | 8.1 ± 1.3% | 6.6 ± 0.3% | 11.9 ± 1.3% | 15.1 ± 0.9% | 6.4 ± 0.7% | 0.8 ± 0.2% | 51.2 ± 2.0% | |
| 4,4'-MDA | 4.8 ± 0.7% | 3.3 ± 0.9% | 4.8 ± 1.1% | 19.5 ± 2.1% | 3.8 ± 2.7% | 0.8 ± 0.8% | 63.0 ± 3.1 % | |
| Fragment Ions for 2,7-DAF | | | | | | | | |
| Standard | 106 | 180 M-17 | 181 M-16 | 182 | 183 | 196 M-1 | 197 | 198 |
| [M+H] ⁺ | 0.0 ± 0.0% | 17.6 ± 7.0% | 18.4 ± 6.1% | 1.3 ± 1.5% | 0.1 ± 0.2% | 62.6 ± 8.7% | | |
| [M] ⁺ | 0.0 ± 0.1% | 95.1 ± 3.5% | 3.5 ± 3.3% | 1.0 ± 1.6% | 0.3 ± 0.5% | | | |

Table 3.1. Percent relative ion current data for the major fragments from the [M+H]⁺, [M-H]⁺, and [M]⁺ for the three 2-ring MDA isomers and 2,7-DAF. See text for details.

part to the higher stability of the 4,4'-MDA isomer, that allows it to behave similarly despite a slightly more energetic ionization source (MALDI). Another reason for the similarities is that the 4,4'-MDA isomer can protonate only on *para* amino-groups, whereas the 2,2'-MDA and 2,4'-MDA species have additional protonation sites on the ring and on the *ortho* amino-groups (**Figure 3.1**), giving rise to the differences in MS/MS spectra seen for ESI and MALDI. The role of charge localization towards directing fragmentation processes of relatively small organic ions is well-established.²⁴

In **Figure 3.4a**, the depletion of the 199 Da parent ion (black, dashed) and the correlated increase in the 106 Da peak (grey, dashed) are consistent with the previously observed behavior of 4,4'-MDA and is due to stability and limited protonation on only the *para*-amino group. The average %RIC curves for 2,2'-MDA and 2,4'-MDA in **Figure 3.4a** clearly indicate that the 198 Da ion (purple) is derived directly from the 199 Da ion (black, solid) and that the 181 Da ion (teal) increases as both 199 and 198 Da ions decline. The 181 Da ion decreases in intensity as the 153 Da ion increases, indicating that the 153 Da ion (yellow) is derived from the 181 Da ion. On the basis of the dissociation curves in **Figure 3.4a** it appears that the 181 Da peak is generated from both the 198 and 199 Da ions. Because there are two possible protonation sites available for *ortho*-substituted MDAs, multiple pathways could occur. Based on the evidence in **Figure 3.4d** and **Table 3.1**, 2,2'-MDA (red) forms the majority of both the 181 and 182 Da fragments corresponding to mass losses of M-18 and M-17. 2,4'-MDA (green) forms the majority of both the 183 and 198 Da fragments corresponding to mass losses of M-16 and M-1. The t-test also indicates that 2,2'-MDA and 2,4'-MDA produce significantly different percentages of the 106 Da ion and that 2,4'-MDA and 4,4'-MDA produce significantly different percentages of the 181 Da ion.

[M-H]⁺ Species

Collision energy curves in **Figure 3.4b** visualize the path that the $[M-H]^+$ isomers follow from precursor to major fragment ions. With increasing collision energy, the 197 Da precursor ion (black) depletes to form the 180 Da ion (teal) which in turn depletes to form the 152 Da ion (yellow) above 30 eV. This observed two-step depletion is similar to $[M+H]^+$ (**Figure 3.4a**), but here for $[M-H]^+$ the 4,4'-MDA isomer behaves similarly to the other two MDA isomers (**Figure 3.4b** averages the %RIC obtained from all three isomers).

Low energy pathways are also examined in **Figure 3.4e** for the MDA isomers and 2,7-DAF (orange). Somewhat parallel trends are observed for 2,7-DAF and 4,4'-MDA in that both contribute to the majority of the 196 Da and 181 Da fragment ions. **Figure 3.1** shows that these two species are more similar in structure, having both of their amino groups in either the *para* or *meta* positions (no *ortho*). The 2,2'-MDA and 2,4'-MDA isomers, which have similar protonation sites, namely an *ortho* amino group and a ring, both primarily form the 180 Da ion. In addition to the ANOVA testing, the t-test applied to the results in **Table 3.1** indicate there are also significant differences between the two lesser peaks for the 196 Da, 182 Da, 181 Da, and 180 Da fragment ions. Based on the %RIC differences of the 196 Da fragment (2,7-DAF >> 4,4'-MDA > 2,4'-MDA > 2,2'-MDA), it is likely this fragmentation mechanism prefers the *para* and *meta* amino groups over the *ortho*. This trend which is repeated for the 181 Da fragment also indicates that the 181 Da fragment results from the 196 Da fragment rather than directly from the 197 Da precursor. In turn, the 180 Da fragment likely results directly from the 197 Da precursor, via neutral loss of NH_3 .

[M]⁺ Species

The $[M]^+$ radical cation peak (198 Da) appears prominently in the MALDI spectra of all MDA isomers. The question naturally arises whether it is formed by direct ionization of the parent MDA oligomer or by H-atom loss from $[M+H]^+$, or possibly by both mechanisms. Direct

ionization of aromatic molecules in MALDI, although not common, is well known.^{10,25} The 198 Da radical cation peak lies between the 197 Da ($[M-H]^+$) and 199 Da ($[M+H]^+$) peaks, both of which typically show greater intensity in the parent ion spectra. Although interference of the neighboring precursor peaks does occur, our experiments with the resolving quadrupole suggest (**Figure C.10**) that the 198 Da peak can be mass-selected with at least 85% purity from the other two species.

Figure 3.4c displays the collision energy curves for $[M]^+$ which are qualitatively similar to those observed for the $[M+H]^+$ precursor ions. The dotted lines indicate minor fragments not present at 20% but still worth noting for $[M]^+$ due to the more complex MS/MS spectra. Here, the $[M]^+$ precursor ion (198 Da, black) depletes to form directly the $[M-1]^+$ (197 Da, purple) and $[M-16]^+$ (182 Da, navy) fragment ion species. The $[M-17]^+$ (181 Da, cyan) and $[M-18]^+$ (180 Da, teal) species appear to be formed from the $[M-1]^+$ species, as their appearance coincides with the depletion of the 197 Da ion. The 180 Da ion then appears to deplete to form the 152 Da ion (yellow), which was also observed for the $[M-H]^+$ ion of all MDA isomers. An analysis of the low energy fragmentation pathways (**Figure 3.4f**) indicates the formation of fragment ions at 197, 180 to 183, and 106 Da. We also observe trends in both **Figure 3.4f** and **Table 3.1** that those fragments favoring either 2,2'- or 4,4'-MDA also occur for 2,4'-MDA. This observation is consistent with the position of amino groups and availability of ring protonation playing a primary role in fragmentation preferences.

Characterization by Ion Mobility-Mass Spectrometry and Computational Modeling

IM-MS results also indicate that the $[M-H]^+$ MDA species are similar to 2,7-DAF. The IM traces in **Figure 3.5a-c** are shown for the $[M-H]^+$ (red) and $[M+H]^+$ (black) MDA species as well as the 2,7-DAF $[M+H]^+$ (blue). For 2,2'-MDA (**Figure 3.5b**) and 2,4'-MDA (**Figure 3.5c**), the $[M-H]^+$ and $[M+H]^+$ mobility traces overlap, but for 4,4'-MDA (**Figure 3.5a**) the $[M-H]^+$

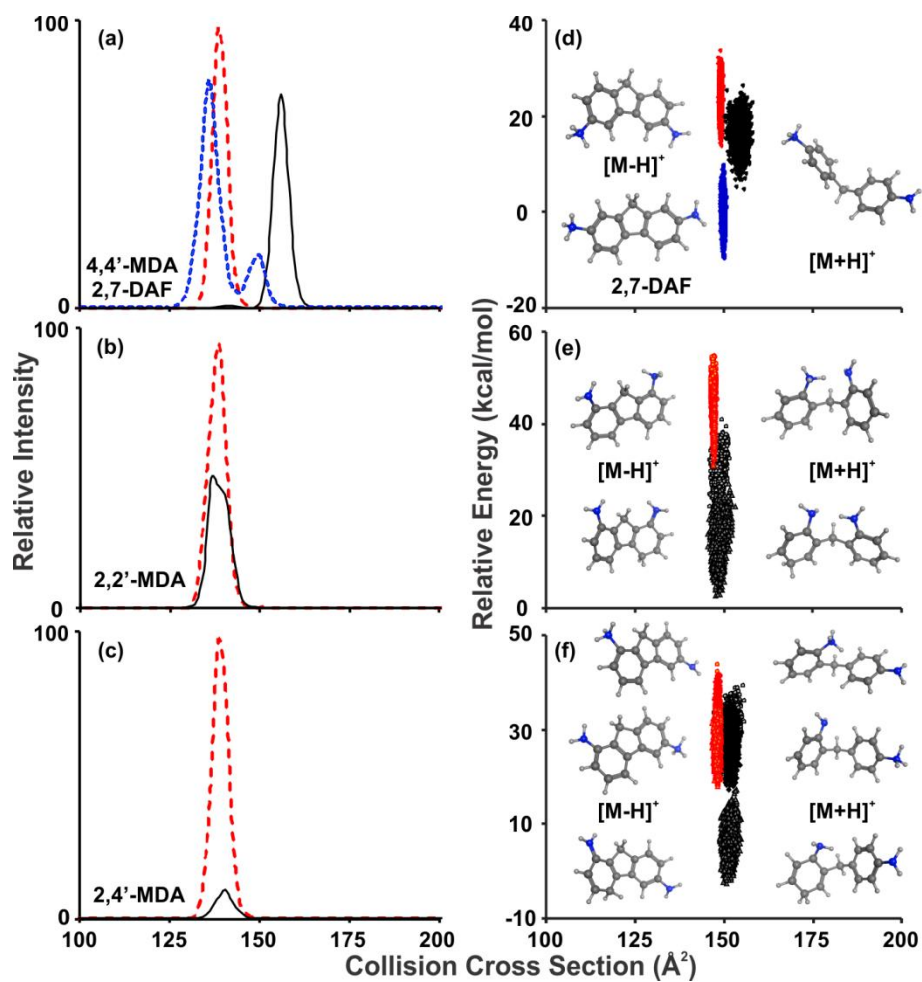


Figure 3.5. Ion mobility traces and computational modeling results for 2-ring MDA. $[\text{M}+\text{H}]^+$ results are shown in black, $[\text{M}-\text{H}]^+$ results are shown in red, and 2,7-DAF results in blue.

species has a smaller CCS than the $[M+H]^+$ species. The smaller CCS observed for the 4,4'-MDA $[M-H]^+$ species in **Figure 3.5a** also closely aligns with the mobility trace for 2,7-DAF, further evidence of the fluorene backbone for the $[M-H]^+$ MDA species. Computational modeling can provide some structural meaning to these observations. Theoretical results are shown in **Figure 3.5d-f** for the three 2-ring isomers and 2,7-DAF. The conformations resulting from simulated annealing calculations are shown for the $[M-H]^+$ (red) and $[M+H]^+$ (black) MDA species as well as 2,7-DAF (blue). **Figure 3.1** is a helpful reference for the number of protonation sites for each regioisomer since each of these is modeled separately: one for 4,4'-MDA, two for 2,2'-MDA, and three for 2,4'-MDA. Each simulated annealing calculations generate clusters of 3,000 unique structures, which in many cases overlap with one another. To avoid complete disappearance of these data points, shading has been utilized in **Figures 3.5d-f** for the various $[M+H]^+$ protonation sites including the *para* (black), *ortho* (light grey), and ring (dark grey), as well as corresponding $[M-H]^+$ charge sites for *para* (red), *ortho* (yellow), and ring (orange) locations. A separate conformational space plot is shown for each protonation site for each precursor species in the **Supporting Information (Figures C.18-C.19)**. It is also important to note that while the magnitude of the predicted CCS is larger here than what is measured experimentally, the relative ordering of theoretical CCS values is in qualitative agreement with the experimental trends observed for IM-MS. The $[M-H]^+$ conformations (red) of 4,4'-MDA, which has only a single protonation site at the *para* amine, are separated in CCS both theoretically (**Figure 3.5d**) and experimentally (**Figure 3.5a**) from the $[M+H]^+$ ions (black). The 2,7-DAF and 4,4'-MDA $[M-H]^+$ conformational space plots and mobility traces also overlap. In contrast, two protonation sites are available for the 2,2'-MDA $[M-H]^+$ and $[M+H]^+$ on both the *ortho* amine and the ring. These protonation sites not only overlap with each other, but the $[M-H]^+$ and $[M+H]^+$ also overlap for both experimental (**Figure 3.5b**) and theoretical results (**Figure 3.5e**). The reduced conformational space of the $[M-H]^+$ species becomes especially apparent in **Figure 3.5e** as the two protonation sites result in a very narrow CCS space (146.5–148.3 Å²) versus the $[M+H]^+$

species which occupies a much wider CCS space (145.7–153.3 Å²). The distribution width in **Figure 3.5b** also suggests the slightly larger conformational flexibility of the [M+H]⁺ species. The 2,4'-MDA results are somewhat more complicated as there are now three possible protonation sites, but qualitatively, the deprotonated conformers (red, orange, and yellow) are all shifted to lower CCS than the protonated conformers (black, dark grey, and light grey) in **Figure 3.5f**. The mobility traces in **Figure 3.5c** do show a very slight shift to a smaller CCS for the [M-H]⁺ species. These protonation site assignments from computational results are supported by observations from the MS/MS experiments and will be further analyzed in the mechanistic discussions.

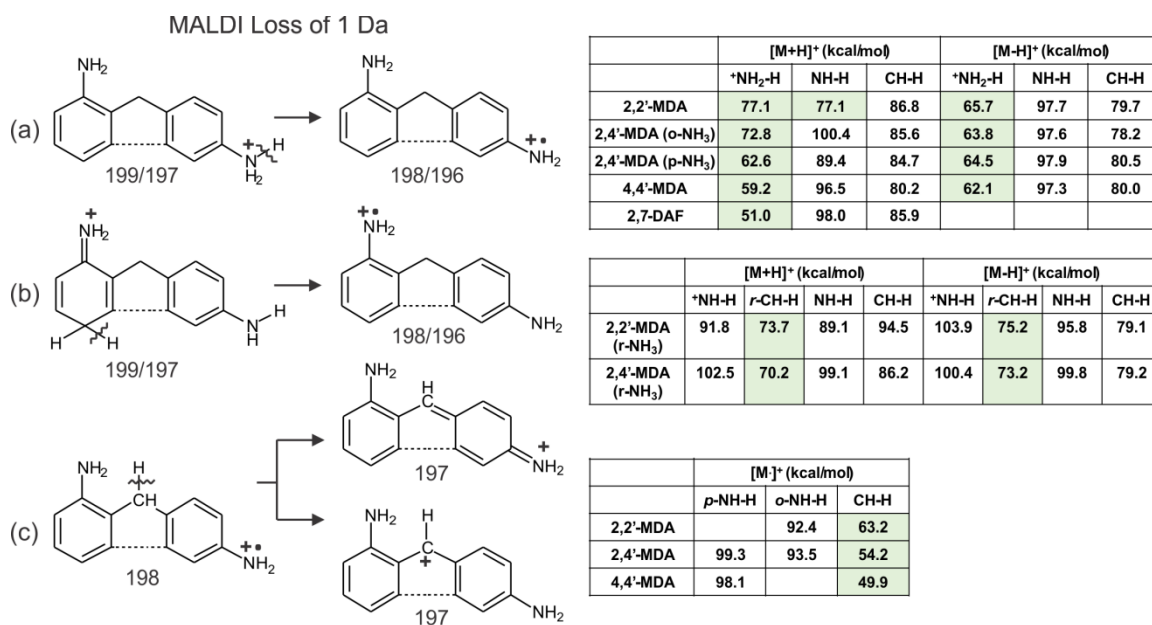
The theoretical conformations (RMSD clustering) in **Figure 3.5d-f** provide a visual representation of the reduced flexibility for [M-H]⁺ regioisomers. While the [M-H]⁺ conformation for 2,2'-MDA and 2,4'-MDA would not be expected to decrease in CCS compared to their [M+H]⁺ forms, it would for the 4,4'-MDA because the external amines become more restricted with the central fluorene motif. The fluorene ring structure for the [M-H]⁺ ion creates a much more compact structure for the 4,4'-MDA (**Figure 3.5d**) and slightly more compact structure for the 2,4'-MDA (**Figure 3.5f**) due to the middle fused ring restricting the flexibility of the central carbon bond, whereas the [M+H]⁺ ion has a more elongated structure and greater flexibility. The overall conformation of the 2,2'-MDA (**Figure 3.5e**) does not change significantly from the [M+H]⁺ ion due to the amine groups being centrally located on the structure. While the conformations of the 2,7-DAF and 4,4'-MDA [M-H]⁺ clearly reflect similarities (**Figure 3.5d**), the second, smaller mobility peak for the 2,7-DAF (**Figure 3.5a**) is difficult to assign to a second conformation as flexibility is clearly restricted due to the fluorene motif, but rather likely represents an impurity, possibly a positional isomer present in the analytical standard. Additional IM-MS, including ESI results for 2,7-DAF are provided as **Supporting Information (Figures C.16-C.17)**, but an in-depth discussion on 2,7-DAF is outside the scope of the current manuscript.

Mechanisms for Fragmentation of MDA Isomers

In addition to the MS/MS and IM-MS data described earlier, bond energy calculations were performed for all the precursor ions listed in **Table 3.1**. The complete results are provided as **Supporting Information (Figures C.20-C.22)**, but bond energies for the weakest bonds are included in **Scheme 3.1**. In general, the weakest bond (highlighted in green) in a molecule is shown to be either the protonated N-H or the protonated ring C-H, where appropriate. Typically, the methylene bridge C-H is the second weakest bond for all cases. The remaining fragmentation mechanism discussions will focus on the MDA species that produces the largest %RIC for each representative fragmentation ion.

M-1 Fragmentation

Scheme 3.1 summarizes M-1 fragmentation for the three MDA isomers and 2,7-DAF. **Scheme 3.1a** describes H-atom loss from species having a protonated amine group that is the weakest bond in all $[M+H]^+$, $[M-H]^+$ and 2,7-DAF species. The dashed lines in the structures indicate that the reaction occurs for both $[M+H]^+$ and $[M-H]^+$ precursor species. **Scheme 3.1b** shows similar reactions for $[M+H]^+$ and $[M-H]^+$ precursor species having ring protonation. Fragmentation of the protonated ring C-H bond is the lowest energy pathway. **Scheme 3.1c** describes H-atom loss from the $[M]^+$ parent ion that does not have a protonated amine, the bridge C-H bond is the weakest bond for the three MDA regioisomers. Loss of the bridge hydrogen has different consequences than loss from an amine group in that the remaining charge is delocalized over the entire aromatic system. The two resulting structures shown in the scheme are Pauling-type resonance structures for the 197 Da fragment ion. It is important to note that this 197 Da fragment ion, derived from the $[M]^+$ parent, is different from the 197 Da $[M-H]^+$ parent ion which cannot be produced by a M-1 reaction.

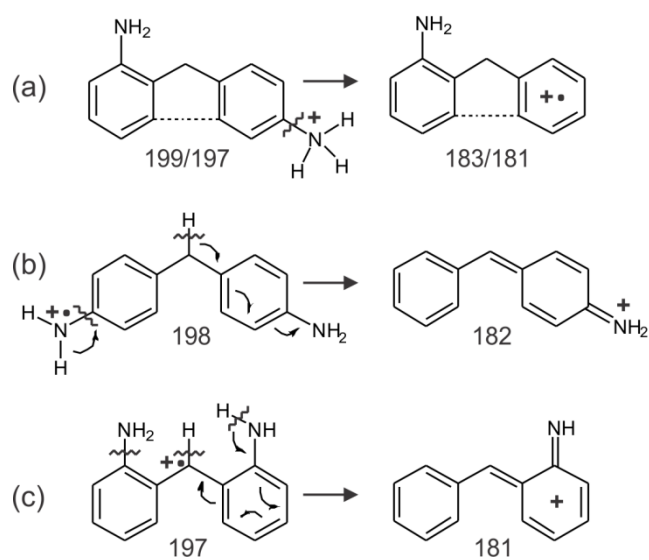


Scheme 3.1. Fragmentation mechanisms for the M-1 mass loss when (a) an N-H bond from a protonated amine is broken, (b) a C-H bond from a protonated ring is broken, and (c) when a bridge C-H bond is broken. Selected bond energies are included for the MDA isomers. Green highlighting specifies the weakest bond.

M-16 Fragmentation

Scheme 3.2 summarizes the reactions involved in loss of 16 Da from the MDA and 2,7-DAF parent ions. The most likely loss is NH_2 from a charge-site reaction involving the protonated amine group. **Scheme 3.2a** indicates transfer of a protonated amine H-atom onto the aromatic ring along with charge transfer to the same ring. The same reaction occurs for 2,7-DAF. The driving force is fracture of an N-H bond and subsequent formation of an aromatic C-H bond. It costs about 60 kcal/mol to break the N-H bond and 140 kcal/mol to break the C-N bond for a protonated amine. About 120 kcal/mol is reclaimed by aromatic C-H formation, giving a net cost of about 80 kcal/mol for the reaction; this is very similar to the energy associated with M-1 loss. Loss of NH_2 is not likely when protonation occurs on the ring, although it could shift into an amine protonated species by a tautomeric equilibrium reaction. Direct loss of an amine group from a $[\text{M}]^+$ parent ion via a simple C-N bond fracture is also not likely, given that the C-N bond energies for unprotonated amines are ~ 110 kcal/mol. **Figure 3.4c** indicates that the 182 Da fragment ion of $[\text{M}]^+$ is formed directly from the parent ion, in parallel with the 197 Da fragment ion. Also, **Table 3.1** indicates it is most prominent for the 4,4'- and 2,4'-MDA parent ions. **Scheme 3.2b** indicates this could be accomplished by a concerted reaction involving N-H transfer to the aromatic ring and bridge C-H loss. The 182 Da fragment has charge delocalization over the whole aromatic system, helping to drive the reaction. The distributions of %RIC intensities are quite similar for the 197 Da and 182 Da fragment ions of $[\text{M}]^+$ (**Figure 3.4f**). Another reaction must also be considered for M-16, namely, loss of 16 Da from the 197 Da fragment of $[\text{M}]^+$ to form the 181 Da fragment, nominally this would be M-17 from the parent ion. The proposed M-16 reaction for 2,2'-MDA is shown in **Scheme 3.2c**. This is based on collective evidence from **Figure 3.4c** which indicates that formation of the 181 Da fragment ion occurs from the 197 Da ion for $[\text{M}]^+$, and evidence from **Table 3.1** which indicates that 181 Da formation is most prominent for the *ortho*-substituted oligomers.

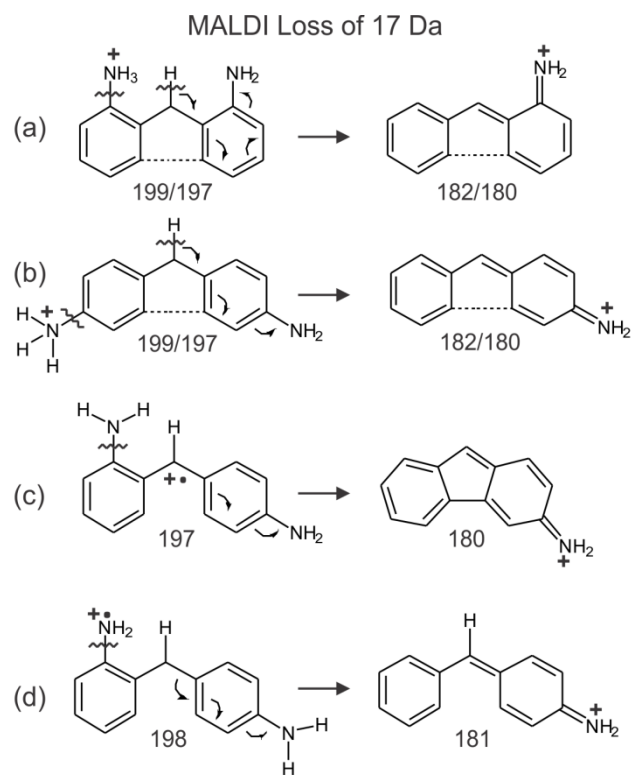
MALDI Loss of 16 Da



Scheme 3.2. Fragmentation mechanisms for the M-16 mass loss when (a) an NH₂ fragment is lost from a protonated amine group, (b) when an NH fragment and a bridge hydrogen are lost, and (c) when an *ortho* NH₂ group is lost by hydrogen rearrangement.

M-17 Fragmentation

Scheme 3.3 summarizes fragmentation reactions involving loss of 17 Da, presumably as ammonia (NH₃). For compounds containing a protonated *ortho*-amino group, this corresponds to transfer of a bridge H-atom to displace NH₃ as shown in **Scheme 3.3a** for both [M+H]⁺ and [M-H]⁺ parent ions. The specific reaction is shown for 2,2'-MDA. Lack of proximity of the protonated amino and bridge C-H groups in the 4,4'-isomers and 2,7-DAF, requires a different mechanism shown in **Scheme 3.3b**. The data in **Table 3.1** for [M-H]⁺ indicate that this is the case based on the decreases of %RIC seen for the M-17 fragment ions from 2,2'-MDA > 2,4'-MDA > 4,4'-MDA. However, both reactions (**Scheme 3.3a,b**) must be significant. This is the major fragmentation reaction for all [M-H]⁺ MDA oligomers, a 89 %RIC is seen for 2,2'-MDA. However, the 4,4'-oligomer shows a 51 %RIC, indicating a very significant influence of the more rigid [M-H]⁺ structure. The M-17 fragments corresponding to the three [M+H]⁺ oligomers are much less intense, averaging about 12 %RIC. The [M]⁺ parent has no protonated amino group but still shows a significant M-17 loss, with a 20 %RIC for the 2,2'-oligomer as discussed above. However, the [M]⁺ parent ion does show a nominal M-18 loss at 180 Da. **Figure 3.4c** indicates that the 197 Da peak is the precursor for the 180 Da ion of [M]⁺, as was the case for the 181 Da ion in **Scheme 3.2**. **Scheme 3.3c** shows such a reaction for the 2,4'- oligomer, which forms the same mass as the [M-H]⁺ parent (180 Da). Another reaction is also possible for the [M]⁺ ion. **Figure 3.4a** indicates that the M-18 ion (181 Da) of [M+H]⁺ can be formed from the [M]⁺ ion produced by the 199 Da parent ion. Also, **Table 3.1** indicates that the 181 Da ion is most prominent for 2,2'-MDA. Based on this evidence, the 181 Da fragment ion is probably produced by a concerted reaction involving loss of an amino group and an amine H-atom as shown in **Scheme 3.3d**.



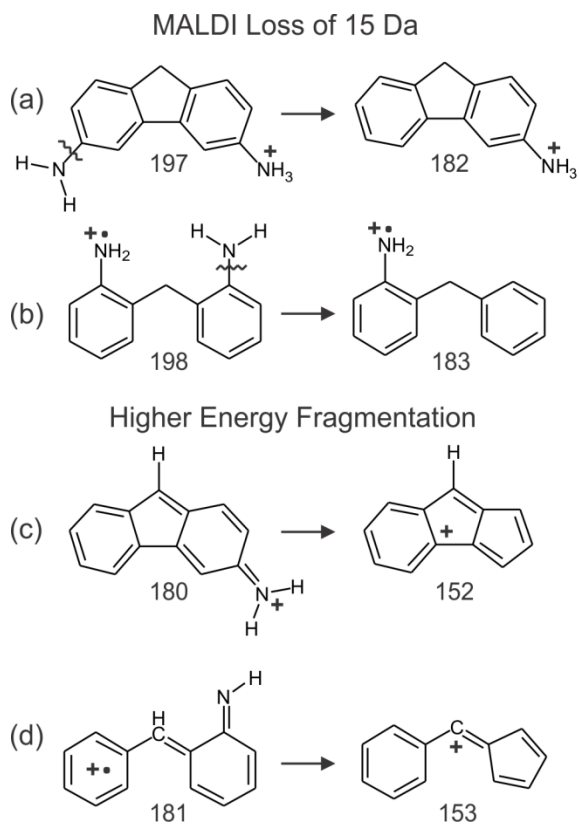
Scheme 3.3. Fragmentation mechanisms for the M-17 mass loss for (a) when an NH_3 group is lost (b) when an NH_2 group and bridge hydrogen are lost, (c) an NH group and two hydrogens are lost from a 197 fragment ion, and (d) loss of NH_2 and an amine hydrogen from $[\text{M}]^+$.

M-15 and Higher Energy Fragmentation

Two MDA species show M-15 losses, $[M-H]^+$ (182 Da) and $[M]^+$ (183 Da), which corresponds to a loss of NH. This can occur in a charge remote reaction involving transfer of an amine H-atom to the ring, as shown in **Scheme 3.4a,b**. The difference in N-H bond energies for protonated and unprotonated amine groups, 62.1 and 97.3 kcal/mol respectively, coupled with lack of charge transfer, make these H-atom reactions less likely than their protonated-amine counterparts. The 152 and 153 Da ions assume prominence in **Figure 3.4a-c** as the fragmentation energy is increased. The 152 Da ion is related to the $[M-H]^+$ and $[M]^+$ parent ions and is formed from the 180 Da fragment, whereas the 153 Da ion is related to the $[M+H]^+$ and originates from the 181 Da fragment. Both the 152 Da and 153 Da fragmentation reactions involve loss of the remaining amine nitrogen atom, a ring carbon atom, and hydrogens. **Scheme 3.4c** shows the reaction for the 180 Da fragment ion formed from $[M-H]^+$. The net effect is converting a six-member ring into a five-member fused ring, by separate loss of HCN and a H-atom. Another high energy fragmentation process, loss of 28 Da from the 181 Da fragment ion, is more challenging to assign a mechanism. While a structure equaling 153 Da could be imagined by replacing the bridge C-H group in the 152 Da structure with a nitrogen atom, how this might happen mechanistically is hard to reconcile. The structure shown in **Scheme 3.4d** for formation of the 153 Da ion probably involves loss of HCN and a H-atom, similarly to the 152 Da mechanism (**Scheme 3.4c**). One hydrogen loss must be remote from the NH group. Bridge H-atom loss is shown in **Scheme 3.4d** because it is the weakest C-H bond in the molecule. However, it is noted here that other 153 Da structures are also possible.

3.4 Conclusions

In this study, 2-ring MDA isomers (2,2'-, 2,4'-, and 4,4'-MDA) have been characterized using a MALDI-TOF MS platform and a variety of other MS techniques. In previous work, we



Scheme 3.4. Fragmentation mechanisms for the M-15 mass loss for (a) loss of NH from $[M-H]^+$ and, (b) loss of NH from $[M]^+$; higher energy fragmentation for (c) loss of nominal H-C=N-H from a 180 fragment ion and (d) loss of nominal H-C=N-H from a 181 fragment ion.

concluded that $[M+H]^+$ is the only parent ion formed in ESI, whereas in this current study, MALDI was observed to form three unique parent ions for all MDA isomers: $[M+H]^+$, and two other ions formed by laser irradiation, $[M]^+$ and $[M-H]^+$. Unique fragment ions observed for each of the respective precursor ions were explored and their origins were determined using energy-resolved MS/MS studies. IM-MS provided further conformational distinctions between parent ions observed in the precursor region. 2,7-DAF confirmed the $[M-H]^+$ proposed fluorene motif structure. Characterizing fragment ions associated with 2,7-DAF allowed for a greater understanding of how the $[M-H]^+$ fragment ion forms from each of the three MDA regioisomers. Analytically, these findings provide important insight into the complex ion formation and associated fragmentation behavior for polymer precursors investigated using MALDI ionization methods. It is anticipated that this work will help further the interpretation and development of MALDI-based polymer studies by MS, which remains a key MS technology for polymer characterization.

3.5 Acknowledgements

The authors thank Dr. Stefan Wershofen for providing 2-ring MDA samples. We also acknowledge the characterization support of Dr. Don Stec and the Vanderbilt NMR facilities, which is supported by the National Institute of Health (NIH S10 RR019022). Additionally, we acknowledge the Vanderbilt Center for Structural Biology and Dr. Terry Lybrand for computational support, Prof. Ned Porter and Dr. Hartmut Nefzger for valuable discussions, and the Searle Systems Biology and Bioengineering Undergraduate Research Experience (SyBBURE) Program at Vanderbilt for summer support for T.M.C. This research was funded by the National Institutes of Health (NIH R01GM092218), the U.S. Army Research Office and the Defense Advanced Research Projects Agency (DARPA) under Cooperative Agreement Number W911 NF-14-2-0022, and the U.S. Environmental Protection Agency (EPA) under Assistance Agreement No. 83573601. This work has not been formally reviewed by EPA and EPA does not

endorse any products or commercial services mentioned in this publication. The views expressed in this document are solely those of the authors and should not be interpreted as representing the official policies, either expressed or implied, of the EPA, the Army Research Office, DARPA, or the U.S. Government.

3.6 References

1. Forsythe, J.G.; Stow, S.M.; Nefzger, H.; Kwiecien, N.W.; May, J.C.; McLean, J.A.; Hercules, D.M. Structural characterization of methylenedianiline regioisomers by ion mobility-mass spectrometry, tandem mass spectrometry, and computational strategies: I. Electrospray spectra of 2-ring isomers. *Anal. Chem.*, 2014, 86 (9), 4362-4370.
2. Stow, S.M.; Onifer, T.M.; Forsythe, J.G.; Nefzger, H.; Kwiecien, N.W.; May, J.C.; McLean, J.A.; Hercules, D.M. Structural Characterization of Methylenedianiline Regioisomers by Ion Mobility-Mass Spectrometry, Tandem Mass Spectrometry, and Computational Strategies. 2. Electrospray Spectra of 3-Ring and 4-Ring Isomers. *Anal. Chem.*, 2015, 87 (12), 6288-6296.
3. Liu, J.; Loewe, R.S.; McCullough, R.D. Employing MALDI-MS on poly (alkylthiophenes): analysis of molecular weights, molecular weight distributions, end-group structures, and end-group modifications. *Macromolecules*, 1999, 32 (18), 5777-5785.
4. Nielen, M.W. MALDI time - of - flight mass spectrometry of synthetic polymers. *Mass Spectrom. Rev.*, 1999, 18 (5), 309-344.
5. Belu, A.M.; DeSimone, J.M.; Linton, R.W.; Lange, G.W.; Friedman, R.M. Evaluation of matrix-assisted laser desorption ionization mass spectrometry for polymer characterization. *Journal of the American Society for Mass Spectrometry*, 1996, 7 (1), 11-24.
6. Montaudo, G.; Samperi, F.; Montaudo, M.S. Characterization of synthetic polymers by MALDI-MS. *Prog. Polym. Sci.*, 2006, 31 (3), 277-357.
7. Bletsos, I.V.; Hercules, D.M.; VanLeyen, D.; Benninghoven, A.; Karakatsanis, C.G.; Rieck, J.N. Structural characterization of model polyester polyurethanes using time-of-flight secondary ion mass spectrometry. *Macromolecules*, 1990, 23 (18), 4157-4163.

8. Gies, A.P.; Ellison, S.T.; Stow, S.M.; Hercules, D.M. Matrix-assisted laser desorption/ionization-time-of-flight/time-of-flight collision-induced dissociation study of poly (p-phenylenediamine terephthalamide) fragmentation reactions. *Anal. Chim. Acta*, 2014, 808, 124-143.
9. Gaskell, S. J. *Electrospray: principles and practice*. *J. Mass Spectrom.* 1997, 32 (7), 677-688.
10. Zenobi, R.; Knochenmuss, R. Ion Formation in MALDI mass spectrometry. *Mass Spectrom. Rev.* 1998, 17 (5), 337-366.
11. May, J.C.; Goodwin, C.R.; Lareau, N.M.; Leaptrot, K.L.; Morris, C.B.; Kurulugama, R.T.; Mordehai, A.; Klein, C.; Barry, W.; Darland, E.; Overney, G.; Conformational ordering of biomolecules in the gas phase: nitrogen collision cross sections measured on a prototype high resolution drift tube ion mobility-mass spectrometer. *Anal. Chem.*, 2014, 86 (4), 2107-2116.
12. Ruotolo, B.T.; Benesch, J.L.; Sandercock, A.M.; Hyung, S.J.; Robinson, C.V.; Ion mobility–mass spectrometry analysis of large protein complexes. *Nat. Protoc.*, 2008, 3 (7), 1139-1152.
13. Hines, K. M.; May, J. C.; McLean, J. A.; Xu, L. Evaluation of collision cross section calibrants for structural analysis of lipids by traveling wave ion mobility-mass spectrometry. *Anal. Chem.* 2016, 88 (14), 7329-7336.
14. Harper, B.; Neumann, E. K.; Stow, S. M.; May, J. C.; McLean, J. A.; Solouki, T. Determination of ion mobility collision cross sections for unresolved isomeric mixtures using tandem mass spectrometry and chemometric deconvolution. *Anal. Chim. Acta* 2016, 939, 64-72.
15. Case, D. A.; Babin, V.; Berryman, J.; Betz, R. M.; Cai, Q.; Cerutti, D. S.; Cheatham, T. E., III; Darden, T. A.; Duke, R. E.; Gohlke, H. et al. *AMBER 14*; University of California: San Francisco, CA, 2014.

16. Mesleh, M.F.; Hunter, J.M.; Shvartsburg, A.A.; Schatz, G.C.; Jarrold, M.F. Structural information from ion mobility measurements: effects of the long-range potential. *J. Phys. Chem.*, 1996, 100 (40), 16082-16086.
17. Shvartsburg, A. A.; Jarrold, M. F. An exact hard-spheres scattering model for the mobilities of polyatomic ions. *Chem. Phys. Letters* 1996, 261 (1), 86-91.
18. Campuzano, I.; Bush, M. F.; Robinson, C. V.; Beaumont, C.; Richardson, K.; Kim, H.; Kim, H. I. Structural characterization of drug-like compounds by ion mobility mass spectrometry: comparison of theoretical and experimentally derived nitrogen collision cross sections. *Anal. Chem.* 2011, 84, 1026-1033.
19. Bleiholder, C.; Wyttenbach, T.; Bowers, M. T. A novel projection approximation algorithm for the fast and accurate computation of molecular collision cross sections (I). *Method. Int. J. Mass Spectrom.* 2011, 308, 1-10.
20. Bleiholder, C.; Contreras, S.; Do, T. D.; Bowers, M. T. A novel projection approximation algorithm for the fast and accurate computation of molecular collision cross sections (II). Model parameterization and definition of empirical shape factors for proteins. *Int. J. Mass Spectrom.* 2013, 345, 89-96.
21. Anderson, S. E.; Bleiholder, C.; Brocker, E. R.; Stang, P. J.; Bowers, M. T. A novel projection approximation algorithm for the fast and accurate computation of molecular collision cross sections (III): Application to supramolecular coordination-driven assemblies with complex shapes. *Int. J. Mass Spectrom.* 2012, 330-332, 78-84.
22. Bleiholder, C.; Contreras, S.; Bowers, M. T. A novel projection approximation algorithm for the fast and accurate computation of molecular collision cross sections (IV). Application to polypeptides. *Int. J. of Mass Spectrom.* 2013, 354, 275-280.
23. Frisch, M. J.; Trucks, G. W.; Schlegel, H. B.; Scuseria, G. E.; Robb, M. A.; Cheeseman, J. R.; Scalmani, G.; Barone, V.; Mennucci, B.; Petersson, G. A., et. al. *Gaussian09*, Revision A.02; Gaussian Inc., Wallingford, CT 2009.

24. McLafferty, F. W.; Tureček, F. Interpretation of Mass Spectra, 4th ed.; University Science Books: Sausalito, CA, 1993.
25. Knochenmuss, R.; Zenobi, R. MALDI ionization: the role of in-plume processes. Chem. Rev. 2003, 103, 441-452.

CHAPTER IV

STRUCTURAL CHARACTERIZATION OF METHYLENEDIANILINE REGIOISOMERS BY ION MOBILITY-MASS SPECTROMETRY AND TANDEM MASS SPECTROMETRY: IV. 3-RING AND 4-RING ISOMERS

4.1 Introduction

Polyurethane (PU) copolymers are one of the most versatile polymeric materials, commonly manufactured for use in rigid and flexible foams, coatings, adhesives, sealants, elastomers, membrane materials, laminates, fibers, and composites. Methylenedianiline (MDA) is a precursor to methylene bisphenyl diisocyanate (MDI), a major hard block component in the manufacturing of PUs. MDA is formed from the reaction between aniline and formaldehyde, generating the 2-ring MDA regioisomers 2,2'-MDA, 2,4'-MDA, and 4,4'-MDA, as well as larger multimeric species including 3-ring and 4-ring MDAs.^{1,2}

In our previous work, 2-ring MDAs (2,2'-MDA, 2,4'-MDA, and 4,4'-MDA) were characterized using electrospray ionization-ion mobility-mass spectrometry (ESI-IM-MS)¹ and matrix assisted laser desorption/ionization-ion mobility-mass spectrometry (MALDI-IM-MS),³ two MS techniques commonly used to analyze PU polymers.⁴⁻⁸ In those studies, one unique parent ion ($[M+H]^+ = 199$ Da) was observed for each isomer using ESI-MS; however, when studied by MALDI-MS we observed three distinct precursor ions, $[M-H]^+ = 197$ Da and $[M]^+ = 198$ Da, in addition to the $[M+H]^+ = 199$ Da species.

More recently, we used ESI-IM-MS to structurally characterize 3-ring and 4-ring MDAs by studying their preferred sites of protonation, gas phase stability, and fragmentation pathways.² In this present study, 3-ring and 4-ring MDAs were similarly characterized using MALDI-IM-MS and the results were compared to our previous ESI-IM-MS findings. In **Figure 4.1**, 3-ring and 4-ring MDA parent species are illustrated with their respective protonation sites denoted with

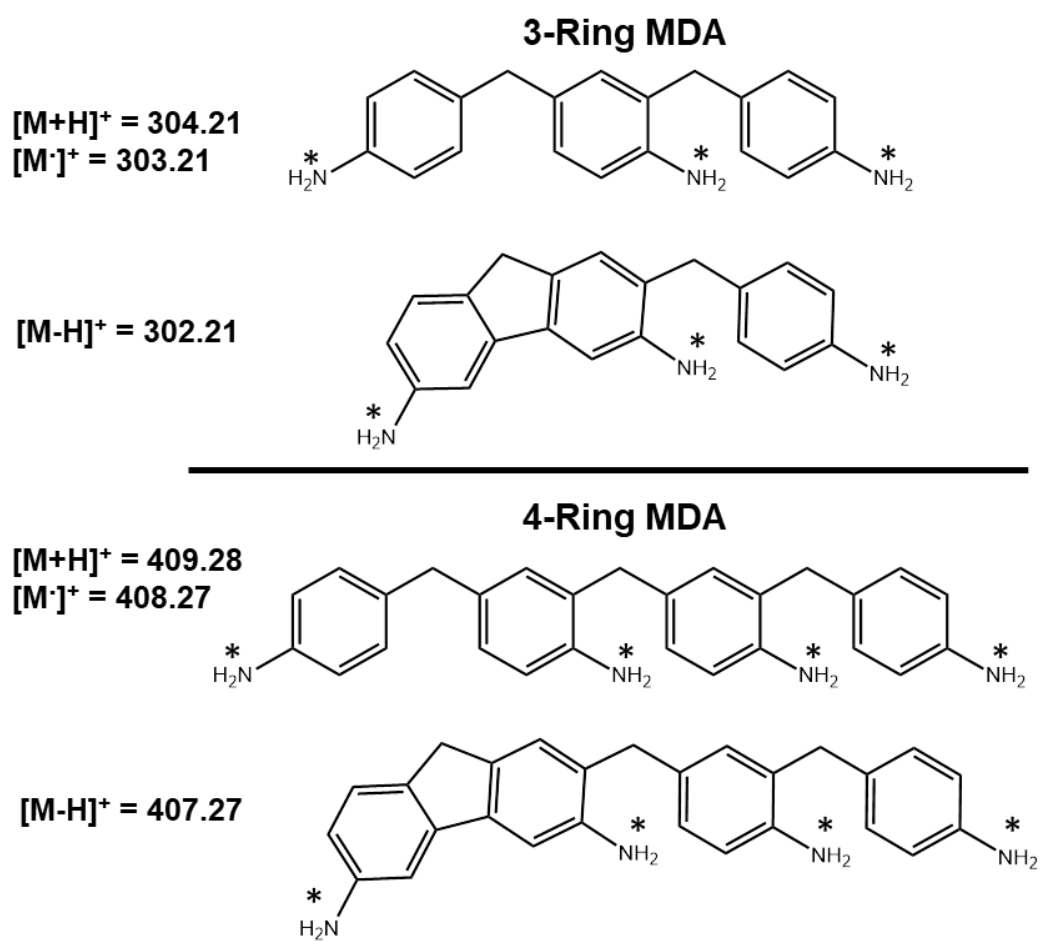


Figure 4.1. MDA 3-ring and 4-ring $[M+H]^+$, $[M]^\cdot$, and $[M-H]^+$ species. Asterisks (*) denote sites of possible protonation.

their respective protonation sites denoted with asterisks. Consistent with our 2-ring MDA study, we observed one unique parent ion formed during ESI for both 3-ring ($[M+H]^+ = 304$ Da) and 4-ring MDA ($[M+H]^+ = 409$ Da). During the MALDI process we observe three parent ions; two of which are unique to the MALDI process for each 3-ring and 4-ring MDA: $[M+H]^+ = 304, 409$ Da, $[M]^+ = 303, 408$ Da, and $[M-H]^+ = 302, 407$ Da, respectively. The additional rings in these species provide greater flexibility and thus more complex consequences for the fragmentation patterns observed. The novelty of this work compares ESI and MALDI-MS ionization and the unique precursor species that arise from 3-ring and 4-ring MDA species. This work highlights the complexity when investigating fragmentation pathways of larger multimeric MDA species. The combination of IM-MS and MS/MS allow for unique structural characterization of the three precursor ions formed and their respective fragment ion pathways observed during the MALDI process.

4.2 Experimental Section

Materials

Sample preparation and experimental details have been reported previously for 3-ring and 4-ring MDA ESI studies² and 2-ring MDA ESI and MALDI studies,^{1,3} but a few details will be mentioned here. Methylenedianiline (MDA) 3-ring and 4-ring samples were provided by Dr. Stefan Wershofen (Bayer MaterialScience AG, 47812 Uerdingen, Germany). Optima grade methanol and water with 0.1% formic acid were obtained from Fisher Scientific (Waltham, MA, USA). Tetralkylammonium salts, α -cyano-4-hydroxycinnamic acid (CHCA) and alkali salts were obtained from Sigma-Aldrich (St. Louis, MO, USA). Samples were dissolved at a concentration of 1 mg/mL in 9:1 methanol/water containing 0.1% formic acid (v/v). Each MDA isomer was combined in a 10:1 CHCA matrix-to-analyte ratio and two or three layers of 0.5 μ L of samples were spotted on a 100-well MALDI plate.

Traveling Wave MALDI-IM-TOF/MS

A traveling wave IM-MS (TWIM-MS) Synapt G2-S (Waters Corporation, Milford, MA) was used for acquiring ESI and MALDI MS, MS/MS, and IM-MS data.⁹ Collision cross section (CCS) values cannot be obtained directly from TWIM experimental drift time values, therefore quaternary ammonium salts were used as CCS calibration standards to obtain CCS data from TWIM.¹⁰⁻¹²

The Synapt G2-S mass spectrometer MALDI source has a frequency-tripled Nd:YAG laser which emits 355 nm at 1kHz pulse repetition rate. Laser attenuation ranged from 190-300 (arbitrary units), with 270 selected for all experiments unless noted otherwise. CHCA matrix cluster peaks were used for TOF calibration. Further experimental details can be found from our earlier study², but briefly the TWIM drift cell settings were as follows: TWIM pressure, 3 mbar nitrogen (2.25 Torr); electrodynamic wave height, 35 V; wave velocity, 700 m/s; TOF resolving power, ca. 18,000 $m/\Delta m$ at 200 m/z . Collision-induced dissociation (CID) experiments were performed using argon gas. In our previous studies, experiments were conducted to evaluate the influence of the MALDI laser fluence and the resolving power of the MS/MS resolving quadrupole on the resulting precursor ion intensities. From those studies, the m/z resolving quadrupole was set to 18 resolving power for the MS/MS experiments providing the best separation of the three precursor ions, without significant loss of signal.³ To perform MS³ experiments, the ion of interest is selected by the quadrupole and is fragmented in the “Trap” region located prior to the TWIM drift cell. The first generation of product ions are then separated by the TWIM and subjected to a second stage of CID in the “Transfer” region to produce 2nd generation and 1st generation product ions (i.e., MS/IM/MS experiments).

4.3 Results and Discussion

Differences between ESI and MALDI Spectra for $[M+H]^+$

The full ESI-MS and MALDI-MS spectra in **Figure 4.2** were acquired for both 3-ring (**Figure 4.2a-b**) and 4-ring MDA (**Figure 4.2c-d**), respectively. The ESI-MS and MALDI-MS spectra for the 3-ring and 4-ring MDA species are vastly different. Using ESI, we observed one precursor species $[M+H]^+$ and additional characteristic peaks at 211 and 106 Da for the 3-ring (**Figure 4.2a**) and 316, 211, and 106 Da for 4-ring MDA (**Figure 4.2c**). In addition, peaks observed at 152.6 m/z and 158.6 m/z correspond to the doubly charged 3-ring and 4-ring MDAs (**Figure 4.2a,c**). With MALDI we observe more complex mass spectra for both 3-ring and 4-ring MDA (**Figure 4.2b,d**). Each of the three unique precursor ions is observed in the 3-ring and 4-ring MALDI spectra, similar to our previous study on 2-ring MDA regioisomers. In MALDI, we observe a characteristic peak at 211 Da for 3-ring MDA and CHCA matrix cluster peaks at 337, 335, 190, and 172 Da (**Figure 4.2b**). In addition, the MALDI spectra for 4-ring MDA show the $[M+Na]^+$ peak at 431 Da, characteristic peaks at 316 and 211 Da, and CHCA matrix cluster peaks at 379, 335, 190, and 172 Da (**Figure 4.2d**). Precursor ions unique to 3-ring MDA include: $[M+H]^+ = 304$ Da, $[M]^+ = 303$ Da, and $[M-H]^+ = 302$ Da (**Figure 4.2b**). In addition, precursor ions characteristic to the 4-ring MDA include: $[M+H]^+ = 409$ Da, $[M]^+ = 408$ Da, and $[M-H]^+ = 407$ Da (**Figure 4.2d**). In MALDI, the 3-ring and 4-ring $[M+H]^+$ precursor is the least abundant precursor ion compared to $[M]^+$ and $[M-H]^+$ species (**Figure 4.2b,d**). In ESI, the 3-ring and 4-ring $[M+H]^+$ species and characteristic fragment peaks appear more stable than the $[M+H]^+$ precursor and fragment ions produced by the MALDI process. This difference observed for the $[M+H]^+$ precursor indicates that these MDA multimers behave significantly differently when ionized by MALDI than by ESI.

Characterization of 3-Ring and 4-Ring MDA by MS/MS

Figure 4.3 details the MALDI MS/MS spectra for each precursor ion formed: 3-ring (**Figure 4.3a-c**) and 4-ring (**Figure 4.3d-f**) MDAs, $[M+H]^+$, $[M]^+$, and $[M-H]^+$. In the MS/MS

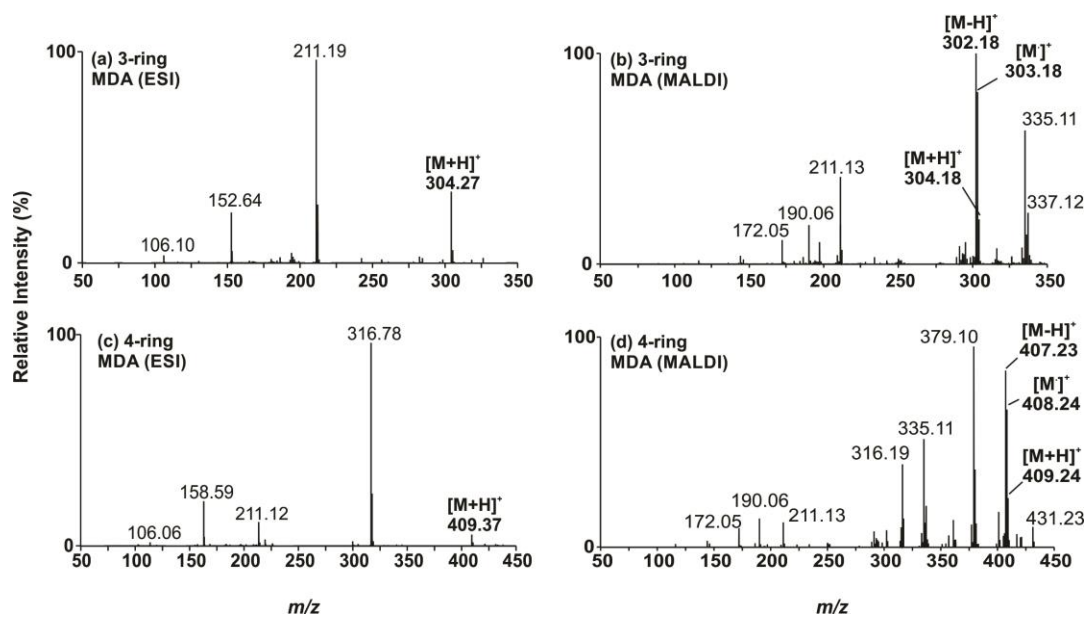


Figure 4.2. Comparison of ESI-MS and MALDI-MS of 3-ring (a-b) and 4-ring (c-d) MDA.

spectra, different collision energies were used to generate fragment ions for each precursor due to differing precursor stabilities. **Figures D.1 and D.2 in Supporting Information** compare all precursor species fragmented at 15 eV compared to 20 eV (laboratory frame). Due to an increase in the number of fragment ions observed for the $[M+H]^+$ species for both 3-ring and 4-ring MDA, a 15 eV collision energy was used to characterize specific fragment ions derived from the $[M+H]^+$ precursor species, and 20 eV was used to characterize fragment ions derived from the $[M]^+$ and $[M-H]^+$ species. The MS/MS spectra in **Figure 4.3** show unique fragment ions for each 3-ring and 4-ring precursor species: 15 eV was used for $[M+H]^+$ (**Figure 4.3a,d**) and 20 eV was used for $[M]^+$ and $[M-H]^+$ species (**Figure 4.3b-c,e-f**). Additional MS/MS spectra at various collision energies for both 3-ring and 4-ring MDA precursors can be found in **Supporting Information (Figures D.3-D.4)**. Due to the numerous fragment ions formed uniquely for each precursor, this manuscript will focus on the interpretation of major low energy fragment ions formed by the MALDI process and will be introduced by schemes proposing fragment ion pathways and collision-induced dissociation ion breakdown curves (CID curves). Additional MS^3 data found in **Supporting Information (Figures D.5 and D.6)** was also acquired and used to support the interpretation of unique fragment ion pathways.

It should be noted that there is a major difference between interpretation of the MALDI spectra of the 3-ring and 4-ring MDAs relative to the 2-ring MDAs from our previous work. This difference arises from the multiple amine groups in the 3-ring and 4-ring compounds. Not only do the amine groups have somewhat differing basicities, but their steric effects can vary significantly. These effects were observed to some extent in the ESI spectra of these compounds,² but the complexities in the MALDI spectra are more severe due to the larger MDA species and formation of three unique precursor ions in the MALDI process. The net result indicates that it is generally not possible to identify a unique structure for a given mass loss. **Supporting Information Figures D.7 and D.8** address this problem in greater detail with an illustration

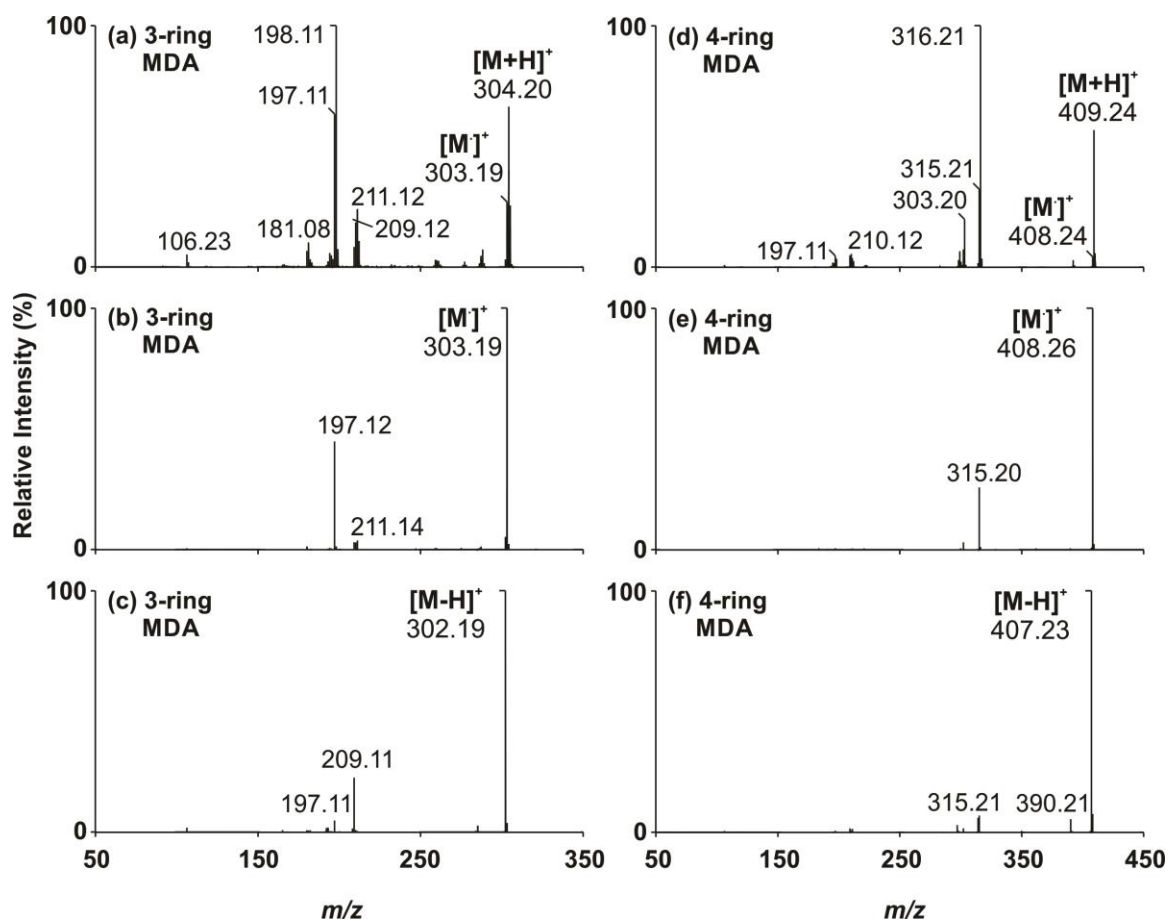


Figure 4.3. MALDI MS/MS spectra for (left) 3-ring MDA and (right) 4-ring MDA. Lab-frame energies are shown; corresponding energies are 15 eV for (a,d) and 20 eV for (b-c,e-f). Results for $[M+H]^+$ are shown in (a,d), for $[M]^+$ in (b,e), and $[M-H]^+$ in (c,f).

provided to highlight the complexity of these specific compounds. Therefore, specific structures described in the manuscript are tentative and may not be the only structures possible for a given fragment ion.

Characterization by Ion Mobility-Mass Spectrometry

The experimental IM spectra provided in **Figure 4.4** are shown for the $[M+H]^+$ (blue), $[M]^+$ (black), and $[M-H]^+$ (red) ion forms of the 3-ring and 4-ring MDA precursor species. In **Figure 4.4a**, the TWIM spectrum obtained for the 3-ring species indicate a single distribution for each precursor, whereas in **Figure 4.4b** the 4-ring MDA species each exhibit two partially-resolved structural populations, indicative of multiple gas-phase conformations. In our previous ESI studies, computational modeling was used to study the $[M+H]^+$ 3-ring and 4-ring MDA. Theoretical structures were generated to align with experimental CCS values. In those studies, the $[M+H]^+$ 3-ring MDA was shown to undergo the most favorable protonation on the internal amine, when compared to the external amines. In the ESI $[M+H]^+$ 4-ring MDA studies, two conformations were seen, which is similar to what is experimentally observed in the MALDI studies described here. These two conformational families were attributed to external amine protonation and internal amine protonation, respectively. Computational modeling in the ESI study suggests protonation on the external amines is more favored due to the 4-ring MDA species wrapping around the proton to share between the two external amine groups. As demonstrated in previous literature, IM-MS separations can differentiate between both aniline protomers coexisting in the gas-phase: N-protonated and ring protonated aniline.¹³⁻¹⁴ Similar to aniline studies, we can confirm that IM-MS techniques can aide in identifying multiple sites of protonation within 3-ring and 4-ring MDA precursor species.

In **Figure 4.4a**, the IM-MS results show 304 Da $[M+H]^+$ and 303 Da $[M]^+$ species to have the same CCS (140.8 \AA^2). However, the 302 Da $[M-H]^+$ species show a smaller CCS (139.2 \AA^2); this difference in CCS for the 3-ring MDA can be attributed to the structural CCS (139.2

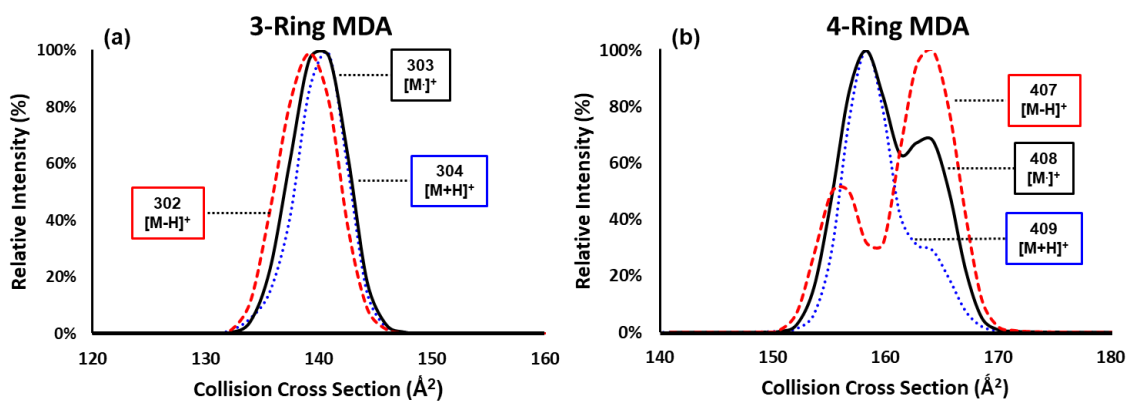


Figure 4.4. MALDI-IM-MS profiles for (a) 3-ring MDA and (b) 4-ring MDA. $[M+H]^+$ results are shown in blue, $[M]^+$ results are shown in black, and $[M-H]^+$ results are in red.

\AA^2); this difference in CCS for the 3-ring MDA can be attributed to the structural differences exhibited by the $[\text{M-H}]^+$ bridged fluorene-backbone, as depicted in **Figure 4.1**. The 4-ring MDA precursors behave much differently than the 3-ring species. First, we notice two conformations present for each precursor, each conformation having different abundances. Next, the 409 Da $[\text{M+H}]^+$ and 408 Da $[\text{M}]^+$ species each share the same CCS both for the larger conformation (158.3 \AA^2) and smaller conformation (164.1 \AA^2). The 407 Da $[\text{M-H}]^+$ species is uniquely different from all of the 3-ring and 4-ring precursors. The 407 Da IM-MS trace shows two isomeric species; the less abundant isomer exhibits the smaller CCS (156.0 \AA^2), whereas the more abundant isomer has the larger CCS (164.2 \AA^2). When comparing the $[\text{M-H}]^+$ species between 3-ring and 4-ring MDAs, we notice that the 302 Da species has a smaller CCS, whereas the 407 Da species (more abundant isomer) has a larger CCS value. The differences observed between the precursors and 3-ring and 4-ring MDA can be attributed to either structural differences or multiple sites of protonation. Structural differences between 3-ring and 4-ring MDA include the addition of a bridged methyl-aniline and differences between $[\text{M+H}]^+$ and $[\text{M-H}]^+$ for each MDA multimer include the bridged fluorene backbone. Possible protonation sites on the 3-ring and 4-ring MDAs are illustrated in **Figure 4.1**, differences include exterior or interior amine protonation. As seen in our previous 3-ring and 4-ring ESI studies, the MDA species must be oriented such that the additional proton is in proximity to the most basic site on the adjacent aniline ring to represent the most energetically favorable position. Curve resolution analysis for the 4-ring MDA precursors (**Supporting Information D.9**) and additional IM-MS data can be found in **Supporting Information** under *Multiple Protonation Example*.

3-Ring MDA

In the MS/MS spectrum for each 3-ring MDA precursor, **Figure 4.3a-c** shows major fragment peaks observed at low lab frame collision energies: $[\text{M+H}]^+ = 15 \text{ eV}$, $[\text{M}]^+ = 20 \text{ eV}$, and $[\text{M-H}]^+ = 20 \text{ eV}$. The conversion from precursor ion to major fragment ion was monitored as a

function of applied collision energy as shown in **Figure 4.5**. Collision energy was ramped from 0 to 50 eV for all unique precursor species in 5 eV increments and performed in triplicate. **Figure 4.5a,c,e** monitors CID of major fragment ions having a percent relative ion current (%RIC) of 20% or more, and **Figure 4.5b,d,f** illustrates %RIC of low abundance fragment ions formed in the range of 5-20% along the 0-50 eV ramp. All of the CID curves in **Figure 4.5** represent %RIC values of 5% or more along the 0-50 eV ramp. Additional CID curves for minor fragment ions formed at 35 eV or higher are provided as **Supporting Information (Figure D.10)**. Major fragment ions observed for each precursor species will be discussed in further detail.

3-Ring MDA [M+H]⁺ Species (304 Da)

In **Figure 4.3a**, the MS/MS spectrum highlights major fragment ions observed for the 304 precursor species at 15 eV. The MS/MS spectrum shows the 304 Da species dissociating into four major fragment ions 303, 211, 209, and 198 Da, as seen in **Scheme 4.1a** and in the total percent ion current table found in **Supporting Information Table D.3**. These fragment ions are derived directly from the 304 Da species and each forms with an intensity greater than 5%. In **Figure 4.5a-b**, the [M+H]⁺ precursor depletes at 15 eV forming fragment ions 303 ([M-1]⁺), 211 ([M-93]⁺), 209 ([M-95]⁺), and 198 Da ([M-106]⁺); a dashed line is drawn for visual alignment of major and minor fragment ion formation at 15 eV. Major fragment ion 303 Da corresponds to the loss of one hydrogen, and the transfer of charge to the ring (8%, 15 eV). Major fragment ion 211 Da forms from the loss of aniline (7%, 15 eV), from its parent species 304 Da. Fragment ion 209 Da corresponds to the loss of aniline and two hydrogens; this fragment ion forms at higher collision energy (6%, 30 eV). In addition, mass 198 Da forms in high abundance due to the loss of methylene-aniline (30%, 15 eV). **Scheme 4.1a** outlines a proposed fragmentation pathway for each fragment ion (>5%) originating from the [M+H]⁺ 304 Da species. As seen in **Scheme 4.1a**, minor fragment ions such as 210 ([M-93]⁺), 197 ([M-106]⁺), 181 ([M-17]⁺), and 180 Da ([M-17]⁺) form by depletion of the major fragment ions at higher collision energy. **Scheme 4.1a**

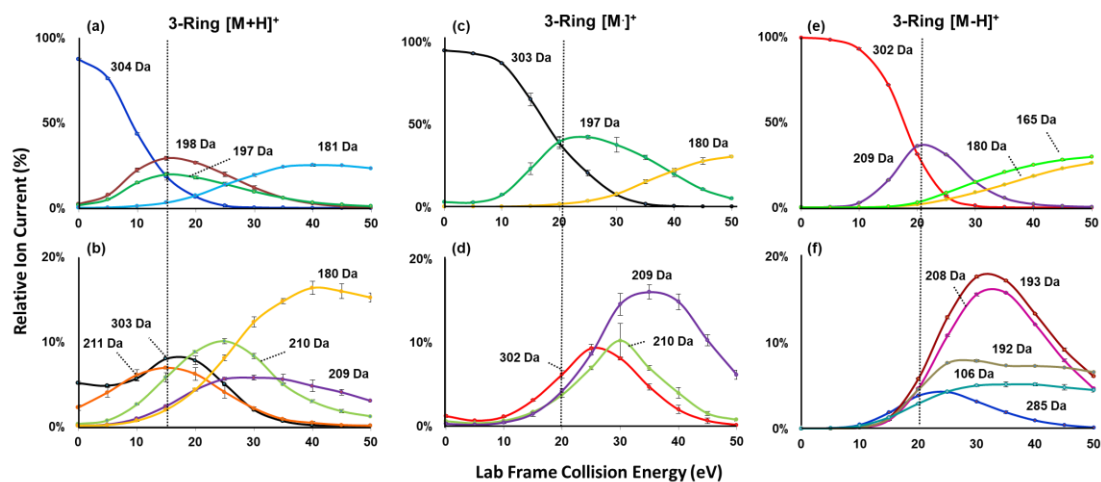


Figure 4.5. Collision-induced dissociation curves monitoring the transition of 3-ring MDA precursor to fragment ions for **(a-b)** $[M+H]^+$ ions, **(c-d)** $[M]^+$ ions, and **(e-f)** $[M-H]^+$ ions. Fragment ions formed above 20% relative ion current are represented in **(a,c,e)**; fragment ions formed between 0-20% relative ion current are represented in **(b,d,f)** for each precursor ion. Dashed lines for visual alignment are added for each precursor species: $[M+H]^+$ dashed line represents 15 eV, precursor $[M]^+$ and $[M-H]^+$ dashed line represents collision energy at 20 eV.

proposes that mass 303 Da can form two possible fragments ions: 210 Da and 197 Da. Mass 210 Da is formed by the loss of aniline (10%, 25 eV) and ion 197 Da forms from the loss of methylene-aniline. In **Figure 4.5a-b** we observe the depletion of mass 198 Da leading to the formation of the 181 Da (25%, 40 eV) species, resulting from the loss of $-NH_2$ and one hydrogen forming the fluorene-bridge. Similarly, minor fragment ion 180 Da (16%, 40 eV) results from the loss of $-NH_2$ and one hydrogen forming the fluorene-bridge, from major fragment ion 197 Da. The MS³ data found in **Supporting Information Figure D.5** is consistent with the proposed **Scheme 4.1a** outline. Additional possible structures of the proposed fragment ions derived from the 304 Da $[M+H]^+$ are outlined in **Supporting Information (Figure D.11)**. Proposed fragment ion pathways, CID curves, and intensity values for additional ions formed at 35 eV or higher are also described in **Supporting Information (Figures D.10)**.

3-Ring MDA $[M]^+$ Species (303 Da)

When comparing the **Figure 4.3b** MS/MS spectrum of the $[M]^+$ species to **Figure 4.3a** $[M+H]^+$ MS/MS spectrum, we observe an increase in ion stability. In **Figure 4.5** precursor $[M]^+$ requires additional collision energy to generate fragment ions compared to the $[M+H]^+$ species. This increase in stability results from delocalization of charge for the 303 Da species. In **Figure 4.5c-d**, fewer fragment ions are observed for the 303 Da $[M]^+$ species at 20 eV collision energy compared to **Figure 4.5a-b** (vertical dashed line is drawn for visual reference). Found in the **Supporting Information, Table D.4** shows percent total ion current values of major and minor fragment ions formed from mass 303 Da depletion. In **Scheme 4.1b**, the major fragment ions observed to form directly from mass 303 Da are outlined: mass 302 ($[M-1]^+$), mass 210 ($[M-93]^+$), and mass 197 ($[M-106]^+$). At 25 eV, fragment ion 302 Da forms from the loss of one hydrogen (9%, 25 eV) and mass 197 Da results from the loss of methylene-aniline (42%, 25 eV). Fragment ion 210 Da forms at higher collision energy (10%, 30 eV), resulting from the loss of aniline. Several minor fragment ions are also observed from the depletion of these major

fragment ions: 209 ($[M-93]^+$), 181 ($[M-29]^+$), 180 ($[M-17]^+$), and 165 Da ($[M-15]^+$). In **Scheme 4.1b**, species 209 Da forms directly from mass 302 Da through an M-93 loss of aniline (16%, 35 eV). At higher collision energy, mass 210 Da fragments into 181 Da due to loss of -NH and -CH₂ (9%, 45 eV). In **Figure 4.5c**, the depletion of 197 Da can be monitored to illustrate the formation of fragment ion 180 Da (30%, 50 eV, loss of -NH₂ and one-hydrogen). Increasing fragmentation energy to 50eV causes mass 180 Da to form mass 165 Da (9%, loss of -NH₂). Additional structures of the major and minor fragment ions formed from the 303 Da species can be found in **Supporting Information Figure D.12**.

3-Ring MDA [M-H]⁺ Species (302 Da)

The $[M-H]^+$ species is the most stable precursor compared to $[M+H]^+$ and $[M]^+$ (see **Figure 4.5**). The increase in stability is due to the fluorene-backbone, as seen in the 2-ring $[M-H]^+$ species versus the $[M+H]^+$ species, discussed previously.³ In **Figure 4.3c**, the MS/MS spectrum shows three major fragment ions deriving from the 302 Da precursor ion at 20 eV: 285 ($[M-17]^+$), 209 ($[M-93]^+$), and 106 Da ($[M-196]^+$). The dashed line in **Figure 4.5e-f** at 20 eV is drawn for visual alignment to illustrate fragment ions formed at %RIC above 5%. Here we observe the increased stability of the $[M-H]^+$ precursor ion, higher collision energy is needed to form fragment ions. Total percent ion current values of major and minor fragment ions formed from the 302 Da species can be found in **Supporting Information Table D.5**. The formation of mass 285 Da corresponds to M-17, loss of ammonia (4%, 20 eV), this species is not one of the more intense fragment ions for the mass 302 Da precursor, but loss of -NH₃ occurs prominently in the MALDI spectra for all species. In **Scheme 4.1c** the proposed fragment ion pathways are illustrated for the 302 Da precursor. The major fragment ion formed from the 302 Da precursor is an ion at mass 209 Da (36%, 20 eV), formally M-93 corresponding to loss of aniline; it can be assumed to come from charge-remote fragmentation (**Supporting Information Figures D.7-D.8**). Fragment ion 106 Da has been consistently characterized for the MDA 2-ring, 3-ring, and

4-ring species. For the 3-ring MALDI MS/MS studies, mass 106 Da forms from a loss of 4,4'-MDA and one hydrogen (5%, 30 eV). There are five additional minor fragment ions of interest, all formed at higher collision energies: 208 ($[M-1]^+$), 193 ($[M-16]^+$), 192 ($[M-1]^+$), 180 ($[M-29]^+$), and 165 Da ($[M-28]^+$). Fragment ion 208 Da (16%, 35 eV) forms from 209 Da due to a loss of one hydrogen localizing the charge on the ring. Fragment ion 193 Da (18%, 30 eV) forms from a loss of $-NH_2$ directly from fragment 209 Da. Furthermore, the 193 Da ion depletes into mass 192 Da (8%, 30 eV) from loss of the bridge-hydrogen; in addition, higher collision energy causes mass 165 Da (30%, 50 eV) to form from the 193 Da species due to the loss of $-CHN-$ from the protonated species. The 180 Da (26%, 50 eV) ion also forms at high collision energy and is formed from the 209 Da species from a loss of $CH_2=NH$. Additional structures of the major and minor fragment ions formed from the 302 Da precursor can be found in the **Supporting Information Figure D.13**.

4-Ring MDA

The three 4-ring MDA precursors behave similarly to the 3-ring MDA. Here we observe $[M+H]^+$ as the least stable precursor amongst $[M]^+$ and $[M-H]^+$ species, forming more fragment ions at lower collision energy (**Figure 4.3d-f**); this is consistent with our previous 2-ring studies.³ The MALDI MS/MS spectra for the 4-ring MDAs show major fragment ion peaks at low collision energy for each precursor species: $[M+H]^+$, $[M]^+$, and $[M-H]^+$. It is interesting to note that an increase in fragment ions is observed in **Figure 4.3d** for the $[M+H]^+$ species (15 eV) compared to $[M]^+$ and $[M-H]^+$ in **Figure 4.3e-f** (20 eV). In **Figure 4.6**, we monitor the depletion of each precursor species as a function of applied collision energy from 0 to 50 eV in 5 eV increments. **Figure 4.6a,c,e** shows CID breakdown curves for the major fragment ions having a %RIC of 20% or more, and **Figure 4.6b,d,f** illustrates the minor fragment ions (less than 20% RIC) formed along the 0-50 eV ramp. Major fragment ions to be discussed form in high

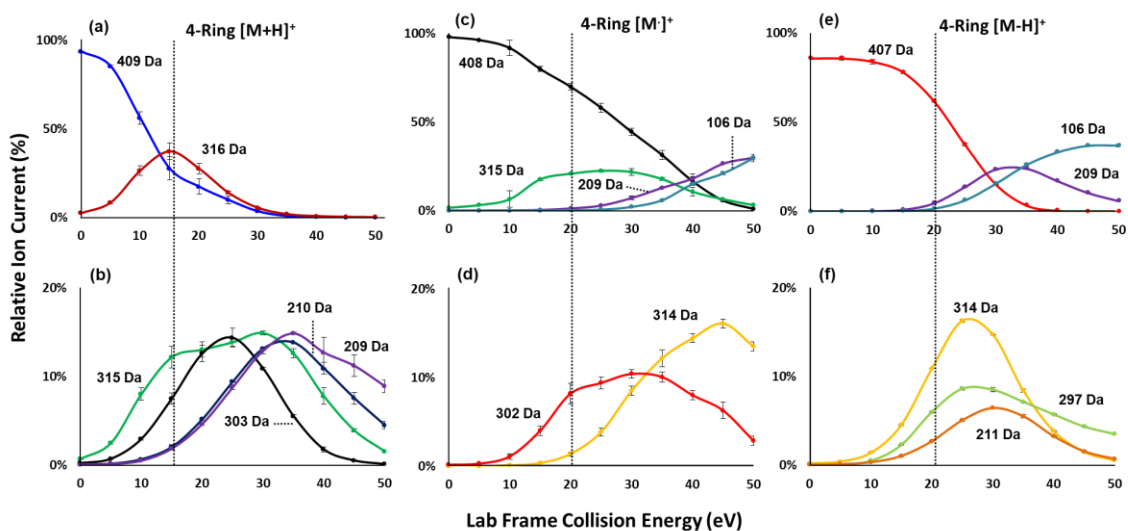
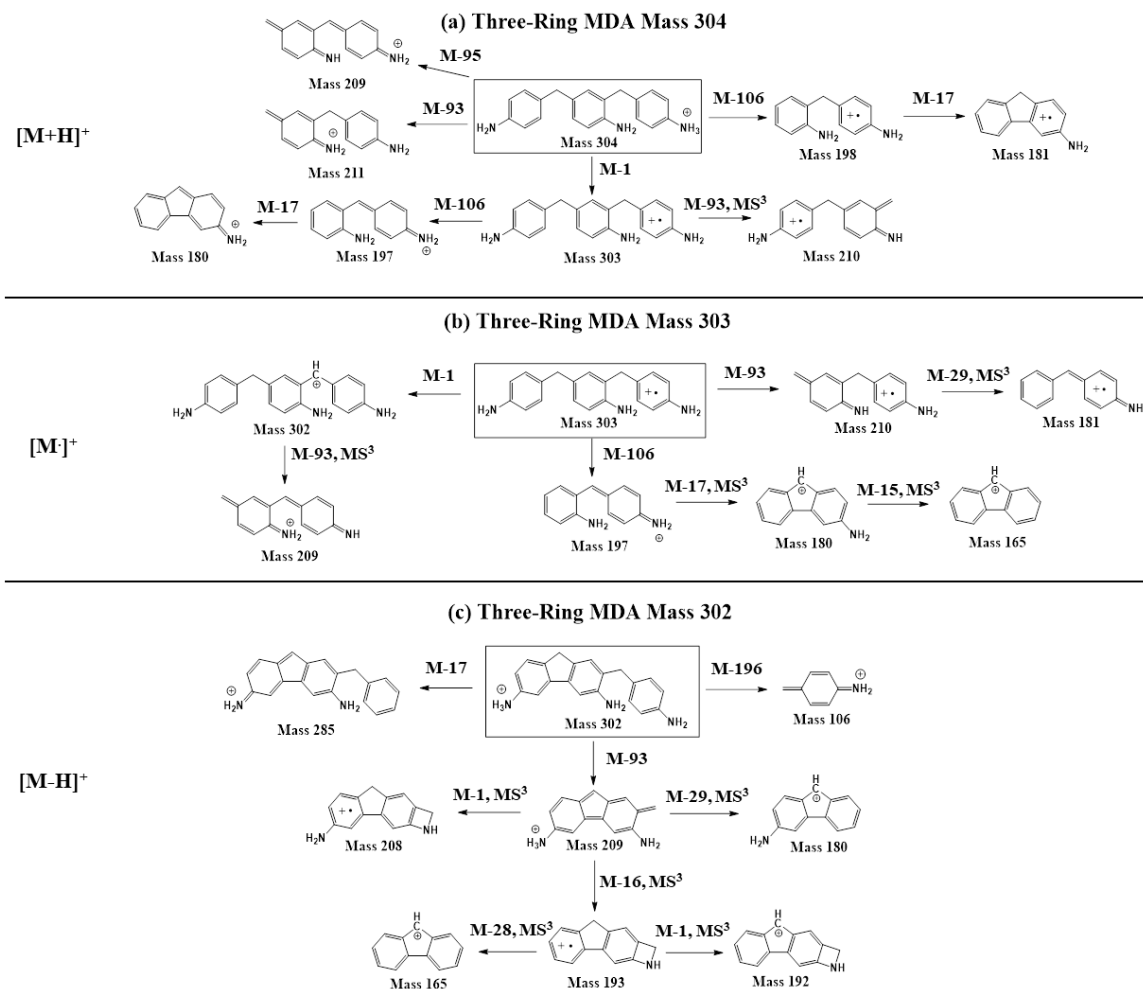


Figure 4.6. Collision-induced dissociation curves monitoring the transition of 4-ring MDA precursor to fragment ions for (a-b) $[M+H]^+$ ions, (c-d) $[M]^+$ ions, and (e-f) $[M-H]^+$ ions. Fragment ions formed above 20% relative ion current are represented in (a,c,e); fragment ions formed between 0-20% relative ion current are represented in (b,d,f) for each precursor ion. Dashed lines for visual alignment are added for each precursor species: $[M+H]^+$ dashed line represents 15 eV, precursor $[M]^+$ and $[M-H]^+$ dashed line represents collision energy at 20 eV.

abundance at collision energies below 35 eV, additional CID curves for fragment ions formed at 35 eV or higher are provided as **Supporting Information (Figure D.14)**. Total percent ion current tables are provided in the **Supporting Information (Table D.6-D.8)** for each precursor; these tables highlight fragment ion (%RIC) formation as CID energy is increased. The major fragment ions observed for each precursor species will be discussed in further detail.

4-Ring MDA [M+H]⁺ Species (409 Da)

The MS/MS spectrum in **Figure 4.3d** highlights the 409 Da [M+H]⁺ precursor forming three major fragment ions at low collision energy (15 eV): 316 Da ([M-93]⁺), 315 Da ([M-94]⁺), and 303 Da ([M-106]⁺). In **Figure 4.6a-b**, the depletion of 409 Da species is monitored over a 0-50 eV span at 5 eV increments, a dashed line is drawn for visual alignment. The three major fragment ions are observed to originate directly from the depletion of 409 Da. Proposed structures of these fragment ions are provided in **Scheme 4.2a**. The CID curves show that the most abundant fragment ion, mass 316 Da (37%, 15 eV), corresponds to the loss of aniline through charge-remote fragmentation. Based on the CID curves and **Supporting Information Table D.6**, mass 209 Da forms directly from the 316 Da species through M-107 loss of methylene-aniline and one hydrogen (15%, 35 eV). The second major fragment ion at mass 315 Da (15%, 30 eV) also forms from the 409 Da species due to the loss of aniline and one hydrogen. The third major fragment ion, mass 303 Da has the same structure as the 3-ring MDA [M]⁺ species discussed above. The charge is delocalized on the ring, and the 303 Da (14%, 35 eV) fragment ion forms from the loss of a methylene-aniline. Additional fragmentation of mass 303 Da leads to the formation of a minor fragment ion, mass 210 Da (M-93, 14%, 35 eV), which represents the loss of aniline through charge remote fragmentation. Higher collision energy fragment ions formed from the [M+H]⁺ precursor can be found in **Supporting Information Figure D.14**.



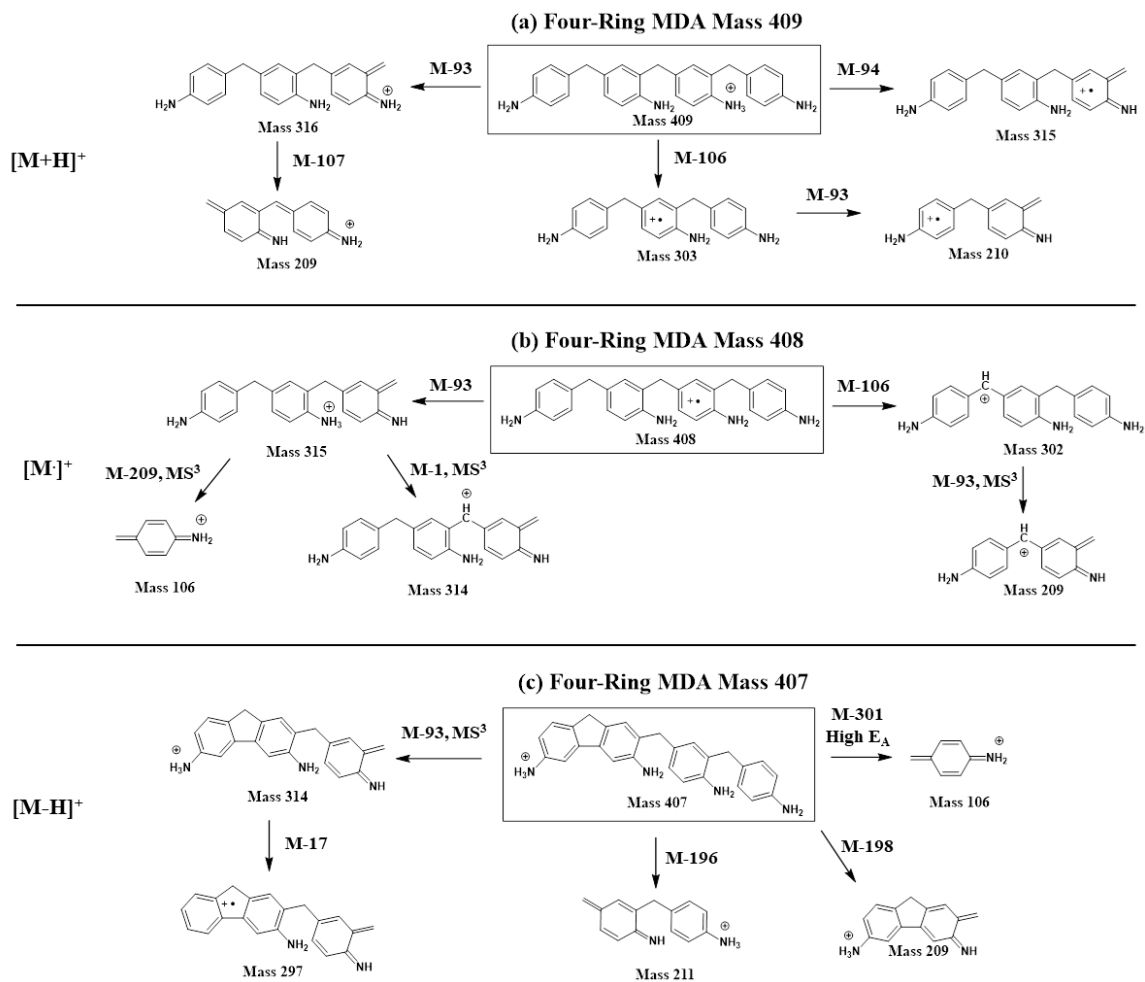
Scheme 4.1. MDA 3-ring (a) $[M+H]^+$, (b) $[M]^+$, and (c) $[M-H]^+$ fragmentation pathways of major low energy fragment ions. Fragment ions identified through MS^3 spectra are denoted, MS^3 .

4-Ring MDA [M]⁺ Species (408 Da)

As observed in **Figure 4.3e**, the 408 Da species is more stable than the 409 Da precursor. The collision energy is increased to 20 eV for the [M]⁺ species and only a few fragment ions are observed compared to the [M+H]⁺ spectrum. In **Figure 4.6c-d**, 408 Da is monitored across an increasing collision energy gradient, here the [M]⁺ species reaches 50% depletion at 25 eV. **Scheme 4.2b** illustrates the two major fragment ions derived from the 408 Da species: mass 315 Da ([M-93]⁺) and 302 Da ([M-106]⁺). Major fragment ion 315 Da initially forms due to loss of aniline (23%, 25 eV). This major fragment ion can further fragment into two minor fragment ions at higher collision energy: 314 Da ([M-1]⁺) and 106 ([M-209]⁺). Fragment 314 Da forms from the loss of one hydrogen at the bridge-carbon (16%, 45 eV), and fragment 106 Da (30%, 50eV) forms due to charge-remote fragmentation. MS³ data support 314 Da and 106 Da species originating from the 315 Da species, see **Supporting Information Figure D.6**. The third major fragment ion formed from the 408 Da precursor is mass 302 Da (11%, 30 eV); this species is formed from the loss of a methylene-aniline and the structure resembles 3-ring MDA with the loss of a hydrogen from the bridged methylene. Further depletion of the mass 302 Da species increases the formation of mass 209 Da (30%, 50 eV) through loss of aniline (M-93). Additional supporting data for 408 Da fragment ions can be found in the **Supporting Information (Figures D.14 and Table D.7)**.

4-Ring MDA [M-H]⁺ Species (407 Da)

The 407 Da [M-H]⁺ species is also more stable than the 409 Da [M+H]⁺ ion. In **Figure 4.3f** the MS/MS spectrum at 20 eV shows few fragment ions and a strong 407 Da precursor peak at 62% relative intensity. **Figure 4.6e-f** illustrates the major and minor fragment ions formed above 5% as the collision energy was monitored from 0-50 eV. As the 407 Da precursor depletes, four major fragment ions are observed to derive directly from the [M-H]⁺ species. **Scheme 4.2c**



Scheme 4.2. MDA 4-ring (a) $[M+H]^+$, (b) $[M]^+$, and (c) $[M-H]^+$ fragmentation pathways of major low energy fragment ions. Fragment ions identified through MS^3 spectra are denoted, MS^3 .

shows mass 314 Da ($[M-93]^+$), 211 Da ($[M-196]^+$), 209 Da ($[M-198]^+$), and 106 Da ($[M-301]^+$) all forming from the 407 Da $[M-H]^+$ precursor. Fragment ion 314 Da (16%, 25 eV) is formed from the loss of aniline and then further depletes into minor fragment ion 297 Da ($[M-17]^+$, 9%, 25 eV), formed from the loss of an ammonia. Additionally, ions 211 Da (6%, 30 eV) and 209 Da (24%, 35 eV) are both formed by fragmentation at the center CH_2 , causing the loss of methylene-dianiline. The difference in these fragment ion masses correspond to alternative structural rearrangement and loss of two hydrogens. The 106 Da fragment forms at high collision energy as seen in our previous studies;² this ion forms in 37% abundance at 50 eV. Further exploration of high energy fragment ions formed due to 407 Da depletion can be found in **Supporting Information (Figures D.14)**. A complete breakdown of fragment ion %RIC over 0-50 eV ramp can also be found in **Supporting Information (Table D.8)**.

4.4 Conclusions

In this study, 3-ring and 4-ring MDA have been extensively characterized using MALDI-MS, MALDI-IM-MS, and multi-stage fragmentation (MS/MS, MS^3) techniques. The combination of MS/MS and IM-MS is demonstrated to be a successful tool in the structural characterization of these unique precursor species and their respective fragment ions. In previous work, we concluded that both the 3-ring and 4-ring MDA only form the $[M+H]^+$ precursor in ESI, whereas in this current MALDI study we observe three unique precursor species as seen in the 2-ring studies: $[M+H]^+$, $[M]^+$, and $[M-H]^+$. Here we observe both the 3-ring and 4-ring MDA forming these three unique precursor species. Using energy-resolved ion fragmentation studies, the $[M+H]^+$ species was found to be the least stable of the three precursor ions. The $[M]^+$ and $[M-H]^+$ species were both more stable, generating fewer fragment ions at a higher collision energy. The IM spectra exhibited one narrow structural population for the 3-ring precursor species, whereas the 4-ring MDA precursors each had two unique conformational families present. IM-MS separations can identify the presence of multiple protonation sites coexisting in the gas-phase.

Future studies will include the characterization of the 4-ring MDA IM-MS spectra. These findings provide insight into the complex nature of PU precursors and their unique fragmentation behavior.

4.5 Acknowledgment

We thank Dr. Stefan Wershofen for providing 3-ring and 4-ring MDA samples. We acknowledge Dr. Don Stec and the Vanderbilt NMR facilities for their characterization support, which are supported by the National Institutes of Health (Grant NIH S10 RR019022). This work was supported in part using the resources of the Center for Innovative Technology (CIT) at Vanderbilt University. Funding was provided by the National Institutes of Health (Grant NIH R01GM092218), the U.S. Army Research Office and the Defense Advanced Research Projects Agency (DARPA) under Cooperative Agreement No. W911 NF-14-2-0022, and the U.S. Environmental Protection Agency (EPA) under Assistance Agreement No. 83573601. This work has not been formally reviewed by EPA, and EPA does not endorse any products or commercial services mentioned in this publication. The views expressed in this document are solely those of the authors and should not be interpreted as representing the official policies, either expressed or implied, of the EPA, the Army Research Office, DARPA, or the U.S. Government.

4.6 References

1. Forsythe, J. G.; Stow, S. M.; Nefzger, H.; Kwiecien, N. W.; May, J. C.; McLean, J. A.; Hercules, D. M. Structural characterization of methylenedianiline regioisomers by ion mobility-mass spectrometry, tandem mass spectrometry, and computational strategies: I. Electrospray spectra of 2-ring isomers. *Anal. Chem.* 2014, 86, 4362–4370.
2. Stow, S. M.; Onifer, T. M.; Forsythe, J. G.; Nefzger, H.; Kwiecien, N. W.; May, J. C.; McLean, J. A.; Hercules, D. M. Structural Characterization of Methylenedianiline Regioisomers by Ion Mobility-Mass Spectrometry, Tandem Mass Spectrometry, and Computational Strategies. 2. Electrospray Spectra of 3-Ring and 4-Ring Isomers. *Anal. Chem.* 2015, 87, 6288-6296.
3. Stow, S. M.; Crescentini, T. M.; Forsythe, J. G.; May, J. C.; McLean, J. A.; Hercules, D. M. Structural Characterization of Methylenedianiline Regioisomers by Ion Mobility-Mass Spectrometry, Tandem Mass Spectrometry, and Computational Strategies. 3. MALDI Spectra of 2-Ring Isomers. *Anal. Chem.* 2017, 89, 9900-9910.
4. Mehl, J. T.; Murgasova, R.; Dong, X.; Hercules, D. M.; Nefzger, H., Characterization of polyether and polyester polyurethane soft blocks using MALDI mass spectrometry. *Anal. Chem.* 2000, 72, 2490-2498.
5. Yontz, D. J.; Hsu, S. L. A mass spectrometry analysis of hard segment length distribution in polyurethanes. *Macromolecules.* 2000, 33, 8415-8420.
6. Aou, K.; Schrock, A. K.; Ginzburg, V. V.; Price, P. C. Characterization of polyurethane hard segment length distribution using soft hydrolysis/MALDI and Monte Carlo simulation. *Polymer.* 2013, 54, 5005-5015.
7. Gies, A. P.; Hercules, D. M.; Collision induced dissociation study of ester-based polyurethane fragmentation reactions. *Anal. Chim. Acta.* 2014, 808, 199-219.

8. Bonnaire, N.; Dannoux, A.; Pernelle, C.; Amekraz, B.; Moulin, C. On the use of electrospray ionization and desorption electrospray ionization mass spectrometry for bulk and surface polymer analysis. *Appl. Spectrosc.* 2010, 64, 810-818.
9. May, J. C.; Goodwin, C. R.; McLean, J. A. In *Encyclopedia of Drug Metabolism and Interactions*; Lyubimov, A. V., Ed.; John Wiley & Sons: Hoboken, New Jersey, USA, 2011.
10. Ruotolo, B. T.; Benesch, J. L. P.; Sandercock, A. M.; Hyung, S. J.; Robinson, C. V. Ion mobility–mass spectrometry analysis of large protein complexes. *Nat. Protoc.* 2008, 3, 1139–1152.
11. Hines, K. M.; May, J. C.; McLean, J. A.; Xu, L. Evaluation of collision cross section calibrants for structural analysis of lipids by traveling wave ion mobility-mass spectrometry. *Anal. Chem.* 2016, 88, 7329–7336.
12. Harper, B.; Neumann, E. K.; Stow, S. M.; May, J. C.; McLean, J. A.; Solouki, T. Determination of ion mobility collision cross sections for unresolved isomeric mixtures using tandem mass spectrometry and chemometric deconvolution. *Anal. Chim. Acta.* 2016, 939, 64–72.
13. Karpas, Z.; Berant, Z.; Stimac, R. M., An ion mobility spectrometry/mass spectrometry (IMS/MS) study of the site of protonation in anilines. *Struct. Chem.* 1990, 1, 201-204.
14. Lalli, P. M.; Iglesias, B. A.; Toma, H. E.; de Sa, G. F.; Daroda, R. J.; Silva Filho, J. C.; Szulejko, J. E.; Araki, K.; Eberlin, M. N. Protomers: formation, separation and characterization via travelling wave ion mobility mass spectrometry. *J. Mass Spectrom.* 2012, 47, 712-719.

CHAPTER V

ALKALI METAL CATION ADDUCT EFFECT ON POLYBUTYLENE ADIPATE OLIGOMERS: ION MOBILITY-MASS SPECTROMETRY

5.1 Introduction

Polyurethanes (PUs) are one of the most versatile synthetic polymers and are well known for their applications in the automotive, construction, and medical industries. PUs are diblock copolymers composed of hard (urethane) and soft (aliphatic) segments which contribute to their diverse applications.¹ Hard segments such as methylene bisphenol diisocyanate (MDI) are known for their ridged urethane backbone when reacted with soft segment diols such as polyesters. When synthesizing PU polymers, polydispersity inevitably adds a level of complexity to a polymer sample.²

Mass spectrometry (MS) has become one of the most useful analytical techniques for accurate mass measurement and detailed end-group analysis of synthetic polymers.³ Coupling ion mobility (IM) separation to MS (IM-MS) can provide valuable information regarding the three-dimensional structure of a polymer's architectural motif. IM-MS is capable of differentiating isomeric species, such as linear and cyclic polymers,^{4,5} and can provide detailed characterization regarding ion size and mass. A molecule's size and shape are described quantitatively by the gas-phase collision cross section (CCS) derived from IM measurements.^{6,7} Additionally, tandem mass spectrometry (MS/MS) promotes the structural characterization of a polymer's sequence. Coupling IM-MS to MS/MS provides multidimensional information that is useful for characterizing a polymer's molecular sequence and configured arrangement.⁸⁻¹¹

Another useful strategy which can be combined with IM-MS characterization is cation coordination. IM-MS cation coordination has been successfully utilized for biopolymers to analyze DNA base pair arrangements,¹²⁻¹⁴ carbohydrates,^{15,16} and peptide sequences.¹⁷ Although

cation coordination for biopolymers has been extensively explored, applying cation coordination studies towards synthetic polymers using IM-MS is relatively new. Prior studies have noted that flexible poly(ethylene glycol) (PEG) oligomers encapsulate Cs^+ , coordinating up to 11 oxygen centers with the large Cs^+ cation to form a near spherical shape.^{18,19} Other PEG studies have focused on low charge state polymer ions in order to characterize globular gas-phase geometries using both experimental and computational methods.²⁰ Other polymer systems such as poly(methyl methacrylate) were found to coordinate with various metal ions via the oxygen atoms along the polymer backbone,²¹ whereas polystyrene was discovered to coordinate with cations via π stacking at its benzene groups, sandwiching the metal ions between the rings.²² Several alkali ions were used to characterize poly(ethylene terephthalate) and the identity of the cation corresponded to the oligomer length.²³ Other polymer studies have investigated the addition of metal ions and their effect on polymer topology^{24–27} and the stepwise folding process.²⁸ More recent studies investigating polymer-cation coordination have progressed towards identification of unique three-dimensional structures; by studying these polymer-cation systems, the transition from an unfolded linear species to a folded globular conformation can be investigated.²⁹ For a given charge state, oligomer chain lengths are observed to fold around the cation in a well-defined manner. As the degree of polymerization (DP) increases for a given polymer, the structural motif was observed to transition towards a globular arrangement.³⁰ Uniquely, charge-induced unfolding of polymers has also been investigated.³¹

In the present study, a telechelic PBA standard ($M_n = 2250$), **Figure 5.1**, was investigated by probing the effects of various Group I monovalent cations (Li, Na, K, Rb, and Cs). IM-MS studies identified multiple charge state (z) trends for each cationized PBA oligomer. Unique transitional folding was noted for all charge state trends observed, including: +1, +2, and +3. Empirical CCS values as obtained from uniform electric field measurements are reported for each alkali metal-adducted PBA oligomer. An analysis of variance (ANOVA) on the measured CCS values was used to determine gas-phase structural differences (different molecular volume) and

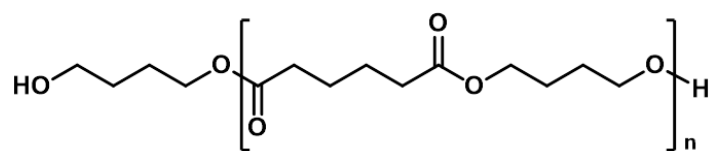


Figure 5.1. Structure of telechelic polybutylene adipate (PBA).

structural similarities (same molecular volume) observed between each PBA-cation. IM-MS/MS was also utilized to study the unique fragmentation patterns associated with cation-oligomer species (DP = 1 and DP = 5). Here the mobility-resolved ion fragmentation results revealed the unique behavior of the Li⁺ and Na⁺ cation to undergo 1,5 H-shift and 1,3 H-shift fragmentation, compared to the larger cations K⁺, Rb⁺, and Cs⁺ which preferentially are lost upon increased activation energy. The combination of monovalent alkali metal cations, IM-MS, IM-MS/MS, and statistical strategies aided in the characterization of PBA's gas-phase structural behavior.

5.2. Materials and Methods

Materials

Optima LC-MS grade acetonitrile and water were purchased from Fisher Scientific (Waltham, MA). The PBA sample was provided by Bayer Material Science, with the number-average molecular weight (M_n) determined by end-group analysis ($M_n = 2250$).³² MALDI analysis of this PBA sample determined $M_n = 2155$.³³ Lithium chloride, sodium chloride, potassium chloride, rubidium chloride, and cesium chloride were purchased from Sigma-Aldrich (St. Louis, MO). The PBA sample was prepared at an initial concentration of 1 mg/mL and subsequently diluted to a final concentration of 10 µg/mL in acetonitrile. Group I monovalent cations were prepared at an initial concentration of 1 mg/mL in water. Then, metal cation solutions were diluted to 5 mM in 10 µg/mL of the PBA sample in acetonitrile.

Instrumentation

All experiments were conducted on a commercially available drift tube IM-MS (6560-IM-QTOF, Agilent Technologies, Santa Clara, CA, USA) as described previously.³⁴ The IM stage of this instrument consists of a uniform field drift tube 78.1 cm in length, filled with nitrogen and operated with a static drift gas pressure of ca. 4 Torr and ~30 °C. All samples were directly infused via a syringe pump (Cole-Palmer, Vernon Hills, IL) at a 10 µL/min flow rate into a

thermally assisted ESI source (Agilent Jet Stream). The instrument was operated in the positive ion mode with 3.8 kV applied to the ion transfer capillary and 1.8 kV applied to the ion focusing nozzle. The sample nebulizer is maintained at ground potential. Source temperatures were kept relatively low (200 °C) to aid in ionization. Ion mobility parameters were adjusted to optimize the IM resolving power and utilize a gate width of 100 μ s.³⁵

CCS Measurements

Collision cross sections (CCS) were determined using a stepped field technique where the applied voltage across the drift tube was varied in 7 uniform increments from 1050 to 1650 V (7.0 – 19.8 V/cm or 6 – 16 Td at 4 Torr) to determine the time ions reside outside the drift tube. The corrected drift times were then used to obtain CCS values based on the Mason-Schamp equation as described previously.^{34,36}

Targeted MS/MS

For targeted MS/MS, all ions were analyzed by IM and then m/z species related to DP = 1 and DP = 5 [M+Li]⁺, [M+Na]⁺, [M+K]⁺, [M+Rb]⁺, and [M+Cs]⁺ oligomer adducts were mass isolated for CID (IM-MS/MS). For IM, the trap fill time was set to 60,000 μ s and 200 μ s for trap release time. For CID, a stepped voltage ramp was used with increments of 10 V between 0 – 100 V (laboratory frame). The IM-MS was tuned and mass calibrated using a commercially-available tuning mixture (ESI-L Tune Mix, Agilent).

5.3. Results and Discussion

5.3.1. IM-MS Characterization

In this study, we monitored the evolution of cationized PBA for changes in CCS as a function of DP for three different charge states: +1, +2, and +3 ions. These charge states were generated by coordination of monovalent alkali cations (Li, Na, K, Rb, and Cs) onto the polymer

chain, and labeled accordingly in **Figure 5.2**. Due to polydispersity within the PBA sample, each charge state trend represents a range of PBA DP coordination with alkali metal cations. The full ESI-MS spectra of each PBA-cationized sample can be found in **Supporting Information (Figures E.1-E.2)**. By using ESI to characterize PBA, we observe multiply charged species, which are characteristic of this technique. The majority of species contained in this PBA polymer sample were telechelic oligomers with –OH end groups. Within this PBA sample, only a few low MW cyclics were detected as seen in **Supporting Information (Figure E.1)**.

Figure 5.2 contains a plot of the CCS as a function of the PBA DP, increasing in chain length from left to right. For charge state +1, we observe a mean constant increase in CCS as the PBA chain length increases for each cationized DP. To ensure that the IM profiles observed are unique to the PBA polymer sample alone and not to the instrument conditions, the IM-MS ion funnel trap RF voltage was increased in 20 V increments from 80 – 200 V_{pp} (**Supporting Information Figure E.3**). Varying the trap RF voltage in this manner can probe for low energy structural transitions (i.e. polymer unfolding that would otherwise go unnoticed).³⁷ There were no changes to the PBA charge state trends in the IM profile, respective to varying the trap RF voltage. As observed similarly by Haler et al. for poly(ethoxyphosphate) and poly(ethylene oxide) polymers,²² CCS evolution for higher charge state species (greater than +1) are known to have a defined structural transition at a specific DP. The structural transition can be characterized by a visual change in a CCS IM plot, and is attributed to a collapse of the polymer’s gas-phase conformation to smaller CCS. The point of structural transition for this PBA system is observed at the beginning of the +2 and +3 charge state trend lines. This is where the polymer ion’s chain length exceeds the coulombic forces induced by the multiple cations. The PBA species are then observed to behave predictably with a near linear increase in CCS respective to the increase in the polymers length. When the polymer cationizes with two metal adducts ($z = +2$), a noticeable “tipping point” in CCS is observed between DP = 4 – 8. Here the polymer species is observed to begin transitional folding around the two cations contained in the PBA ion structure. A similar

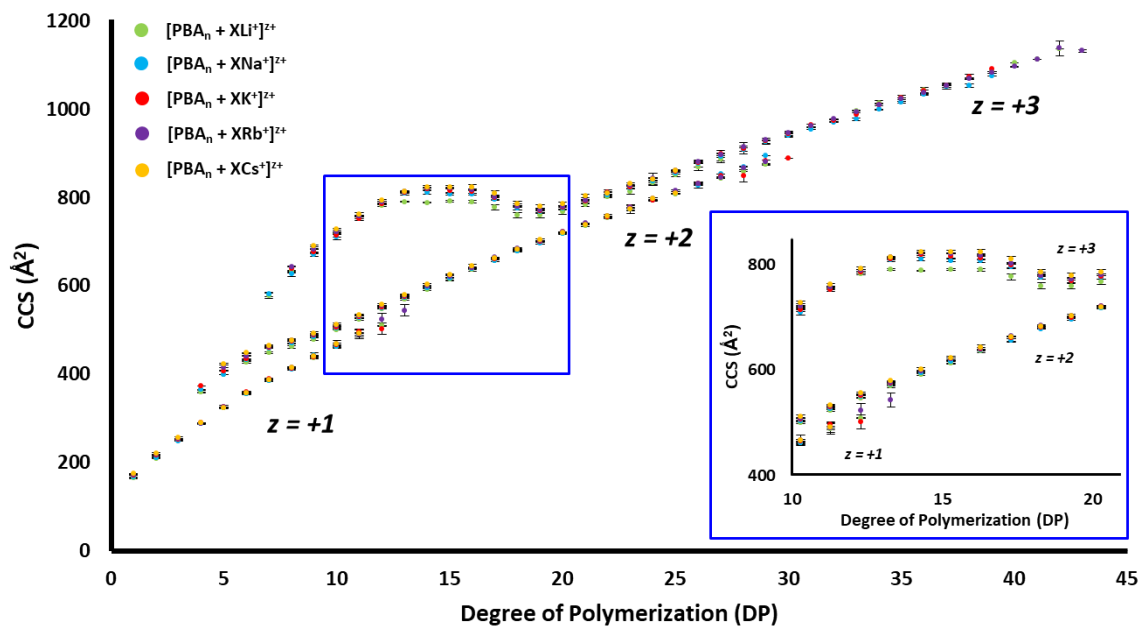


Figure 5.2. IM-MS mobility plot of CCS versus degree of polymerization (DP) of cationized linear PBA oligomers (n) for different charge states ($z = +1, +2,$ and $+3$). Cations used to ionize PBA are annotated by color (Li = green, Na = blue, K = red, Rb = purple, and Cs = yellow), where X is the number of cations ionizing PBA_n .

region of structural folding is more dramatically observed for the higher +3 charge state trend line, where PBA coordinates with three cations. Here the tipping point in CCS is observed to reach its peak transition from DP = 7 – 14. This transition is characterized by a decrease in CCS between DP = 15 – 19 after which the CCS increases with polymer chain length in a linear trend for DP > 20. We hypothesize that this positive linear trend in CCS following the region of fold change indicates when the PBA chain wraps around the attached cations.

It is expected that longer PBA oligomer chains can accommodate more cations than shorter chains and this bears out in the observations made in this study. For instance, singly charged PBA oligomers are first observed for DP = 1, doubly charged species are observed at DP = 4, and triply charged species begin to form at DP = 7. As the PBA chain length increases in size, the polymer's ability to coordinate with additional cation species increases. The full IM-MS profile of each PBA-cation sample can be found in **Supporting Information (Figure E.4)**.

5.3.2. Structural Transition

Figure 5.3 shows plots of the first derivative of CCS ($\Delta\text{CCS}/\Delta\text{DP}$) for each PBA-cation at charge states +1, +2, and +3. **Figure 5.3a** illustrates that the point of change is indicated by a valley, where the data indicate that a structural transition in a polymer's topology occurs respective to DP. The point at which ΔCCS converges to the smallest number represents the tipping point, that is, the point where the polymer chain wraps around the attached cations, previously referred to as "beads-on-a-string".²⁹ In **Figure 5.3b-f**, ΔCCS was calculated for each PBA's cationized charge state trend and illustrated accordingly: +1 (dotted-line), +2 (dashed-line), and +3 (solid-line). Blue dashed lines are drawn for visual alignment of the point of structural change represented by the negative apex for each charge state. Along the charge state +1 trend line, we observed minor transitional folding for PBA-Na, PBA-K, PBA-Rb, and PBA-Cs between DP = 2 - 3, (**Figure 5.3c-f**). However, PBA-Li species were not observed to undergo any fold change in the charge state +1 trend for DP = 2 – 3 (**Figure 5.3b**).

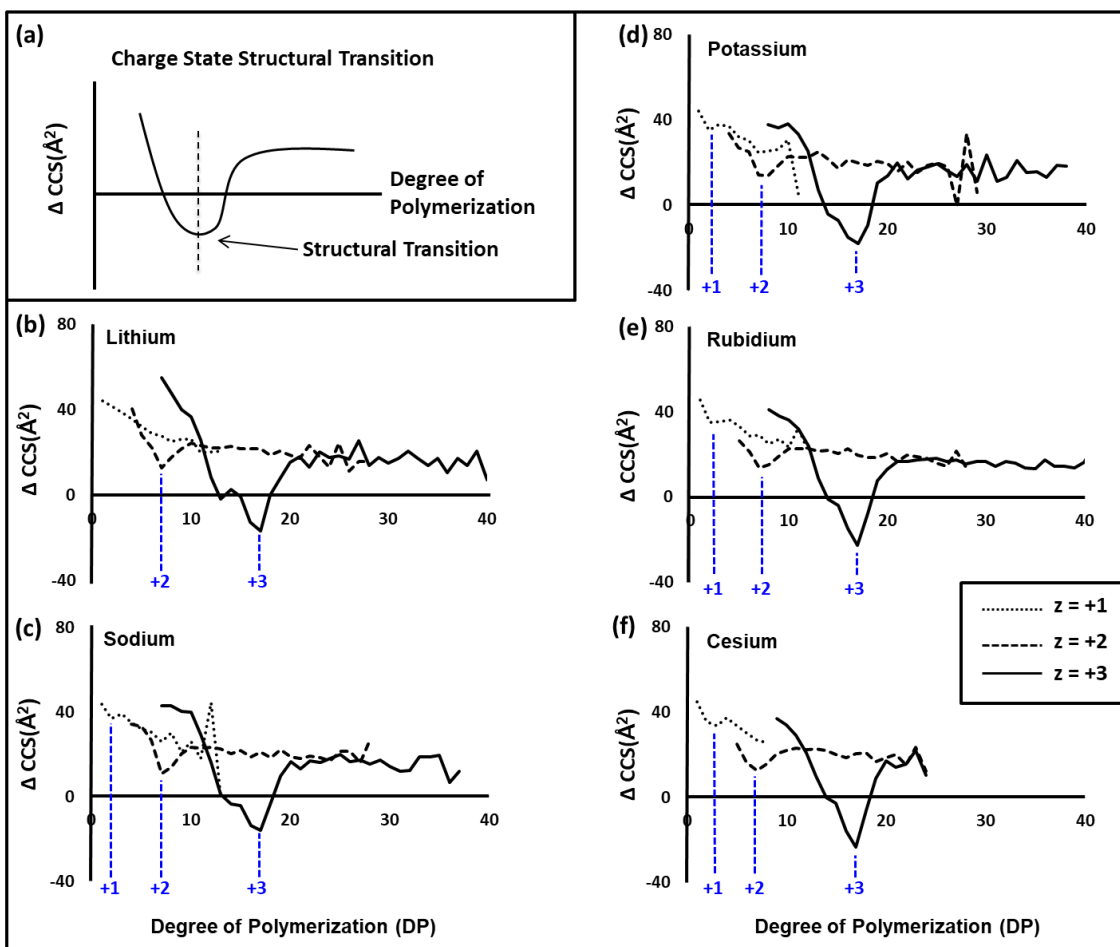


Figure 5.3. Plots of ΔCCS vs DP which assist in monitoring gas-phase structural trends. **(a)** Conceptual illustration of a polymer undergoing charge dependent structural transition as indicated by a well-defined negative apex. **(b)** Charge state trends observed for each cationized PBA DP include: $z = +1$ (dotted line), $z = +2$ (dashed line), and $z = +3$ (solid line). Blue dashed lines are drawn for visual alignment of transition.

In **Figure 5.3b-f**, the valleys indicate that significant structural changes occur for charge states +2 and +3. **Table 5.1** summarizes the region of significant structural change along the +2 and +3 charge state trend lines as recorded for each cation: Li, Na, K, Rb, and Cs. The +2 charge state structural transition region occurs between DP = 6 – 10 for all five cations. However, the +3 charge state structural transition region changes with respect to cation size. In **Table 5.1**, the +3 charge state structural transitions for Li start at chain length DP = 11. As the cation size increases to Na and K, the region of structural transition starts at DP = 12. Similarly, the larger cations Rb and Cs undergo structural changes at a longer chain length of DP = 13. This pattern highlights the effect that cation size has on the polymer's gas-phase structure. Although we observed these cation species to undergo structural change at different DP values, all cations were found to end their transitions at DP = 20. The structural transition region for Li spanned a range of 10 PBA DPs, Na and K spanned 9 PBA DPs, and Rb and Cs transitioned across only 8 PBA DP additions. **Table 5.1** also shows the tipping points for each PBA-cation at charge states +2 and +3. The tipping point, or point of greatest change for charge state +2 was observed to be DP = 7 for all five cations. The tipping point for charge state +3 occurred at DP = 17 for all cation species. As stated above, we observed the PBA region of structural folding to be directly related to cation coordination and size. As a general observation, the smaller cations, such as Li, Na, and K were found to start transition folding at a shorter PBA chain length, compared to Rb and Cs.

5.3. Ion Mobility Plots

IM distributions of PBA-cationized by Li (green), Na (blue), K (red), Rb (purple), and Cs (yellow) are shown in **Figure 5.4** for DP = 1, 3, and 5 at charge state +1. The corresponding CCS means for each PBA species and their respective standard deviations are represented by error bars at the top of each mobility trace. The vertical dashed lines are drawn for visual alignment within

| Region of Structural Transition (DP) | | | | | |
|--------------------------------------|---------|---------|---------|---------|---------|
| Charge (z) | Li | Na | K | Rb | Cs |
| +1 | NA | 2 - 3 | 2 - 3 | 2 - 3 | 2 - 3 |
| +2 | 6 - 10 | 6 - 10 | 6 - 10 | 6 - 10 | 6 - 10 |
| +3 | 11 - 20 | 12 - 20 | 12 - 20 | 13 - 20 | 13 - 20 |

| Tipping Point (DP) | | | | | |
|--------------------|----|----|----|----|----|
| Charge (z) | Li | Na | K | Rb | Cs |
| +2 | 7 | 7 | 7 | 7 | 7 |
| +3 | 17 | 17 | 17 | 17 | 17 |

Table 5.1. Region of structural transition and tipping point as degree of polymerization (DP) increases for charge states +1, +2 and +3.

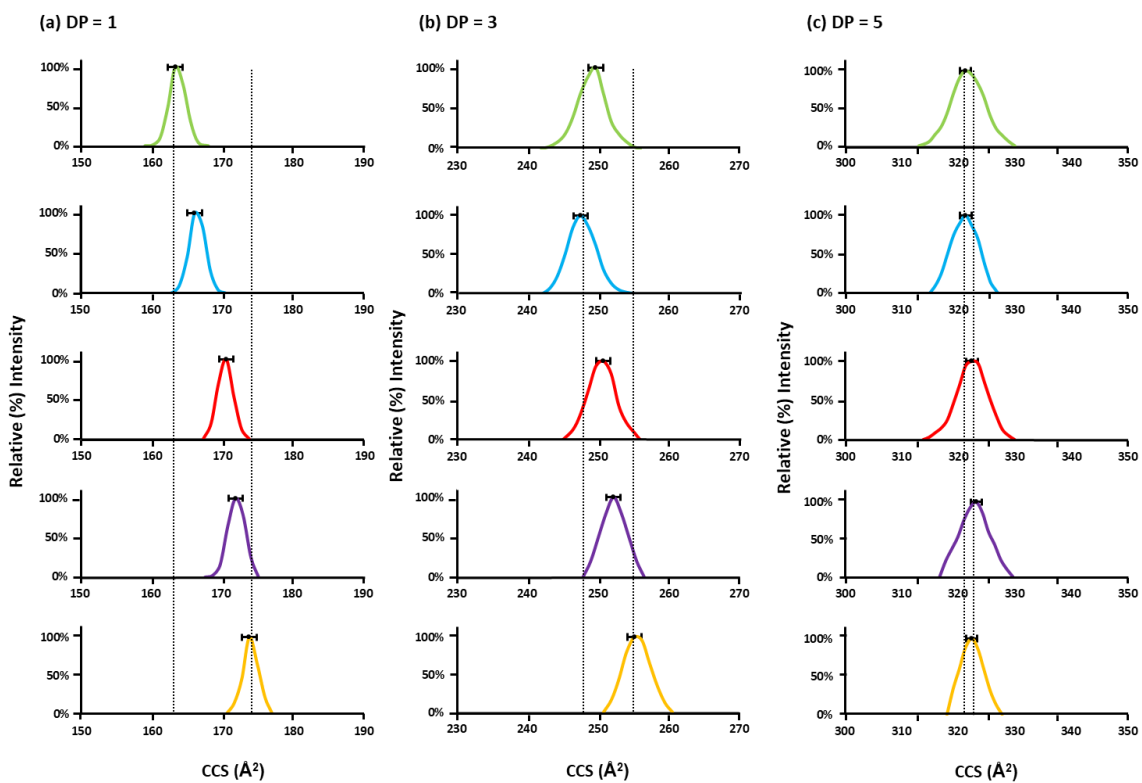


Figure 5.4. IM plots of PBA-cations having charge state +1 are shown above. Experimental CCS and their respective standard deviations are given for (a) DP= 1, (b) DP = 3, and (c) DP = 5. Cations are notated by color: Li = green, Na = blue, K = red, Rb = purple, and Cs = yellow. Dotted lines are drawn for visual alignment representing maximum and minimum CCS values.

Figure 5.4a-c and represent the maximum and minimum CCS values (means) observed for all five PBA-cation species. In **Figure 5.4a**, PBA-cation species (DP = 1) have a CCS range that spans approximately 18 Å²: PBA-Li = 163 ± 0.4 Å², PBA-Na = 166 ± 0.3 Å², PBA-K = 171 ± 0.4 Å², PBA-Rb = 172 ± 0.8 Å², and PBA-Cs = 174 ± 0.5 Å². As cation size increases from Li to Cs, we observed a corresponding increase in CCS for PBA-cation species known as a periodic trend. In **Figure 5.4b**, for a PBA chain length of DP = 3, the maximum and minimum CCS values are observed to span 8 Å². It is interesting to note that for DP = 3, the CCS values are much closer to one another and do not follow a periodic trend. Here, PBA-Na has a smaller mean CCS than PBA-Li: PBA-Li = 249 ± 0.3 Å², PBA-Na = 247 ± 0.4 Å², PBA-K = 250 ± 0.3 Å², PBA-Rb = 252 ± 0.8 Å², and PBA-Cs = 255 ± 0.5 Å². In **Figure 5.4c**, for chain length of DP = 5, the observed CCS range maximum and minimum values converge toward the same CCS, a 2 Å² range. This is within the scale of the standard deviation of the measurements, and there are no periodic trends that can be derived from these measurements. The corresponding PBA CCS values are: PBA-Li = 321 ± 0.5 Å², PBA-Na = 321 ± 0.7 Å², PBA-K = 322 ± 0.4 Å², PBA-Rb = 323 ± 0.8 Å², and PBA-Cs = 322 ± 0.5 Å². Taken collectively, these observations indicate that as the PBA DP increases from DP = 1 to DP = 5, the PBA-cationized CCS values converge. This convergence in CCS is attributed to the polymer's structural transition. As the polymer chain length increases, more ester functional groups become available for cation interaction allowing the polymer to more efficiently coordinate the cation(s). As the PBA chain increases from DP = 1 to DP = 5, the peak width of the IM plot increases in size. A larger peak width could indicate either the presence multiple conformations or the existence of a conformational change during the IM separation.

5.3.4. Statistical Analysis of Charge State +1, +2, and +3

To better understand coordination similarities among PBA-cation DP groups, we performed single-factor analysis of variance (ANOVA) on CCS values obtained for each DP

along the various charge states. ANOVA was used to compare PBA-Li, PBA-Na, PBA-K, PBA-Rb, and PBA-Cs species to one another. In **Figure 5.4**, the CCS values are compared against the same DP chain length, and as notated previously are observed to converge towards the same CCS as the DP chain length increases from DP = 1 to DP = 5. While converging of CCS values is clearly observed for charge state +1 in **Figure 5.4**, we investigated CCS trends within charge state +2 and +3 which are somewhat more difficult to interpret. In **Figure 5.2**, the DP chain lengths represent oligomers ranging from DP = 1 – 43 among the three charge states observed; each CCS value was measured in triplicate for all 5 metal ions, totaling 1,125 data points. In this situation, it is best to use statistical methodology to check for significant differences, and this present problem is well suited for single-factor ANOVA. ANOVA compares the variance *between* CCS values measured for each of the different metal ions variance (*between*) with the collective variance from the reproducibility in measurement of each metal cations CCS value (*within*). The F ratio of the variances, $F = \text{variance (between)} / \text{variance (within)}$, is compared to the critical F value using the appropriate degrees of freedom in the two variables: 4 and 10, respectively. The results were compared to determine if they were significant at the 95% confidence level ($\alpha = 0.05$); this confidence level is typically chosen for scientific experiments. The ANOVA results identified structural differences and similarities between the polymer topologies in the gas-phase that were not qualitatively evident. A detailed description and example of the ANOVA test conducted in this study can be found in **Supporting Information (Figure E.5)**.

In **Table 5.2** for charge state +1 species, the CCS values for each PBA-cation measured between DP = 1 – 3 are determined to be significantly different. However, the CCS values for PBA-cations at DP = 4 – 11 are considered to be significantly the same at the 95% confidence level. This is consistent with the data of **Figure 5.4**. Raw data and detailed statistical analysis for charge state +1 trend can be found in **Supporting Information (Figure E.6)**. For charge state +2, the CCS values for PBA-cation species

| Charge | Cations | DP: | 1 | 2 | 3 | 4 | 5 | 6 | 7 | 8 | 9 | 10 | 11 | 12 | 13 | 14 |
|--------|---------------|-----|-----------|---|---|------|---|---|---|---|---|----|----|----|----|----|
| +1 | Li Na K Rb Cs | | DIFFERENT | | | SAME | | | | | | | | | | |

| Charge | Cations | DP: | 5 | 6 | 7 | 8 | 9 | 10 | 11 | 12 | 13 | 14 | 15 | 16 | 17 | 18 | 19 | 20 | 21 | 22 | 23 | 24 | 25 | 26 | 27 | 28 | 29 | 30 |
|--------|---------------|-----|-----------|------|---|---|---|-----------|------|-----------|------|----|----|----|----|----|----|----|----|----|----|----|----|------|----|----|----|----|
| +2 | Li Na K Rb Cs | | D. | SAME | | | | | | | | | | | | | | | | | | | | | | | | |
| +3 | Li Na K Rb Cs | | DIFFERENT | | | | | | | | | | | | | | | | | | | | | | | | | |
| +3 | Na K Rb Cs | | | | | | | DIFFERENT | SAME | DIFFERENT | SAME | | | | | D. | | | | | | | | | | | | |
| +3 | Li Na K Rb | | | | | | | | | | | | | | | | | | | | | | | SAME | D. | | | |

Table 5.2. Summary of ANOVA analysis on CCS measurements for charge states +1, +2, and +3. For charge state +1, all five cations are compared. For charge state +2, the PBA-Cs species was not detected beyond DP = 25. ANOVA results for charge state +3 data are shown for three separate comparisons (1) all 5 cations, (2) without-Li, and (3) without-Cs. For all ANOVA comparisons, significant differences in CCS means are represented in blue, and significant similarities in CCS means are represented in green for the 95% confidence level.

between DP = 4 – 6 are significantly different, but significantly the same for DP = 7 – 22. Note, only charge state +2 PBA-Li, PBA-Na, and PBA-K species for DP = 4 were detected. Larger cations Rb and Cs were observed to cationize with PBA starting at DP = 5 chain length.

In **Figure 5.2**, a folding region is observed for both the +2 and +3 charge states. When investigating the +3 charge state in detail, unique behavior was noted for the PBA-Li species during the structural transition region (described below). The +3 charge state trend is quite different from the other charge state trends. Here, all five of the PBA-cation species have significantly different CCS values for the metal cations between DP = 7 – 25. However, inspection indicated that the CCS values for Li +3 are typically smaller than the +3 CCS values for the other four metal cations. When the PBA-Li data are removed from the data set, the remaining PBA-cation (Na, K, Rb, and Cs) CCS values are considered to be significantly different for DP = 9 – 11, to be the same for DP = 12 – 13, different for DP = 14 – 16, and significantly the same for DP = 17 – 24, with one outlier at DP = 25. As the PBA chain length increases beyond DP = 25, PBA-Cs is not detected in the IM-MS spectra. Interestingly, given the odd behavior of Li for the +3 charge state structural transition region, here we observed significant similarities among PBA-cation (Li, Na, K, and Rb) species between DP = 26 – 29, and structural differences for DP = 30. The ANOVA test aided in differentiating the similarities and differences between PBA-cation CCS means and their gas-phase behavior. Raw data used for ANOVA test can be found in **Supporting Information Figures E.7-E.12**, for charge states +2 and +3.

5.3.5. Mass Targeted Experiments

Previous MALDI-TOF/TOF CID studies explored cyclic and linear PBA low energy fragmentation mechanisms using Li and Na cations.³⁸ In this study, we explored the unique fragmentation behavior of each alkali metal cation (Li, Na, K, Rb, and Cs) for DP = 1 and DP = 5 in the +1 charge state. When characterizing DP = 1 species, informative fragment ions were

observed only for PBA-Li species as seen in **Supporting Information Figure E.13**, with unique fragment ion structures attributed to PBA-Li species outlined in **Supporting Information Figure E.14**. Here, at relatively low energy, PBA-Li is observed to produce fragment ions attributed to 1,5 H-shift fragmentation. The small atomic radius of Li, aids in its ability to fit within the polyester pocket, stabilizing the charge on the fragment ion. When monitoring PBA-Na, PBA-K, PBA-Rb, and PBA-Cs for DP = 1, fragment ions were not observed. Instead each PBA-cationized species was observed to lose its respective cation as CID energy increased. IM-MS/MS fragmentation spectra for each PBA-cationized species for DP = 1 can be found in **Supporting Information Figure E.13, E.15-E.16**.

When monitoring CID energy with respect to DP = 5, we observed unique fragment ions for both PBA-Li and PBA-Na species. **Figure 5.5a** illustrates 1,5 H-shift fragmentation, commonly referred to as a McLafferty Rearrangement mechanism, where fragment ions result from a single chain fracture. There are only two series of peaks that can be formed from the 1,5 H-shift of a symmetrical PBA precursor. Fragmentation occurs by hydrogen transfer from the diol chain to the ester carbonyl, but not from the acid segment. Both PBA-Li and PBA-Na species were observed to undergo 1,5 H-shift, promoting fragmentation at the C(O)O-CH₂ bond generating butanol-carboxyl and butanol-butene species. Both sets of fragment ions from the 1,5 H-shift were observed in the MS/MS spectra, as seen in **Supporting Information Figure E.17**.

Figure 5.5b illustrates the 1,3 H-shift, which was also observed for both PBA-Li and PBA-Na species. This hydrogen transfer reaction causes fragmentation at the C(O)-O bond producing two stable fragments: (1) diol terminus and (2) ketene end group. These results correspond to what has previously been reported regarding DP = 5 PBA-Li and PBA-Na species. Fragment ion series (i.e. PBA-Li: 297, 497, 697, etc. and PBA-Na: 213, 413, 613, etc.) associated with -OH terminus in the 1,3 H-shift pathway, are in low abundance for ESI-MS. In previous MALDI-MS studies, this 1,3 H-shift fragment ion series was observed at higher signal intensity,

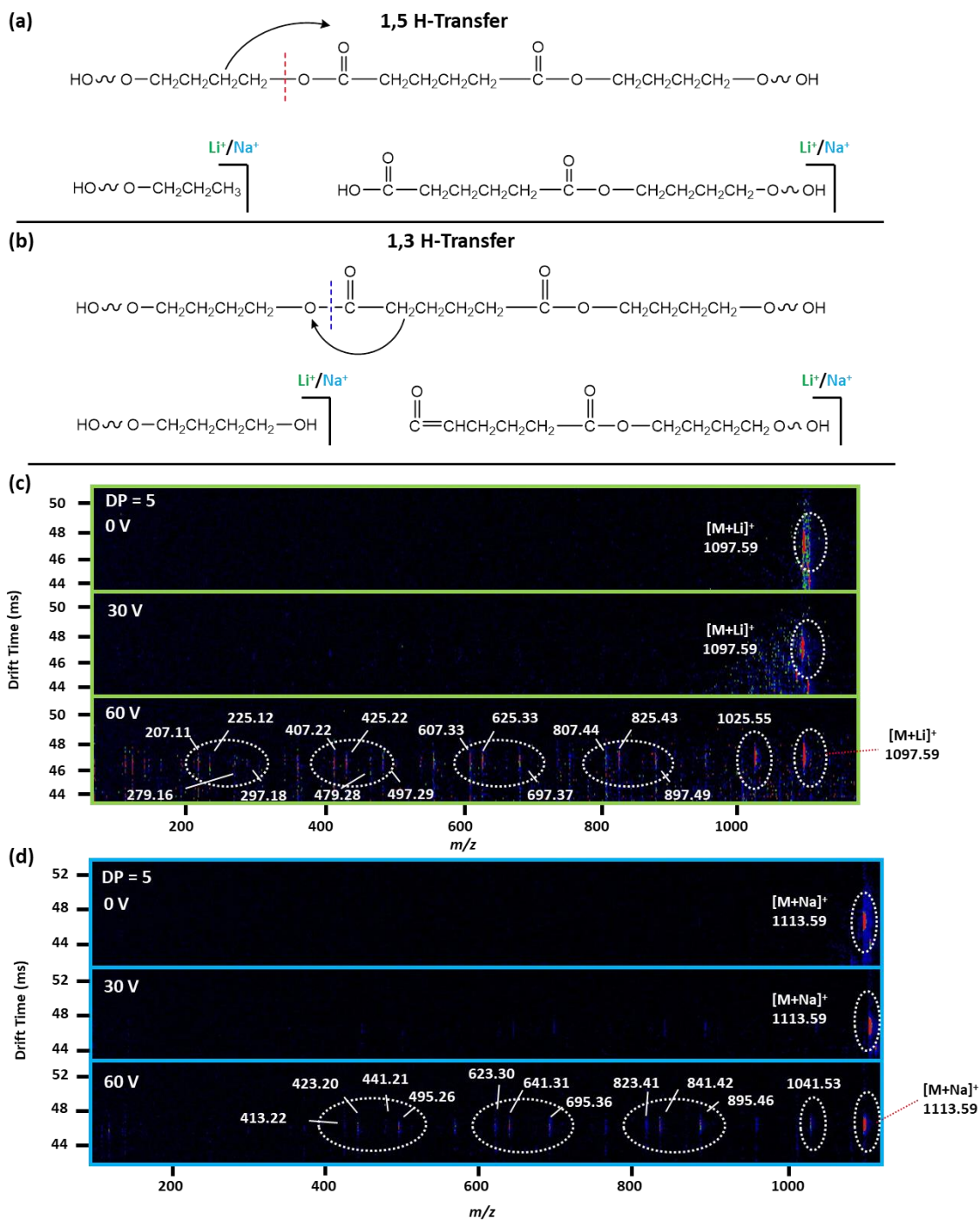


Figure 5.5. Fragmentation reaction mechanisms and results for singly charged PBA DP = 5. (a) 1,5 H-shift and (b) 1,3 H-shift produces two stable fragment ions. (c) IM-MS/MS spectrum for PBA-Li at 0, 30, and 60 V collision energies and (d) IM-MS/MS spectrum for PBA-Na at 0, 30, and 60 V collision energies. Respective fragment and precursor species are outlined.

this difference in peak intensity can most likely be attributed to ionization differences between the MALDI and ESI process.

Respective fragment ions (m/z) and their mechanistic pathways observed for both PBA-Li and PBA-Na species can be found in **Supporting Information Figure E.18**. IM-MS/MS spectra of PBA-Li and PBA-Na are shown in **Figure 5.5c-d**. Fragment ion generation was monitored for each PBA-cationized species at CID energies 0 – 110 V in 10 V increments; see **Supporting Information Figures E.19-E.20**. In **Figure 5.5c-d**, CID spectra for 0 V, 30 V, and 60 V have dotted lines drawn around fragment ions and precursor species. As similarly seen with DP = 1 PBA-Li species, there were no fragment ions detected for PBA-K, PBA-Rb, and PBA-Cs, these species preferentially lost their respective cation as CID energy increased. We observe both PBA-Li and PBA-Na species to undergo charge remote 1,5 H-shift and 1,3 H-shift fragmentation as CID energy increases.

In this study, no unique fragment ions were observed for either Li or Na cationized PBA. However, Li did produce more intense fragment ion peaks relative to PBA-Na fragment ions. In addition to 1,5 H-shift and 1,3 H-shift fragment ions, other fragment ions are formed such as a diacid (carboxyl end groups), most likely formed by an intra-chain fragmentation mechanism. Moreover, this data is consistent with the previously reported MALDI-TOF/TOF CID studies.³⁸

5.4. Conclusions

In this study, PBA ($M_n = 2250$) has been extensively characterized with monovalent alkali metal cations (Li, Na, K, Rb, and Cs) using IM-MS, IM-MS/MS, and statistical analysis. Unique charge state trend lines were observed for this polymer and it was concluded that these structural trends were native to the polymer and not specific to either the cationizing agents or instrumentation used in this study. Charge state +1, +2, and +3 trend lines increased in CCS respective to increasing PBA chain length. Regions of structural transitions representing gas-phase polymer folding were more distinctly observed for charge states +2 and +3, although PBA-

cations Na, K, Rb, and Cs were also observed to undergo structural transitions along the +1 charge state trend line. The tipping point at which the gas-phase structural behavior begins to change was determined to be the same for each cation tested within the same charge state trend line. ANOVA statistical analysis aided in evaluating unique gas-phase behavior of the PBA-cations. Significant differences and similarities between PBA-cation CCS means, were compared to characterize gas-phase behavior. Tandem IM-MS/MS revealed that PBA-Li and PBA-Na species preferentially promote charge remote fragmentation to produce 1,5 H-shift and 1,3 H-shift fragment ions at DP = 5. Other PBA-cation species (K, Rb, and Cs) preferentially lost their cationizing agent as CID energy increased yielding no structurally useful information.

5.5. Future Directions

Probing PBA with monovalent cations (Li, Na, K, Rb, and Cs) revealed the unique behavior of this polymers increasing DP chain length in the gas-phase. Future studies using Group II divalent cations (Mg and Ca), may provide additional information on how the polyester back-bone interacts with a divalent system. There are limited IM-MS papers on the use of divalent cations to probe synthetic polymers gas-phase behavior. Comparing monovalent and divalent cation coordination with PBA is of interest to further investigate. Statistical tests such as ANOVA will be useful to compare these large data sets, and highlight the unique structural similarities and differences of the multi-charged cations. It is also of interest to further characterize the behavior of the PBA structural transition regions respective to a wide variety of charge states and cation sizes. Preliminary data of PBA-Mg and PBA-Ca systems reveal charge state trends increasing from $z = +2, +4, +6$ etc., as seen in **Figure 5.6**. Probing with divalent cations, may also be a useful technique for ionizing high molecular weight synthetic polymers using MS-based techniques. Cation-polymer complexes characterized by IM-MS methods can help elucidate the unique structural motif of a specific polymer system.

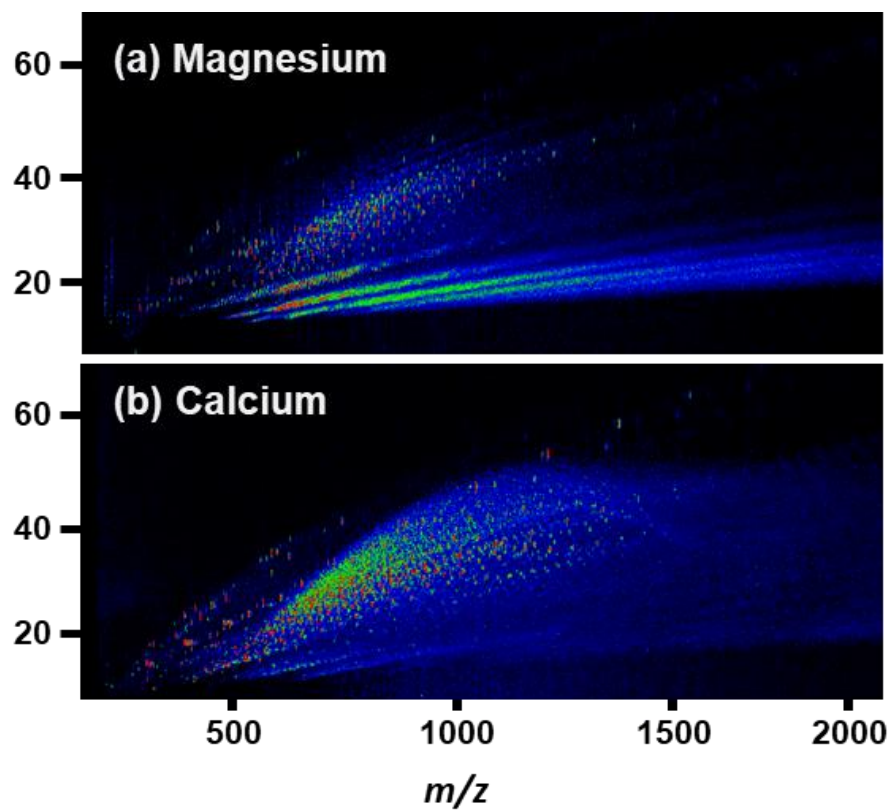


Figure 5.6. Ion mobility spectra of PBA ($M_n = 2200$) ionized by alkali monovalent cations. PBA samples were independently spiked with either formic acid or one cation of interest: (a) magnesium chloride and (b) calcium chloride.

5.6. Acknowledgments

We thank Hartmut Nefzger and Bayer Material Sciences for providing the poly(butylene adipate) ($M_n = 2250$) sample. This work was funded and supported in part by the resources of the Center for Innovative Technology (CIT) at Vanderbilt University. Financial support for this research was provided by the National Institutes of Health (NIH NIGMS R01GM092218 and NIH NCI 1R03CA222452-01).

5.7. References

1. Oertel, G. *Polyurethane Handbook*; Carl Hanser Verlag, 1985.
2. Oschmann, B.; Lawrence, J.; Schulze, M. W.; Ren, J. M.; Anastasaki, A.; Luo, Y.; Nothling, M. D.; Pester, C. W.; Delaney, K. T.; Connal, L. A.; et al. Effects of Tailored Dispersity on the Self-Assembly of Dimethylsiloxane-Methyl Methacrylate Block Co-Oligomers. *ACS Macro Lett.* 2017, 6 (7), 668–673.
3. Crotty, S.; Gerişlioğlu, S.; Endres, K. J.; Wesdemiotis, C.; Schubert, U. S. Polymer Architectures via Mass Spectrometry and Hyphenated Techniques: A Review. *Anal. Chim. Acta* 2016, 932, 1–21.
4. Hoskins, J. N.; Trimpin, S.; Grayson, S. M. Architectural Differentiation of Linear and Cyclic Polymeric Isomers by Ion Mobility Spectrometry-Mass Spectrometry. *Macromolecules* 2011, 44 (17), 6915–6918.
5. Bennett, J. R. M.-B. J. M.; McLean, J. A.; Hercules, D. M. Novel Behavior of the Chromatographic Separation of Linear and Cyclic Polymers. *Anal. Bioanal. Chem.* 2016, 408 (3), 677–681.
6. Wesdemiotis, C. Multidimensional Mass Spectrometry of Synthetic Polymers and Advanced Materials. *Angew. Chemie - Int. Ed.* 2017, 56 (6), 1452–1464.
7. Forsythe, J. G.; Stow, S. M.; Nefzger, H.; Kwiecien, N. W.; May, J. C.; McLean, J. A.; Hercules, D. M. Structural Characterization of Methylenedianiline Regioisomers by Ion Mobility-Mass Spectrometry, Tandem Mass Spectrometry, and Computational Strategies: I. Electrospray Spectra of 2-Ring Isomers. *Anal. Chem.* 2014, 86 (9), 4362–4370.
8. Gies, A. P.; Hercules, D. M. Collision Induced Dissociation Study of Ester-Based Polyurethane Fragmentation Reactions. *Anal. Chim. Acta* 2014, 808, 199–219.
9. Barrere, C.; Selmi, W.; Hubert-Roux, M.; Coupin, T.; Assumani, B.; Afonso, C.; Giusti, P. Rapid Analysis of Polyester and Polyethylene Blends by Ion Mobility-Mass Spectrometry. *Polym. Chem.* 2014, 5 (11), 3576–3582.

10. Alexander, N. E.; Swanson, J. P.; Joy, A.; Wesdemiotis, C. Sequence Analysis of Cyclic Polyester Copolymers Using Ion Mobility Tandem Mass Spectrometry. *Int. J. Mass Spectrom.* 2018, 429, 151–157.
11. Liu, X.; Cool, L. R.; Lin, K.; Kasko, A. M.; Wesdemiotis, C. Tandem Mass Spectrometry and Ion Mobility Mass Spectrometry for the Analysis of Molecular Sequence and Architecture of Hyperbranched Glycopolymers. *Analyst* 2015, 140 (4), 1182–1191.
12. Arcella, A.; Portella, G.; Ruiz, M. L.; Eritja, R.; Vilaseca, M.; Gabelica, V.; Orozco, M. Structure of Triplex DNA in the Gas Phase. *J. Am. Chem. Soc.* 2012, 134 (15), 6596–6606.
13. Koomen, J. M.; Ruotolo, B. T.; Gillig, K. J.; McLean, J. A.; Russell, D. H.; Kang, M.; Dunbar, K. R.; Fuhrer, K.; Gonin, M.; Schultz, J. A. Oligonucleotide Analysis with MALDI-Ion-Mobility-TOFMS. *Anal. Bioanal. Chem.* 2002, 373 (7), 612–617.
14. Burmistrova, A.; Gabelica, V.; Duwez, A. S.; De Pauw, E. Ion Mobility Spectrometry Reveals Duplex DNA Dissociation Intermediates. *J. Am. Soc. Mass Spectrom.* 2013, 24 (11), 1777–1786.
15. Fenn, L. S.; Kliman, M.; Mahsut, A.; Zhao, S. R.; McLean, J. A. Characterizing Ion Mobility-Mass Spectrometry Conformation Space for the Analysis of Complex Biological Samples. *Anal. Bioanal. Chem.* 2009, 394 (1), 235–244.
16. Fenn, L. S.; McLean, J. A. Structural Resolution of Carbohydrate Positional and Structural Isomers Based on Gas-Phase Ion Mobility-Mass Spectrometry. *Phys. Chem. Chem. Phys.* 2011, 13 (6), 2196–2205.
17. McLean, J. A.; Ruotolo, B. T.; Gillig, K. J.; Russell, D. H. Ion Mobility-Mass Spectrometry: A New Paradigm for Proteomics. *Int. J. Mass Spectrom.* 2005, 240 (3), 301–315.
18. Helden, G. Von; Bowers, M. T.; Wytenbach, T. Inclusion of a MALDI Ion Source in the Ion Chromatography Technique: Conformational Information on Polymer and Biomolecular Ions. *Int. J. Mass Spectrom. Ion Process.* 1995, 147, 349–364.

19. Wytttenbach, T.; von Helden, G.; Bowers, M. T. Conformations of Alkali Ion Cationized Polyethers in the Gas Phase: Polyethylene Glycol and Bis[(Benzo-15-Crown-5)-15-Ylmethyl] Pimelate. *Int. J. Mass Spectrom. Ion Process.* 1997, 165–166, 377–390.
20. Ernesto Criado-Hidalgo, Juan Fernández-García, J. F. de la M. Mass and Charge Distribution Analysis in Negative Electrosprays of Large Polyethylene Glycol Chains by Ion Mobility Mass Spectrometry. *Anal. Chem.* 2013, 85, 2710–2716.
21. Gidden, J.; Jackson, A. T.; Scrivens, J. H.; Bowers, M. T. Gas Phase Conformations of Synthetic Polymers: Poly(Methyl Methacrylate) Oligomers Cationized by Sodium Ions. *Int. J. Mass Spectrom.* 1999, 188, 121–130.
22. Gidden, J.; Bowers, M. T.; Jackson, A. T.; Scrivens, J. H. Gas-Phase Conformations of Cationized Poly(Styrene) Oligomers. *J. Am. Soc. Mass Spectrom.* 2002, 13 (5), 499–505.
23. Gidden, J.; Wytttenbach, T.; Batka, J. J.; Weis, P.; Bowers, M. T.; Jackson, A. T.; Scrivens, J. H. Poly (Ethylene Terephthalate) Oligomers Cationized by Alkali Ions: Structures, Energetics, and Their Effect on Mass Spectra and the Matrix-Assisted Laser Desorption/Ionization Process. *J. Am. Soc. Mass Spectrom.* 1999, 10 (9), 883–895.
24. Morsa, D.; Defize, T.; Dehareng, D.; Jérôme, C.; De Pauw, E. Polymer Topology Revealed by Ion Mobility Coupled with Mass Spectrometry. *Anal. Chem.* 2014, 86 (19), 9693–9700.
25. Haler, J. R. N.; Morsa, D.; Lecomte, P.; Jérôme, C.; Far, J.; De Pauw, E. Predicting Ion Mobility-Mass Spectrometry Trends of Polymers Using the Concept of Apparent Densities. *Elsevier Methods* 2018, 144, 125–133.
26. Foley, C. D.; Zhang, B.; Alb, A. M.; Trimpin, S.; Grayson, S. M. Use of Ion Mobility Spectrometry-Mass Spectrometry to Elucidate Architectural Dispersity within Star Polymers. *ACS Macro Lett.* 2015, 4 (7), 778–782.
27. Kim, K.; Lee, J. W.; Chang, T.; Kim, H. I. Characterization of Polylactides with Different Stereoregularity Using Electrospray Ionization Ion Mobility Mass Spectrometry. *J. Am. Soc. Mass Spectrom.* 2014, 25 (10), 1771–1779.

28. Duez, Q.; Josse, T.; Lemaur, V.; Chirot, F.; Choi, C. M.; Dubois, P.; Dugourd, P.; Cornil, J.; Gerbaux, P.; De Winter, J. Correlation between the Shape of the Ion Mobility Signals and the Stepwise Folding Process of Polylactide Ions. *J. Mass Spectrom.* 2017, 52 (3), 133–138.
29. Trimpin, S.; Plasencia, M.; Isailovic, D.; Clemmer, D. E. Resolving Oligomers from Fully Grown Polymers with IMS-MS. *Anal. Chem.* 2007, 79 (21), 7965–7974.
30. Trimpin, S.; Clemmer, D. E. Ion Mobility Spectrometry/Mass Spectrometry Snapshots for Assessing the Molecular Compositions of Complex Polymeric Systems. *Anal. Chem.* 2008, 80 (23), 9073–9083.
31. Ude, S.; Fernández De La Mora, J.; Thomson, B. A. Charge-Induced Unfolding of Multiply Charged Polyethylene Glycol Ions. *J. Am. Chem. Soc.* 2004, 126 (38), 12184–12190.
32. Nefzger, H. Personal Communication; 2011.
33. Chakraborty, A. Mass Spectrometric Study of Poly(1,4-Butylene Adipate)-Based Model Polyurethanes, Vanderbilt University, Honors Thesis, 2012.
34. May, J. C.; Goodwin, C. R.; Lareau, N. M.; Leaptrot, K. L.; Morris, C. B.; Kurulugama, R. T.; Mordehai, A.; Klein, C.; Barry, W.; Darland, E.; et al. Conformational Ordering of Biomolecules in the Gas Phase: Nitrogen Collision Cross Sections Measured on a Prototype High Resolution Drift Tube Ion Mobility-Mass Spectrometer. *Anal. Chem.* 2014, 86 (4), 2107–2116.
35. May, J. C.; Dodds, J. N.; Kurulugama, R. T.; Stafford, G. C.; Fjeldsted, J. C.; McLean, J. A. Broadscale Resolving Power Performance of a High Precision Uniform Field Ion Mobility-Mass Spectrometer. *Analyst* 2015, 140 (20), 6824–6833.
36. Stow, S. M.; Causon, T. J.; Zheng, X.; Kurulugama, R. T.; Mairinger, T.; May, J. C.; Rennie, E. E.; Baker, E. S.; Smith, R. D.; McLean, J. A.; et al. An Interlaboratory Evaluation of Drift Tube Ion Mobility - Mass Spectrometry Collision Cross Section Measurements. 2017, 89 (17), 9048–9055.

37. Gabelica, V.; Livet, S.; Rosu, F. Optimizing Native Ion Mobility Q-TOF in Helium and Nitrogen for Very Fragile Noncovalent Structures. *J. Am. Soc. Mass Spectrom.* 2018, 29 (11), 2189–2198.
38. Gies, A. P.; Ellison, S. T.; Chakraborty, A. K.; Kwiecien, N. W.; Hercules, D. M. MALDI-TOF/TOF CID Study of Poly(Butylene Adipate) Fragmentation Reactions. *RSC Adv.* 2012, 2 (10), 4135–4151.

CHAPTER VI

STEPWISE ADDITION AND CHARACTERIZATION OF POLYURETHANE BLOCK COPOLYMERS

6.1. Introduction

Polyurethane (PU) di-block copolymers are one of the most versatile polymeric materials, commonly manufactured in the form of foams, thermoplastics, coatings, adhesives, sealants, and elastomers.¹ PUs' resourcefulness comes from their di-block copolymer system comprised of hard and soft segments. Soft segments commonly used in PU synthesis are known as polyester or polyether polyols, which contribute to PUs' elasticity. Commonly used hard segments include aromatic isocyanates such as methylene bisphenyl diisocyanate (MDI), which contributes to PUs rigidity. The reaction between nucleophilic polyol hydroxyl groups and electrophilic isocyanates result in the formation of a urethane back-bone within a PU system.² PUs are extremely complex materials, which can be challenging to characterize due to intrinsic polydispersity, cross-linking, and structural heterogeneity among the most purified samples.³ PUs can also form through random or block polyaddition. One major limitation towards characterizing PUs, is the ability to determine the exact sequential arrangement of a PU oligomer. Therefore, utilizing advanced analytical techniques may provide insight into the chemical make-up of di-block copolymer systems. In addition to using advanced analytical techniques, there is also a need for novel synthetic strategies to generate monodisperse PU oligomers with defined architectural arrangements.

Over the years, bio-polymers such as proteins and oligonucleotides have utilized a stepwise mono-addition method to synthetically control the synthesis of discrete oligomeric compounds. Similarly, this synthetic strategy to form discrete bio-polymers can also be used to create monodisperse synthetic polymers. The present study was inspired by the previous work of

Williams et al., where a series of discrete mass polybutylene glutarate (PBG) oligomers were synthesized using mono protecting group addition.⁴ In Williams' study, these monodisperse PBG species were not only synthesized, but characterized using a variety of analytical techniques so that these PBG oligomers could be used as analytical standards in future studies. Williams used PBG as a model system to show how mono protecting group addition can generate pure polymeric oligomers with a defined monomeric arrangement. In this present study, monodisperse PU oligomers with a specific arrangement of soft and hard segments were synthesized using a similar mono protecting group addition method. In this study, hard segment MDI and telechelic polybutylene adipate (PBA) were used to generate symmetrical P(1,2) and P(1,4) monodisperse PU oligomers as seen in **Figure 6.1a-b**, respectively. PUs will be indicated in the text by "P" with the number of MDI and PBA groups in parentheses separated by a comma. For example a PU having 1 MDI unit and 2 PBA units would be P(1,2).

The inspiration for synthesizing monodisperse PU oligomers, comes from the work of Gies et al., where PBA polyesters and PBA PUs were characterized.^{5,6} Gies used a combination of mass spectrometry (MS) based experiments to characterize a PU sample which contained a wide distribution of polydispersity. He performed fragmentation studies at relatively low collision energies on linear soft segment PUs such as the 830 Da (P(1,2)) and 1230 Da (P(1,4)) species that were observed in the spectrum. The 830 Da species, which was observed by Gies was composed of 2 soft segments (PBA) and 1 hard segment (MDI), and called P(1,2). However in this work, the 830 Da species was identified to contain two isomers: an asymmetrical and a symmetrical P(1,2) compound. This finding highlights the need for discrete mono-disperse PU oligomers to be synthesized, more specifically symmetrical and asymmetrical P(1,2) compounds. Furthermore, structural characterization of these discrete mass PUs may pose as analytical standards for polydisperse samples in the future.

MS is a powerful tool that can be used to identify and characterize synthetic polymers, their end-groups, direct mass measurement, molecular weight distribution, and detection of

Polyester Polyurethanes and Precursors

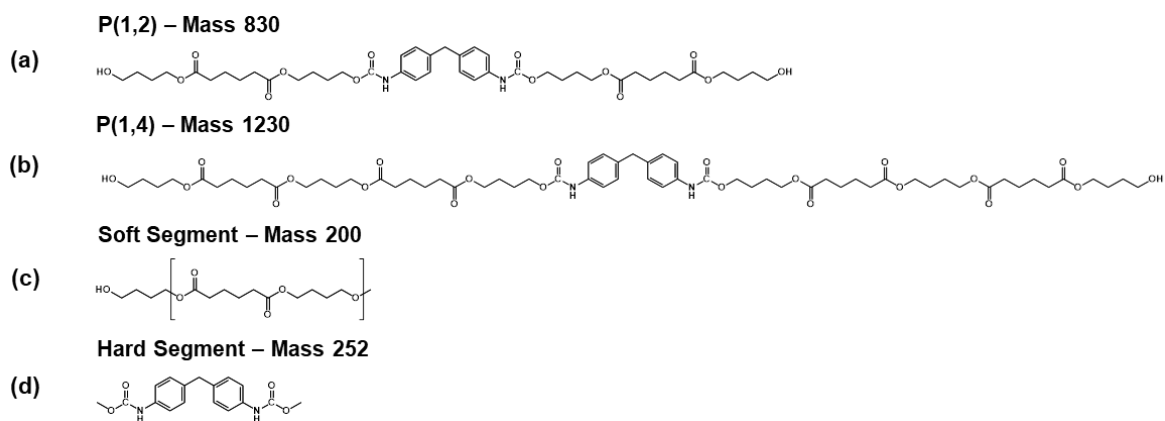


Figure 6.1. Polybutylene adipate polyurethanes synthesized using stepwise addition (a) P(1,2) and (b) P(1,4). Soft segment (c) polybutylene adipate (PBA) has a repeat unit of 200 mass. Hard segment (d) methylene bisphenyl diisocyanate (MDI) has a repeat unit of 252 mass.

impurities or additives. However, MS is still a limited technique when used to fully characterize isomeric species within a polydisperse system.^{7,8} Analytical techniques such as ion mobility-mass spectrometry (IM-MS) are needed in tangent with MS studies to add a multidimensional approach for further insight into a molecule's gas-phase size. IM-MS is a gas-phase separation technique where ions are separated by their shape, in addition to their mass and charge. In previous IM-MS studies, structural elucidation of polymeric samples containing cyclic and linear species,^{9,10} and isomeric¹¹⁻¹⁴ species have been outlined. However, when it comes to detailed structural determination of a polydisperse sample, there is still a need for additional tools towards fully characterizing polymeric materials.

Currently, tandem mass spectrometry (MS/MS) is the leading method for deciphering the sequence of a synthetic polymer. MS/MS sequencing is a key technique to determine the architectural make-up within a polymeric chain.¹⁵ Similar to bio-polymers such as peptides, oligonucleotides, or carbohydrates, collision-induced dissociation (CID) studies can provide useful information about the chemical makeup of a synthetic polymer system. For instance, when the sequence of a polymer is unknown, CID studies can aid in structural elucidation of fragment ions, to help reveal the intact chemical makeup of the polymer system.³

In this study, IM-MS and MS/MS methods such as CID experiments will be incorporated to assist in characterizing the unique fragmentation pathways of mono discrete PU species. The goal of this research is to outline a new direction for sequencing ester-urethane derivatives. In this study, we have developed several synthetic routes towards creating mono disperse polyester PUs using a protecting group stepwise approach. The symmetrical P(1,2) and P(1,4) oligomers were synthesized and characterized using MS-based techniques. In future studies, the asymmetrical P(1,2) and P(1,4) compounds will be synthesized and their unique fragmentation pathways will be compared to the symmetrical compounds. The starting material used to generate the P(1,2) and P(1,4) compounds was also characterized, this includes telechelic PBA $n = 1$ and $n = 2$ species. Each species unique fragmentation pathways were probed using a variety of cations such as

monovalent Li^+ and Na^+ , and transition metal Ag^+ . Similar to previous studies, alkali-metal ions and transition metal ions such as Li^+ , Na^+ , and Ag^+ are known to take on an encapsulation motif around the metal ion and form a π -stacking configuration between phenyl rings.¹⁶ In this study, unique fragment ions associate with each cation-coordinated PBA or PU system was explored. We also probed for unique gas-phase cation-coordination through the use of IM drift plots.

6.2. Material and Methods

6.2.1. Mono-Addition Synthesis of P(1,2) and P(1,4)

The target products of this synthesis were discrete mass telechelic PBA oligomers containing 1 and 2 mass units, and P(1,2) and P(1,4) symmetrical PUs, as seen in **Figure 6.1a-b**. The telechelic PUs polymers contained a defined number of adipic acid, 1,4-butanediol, and MDI residues within the polymer chain. In **Figure 6.1c**, the PBA soft segment contains one adipic acid and one 1,4-butanediol to have the 200 mass repeat unit. In **Figure 6.1d**, the hard segment MDI has a mass of 252 Da.

To synthesize P(1,2) and P(1,4), synthetic control was accomplished through monoprotection of the 1,4-butanediol starting material, and cyclization of the adipic acid to make the adipic anhydride. In this experiment, trytl chloride was used to monoprotect 1,4-butanediol. Condensation reagents such as dicyclohexylcarbodiimide (DCC) with catalytic amounts of (*N,N*-dimethylamino)pyridine (DMAP) were also used to form the ester bond. Detailed analysis of the mono-addition stepwise synthetic approach can be found in section 6.5. *Synthetic Procedures*.

6.2.2. Instrument Conditions

IM-MS Sample Preparation

Optima LC-MS grade acetonitrile, water, and formic acid was purchased from Fisher Scientific (Waltham, MA). Lithium chloride, sodium chloride, and silver nitrate were purchased from Sigma-Aldrich (St. Louis, MO). The monodisperse PU samples were synthesized

specifically for this study. The telechelic PBA $n = 1$, $n = 2$, and PU P(1,2) and P(1,4) samples were prepared at an initial concentration of 1 mg/mL in acetonitrile. Cations were prepared at an initial concentration of 1 mg/mL in water. Then, metal cation solutions were diluted to 5 mM in 10 $\mu\text{g/mL}$ of the synthesized samples in acetonitrile.

Instrumentation

All experiments were carried out in the positive ion mode using a commercially available Agilent 6560 (Agilent Technologies, Santa Clara, CA, USA) as previously described.¹⁷ The drift tube is 78.1 cm in length, filled with nitrogen for the drift gas pressure of ca. 4 Torr. In nitrogen, the collision gas pressure was approximately 4.00 Torr, ~ 30 °C. All samples were directly infused via a syringe pump (Cole-Palmer, Vernon Hills, IL) at 10 $\mu\text{L/min}$ flow rate into a thermally assisted ESI (Agilent Jet Stream). The instrument was operated in the positive ion mode with 3.8 kV applied to the ion transfer capillary and 1.8 kV applied to the ion focusing nozzle. Source temperatures were kept low (200 °C) to aid in ionization. Ion mobility parameters were adjusted to optimize the IM resolving power gate width of 100 μs .¹⁸

CCS Measurements

Collisional cross sections were determined using a stepped field technique where the applied voltage across the drift tube was varied in 7 increments from 1050 to 1650 V (7.0–19.8 V/cm or 6–16 Td at 4 Torr) to determine the time ions reside outside the drift cell. The corrected drift times were then used to obtain CCS values based on the Mason-Schamp equation as described previously.^{17,19}

Untargeted IM-MS/MS

For this method, all species ionized between 50-1700 m/z were introduced to a step voltage ramp set to increase collision energy (CE) at 5 and 10 CE increments: 0-50 CE and 0-100

CE. The IM-MS/MS trap fill time was set to 60000 μ s, 200 μ s for trap release time, and 20 K trap fill. The instrument was tuned using an Agilent tune mix and calibrated to correct for small mass drifts during acquisition.

6.3. Results and Discussions

6.3.1. Characterization of $n = 1$ Polybutylene Adipate by MS/MS

Figure 6.2 details the ESI MS/MS spectra for $n = 1$ cationized PBA; $[M+Li]^+$ (**Figure 6.2a-b**), $[M+Na]^+$ (**Figure 6.2c-d**), and $[M+Ag]^+$ (**Figure 6.2e-f**). In the MS/MS spectra, different collision energies were used to generate fragment ions for each cation coordinated precursor. In **Figure 6.2**, precursor species fragmented at 0 eV and 20 eV (laboratory frame) are compared. The MS/MS spectra in **Figure 6.2** show the unique fragmentation behavior of each cation coordinated to PBA $n = 1$ species. At 0 eV, both $[M+Li]^+$ and $[M+Ag]^+$ were observed to form minor fragment ions, and the $[M+Na]^+$ species appeared to be more stable and therefore did not generate as many fragment ions. However, when comparing the MS/MS spectra at 20 eV for all three cationized precursors, we observe an increase in fragment ions for the $[M+Li]^+$ and $[M+Ag]^+$ species, and a few fragment ions from the $[M+Na]^+$ species. In **Figure 6.3**, the conversion from precursor ion to major fragment ions was monitored as a function of applied collision energy. Collision energy was ramped from 0 eV to 50 eV for all unique precursor species in 5 eV increments and performed in triplicate. The masses listed in **Figure 6.3** are without the charge producing cation, and for comparison purposes. **Figure 6.3a-c** monitors the collision induced dissociation (CID) of major fragment ions formed having a percent relative ion current (%RIC) of 5% or more. Percent relative standard deviations (%RSD) are also plotted for each CID curve.

In **Figure 6.2b**, the MS/MS spectrum highlights major fragment ions observed for the $[M+Li]^+ = 297$ Da species. The MS/MS spectrum shows the 297 Da species dissociating into three major fragment ions at low collision energies: 225, 153, and 135 Da species which

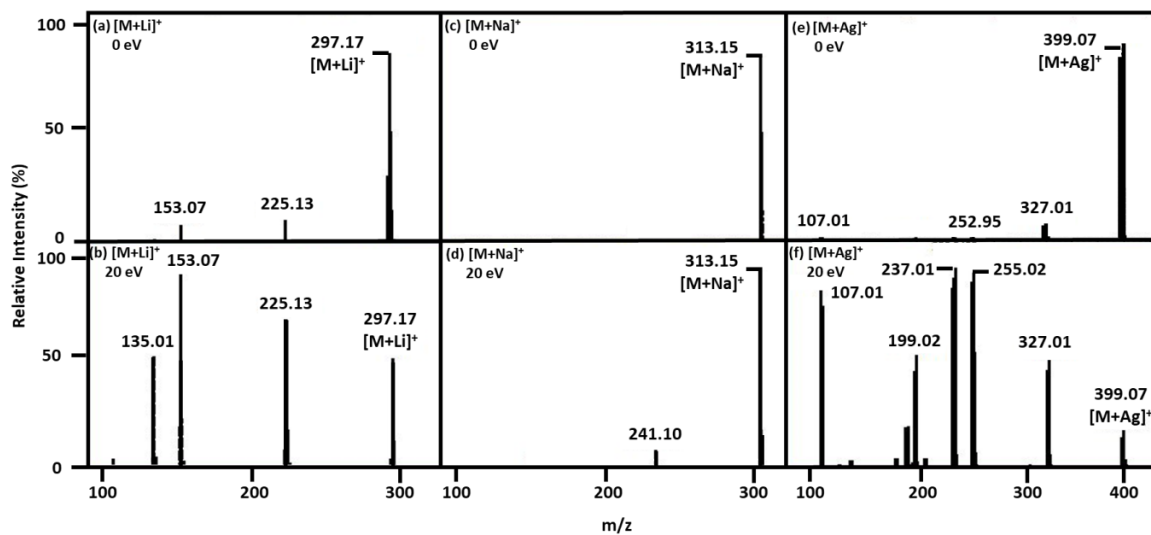


Figure 6.2. ESI MS/MS spectra for $n = 1$ PBA at corresponding lab-frame energies of 0 eV for (a,c,e) and 20 eV for (b,d,f). Results for $[M+Li]^+$ are shown in (a-b), $[M+Na]^+$ in (c-d), and $[M+Ag]^+$ in (e-f).

correspond to the nominal fragment ion masses of 218, 146, and 128 Da, as seen in **Figure 6.3a**. In **Figure 6.3a**, a dotted line was drawn for visual alignment marking the point of low energy for the PBA $n = 1$ precursor (≤ 20 eV). In **Figure 6.4**, fragment ion pathways are illustrated, proposed fragment ion pathways are shown and their corresponding mechanisms. In **Figure 6.3a**, the 290 Da precursor was observed to deplete 100% at 30 eV. Low energy fragment ion 218 Da (29%, 15 eV) formed due to a 1,5 H-shift, generating the PBA $n = 1$ species having acid and hydroxyl end-groups (**Figure 6.4**). Fragment ion 146 Da (46%, 30 eV) is observed to form from a 1,5 H-shift along the 218 Da species (2X 1,5 H-shift), producing the adipic acid (di-acid terminated) fragment ion. Fragment ion 128 Da was observed to form from the 218 Da species, through a combination reaction. Fragment ion 128 Da reaches its peak ion formation at 45 eV (46%) and forms due to a 1,3 H-shift along the 218 Da species, forming an =C=O end group. At higher CID energy, fragment ion 100 Da (41%, 50 eV) was observed to form from the 146 Da species, as seen in **Figure 6.4**.

In **Figure 6.2d**, the MS/MS spectrum highlights major fragment ions formed from the depletion of $[M+Na]^+ = 313$ Da precursor at 20 eV. The MS/MS spectrum shows the 313 Da species having greater stability compared to $[M+Li]^+$ and $[M+Ag]^+$ species, dissociating into one major fragment ions at low CID energies. As seen in **Figure 6.2d**, fragment ions 241 Da corresponds to nominal masses 218 Da in **Figure 6.3b**. Fragment ion 218 Da (31%, 35 eV) is observed to form from the 1,5 H-shift, as seen in **Figure 6.4**. At high CID energies, the major fragment ion 128 Da (as seen for the $[M+Li]^+$ species) was observed to form from the depletion of the 218 Da fragment ion (40 eV 100%), from a 1,3 H-shift pathway. The 128 Da species formed from a combination reaction (1,5 and 1,3 H-shift). The Na cation is known for having a larger atomic radius compared to Li, therefore it can be hypothesized that Li's

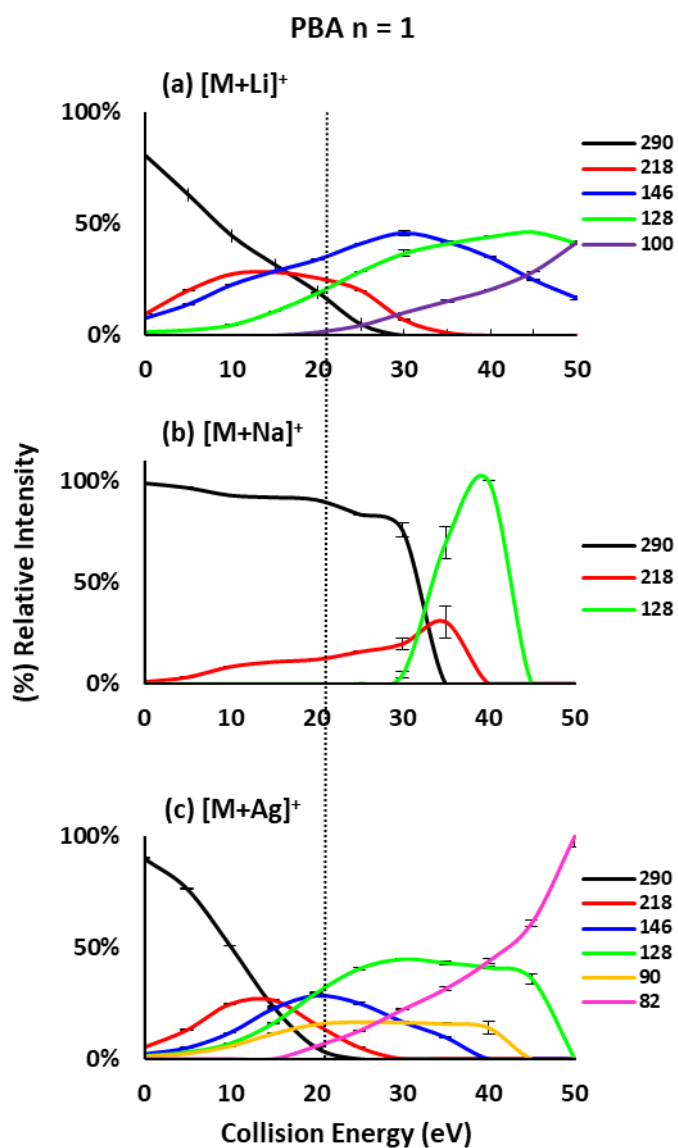


Figure 6.3. Collision-induced dissociation curves monitoring the unique transition of $n = 1$ PBA precursor to fragment ions when coordinated with cations (a) $[M+Li]^+$, (b) $[M+Na]^+$, and (c) $[M+Ag]^+$. The dotted line is drawn at 20 eV for visual alignment of low energy fragment ions.

PBA n = 1 Fragment Ion Pathway

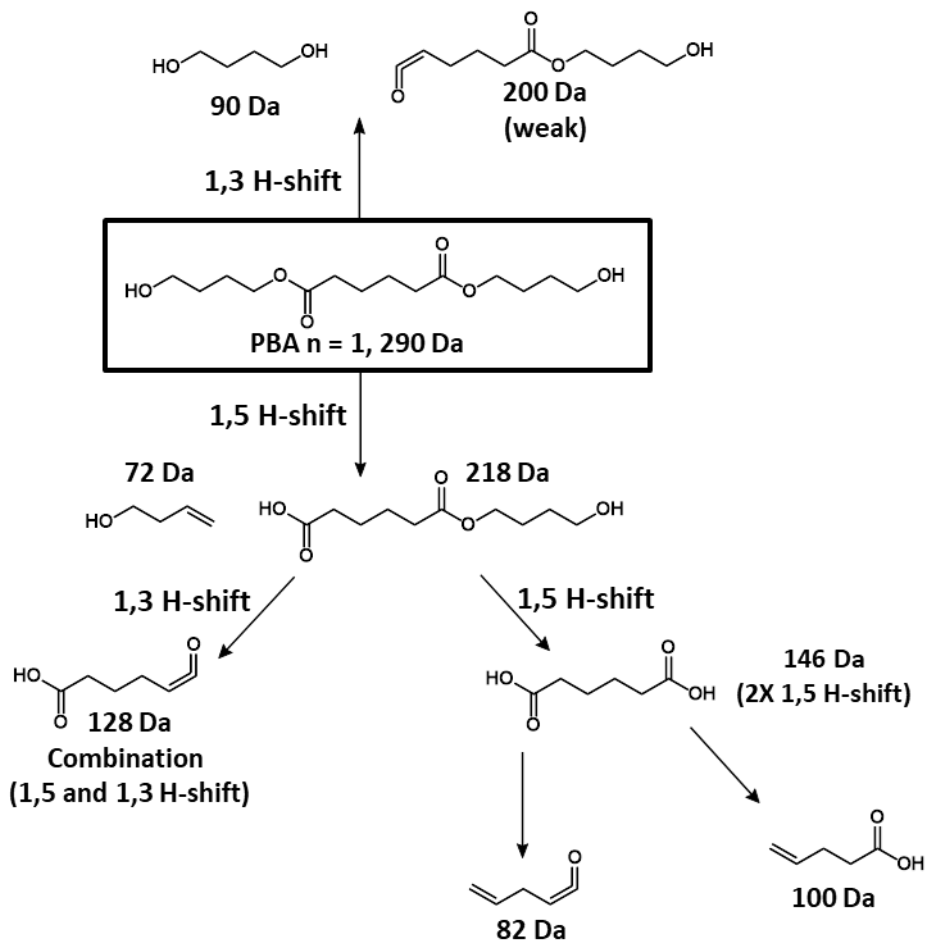


Figure 6.4. Fragmentation ion pathway monitoring the unique transition of n = 1 PBA precursor into fragment ions.

small atomic radius increases its ability to fit between the ester functional group, therefore promoting more fragment ions than Na.

The Ag cation has two major isotopes ^{107}Ag (51%) and ^{109}Ag (49%). The fragment ions observed contained the Ag isotopic distribution, therefore the CID curves represent the summation of both ^{107}Ag and ^{109}Ag isotopes for each fragment ion. The MS/MS spectrum may not have every isotopic peak notated; however both peaks were represented and accounted for in the calculations. The ^{109}Ag isotope intensity appears higher than the 107 Da because of the two underlying ^{13}C isotopes. The MS/MS spectrum in **Figure 6.2f**, highlights the major fragment ions formed from the depletion of the $[\text{M}+\text{Ag}]^+$ precursor at 20 eV. Similar to $[\text{M}+\text{Li}]^+$, the $[\text{M}+\text{Ag}]^+$ species was observed to generate numerous fragment ions at relatively low CID energies. In **Figure 6.2f**, major fragment ions 327, 255, 237, and 199 Da correspond to nominal masses 218, 146, 128, and 90 Da as seen in **Figure 6.3c**. The 82 Da ion in **Figure 6.3c** was only observed in low intensity in the MS/MS spectra, as CID energy increased, fragment ion 82 Da became a more intense ion. In **Figure 6.3c**, the 290 Da species is observed to deplete at 25 eV, forming major fragment ion 218 Da (25%, 10 eV) from a 1,5 H-shift. Fragment ion 146 Da (30%, 20 eV) is also observed to form at low CID energies from the 218 Da species (2X 1,5 H-shift) as seen in **Figure 6.4**. Major fragment ion 128 Da was also observed to form from the 218 Da species (combination reaction), due to a 1,3 H-shift (45%, 30 eV) forming both acid and $=\text{C}=\text{O}$ end groups. Fragment ion 90 Da (22%, 30 eV) was only observed for the $[\text{M}+\text{Ag}]^+$ precursor, corresponding fragment ion 200 Da was observed at weak intensities. The major fragment ion 82 Da (100%, 50 eV), is only observed at high CID energies and proposed to form from the depletion of the 128 Da species, as seen in **Figure 6.4**. The total percent ion current tables can be found in **Table 6.1** for $n = 1$ PBA $[\text{M}+\text{Li}]^+$, $[\text{M}+\text{Na}]^+$, and $[\text{M}+\text{Ag}]^+$ species.

For each of the cationized $n = 1$ species, the 1,5 H-shift reaction appeared to occur more frequent along the PBA chain compared to the 1,3 H-shift reaction. Fragment ion 200 Da from the 1,3 H-shift appeared in the MS/MS spectra for each cationized species, at a weak intensity.

The 1,5 H-shift fragment ion 218 Da appeared in all three cation spectra. The 218 Da fragment ion was observed to transition into many fragment ions observed at high CID energies (**Figure 6.4**). The 218 Da species contributed to the observation of both (1) 2X 1,5 H-shift reactions forming the 146 Da ion, and (2) combination reaction forming the 128 Da ion from a 1,3 H-shift.

6.3.2. Characterization of $n = 2$ Polybutylene Adipate by MS/MS

In **Figure 6.5**, the ESI MS/MS spectra highlight fragment ions generated for PBA $n = 2$ species at 0 eV and 30 eV CID energies for $[M+Li]^+$ (**Figure 6.5a-b**), $[M+Na]^+$ (**Figure 6.5c-d**), and $[M+Ag]^+$ (**Figure 6.5e-f**). **Figure 6.6a-f** monitors the CID of major fragment ions formed from the PBA $n = 2$ species forming at 5% RIC or more. The dashed line is drawn for visual alignment at 30 eV to represent low energy fragment ion formation. The PBA $n = 2$ species appears to be more stable than the PBA $n = 1$ species, requiring additional CID energies to generate fragment ions (i.g. $n = 1$ requires 20 eV, and $n = 2$ requires 30 eV). This increase in stability may also result from an increase in the degree of polymerization (DP) along the PBA chain. In **Figure 6.6a-c** full CID curves are represented for each cation coordinated to PBA $n = 2$, in **Figure 6.6d-f** ions of low abundance are highlighted between 30 – 0 %RIC. In **Figure 6.5a,c,e** all cationized PBA species are observed to be stable at 0 eV. When the collision energy increases to 30 eV, both $[M+Li]^+$ and $[M+Ag]^+$ species are observed to form many fragment ions (**Figure 6.5b,f**). However, at 30 eV, the $[M+Na]^+$ species appears to be more stable relative to Li or Ag, forming less fragment ions as CID energies increase (**Figure 6.5.d**).

In **Figure 6.5b**, the MS/MS spectrum highlights major fragment ions formed from the depletion of the $[M+Li]^+ = 497$ Da species at 30 eV. Major fragment ions that form at relatively low CID energies include: 425, 353, 297, 279, 225, 207, 153, and 135 Da species as seen in **Figure 6.5b**. The corresponding nominal masses of each ion is represented in the CID curves in

| (a) | Mass (without Li) | [M+Li] ⁺ | 0 | 5 | 10 | 15 | 20 | 25 | 30 | 35 | 40 | 45 | 50 | |
|-----|-------------------|---------------------|-------|-------|-------|-------|-------|-------|-------|-------|-------|-------|-------|----|
| | 128 | 135 | 1.6% | 2.5% | 4.7% | 10.9% | 19.1% | 28.9% | 36.8% | 41.2% | 44.3% | 46.4% | 41.4% | AV |
| | | | 0.1% | 0.1% | 0.1% | 0.0% | 0.1% | 0.0% | 1.6% | 0.2% | 0.4% | 0.1% | 0.8% | SD |
| | 146 | 153 | 7.9% | 14.1% | 22.8% | 28.9% | 34.1% | 41.3% | 46.0% | 42.1% | 35.1% | 25.0% | 16.9% | AV |
| | | | 0.2% | 0.2% | 0.1% | 0.0% | 0.1% | 0.1% | 1.1% | 0.2% | 0.2% | 0.2% | 1.0% | SD |
| | 218 | 225 | 9.8% | 20.4% | 27.6% | 28.4% | 25.8% | 20.2% | 6.9% | 1.3% | 0.0% | 0.0% | 0.0% | AV |
| | | | 0.1% | 0.4% | 0.1% | 0.0% | 0.1% | 0.1% | 0.2% | 0.1% | 0.0% | 0.0% | 0.0% | SD |
| | 290 | 297 | 80.7% | 63.0% | 44.8% | 31.8% | 19.4% | 5.0% | 0.0% | 0.0% | 0.0% | 0.0% | 0.0% | AV |
| | | | 0.2% | 0.6% | 0.1% | 0.0% | 0.0% | 0.0% | 0.0% | 0.0% | 0.0% | 0.0% | 0.0% | SD |
| | 100 | 107 | 0.0% | 0.0% | 0.0% | 0.0% | 1.5% | 4.6% | 10.2% | 15.4% | 20.6% | 28.6% | 41.7% | AV |
| | | | 0.0% | 0.0% | 0.0% | 0.0% | 0.0% | 0.1% | 0.3% | 0.3% | 0.2% | 0.0% | 0.3% | SD |

| (b) | Mass (without Na) | [M+Na] ⁺ | 0 | 5 | 10 | 15 | 20 | 25 | 30 | 35 | 40 | 45 | 50 | |
|-----|-------------------|---------------------|-----|-----|-----|-----|-----|-----|-----|-----|------|----|----|----|
| | 218 | 241 | 1% | 3% | 8% | 11% | 12% | 16% | 20% | 31% | 0% | 0% | 0% | AV |
| | | | 0% | 0% | 0% | 0% | 0% | 0% | 3% | 8% | 0% | 0% | 0% | SD |
| | 290 | 313 | 99% | 97% | 93% | 92% | 91% | 84% | 76% | 0% | 0% | 0% | 0% | AV |
| | | | 0% | 0% | 0% | 0% | 0% | 0% | 3% | 0% | 0% | 0% | 0% | SD |
| | 146 | 169 | 0% | 0% | 0% | 0% | 0% | 0% | 0% | 0% | 0% | 0% | 0% | AV |
| | | | 0% | 0% | 0% | 0% | 0% | 0% | 0% | 0% | 0% | 0% | 0% | SD |
| | 128 | 151 | 0% | 0% | 0% | 0% | 0% | 0% | 5% | 69% | 100% | 0% | 0% | AV |
| | | | 0% | 0% | 0% | 0% | 0% | 0% | 1% | 8% | 0% | 0% | 0% | SD |

| (c) | Mass (without Ag) | [M+Ag] ⁺ | 0 | 5 | 10 | 15 | 20 | 25 | 30 | 35 | 40 | 45 | 50 | |
|-----|-------------------|---------------------|-----|-----|-----|-----|-----|-----|-----|-----|-----|-----|------|----|
| | 290 | 399/397 | 90% | 76% | 51% | 24% | 5% | 0% | 0% | 0% | 0% | 0% | 0% | AV |
| | | | 0% | 0% | 0% | 0% | 0% | 0% | 0% | 0% | 0% | 0% | 0% | SD |
| | 218 | 327/325 | 5% | 13% | 25% | 26% | 15% | 5% | 0% | 0% | 0% | 0% | 0% | AV |
| | | | 0% | 0% | 0% | 0% | 0% | 0% | 0% | 0% | 0% | 0% | 0% | SD |
| | 146 | 255/253 | 2% | 5% | 12% | 23% | 28% | 25% | 17% | 10% | 0% | 0% | 0% | AV |
| | | | 0% | 0% | 0% | 0% | 0% | 0% | 0% | 0% | 0% | 0% | 0% | SD |
| | 128 | 237/235 | 1% | 3% | 7% | 16% | 30% | 41% | 45% | 43% | 41% | 36% | 0% | AV |
| | | | 0% | 0% | 0% | 0% | 0% | 1% | 0% | 1% | 1% | 2% | 0% | SD |
| | 90 | 199/197 | 1% | 2% | 6% | 11% | 16% | 17% | 16% | 16% | 14% | 0% | 0% | AV |
| | | | 0% | 0% | 0% | 0% | 0% | 0% | 0% | 1% | 3% | 0% | 0% | SD |
| | 82 | 191/189 | 0% | 0% | 0% | 0% | 6% | 13% | 22% | 31% | 44% | 61% | 100% | AV |
| | | | 0% | 0% | 0% | 0% | 0% | 0% | 0% | 1% | 1% | 2% | 5% | SD |

Table 6.1. Total percent ion currents observed for n = 1 polybutylene adipate, 290 Da: (a) [M+Li]⁺, (b) [M+Na]⁺, and (c) [M+Ag]⁺. Percent averages and %RSD are shown above for each ion.

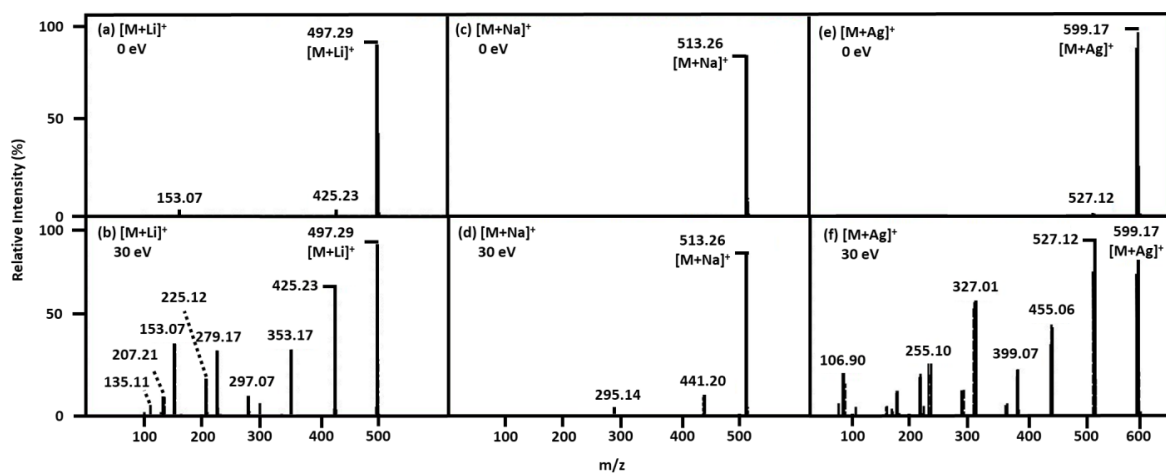


Figure 6.5. ESI MS/MS spectra for $n = 2$ PBA at corresponding lab-frame energies of 0 eV for (a,c,e) and 30 eV for (b,d,f). Results for $[M+Li]^+$ are shown in (a-b), $[M+Na]^+$ in (c-d), and $[M+Ag]^+$ in (e-f).

PBA n = 2

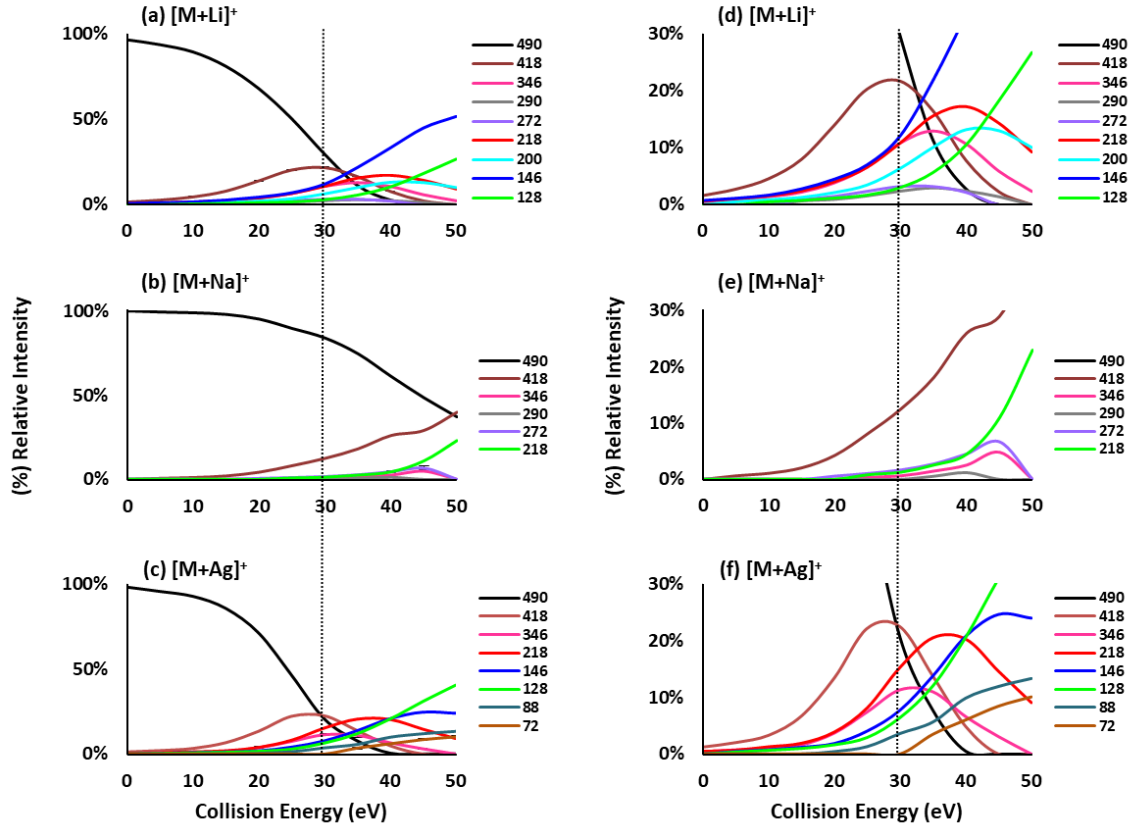


Figure 6.6. Collision-induced dissociation (CID) curves monitoring the unique transition of $n = 2$ PBA precursor to fragment ions when coordinated with cations (a,d) $[M+Li]^+$, (b,e) $[M+Na]^+$, and (c,f) $[M+Ag]^+$. CID curves (a-c) monitor fragment ions formed from 0 – 100 %RIC, In CID curves (d-f), zoomed view of fragment ions formed between 0 – 30 %RIC are observed. The dotted line is drawn at 30 eV for visual alignment of low energy fragment ions.

Figure 6.6a,d, these include: 418, 346, 290, 272, 218, 200, 146, and 128 Da. In **Figure 6.7**, major fragment ions resulting from a 1,5 H-shift fragmentation mechanism include: 418 Da (22%, 30 eV) forming the PBA $n = 2$ species with acid and hydroxyl end groups, and corresponding fragment ion 72 Da which was only observed at relatively low abundance ($\leq 1\%$). Fragment ions 218 Da (17%, 40 eV) and 272 Da (5%, 35 eV) species was also observed to form from a 1,5 H-shift as seen in **Figure 6.7**. Fragment ions formed from the 1,3 H-shift include 200 Da (13%, 45 eV) and 290 Da (5%, 35 eV) as seen in **Figure 6.7**. The 1,3 H-shift fragmentation mechanism cleaves the bond between the $-O-C(O)-$, yielding hydroxyl and $=C=O$ terminated fragment ion. However, 1,3 H-shift fragment ions 400 and 90 Da were not observed above 5% RIC. These fragment ions were only observed in the MS/MS spectra at low ion intensities. In **Figure 6.7**, fragment ions 346 and 146 Da were both observed to form from a 1,5 H-shift from the 418 and 218 Da, respectively. Fragment ions 346 Da (10%, 30 eV) and 146 Da (51%, 50 eV) are products of a high energy pathway and are considered to form from a 2X 1,5 H-shift pathway. The 128 Da fragment ion (27%, 50 eV) was also observed at high CID energy. The 128 Da species forms from a combination reaction from the 218 or 418 Da species first (1,5 H-shift), and then a 1,3 H-shift pathway. Additional CID depletion curves with %RSD can be found in **Figure 6.8a,d**.

In **Figure 6.5d**, the MS/MS spectrum highlights the smaller number of fragment ions formed from the depletion of the $[M+Na]^+ = 513$ Da species at 30 eV. Major fragment ions that form at relatively low CID energies are the 441 and 295 Da species which correspond to nominal masses: 418 Da (13%, 30 eV) and 218 Da (1%, 30 eV). As seen in **Figure 6.7**, the 418 and 218Da species are products of the 1,5 H-shift pathway, and form corresponding fragment ions 72 and 272 Da, respectively. Additional fragment ions observed at higher CID energies include: 346 Da (6%, 45 eV), 290 Da (5%, 40 eV), and 272 Da (7%, 45 eV). In **Figure 6.6b,e** the 272 Da species is observed at intensities above 5% RIC, however the 72 Da ion was only observed at relatively low ion intensity in the MS/MS spectra. Fragment ion 290 Da was the only ion

PBA n = 2 Fragment Ion Pathway

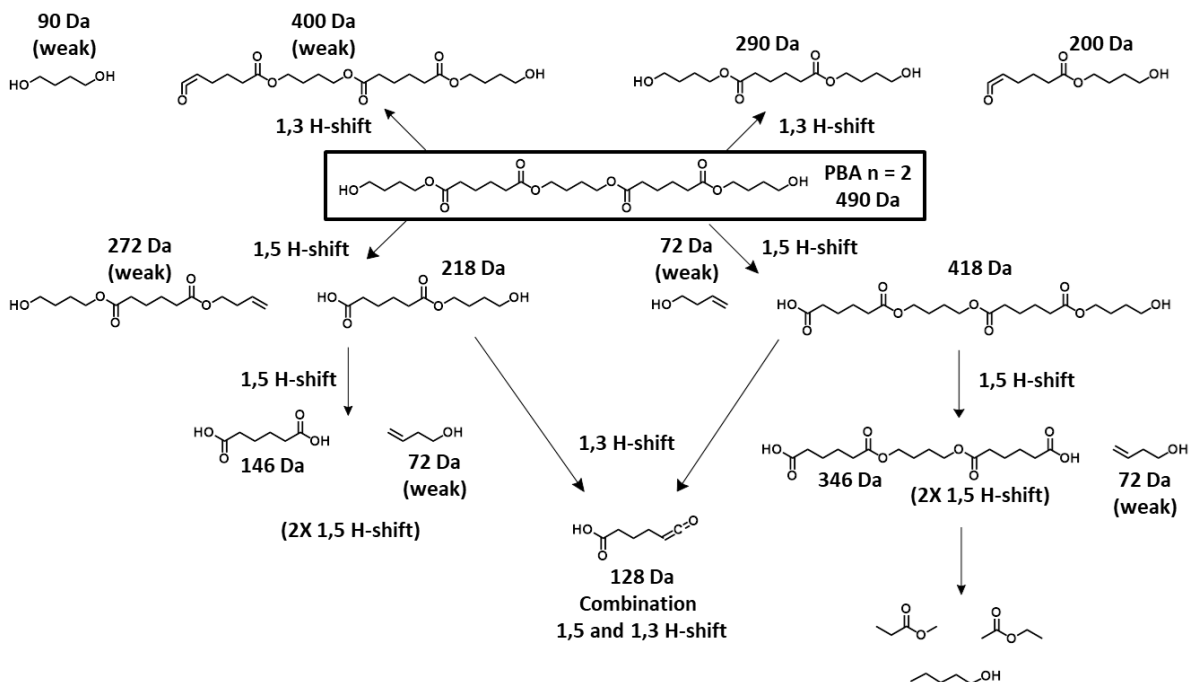


Figure 6.7. Fragmentation ion pathway monitoring the unique transition of n = 2 PBA precursor into fragment ions.

observed at 5% RIC to form from a 1,3 H-shift pathway. Corresponding 200 Da species was observed at low abundance. Also, PBA $n = 2$ precursor can also form the 400 and 90 Da species from a 1,3 H-shift, however these ions were not observed at high %RIC intensities. Fragment ion 346 Da, as illustrated in **Figure 6.7** was observed at high CID energies to form from the 418 Da species. Additional CID depletion curves with %RSD can be found in **Figure 6.8b,e**.

In **Figure 6.5f**, the MS/MS spectrum highlights the major fragment ions formed from depletion of the $[M+Ag]^+$ precursor at 30 eV. Similar to $[M+Li]^+$, the $[M+Ag]^+$ species generated many fragment ions at relatively low collision energies. In **Figure 6.6c,f**, we observe many fragment ions that form below 30 eV. The fragment ions annotated in the MS/MS spectrum (**Figure 6.5f**) include: 527, 455, 399, 327, and 255 Da. The peak at 106.9 is from the Ag cation. Low abundant fragment ions also observed at 30 eV in the MS/MS spectra include: 237, 199, and 181 Da, these fragment ions are observed at higher intensities as CID energies increase. In **Figure 6.6c,f**, the $[M+Ag]^+$ species was observed to deplete 100% by 40 eV. The nominal masses of each fragment ion are represented from above 10%RIC and include: 418, 346, 218, 146, 128, 88, and 72 Da. Fragment ion 399 Da as observed in the MS/MS spectra forms at 6% intensity at 30 eV and is observed as a minor fragment ion in **Table 6.4**, as nominal mass 290 Da. Fragment ions observed to form from a 1,5 H-shift include: 418 (22%, 30 eV) and 218 (20%, 35 eV) Da species. Only the 418 Da corresponding 72 Da (10%, 50 eV) ion was observed at relatively high %RIC. The 218 Da corresponding 272 Da ion was only observed at relatively low abundance, as illustrated in **Figure 6.7**. Fragment ion 290 Da, observed in the MS/MS spectra and in **Table 6.4** forms from a 1,3 H-shift, corresponding 200 Da ion was also observed at low intensities (6%, 40 eV). The 346 (11%, 30 eV) and 146 Da (24%, 50 eV) species, as seen in **Figure 6.7**, directly form from a 1,5 H-shift of the 418 and 218 Da species, respectively (2X 1,5 H-shift). Fragment ion 128 Da (40%, 50 eV) was observed to form from a combination reaction (1,5 and 1,3 H-shift) from the 418 and 218 Da species. The 88 Da (13%, 50 eV) species was uniquely observed to

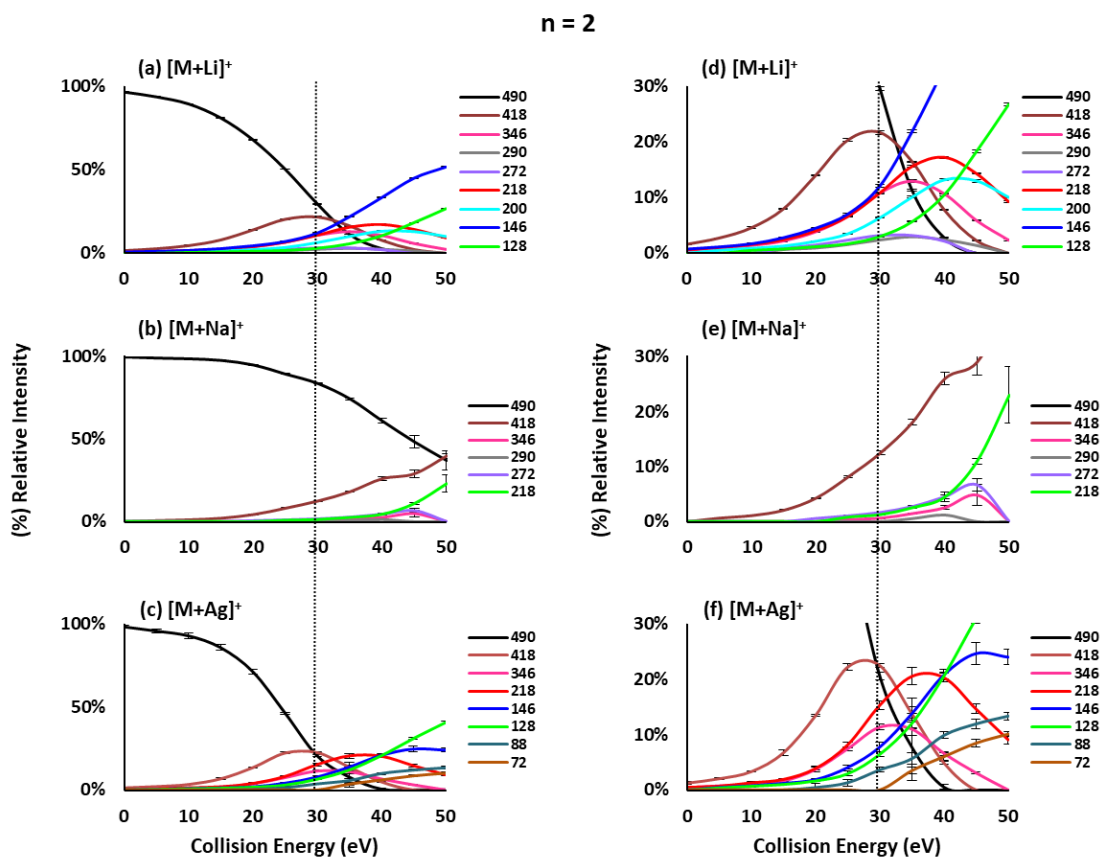


Figure 6.8. Collision-induced dissociation (CID) curves monitoring the unique transition of $n = 2$ PBA precursor to fragment ions when coordinated with cations (a,d) $[M+Li]^+$, (b,e) $[M+Na]^+$, and (c,f) $[M+Ag]^+$. CID curves (a-c) monitor fragment ions formed from 0 – 100 %RIC, In CID curves (d-f), zoomed view of fragment ions formed between 0 – 30 %RIC are observed. The dotted line is drawn at 30 eV for visual alignment of low energy fragment ions and with %RSD.

formed for the $[M+Ag]^+$ precursor, and is proposed to form from the 128 Da species at high CID energies. In **Figure 6.7**, proposed fragment ion structures and their respective pathway are illustrated. The total %RIC of PBA $n = 2$ precursor species can be found in **Tables 6.2-6.4**.

6.3.3. Polybutylene Adipate Literature MS/MS Comparison

Gies et al., used MALDI-TOF/TOF CID to explore fragmentation reactions associated with PBA.⁶ In that study, a telechelic polydisperse PBA sample was characterized for both linear and cyclic PBA species, and fragmented using Li and Na cations. Unique low energy fragmentation pathways were documented. PBA oligomers were found to undergo a number of low energy degradation pathways: (1) 1,5 H-shift, (2) 1,3 H-shift, (3) remote hydrogen abstraction reactions, and (4) a combination of (1-3). In the present study, characterizing monodisperse PBA $n = 1$ and $n = 2$ species, we observed similar findings to those of Gies et al., however we did not observe hydrogen abstraction reactions. Fragmentation pathways of PBA $n = 1$ and $n = 2$ species were monitored with respect to Li, Na, and Ag cation coordination. We observed the Na cation to generate a more stable precursor for the PBA species compared to Li or Ag coordination. With respect to fragmentation patterns, we observed both 1,5 and 1,3 H-shift fragmentation mechanism for all coordinated cation species. We also observed higher energy combination reactions which included both 1,5 and 1,3 H-shift mechanisms and 2X 1,5 H-shift reactions along the polyester backbone. Unique fragment ions were also observed for PBA cation coordinated precursors. Those fragment ions are low mass species, resulting in the fragmentation of the 146 Da and 126 Da species.

| Mass without Li | 0 | 5 | 10 | 15 | 20 | 25 | 30 | 35 | 40 | 45 | 50 |
|--------------------|-------|-------|-------|-------|-------|-------|-------|-------|-------|-------|-------|
| 490 | 96.5% | 93.6% | 89.3% | 81.0% | 67.9% | 50.3% | 29.6% | 11.3% | 2.8% | 0.0% | 0.0% |
| | 0.1% | 0.2% | 0.1% | 0.2% | 0.3% | 0.2% | 0.3% | 0.2% | 0.1% | 0.0% | 0.0% |
| | | | | | | | | | | | |
| 418 | 1.6% | 2.7% | 4.6% | 8.0% | 14.0% | 20.3% | 21.7% | 16.4% | 7.8% | 2.3% | 0.0% |
| | 0.1% | 0.0% | 0.2% | 0.2% | 0.2% | 0.2% | 0.4% | 0.1% | 0.1% | 0.1% | 0.0% |
| | | | | | | | | | | | |
| 346 | 0.5% | 0.9% | 1.4% | 2.2% | 3.8% | 6.6% | 10.8% | 12.9% | 10.7% | 5.9% | 2.3% |
| | 0.1% | 0.1% | 0.1% | 0.1% | 0.1% | 0.1% | 0.2% | 0.3% | 0.1% | 0.1% | 0.1% |
| | | | | | | | | | | | |
| 290 | 0.0% | 0.0% | 0.0% | 0.7% | 1.0% | 1.6% | 2.4% | 3.0% | 2.4% | 1.4% | 0.0% |
| | 0.0% | 0.0% | 0.0% | 0.0% | 0.1% | 0.0% | 0.1% | 0.1% | 0.1% | 0.1% | 0.0% |
| | | | | | | | | | | | |
| 272 | 0.0% | 0.0% | 0.0% | 0.9% | 1.5% | 2.4% | 3.2% | 3.2% | 2.2% | 0.0% | 0.0% |
| | 0.0% | 0.0% | 0.0% | 0.0% | 0.1% | 0.1% | 0.1% | 0.1% | 0.0% | 0.0% | 0.0% |
| | | | | | | | | | | | |
| 218 | 0.6% | 1.1% | 1.6% | 2.4% | 4.0% | 6.6% | 10.8% | 15.6% | 17.2% | 14.3% | 9.3% |
| | 0.0% | 0.1% | 0.0% | 0.1% | 0.1% | 0.1% | 0.0% | 0.2% | 0.2% | 0.1% | 0.2% |
| | | | | | | | | | | | |
| 200 | 0.0% | 0.5% | 0.9% | 1.3% | 2.1% | 3.5% | 6.4% | 10.1% | 13.2% | 13.0% | 10.0% |
| | 0.0% | 0.0% | 0.1% | 0.0% | 0.0% | 0.1% | 0.0% | 0.2% | 0.2% | 0.2% | 0.1% |
| | | | | | | | | | | | |
| 146 | 0.8% | 1.1% | 1.7% | 2.8% | 4.5% | 7.0% | 12.1% | 21.8% | 33.3% | 44.9% | 51.6% |
| | 0.1% | 0.0% | 0.1% | 0.1% | 0.1% | 0.1% | 0.2% | 0.2% | 0.3% | 0.0% | 0.1% |
| | | | | | | | | | | | |
| 128 | 0.0% | 0.0% | 0.5% | 0.8% | 1.2% | 1.7% | 3.0% | 5.7% | 10.5% | 18.3% | 26.7% |
| | 0.0% | 0.0% | 0.1% | 0.1% | 0.1% | 0.1% | 0.1% | 0.1% | 0.1% | 0.2% | 0.2% |

Table 6.2. Total percent ion currents observed for $[M+Li]^+$ PBA $n = 2$. Percent averages and %RSD are shown above for each ion.

| Mass without Na | 0 | 5 | 10 | 15 | 20 | 25 | 30 | 35 | 40 | 45 | 50 |
|-----------------|------|-----|-----|-----|-----|-----|-----|-----|-----|-----|-----|
| 490 | 100% | 99% | 99% | 98% | 95% | 90% | 84% | 75% | 61% | 48% | 37% |
| | 0% | 0% | 0% | 0% | 0% | 0% | 0% | 1% | 1% | 4% | 6% |
| | | | | | | | | | | | |
| 418 | 0% | 1% | 1% | 2% | 4% | 8% | 13% | 18% | 26% | 29% | 40% |
| | 0% | 0% | 0% | 0% | 0% | 0% | 0% | 0% | 1% | 2% | 1% |
| | | | | | | | | | | | |
| 346 | 0% | 0% | 0% | 0% | 0% | 0% | 1% | 1% | 3% | 5% | 0% |
| | 0% | 0% | 0% | 0% | 0% | 0% | 0% | 0% | 0% | 2% | 0% |
| | | | | | | | | | | | |
| 290 | 0% | 0% | 0% | 0% | 0% | 0% | 0% | 1% | 1% | 0% | 0% |
| | 0% | 0% | 0% | 0% | 0% | 0% | 0% | 0% | 0% | 0% | 0% |
| | | | | | | | | | | | |
| 272 | 0% | 0% | 0% | 0% | 1% | 1% | 2% | 3% | 5% | 7% | 0% |
| | 0% | 0% | 0% | 0% | 0% | 0% | 0% | 0% | 0% | 1% | 0% |
| | | | | | | | | | | | |
| 218 | 0% | 0% | 0% | 0% | 0% | 1% | 1% | 3% | 5% | 11% | 23% |
| | 0% | 0% | 0% | 0% | 0% | 0% | 0% | 0% | 1% | 1% | 5% |

Table 6.3. Total percent ion currents observed for $[M+Na]^+$ PBA $n = 2$. Percent averages and %RSD are shown above for each ion.

| Mass without Ag | 0 | 5 | 10 | 15 | 20 | 25 | 30 | 35 | 40 | 45 | 50 |
|-----------------|-------|-------|-------|-------|-------|-------|-------|-------|-------|-------|-------|
| 490 | 97.9% | 95.4% | 92.5% | 85.4% | 70.9% | 46.2% | 20.5% | 7.7% | 0.5% | 0.0% | 0.0% |
| | 0.8% | 1.2% | 1.8% | 1.8% | 1.3% | 0.6% | 0.6% | 6.0% | 0.4% | 0.0% | 0.0% |
| | | | | | | | | | | | |
| 418 | 1.2% | 2.0% | 3.3% | 6.7% | 13.4% | 22.1% | 22.4% | 13.7% | 4.8% | 0.0% | 0.0% |
| | 0.2% | 0.2% | 0.1% | 0.5% | 0.2% | 0.6% | 0.4% | 2.8% | 0.3% | 0.0% | 0.0% |
| | | | | | | | | | | | |
| 346 | 0.4% | 0.7% | 1.0% | 1.6% | 3.7% | 7.4% | 11.3% | 11.0% | 6.6% | 3.1% | 0.0% |
| | 0.0% | 0.1% | 0.2% | 0.1% | 0.5% | 0.3% | 0.5% | 1.2% | 0.4% | 0.2% | 0.0% |
| | | | | | | | | | | | |
| 290 | 0.0% | 0.4% | 0.5% | 1.0% | 1.7% | 3.7% | 6.0% | 5.9% | 4.1% | 1.4% | 0.0% |
| | 0.0% | 0.0% | 0.1% | 0.2% | 0.1% | 0.4% | 0.5% | 0.2% | 0.5% | 0.7% | 0.0% |
| | | | | | | | | | | | |
| 272 | 0.0% | 0.0% | 0.0% | 0.1% | 0.7% | 1.7% | 2.0% | 0.0% | 0.0% | 0.0% | 0.0% |
| | 0.0% | 0.0% | 0.0% | 0.2% | 0.6% | 0.1% | 0.8% | 0.0% | 0.0% | 0.0% | 0.0% |
| | | | | | | | | | | | |
| 268 | 0.0% | 0.0% | 0.0% | 0.8% | 0.9% | 0.0% | 0.0% | 0.0% | 0.0% | 0.0% | 0.0% |
| | 0.0% | 0.0% | 0.0% | 0.3% | 0.4% | 0.0% | 0.0% | 0.0% | 0.0% | 0.0% | 0.0% |
| | | | | | | | | | | | |
| 218 | 0.5% | 0.7% | 1.3% | 1.9% | 3.9% | 8.1% | 15.2% | 20.5% | 20.2% | 14.6% | 9.0% |
| | 0.1% | 0.1% | 0.2% | 0.1% | 0.3% | 0.5% | 0.8% | 1.5% | 0.8% | 0.9% | 0.8% |
| | | | | | | | | | | | |
| 200 | 0.0% | 0.0% | 0.0% | 0.4% | 1.0% | 2.6% | 4.8% | 6.4% | 6.7% | 5.2% | 3.2% |
| | 0.0% | 0.0% | 0.0% | 0.0% | 0.1% | 0.3% | 0.6% | 0.6% | 0.3% | 0.3% | 0.4% |
| | | | | | | | | | | | |
| 146 | 0.0% | 0.5% | 0.7% | 1.2% | 1.9% | 4.0% | 7.7% | 13.7% | 20.7% | 24.6% | 23.9% |
| | 0.0% | 0.0% | 0.1% | 0.2% | 0.2% | 0.3% | 0.8% | 1.2% | 0.9% | 2.0% | 1.3% |
| | | | | | | | | | | | |
| 128 | 0.0% | 0.4% | 0.7% | 1.0% | 1.6% | 2.9% | 6.4% | 12.0% | 20.6% | 30.9% | 40.5% |
| | 0.0% | 0.0% | 0.2% | 0.1% | 0.1% | 0.4% | 0.4% | 0.9% | 0.6% | 0.8% | 1.0% |
| | | | | | | | | | | | |
| 88 | 0.0% | 0.0% | 0.0% | 0.0% | 0.4% | 1.3% | 3.6% | 5.6% | 9.8% | 11.9% | 13.3% |
| | 0.0% | 0.0% | 0.0% | 0.0% | 0.7% | 0.6% | 0.4% | 1.0% | 0.6% | 0.8% | 0.7% |
| | | | | | | | | | | | |
| 72 | 0.0% | 0.0% | 0.0% | 0.0% | 0.0% | 0.0% | 0.0% | 3.5% | 6.0% | 8.4% | 10.1% |
| | 0.0% | 0.0% | 0.0% | 0.0% | 0.0% | 0.0% | 0.0% | 0.6% | 0.7% | 0.6% | 0.5% |

Table 6.4. Total percent ion currents observed for $[M+Ag]^+$ PBA n = 2. Percent averages and %RSD are shown above for each ion.

6.3.4. Characterization of P(1,2) by MS/MS

In this present study, we probed for unique fragmentation pathways for the P(1,2) species coordinated to Li^+ , Na^+ , and Ag^+ cations. We monitored the formation of major and minor fragment ions with respect to increasing CID energies. Major fragment ions observed for the $[\text{M}+\text{Li}]^+$, $[\text{M}+\text{Na}]^+$, and $[\text{M}+\text{Ag}]^+$ that formed above 10%RIC can be found in **Figure 6.9**. The dashed line is drawn for visual alignment at 50 eV to represent low energy fragment ion formation. Similar to the PBA $n = 1$ and $n = 2$ findings, the P(1,2) was also observed to undergo 1,5 and 1,3 H-shift pathways along both the polyester and urethane chain. The findings discussed in this paper correlate strongly to the previous findings of Gies and Hercules,⁵ and will be discussed further in the sections to come.

The ESI MS/MS spectra of P(1,2) coordinated to $[\text{M}+\text{Li}]^+$ at different CID energies can be found in **Figure 6.10**. The $[\text{M}+\text{Li}]^+$ MS/MS spectra at 0 eV (**Figure 6.10a-b**), 30 eV (**Figure 6.10c-d**), and 50 eV (**Figure 6.10e-f**) shows both full (**Figure 6.10a,c,e**) MS/MS spectra and zoomed (**Figure 6.10b,d,f**) regions for each of these CID energies. Both major and minor fragment ions are annotated to show the unique polyester and urethane fragmentation pathways for P(1,2) coordinated to Li^+ . In **Figure 6.9**, major fragment ions that formed above 10%RIC include (nominal mass) 758, 218, 146, and 128 Da, which corresponds to 837, 765, 225, 153, and 135 Da (mass with Li^+ cation). In **Figure 6.10**, additional fragment ions are notated in the MS/MS spectra. These are considered to be minor fragment ions. These minor fragment ions were monitored with respect to increasing CID energies in **Figure 6.11a**. As an example, the P(1,2) $[\text{M}+\text{Li}]^+$ species MS/MS spectra at 50 eV was enlarged in **Figure 6.12a-d** to highlight the unique major and minor fragment ions observed for this precursor.

In **Figure 6.9a**, the depletion of the $[\text{M}+\text{Li}]^+$ precursor species was monitored with respect to increasing CID energies. The 830 Da precursor was observed to deplete 100% by 70 eV. Only one low energy fragment ion was observed to form under 50 eV and above 10% RIC. This was the 758 Da fragment ion (15%, 50 eV), which formed from the 1,5 H-shift along the

polyester chain as seen in **Table 6.5**. The corresponding 72 Da fragment ion was observed in relatively low abundance in the MS/MS spectrum. High energy fragment ions were also observed; these include: 218, 146, and 128 Da species. The 218 Da (12%, 70 eV) fragment ion can form from two pathways. The 218 Da species can form from a 1,5 H-shift around the ester functional group, forming the corresponding 72 Da fragment ion. The 218 Da species can also form from a 1,3 H-shift around the urethane group as seen in **Table 6.5**. The corresponding 642 Da fragment species was only observed in relatively low abundance in **Figure 6.12c**. The 146 Da (52%, 90 eV) fragment ion as described in the PBA section, forms from a two 1,5 H-shift along the polyester chain. Additionally, major fragment ion 128 Da (37%, 100 eV) was also observed to form from both the 1,5 H-shift and the 1,3 H-shift along the polyester chain, due to high-energy fragmentation as seen in **Table 6.5**. The Li⁺ coordinated P(1,2) species was found to form many fragment ions as CID energies increased. Li is notoriously known to cause increased fragment ion formation. Due to Li's small atomic radius, we propose that Li is coordinating with the ester functional groups along the soft segment chain, in addition to coordination with the hard segment phenyl rings. Additional total %RIC data can be found in **Tables 6.6** for both major and minor fragment ions generated from the [M+Li]⁺ species.

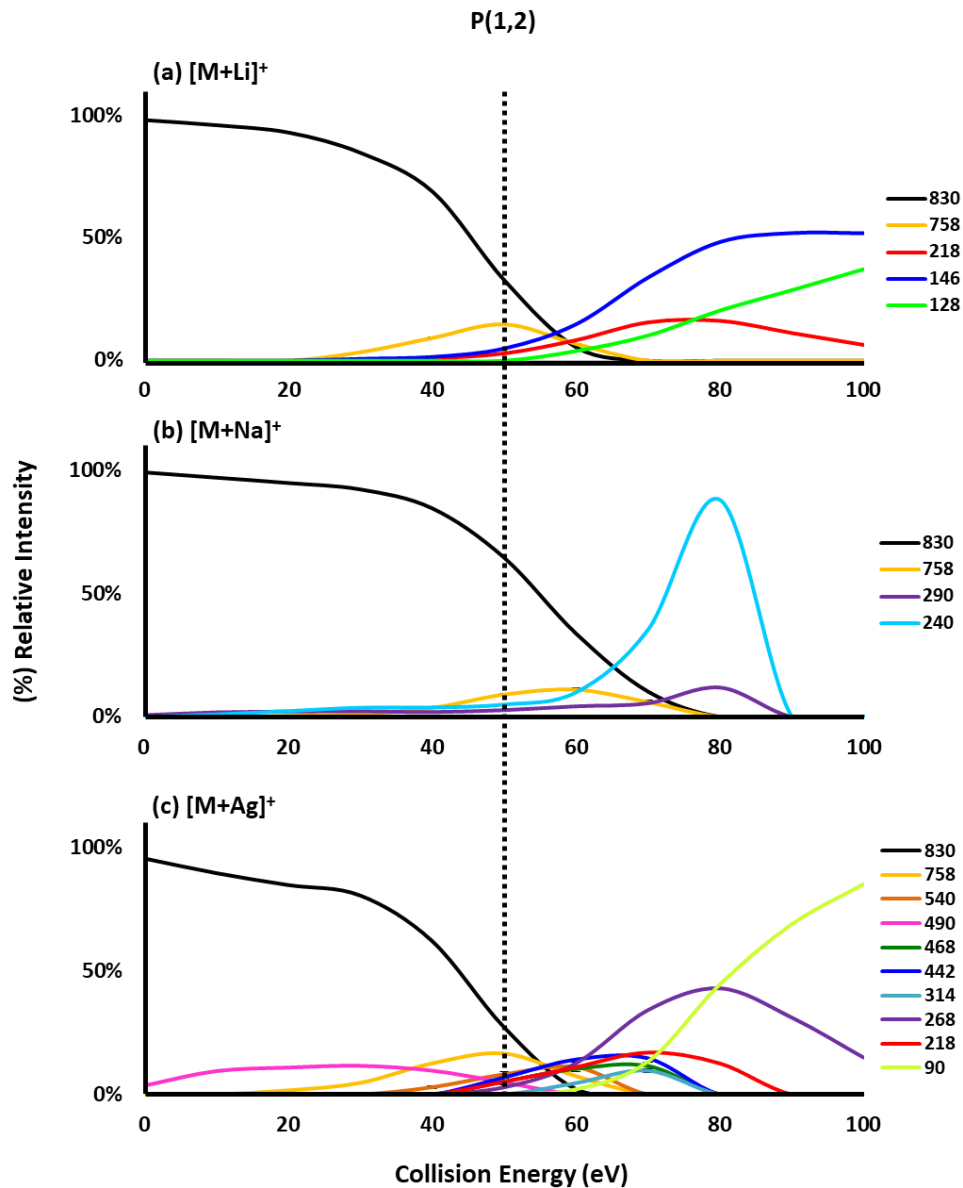


Figure 6.9. Collision-induced dissociation (CID) curves monitoring the unique transition of P(1,2) precursor to fragment ions when coordinated with cations (a) $[M+Li]^+$, (b) $[M+Na]^+$, and (c) $[M+Ag]^+$. The dotted line is drawn at 50 eV for visual alignment of low energy fragment ions.

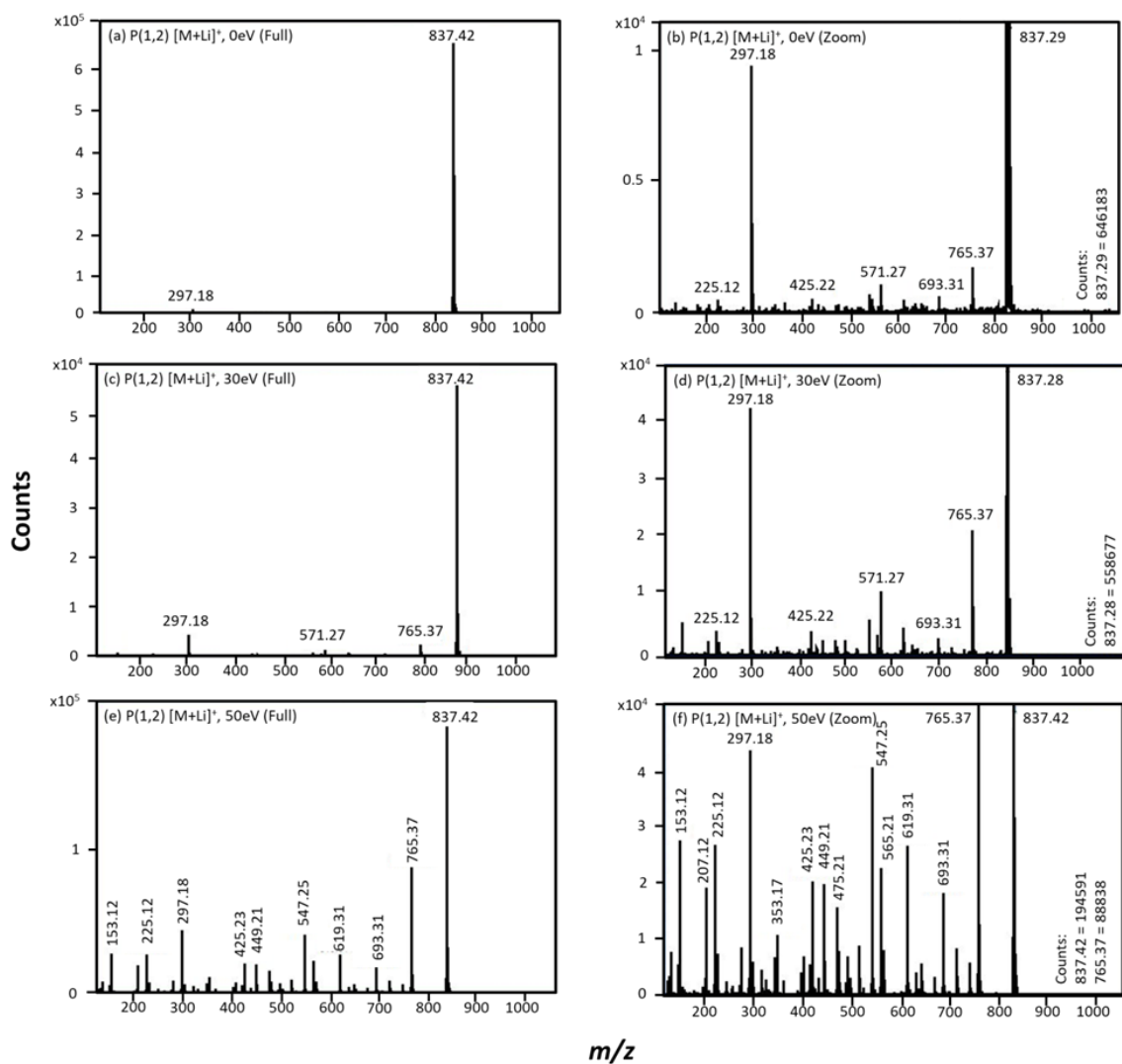


Figure 6.10. ESI MS/MS spectra of the P(1,2) $[M+Li]^+$ at corresponding lab-frame energies of 0 eV for (a-b), 30 eV (c-d), and 50 eV (e-d). Both full (a,c,e) MS/MS spectra and zoomed-in (b,d,f) regions are represented each lab-frame energy. Counts represent max intensities for precursor ions in each zoomed spectra.

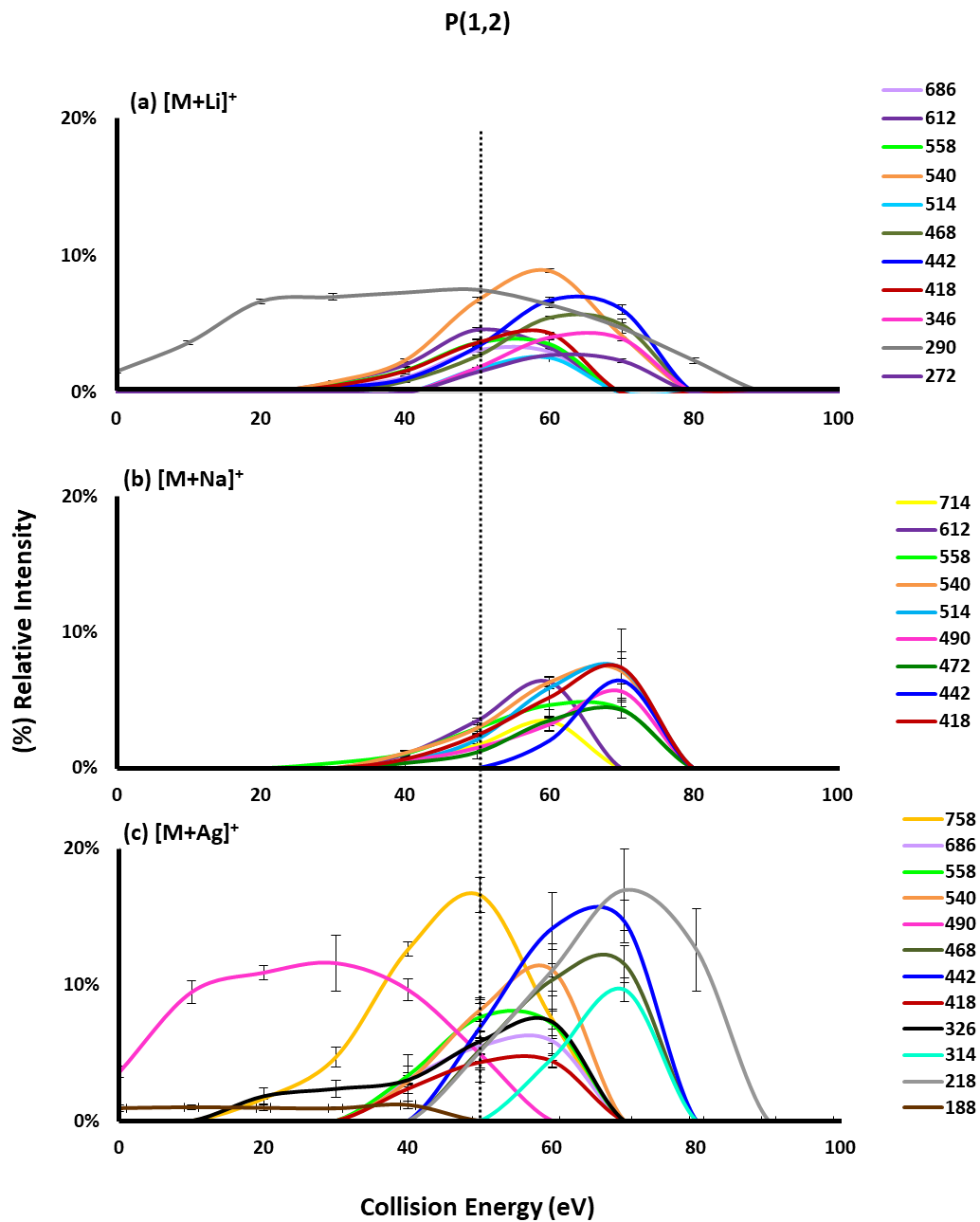


Figure 6.11. Collision-induced dissociation (CID) curves monitoring the unique transition of P(1,2) precursor to minor fragment ions when coordinated with cations (a) [M+Li]⁺, (b) [M+Na]⁺, and (c) [M+Ag]⁺. The dotted line is drawn at 50 eV for visual alignment of low energy fragment ions with %RSD.

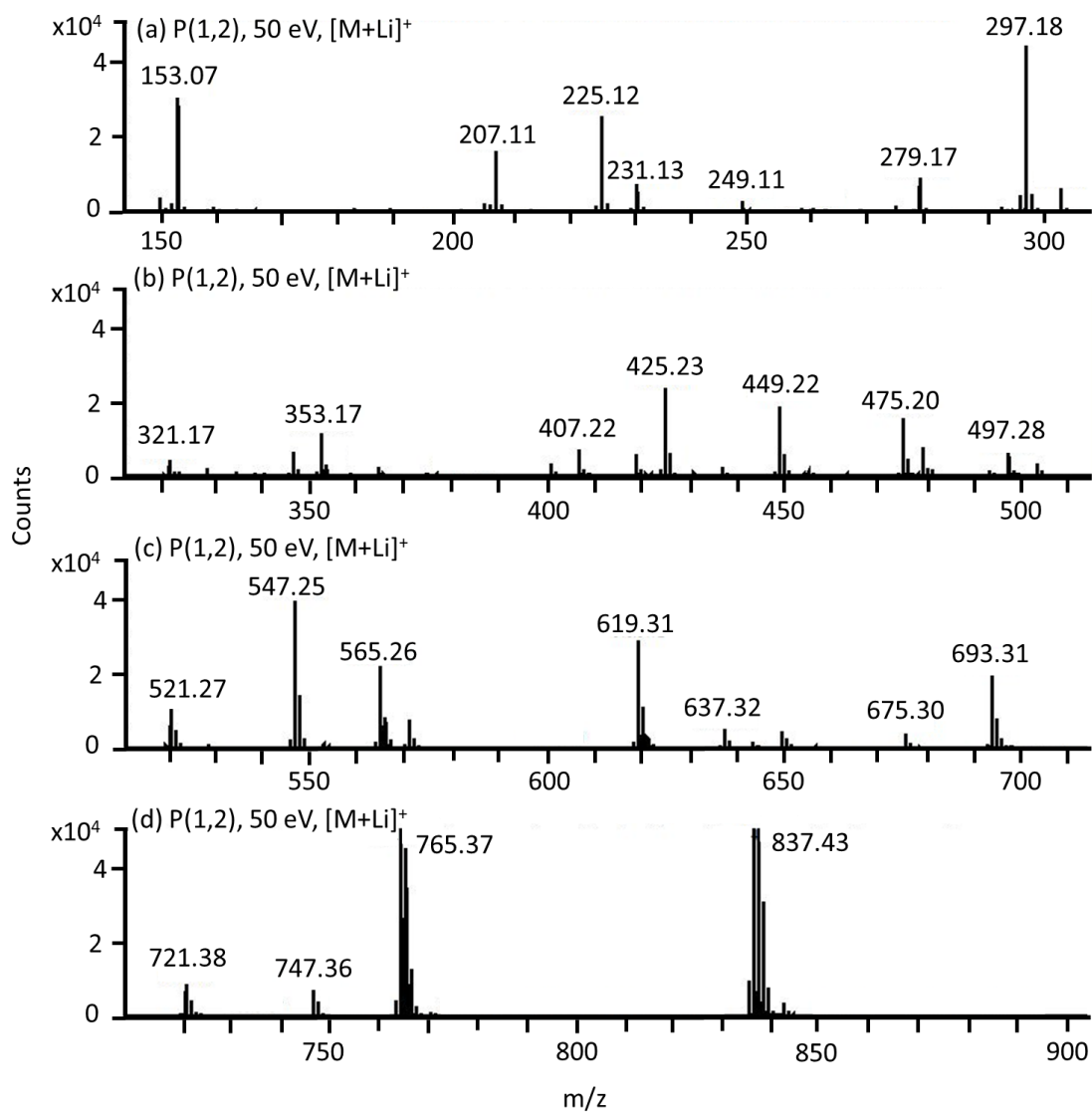


Figure 6.12. ESI MS/MS spectra of the P(1,2) [M+Li]⁺ at 50 eV. Zoomed-in regions include: (a) 150 – 300 m/z, (b) 300 – 500 m/z, (c) 500 – 700 m/z, and (d) 700 – 900 m/z.

| [M+Li] ⁺ | [M+Na] ⁺ | [M+Ag] ⁺ | mass | Fragmentation Pathway | Structures |
|---------------------|---------------------|---------------------|------|-----------------------------------|------------|
| 837 | 853 | 937 | 830 | Precursor P(1,2) | |
| 765 | 781 | 865 | 758 | 1,5 H-shift | |
| 547 | 563 | 647 | 540 | 1,3 H-shift | |
| 497 | 513 | 597 | 490 | 1,5 and 1,3 H-shift (combination) | |
| 475 | 491 | 575 | 468 | 1,5 and 1,3 H-shift (combination) | |
| 449 | 465 | 549 | 442 | 2X 1,5 H-shift | |
| 321 | 337 | 421 | 314 | 1,5 and 1,3 H-shift (combination) | |
| 297 | 313 | 397 | 290 | 1,3 H-shift | |
| 275 | 291 | 375 | 268 | 2X 1,3 H-shift | |
| 247 | 263 | 347 | 240 | high energy | |
| 225 | 241 | 325 | 218 | 1,5 H-shift | |
| 153 | 169 | 253 | 146 | 2X 1,5 H-shift | |
| 135 | 151 | 235 | 128 | 1,5 and 1,3 H-shift (combination) | |
| 97 | 113 | 197 | 90 | 1,3 H-shift | |

Table 6.5. Provides mass lists for each cation coordinated to P(1,2) precursor and nominal masses as listed in CID curves. The fragmentation pathway and corresponding structure for each species is represented above. Only major fragment ions monitored in CID curves are represented above.

| HOBABMBAOH (with Li) | | | | | | | | | | | | |
|----------------------|----------------|-------|-------|-------|-------|-------|-------|-------|-------|-------|-------|-------|
| (mass without Li) | (mass with Li) | 0 | 10 | 20 | 30 | 40 | 50 | 60 | 70 | 80 | 90 | 100 |
| 830 | 837 | 98.5% | 96.4% | 93.3% | 85.0% | 69.1% | 32.8% | 5.4% | 0.0% | 0.0% | 0.0% | 0.0% |
| | | 0.1% | 0.1% | 0.2% | 0.6% | 0.6% | 0.7% | 0.3% | 0.0% | 0.0% | 0.0% | 0.0% |
| 758 | 765 | 0.0% | 0.0% | 0.0% | 3.5% | 9.3% | 14.9% | 6.8% | 0.0% | 0.0% | 0.0% | 0.0% |
| | | 0.0% | 0.0% | 0.0% | 0.2% | 0.2% | 0.1% | 0.1% | 0.0% | 0.0% | 0.0% | 0.0% |
| 686 | 693 | 0.0% | 0.0% | 0.0% | 0.4% | 1.1% | 3.1% | 3.0% | 0.0% | 0.0% | 0.0% | 0.0% |
| | | 0.0% | 0.0% | 0.0% | 0.1% | 0.1% | 0.2% | 0.2% | 0.0% | 0.0% | 0.0% | 0.0% |
| 612 | 619 | 0.0% | 0.0% | 0.0% | 0.7% | 2.0% | 4.6% | 3.3% | 0.0% | 0.0% | 0.0% | 0.0% |
| | | 0.0% | 0.0% | 0.0% | 0.1% | 0.2% | 0.1% | 0.2% | 0.0% | 0.0% | 0.0% | 0.0% |
| 558 | 565 | 0.0% | 0.0% | 0.0% | 0.5% | 1.6% | 3.6% | 3.6% | 0.0% | 0.0% | 0.0% | 0.0% |
| | | 0.0% | 0.0% | 0.0% | 0.0% | 0.3% | 0.3% | 0.4% | 0.0% | 0.0% | 0.0% | 0.0% |
| 540 | 547 | 0.0% | 0.0% | 0.0% | 0.8% | 2.4% | 6.7% | 8.9% | 4.2% | 0.0% | 0.0% | 0.0% |
| | | 0.0% | 0.0% | 0.0% | 0.1% | 0.1% | 0.2% | 0.1% | 0.2% | 0.0% | 0.0% | 0.0% |
| 514 | 521 | 0.0% | 0.0% | 0.0% | 0.0% | 0.0% | 1.7% | 2.6% | 0.0% | 0.0% | 0.0% | 0.0% |
| | | 0.0% | 0.0% | 0.0% | 0.0% | 0.0% | 0.2% | 0.0% | 0.0% | 0.0% | 0.0% | 0.0% |
| 490 | 497 | 0.0% | 0.0% | 0.0% | 0.0% | 0.0% | 0.0% | 0.0% | 0.0% | 0.0% | 0.0% | 0.0% |
| | | 0.0% | 0.0% | 0.0% | 0.0% | 0.0% | 0.0% | 0.0% | 0.0% | 0.0% | 0.0% | 0.0% |
| 468 | 475 | 0.0% | 0.0% | 0.0% | 0.0% | 0.8% | 2.7% | 5.5% | 5.0% | 0.0% | 0.0% | 0.0% |
| | | 0.0% | 0.0% | 0.0% | 0.0% | 0.1% | 0.1% | 0.1% | 0.1% | 0.0% | 0.0% | 0.0% |
| 442 | 449 | 0.0% | 0.0% | 0.0% | 0.4% | 1.0% | 3.4% | 6.7% | 6.1% | 0.0% | 0.0% | 0.0% |
| | | 0.0% | 0.0% | 0.0% | 0.0% | 0.2% | 0.2% | 0.2% | 0.3% | 0.0% | 0.0% | 0.0% |
| 418 | 425 | 0.0% | 0.0% | 0.0% | 0.5% | 1.6% | 3.7% | 4.4% | 0.0% | 0.0% | 0.0% | 0.0% |
| | | 0.0% | 0.0% | 0.0% | 0.1% | 0.1% | 0.2% | 0.0% | 0.0% | 0.0% | 0.0% | 0.0% |
| 346 | 353 | 0.0% | 0.0% | 0.0% | 0.0% | 0.0% | 1.8% | 4.0% | 3.9% | 0.0% | 0.0% | 0.0% |
| | | 0.0% | 0.0% | 0.0% | 0.0% | 0.0% | 0.0% | 0.2% | 0.1% | 0.0% | 0.0% | 0.0% |
| 290 | 297 | 1.5% | 3.6% | 6.7% | 7.0% | 7.3% | 7.5% | 6.4% | 4.7% | 2.3% | 0.0% | 0.0% |
| | | 0.1% | 0.1% | 0.2% | 0.3% | 0.1% | 0.1% | 0.2% | 0.6% | 0.2% | 0.0% | 0.0% |
| 272 | 279 | 0.0% | 0.0% | 0.0% | 0.0% | 0.0% | 1.5% | 2.7% | 2.3% | 0.0% | 0.0% | 0.0% |
| | | 0.0% | 0.0% | 0.0% | 0.0% | 0.0% | 0.1% | 0.1% | 0.1% | 0.0% | 0.0% | 0.0% |
| 218 | 225 | 0.0% | 0.0% | 0.0% | 0.6% | 1.4% | 4.4% | 9.4% | 12.2% | 9.9% | 5.7% | 3.2% |
| | | 0.0% | 0.0% | 0.0% | 0.1% | 0.0% | 0.2% | 0.5% | 1.4% | 0.5% | 0.5% | 0.1% |
| 200 | 207 | 0.0% | 0.0% | 0.0% | 0.0% | 1.0% | 3.0% | 8.5% | 15.7% | 16.3% | 11.3% | 6.5% |
| | | 0.0% | 0.0% | 0.0% | 0.0% | 0.1% | 0.3% | 0.2% | 2.0% | 1.1% | 0.8% | 1.1% |
| 146 | 153 | 0.0% | 0.0% | 0.0% | 0.8% | 1.6% | 5.0% | 15.0% | 34.1% | 48.6% | 52.2% | 52.2% |
| | | 0.0% | 0.0% | 0.0% | 0.1% | 0.2% | 0.3% | 0.8% | 0.7% | 3.2% | 2.7% | 1.0% |
| 128 | 135 | 0.0% | 0.0% | 0.0% | 0.0% | 0.0% | 0.0% | 4.0% | 10.3% | 20.6% | 28.9% | 37.5% |
| | | 0.0% | 0.0% | 0.0% | 0.0% | 0.0% | 0.0% | 0.1% | 0.6% | 0.5% | 0.3% | 0.9% |

Table 6.6. Total percent ion currents observed for $[M+Li]^+$ P(1,2). Percent averages and %RSD are shown above for each ion.

The ESI MS/MS spectra of P(1,2) coordinated to $[M+Na]^+$ at different CID energies can be found in **Figure 6.13**. The $[M+Na]^+$ MS/MS spectra at 0 eV (**Figure 6.13a-b**), 30 eV (**Figure 6.13c-d**), and 50 eV (**Figure 6.13e-f**) shows both full (**Figure 6.13a,c,e**) MS/MS spectra and zoomed (**Figure 6.13b,d,f**) regions for each of these CID energies. In **Figure 6.9b**, the depletion of the $[M+Na]^+$ precursor was monitored with respect to increasing CID energies (0 – 110 eV). The CID curves for $[M+Na]^+$ species show an increased stability in P(1,2) coordinated to Na cation, compared to Li and Ag cations. The P(1,2) species (830 Da) was observed to deplete 100% by 80 eV, forming three major fragment ions: 758, 290, and 240 Da, which correspond to 781, 313, and 263 Da (cation masses as seen in **Figure 6.13**). All ions that were observed to form above 10% RIC are considered major fragment ions.

In **Figure 6.9b**, major fragment ions 758, 290, and 240 Da were observed to start forming at low CID energies (≤ 50 eV), however these fragment ions formed in greatest abundance at high energies (≥ 50 eV). Fragment ion 758 Da (11%, 60 eV), as discussed previously forms from the 1,5 H-shift; in the MS/MS spectra, the corresponding 72 Da fragment ion was observed to form at relatively low intensity. The next major fragment ion, 290 Da (12%, 80 eV) species forms from a 1,3 H-shift around the urethane group yielding the $n = 1$ PBA chain. The corresponding 540 Da species was observed as a minor fragment ion observed in **Table 6.5** and **Figure 6.11b**. The 540 Da structure includes the MDI hard segment with an exposed isocyanate group and a urethane PBA $n = 1$ chain. The most interesting fragment ion formed in the $[M+Na]^+$ spectra was the 240 Da species as seen in **Table 6.5**. This fragment ion was observed to form at high energy only, and was uniquely observed only for the P(1,2) precursor coordinated to an Na alkali cation. The 240 Da fragment ion forms at high activation energy (88%, 80 eV), and results in an NH group and

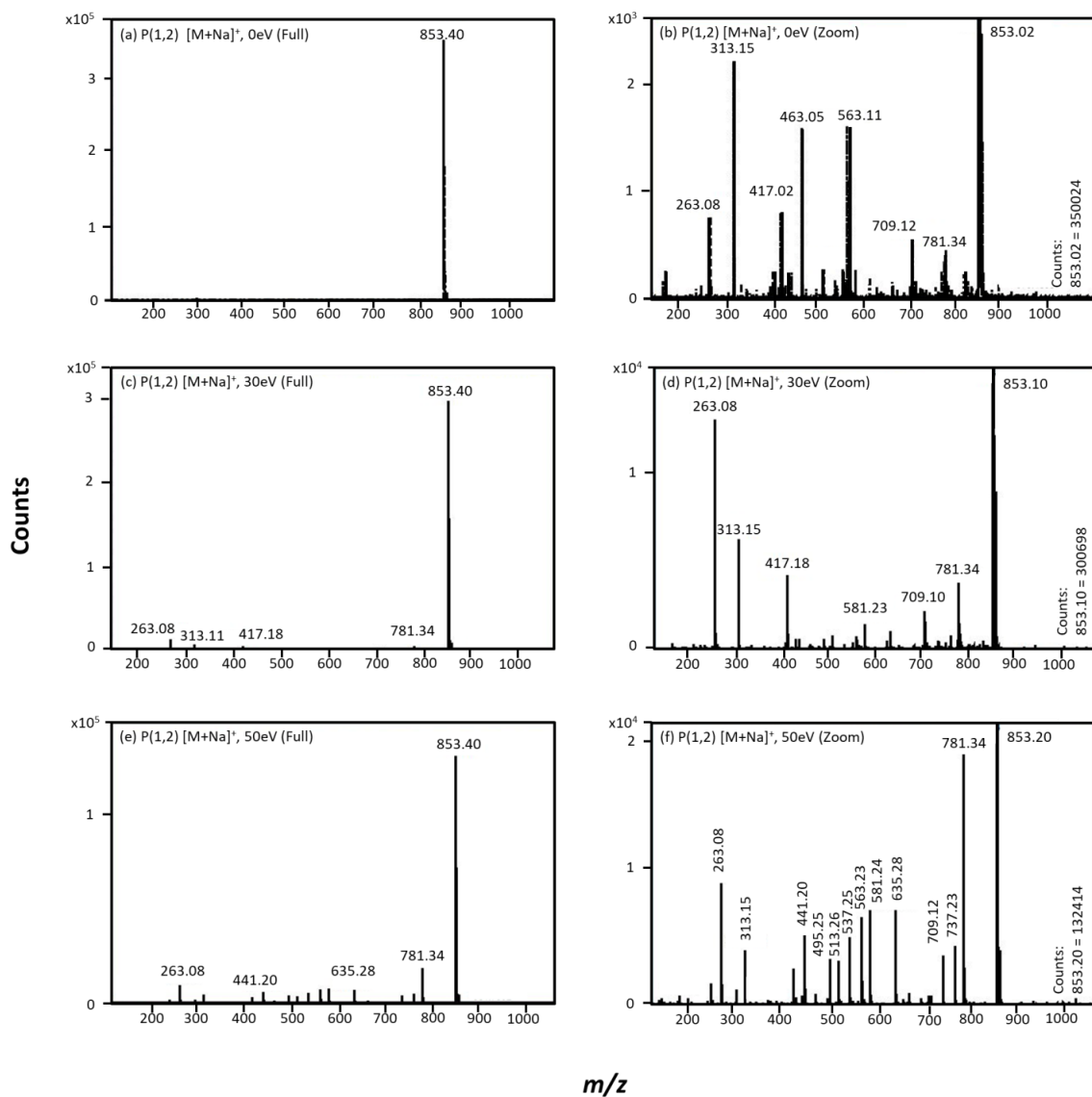


Figure 6.13. ESI MS/MS spectra of the P(1,2) $[M+Na]^+$ at corresponding lab-frame energies of 0 eV for (a-b), 30 eV (c-d), and 50 eV (e-f). Both full (a,c,e) MS/MS spectra and zoomed-in (b,d,f) regions are represented each lab-frame energy. Counts represent max intensities for precursor ions in each zoomed spectra.

| HOBABMBAOH (with Na) | | | | | | | | | | | | |
|----------------------|----------------|-------|-------|-------|-------|-------|-------|-------|-------|-------|------|------|
| (mass without Na) | (mass with Na) | 0 | 10 | 20 | 30 | 40 | 50 | 60 | 70 | 80 | 90 | 100 |
| 830 | 853 | 99.3% | 97.1% | 95.0% | 92.4% | 84.7% | 64.7% | 33.9% | 10.3% | 0.0% | 0.0% | 0.0% |
| | | 0.1% | 0.2% | 0.5% | 0.1% | 0.6% | 1.0% | 0.6% | 1.7% | 0.0% | 0.0% | 0.0% |
| 758 | 781 | 0.0% | 0.0% | 0.5% | 1.2% | 3.6% | 9.1% | 11.1% | 6.0% | 0.0% | 0.0% | 0.0% |
| | | 0.0% | 0.0% | 0.1% | 0.1% | 0.1% | 0.3% | 0.6% | 0.8% | 0.0% | 0.0% | 0.0% |
| 714 | 737 | 0.0% | 0.0% | 0.0% | 0.0% | 0.5% | 1.7% | 3.5% | 0.0% | 0.0% | 0.0% | 0.0% |
| | | 0.0% | 0.0% | 0.0% | 0.0% | 0.1% | 0.1% | 0.3% | 0.0% | 0.0% | 0.0% | 0.0% |
| 612 | 635 | 0.0% | 0.0% | 0.0% | 0.0% | 1.0% | 3.5% | 6.4% | 0.0% | 0.0% | 0.0% | 0.0% |
| | | 0.0% | 0.0% | 0.0% | 0.0% | 0.2% | 0.2% | 0.3% | 0.0% | 0.0% | 0.0% | 0.0% |
| 558 | 581 | 0.0% | 0.0% | 0.0% | 0.4% | 1.1% | 3.0% | 4.7% | 4.4% | 0.0% | 0.0% | 0.0% |
| | | 0.0% | 0.0% | 0.0% | 0.0% | 0.2% | 0.5% | 1.2% | 0.7% | 0.0% | 0.0% | 0.0% |
| 540 | 563 | 0.0% | 0.0% | 0.0% | 0.0% | 1.1% | 3.0% | 6.3% | 7.1% | 0.0% | 0.0% | 0.0% |
| | | 0.0% | 0.0% | 0.0% | 0.0% | 0.1% | 0.3% | 0.1% | 0.9% | 0.0% | 0.0% | 0.0% |
| 514 | 537 | 0.0% | 0.0% | 0.0% | 0.0% | 0.5% | 2.1% | 5.9% | 7.4% | 0.0% | 0.0% | 0.0% |
| | | 0.0% | 0.0% | 0.0% | 0.0% | 0.0% | 0.4% | 0.1% | 1.2% | 0.0% | 0.0% | 0.0% |
| 490 | 513 | 0.0% | 0.0% | 0.0% | 0.0% | 0.5% | 1.5% | 3.2% | 5.7% | 0.0% | 0.0% | 0.0% |
| | | 0.0% | 0.0% | 0.0% | 0.0% | 0.1% | 0.1% | 0.5% | 0.5% | 0.0% | 0.0% | 0.0% |
| 472 | 495 | 0.0% | 0.0% | 0.0% | 0.0% | 0.4% | 1.2% | 3.5% | 4.3% | 0.0% | 0.0% | 0.0% |
| | | 0.0% | 0.0% | 0.0% | 0.0% | 0.3% | 0.5% | 0.8% | 0.6% | 0.0% | 0.0% | 0.0% |
| 442 | 465 | 0.0% | 0.0% | 0.0% | 0.0% | 0.0% | 0.0% | 2.0% | 6.5% | 0.0% | 0.0% | 0.0% |
| | | 0.0% | 0.0% | 0.0% | 0.0% | 0.0% | 0.0% | 0.3% | 0.8% | 0.0% | 0.0% | 0.0% |
| 418 | 441 | 0.0% | 0.0% | 0.0% | 0.0% | 0.7% | 2.4% | 5.2% | 7.4% | 0.0% | 0.0% | 0.0% |
| | | 0.0% | 0.0% | 0.0% | 0.0% | 0.1% | 0.1% | 1.6% | 2.9% | 0.0% | 0.0% | 0.0% |
| 290 | 313 | 0.7% | 1.9% | 2.2% | 2.3% | 2.0% | 2.8% | 4.3% | 5.6% | 11.9% | 0.0% | 0.0% |
| | | 0.1% | 0.3% | 0.2% | 0.4% | 0.2% | 0.6% | 0.6% | 0.5% | 5.9% | 0.0% | 0.0% |
| 240 | 263 | 0.0% | 1.0% | 2.4% | 3.8% | 3.9% | 5.0% | 10.0% | 35.4% | 88.1% | 0.0% | 0.0% |
| | | 0.0% | 0.2% | 0.3% | 0.3% | 0.2% | 0.3% | 1.2% | 1.3% | 5.9% | 0.0% | 0.0% |

Table 6.7. Total percent ion currents observed for $[M+Na]^+ P(1,2)$. Percent averages and %RSD are shown above for each ion.

carbamic acid around the hard segment. Carbamic acids are unstable end groups which can easily undergo loss of CO₂ to form the amine. Additional total %RIC data can be found in **Tables 6.7** for both major and minor fragment ions generated from the [M+Na]⁺ species.

The ESI MS/MS spectra of P(1,2) coordinated to [M+Ag]⁺ at different CID energies can be found in **Figure 6.14**. The [M+Ag]⁺ MS/MS spectra at 0 eV (**Figure 6.14a-b**), 30 eV (**Figure 6.14c-d**), and 50 eV (**Figure 6.14e-f**) shows both full (**Figure 6.14a,c,e**) MS/MS spectra and zoomed (**Figure 6.14b,d,f**) regions for each of these CID energies. In **Figure 6.9.c**, the depletion of the [M+Ag]⁺ precursor was monitored with respect to increasing CID energies. In the case where Ag is coordinated to P(1,2), there is an increase in fragment ions formed from the depletion of the 830 Da precursor. Here, the precursor species is observed to deplete to 100% completion at 60 eV, therefore making this species the least stable of the three cationized P(1,2) species. At relatively low CID energies, two major fragment ions were observed to form: 758 and 490 Da species. The 758 Da (17%, 50 eV) species forms from the 1,5 H-shift and its corresponding fragment ion, 72 Da was only observed in low ion abundance in the MS/MS spectra. The other low energy fragment ion formed is the 490 Da species (12%, 30 eV) as seen in **Table 6.5**. This species is appears in relatively high intensities for the Ag⁺ species, and is also seen for the Li⁺ species (**Figure 6.12b** as 497 Da). It appears that the 490 Da species forms from both a combination reaction between the 1,5 and 1,3 H-shift along the urethane and polyester chain, as seen in **Table 6.5**. Other major fragment ions observed at higher collision energies include: 540, 468, 442, 314, 268, 218, and 90 Da species. The 442 Da (15%, 70 eV) formed due to high energies from a 1,5 H-shift around the urethane forming an amine and corresponding 318 Da fragment ion (observed in low abundance in MS/MS spectra). Additionally, the 442 Da (**Figure 6.14f**) formed due to a 1,5 H-shift along the polyester backbone forming the corresponding 72 Da fragment ion, also observed at low ion intensities in MS/MS spectra. Fragment ion 218 Da (17%, 70 eV) was also observed to form due to 1,5 H-shift along the polyester backbone, resulting in fragment ion 612 Da, also observed in low ion intensity in the MS/MS spectra (**Figure 6.14f** as

the 721 Da, cation mass included). The 540 Da (11%, 60 eV) fragment ion forms from the 1,3 H-shift around the urethane bond (**Table 6.5**), resulting in the formation of the 290 Da species which was not observed in the MS/MS spectra. Fragment ion 268 Da (43%, 80 eV) formed due to a 1,3 H-shift around the PU hard segment, leaving isocyanate and carbamic acid end groups as seen in **Table 6.5**. Fragment ion 90 Da (85%, 100 eV) also forms from a 1,3 H-shift along the polyester chain. The corresponding 740 Da species was not observed as a minor fragment ion, however it was observed in low ion intensity in the MS/MS spectra. The 468 Da (11%, 70 eV) species uniquely forms from both a 1,3 H-shift around the urethane and a 1,5 H-shift around the polyester backbone. Fragment ion 314 Da (10%, 70 eV) is also formed at relatively high CID energies due to a combination reaction of 1,5 and 1,3 H-shift, forming the hard segment with an amine (-NH₂) and a 1,3 H-shift fragmentation mechanism along the polyester chain (**Table 6.5**). Similar to the [M+Li]⁺ P(1,2) species, the Ag⁺ cation is observed to generate many fragment ions both along the polyester chain as well as around the urethane hard segment. Additional total %RIC data of major and minor fragment ions can be found in **Tables 6.8**. In **Figure 6.15**, the major P(1,2) fragment ions CID curves with %RSD error bars can be found for each cation.

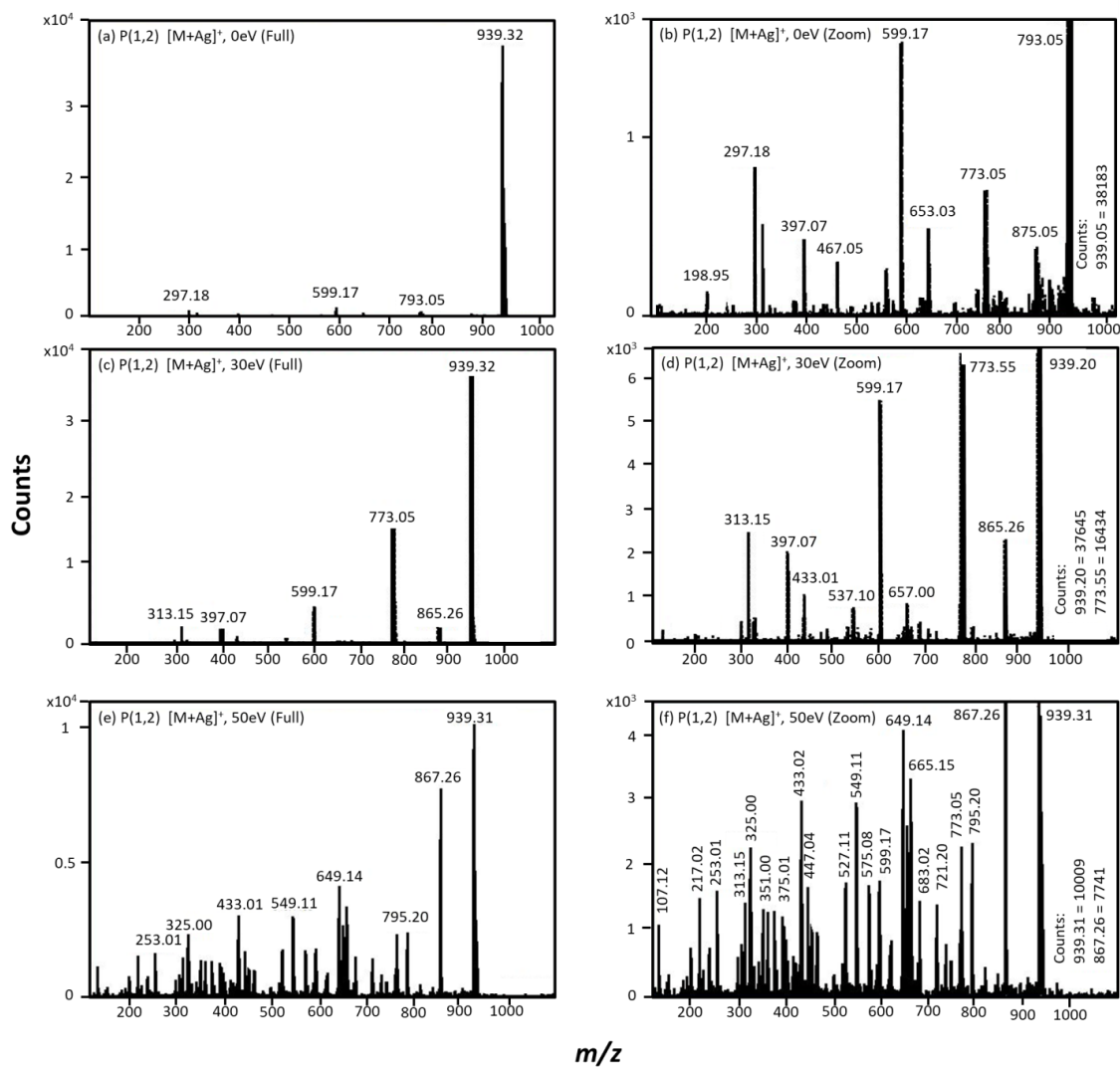


Figure 6.14. ESI MS/MS spectra of the P(1,2) [M+Ag]⁺ at corresponding lab-frame energies of 0 eV for (a-b), 30 eV (c-d), and 50 eV (e-d). Both full (a,c,e) MS/MS spectra and zoomed-in (b,d,f) regions are represented each lab-frame energy. Counts represent max intensities for precursor ions in each zoomed spectra.

| HOBABMBABOH (With Ag) | | | | | | | | | | | |
|-----------------------|-----|-----|-----|-----|-----|-----|-----|-----|-----|-----|-----|
| | 0 | 10 | 20 | 30 | 40 | 50 | 60 | 70 | 80 | 90 | 100 |
| 830 | 95% | 90% | 85% | 81% | 62% | 27% | 2% | 0% | 0% | 0% | 0% |
| 939/937 | 1% | 3% | 2% | 4% | 6% | 5% | 0% | 0% | 0% | 0% | 0% |
| 758 | 0% | 0% | 2% | 5% | 13% | 17% | 7% | 0% | 0% | 0% | 0% |
| 867/865 | 0% | 0% | 0% | 1% | 1% | 1% | 1% | 0% | 0% | 0% | 0% |
| 686 | 0% | 0% | 0% | 0% | 3% | 5% | 6% | 0% | 0% | 0% | 0% |
| 795/793 | 0% | 0% | 0% | 0% | 0% | 1% | 0% | 0% | 0% | 0% | 0% |
| 558 | 0% | 0% | 0% | 0% | 3% | 8% | 7% | 0% | 0% | 0% | 0% |
| 667/665 | 0% | 0% | 0% | 0% | 1% | 1% | 1% | 0% | 0% | 0% | 0% |
| 540 | 0% | 0% | 0% | 0% | 3% | 8% | 11% | 0% | 0% | 0% | 0% |
| 649/647 | 0% | 0% | 0% | 0% | 0% | 1% | 2% | 0% | 0% | 0% | 0% |
| 490 | 4% | 9% | 11% | 12% | 10% | 5% | 0% | 0% | 0% | 0% | 0% |
| 599/597 | 0% | 1% | 1% | 2% | 1% | 1% | 0% | 0% | 0% | 0% | 0% |
| 468 | 0% | 0% | 0% | 0% | 0% | 5% | 10% | 11% | 0% | 0% | 0% |
| 577/575 | 0% | 0% | 0% | 0% | 0% | 1% | 1% | 1% | 0% | 0% | 0% |
| 442 | 0% | 0% | 0% | 0% | 0% | 7% | 14% | 15% | 0% | 0% | 0% |
| 551/549 | 0% | 0% | 0% | 0% | 0% | 1% | 3% | 2% | 0% | 0% | 0% |
| 418 | 0% | 0% | 0% | 0% | 2% | 4% | 4% | 0% | 0% | 0% | 0% |
| 527/525 | 0% | 0% | 0% | 0% | 0% | 1% | 1% | 0% | 0% | 0% | 0% |
| 326 | 0% | 0% | 2% | 2% | 3% | 6% | 7% | 0% | 0% | 0% | 0% |
| 435/433 | 0% | 0% | 1% | 1% | 2% | 3% | 3% | 0% | 0% | 0% | 0% |
| 314 | 0% | 0% | 0% | 0% | 0% | 0% | 5% | 10% | 0% | 0% | 0% |
| 423/421 | 0% | 0% | 0% | 0% | 0% | 0% | 0% | 1% | 0% | 0% | 0% |
| 268 | 0% | 0% | 0% | 0% | 0% | 3% | 13% | 34% | 43% | 31% | 15% |
| 377/375 | 0% | 0% | 0% | 0% | 0% | 1% | 2% | 4% | 5% | 5% | 4% |
| 218 | 0% | 0% | 0% | 0% | 0% | 5% | 11% | 17% | 13% | 0% | 0% |
| 327/325 | 0% | 0% | 0% | 0% | 0% | 1% | 2% | 4% | 6% | 0% | 0% |
| 188 | 1% | 1% | 1% | 1% | 1% | 0% | 0% | 0% | 0% | 0% | 0% |
| 297/295 | 0% | 0% | 0% | 0% | 0% | 0% | 0% | 0% | 0% | 0% | 0% |
| 90 | 0% | 0% | 0% | 0% | 0% | 0% | 2% | 13% | 45% | 69% | 85% |
| 199/197 | 0% | 0% | 0% | 0% | 0% | 0% | 2% | 4% | 5% | 5% | 6% |

Table 6.8. Total percent ion currents observed for $[M+Ag]^+ P(1,2)$. Percent averages and %RSD are shown above for each ion.

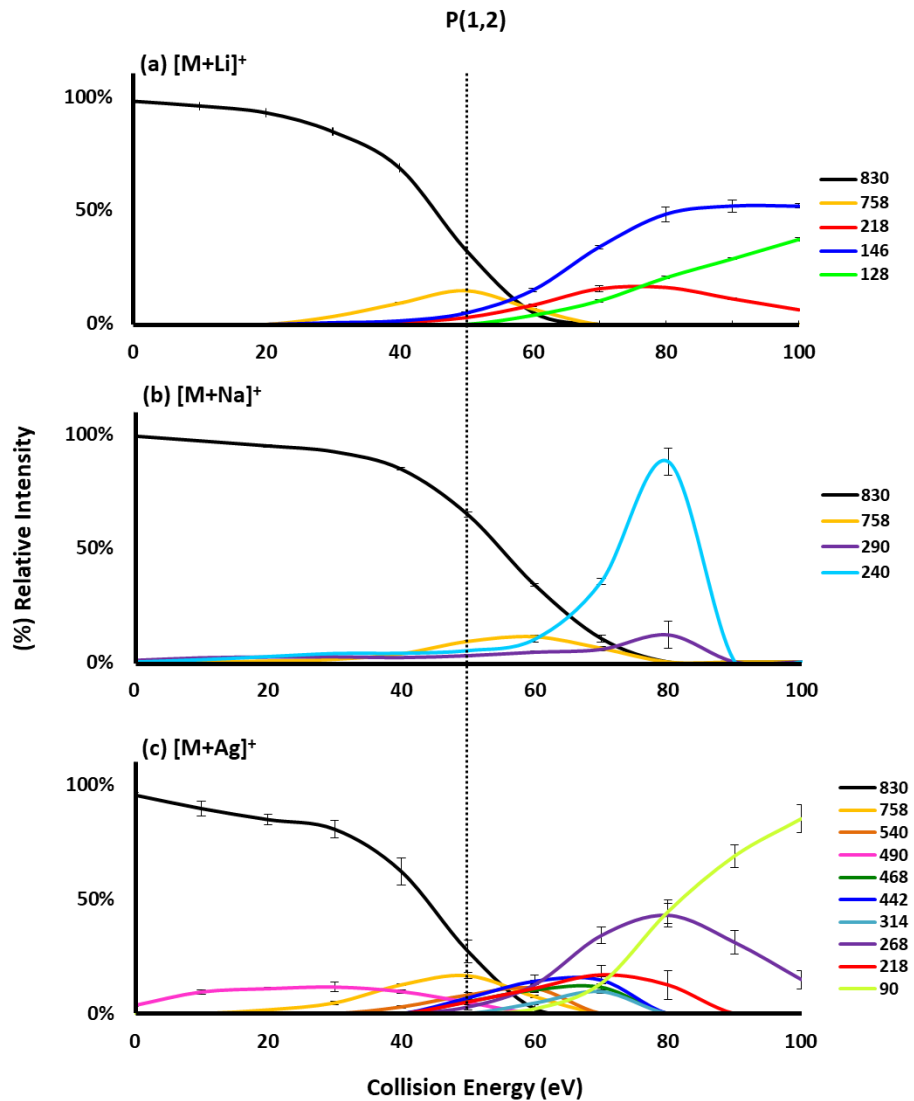


Figure 6.15. Collision-induced dissociation (CID) curves monitoring the unique transition of P(1,2) precursor to major fragment ions when coordinated with cations (a) $[M+Li]^+$, (b) $[M+Na]^+$, and (c) $[M+Ag]^+$. The dotted line is drawn at 50 eV for visual alignment of low energy fragment ions with %RSD.

6.3.5. Characterization of P(1,4) by MS/MS

The P(1,4) species produced similar results to what was found in the P(1,2) studies. Here, P(1,4) has two polyester repeat units on each side of the hard segment urethane as seen in **Figure 6.1b**. When probing the unique fragmentation pathways associated with this symmetrical P(1,4), we found that the P(1,4) was more stable than the symmetrical P(1,2) species. For instance, the P(1,4) precursor, irrespective of coordinated cation, appeared to deplete 100% by CID energies of 100 – 110 eV compared to 60 – 80 eV as seen in the P(1,2) findings. In this present study, we probed for unique fragmentation pathways for the P(1,4) species coordinated to Li^+ , Na^+ , and Ag^+ cations. We monitored the formation of major and minor fragment ions with respect to increasing CID energies. Major fragment ions observed for the $[\text{M}+\text{Li}]^+$, $[\text{M}+\text{Na}]^+$, and $[\text{M}+\text{Ag}]^+$ that formed above 10%RIC can be found in **Figure 6.16a-c**. The dashed line is drawn for visual alignment at 70 eV to represent low energy fragment ion formation.

The ESI MS/MS spectra of P(1,4) coordinated to $[\text{M}+\text{Li}]^+$ at different CID energies can be found in **Figure 6.17**. The $[\text{M}+\text{Li}]^+$ MS/MS spectra at 0 eV (**Figure 6.17a-b**), 50 eV (**Figure 6.17c-d**), and 70 eV (**Figure 6.17e-f**) shows both full (**Figure 6.17a,c,e**) MS/MS spectra and zoomed (**Figure 6.17b,d,f**) regions for each of these CID energies. Both major and minor fragment ions are annotated to show the unique polyester and urethane fragmentation pathways for P(1,4) coordinated to Li^+ . In **Figure 6.16**, major fragment ions that formed above 10%RIC include (nominal mass) 1158, 740, 418, 400, 346, 218, 200, 146, and 104 Da, which corresponds to 1165, 747, 425, 407, 353, 225, 207, 153, and 111 Da (mass with Li^+ cation). In **Figure 6.17**, additional fragment ions are notated in the MS/MS spectra. These are considered to be minor fragment ions, which were formed under 10%RIC, as seen

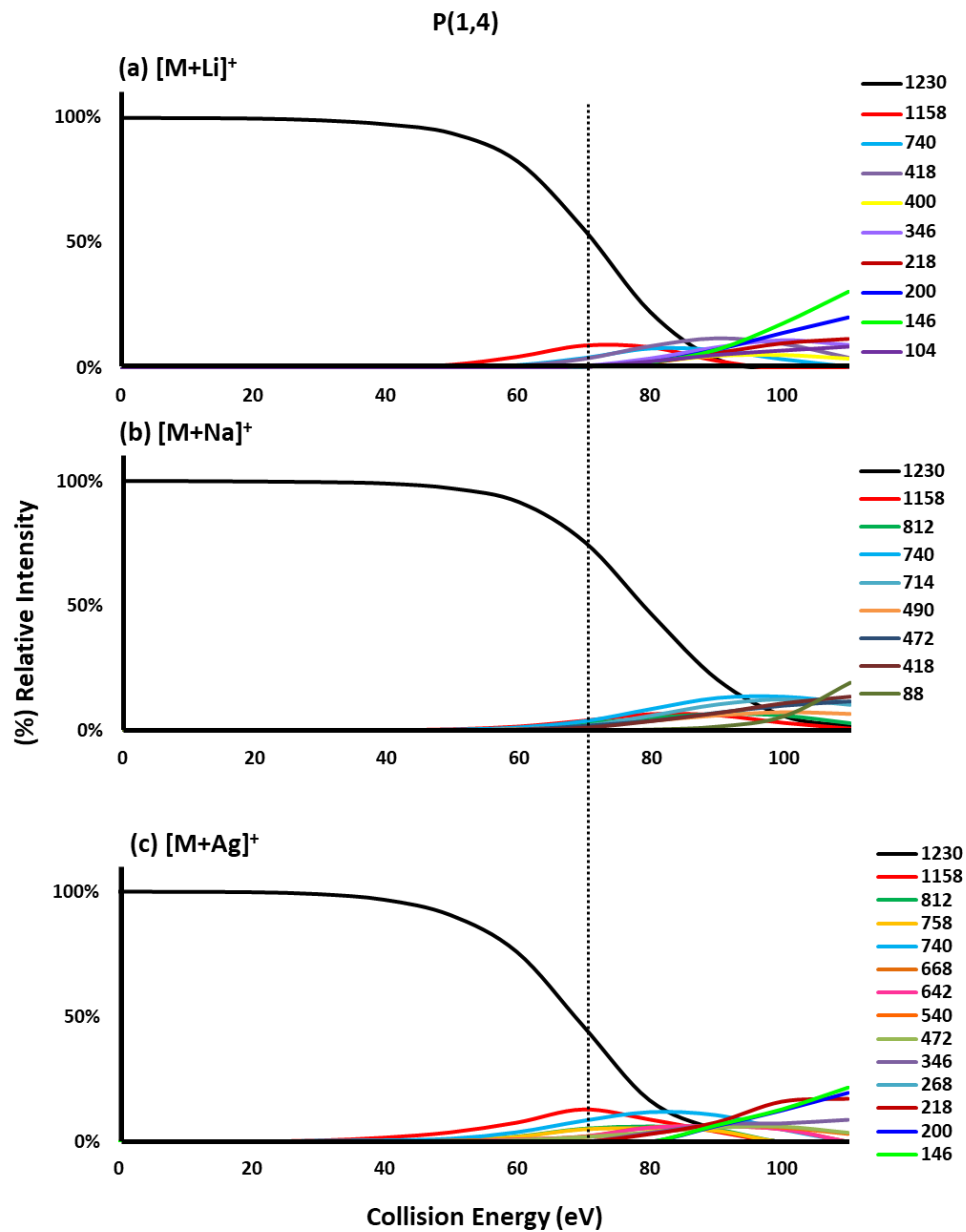


Figure 6.16. Collision-induced dissociation (CID) curves monitoring the unique transition of P(1,4) precursor to fragment ions when coordinated with cations (a) $[M+Li]^+$, (b) $[M+Na]^+$, and (c) $[M+Ag]^+$. The dotted line is drawn at 70 eV for visual alignment of low energy fragment ions.

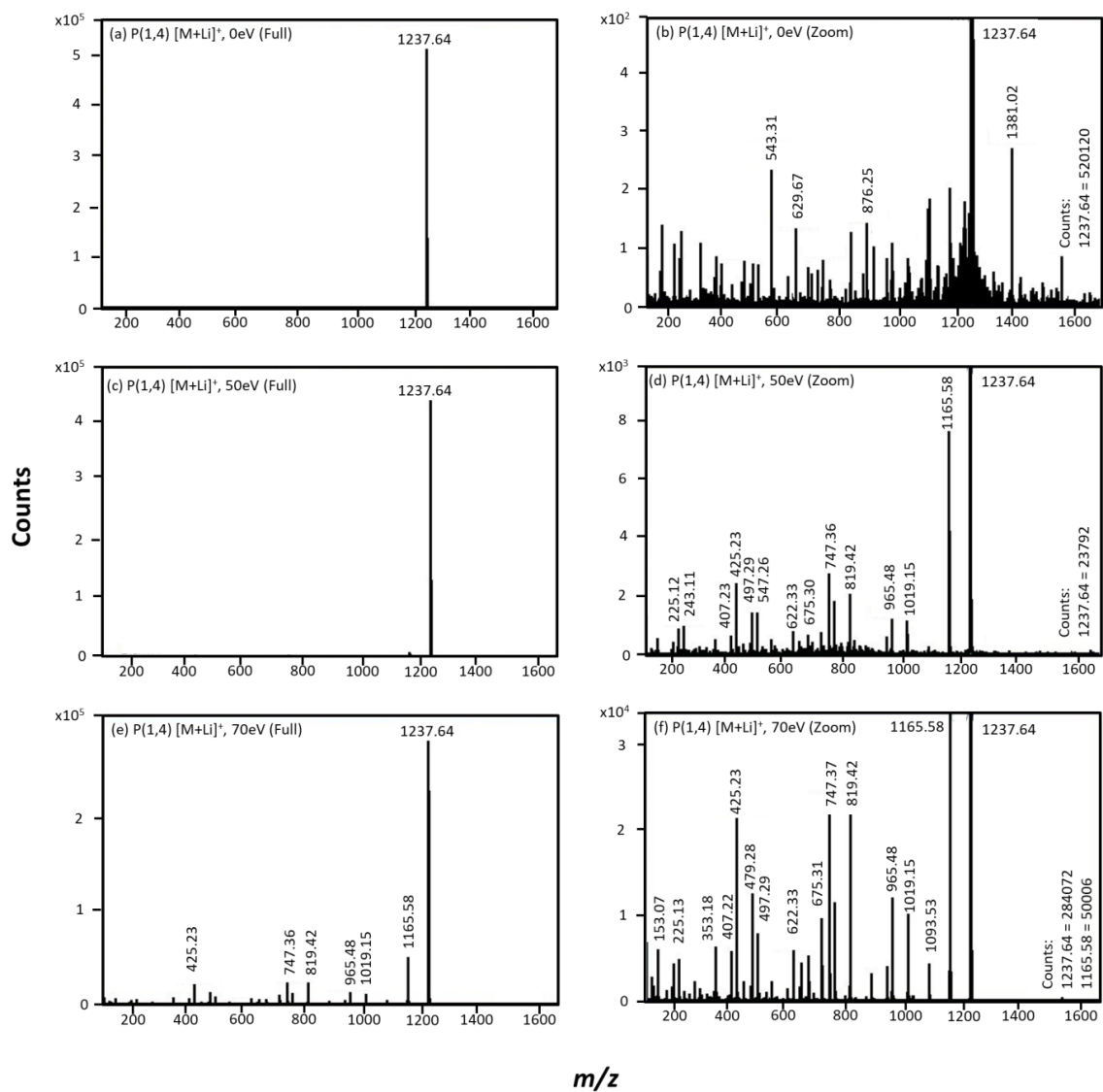


Figure 6.17. ESI MS/MS spectra of the P(1,4) [M+Li]⁺ at corresponding lab-frame energies of 0 eV for (a-b), 30 eV (c-d), and 50 eV (e-d). Both full (a,c,e) MS/MS spectra and zoomed-in (b,d,f) regions are represented each lab-frame energy. Counts represent max intensities for precursor ions in each zoomed spectra.

in **Figure 18a**. As an example, the P(1,4) $[M+Li]^+$ species MS/MS spectra at 70 eV was enlarged in **Figure 6.19a-d** to highlight the unique major and minor fragment ions observed for this precursor.

In **Figure 6.16a**, the depletion of the $[M+Li]^+$ precursor species (1230 Da) was monitored with respect to increasing CID energies. The CID curves for the $[M+Li]^+$ species show an increase in stability of the P(1,4) precursor with increasing CID energies. Here, the precursor is observed to deplete to 100% by 100 eV, therefore making this species more stable than the P(1,2) $[M+Li]^+$ precursor. At relatively low collision energies, only the 1158 Da (9%, 70 eV) is observed to form. The 1158 Da fragment ion is the product of a 1,5 H-shift around the polyester chain, as seen in **Table 6.9**. The corresponding 72 Da species was observed at low ion intensity. All other fragment ions observed formed at high CID energies. High energy fragment ions observed include: 740, 418, 400, 346, 218, 200, 146, and 104 Da species (as seen in **Figure 6.17** and **Figure 6.19**). The 418 Da (12%, 90 eV) and 218 Da (12%, 110 eV) species both formed from a 1,5 H-shift around the polyester as seen previously for PBA $n = 2$ (**Table 6.9**). The 740 Da (8%, 80 eV) species was observed to form from one 1,3 H-shift around the urethane hard segment, or two 1,3 H-shifts along the polyester chain, both 740 Da structures are illustrated in **Table 6.9**. As observed for PBA $n = 2$, both fragment ions 400 Da (5%, 100 eV) and 200 Da (20%, 110 eV) form from a 1,3 H-shift along the polyester chain. Likewise, fragment ions 346 Da (11%, 100 eV) and 146 Da (31%, 110 eV) species were also observed for PBA $n = 2$, and these fragment ions form from two 1,5 H-shifts along the polyester chain, leaving a di-acid product. The 104 Da (9%, 110 eV) species was uniquely observed for the $[M+Li]^+$ precursor species at high CID energies. Additional total %RIC data of major and minor fragment ions can be found in **Tables 6.10**.

P(1,4)

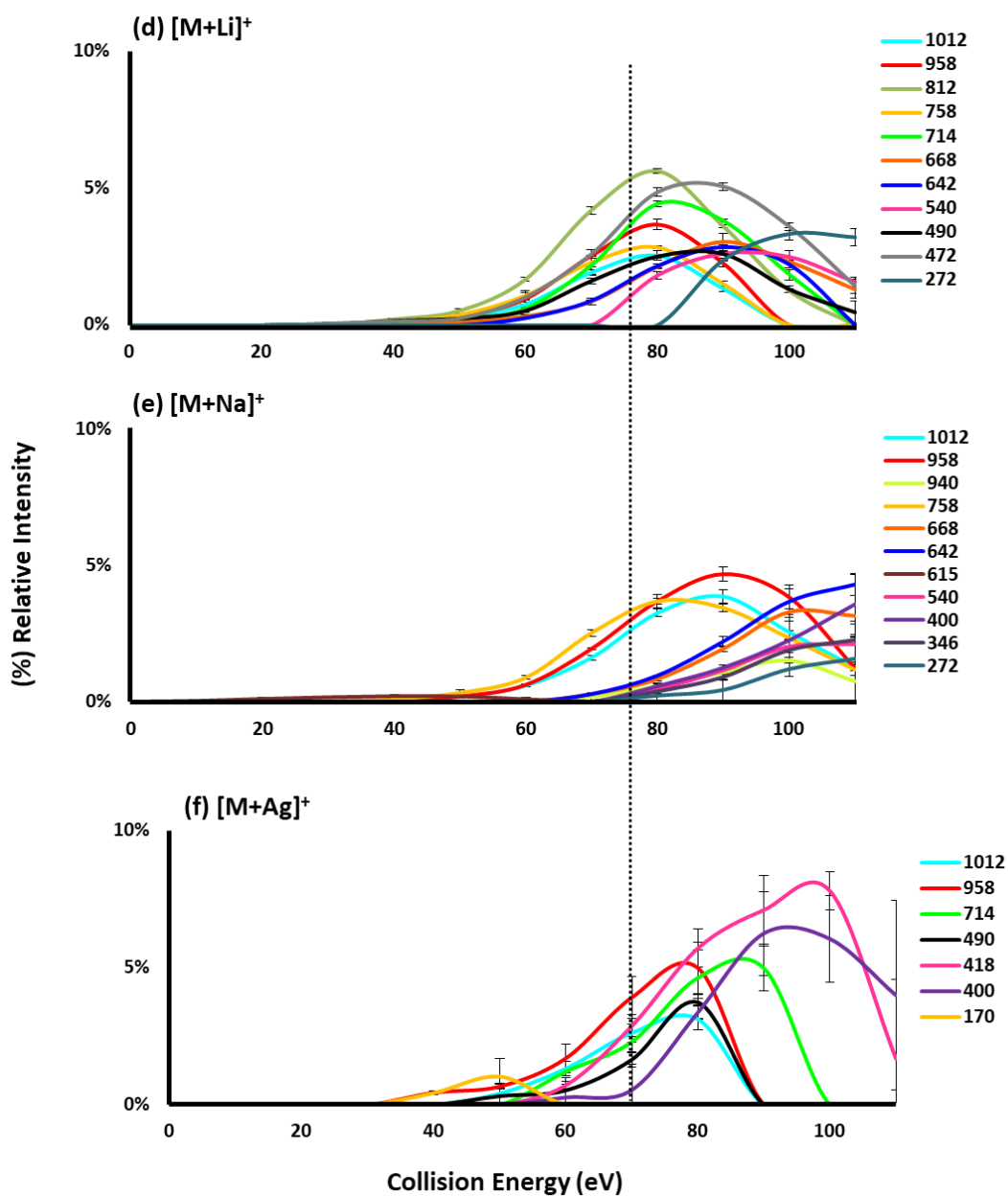


Figure 6.18. Collision-induced dissociation (CID) curves monitoring the unique transition of P(1,4) precursor to minor fragment ions when coordinated with cations (a) [M+Li]⁺, (b) [M+Na]⁺, and (c) [M+Ag]⁺. The dotted line is drawn at 70 eV for visual alignment of low energy fragment ions with %RSD.

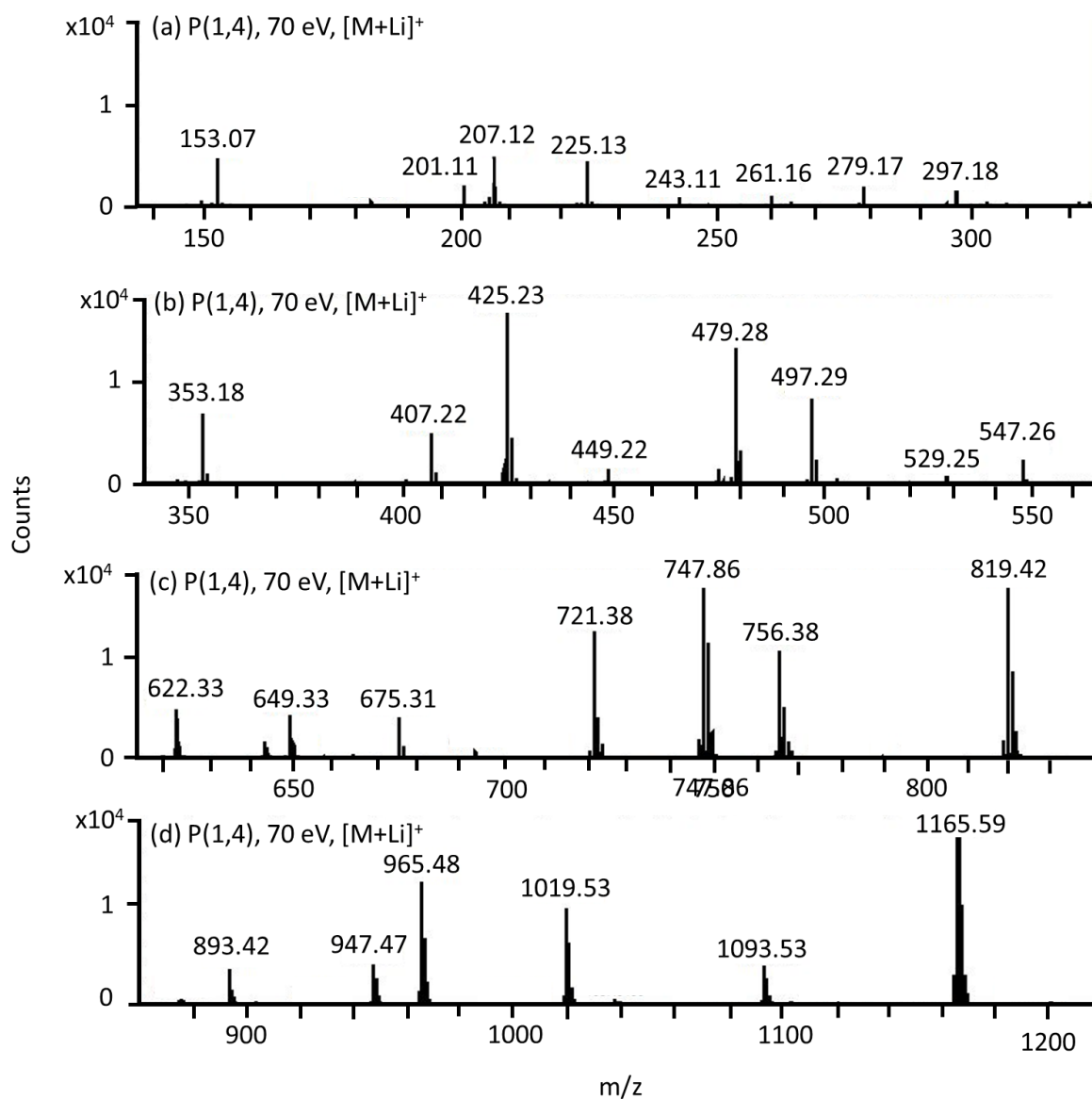


Figure 6.19. ESI MS/MS spectra of the P(1,4) [M+Li]⁺ at 70 eV. Zoomed-in regions include: (a) 150 – 350 m/z, (b) 350 – 550 m/z, (c) 600 – 850 m/z, and (d) 900 – 1200 m/z.

| [M+Li] ⁺ | [M+Na] ⁺ | [M+Ag] ⁺ | mass | Fragmentation Pathway | Structures |
|---------------------|---------------------|---------------------|------|--|------------|
| 1237 | 1253 | 1337 | 1230 | Precursor P(1,4) | |
| 1165 | 1181 | 1265 | 1158 | 1,5 H-shift | |
| 819 | 835 | 919 | 812 | 1,5 H-shift | |
| 765 | 781 | 865 | 758 | 1,5 and 1,3 H-shift (combination) | |
| 747 | 763 | 847 | 740 | 1,3 H-shift or 2X 1,3 H-shift | |
| 721 | 737 | 821 | 714 | 1,5 H-shift | |
| 675 | 691 | 775 | 668 | 1,5 and 1,3 H-shift (combination) | |
| 649 | 665 | 749 | 642 | 1,3 H-shift | |
| 547 | 563 | 647 | 540 | 2X 1,3 H-shift | |
| 497 | 513 | 597 | 490 | 1,3 H-shift | |
| 479 | 495 | 579 | 472 | 1,5 H-shift | |
| 425 | 441 | 525 | 418 | 1,5 H-shift | |
| 407 | 423 | 507 | 400 | 1,3 H-shift | |
| 353 | 369 | 453 | 346 | 2X 1,5 H-shift | |
| 275 | 291 | 375 | 268 | 1,5 and 1,3 H-shift (combination) | |
| 225 | 241 | 325 | 218 | 1,5 H-shift or 1,5 and 1,3 H-shift (combination) | |
| 207 | 223 | 307 | 200 | 1,3 H-shift | |
| 153 | 169 | 253 | 146 | 2X 1,5 H-shift | |
| 111 | 127 | 211 | 104 | high energy | |
| 95 | 111 | 195 | 88 | high energy | |

Table 6.9. Provides mass lists for each cation coordinated to P(1,2) precursor and nominal masses as listed in CID curves. The fragmentation pathway and corresponding structure for each species is represented above. Only major fragment ions monitored in CID curves are represented above.

| | | M+Li | | | | | | | | | | | | |
|------|------|--------|-------|-------|-------|-------|-------|-------|-------|-------|-------|-------|-------|--|
| | | 0 | 10 | 20 | 30 | 40 | 50 | 60 | 70 | 80 | 90 | 100 | 110 | |
| 1237 | 1230 | 100.0% | 99.9% | 99.7% | 99.0% | 97.4% | 93.8% | 82.6% | 55.6% | 22.8% | 4.1% | 0.0% | 0.0% | |
| | | 0.0% | 0.0% | 0.0% | 0.2% | 0.1% | 0.2% | 0.3% | 0.5% | 0.4% | 0.0% | 0.0% | 0.0% | |
| 1165 | 1158 | 0.0% | 0.1% | 0.1% | 0.2% | 0.7% | 1.8% | 5.0% | 9.4% | 8.8% | 3.4% | 0.0% | 0.0% | |
| | | 0.0% | 0.0% | 0.0% | 0.0% | 0.1% | 0.1% | 0.1% | 0.4% | 0.4% | 0.2% | 0.0% | 0.0% | |
| 1019 | 1012 | 0.0% | 0.0% | 0.0% | 0.0% | 0.0% | 0.3% | 0.8% | 1.9% | 2.5% | 1.3% | 0.0% | 0.0% | |
| | | 0.0% | 0.0% | 0.0% | 0.0% | 0.0% | 0.1% | 0.1% | 0.1% | 0.2% | 0.1% | 0.0% | 0.0% | |
| 965 | 958 | 0.0% | 0.0% | 0.0% | 0.0% | 0.1% | 0.3% | 1.0% | 2.5% | 3.7% | 2.3% | 0.0% | 0.0% | |
| | | 0.0% | 0.0% | 0.0% | 0.0% | 0.0% | 0.1% | 0.0% | 0.0% | 0.2% | 0.1% | 0.0% | 0.0% | |
| 819 | 812 | 0.0% | 0.0% | 0.0% | 0.0% | 0.2% | 0.5% | 1.7% | 4.2% | 5.6% | 3.6% | 1.3% | 0.0% | |
| | | 0.0% | 0.0% | 0.0% | 0.0% | 0.0% | 0.1% | 0.1% | 0.1% | 0.1% | 0.1% | 0.1% | 0.0% | |
| 765 | 758 | 0.0% | 0.0% | 0.0% | 0.0% | 0.1% | 0.4% | 1.1% | 2.3% | 2.8% | 1.5% | 0.0% | 0.0% | |
| | | 0.0% | 0.0% | 0.0% | 0.0% | 0.0% | 0.0% | 0.1% | 0.2% | 0.0% | 0.1% | 0.0% | 0.0% | |
| 747 | 740 | 0.0% | 0.0% | 0.0% | 0.1% | 0.3% | 0.6% | 1.6% | 4.4% | 8.2% | 7.6% | 4.0% | 1.0% | |
| | | 0.0% | 0.0% | 0.0% | 0.0% | 0.0% | 0.1% | 0.1% | 0.1% | 0.2% | 0.2% | 0.2% | 0.1% | |
| 721 | 714 | 0.0% | 0.0% | 0.0% | 0.0% | 0.1% | 0.2% | 0.6% | 2.2% | 4.4% | 3.8% | 1.9% | 0.0% | |
| | | 0.0% | 0.0% | 0.0% | 0.0% | 0.1% | 0.1% | 0.0% | 0.3% | 0.1% | 0.0% | 0.2% | 0.0% | |
| 675 | 668 | 0.0% | 0.0% | 0.0% | 0.0% | 0.0% | 0.1% | 0.3% | 0.9% | 2.1% | 3.1% | 2.3% | 1.3% | |
| | | 0.0% | 0.0% | 0.0% | 0.0% | 0.0% | 0.1% | 0.1% | 0.1% | 0.1% | 0.3% | 0.0% | 0.3% | |
| 649 | 642 | 0.0% | 0.0% | 0.0% | 0.0% | 0.0% | 0.0% | 0.3% | 0.9% | 2.2% | 2.9% | 2.2% | 0.0% | |
| | | 0.0% | 0.0% | 0.0% | 0.0% | 0.0% | 0.0% | 0.0% | 0.0% | 0.1% | 0.1% | 0.1% | 0.0% | |
| 547 | 540 | 0.0% | 0.0% | 0.0% | 0.0% | 0.0% | 0.0% | 0.0% | 0.0% | 1.8% | 2.6% | 2.5% | 1.6% | |
| | | 0.0% | 0.0% | 0.0% | 0.0% | 0.0% | 0.0% | 0.0% | 0.0% | 0.1% | 0.1% | 0.2% | 0.2% | |
| 497 | 490 | 0.0% | 0.0% | 0.0% | 0.0% | 0.2% | 0.2% | 0.5% | 1.6% | 2.5% | 2.6% | 1.3% | 0.5% | |
| | | 0.0% | 0.0% | 0.0% | 0.1% | 0.0% | 0.1% | 0.1% | 0.1% | 0.1% | 0.1% | 0.1% | 0.4% | |
| 479 | 472 | 0.0% | 0.0% | 0.0% | 0.1% | 0.1% | 0.3% | 1.0% | 2.6% | 4.9% | 5.1% | 3.6% | 1.4% | |
| | | 0.0% | 0.0% | 0.0% | 0.1% | 0.0% | 0.0% | 0.3% | 0.2% | 0.1% | 0.1% | 0.1% | 0.3% | |
| 425 | 418 | 0.0% | 0.0% | 0.0% | 0.1% | 0.3% | 0.5% | 1.3% | 4.1% | 9.2% | 12.3% | 10.1% | 4.6% | |
| | | 0.0% | 0.0% | 0.0% | 0.0% | 0.0% | 0.0% | 0.0% | 0.3% | 0.1% | 0.2% | 0.3% | 0.2% | |
| 407 | 400 | 0.0% | 0.0% | 0.0% | 0.0% | 0.0% | 0.0% | 0.4% | 1.1% | 2.8% | 5.3% | 5.6% | 4.2% | |
| | | 0.0% | 0.0% | 0.0% | 0.1% | 0.1% | 0.1% | 0.1% | 0.1% | 0.2% | 0.2% | 0.2% | 0.6% | |
| 353 | 346 | 0.0% | 0.0% | 0.0% | 0.0% | 0.1% | 0.1% | 0.4% | 1.3% | 4.3% | 8.7% | 11.5% | 9.7% | |
| | | 0.0% | 0.0% | 0.0% | 0.1% | 0.1% | 0.1% | 0.1% | 0.1% | 0.1% | 0.3% | 0.3% | 0.3% | |
| 279 | 272 | 0.0% | 0.0% | 0.0% | 0.0% | 0.0% | 0.0% | 0.0% | 0.0% | 0.0% | 2.4% | 3.3% | 3.2% | |
| | | 0.0% | 0.0% | 0.0% | 0.0% | 0.0% | 0.0% | 0.0% | 0.0% | 0.0% | 0.1% | 0.2% | 0.3% | |
| 225 | 218 | 0.0% | 0.0% | 0.0% | 0.0% | 0.1% | 0.1% | 0.2% | 1.0% | 2.6% | 6.4% | 10.3% | 12.1% | |
| | | 0.0% | 0.0% | 0.0% | 0.0% | 0.1% | 0.1% | 0.2% | 0.1% | 0.3% | 0.2% | 0.4% | 0.2% | |
| 207 | 200 | 0.0% | 0.0% | 0.0% | 0.0% | 0.1% | 0.2% | 0.3% | 1.0% | 2.9% | 7.8% | 14.4% | 20.6% | |
| | | 0.0% | 0.0% | 0.1% | 0.0% | 0.0% | 0.0% | 0.3% | 0.1% | 0.3% | 0.3% | 0.5% | 0.6% | |
| 153 | 146 | 0.0% | 0.0% | 0.0% | 0.1% | 0.2% | 0.2% | 0.5% | 1.0% | 2.8% | 7.7% | 18.1% | 30.9% | |
| | | 0.0% | 0.0% | 0.0% | 0.1% | 0.0% | 0.0% | 0.1% | 0.1% | 0.3% | 0.3% | 0.2% | 0.4% | |
| 111 | 104 | 0.0% | 0.0% | 0.0% | 0.0% | 0.0% | 0.1% | 0.2% | 1.1% | 3.1% | 5.7% | 7.4% | 9.0% | |
| | | 0.0% | 0.0% | 0.0% | 0.0% | 0.0% | 0.1% | 0.2% | 0.2% | 0.4% | 0.3% | 0.3% | 0.7% | |

Table 6.10. Total percent ion currents observed for $[M+Li]^+$ P(1,4). Percent averages and %RSD are shown above for each ion.

The ESI MS/MS spectra of P(1,4) coordinated to $[M+Na]^+$ at different CID energies can be found in **Figure 6.20**. The $[M+Na]^+$ MS/MS spectra at 0 eV (**Figure 6.20a-b**), 50 eV (**Figure 6.20c-d**), and 70 eV (**Figure 6.20e-f**) shows both full (**Figure 6.20a,c,e**) MS/MS spectra and zoomed (**Figure 6.20b,d,f**) regions for each of these CID energies. Both major and minor fragment ions are annotated to show the unique polyester and urethane fragmentation pathways for P(1,4) coordinated to Na^+ . In **Figure 6.16**, major fragment ions that formed above 10% RIC include (nominal mass) 1158, 812, 740, 714, 490, 472, 418, and 88 Da, which corresponds to 1181, 835, 763, 737, 513, 495, 441, and 111 Da (mass with Na^+ cation). In **Figure 6.20**, additional fragment ions are notated in the MS/MS spectra. These are considered to be minor fragment ions, which formed at %RIC under 10% as seen in **Figure 6.18b**. In **Figure 6.16b**, the depletion of the $[M+Na]^+$ precursor species (1230 Da) was monitored with respect to increasing CID energies. The CID curves for the $[M+Na]^+$ species show an increase in stability of the P(1,4) precursor with increasing CID energies. Here, the precursor is observed to deplete to 100% by 110 eV, therefore making this species more stable than the P(1,2) $[M+Na]^+$ and the P(1,4) $[M+Li]^+$ and $[M+Ag]^+$ precursors. At relatively high CID energies, fragment ions were only observed to form. Major fragment ions to be discussed include: 1158, 812, 740, 714, 490, 472, 418, and 88 Da species. As mentioned above, the 1158 Da (7%, 80 eV) fragment ion formed from the 1,5 H-shift fragmentation mechanism along the polyester chain, as seen in **Table 6.9**. The 812 Da fragment ion is unique to the Na and Ag precursors, we do not observed the 812 species for the Li precursor. The 812 Da (6.7%, 90 eV) fragment ion forms from a 1,5 H-shift along the polyester chain as seen in **Table 6.9**. Another fragment ion, such as 714 Da (12%, 100 eV) was also observed at high CID energies to form from an 1,5 H-shift around the urethane

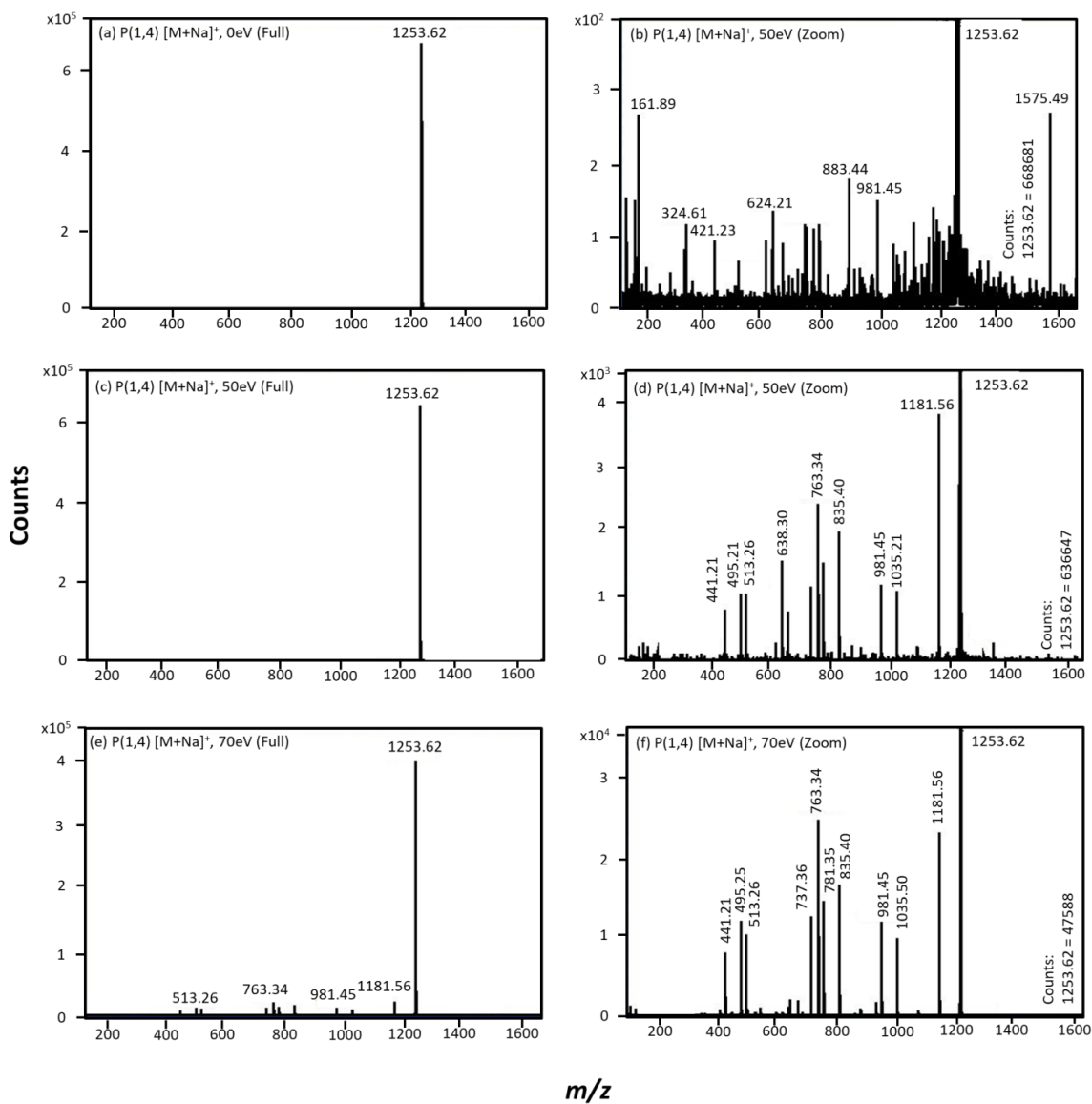


Figure 6.20. ESI MS/MS spectra of the P(1,4) [M+Na]⁺ at corresponding lab-frame energies of 0 eV for (a-b), 30 eV (c-d), and 50 eV (e-d). Both full (a,c,e) MS/MS spectra and zoomed-in (b,d,f) regions are represented each lab-frame energy. Counts represent max intensities for precursor ions in each zoomed spectra.

| | | M+Na | | | | | | | | | | | | |
|------|------|--------|--------|-------|-------|-------|-------|-------|-------|-------|-------|-------|-------|--|
| | | 0 | 10 | 20 | 30 | 40 | 50 | 60 | 70 | 80 | 90 | 100 | 110 | |
| 1253 | 1230 | 100.0% | 100.0% | 99.8% | 99.6% | 99.0% | 97.0% | 91.5% | 75.3% | 46.6% | 20.3% | 5.8% | 1.7% | |
| | | 0.0% | 0.0% | 0.0% | 0.1% | 0.2% | 0.2% | 0.2% | 0.7% | 0.6% | 1.2% | 0.7% | 0.5% | |
| 1181 | 1158 | 0.0% | 0.0% | 0.0% | 0.1% | 0.2% | 0.6% | 1.7% | 4.1% | 6.7% | 6.2% | 3.1% | 0.9% | |
| | | 0.0% | 0.0% | 0.0% | 0.0% | 0.0% | 0.1% | 0.0% | 0.2% | 0.3% | 0.4% | 0.1% | 0.8% | |
| 1035 | 1012 | 0.0% | 0.0% | 0.0% | 0.0% | 0.1% | 0.2% | 0.6% | 1.6% | 3.3% | 3.9% | 2.5% | 1.3% | |
| | | 0.0% | 0.0% | 0.0% | 0.0% | 0.0% | 0.0% | 0.1% | 0.1% | 0.1% | 0.3% | 0.6% | 0.3% | |
| 981 | 958 | 0.0% | 0.0% | 0.0% | 0.0% | 0.0% | 0.2% | 0.6% | 1.9% | 3.7% | 4.7% | 3.8% | 1.2% | |
| | | 0.0% | 0.0% | 0.0% | 0.0% | 0.0% | 0.0% | 0.0% | 0.0% | 0.1% | 0.2% | 0.4% | 0.1% | |
| 963 | 940 | 0.0% | 0.0% | 0.0% | 0.0% | 0.0% | 0.0% | 0.0% | 0.2% | 0.6% | 1.1% | 1.5% | 0.8% | |
| | | 0.0% | 0.0% | 0.0% | 0.0% | 0.0% | 0.0% | 0.0% | 0.2% | 0.1% | 0.1% | 0.1% | 0.7% | |
| 835 | 812 | 0.0% | 0.0% | 0.0% | 0.1% | 0.1% | 0.3% | 1.0% | 2.9% | 5.1% | 6.7% | 6.1% | 3.0% | |
| | | 0.0% | 0.0% | 0.0% | 0.0% | 0.0% | 0.0% | 0.1% | 0.3% | 0.0% | 0.2% | 0.5% | 0.1% | |
| 781 | 758 | 0.0% | 0.0% | 0.0% | 0.0% | 0.1% | 0.3% | 0.9% | 2.5% | 3.7% | 3.4% | 2.3% | 1.2% | |
| | | 0.0% | 0.0% | 0.0% | 0.0% | 0.0% | 0.1% | 0.1% | 0.1% | 0.2% | 0.1% | 0.3% | 1.2% | |
| 763 | 740 | 0.0% | 0.0% | 0.0% | 0.1% | 0.2% | 0.5% | 1.3% | 3.9% | 8.7% | 13.1% | 13.6% | 11.3% | |
| | | 0.0% | 0.0% | 0.0% | 0.0% | 0.1% | 0.1% | 0.1% | 0.4% | 0.2% | 0.4% | 1.3% | 2.4% | |
| 737 | 714 | 0.0% | 0.0% | 0.0% | 0.0% | 0.0% | 0.2% | 0.6% | 2.0% | 6.1% | 10.6% | 12.5% | 10.4% | |
| | | 0.0% | 0.0% | 0.0% | 0.0% | 0.0% | 0.0% | 0.0% | 0.2% | 0.4% | 0.5% | 0.3% | 2.4% | |
| 691 | 668 | 0.0% | 0.0% | 0.0% | 0.0% | 0.0% | 0.0% | 0.0% | 0.3% | 0.8% | 1.9% | 3.3% | 3.2% | |
| | | 0.0% | 0.0% | 0.0% | 0.0% | 0.0% | 0.0% | 0.0% | 0.0% | 0.1% | 0.1% | 0.3% | 0.8% | |
| 665 | 642 | 0.0% | 0.0% | 0.0% | 0.0% | 0.0% | 0.0% | 0.0% | 0.3% | 1.0% | 2.2% | 3.7% | 4.3% | |
| | | 0.0% | 0.0% | 0.0% | 0.0% | 0.0% | 0.0% | 0.0% | 0.0% | 0.0% | 0.2% | 0.5% | 0.4% | |
| 659 | 636 | 0.0% | 0.0% | 0.0% | 0.0% | 0.0% | 0.1% | 0.1% | 0.1% | 0.0% | 0.0% | 0.0% | 0.0% | |
| | | 0.0% | 0.0% | 0.0% | 0.0% | 0.0% | 0.0% | 0.1% | 0.1% | 0.0% | 0.0% | 0.0% | 0.0% | |
| 638 | 615 | 0.0% | 0.0% | 0.1% | 0.2% | 0.2% | 0.2% | 0.1% | 0.0% | 0.0% | 0.0% | 0.0% | 0.0% | |
| | | 0.0% | 0.0% | 0.1% | 0.0% | 0.1% | 0.1% | 0.1% | 0.0% | 0.0% | 0.0% | 0.0% | 0.0% | |
| 563 | 540 | 0.0% | 0.0% | 0.0% | 0.0% | 0.0% | 0.0% | 0.0% | 0.0% | 0.5% | 1.2% | 2.0% | 2.1% | |
| | | 0.0% | 0.0% | 0.0% | 0.0% | 0.0% | 0.0% | 0.0% | 0.0% | 0.0% | 0.1% | 0.2% | 0.7% | |
| 513 | 490 | 0.0% | 0.0% | 0.0% | 0.0% | 0.0% | 0.2% | 0.6% | 1.6% | 4.0% | 6.1% | 7.4% | 6.7% | |
| | | 0.0% | 0.0% | 0.0% | 0.0% | 0.0% | 0.0% | 0.1% | 0.1% | 0.2% | 0.3% | 1.0% | 0.7% | |
| 495 | 472 | 0.0% | 0.0% | 0.0% | 0.0% | 0.1% | 0.2% | 0.5% | 2.0% | 4.0% | 7.3% | 10.1% | 11.8% | |
| | | 0.0% | 0.0% | 0.0% | 0.0% | 0.0% | 0.0% | 0.1% | 0.1% | 0.2% | 0.4% | 0.8% | 1.4% | |
| 441 | 418 | 0.0% | 0.0% | 0.0% | 0.0% | 0.1% | 0.1% | 0.4% | 1.2% | 3.9% | 7.1% | 11.0% | 13.6% | |
| | | 0.0% | 0.0% | 0.0% | 0.0% | 0.0% | 0.0% | 0.0% | 0.2% | 0.2% | 0.5% | 1.2% | 0.8% | |
| 423 | 400 | 0.0% | 0.0% | 0.0% | 0.0% | 0.0% | 0.0% | 0.0% | 0.0% | 0.6% | 1.2% | 2.3% | 3.6% | |
| | | 0.0% | 0.0% | 0.0% | 0.0% | 0.0% | 0.0% | 0.0% | 0.0% | 0.1% | 0.1% | 0.3% | 1.1% | |
| 369 | 346 | 0.0% | 0.0% | 0.0% | 0.0% | 0.0% | 0.0% | 0.0% | 0.0% | 0.4% | 0.9% | 1.9% | 2.3% | |
| | | 0.0% | 0.0% | 0.0% | 0.0% | 0.0% | 0.0% | 0.0% | 0.0% | 0.1% | 0.1% | 0.4% | 0.7% | |
| 295 | 272 | 0.0% | 0.0% | 0.0% | 0.0% | 0.0% | 0.0% | 0.0% | 0.0% | 0.2% | 0.4% | 1.2% | 1.6% | |
| | | 0.0% | 0.0% | 0.0% | 0.0% | 0.0% | 0.0% | 0.0% | 0.0% | 0.2% | 0.4% | 0.3% | 0.8% | |
| 111 | 88 | 0.0% | 0.0% | 0.0% | 0.0% | 0.0% | 0.0% | 0.0% | 0.1% | 0.5% | 1.7% | 5.8% | 19.2% | |
| | | 0.0% | 0.0% | 0.0% | 0.0% | 0.0% | 0.0% | 0.0% | 0.1% | 0.0% | 0.3% | 0.2% | 1.0% | |

Table 6.11. Total percent ion currents observed for $[M+Na]^+$ P(1,4). Percent averages and %RSD are shown above for each ion.

(-NH₂). The 472 Da (12%, 110 eV) species, as seen in **Table 6.9** was also observed to form from a 1,5 H-shift along the polyester chain. The 418 Da (13%, 110 eV) fragment ion, as seen in the previous PBA n = 2 section, also formed from a 1,5 H-shift. The 740 Da (13%, 100 eV) fragment ion is unique. This species could have formed through two mechanistic pathways: (1) 1,3 H-shift around the urethane hard segment, yielding the corresponding 490 Da (7%, 100 eV) fragment ion, and (2) two 1,3 H-shifts along the polyester chain as seen in **Table 6.9**. Similarly, the 88 Da (19%, 110 eV) fragment ion is unique to the P(1,4) [M+Na]⁺ precursor and was observed to form at high CID energies due to a combination of 1,5 and 1,3 H-shifts along the polyester chain. Additional total %RIC data of major and minor fragment ions can be found in **Tables 6.11**.

In this section, we will discuss the unique behavior of the P(1,4) species coordinated to transition metal Ag⁺, as [M+Ag]⁺ precursor. Here we observed similar fragment ions as seen for the [M+Li]⁺ species. The ESI MS/MS spectra of P(1,4) coordinated to [M+Ag]⁺ at different CID energies can be found in **Figure 6.21**. The [M+Ag]⁺ MS/MS spectra at 0 eV (**Figure 6.21a-b**), 50 eV (**Figure 6.21c-d**), and 70 eV (**Figure 6.21e-f**) shows both full (**Figure 6.21a,c,e**) MS/MS spectra and zoomed (**Figure 6.21b,d,f**) regions for each of these CID energies. Both major and minor fragment ions are annotated to show the unique polyester and urethane fragmentation pathways for P(1,4) coordinated to Ag⁺. In **Figure 6.16**, major fragment ions that formed above 10%RIC include (nominal mass) 1158, 812, 758, 740, 668, 642, 540, 472, 346, 268, 218, 200, and 146 Da, which corresponds 1265, 919, 865, 847, 775, 749, 647, 572, 453, 375, 325, 307, and 253 Da (mass with ¹⁰⁷Ag cation, as seen in **Figure 6.21**).

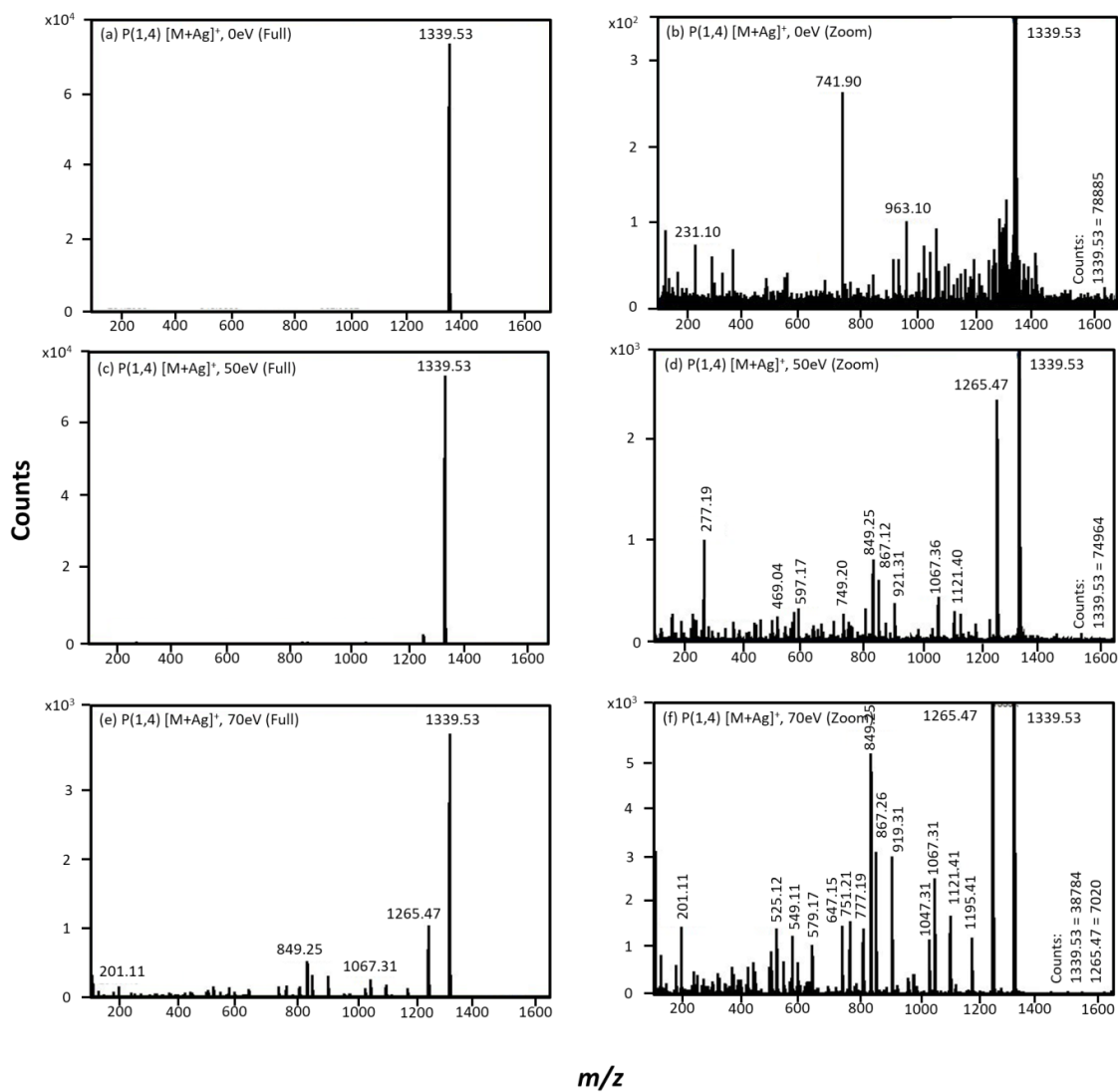


Figure 6.21. ESI MS/MS spectra of the P(1,4) [M+Ag]⁺ at corresponding lab-frame energies of 0 eV for (a-b), 30 eV (c-d), and 50 eV (e-d). Both full (a,c,e) MS/MS spectra and zoomed-in (b,d,f) regions are represented each lab-frame energy. Counts represent max intensities for precursor ions in each zoomed spectra.

In **Figure 6.16c**, the depletion of the $[M+Ag]^+$ precursor species was also monitored against increasing CID energies. The CID curves for the $[M+Ag]^+$ species show an increase in PU stability from P(1,2) to P(1,4). However when comparing P(1,4) cations, the $[M+Ag]^+$ species was observed to form more major fragment ions compared to the other cationized P(1,4) species. The $[M+Ag]^+$ precursor was observed to deplete 100% at 100 eV. There were three major fragment ions that formed at the low CID region (≤ 70 eV), these include: 1158, 758, and 740 Da species (**Figure 6.16c** and **Figure 6.21c-d**). Low energy fragment ion 1158 Da (13%, 70 eV) forms from a 1,5 H-shift along the polyester chain as seen in **Table 6.9**. Fragment ion 740 Da (12%, 80 eV), as discussed above can form through two different pathways: (1) 1,3 H-shift along the urethane, or (2) two 1,3 H-shifts along the polyester chain. Uniquely, fragment ion 758 Da (5%, 70 eV) forms from both a 1,5 and 1,3 H-shift along the polyester chain (structure provided in **Table 6.9**). High energy fragment ions observed include: 812, 668, 642, 540, 472, 346, 270, 218, 200, and 146 Da. Major high energy fragment ion 812 Da (6%, 80 eV) was observed to form from a 1,5 H-shift along the polyester chain. The 472 Da (6%, 100 eV) fragment ion, as previously observed for the $[M+Na]^+$ precursor formed due to a 1,5 H-shift along the polyester chain. Fragment ions 346 Da (9%, 110 eV) and 146 Da (22%, 110 eV) species form from two 1,5 H-shifts along the polyester chain leaving a di-acid product. Fragment ions 540 Da (6%, 90 eV) formed due to two 1,3 H-shifts, one around the urethane and the other along the polyester chain (**Table 6.9**). The 200 Da (20%, 110 eV) species was also observed, this fragment ion forms from a 1,3 H-shift along the polyester chain. Fragment ion 668 Da (6%, 90 eV) formed from both a 1,5 H-shift and 1,3 H-shift fragmentation pathway yielding a product with both $=C=O$ and acid end groups. Fragment ion 218 Da (17%, 110 eV) was observed to form due to a 1,5 and 1,3 H-shift along the polyester chain. Another high energy fragment ion, 268 Da (20%, 110 eV) formed uniquely for the $[M+Ag]^+$ precursor, from both a 1,3 H-shift around the urethane yielding an isocyanate group, and a 1,5 H-shift forming carbamic acid. The carbamic acid is a very unstable fragment ion, and easily transitions into an amine due to the loss of CO_2 , as seen in **Table 6.9**.

The $[M+Ag]^+$ precursor produced more major fragment ions from the polyester chain compared to Li and Na cations. Additional total %RIC data of major and minor fragment ions can be found in **Tables 6.12**. The full CID curves with %RSD error bars can be found in **Figure 6.22**.

6.3.5. *P(1,2) and P(1,4) MS/MS Literature Comparison*

In previous work, Gies and Hercules studied a complex mixture composed of PBA based PUs using MALDI-TOF/TOF MS and IM-MS.⁵ In their work, CID fragmentation identifiers were used to characterize the unique fragmentation pathways associated with PUs. They predicted fragment ions series to distinguish the linear and cyclic architectures with the polydisperse sample as well as characterizing isomeric and isobaric structural differences. Two major fragmentation pathways were observed to form the predominant fragment ions observed for the polyester based urethanes. In their study, a series of P(1,2) and P(1,4) ester urethanes were fragmented to characterize unique degradation pathways associated with these species. These PU species were cationized with Na during all of the fragmentation studies. Gies found that these PU systems underwent (1) 1,5 H-shift, (2) 1,3 H-shift, (3) multiple 1,5 H-shift, (4) multiple 1,3 H-shift, (5) combination of 1,5 and 1,3 H-shift, and (6) retro polymerization fragmentation mechanism.

In this current study, we characterized symmetrical P(1,2) and P(1,4) PBA ester urethanes using a combination of cations (Li^+ , Na^+ , and Ag^+) to probe unique fragment ions. In this study, we investigated these PU species under both low and high CID energies. We observed similar findings to what Gies and Hercules reported. Each cation investigated in this study was observed to have unique fragment ions formed at both high and low CID energies. For instance, Na cation in this study was observed to be the most stable cation when coordinated with both P(1,2) and P(1,4). Both Li and Ag cations were observed to generate multiple fragment ions,

| | | M+Ag | | | | | | | | | | | |
|------|------|---------|--------|--------|--------|--------|--------|--------|--------|--------|--------|--------|--------|
| | ion | 0 | 10 | 20 | 30 | 40 | 50 | 60 | 70 | 80 | 90 | 100 | 110 |
| 1337 | 1230 | 100.00% | 99.92% | 99.78% | 99.01% | 96.77% | 90.63% | 75.96% | 46.37% | 16.74% | 5.13% | 0.00% | 0.00% |
| | | 0.00% | 0.15% | 0.19% | 0.20% | 0.72% | 1.00% | 1.02% | 2.33% | 1.52% | 0.81% | 0.00% | 0.00% |
| 1265 | 1158 | 0.00% | 0.08% | 0.22% | 0.53% | 1.72% | 3.82% | 7.71% | 12.96% | 8.98% | 4.16% | 0.00% | 0.00% |
| | | 0.00% | 0.15% | 0.19% | 0.11% | 0.77% | 0.44% | 0.63% | 1.10% | 0.64% | 0.21% | 0.00% | 0.00% |
| 1119 | 1012 | 0.00% | 0.00% | 0.00% | 0.00% | 0.00% | 0.41% | 1.32% | 2.62% | 3.12% | 0.00% | 0.00% | 0.00% |
| | | 0.00% | 0.00% | 0.00% | 0.00% | 0.00% | 0.38% | 0.27% | 0.33% | 0.02% | 0.00% | 0.00% | 0.00% |
| 1065 | 958 | 0.00% | 0.00% | 0.00% | 0.00% | 0.44% | 0.66% | 1.69% | 3.91% | 4.99% | 0.00% | 0.00% | 0.00% |
| | | 0.00% | 0.00% | 0.00% | 0.00% | 0.03% | 0.10% | 0.52% | 0.77% | 0.94% | 0.00% | 0.00% | 0.00% |
| 919 | 812 | 0.00% | 0.00% | 0.00% | 0.00% | 0.00% | 0.63% | 2.15% | 5.27% | 6.18% | 4.96% | 0.00% | 0.00% |
| | | 0.00% | 0.00% | 0.00% | 0.00% | 0.00% | 0.04% | 0.12% | 0.79% | 0.64% | 0.71% | 0.00% | 0.00% |
| 865 | 758 | 0.00% | 0.00% | 0.00% | 0.00% | 0.00% | 0.69% | 2.00% | 5.03% | 5.37% | 4.49% | 0.00% | 0.00% |
| | | 0.00% | 0.00% | 0.00% | 0.00% | 0.00% | 0.30% | 0.54% | 0.40% | 0.11% | 0.29% | 0.00% | 0.00% |
| 847 | 740 | 0.00% | 0.00% | 0.00% | 0.46% | 0.63% | 1.29% | 3.87% | 8.41% | 11.90% | 10.74% | 5.04% | 0.00% |
| | | 0.00% | 0.00% | 0.00% | 0.11% | 0.05% | 0.18% | 0.38% | 0.70% | 1.14% | 0.09% | 0.40% | 0.00% |
| 821 | 714 | 0.00% | 0.00% | 0.00% | 0.00% | 0.00% | 0.00% | 1.21% | 2.30% | 4.63% | 4.97% | 0.00% | 0.00% |
| | | 0.00% | 0.00% | 0.00% | 0.00% | 0.00% | 0.00% | 0.06% | 0.35% | 1.00% | 0.82% | 0.00% | 0.00% |
| 775 | 668 | 0.00% | 0.00% | 0.00% | 0.00% | 0.00% | 0.52% | 1.01% | 2.13% | 5.81% | 6.13% | 5.12% | 0.00% |
| | | 0.00% | 0.00% | 0.00% | 0.00% | 0.00% | 0.04% | 0.05% | 0.44% | 0.44% | 0.69% | 0.89% | 0.00% |
| 749 | 642 | 0.00% | 0.00% | 0.00% | 0.00% | 0.00% | 0.00% | 0.90% | 2.04% | 5.69% | 6.27% | 5.07% | 0.00% |
| | | 0.00% | 0.00% | 0.00% | 0.00% | 0.00% | 0.00% | 0.14% | 0.28% | 1.32% | 1.36% | 0.62% | 0.00% |
| 647 | 540 | 0.00% | 0.00% | 0.00% | 0.00% | 0.00% | 0.00% | 0.00% | 1.98% | 3.32% | 6.49% | 5.75% | 3.22% |
| | | 0.00% | 0.00% | 0.00% | 0.00% | 0.00% | 0.00% | 0.00% | 0.19% | 0.33% | 0.46% | 0.83% | 2.79% |
| 597 | 490 | 0.00% | 0.00% | 0.00% | 0.00% | 0.00% | 0.32% | 0.53% | 1.65% | 3.73% | 0.00% | 0.00% | 0.00% |
| | | 0.00% | 0.00% | 0.00% | 0.00% | 0.00% | 0.28% | 0.46% | 0.26% | 0.15% | 0.00% | 0.00% | 0.00% |
| 579 | 472 | 0.00% | 0.00% | 0.00% | 0.00% | 0.00% | 0.00% | 0.67% | 1.92% | 3.80% | 5.74% | 6.13% | 3.67% |
| | | 0.00% | 0.00% | 0.00% | 0.00% | 0.00% | 0.00% | 0.60% | 0.24% | 0.47% | 0.79% | 0.54% | 3.18% |
| 525 | 418 | 0.00% | 0.00% | 0.00% | 0.00% | 0.00% | 0.00% | 0.71% | 2.87% | 5.71% | 7.10% | 7.79% | 1.67% |
| | | 0.00% | 0.00% | 0.00% | 0.00% | 0.00% | 0.00% | 0.13% | 0.41% | 0.69% | 1.24% | 0.70% | 2.90% |
| 507 | 400 | 0.00% | 0.00% | 0.00% | 0.00% | 0.00% | 0.00% | 0.27% | 0.54% | 3.37% | 6.25% | 6.05% | 3.99% |
| | | 0.00% | 0.00% | 0.00% | 0.00% | 0.00% | 0.00% | 0.46% | 0.94% | 0.64% | 1.53% | 1.59% | 3.46% |
| 453 | 346 | 0.00% | 0.00% | 0.00% | 0.00% | 0.00% | 0.00% | 0.00% | 0.00% | 3.57% | 7.02% | 7.40% | 8.86% |
| | | 0.00% | 0.00% | 0.00% | 0.00% | 0.00% | 0.00% | 0.00% | 0.00% | 0.66% | 1.30% | 1.62% | 2.36% |
| 375 | 268 | 0.00% | 0.00% | 0.00% | 0.00% | 0.00% | 0.00% | 0.00% | 0.00% | 0.00% | 0.00% | 9.94% | 20.00% |
| | | 0.00% | 0.00% | 0.00% | 0.00% | 0.00% | 0.00% | 0.00% | 0.00% | 0.00% | 0.00% | 2.14% | 2.55% |
| 325 | 218 | 0.00% | 0.00% | 0.00% | 0.00% | 0.00% | 0.00% | 0.00% | 0.00% | 3.10% | 7.72% | 16.11% | 17.23% |
| | | 0.00% | 0.00% | 0.00% | 0.00% | 0.00% | 0.00% | 0.00% | 0.00% | 0.53% | 0.78% | 0.79% | 5.00% |
| 307 | 200 | 0.00% | 0.00% | 0.00% | 0.00% | 0.00% | 0.00% | 0.00% | 0.00% | 0.00% | 6.27% | 12.58% | 19.62% |
| | | 0.00% | 0.00% | 0.00% | 0.00% | 0.00% | 0.00% | 0.00% | 0.00% | 0.00% | 0.11% | 1.81% | 6.56% |
| 277 | 170 | 0.00% | 0.00% | 0.00% | 0.00% | 0.43% | 1.03% | 0.00% | 0.00% | 0.00% | 0.00% | 0.00% | 0.00% |
| | | 0.00% | 0.00% | 0.00% | 0.00% | 0.08% | 0.65% | 0.00% | 0.00% | 0.00% | 0.00% | 0.00% | 0.00% |
| 253 | 146 | 0.00% | 0.00% | 0.00% | 0.00% | 0.00% | 0.00% | 0.00% | 0.00% | 0.00% | 6.57% | 13.01% | 21.75% |
| | | 0.00% | 0.00% | 0.00% | 0.00% | 0.00% | 0.00% | 0.00% | 0.00% | 0.00% | 0.62% | 2.13% | 3.49% |

Table 6.12. Total percent ion currents observed for $[M+Ag]^+ P(1,4)$. Percent averages and %RSD are shown above for each ion.

P(1,4)

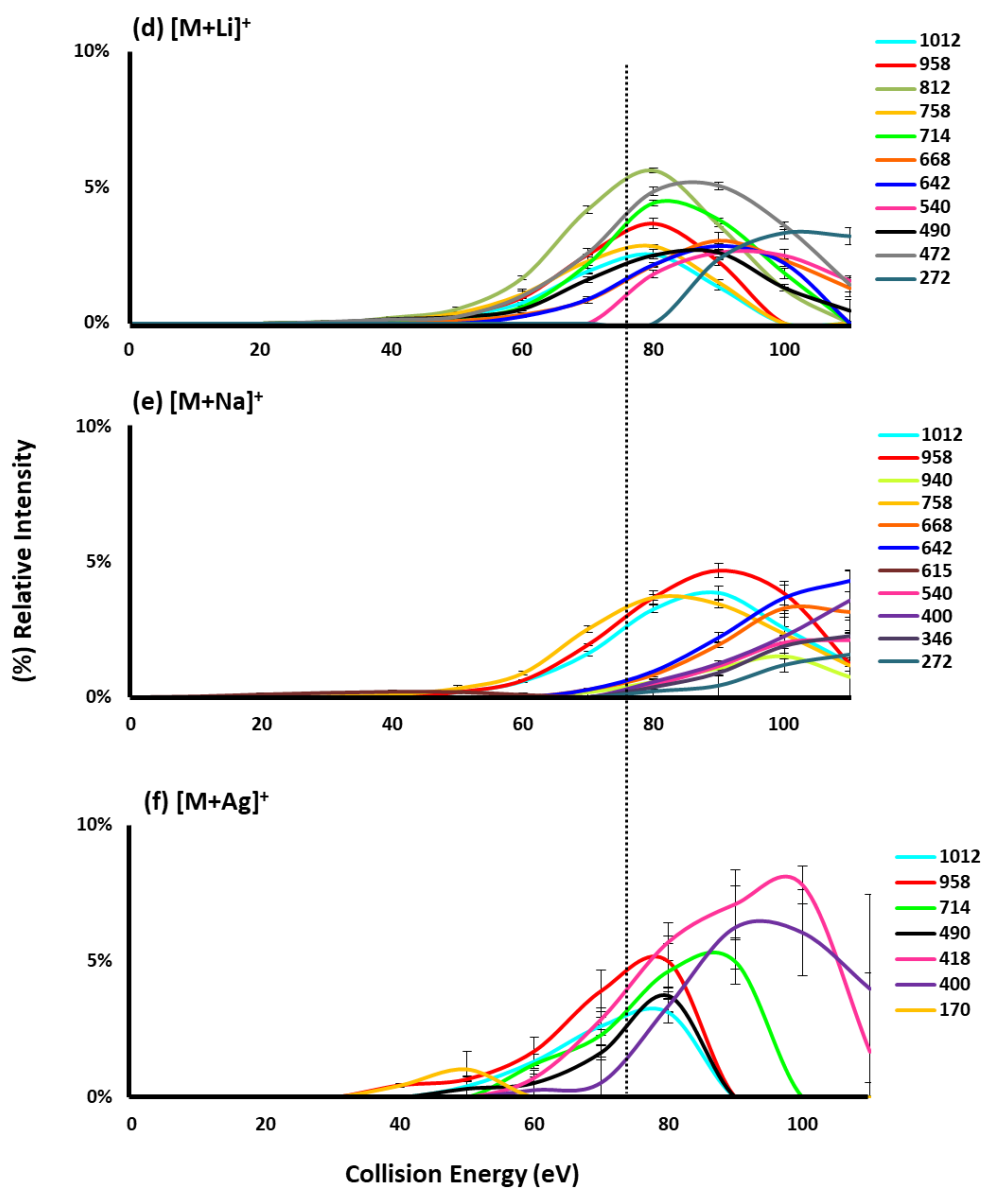
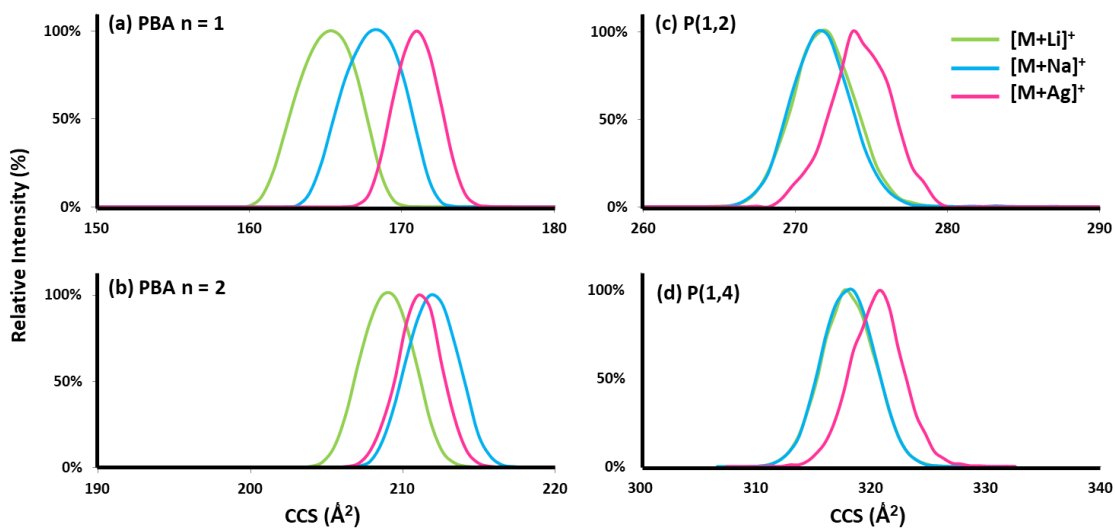


Figure 6.22. Collision-induced dissociation (CID) curves monitoring the unique transition of P(1,4) precursor to minor fragment ions when coordinated with cations (a) $[M+Li]^+$, (b) $[M+Na]^+$, and (c) $[M+Ag]^+$. The dotted line is drawn at 70 eV for visual alignment of low energy fragment ions with %RSD.

which can be attributed to Li's small atomic radius, and Ag's strong affinity for aromatic systems. We observed all 6 fragmentation mechanisms between each precursor tested. In addition, we observed unique fragment ions that only occurred at high CID energies. For instance, the P(1,2) $[M+Na]^+$ species was observed to generate fragment ion 240 Da. As observed in **Table 6.5**, the structure of the 240 Da species formed unique to the high CID energy and retro polymerization further reducing the isocyanate to an amine (NH_2), and then $-NH$ group. Cation coordination is a useful technique to probe unique fragment ions associated with PU systems. When characterizing asymmetrical compounds, we propose fragment ions to form from the 6 fragmentation mechanisms and even form from unique fragmentation pathways not currently observed.

6.3.6. Characterization of PBA $n = 1, 2$, P(1,2) and P(1,4) by IM-MS

The experimental IM spectra provided in **Figure 6.23a-d** are shown for the PBA $n = 1$, PBA $n = 2$, P(1,2), and P(1,4) species. Each species gas-phase CCS was monitored with respect to cation coordination between Li (green), Na (blue), and Ag (pink). In **Figure 6.23a**, a unique IM plot distribution is represented for each PBA $n = 1$ species coordinated to the different cations. In **Figure 6.23e**, the IM-MS results show PBA $n = 1$ $[M+Li]^+$ species to have a smaller CCS (165.5 \AA^2), compared to $[M+Na]^+$ (168.6 \AA^2) and $[M+Ag]^+$ (170.9 \AA^2). When the PBA chain elongates to $n = 2$ (**Figure 6.23b**), converging starts to occur. Here we observe PBA $n = 2$ species coordinated with Ag (211.0 \AA^2) causing the polyester to elute out of the drift tube faster than PBA $n = 2$ coordinated with Na (211.7 \AA^2). IM-MS results still showed the $[M+Li]^+$ species having a smaller CCS (208.6 \AA^2) compared to Na and Ag. The similarities in CCS for the $[M+Na]^+$ and $[M+Ag]^+$ species may result from similarities in the way the Na and Ag cation have coordinated with the PBA $n = 2$ species. In **Figure 6.23c**, the IM drift plots of the P(1,2) species showed a similar gas-phase shape between $[M+Li]^+$ (272.1 \AA^2) and $[M+Na]^+$ (271.3 \AA^2) coordination, however the $[M+Ag]^+$ species resulted in a larger CCS (274.0 \AA^2). When comparing the P(1,4) to the P(1,2) species (**Figure 6.23c-d**), we still observe similar gas-phase structural behavior when



(e) PU Species CCS

| PU Species | [M+Li] ⁺ (Å ²) | [M+Na] ⁺ (Å ²) | [M+Ag] ⁺ (Å ²) |
|------------|---------------------------------------|---------------------------------------|---------------------------------------|
| PBA n = 1 | 165.5 ± 0.0 | 168.6 ± 0.0 | 170.9 ± 0.0 |
| PBA n = 2 | 208.6 ± 0.0 | 211.7 ± 0.0 | 211.0 ± 0.0 |
| P(1,2) | 272.1 ± 0.0 | 271.3 ± 0.0 | 274.0 ± 0.4 |
| P(1,4) | 317.6 ± 0.0 | 318.1 ± 0.4 | 320.5 ± 0.4 |

Figure 6.23. IM-MS profiles for (a) n = 1 PBA, (b) n = 2 PBA, (c) P(1,2), (d) P(1,4), and (e) CCS_{av} and %RSD. Results are shown in green for [M+Li]⁺, blue for [M+Na]⁺, and pink for [M+Ag]⁺.

the PU system has PBA $n = 1$ comparative to an elongated PBA chain of $n = 2$. For P(1,4), the $[M+Li]^+$ species has the smallest CCS (317.6 \AA^2), the $[M+Na]^+$ species CCS is slightly larger than Li (318.1 \AA^2), and $[M+Ag]^+$ species has the largest CCS (320.5 \AA^2). For the P(1,2), only the $[M+Ag]^+$ species showed two conformers in IM. All other species monitored in this experiment exhibited one unique conformation.

6.4. Conclusions

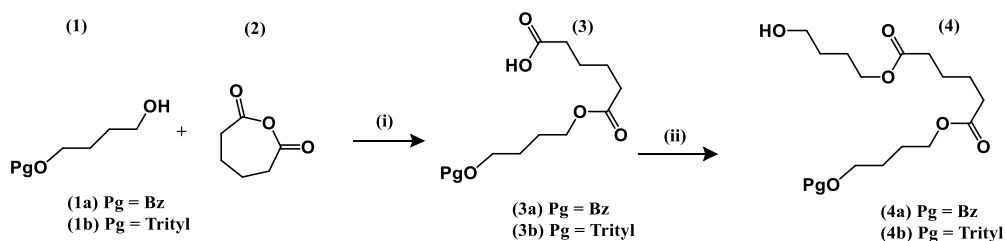
In this study, a series of PBA ($n = 1$ and $n = 2$) and symmetrical PU oligomers (P(1,2) and P(1,4)) were synthesized using a stepwise mono-addition approach and extensively characterized using a series of monovalent cations (Li^+ , Na^+ , and Ag^+) using IM-MS/MS. Unique fragment ions were observed to form from each coordinated cation studied. Coordination of Na^+ was observed to produce fewer fragment ions compared to Li^+ and Ag^+ for PBA $n = 1$, $n = 2$, P(1,2), and P(1,4) species characterized. Another unique difference observed in this study, compared to previous literature findings resulted in the formation of carbamic acid end groups. In the previous work by Gies and Hercules studying polyester PU's, they reported that carbamic acids were extremely unstable and they did not detect many fragment ions with this end group. Carbamic acid is known to rapidly decompose into the amine, resulting in the loss of CO_2 . In this present study, we observed several fragment ions forming with the carbamic acid end group, and in relatively high abundance. For instance, the $[M+Na]^+$ P(1,2) compound transitioned into the 240 Da fragment ion. These results differ from what was previously reported, and this could be the result in different ionization techniques. Previous studies utilized MALDI-MS/MS and we used ESI-MS/MS. It may be interesting to probe the unique carbamic acid fragment ions in future studies. Additionally, IM-MS experiments showed the unique coordination of Li^+ , Na^+ , and Ag^+ cation with the polyesters and polyester-urethane systems tested. Future work will include the synthesis and characterization of asymmetrical P(1,2) and P(1,4) compounds and computational

studies to characterize the unique coordination behavior of these cations with the PBA and PU systems.

6.5. Synthetic Procedures

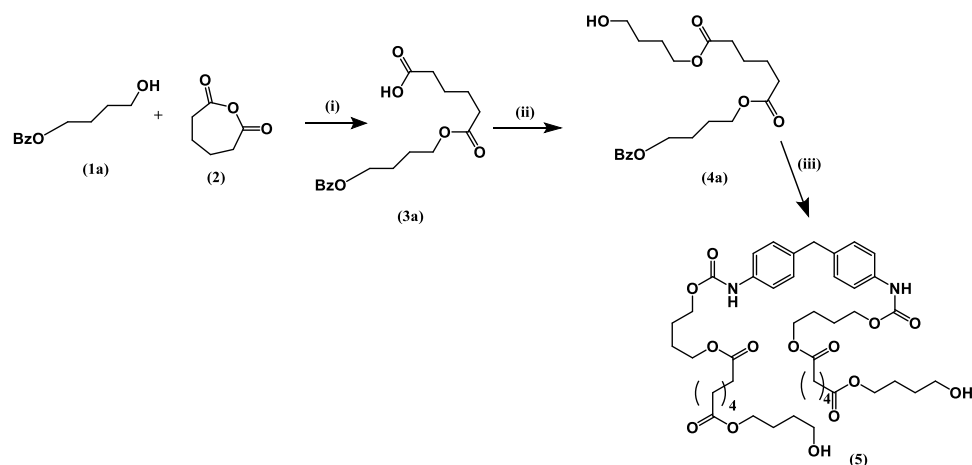
6.5.1. Synthetic Protocol for PBA $n = 1$, $n = 2$, $P(1,2)$, and $P(1,4)$

We hypothesized that it may be possible to synthesize mono protected polybutylene adipate (PBA) monomers from a mono protected derivative of 1,4-butanediol (1) with adipic anhydride (2). The resultant intermediate mono functionalized acid (3) may be reacted with an excess of 1,4-butane diol utilizing a DCC coupling resulting in the mono protected compound $n = 1$ (4) (**Scheme 6.1**) subsequent chain extension may be accomplished by reacting this monomer with adipic anhydride and 1,4-butane diol in a stepwise manner.



Scheme 6.1. (i) DCM, EtN_3 ; (ii) DCM, EtN_3 , DCC, 1,4-butanediol (25 equiv.).

Our initial trials utilized 4-(benzyloxy)butan-1-ol (1a) which was reacted with adipic anhydride (2) resulting in (3a). We hoped to react this intermediate acid with butane diol to give (4a), which may be reacted with MDI and deprotected via catalytic hydrogenation to yield the desired product (5) (**Scheme 6.2**).



Scheme 6.2. (i) methylene chloride, pyridine, DMAP (cat), 0° to 18°C 48hrs; (ii) DCC, DMAP, 1,4-butane diol; (iii) (a) methylene chloride (4a) 2.2 equiv, MDI, triethylamine (cat), 24hrs, room temp, (b) Pd/C, H₂, EtOH.

Attempts to synthesize (3a) gave the desired compound however this was contaminated with the bis benzyl product (6) (**Figure 6.1**).

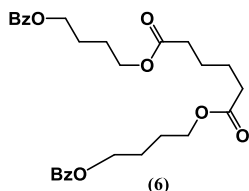
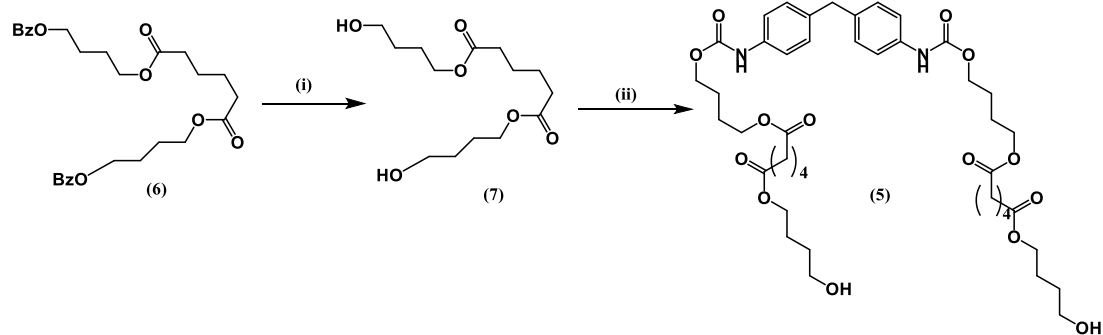


Figure 6.1. Bis benzyl product.

We were able to purify a sample of compound (6) by column chromatography, however a pure sample of the acid (3a) proved to be elusive. To determine if the reaction between MDI and the ester would work, we deprotected the intermediate (6) using catalytic hydrogenation yielding give deprotected butylene adipate (7) in a 52% yield. Reaction of 15 equivalents of (7) with MDI (**Scheme 6.3**) gave a crude sample of the MDI derivative (5). Compound (5) was purified by column chromatography on silica eluted with 95% DCM to 5% MeOH to give (5) in a 34% yield.



Scheme 6.3. (i) 10% Pd/C, H₂, EtOH, 18 hours; (ii) MDI, CH₂Cl₂, Et₃N

Encouraged by these results we modified our synthetic route replacing the benzyl protecting group with a trityl group this gave pure acid (3b) in a 50% yield, reaction with DCC and excess 1,4-butanediol gave a mixture of the desired product (4b) in a 60% yield plus a dimerized product (8) in a 20% yield (**Figure 6.2**). (8) and (4b) may be separated utilizing column chromatography eluted with a 50:50 mixture of EtOAc/hexanes.

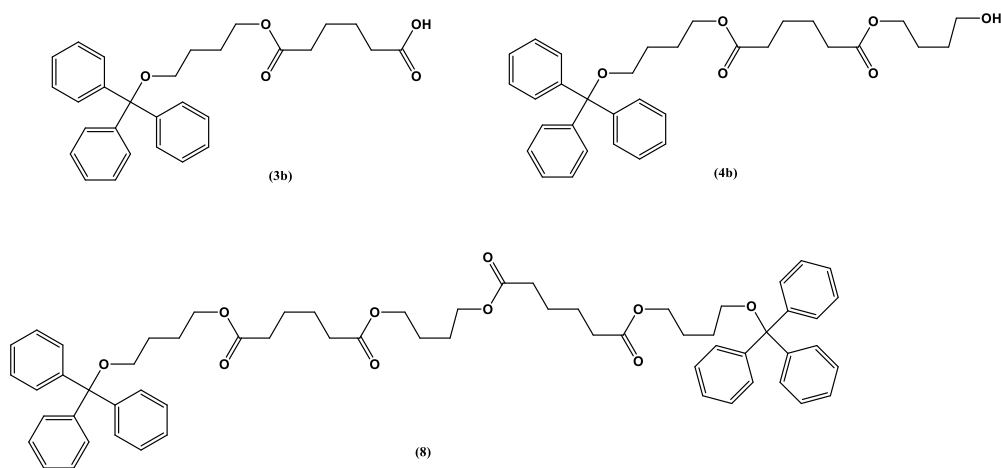
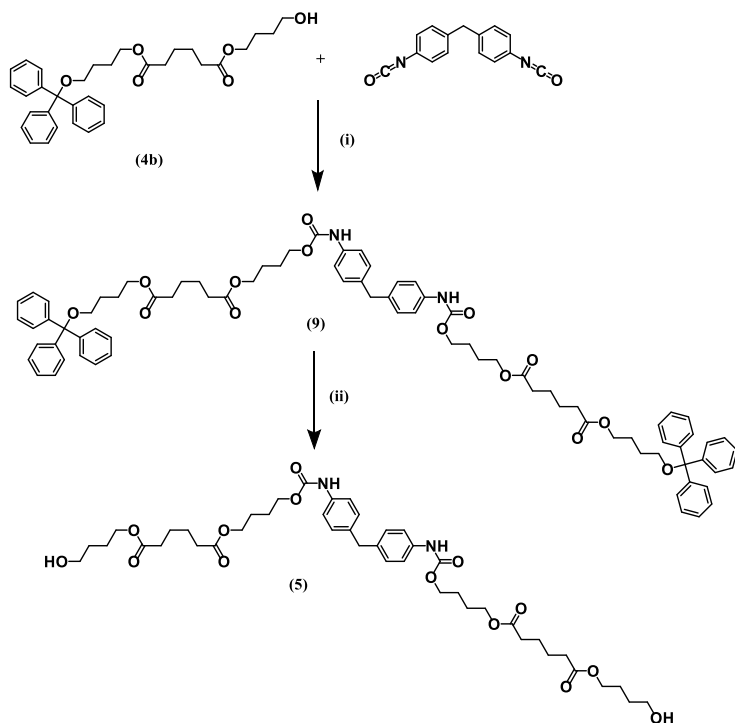


Figure 6.2. Mixture of desired product separated by column chromatography. (a) mono protected butanol adipate, (b) mono protected n = 1 PBA, (c) bis protected n = 2 PBA.

We have reacted 4-hydroxybutyl (4-(trityloxy)butyl) adipate (4b) with MDI to give (9) in a 43% yield as shown in **Scheme 6.4**. Attempts to remove the trityl substituents using a biphasic system

composed of methylene chloride and concentrated hydrochloric acid gave mainly hydrolysis products and not the desired compound (5).



Scheme 6.4. (i) CH_2Cl_2 , Et_3N , 18 hours;

Compound (8) has been deprotected using a biphasic system of DCM and concentrated hydrochloric acid to give the bis ester (10) in a 90% yield. This was reacted with MDI in a 1:10 mol equiv. giving (11) in a 10 % yield (**Figure 6.3**).

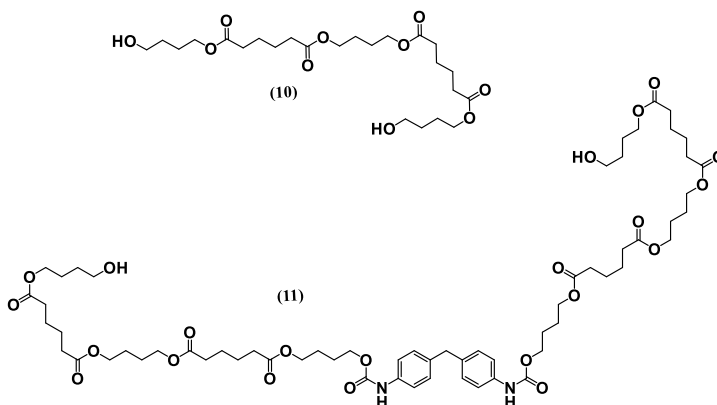


Figure 6.3. (10) Deprotected $n = 1$ PBA and (11) symmetrical $n = 1$ PBA MDI derivative.

Mono-tritylated $n = 2$ ester (13) was synthesized using the same protocol as outlined in **Scheme 6.1**. from the $n = 1$ ester (4b) by reacting it with adipic anhydride to give the intermediate acid (12) in a 58% yield followed by a DCC coupling with excess 1,4-butanediol giving the mono trityl protected $n = 2$ ester (13) in a 63% yield.

Experimental

4-(benzyloxy)butan-1-ol (1a)

Potassium hydroxide (80g, 1.42mols) was added to a stirred solution of 1,4-butanediol (132ml). Potassium iodide (0.2g) and benzylchloride (42.53g, 0.34mols) were added in 4 portions over 1 hour at ambient temperature. Then the reaction was stirred for 18 hours after which water (200ml) was added. The solution was extracted with diethyl ether (3x100ml). The combined ethereal extracts were dried over magnesium sulfate, filtered and evaporated. Then the product was purified by column chromatography on silica eluted with methylene chloride to give 29g of 4-(benzyloxy)butan-1-ol (1a) in a 48% yield as a clear oil.

4-(trityloxy)butan-1-ol (1b)

1,4-Butane diol (156.08g) was added to methylene chloride (400ml) followed by triethylamine (100ml). The solution was cooled in an ice/acetone bath to 0°C and trityl chloride (50g, 0.18mols) in methylene chloride (50ml) was added dropwise over 30 minutes with stirring. The solution was allowed to warm to ambient temperature and stirred for 18 hours. After which it was evaporated under reduced pressure and methylene chloride (200ml) was added. The organic solution was washed with deionized water (3 x 200ml) dried over magnesium sulfate filtered and evaporated under reduced pressure. Then 46g of 4-(trityloxy)butan-1-ol was obtained as a colorless solid in a 77% yield by crystallizing the crude product from hexanes (100ml).

6-oxo-6-(4-(trityloxy)butoxy)hexanoic acid (3b)

Adipic acid (3g, 0.021 mols) was added to a 50ml round bottomed flask equipped with a magnetic follower and acetic anhydride (12ml) was added. The solution was heated at reflux for 18 hours after which it was evaporated to dryness under reduced pressure. The crude adipic anhydride (2) was dissolved in methylene chloride (120ml). This solution was stirred and cooled to 0°C. After which pyridine (20ml) and dimethyl amino pyridine (80mg) were added followed by 4-(trityloxy)butan-1-ol (6.8g, 0.02mols). The solution was allowed to warm to ambient temperature and stirred for 48 hours. Then it was evaporated under reduced pressure and dissolved in methylene chloride (100ml). The organic solution was washed with a citric acid solution (100ml, 10% w.w. in deionized water), water (2 x 50ml) and dried over magnesium sulfate. After filtration the methylene chloride was removed under reduced pressure and 6-oxo-6-(4-(trityloxy)butoxy)hexanoic acid (3b) was purified by column chromatography on silica eluted with methylene chloride 99% / methanol 1% to give 4.9g of (3b) in a 52% yield as a pale yellow oil.

4-Hydroxybutyl (4-(trityloxy)butyl) adipate (4b) and O,O'-(butane-1,4-diyl)bis(4-trityloxy)butyl diadipate (8)

6-oxo-6-(4-(trityloxy)butoxy)hexanoic acid (3b) (6.9g, 0.015mols) was dissolved in methylene chloride (70ml), 1,4-butane diol (31.44g, 0.35mols) and dimethyl amino pyridine (0.184g) were added and the solution was cooled with stirring to 0°C. Then dicylohexylcarbodiimide (4.64g) was added. The solution was allowed to warm to ambient temperature and was stirred for 18 hours. The resultant N,N'-dicylohexylurea was removed by filtration and the organic solution was washed with deionized water (2 x 100ml). After drying over magnesium sulfate filtering and evaporating under reduced pressure 4-hydroxybutyl (4-(trityloxy)butyl) adipate (4b) and O,O'-(butane-1,4-diyl)bis(4-trityloxy)butyl diadipate (8) were purified by column chromatography on silica eluted with a 50:50 mixture of EtOAc to hexanes. This gave 4.9g of 4-Hydroxybutyl (4-

(trityloxy)butyl) adipate (4b) in a 60% yield as a pale yellow viscous oil and 3g of O,O'-(butane-1,4-diyl)bis(4-trityloxy)butyl) diadipate (8) in a 20% yield as a pale yellow tar.

Bis(4-(benzyloxy)butyl) adipate (6)

Adipic acid (7g, 0.048 mols) was added to a 25ml round bottomed flask equipped with a magnetic follower. Then acetic anhydride (15ml) was added and the mixture was heated at reflux for 4 hours. After which the acetic anhydride was removed under reduced pressure and the crude adipic anhydride was dissolved in methylene chloride (50ml). Pyridine (11ml) and dimethyl amino pyridine (0.2g) were added to a 250ml flask equipped with a magnetic follower and cooled to 0°C. Then 4-(benzyloxy)butan-1-ol (1a) (15.48g, 0.086 mols) dissolved in methylene chloride was added. The solution was stirred and allowed to warm to ambient temperature after which it was stirred for 18h and subsequently evaporated under reduced pressure column chromatography on silica eluted with hexanes / ethyl acetate 50:50 gave 0.9g of pure bis(4-(benzyloxy)butyl) adipate in a 4% yield as a colorless oil. 6-(4-(benzyloxy)butoxy)-6-oxohexanoic acid (3a) was also obtained from this column but was contaminated with (6) and other products. All attempts to purify (3a) failed.

Bis (4-hydroxybutyl) adipate (7)

Bn-B-A-B-Bn (1.5g) was added to RBF and stirred with 120 mL ethanol. Catalyst Pb/C (0.1g) was added to the RBF. The reaction was degassed and put under vacuum using an aspirator to remove all oxygen. Then the reaction was placed under H_{2(gas)}. The reaction was left overnight. Then using a frit and a celite pad, the excess Pd/C was filtered and concentrated down. Product was purified using column chromatography DCM/MeOH 95:5 and gave 0.5g of Bis (4-hydroxybutyl) adipate (7).

Bis(4-hydroxybutyl) *O,O'*-((((methylenebis(4,1-phenylene))bis(azanediyl))bis(carbonyl))bis(oxy))bis(butane-1,4-diyl) diadipate (5)

Trt-B-A-B-M-B-A-B-Trt (2.2g) was added to RBF with 60mL of DCM. The reaction stirred for 30min, then 10 drops of concentrated HCl was added to the reaction mixture. After 60 min, the reaction was stopped, concentrated down, and the product was determined to hydrolyze, yielding no desired product. This method proved that less concentrated acid is needed for the deprotection of the Trytl groups.

***O,O'*-((((methylenebis(4,1-phenylene))bis(azanediyl))bis(carbonyl))bis(oxy))bis(butane-4,1-diyl))bis(4-(trityloxy)butyl)diadipate (9)**

Monoprotected $n = 1$ PBA ester (4b) was dissolved (0.1g) in 50mL DCM, then (0.5mol equiv.) of MDI was added to the reaction vessel and left to stir overnight. The product was washed and DCM, dried over MgSO₄ and concentrated down. Column chromatography was used to purify the (9) using DCM / MeOH 95:5 mobile phase to isolate desired product.

***O,O'*-(butane-1,4-di-diyl) bis (4-hydroxybutyl) diadipate (10)**

In a RBF, 1.2g of compound (8) was dissolved in 50mL of DCM, then a few drops of concentrated HCl was added and the reaction was left to stir for 30min. Then quenched and purified using column chromatography DCM / MeOH 99:1 to remove trytl protecting groups, leaving desired product (10).

Bis(4-((6-(4-hydroxybutoxy)-6-oxohexanoyl)oxo)butyl) *O,O'*-((((methylenebis(4,1-phenylene))bis(azanediyl))bis(carbonyl))bis(oxo))bis(butane-4,1-diyl) diadipate (11)

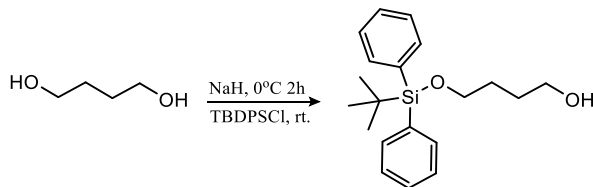
Compound (10) (0.9g) was dissolved in 50mL of DCM and stirred in RBF. Using an addition funnel, MDI (1:10 mol equiv.) was dissolved in 20mL of DCM and was added over 2hrs to the reaction mixture. The reaction was left to run overnight and monitored using ESI-MS. On the

second day, and additional (1:10 mol equiv.) of MDI in 20mL of DCM was added again to the reaction vessel. The product was observed to form, mono selectively using the slow addition process of MDI. The product remained a mixture of compound (10) and product (11) and was not purified.

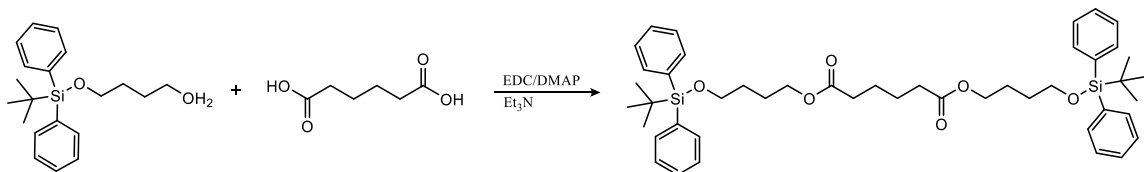
8,13,20-trioxo-1,1,1-triphenyl-2,7,14,19-tetraoxopentacosan-25-oic acid (12)

Acetic anhydride (6ml) was added to adipic acid (1.5g, 0.01mols) in a 25ml round bottomed flask equipped with a magnetic follower. This mixture was heated at reflux for 18 hours under nitrogen with stirring. Excess acetic anhydride was removed under reduced pressure and the crude adipic anhydride was dissolved in methylene chloride (50ml). Pyridine (10ml) and dimethylamino pyridine (0.05g) were added to the solution in a 250ml round bottomed flask equipped with a stir bar. The solution was stirred and cooled to 0° C and a solution of 4-Hydroxybutyl (4-(trityloxy)butyl) adipate (4b) (5.2g, 0.0098 mols) in methylene chloride was added dropwise. Upon complete addition of 4b the solution was allowed to warm to ambient temperature and stirred at ambient temperature for 48 hours. Then the solvent was removed under reduced pressure and the residue was dissolved in methylene chloride (100ml). This solution was washed with a solution of citric acid (10% w.w. in water, 100ml) and deionized water (2 x 100ml). After which it was dried over magnesium sulfate, filtered and evaporated under reduced pressure. 8,13,20-trioxo-1,1,1-triphenyl-2,7,14,19-tetraoxopentacosan-25-oic acid (12) was purified by column chromatography on silica eluted with methylene chloride / methanol 98:2. This gave 3.8g of pure (12) as an oil in a 58% yield.

6.5.2. Other Experimental Synthesis

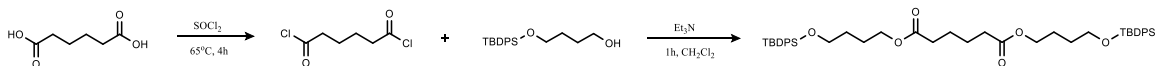


Synthesis of 4-((tert-butyldiphenylsilyl)oxy)butan-1-ol. A suspension of (0.73g, 18mmol) sodium hydride (60% dispersed in mineral oil) in CH_2Cl_2 (55mL) stirred at 0°C for 30min. 1,4-Butanediol (1.62mL, 17.7mmol) was added to the cold solution dropwise over 30min and left to react at 0°C for 2h. *Tert*-Butyl(chloro)diphenylsilane (4.59mL, 15.8mmol) was added to the reaction mixture and allowed to return to rt. After stirring overnight, the reaction mixture was neutralized with saturated ammonium chloride, extracted with EtOAc, and dried over MgSO_4 . The product was purified by column chromatography (17:3, Hexanes: EtOAc, $R_f = 0.35$) and isolated as a clear yellow viscous liquid (4.9 g, 94 %). ^1H (CDCl_3) δ 7.71 (dd, 4H), 7.42 (m, 6H), 4.14 (q, 2H), 3.69 (dt, 2H), 1.68 (m, 4H), 1.09 (s, 9H); ^{13}C (CDCl_3) δ 135.5, 129.6, 127.6, 63.9, 62.7, 31.7, 29.7, 29.2, 26.7; HESI-MS observed $[\text{M} + \text{H}]^+ = 329.10$ m/z.



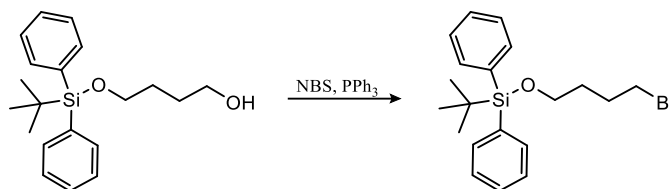
Synthesis of bis(4-((tert-butyldiphenylsilyl)oxy)butyl) adipate.

Adipic acid (1.52g, 10.42mmol) was added to a solution of EDC (3.23g, 20.79mmol), DMAP (0.39g, 3.19mmol) and Et_3N (5.8mL, 79.00mmol) in CH_2Cl_2 (90mL). After 30min, 4-((tert-butyldiphenylsilyl)oxy)butan-1-ol (7.2mL, 21.93mmol) was added. After stirring overnight, the reaction mixture was diluted CH_2Cl_2 and washed with brine. The organic layer was dried over MgSO_4 , filtered, and concentrated. Purification by column chromatography (7:3, Hexanes:EtOAc) yielded the product as a light yellow viscous liquid (2.5g, 32%).



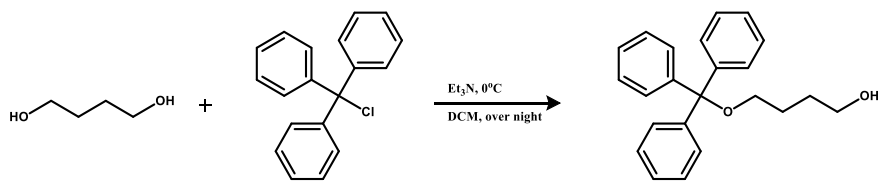
Synthesis of bis(4-((tert-butyldiphenylsilyl)oxy)butyl) adipate.

SOCl₂ (15mL) was added to a solution of adipic acid in anhydrous toluene (10mL) at 65°C. After 4 h the reaction mixture was cooled to rt. and concentrated. The crude product was reconstituted in anhydrous CH₂Cl₂ and cooled in an ice bath at 0°C. 4-((tert-butyldiphenylsilyl)oxy)butan-1-ol was added to this cold solution followed by the addition of Et₃N dropwise over 30 min. During the addition of Et₃N, a cloudy pink solution developed. The resulting mixture stirred at 0°C for 1 h then returned to rt and left overnight.



Synthesis of (4-bromobutoxy)(tert-butyl)diphenylsilane.

N-bromosuccinimide (1.98g, 11.11mmol) was added to a solution of PPh₃ (3.23g, 12.315mmol) and 4-((tert-butyldiphenylsilyl)oxy)butan-1-ol (3.87g, 11.79mmol) in CH₂Cl₂. After 2h, an additional 0.5eq of NBS and PPh₃ was added to convert the remaining starting material into product. Upon completion, the reaction mixture was diluted with an equal amount of ether and filtered through a small silica funnel and concentrated. To eliminate excess PPh₃ from the reaction, additional NBS was added till all PPh₃ was turned into phosphotriphenyl oxide. Reaction mixture was purified as follows, and equal amount of ether to DCM was added, black precipitate was formed (NBS and PPh₃=O). Product was filtered through a small silica funnel and concentrated down using the rotovap.



Selectively Half Protect 1,4-Butane-diol

4-Trityloxybutan-1-ol. To a 0°C solution of 1,4-butanediol in CH₂Cl₂, Et₃N was added dropwise and left to stir at 0°C. After 2 hours, TrCl was added and the solution was left to return to room temperature and stir overnight. To purify the reaction, the reaction was quenched with sodium bicarbonate (sat.), and then washed with DCM. The organic layer was dried over MgSO₄ and concentrated down. Then a TLC was run at 100% DCM. There were 2 distinct spots R_f = 0.9 was the fully protected butanediol, the R_f = 0.3 spot was the ½ protected butanediol. Then a shot column was run *in vacu* with a short frit/silica pad. Fractions up to 1L were collected and concentrated down. Column was run on a short silica pad at 100% DCM solvent, fractions were collected till ½ protected butanol was recovered and concentrated down. ¹H NMR (600MHz, CDCl₃) δ 1.69 (m, 4H, CH₂), δ 3.14 (t, 2H, CH₂), δ 3.64 (t, 2H, CH₂), δ 7.27 (m), and δ 7.45 (m). ¹³C NMR (CDCl₃) δ 144.2 3C, δ 128.6 3C, δ 127.7 6C, δ 126.9 6C, δ 86.6 1C, δ 77.3 1C, δ 77.0 1C, δ 76.7 1C, δ 53.4 1C, δ 29.9 1C, δ 26.5 1C.

6.6. Future Directions

Due to the unique fragmentation patterns observed for both PBA n = 1, n = 2, P(1,2), and P(1,4) species, the future directions include the synthesis of the asymmetrical P(1,2) and P(1,4) compounds as seen in **Figure 6.24**. Symmetrical P(1,2) and P(1,4) compounds synthesized in this study include **Figure 6.24a,c**. Asymmetrical P(1,2) and P(1,4) compounds to synthesize in future studies include **Figure 6.24b,d-e**. These sets of PU oligomers have a different structural arrangement regarding the placement of hard and soft segments, within the PU chain. Additional

studies include probing the asymmetrical compounds using monovalent Li^+ and Na^+ , and transition metal Ag^+ . These studies will guide our understanding into the unique cation coordination between polyester and urethane functional groups. In the above study, lower and high CID energy fragment ions were extensively groups. In the above study, lower and high CID energy fragment ions were extensively characterized. The above analysis of PBA and PU species may act as a model system for how to characterize these asymmetrical compounds in the future. It will be interesting to observe the unique fragment ions formed when the hard segment is exposed on the terminal end compared to a centrally located placement along the PU chain. The specific placement of the MDI hard segment may result in an increase or decrease in fragment ion observed to form from the urethane functional group. Additional future studies include the detailed IM characterization of longer PBA chains respective to their coordination to Li^+ , Na^+ , and Ag^+ . A detailed study of the unique structural differences or similarities among these species will aid in the understanding of how these PU systems behave in the gas phase. These future studies are aimed towards the creation and characterization of these PU compounds to be used as analytical standards. Coupling computational models to the experimental IM studies will aid in predication of polymer behavior, and the which compounds are of interest to synthesize using the stepwise addition method.

6.7. Acknowledgements

We would like to acknowledge Ian Tomlinson for his development of the polyester and urethane synthesis reaction. This work was funded and supported in part by the resources of the Center for Innovative Technology (CIT) at Vanderbilt University. Financial support for this research was provided by the National Institutes of Health (NIH NIGMS R01GM092218 and NIH NCI 1R03CA222452-01).

Polyester Polyurethane Oligomers to Synthesize

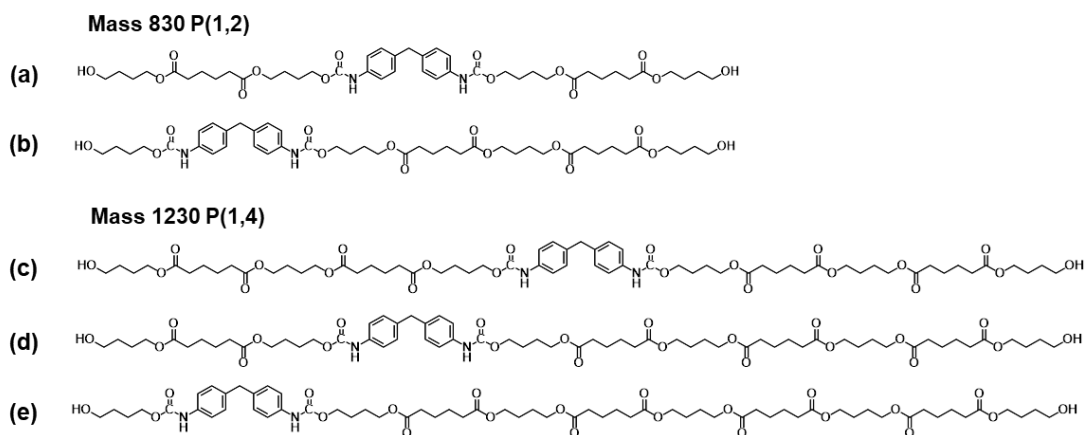


Figure 6.24. Symmetrical and asymmetrical (a-b) P(1,2) and (c-e) P(1,4) oligomers to be synthesized using stepwise addition and further characterized using IM-MS and IM-MS/MS methods.

6.8. References

- (1) Szycher, M. *Szycher's Handbook of Polyurethanes*; CRC press, 1999.
- (2) Oertel, G. *Polyurethane Handbook*; Carl Hanser Verlag, 1985.
- (3) Altuntaş, E.; Schubert, U. S. "Polymeromics": Mass Spectrometry Based Strategies in Polymer Science toward Complete Sequencing Approaches: A Review. *Anal. Chim. Acta* **2014**, *808*, 56–69.
- (4) Williams, J. B.; Chapman, T. M.; Hercules, D. M. Synthesis of Discrete Mass Poly(Butylene Glutarate) Oligomers. *Macromolecules* **2003**, *36* (11), 3898–3908.
- (5) Gies, A. P.; Hercules, D. M. Collision Induced Dissociation Study of Ester-Based Polyurethane Fragmentation Reactions. *Anal. Chim. Acta* **2014**, *808*, 199–219.
- (6) Gies, A. P.; Ellison, S. T.; Chakraborty, A. K.; Kwiecien, N. W.; Hercules, D. M. MALDI-TOF/TOF CID Study of Poly(Butylene Adipate) Fragmentation Reactions. *RSC Adv.* **2012**, *2* (10), 4135–4151.
- (7) Weidner, S. M.; Trimpin, S. Mass Spectrometry of Synthetic Polymers. **2010**, *82* (12), 4811–4829.
- (8) Wesdemiotis, C. Multidimensional Mass Spectrometry of Synthetic Polymers and Advanced Materials. *Angew. Chemie Int. Ed.* **2017**, *56* (6), 1452–1464.
- (9) Hoskins, J. N.; Trimpin, S.; Grayson, S. M. Architectural Differentiation of Linear and Cyclic Polymeric Isomers by Ion Mobility Spectrometry-Mass Spectrometry. *Macromolecules* **2011**, *44* (17), 6915–6918.
- (10) Montenegro-Burke, J. R.; Bennett, J. M.; McLean, J. A.; Hercules, D. M. Novel Behavior of the Chromatographic Separation of Linear and Cyclic Polymers. *Anal. Bioanal. Chem.* **2016**, *408* (3), 677–681.
- (11) Forsythe, J. G.; Stow, S. M.; Nefzger, H.; Kwiecien, N. W.; May, J. C.; McLean, J. A.;

- Hercules, D. M. Structural Characterization of Methylenedianiline Regioisomers by Ion Mobility-Mass Spectrometry, Tandem Mass Spectrometry, and Computational Strategies: I. Electrospray Spectra of 2-Ring Isomers. *Anal. Chem.* **2014**, *86* (9), 4362–4370.
- (12) Stow, S. M.; Onifer, T. M.; Forsythe, J. G.; Nefzger, H.; Kwiecien, N. W.; May, J. C.; McLean, J. A.; Hercules, D. M. Structural Characterization of Methylenedianiline Regioisomers by Ion Mobility-Mass Spectrometry, Tandem Mass Spectrometry, and Computational Strategies. 2. Electrospray Spectra of 3-Ring and 4-Ring Isomers. *Anal. Chem.* **2015**, *87* (12), 6288–6296.
- (13) Stow, S. M.; Crescentini, T. M.; Forsythe, J. G.; May, J. C.; McLean, J. A.; Hercules, D. M. Structural Characterization of Methylenedianiline Regioisomers by Ion Mobility-Mass Spectrometry, Tandem Mass Spectrometry, and Computational Strategies. 3. MALDI Spectra of 2-Ring Isomers. *Anal. Chem.* **2017**, *89* (18).
- (14) Crescentini, T. M.; Stow, S. M.; Forsythe, J. G.; May, J. C.; McLean, J. A.; Hercules, D. M. Structural Characterization of Methylenedianiline Regioisomers by Ion Mobility-Mass Spectrometry and Tandem Mass Spectrometry. 4. 3-Ring and 4-Ring Isomers. *Anal. Chem.* **2018**, *90* (24).
- (15) Crotty, S.; Gerişlioğlu, S.; Endres, K. J.; Wesdemiotis, C.; Schubert, U. S. Polymer Architectures via Mass Spectrometry and Hyphenated Techniques: A Review. *Anal. Chim. Acta* **2016**, *932*, 1–21.
- (16) Dunbar, R. C.; Steill, J. D.; Oomens, J. Encapsulation of Metal Cations by the PhePhe Ligand: A Cation- π Ion Cage. *J. Am. Chem. Soc.* **2011**, *133* (24), 9376–9386.
- (17) May, J. C.; Goodwin, C. R.; Lareau, N. M.; Leaptrot, K. L.; Morris, C. B.; Kurulugama, R. T.; Mordehai, A.; Klein, C.; Barry, W.; Darland, E.; et al. Conformational Ordering of Biomolecules in the Gas Phase: Nitrogen Collision Cross Sections Measured on a Prototype High Resolution Drift Tube Ion Mobility-Mass Spectrometer. *Anal. Chem.* **2014**, *86* (4), 2107–2116.

- (18) May, J. C.; Dodds, J. N.; Kurulugama, R. T.; Stafford, G. C.; Fjeldsted, J. C.; McLean, J. A. BROADSCALE RESOLVING POWER PERFORMANCE OF A HIGH PRECISION UNIFORM FIELD ION MOBILITY-MASS SPECTROMETER. *Analyst* **2015**, *140* (20), 6824–6833.
- (19) Stow, S. M.; Causon, T. J.; Zheng, X.; Kurulugama, R. T.; Mairinger, T.; May, J. C.; Rennie, E. E.; Baker, E. S.; Smith, R. D.; McLean, J. A.; et al. AN INTERLABORATORY EVALUATION OF DRIFT TUBE ION MOBILITY - MASS SPECTROMETRY COLLISION CROSS SECTION MEASUREMENTS. **2017**, *89* (17), 9048–9055.

APPENDIX A

REPRINT PERMISSION FOR CHAPTERS

- Chapter I. **Crescentini, T.M.**, May, J.C., McLean, J.A. and Hercules, D.M. *Mass Spectrometry of Polyurethanes. Elsevier Polymer*, (2019) *In Preparation*.
- Chapter II. Stow, S.M., **Onifer, T.M.**, Forsythe, J.G., Nefzger, H., Kwiecien, N.W., May, J.C., McLean, J.A. and Hercules, D.M. *Structural Characterization of Methylenedianiline Regioisomers by Ion Mobility-Mass Spectrometry, Tandem Mass Spectrometry, and Computational Strategies. 2. Electrospray Spectra of 3-Ring and 4-Ring Isomers, Analytical Chemistry*, 87 (2015) 6288-6296.
- Chapter III. Stow, S.M., **Crescentini, T.M.**, Forsythe, J.G., May, J.C., McLean, J.A. and Hercules, D.M. *Structural Characterization of Methylenedianiline Regioisomers by Ion Mobility-Mass Spectrometry, Tandem Mass Spectrometry, and Computational Strategies. 3. MALDI Spectra of 2-Ring Isomers, Analytical Chemistry*, 89 (2017) 9900-9910.
- Chapter IV. **Crescentini, T.M.**, Stow, S.M., Forsythe, J.G., May, J.C., McLean, J.A. and Hercules, D.M. *Structural Characterization of Methylenedianiline Regioisomers by Ion Mobility-Mass Spectrometry and Tandem Mass Spectrometry. 4. 3-Ring and 4-Ring Isomers. Analytical Chemistry*, 90 (2018) 14453-14461.
- Chapter V. **Crescentini, T.M.**, May, J.C., McLean, J.A. and Hercules, D.M. *Alkali Metal Cation Adduct Effect on Polybutylene Adipate Oligomers: Ion Mobility-Mass Spectrometry. Elsevier Polymer*, (2019) *Submitted*.

APPENDIX B

SUPPORTING INFORMATION FOR CHAPTER II

B.1. NMR Spectroscopy of Purified MDA Isomers

NMR experiments were acquired using a 14.0 T Bruker magnet equipped with a Bruker AV-III console operating at 600.13 MHz. All spectra were acquired in 5 mm NMR tube using a Bruker 5 mm TCI cryogenically cooled NMR probe. Chemical shifts were referenced internally to DMSO (2.49 ppm), which also served as the ^2H lock solvents. For 1D NMR, typical experimental conditions included 32 K data points, 13 ppm sweep width, a recycled delay of 1.5 seconds and 64 scans.

B.1. ^1H NMR 3-Ring MDA

^1H NMR of Sample 4 in DMSO 5mm NMR tube

```
NAME      May30-2014-stowsm
EXEN0     2
PROCNO    1
Date_     20140330
Time      14.48
INSTRUM   spect
PROBHD    5 mm PABBO BB-
PULPROG   zg30
TD        32768
SOLVENT   DMSO
NS        32
DS        0
SWH       5208.333 Hz
FIDRES    0.158946 Hz
AQ        3.1457779 sec
RG        161.3
DM        96.000 usec
DE        25.61 usec
TE        298.0 K
D1        1.5000000 sec
TD0       1
***** CHANNEL f1 *****
NUC1      1H
P1        11.38 usec
PL1       -2.50 dB
PL1W      18.35869398 W
SFO1      400.1320007 MHz
SI        32768
SF        400.1300065 MHz
WDW       EM
SSB       0
LB        0.30 Hz
GB        0
FC        1.00
```

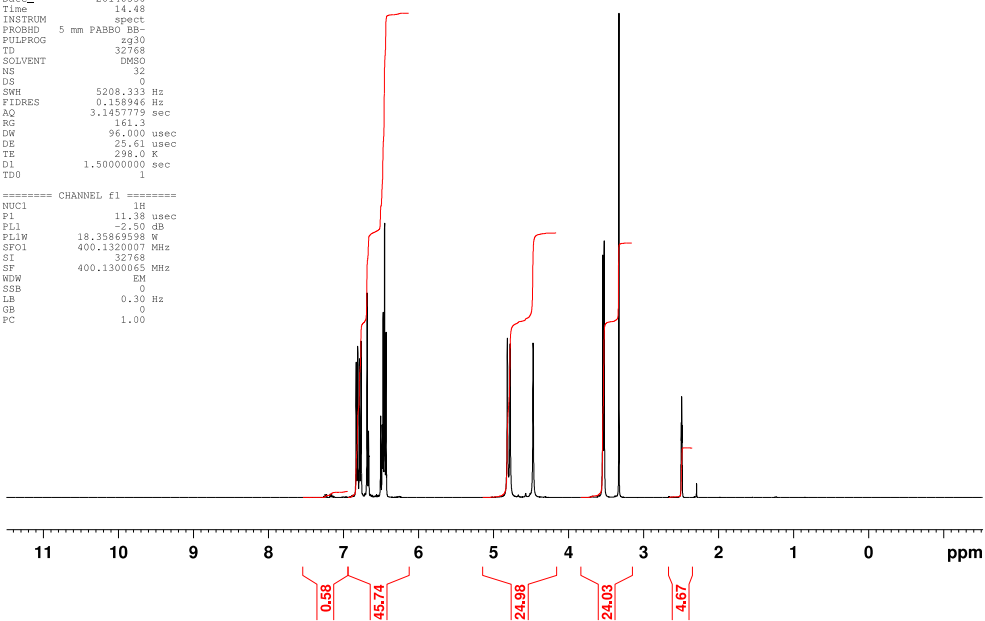


Figure B.1. ^1H NMR 3-Ring MDA.

B.2. ¹H NMR 4-Ring MDA

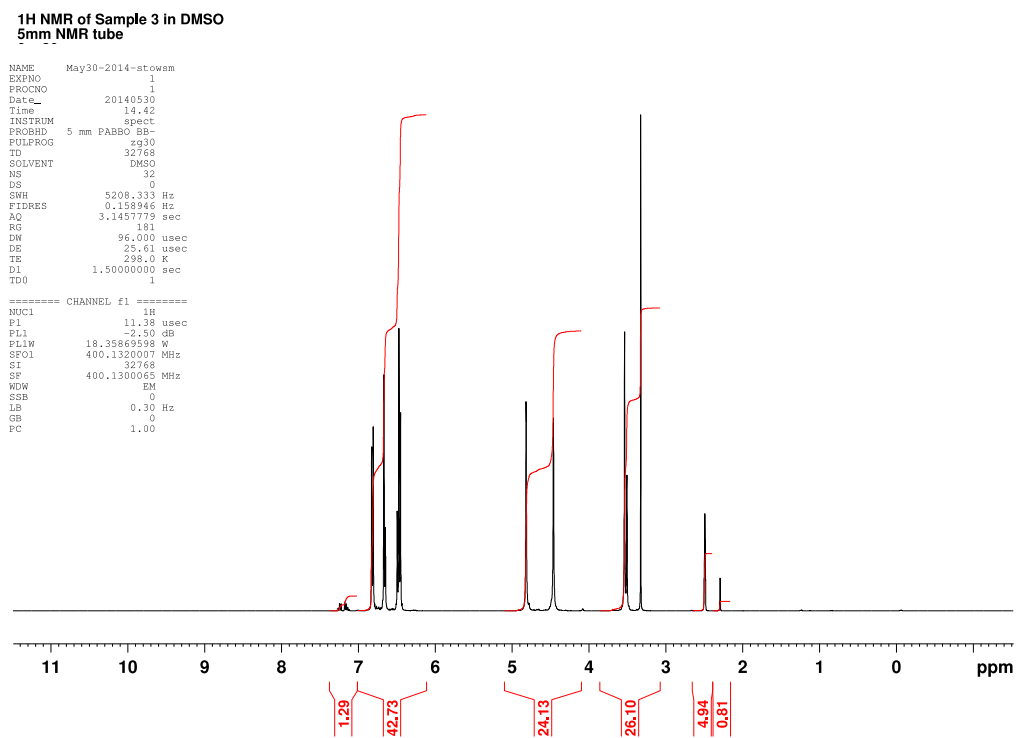


Figure B.2. ¹H NMR of 4-Ring MDA

B.3. Conformational Space Plots 3-Ring MDA

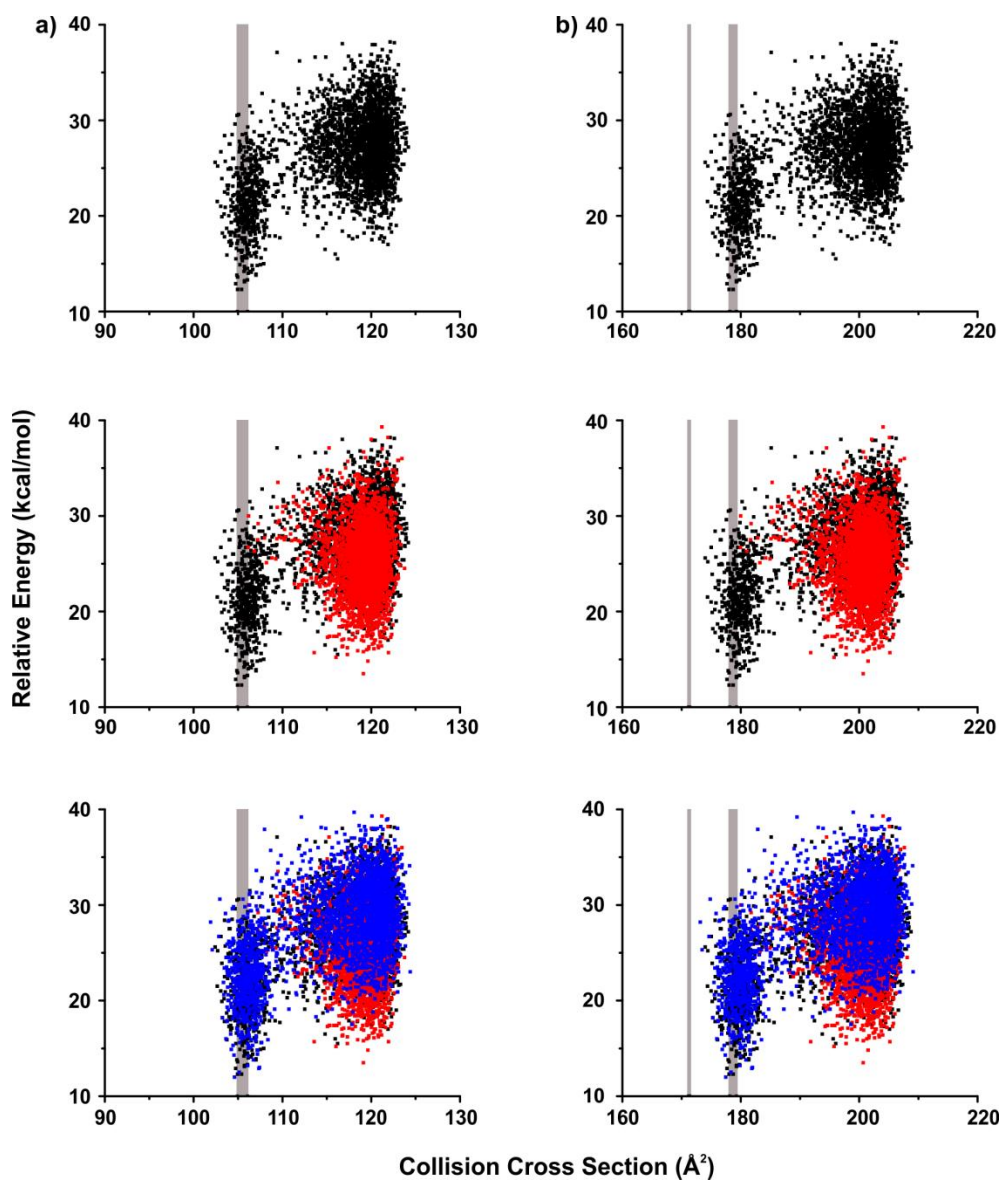


Figure B.3. Overlaid conformational space plots for the different protonation sites of 3-ring MDA. Plots are ordered to represent protonation from left to right across 3-ring MDA. Conformations from protonation on the amine on the first amine are shown in black, on the amine on the second amine in red and on the amine on the third ring in blue. These plots are zoomed in to show alignment with experimental CCS values from both (a) helium and (b) nitrogen. Experimental CCS ranges are indicated with the vertical gray bars. The vertical bars that align with the data are from the uniform field MS whereas the vertical bar in (b) that falls to the left of the plot represents the traveling wave MS.

B.4. Conformational Space Plots 4-Ring MDA

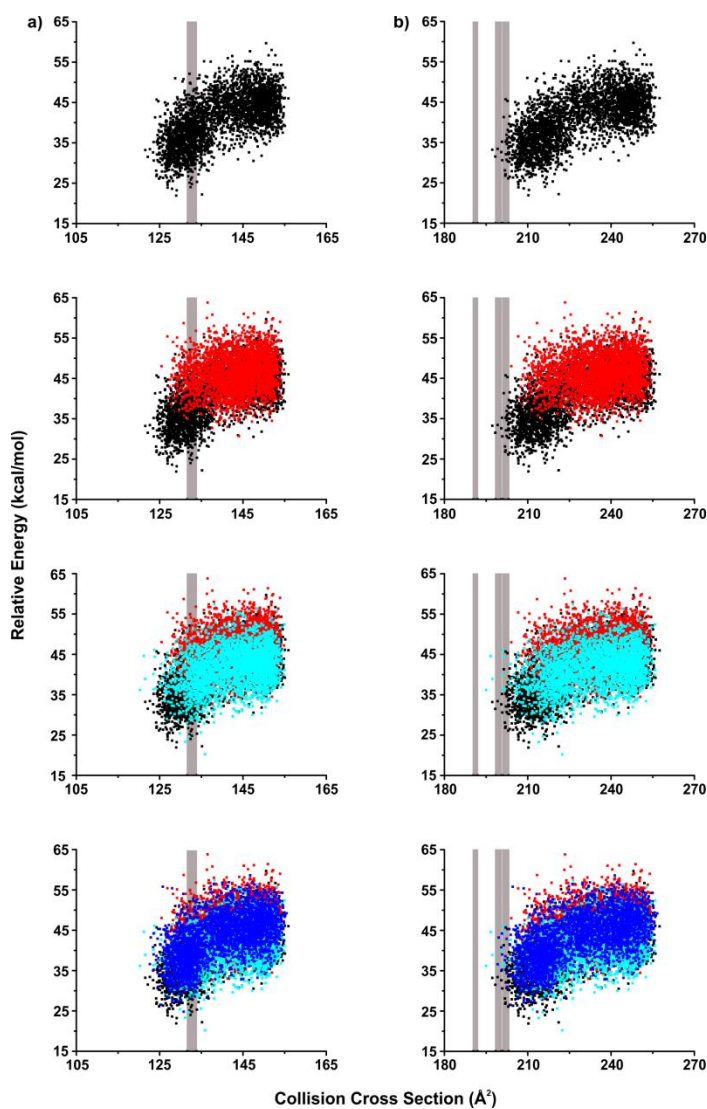


Figure B.4. Overlaid conformational space plots for the different protonation sites of 4-ring MDA. Plots are ordered to represent protonation from left to right across 4-ring MDA. Conformations from protonation on the amine on the first amine are shown in black, on the amine on the second ring in red and on the amine on the third ring in light blue, and on the amine on the fourth ring in blue. These plots are zoomed in to show alignment with experimental CCS values from both (a) helium and (b) nitrogen. Experimental CCS ranges are indicated with the vertical gray bars. The vertical bars that align with the data are from the uniform field MS whereas the vertical bar in (b) that falls to the left of the plot represents the traveling wave MS.

B.5. MS Doubly Charged Species

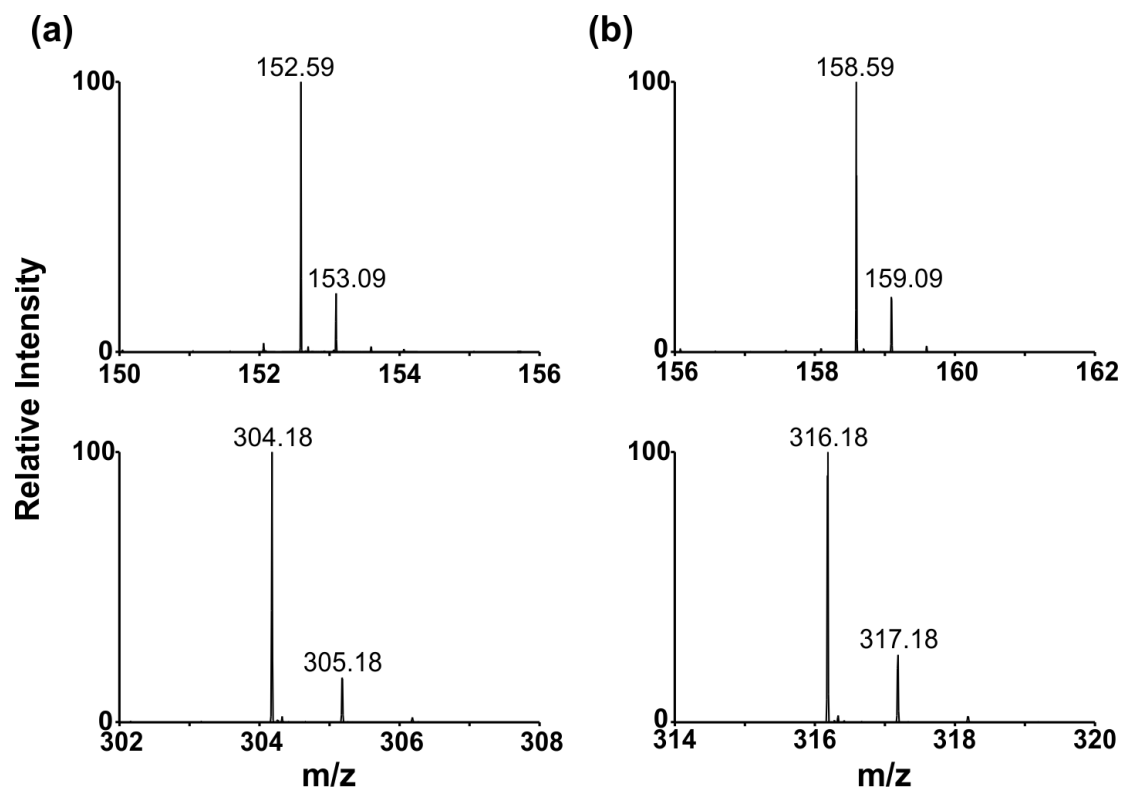


Figure B.5. Mass spectra of the doubly charged peaks and their respective singly charged peaks for (a) the 3-ring MDA and (b) the 4-ring MDA.

B.6. MS/MS Doubly Charged Fragment Ions

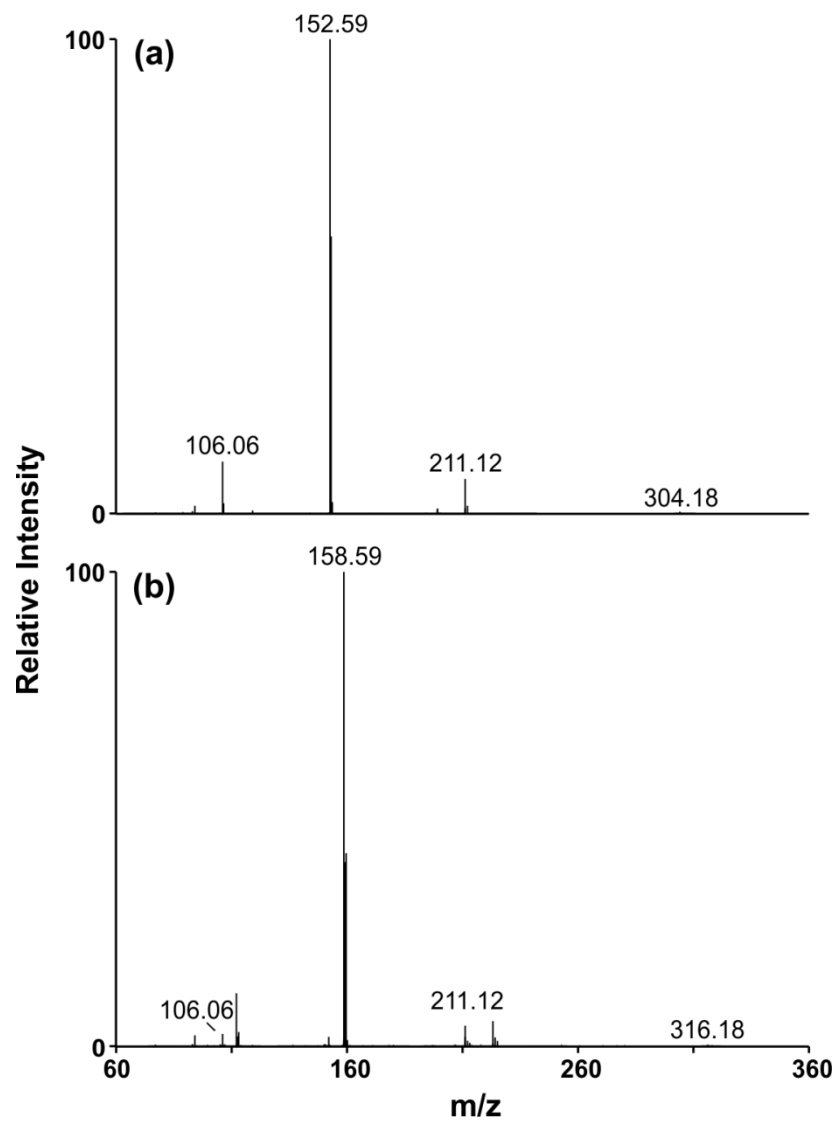


Figure B.6. Tandem mass spectra of the 152.59 and 158.59 doubly charged fragment ions showing the higher m/z fragments that result from fragmenting the doubly charged species.

B.7. Conformational Space Plot 3-Ring MDA

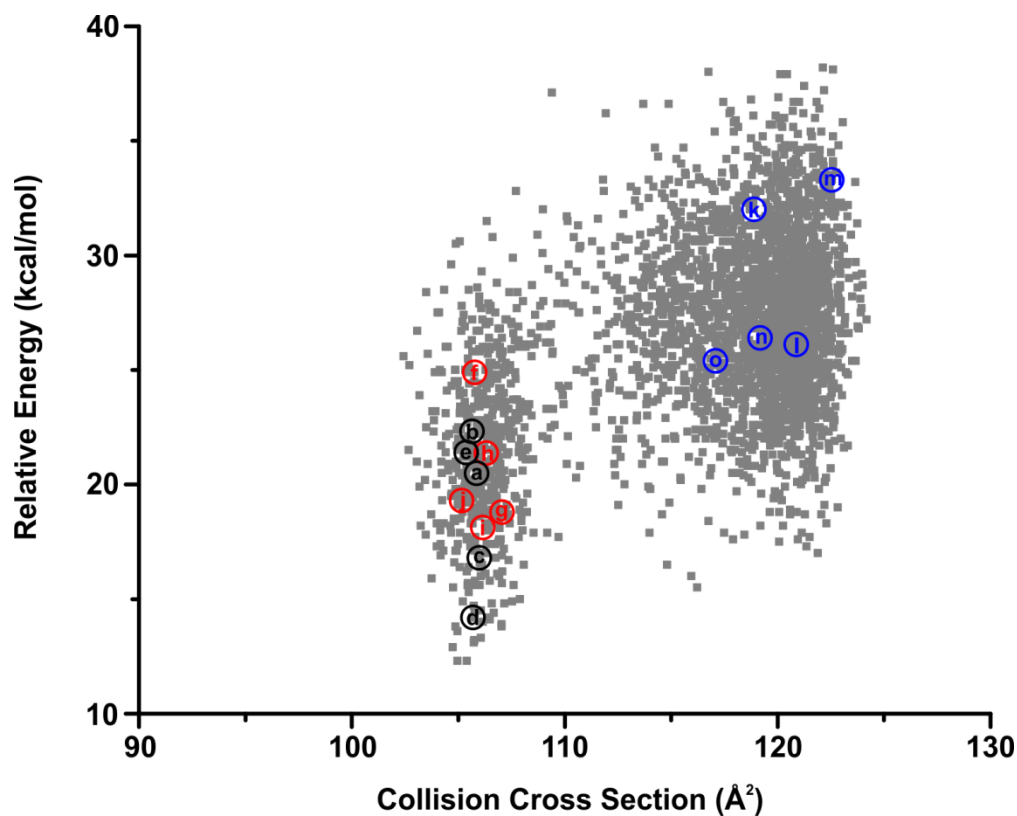


Figure B.7. Conformational space plot for the first ring amine protonated 3-Ring MDA. The 3,000 generated conformations are represented in grey; the clustering representative conformations are labeled with letters that correspond to the structures in **Figures B.7-10**. The conformations labeled in black fall within the experimental range, the conformations labeled in red are representative of conformations from the left conformational cloud, and the conformations labeled in blue are representative of conformations from the right conformational cloud.

B.8. Clustering Analysis 3-Ring MDA

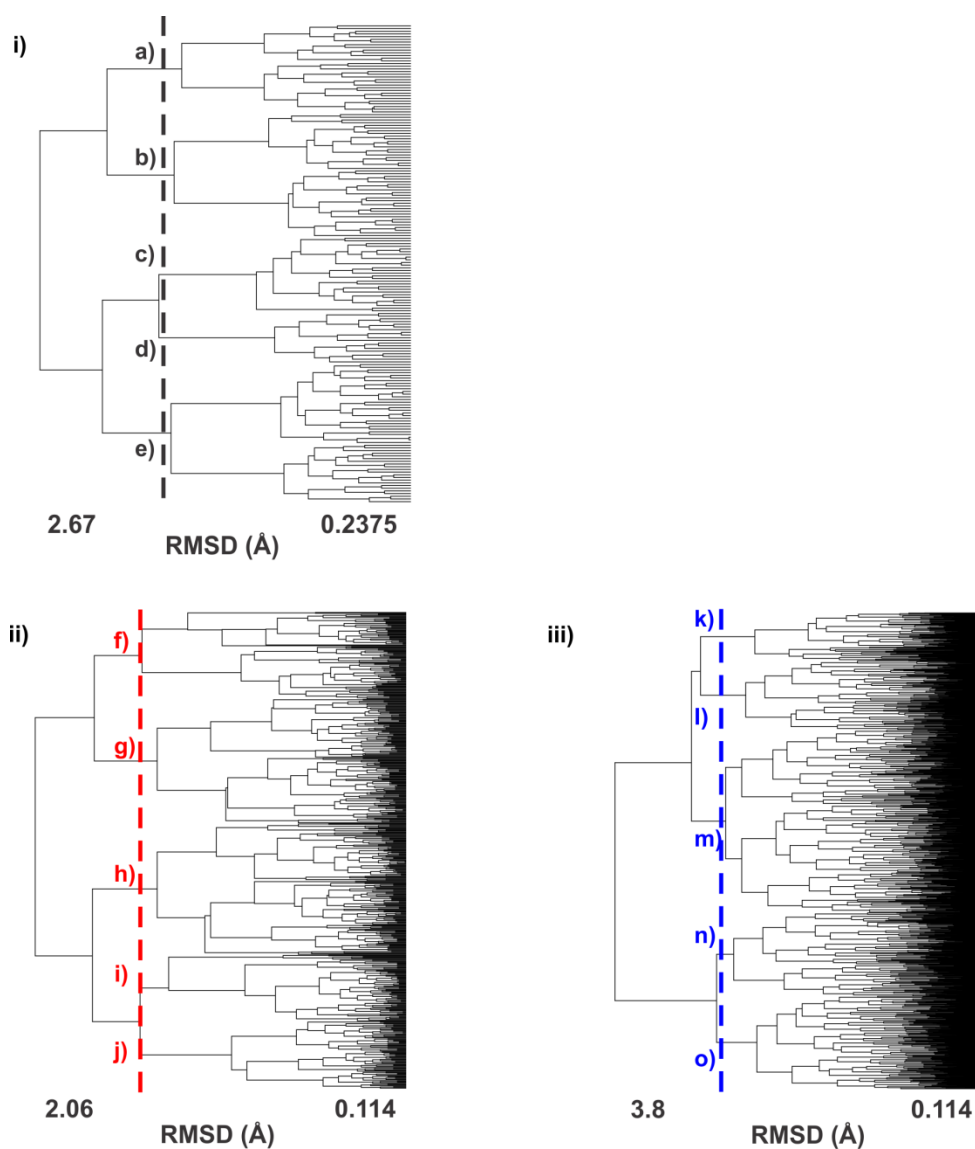


Figure B.8. Clustering analysis of 3,000 conformations of the first ring amine protonated 3-ring MDA. In **(i)** the conformations that fall within the experimental CCS range are clustered, in **(ii)** the conformations in the left conformational cloud are clustered, and in **(iii)** the conformations in the right conformational cloud are clustered. Clustering is based on root mean square distance of atoms of superimposed structures. The vertical bars indicate the RMSD cutoff used to select the conformations for further analysis.

B.9. Conformational Structures 3-Ring MDA

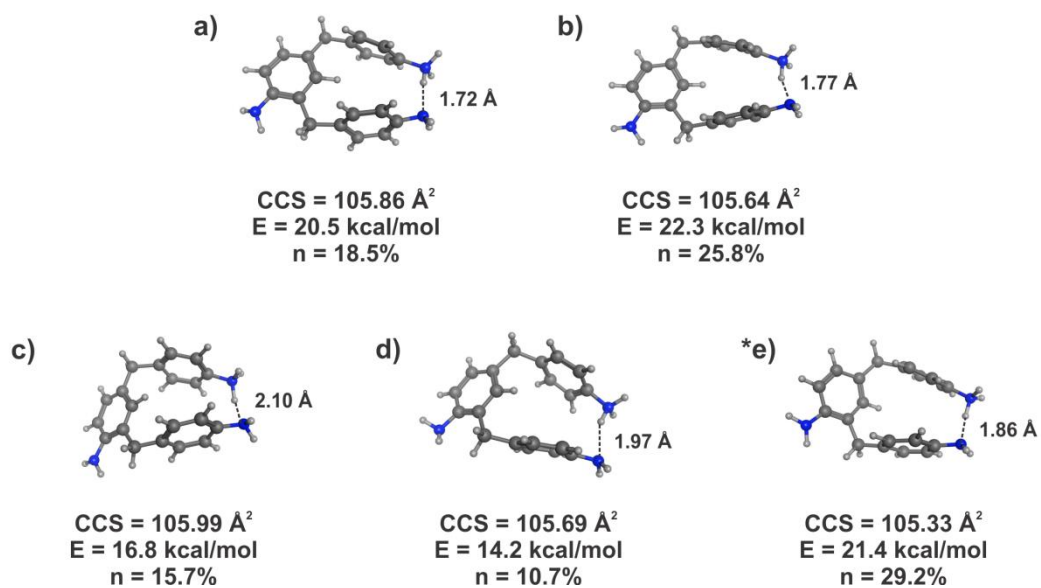


Figure B.9. Representative conformations from clustering analysis of the experimental range region of the first ring amine protonated 3-ring MDA generated from the simulated annealing calculation. Carbon atoms are shown in dark grey, hydrogen in light grey, and nitrogen in blue. Distances are labeled to show the proximity of the additional proton to other atoms in the molecule. The asterisk represents the structures shown in the manuscript. The theoretical CCS, relative energy, and percentage of conformations each of these represents from clustering are shown below each conformer.

B.10. Conformational Structures 3-Ring MDA

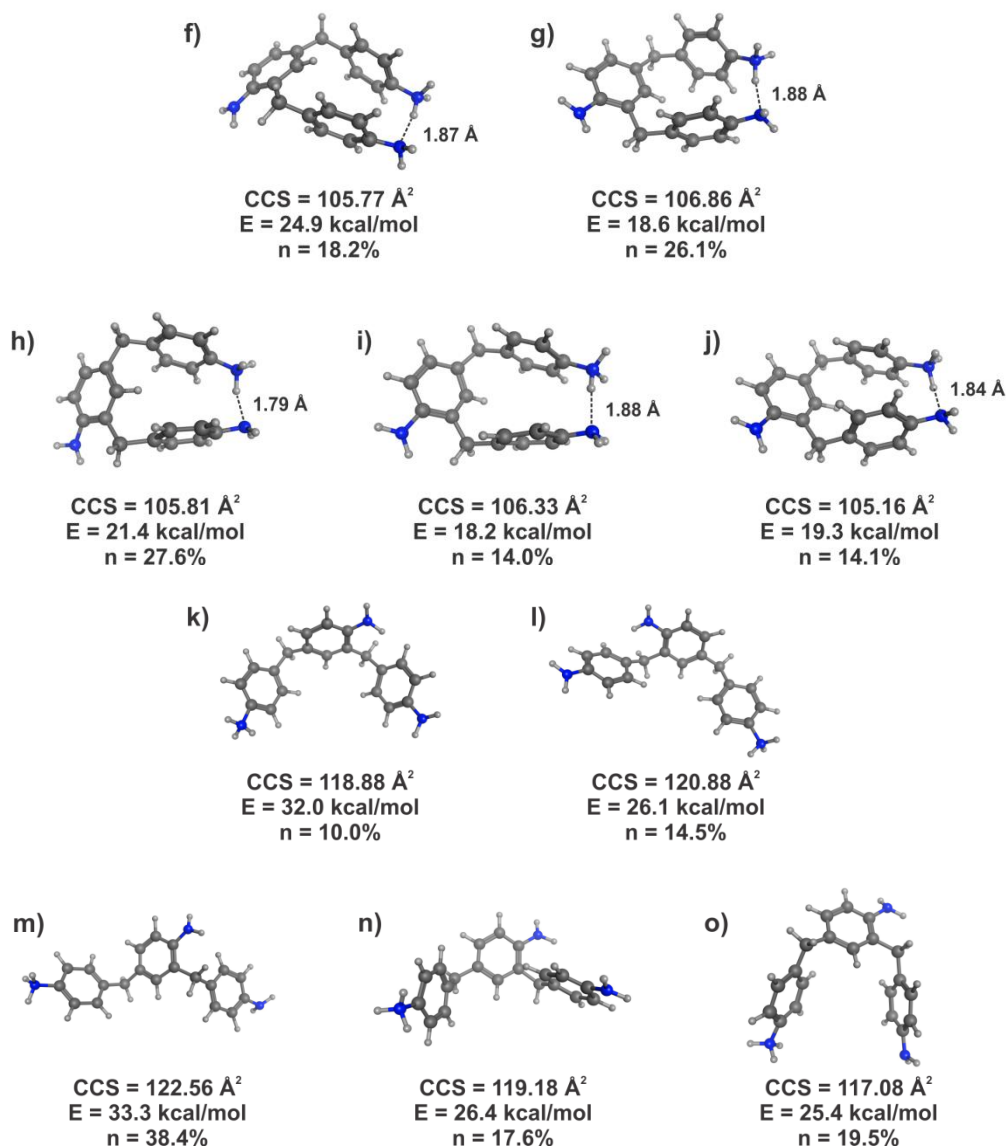


Figure B.10. Representative conformations from clustering analysis of the two conformational space clouds (left cloud (f-j) and right cloud (k-o)) of the first ring amine protonated 3-ring MDA generated from the simulated annealing calculation. Carbon atoms are shown in dark grey, hydrogen in light grey, and nitrogen in blue. Distances are labeled to show the proximity of the additional proton to other atoms in the molecule. The theoretical CCS, relative energy, and percentage of conformations each of these represents from clustering are shown below each conformer.

B.11. Conformational Space Plot 3-Ring MD

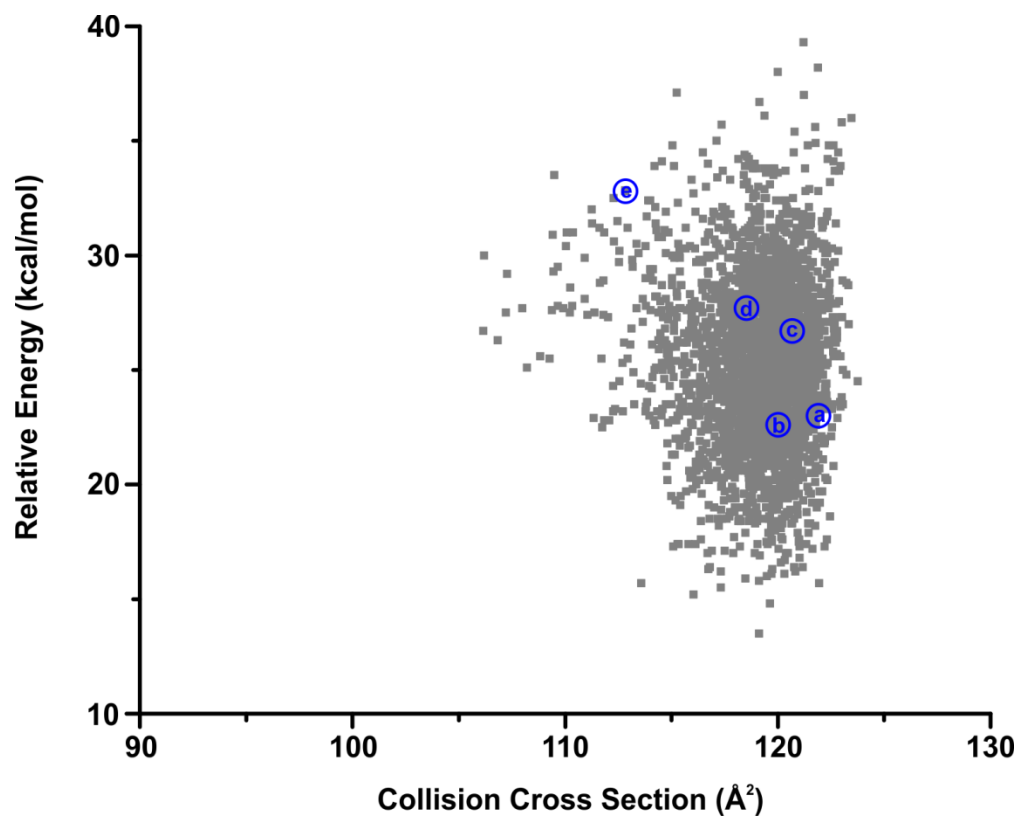


Figure B.11. Conformational space plot for the second ring amine protonated 3-ring MDA. The 3,000 generated conformations are represented in grey; the clustering representative conformations are labeled with letters that correspond to the structures in **Figures B.12-13**.

B.12. Clustering Analysis 3-Ring MDA

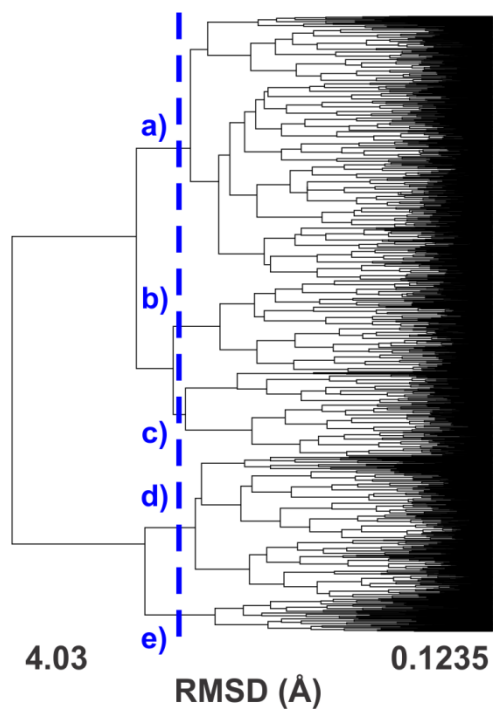


Figure B.12. Clustering analysis of 3,000 conformations of the second ring amine protonated 3-ring MDA. Clustering is based on root mean square distance of atoms of superimposed structures. The vertical bar indicates the RMSD cutoff used to select the conformations for further analysis.

B.13. Conformational Structures 3-Ring MDA

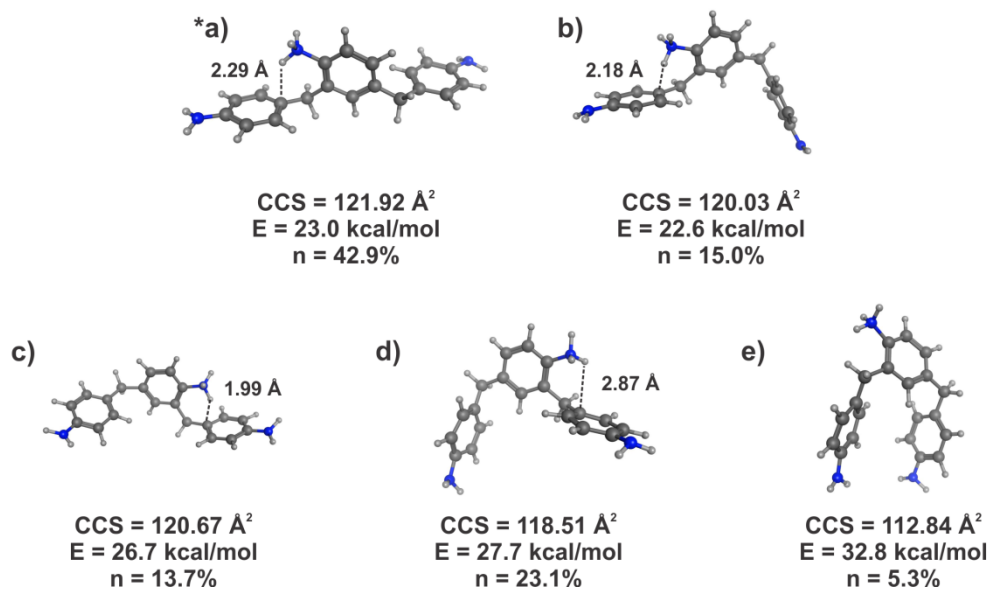


Figure B.13. Representative conformations from clustering analysis of the second ring amine protonated 3-ring MDA generated from an elevated temperate molecular dynamic protocol. Carbon atoms are shown in dark grey, hydrogen in light grey, and nitrogen in blue. The asterisk represents the structures shown in the paper. The number of conformations each of these represents from clustering is shown below the conformation.

B.14. Conformational Space Plot 3-Ring MDA

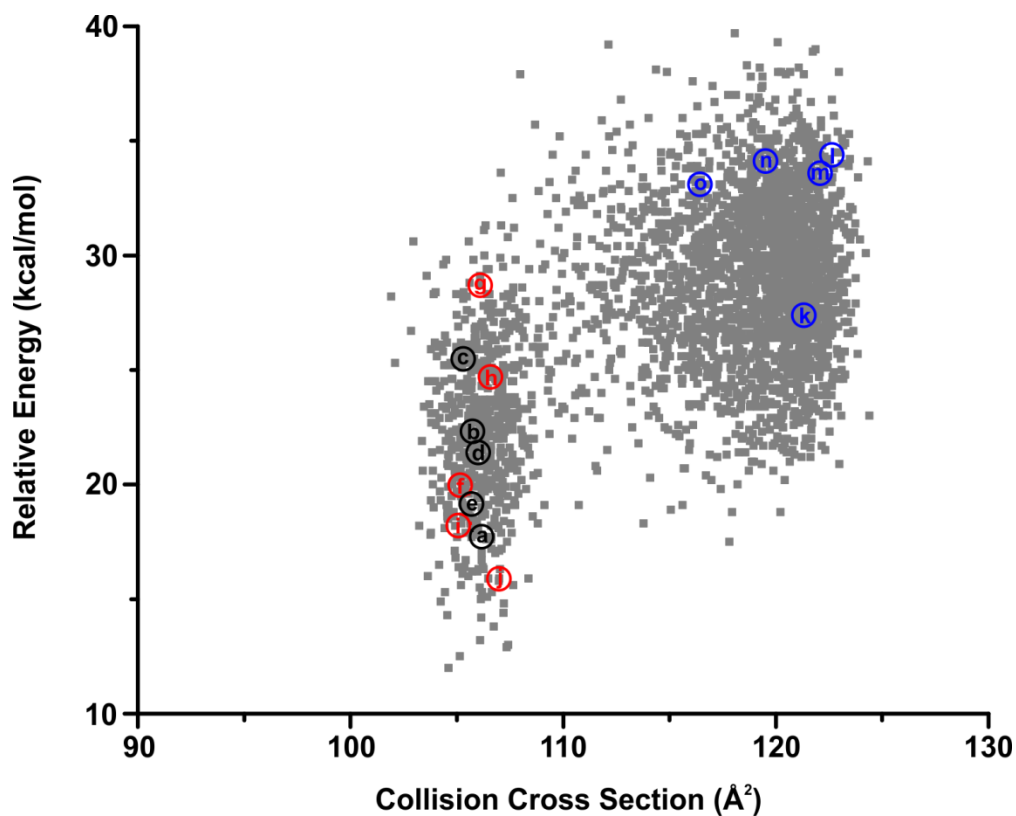


Figure B.14. Conformational space plot for the third ring amine protonated 3-ring MDA. The 3,000 generated conformations are represented in grey; the clustering representative conformations are labeled with letters that correspond to the structures in **Figures B.15-17**. The conformations labeled in black fall within the experimental range, the conformations labeled in red are representative of conformations from the left conformational cloud, and the conformations labeled in blue are representative of conformations from the right conformational cloud.

B.15. Clustering Analysis 3-Ring MDA

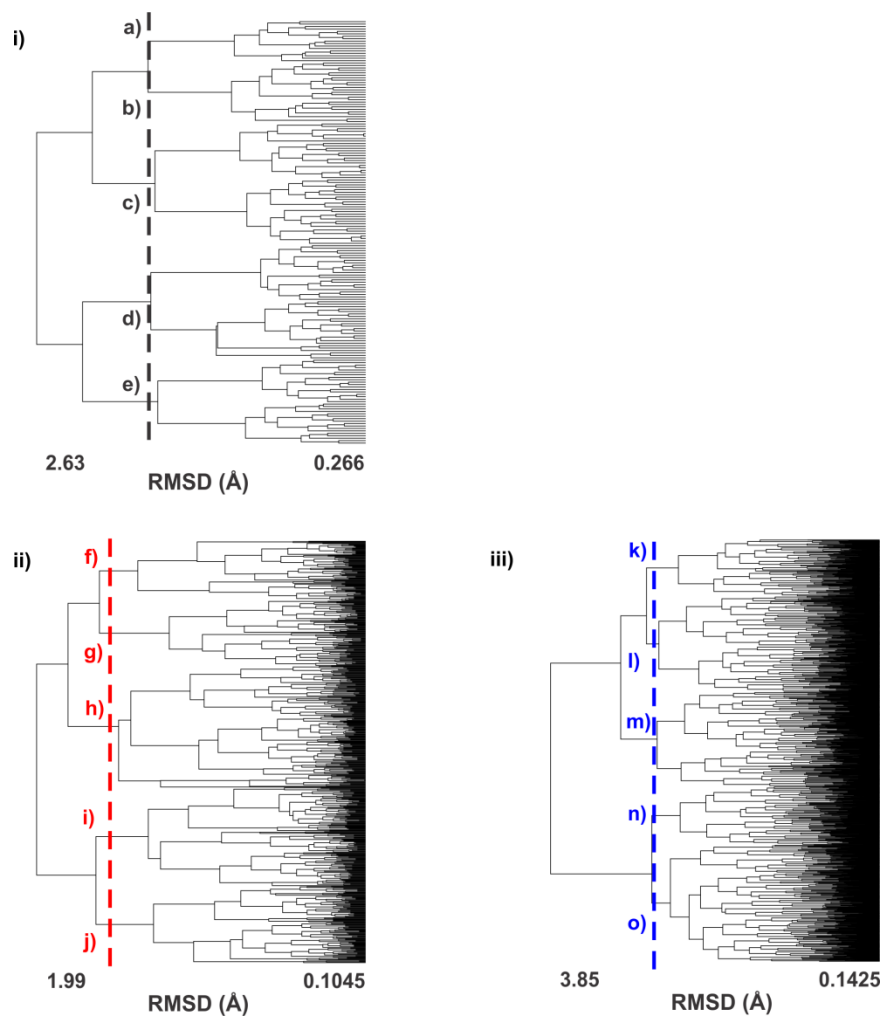


Figure B.15. Clustering analysis of 3,000 conformations of the third ring amine protonated 3-ring MDA. In (i) the conformations that fall within the experimental CCS range are clustered, in (ii) the conformations in the left conformational cloud are clustered, and in (iii) the conformations in the right conformational cloud are clustered. Clustering is based on root mean square distance of atoms of superimposed structures. The vertical bars indicate the RMSD cutoff used to select the conformations for further analysis.

B.16. Conformational Structures 3-Ring MDA

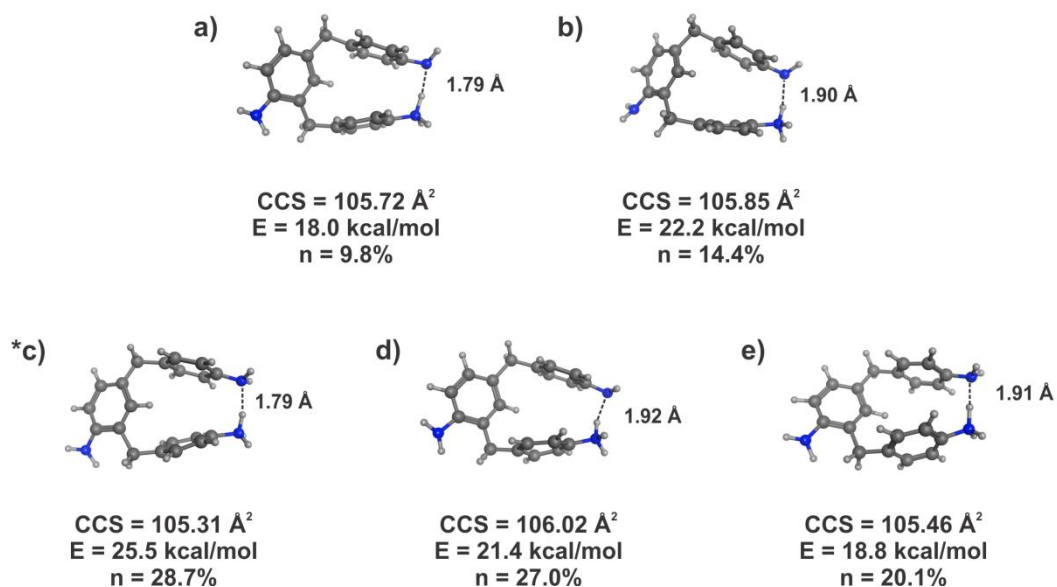


Figure B.16. Representative conformations from clustering analysis of the experimental range region of the third ring amine protonated 3-ring MDA generated from the simulated annealing calculation. Carbon atoms are shown in dark grey, hydrogen in light grey, and nitrogen in blue. Distances are labeled to show the proximity of the additional proton to other atoms in the molecule. The asterisk represents the structures shown in the manuscript. The theoretical CCS, relative energy, and percentage of conformations each of these represents from clustering are shown below the conformation.

B.17. Conformational Structures 3-Ring MDA

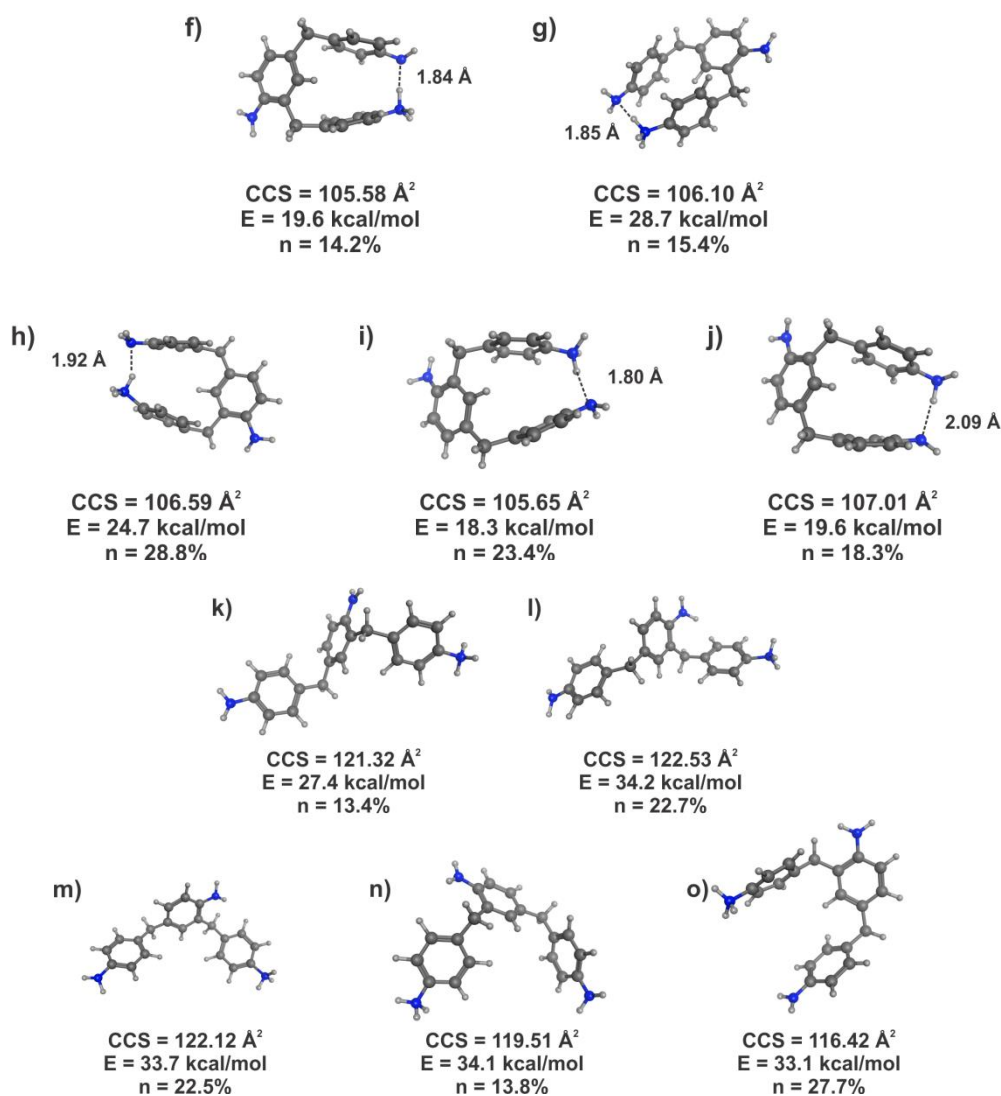


Figure B.17. Representative conformations from clustering analysis of the two conformational space clouds (left cloud (f-j) and right cloud (k-o)) of the third ring amine protonated 3-ring MDA generated from the simulated annealing calculation. Carbon atoms are shown in dark grey, hydrogen in light grey, and nitrogen in blue. Distances are labeled to show the proximity of the additional proton to other atoms in the molecule. The theoretical CCS, relative energy, and percentage of conformations each of these represents from clustering are shown below the conformation.

B.18. Conformational Space Plots 4-Ring MDA

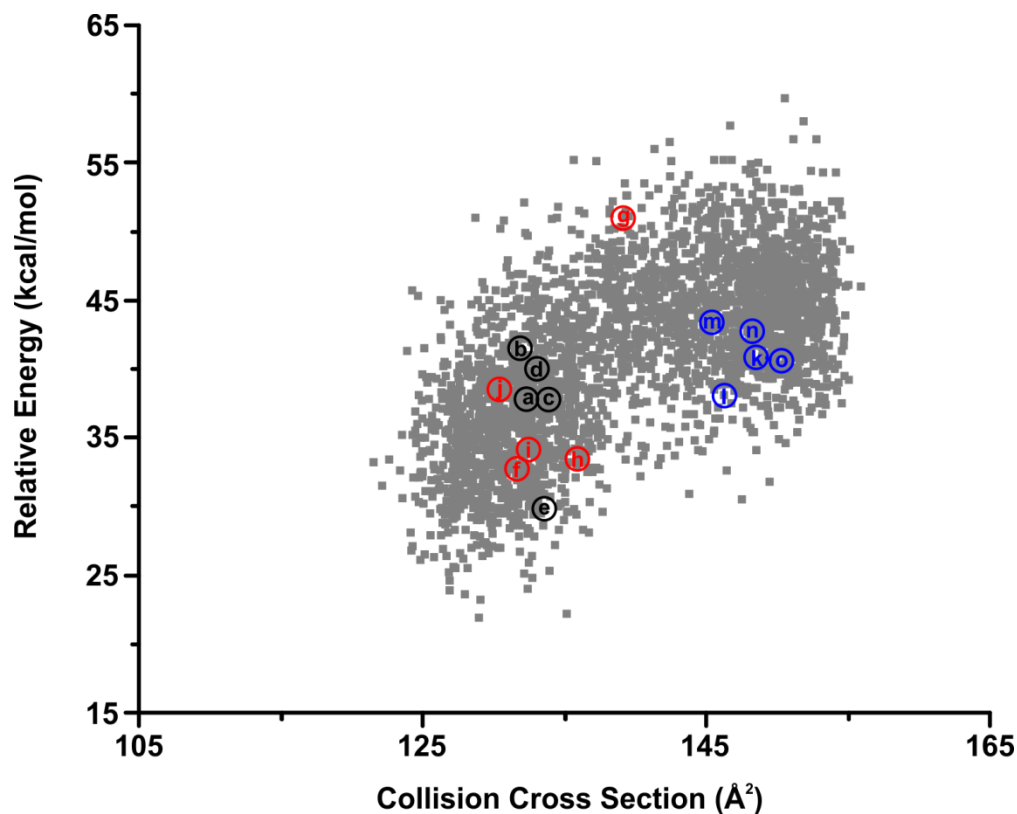


Figure B.18. Conformational space plot for the first ring amine protonated 4-ring MDA. The 3,000 generated conformations are represented in grey; the clustering representative conformations are labeled with letters that correspond to the structures in **Figures B.19-21**. The conformations labeled in black fall within the experimental range, the conformations labeled in red are representative of conformations from the left conformational cloud, and the conformations labeled in blue are representative of conformations from the right conformational cloud.

B.19. Clustering Analysis 4-Ring MDA

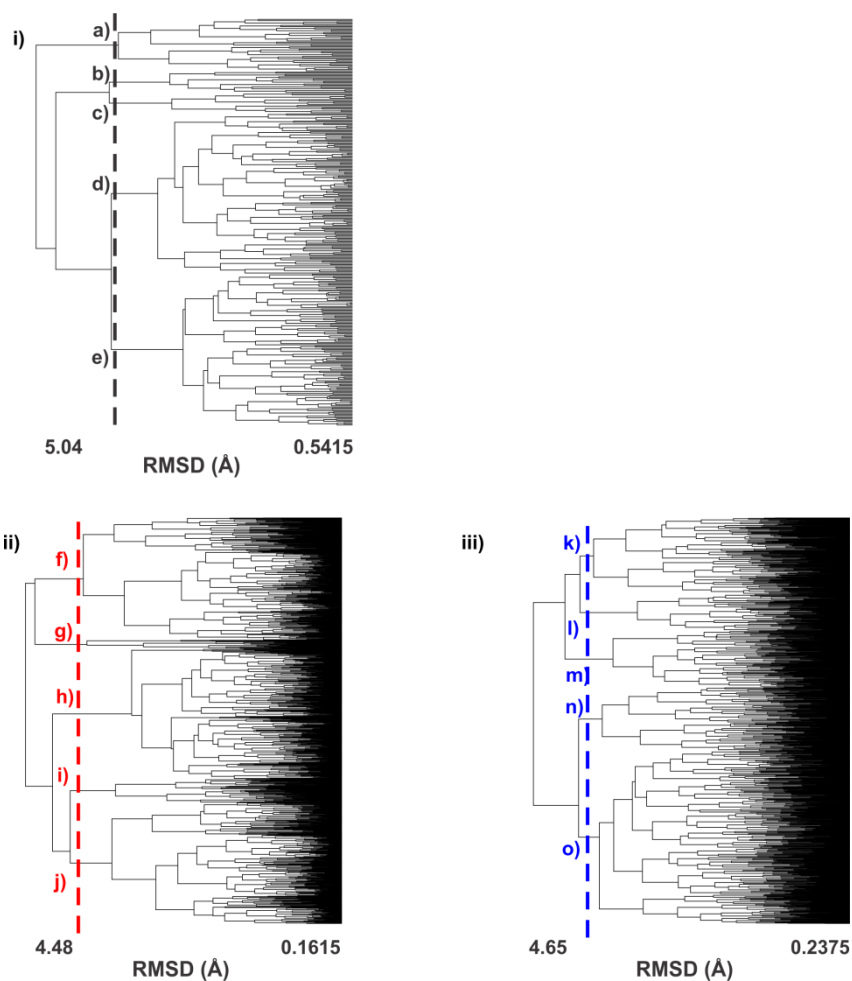


Figure B.19. Clustering analysis of 3,000 conformations of the first ring amine protonated 4-ring MDA. In **(i)** the conformations that fall within the experimental CCS range are clustered, in **(ii)** the conformations in the left conformational cloud are clustered, and in **(iii)** the conformations in the right conformational cloud are clustered. Clustering is based on root mean square distance of atoms of superimposed structures. The vertical bars indicate the RMSD cutoff used to select the conformations for further analysis.

B.20. Conformational Structures 4-Ring MDA

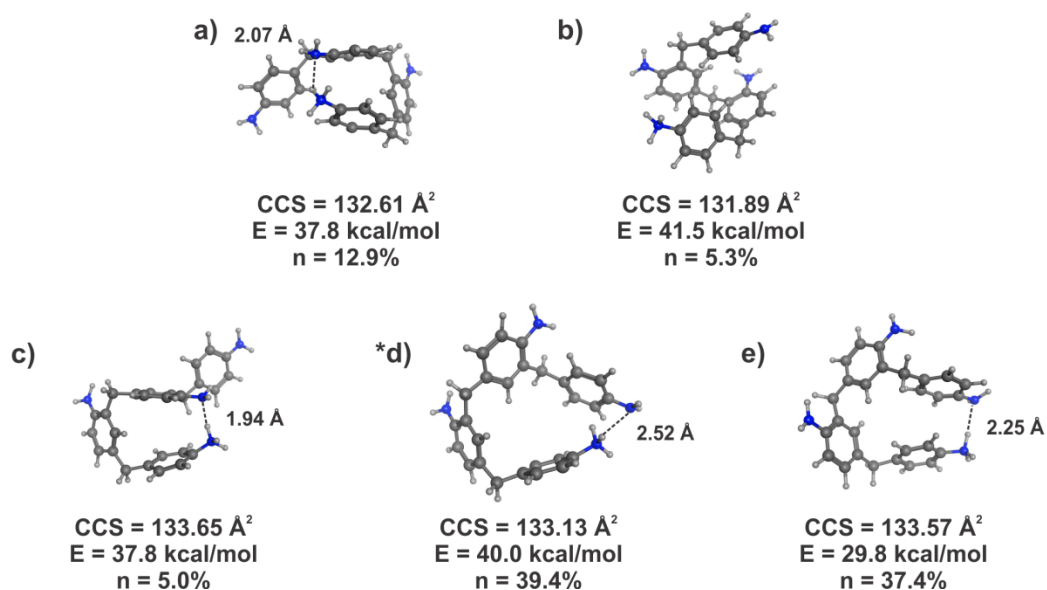


Figure B.20. Representative conformations from clustering analysis of the experimental range region of the first ring amine protonated 4-ring MDA generated from the simulated annealing calculation. Carbon atoms are shown in dark grey, hydrogen in light grey, and nitrogen in blue. Distances are labeled to show the proximity of the additional proton to other atoms in the molecule. The asterisk represents the structures shown in the manuscript. The theoretical CCS, relative energy, and percentage of conformations each of these represents from clustering are shown below the conformation.

B.19. Conformational Structures 4-Ring MDA

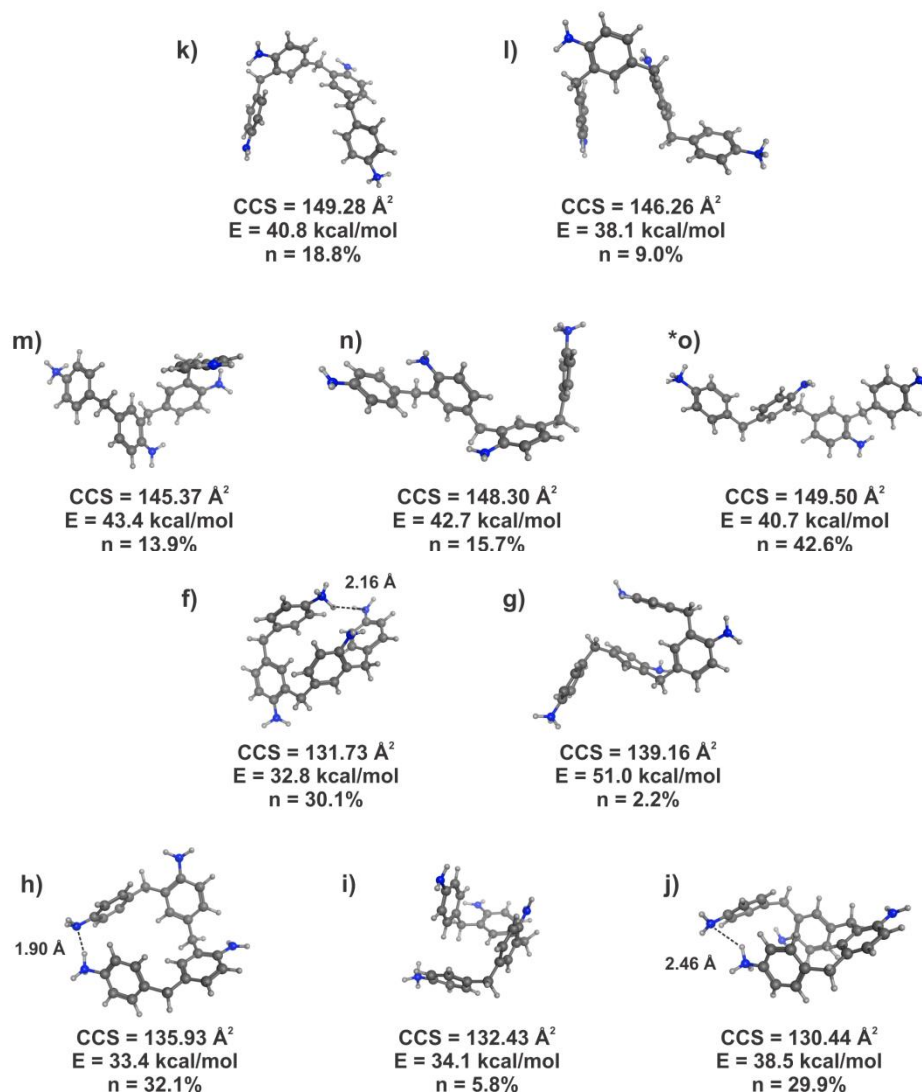


Figure B.21. Representative conformations from clustering analysis of the two conformational space clouds (left cloud (f-j) and right cloud (k-o)) of the first ring amine protonated 4-ring MDA generated from the simulated annealing calculation. Carbon atoms are shown in dark grey, hydrogen in light grey, and nitrogen in blue. Distances are labeled to show the proximity of the additional proton to other atoms in the molecule. The asterisk represents the structure shown in the manuscript. The theoretical CCS, relative energy, and percentage of conformations each of these represents from clustering are shown below the conformation.

B.22. Conformational Space Plots 4-Ring MDA

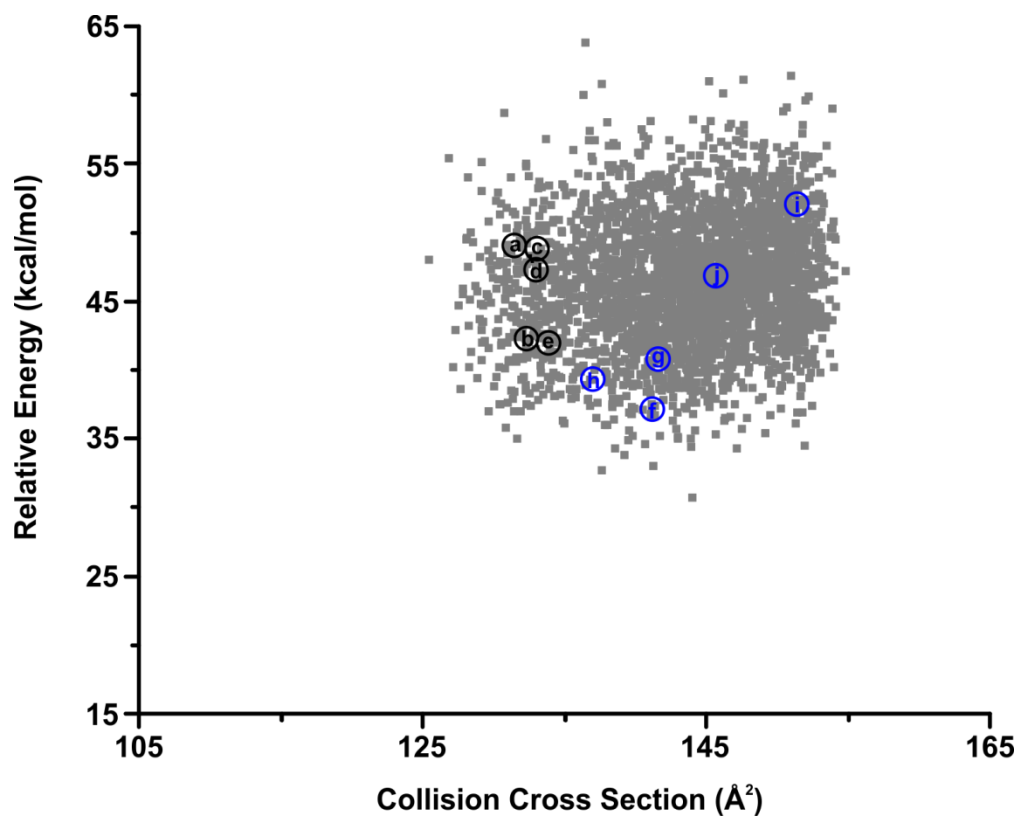


Figure B.22. Conformational space plot for the second ring amine protonated 4-ring MDA. The 3,000 generated conformations are represented in grey; the clustering representative conformations are labeled with letters that correspond to the structures in **Figures B.23-24**. The conformations labeled in black fall within the experimental range and the conformations labeled in blue are representative of conformations from the whole conformational cloud.

B.23. Clustering Analysis 4-Ring MDA

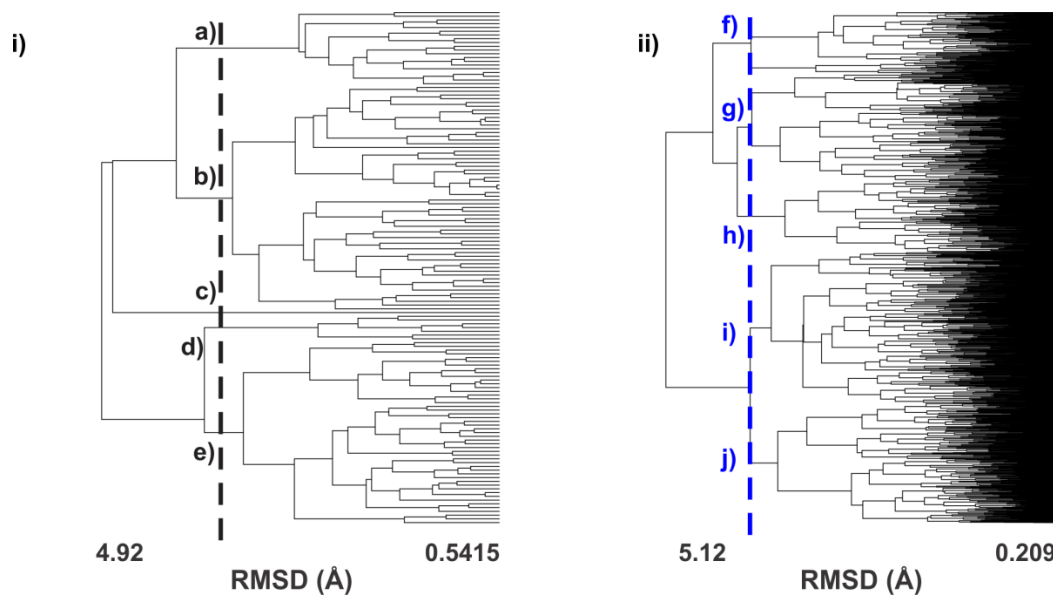


Figure B.23. Clustering analysis of 3,000 conformations of the second ring amine protonated 4-ring MDA. In (i) the conformations that fall within the experimental CCS range are clustered and in (ii) all 3,000 of the conformations are clustered. Clustering is based on root mean square distance of atoms of superimposed structures. The vertical bar indicates the RMSD cutoff used to select the conformations (circled) for further analysis. The asterisk represents the structures shown in the paper.

B.24. Conformational Clustering 4-Ring MDA

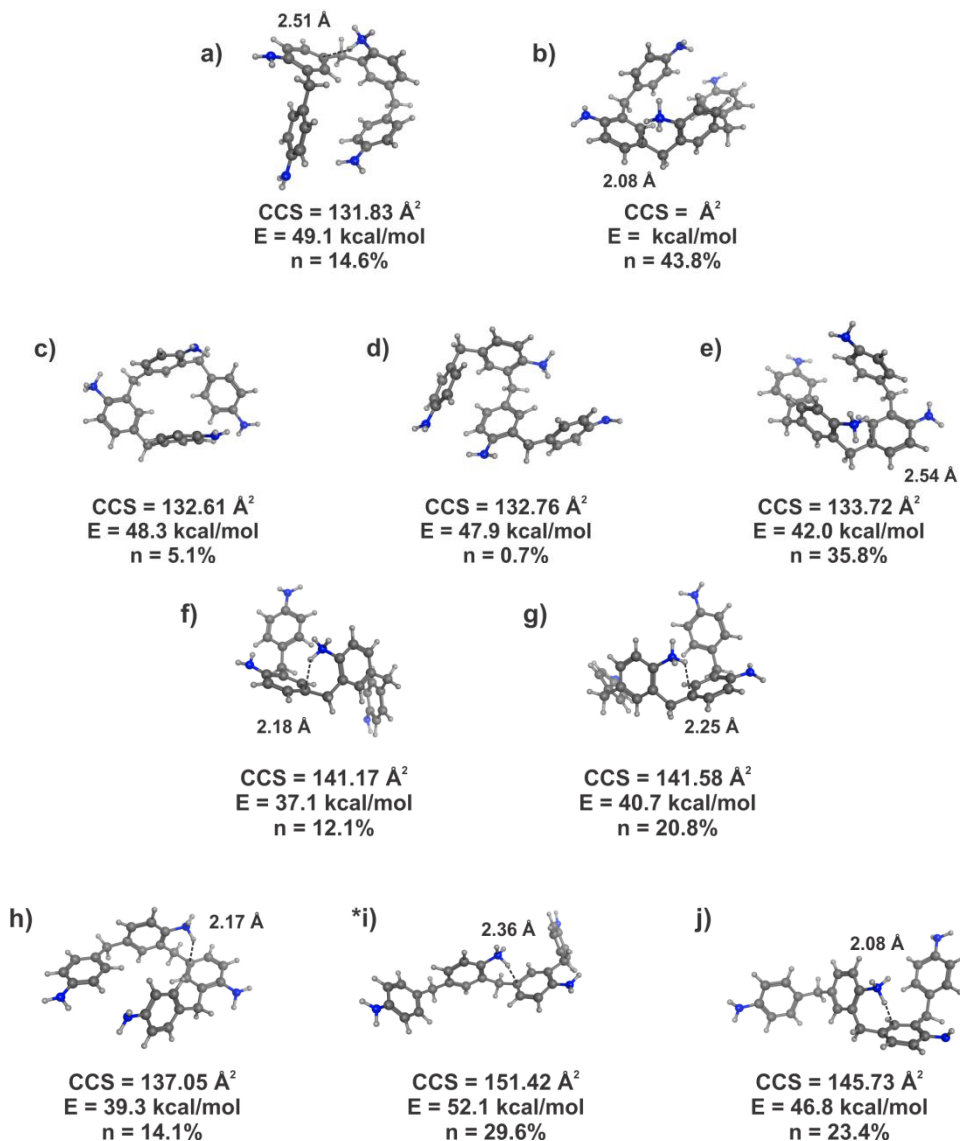


Figure B.24. Representative conformations from clustering analysis of the experimental range (a-e) and the whole conformational space cloud (f-j) of the second ring amine protonated 4-ring MDA generated from the simulated annealing calculation. Carbon atoms are shown in dark grey, hydrogen in light grey, and nitrogen in blue. Distances are labeled to show the proximity of the additional proton to other atoms in the molecule. The asterisk represents the structure shown in the manuscript. The theoretical CCS, relative energy, and percentage of conformations each of these represents from clustering are shown below the conformation.

B.25. Conformational Space Plot 4-Ring MDA

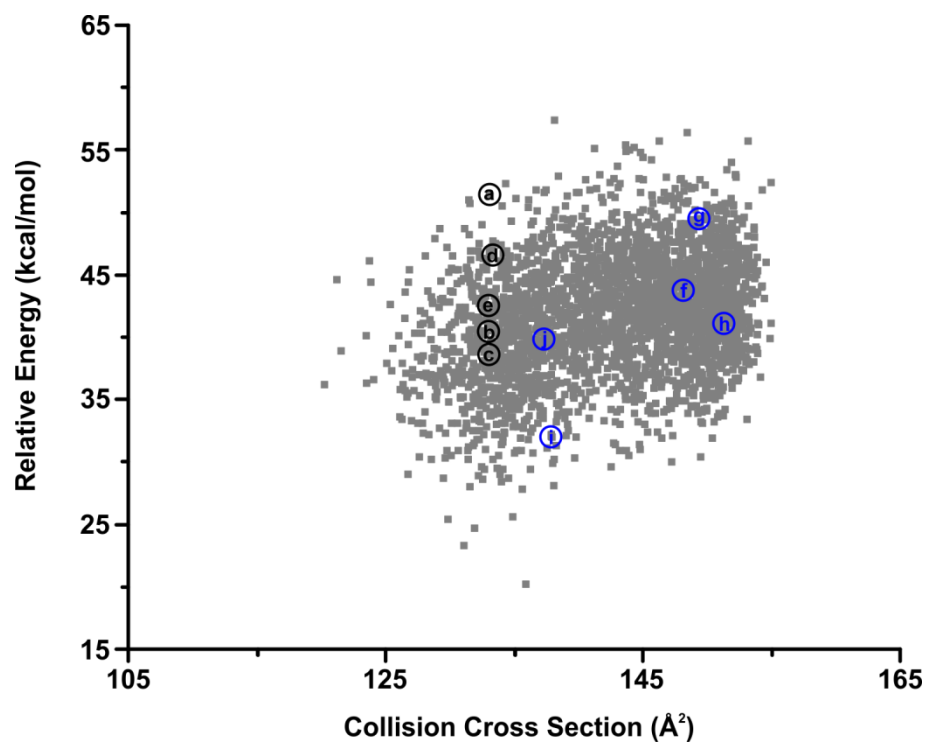


Figure B.25. Conformational space plot for the third ring amine protonated 4-ring MDA. The 3,000 generated conformations are represented in grey; the clustering representative conformations are labeled with letters that correspond to the structures in **Figures B.26-27**. The conformations labeled in black fall within the experimental range and the conformations labeled in blue are representative of conformations from the whole conformational cloud.

B.26. Clustering Analysis 4-Ring MDA

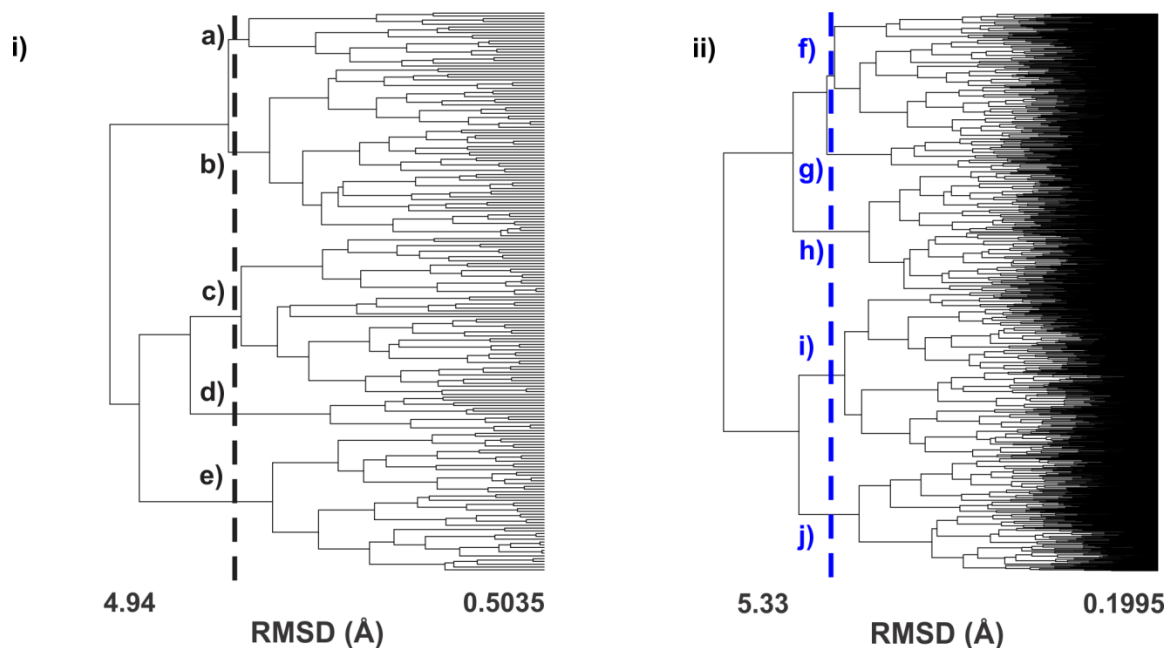


Figure B.26. Clustering analysis of 3,000 conformations of the third ring amine protonated 4-ring MDA. In (i) the conformations that fall within the experimental CCS range are clustered and in (ii) all 3,000 of the conformations are clustered. Clustering is based on root mean square distance of atoms of superimposed structures. The vertical bar indicates the RMSD cutoff (Å) used to select the conformations (circled) for further analysis. The asterisk represents the structures shown in the paper.

B.27. Conformational Structures 4-Ring MDA

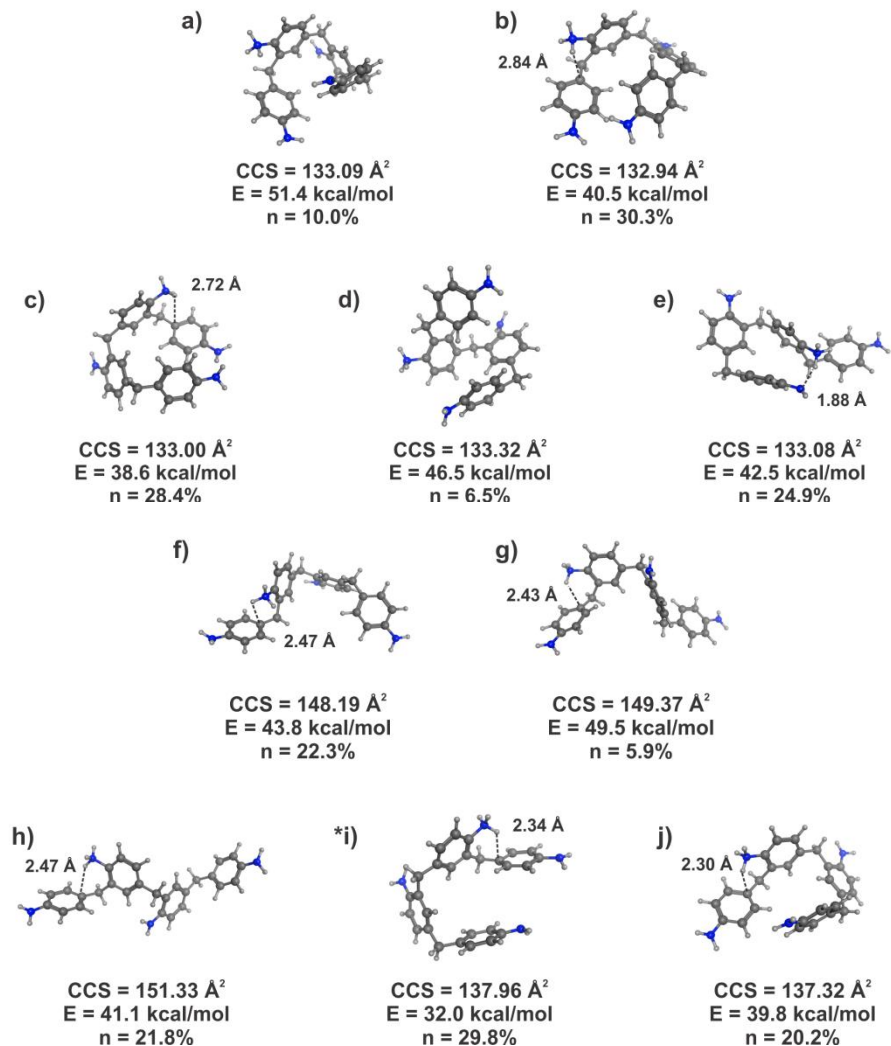


Figure B.27. Representative conformations from clustering analysis of the experimental range (a-e) and the whole conformational space cloud (f-j) of the third ring amine protonated 4-ring MDA generated from the simulated annealing calculation. Carbon atoms are shown in dark grey, hydrogen in light grey, and nitrogen in blue. Distances are labeled to show the proximity of the additional proton to other atoms in the molecule. The asterisk represents the structure shown in the manuscript. The theoretical CCS, relative energy, and percentage of conformations each of these represents from clustering are shown below the conformation.

B.28. Conformational Space Plot 4-Ring MDA

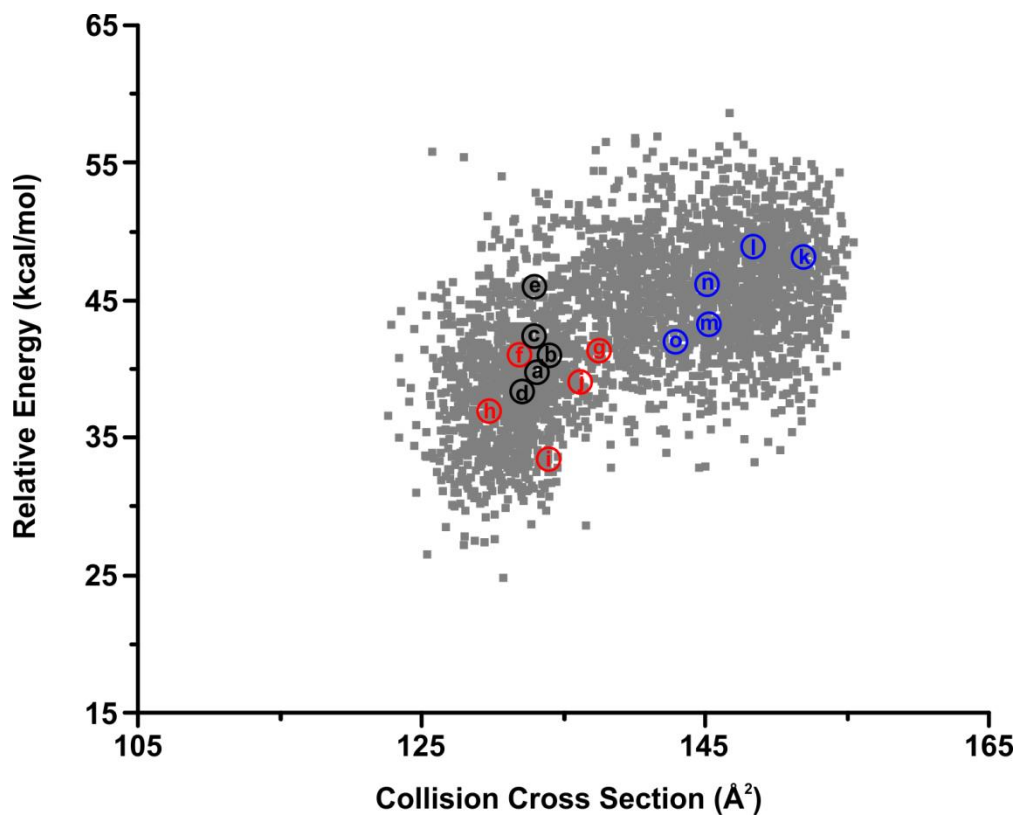


Figure B.28. Conformational space plot for the fourth ring amine protonated 4-ring MDA. The 3,000 generated conformations are represented in grey; the clustering representative conformations are labeled with letters that correspond to the structures in **Figures B.29-31**. The conformations labeled in black fall within the experimental range, the conformations labeled in red are representative of conformations from the left conformational cloud, and the conformations labeled in blue are representative of conformations from the right conformational cloud.

B.29. Clustering Analysis 4-Ring MDA

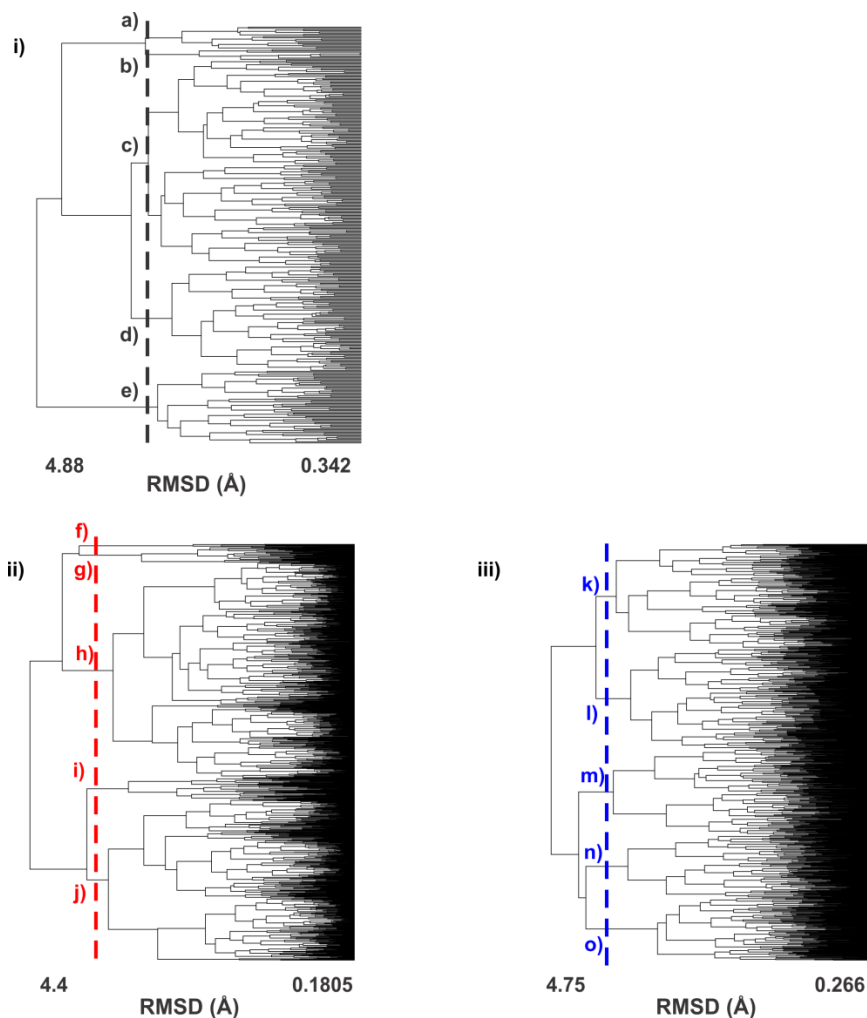


Figure B.29. Clustering analysis of 3,000 conformations of the fourth ring amine protonated 4-ring MDA. In **(i)** the conformations that fall within the experimental CCS range are clustered, in **(ii)** the conformations in the left conformational cloud are clustered, and in **(iii)** the conformations in the right conformational cloud are clustered. Clustering is based on root mean square distance of atoms of superimposed structures. The vertical bars indicate the RMSD cutoff used to select the conformations for further analysis.

B.30. Conformational Structures 4-Ring MDA

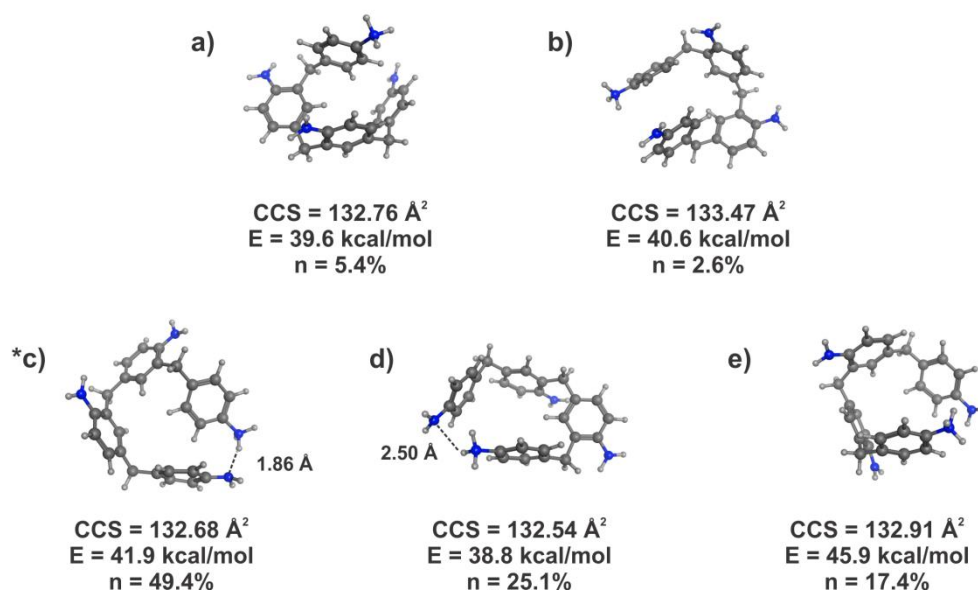


Figure B.30. Representative conformations from clustering analysis of the experimental range region of the fourth ring amine protonated 4-ring MDA generated from the simulated annealing calculation. Carbon atoms are shown in dark grey, hydrogen in light grey, and nitrogen in blue. Distances are labeled to show the proximity of the additional proton to other atoms in the molecule. The asterisk represents the structures shown in the manuscript. The theoretical CCS, relative energy, and percentage of conformations each of these represents from clustering are shown below the conformation.

B.31. Conformational Structures 4-Ring MDA

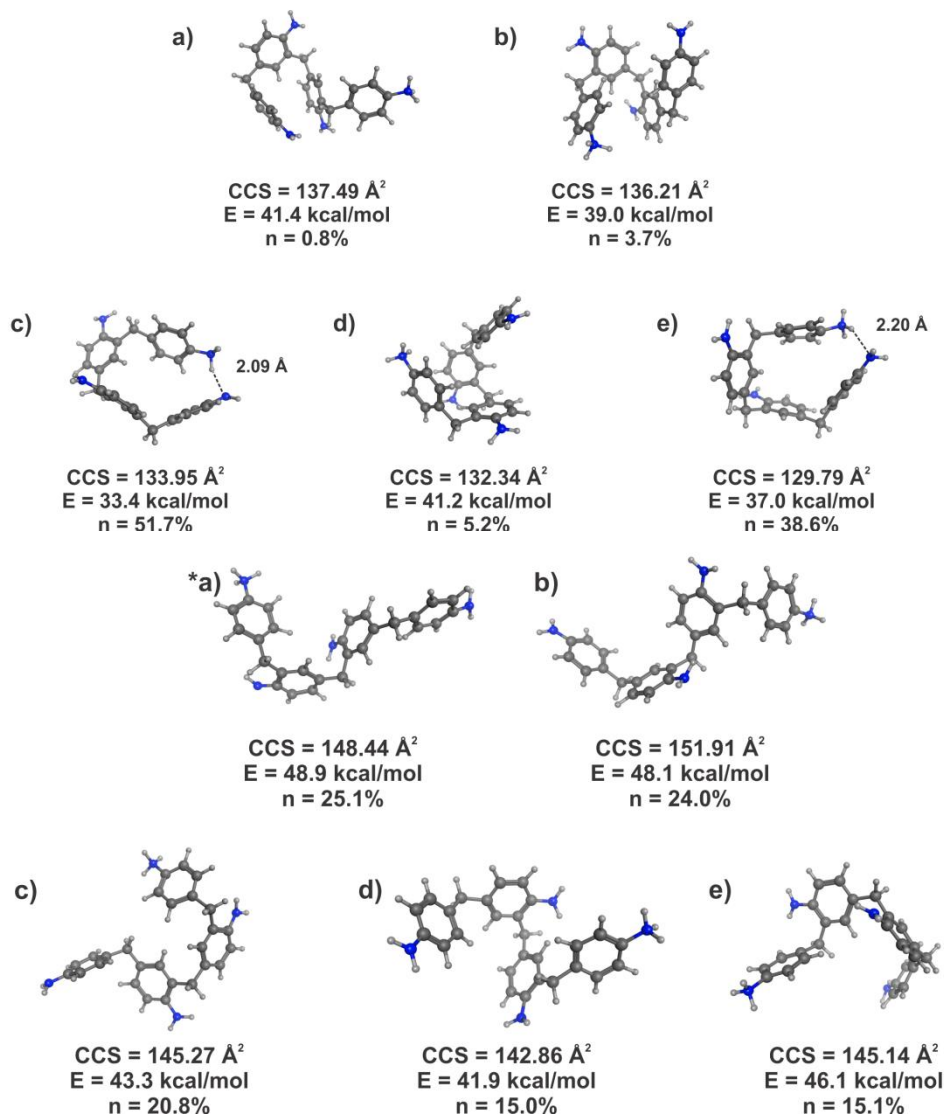


Figure B.31. Representative conformations from clustering analysis of the two conformational space clouds (left cloud (f-j) and right cloud (k-o)) of the first ring amine protonated 4-ring MDA generated from the simulated annealing calculation. Carbon atoms are shown in dark grey, hydrogen in light grey, and nitrogen in blue. Distances are labeled to show the proximity of the additional proton to other atoms in the molecule. The asterisk represents the structures shown in the manuscript. The theoretical CCS, relative energy, and percentage of conformations each of these represents from clustering are shown below the conformation.

APPENDIX C

SUPPORTING INFORMATION FOR CHAPTER III

C.1. 4,4'-MDA MS^3 Spectra

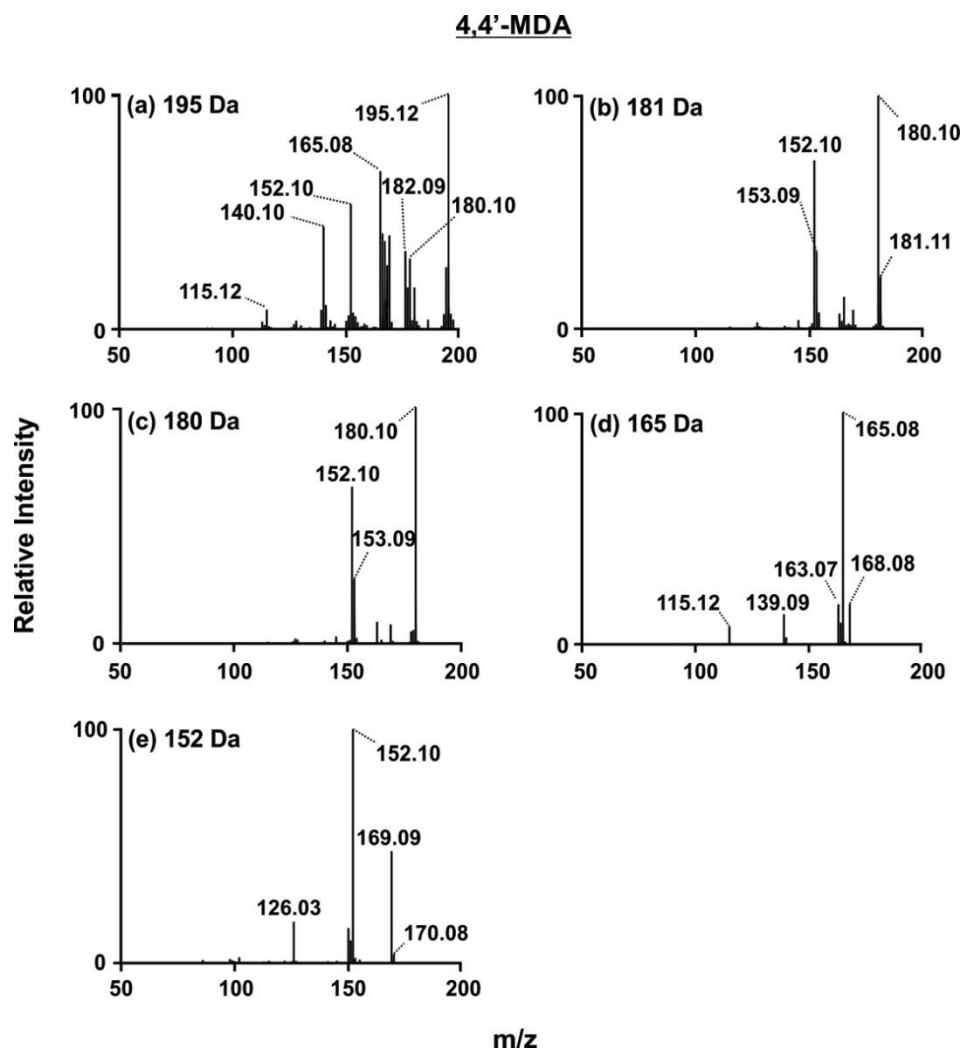


Figure C.1. 4,4'-MDA $[M + H]^+ = 199$ Da parent ion was mass selected then additional major fragment ions were mass selected to acquire MS^3 data. (a) 195 Da, (b) 181 Da, (c) 180 Da, (d) 165 Da, and (e) 152 Da.

C.2. 2,2'-MDA MS³ Spectra

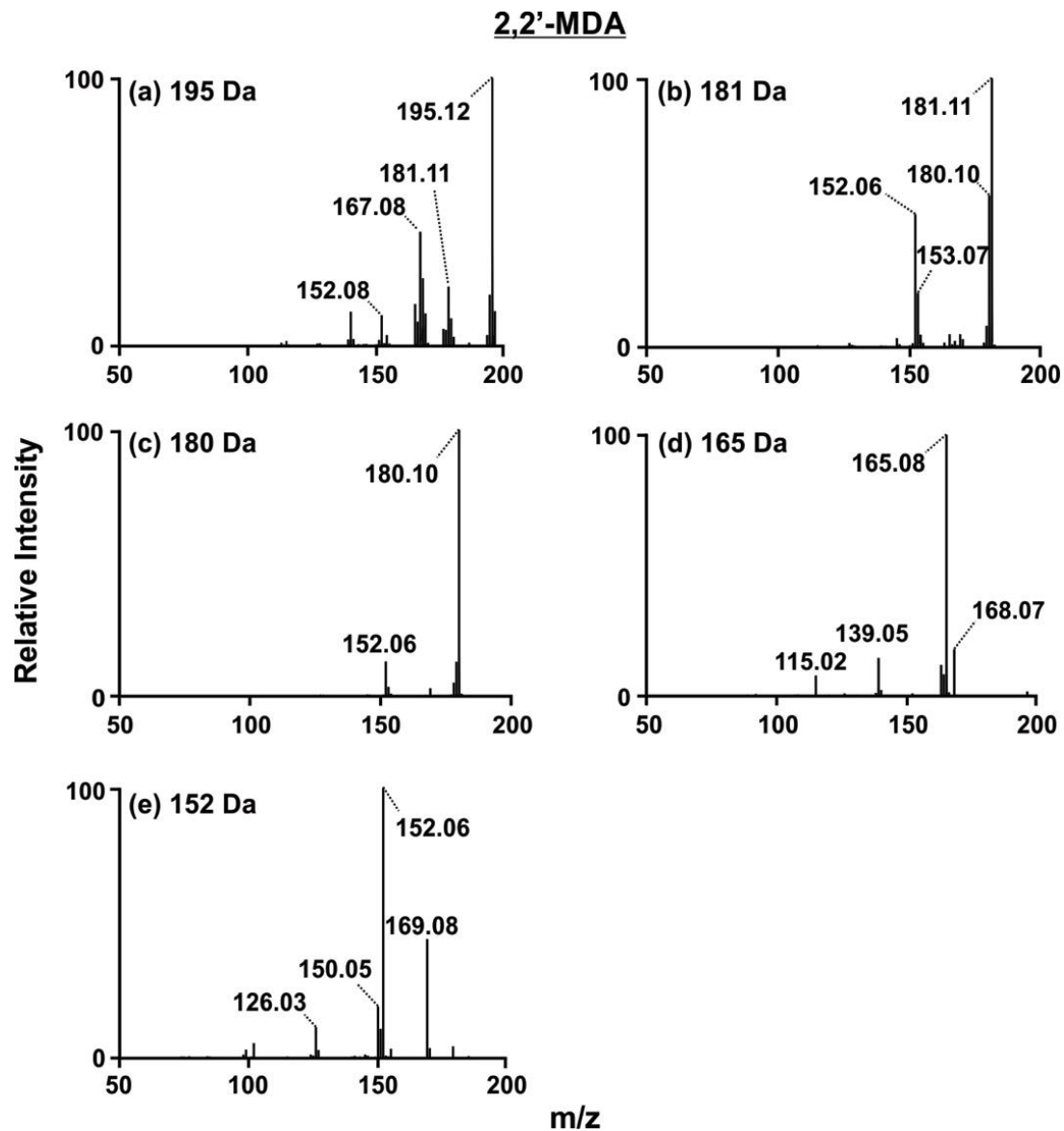


Figure C.2. 2,2'-MDA [M + H]⁺ = 199 Da parent ion was mass selected then additional major fragment ions were mass selected to acquire MS³ data. (a) 195 Da, (b) 181 Da, (c) 180 Da, (d) 165 Da, and (e) 152 Da.

C.3. 2,4'-MDA MS³ Spectra

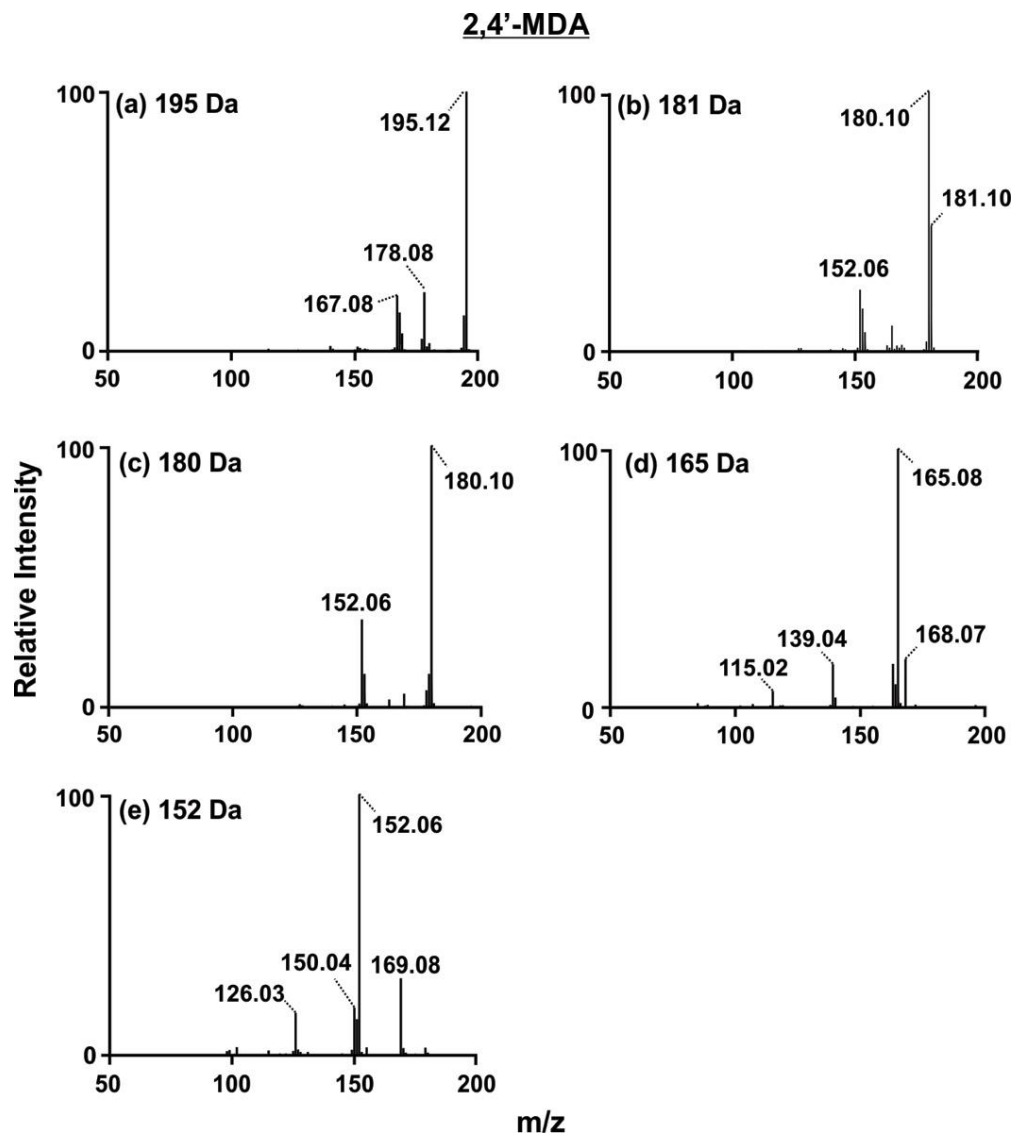


Figure C.3. 2,4'-MDA [M + H]⁺ = 199 Da parent ion was mass selected then additional major fragment ions were mass selected to acquire MS³ data. (a) 195 Da, (b) 181 Da, (c) 180 Da, (d) 165 Da, and (e) 152 Da.

C.4. 2,7'-DAF MS³ Spectra

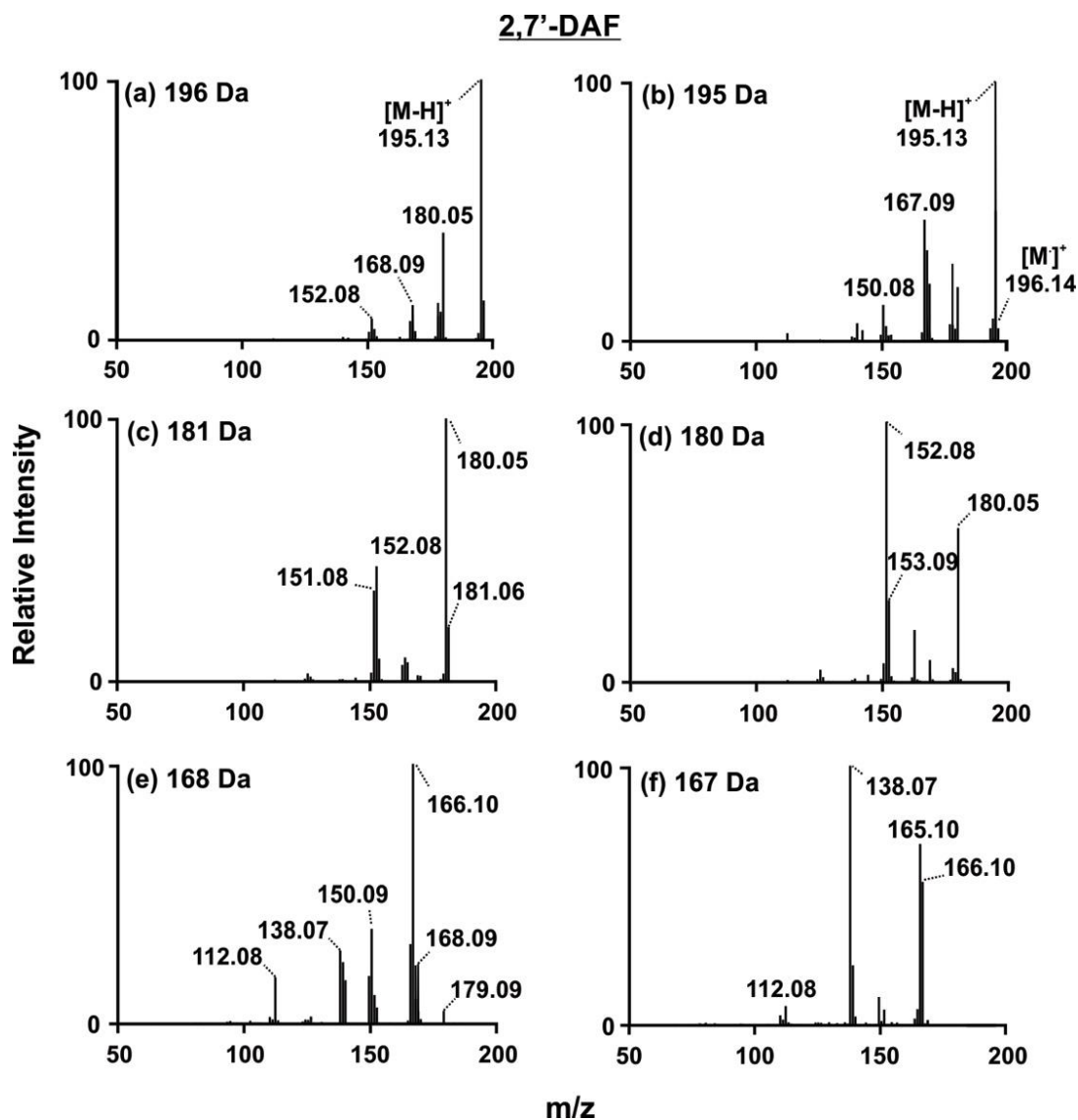


Figure C.4. 2,7'-DAF's $[M + H]^+ = 197$ Da parent ion was mass selected then additional major fragment ions were mass selected to acquire MS³ data. (a) 196 Da = $[M]^+$, (b) 195 Da = $[M - H]^+$, (c) 181 Da, (d) 180 Da, (e) 168 Da, and (f) 167 Da.

C.5. 4,4'-MDA ESI and MALDI Spectra

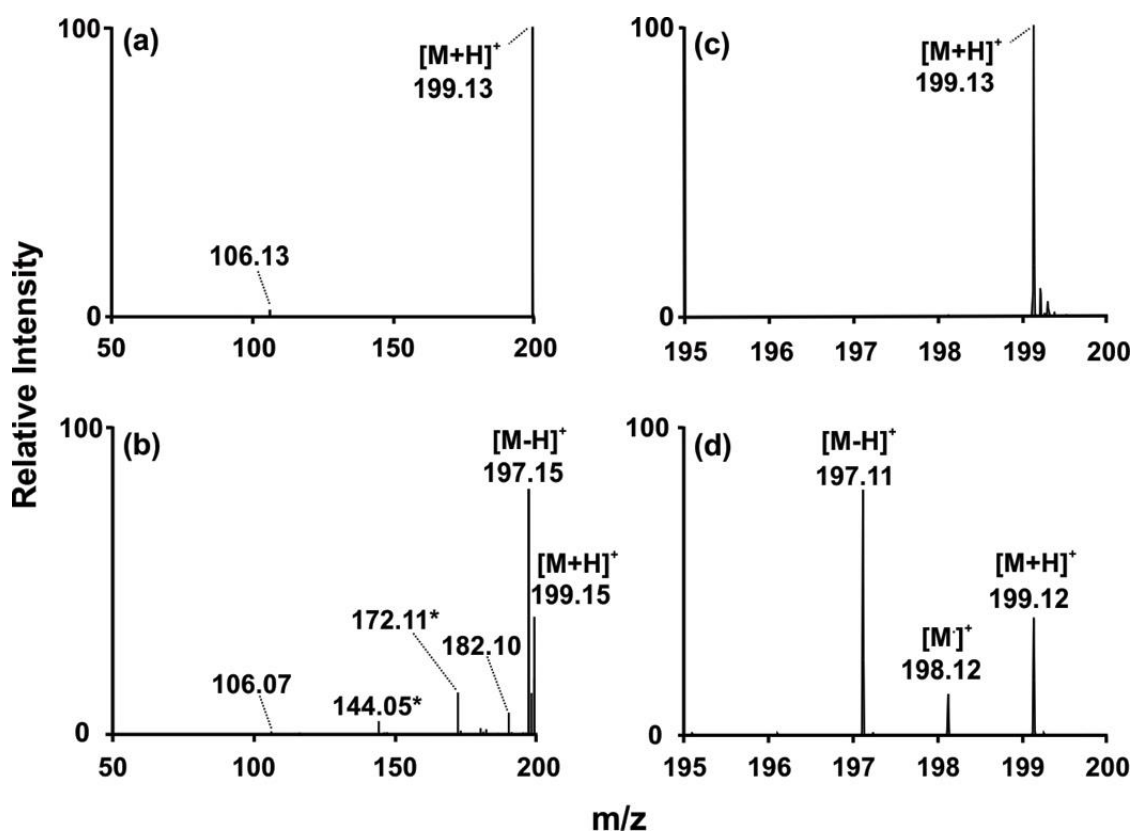


Figure C.5. (Top) Mass spectra of 4,4'-MDA isomer using ESI-TOFMS. (Bottom) Mass spectra of 4,4'-MDA isomer using MALDI-TOFMS. (a) Full ESI mass spectrum and (b) full MALDI mass spectrum of 4,4'-MDA isomer. (c) 195 – 200 m/z ESI mass spectral region and (d) 195 – 200 m/z MALDI mass spectral region of 4,4'-MDA isomer. Parent ions labeled as $[M + H]^+ = 199$ Da, $[M]^+ = 198$ Da, and $[M - H]^+ = 197$ Da. Asterisk (*) notes CHCA matrix peaks.

C.6. 2,4'-MDA ESI and MALDI Spectra

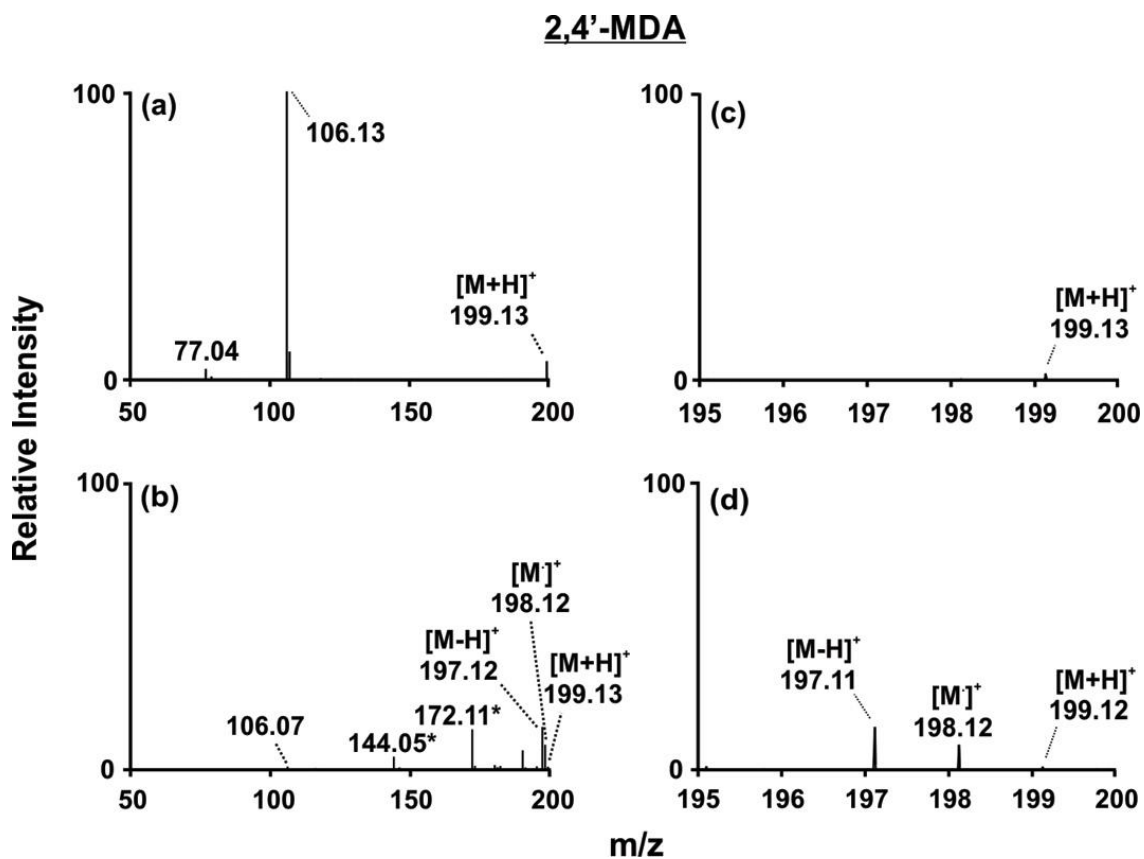


Figure C.6. (Top) Mass spectra of 2,4'-MDA isomer using ESI-TOFMS. (Bottom) Mass spectra of 2,4'-MDA isomer using MALDI-TOFMS. (a) Full ESI mass spectrum and (b) full MALDI mass spectrum of 2,4'-MDA isomer. (c) 195 – 200 m/z ESI mass spectral region and (d) 195 – 200 m/z MALDI mass spectral region of 2,4'-MDA isomer. Parent ions labeled as $[M + H]^+ = 199$ Da, $[M]^+ = 198$ Da, and $[M - H]^+ = 197$ Da. Asterisk (*) notes CHCA matrix peaks.

C.7. 2,2'-MDA ESI and MALDI Spectra

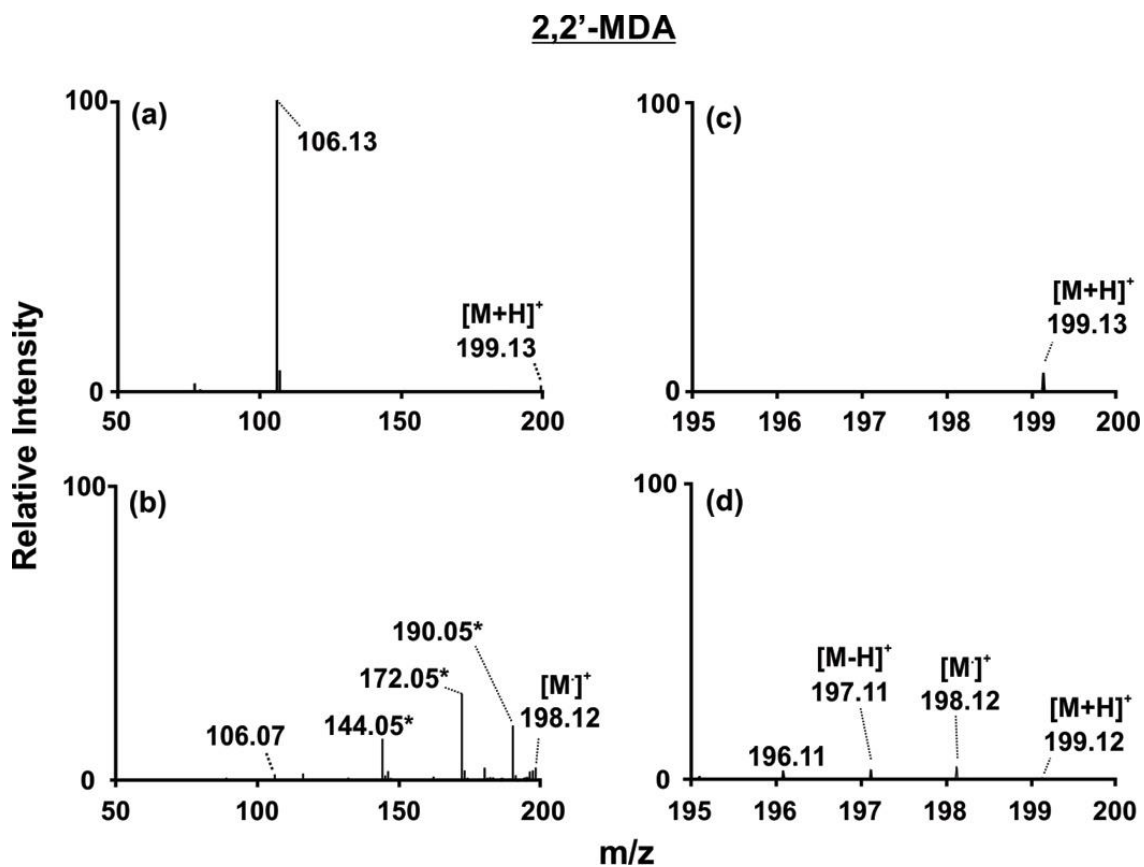


Figure C.7. (Top) Mass spectra of 2,2'-MDA isomer using ESI-TOFMS. (Bottom) Mass spectra of 2,2'-MDA isomer using MALDI-TOFMS. (a) Full ESI mass spectrum and (b) full MALDI mass spectrum of 2,2'-MDA isomer. (c) 195 – 200 m/z ESI mass spectral region and (d) 195 – 200 m/z MALDI mass spectral region of 2,2'-MDA isomer. Parent ions labeled as $[M + H]^+ = 199$ Da, $[M]^+ = 198$ Da, and $[M - H]^+ = 197$ Da. Asterisk (*) notes CHCA matrix peaks.

C.8. 2,7-DAF ESI and MALDI Spectra

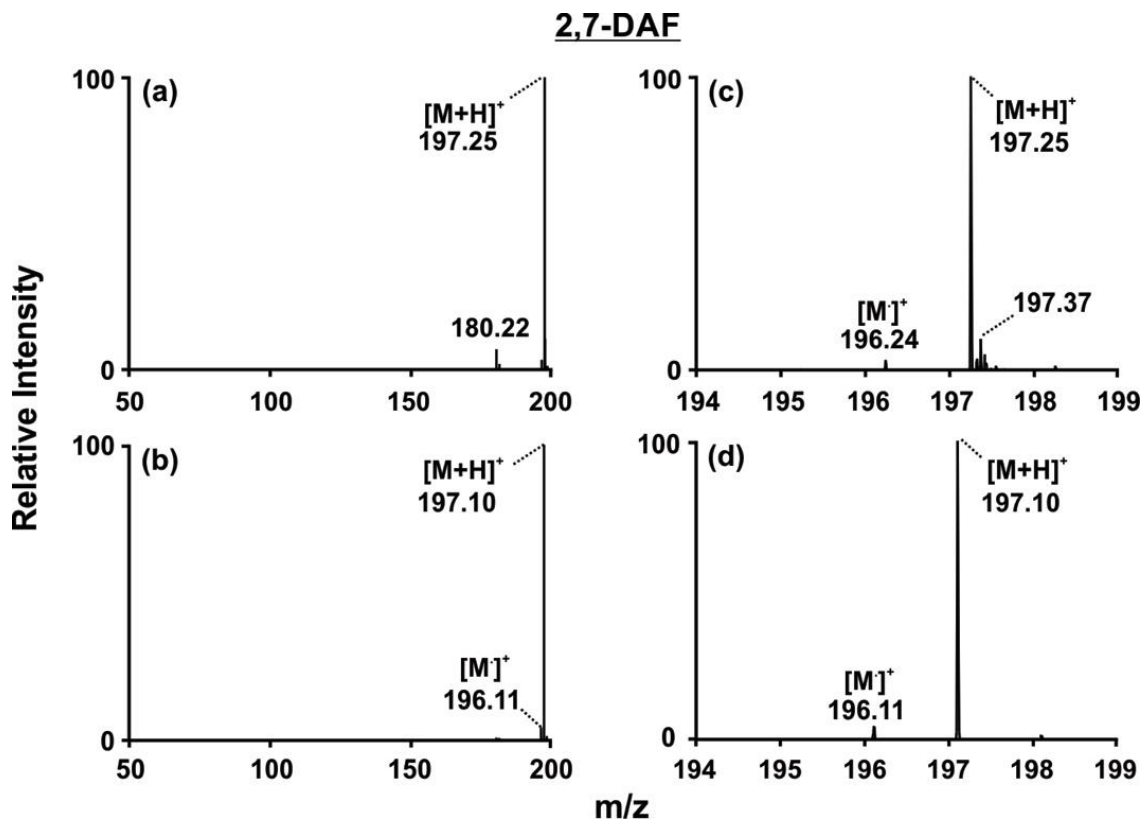


Figure C.8. (Top) Mass spectra of 2,7-DAF using ESI-TOFMS. (Bottom) Mass spectra of 2,7-DAF using MALDI-TOFMS. (a) Full ESI mass spectrum and (b) full MALDI mass spectrum of 2,7-MDA isomer. (c) 194 – 199 m/z ESI mass spectral region and (d) 194 – 199 m/z MALDI mass spectral region of 2,7-MDA isomer. Parent ions labeled as $[M + H]^+ = 197$ Da and $[M]^+ = 196$ Da.

C.9. MS/MS MALDI Spectra

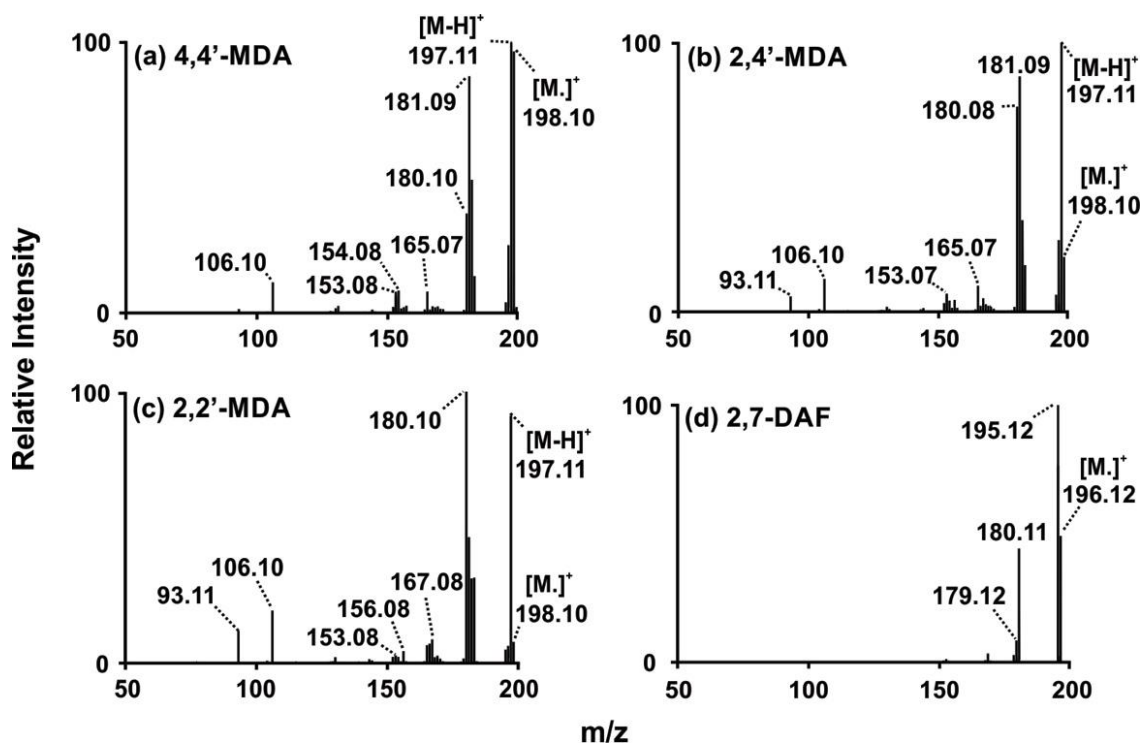


Figure C.9. Tandem MALDI mass spectra of the three 2-Ring MDA [M - H]⁺ species and 2,7-diaminofluorene. The [M]⁺ ions mass selected and fragmented with 25 collision energy. Results are shown for (a) 4,4'-MDA, (b) 2,4'-MDA, (c) 2,2'-MDA, and (d) 2,7-DAF.

C.10. Analysis of Instrument Parameters

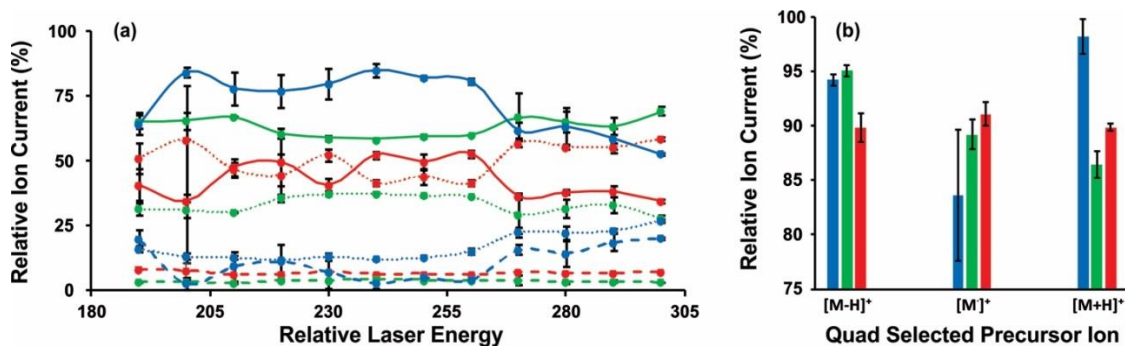


Figure C.10. The effect of (a) laser energy and (b) resolving power of the resolving quadrupole are shown for the three MDA isomers. The color scheme for the ions is as follows: 4,4'-MDA (blue), 2,2'-MDA (red), and 2,4'-MDA (green). A dashed line is used for [M+H]⁺ ions, a dotted line for [M]⁺ ions and a solid line for [M-H]⁺ ions.

Figure C.10.1 Analysis of Instrument Parameters

Experiments were conducted in order to evaluate the influence of the MALDI laser fluence and the resolving power of the MS/MS resolving quadrupole on the resulting intensities of the precursor ions. **Figure 3.2a** traces the relative intensities of the three MDA precursor ions as laser fluence is increased from 190 to 300 arbitrary units. The MS results with no quadrupole selection are shown for 4,4'-MDA (blue traces), 2,4'-MDA (green traces), and 2,2'-MDA (red traces). Ion forms are depicted with different lines types and include the $[M+H]^+$ (dashed line), $[M]^+$ (dotted line), and the $[M-H]^+$ ion (solid line). The average relative ion current across the laser fluence ramp were observed to be 72.2%, 63.2%, and 42.9% for 4,4'-, 2,4'-, and 2,2'-MDA for the $[M-H]^+$ species, respectively, and 10.9%, 3.6%, and 6.8% for the $[M+H]^+$ species. Regardless of laser power, $[M-H]^+$ species are preferentially formed over $[M+H]^+$ ions for all three isomers. The intensity of $[M]^+$ appears to increase with the presence of *ortho* amino groups, as relative ion currents of 16.8%, 33.2%, and 50.3% are obtained for 4,4'-, 2,4'-, and 2,2'-MDA, respectively. Collectively, these observations demonstrate that the laser fluence does not affect the relative intensities of these different ion forms.

Figure 3.2b highlights the capability of the resolving quadrupole to isolate the precursor ions for MS/MS analysis. The bars indicate the percent intensity of the selected ion relative to the intensities of the other two ions, all of which are ± 1 Da apart in nominal mass. The $[M-H]^+$ and $[M+H]^+$ ions can be isolated with typically greater than 90% efficiency from the other two precursor ion species. Although the $[M]^+$ ion falls between the other two species, it can still be separated with about 85% efficiency. This indicates that the precursor ions can be separated with high efficiency. Therefore, the presence of *m/z* values corresponding to the other two precursor ions in MS/MS spectra predominantly results from parent ion fragmentation and not the inability of the quadrupole to resolve these ions.

Figure C.10.2. ANOVA and t-test Details

We conducted an analysis of variance (ANOVA) of the %RIC data for all fragment-ion peaks from a specific parent ion. Using **Table 3.2** (in the manuscript) as an example, ANOVA would test the significance of the differences among the three %RIC values (41.5, 60.7, 42.3) for the 198 mass peak derived from the $[M+H]^+$ parent ion, shown at the top of **Table 3.2**. Each ANOVA was done using a set of 27 measurements from the three MDA oligomers, allowing 26 degrees of freedom for the statistical analysis (2 degrees between oligomers and 24 degrees for variance within the measurements), and a 99+ percent confidence level for a result to be considered as significant. The fragment ions colored in yellow in **Table 3.2** showed a significant difference by ANOVA. A detailed summary of ANOVA is given in **Tables C.1, C.3, C.5** below. ANOVA testing can tell us that the largest and smallest values, 41.5 and 60.7 %RIC, are definitely different for the 198 peak of $[M+H]^+$, but it does not say where the third value (42.3%) lies. In the case of the 198 peak for $[M+H]^+$ in **Table 3.2**, a simple t-test on the average values between the middle value %RIC and the value of its closer neighbor can provide more insight into the difference between 41.5 and 42.3 %RIC. For a two-mean t-test there are 18 measurements in an analysis data set and therefore 16 degrees of freedom, allowing an adequate analysis by the t-test at the 99+% confidence level. There is no difference between 41.5 and 42.3%. The pairs of values for which the t-tests showed significant differences are colored pink in **Table 3.2**. The t-test results are also shown in **Tables 3.2, 3.4, 3.6** below. The results of ANOVA and t-tests identify the differences within each data set (fragment ion peak) and will be helpful in establishing differences in fragmentation mechanisms among the MDA oligomers.

Table C.1. ANOVA for MDA Fragments

| Analysis of Variance | | | | |
|---|---------|-----|-------------|--------|
| F-critical for 2,24 DoF @ 99% Confidence Level = 5.61 | | | | |
| Mass 198 Fragment | | | | |
| Sum of Squares | | DoF | Mean Square | F-test |
| Between | 2107 | 2 | 1053.51 | --- |
| Within | 1264 | 24 | 52.68 | --- |
| Total | 3371 | 26 | --- | 20.00 |
| Mass 183 Fragment | | | | |
| Sum of Squares | | DoF | Mean Square | F-test |
| Between | 137.6 | 2 | 68.80 | --- |
| Within | 153.6 | 24 | 6.40 | --- |
| Total | 291.2 | 26 | --- | 10.75 |
| Mass 182 Fragment | | | | |
| Sum of Squares | | DoF | Mean Square | F-test |
| Between | 227.2 | 2 | 113.58 | --- |
| Within | 102.8 | 24 | 4.28 | --- |
| Total | 330 | 26 | --- | 26.54 |
| Mass 181 Fragment | | | | |
| Sum of Squares | | DoF | Mean Square | F-test |
| Between | 1665 | 2 | 832.5 | --- |
| Within | 61.52 | 24 | 2.56 | --- |
| Total | 1726.52 | 26 | --- | 325.23 |
| Mass 106 Fragment | | | | |
| Sum of Squares | | DoF | Mean Square | F-test |
| Between | 2642 | 2 | 1321 | --- |
| Within | 1098 | 24 | 45.75 | --- |
| Total | 3740 | 26 | --- | 28.87 |

Table C.1. Statistical Analysis of MDA Fragmentation Reactions: $[M + H]^+$ Fragmentation

Table C.2. The t-test of Means for MDA Fragments

| Fragment Mass | Compared Species | t-Calculated | t-Critical | Result |
|----------------------|-------------------------|---------------------|-------------------|-----------------|
| 198 | 4,4' and 2,2' | 0.195 | 2.92 | Not Significant |
| 183 | 4,4' and 2,2' | 0.348 | 2.92 | Not Significant |
| 182 | 4,4' and 2,4' | 0.195 | 2.92 | Not Significant |
| 181 | 4,4' and 2,4' | 6.70 | 2.92 | Significant |
| 106 | 2,2' and 2,4' | 3.087 | 2.92 | Significant |

Table C.2. Analysis Using t-test of Means for $[M + H]^+$ Fragmentation

Table C.3. Statistical Analysis of MDA Fragmentation Reactions: $[M - H]^+$ Fragmentation

| Analysis of Variance | | | | |
|---|--------|-----|-------------|--------|
| F-critical for 2,24 DoF @ 99% Confidence Level = 5.61 | | | | |
| Mass 198 Fragment | | | | |
| Sum of Squares | | DoF | Mean Square | F-test |
| Between | 2107 | 2 | 1053.51 | --- |
| Within | 1264 | 24 | 52.68 | --- |
| Total | 3371 | 26 | --- | 20.00 |
| Mass 182 Fragment | | | | |
| Sum of Squares | | DoF | Mean Square | F-test |
| Between | 335.4 | 2 | 167.7 | --- |
| Within | 37.17 | 24 | 1.55 | --- |
| Total | 372.6 | 26 | --- | 108.2 |
| Mass 181 Fragment | | | | |
| Sum of Squares | | DoF | Mean Square | F-test |
| Between | 1334 | 2 | 666.91 | --- |
| Within | 436.6 | 24 | 18.19 | --- |
| Total | 1770.6 | 26 | --- | 36.6 |
| Mass 180 Fragment | | | | |
| Sum of Squares | | DoF | Mean Square | F-test |
| Between | 6216.3 | 2 | 3108 | --- |
| Within | 209.6 | 24 | 8.73 | --- |
| Total | 6425.9 | 26 | --- | 356.0 |

Table C.3. Statistical Analysis of MDA Fragmentation Reactions: $[M - H]^+$ Fragmentation

Table C.4. Analysis Using t-test of Means for [M-H]⁺ Fragmentation

| Fragment Mass | Compared Species | t-Calculated | t-Critical | Result |
|----------------------|-------------------------|---------------------|-------------------|------------------|
| 196 | 2,2' and 2,4' | 12.15 | 2.92 | Very Significant |
| 182 | 2,2' and 2,4' | 5.30 | 2.92 | Significant |
| 181 | 2,2' and 2,4' | 16.10 | 2.92 | Very Significant |
| 180 | 4,4' and 2,4' | 11.60 | 2.92 | Very Significant |

Table C.4. Analysis Using t-test of Means for [M-H]⁺ Fragmentation

Table C.5. Statistical Analysis of MDA Fragmentation Reactions: $[M]^+$ Fragmentation

| Analysis of Variance | | | | |
|--|----------------|------------|--------------------|---------------|
| F-critical for 2,24 DoF @ 99% Confidence Level = 5.61 | | | | |
| Mass 197 Fragment | | | | |
| Sum of Squares | | DoF | Mean Square | F-test |
| Between | 5425.6 | 2 | 2712.8 | --- |
| Within | 115.82 | 24 | 4.83 | --- |
| Total | 5541.4 | 26 | --- | 561.7 |
| Mass 183 Fragment | | | | |
| Sum of Squares | | DoF | Mean Square | F-test |
| Between | 503.97 | 2 | 251.99 | --- |
| Within | 73.85 | 24 | 3.08 | --- |
| Total | 577.83 | 26 | --- | 81.81 |
| Mass 182 Fragment | | | | |
| Sum of Squares | | DoF | Mean Square | F-test |
| Between | 457.21 | 2 | 228.6 | --- |
| Within | 45.86 | 24 | 1.91 | --- |
| Total | 503.07 | 26 | --- | 119.7 |
| Mass 181 Fragment | | | | |
| Sum of Squares | | DoF | Mean Square | F-test |
| Between | 1110 | 2 | 554.98 | --- |
| Within | 65.15 | 24 | 2.71 | --- |
| Total | 1175.15 | 26 | --- | 204.8 |
| Mass 180 Fragment | | | | |
| Sum of Squares | | DoF | Mean Square | F-test |
| Between | 993.36 | 2 | 496.68 | --- |
| Within | 12.98 | 24 | 0.54 | --- |
| Total | 1006.3 | 26 | --- | 919.8 |
| Mass of 106 Fragment | | | | |
| Sum of Squares | | DoF | Mean Square | F-test |
| Between | 202.43 | 2 | 101.2 | --- |
| Within | 58.96 | 24 | 2.46 | --- |
| Total | 261.4 | 26 | --- | 41.5 |

Table C.5. Statistical Analysis of MDA Fragmentation Reactions: $[M]^+$ Fragmentation

Table C.6. Analysis Using t-test of Means for [M]⁺ Fragmentation

| Fragment Mass | Compared Species | t-Calculated | t-Critical | Result |
|---------------|------------------|--------------|------------|------------------|
| 183 | 4,4' and 2,4' | 2.80 | 2.92 | Not Significant |
| 182 | 4,4' and 2,4' | 5.78 | 2.92 | Significant |
| 180 | 2,2' and 2,4' | 10.43 | 2.92 | Very Significant |
| 106 | 4,4' and 2,4' | 11.60 | 2.92 | Very Significant |
| 106 | 2,2' and 2,4' | 1.89 | 2.92 | Not Significant |
| 106 | 4,4' and 2,4' | 6.70 | 2.92 | Significant |

Table C.6. Analysis Using t-test of Means for [M]⁺ Fragmentation

Table C.7. Total percent ion current for the three 2,2'-MDA ion species.

| Fragment Ion | 0-10 CE | | | 15-30 CE | | | 35-50 CE | | |
|--------------|--------------------|------------------|--------------------|--------------------|------------------|--------------------|--------------------|------------------|--------------------|
| | [M-H] ⁺ | [M] ⁺ | [M+H] ⁺ | [M-H] ⁺ | [M] ⁺ | [M+H] ⁺ | [M-H] ⁺ | [M] ⁺ | [M+H] ⁺ |
| 198 | | | 40.6 ± 3.1% | | | 34.5 ± 13.6% | | | 2.9 ± 2.5% |
| 197 | | 28.3 ± 2.1% | 1.4 ± 1.0% | | 22.0 ± 14.4% | 2.2 ± 1.3% | | 2.6 ± 1.7% | 2.3 ± 0.7% |
| 196 | 1.3 ± 0.7% | 0.2 ± 0.1% | 0.2 ± 0.1% | 5.9 ± 3.1% | 4.4 ± 5.9% | 1.4 ± 1.2% | 3.1 ± 1.3% | 2.2 ± 0.3% | 5.9 ± 0.6% |
| 195 | 0.6 ± 0.2% | 0.1 ± 0.1% | 0.0 ± 0.0% | 3.6 ± 2.2% | 1.0 ± 1.2% | 0.1 ± 0.0% | 7.7 ± 0.8% | 5.3 ± 0.5% | 0.4 ± 0.2% |
| 183 | 1.8 ± 0.7% | 13.7 ± 1.7% | 10.2 ± 3.6% | 2.1 ± 1.1% | 25.5 ± 26.9% | 10.7 ± 1.7% | 0.3 ± 0.2% | 1.4 ± 0.7% | 6.1 ± 1.6% |
| 182 | 1.5 ± 0.2% | 9.3 ± 0.4% | 15.9 ± 1.3% | 5.1 ± 1.6% | 7.6 ± 3.7% | 10.4 ± 1.1% | 3.6 ± 1.3% | 6.6 ± 1.5% | 8.0 ± 0.8% |
| 181 | 4.3 ± 1.1% | 20.1 ± 2.2% | 21.3 ± 2.5% | 7.5 ± 1.1% | 11.2 ± 5.9% | 29.2 ± 8.0% | 8.0 ± 0.7% | 10.4 ± 0.9% | 32.5 ± 6.0% |
| 180 | 87.9 ± 1.9% | 17.2 ± 1.0% | 1.3 ± 0.6% | 68.0 ± 11.0% | 19.1 ± 11.0% | 1.6 ± 0.8% | 36.1 ± 10.0% | 31.8 ± 3.9% | 6.4 ± 1.4% |
| 170 | 0.2 ± 0.2% | 0.2 ± 0.1% | 0.6 ± 0.1% | 0.4 ± 0.1% | 0.3 ± 0.2% | 0.7 ± 0.1% | 0.8 ± 0.4% | 0.5 ± 0.1% | 1.2 ± 0.4% |
| 169 | 0.1 ± 0.0% | 0.6 ± 0.1% | 0.3 ± 0.2% | 0.6 ± 0.4% | 0.6 ± 0.3% | 0.6 ± 0.3% | 2.7 ± 1.2% | 1.4 ± 0.5% | 1.7 ± 0.4% |
| 168 | 0.2 ± 0.1% | 0.1 ± 0.1% | 0.4 ± 0.1% | 1.0 ± 0.6% | 0.4 ± 0.4% | 2.0 ± 1.6% | 3.9 ± 0.9% | 2.8 ± 1.6% | 5.5 ± 0.8% |
| 165 | 0.0 ± 0.0% | 0.2 ± 0.0% | 0.1 ± 0.1% | 0.3 ± 0.3% | 1.2 ± 1.3% | 0.3 ± 0.2% | 1.1 ± 0.2% | 4.3 ± 0.4% | 1.4 ± 0.5% |
| 153 | 0.1 ± 0.1% | 0.1 ± 0.0% | 0.1 ± 0.1% | 1.3 ± 0.9% | 0.8 ± 1.0% | 0.9 ± 0.9% | 4.5 ± 0.9% | 5.0 ± 1.7% | 12.7 ± 5.0% |
| 152 | 0.1 ± 0.1% | 0.0 ± 0.0% | 0.1 ± 0.1% | 2.2 ± 2.2% | 0.6 ± 0.9% | 0.3 ± 0.3% | 20.3 ± 6.2% | 13.6 ± 6.0% | 4.0 ± 1.7% |
| 141 | 0.0 ± 0.0% | 0.0 ± 0.1% | 0.1 ± 0.1% | 0.1 ± 0.0% | 0.1 ± 0.1% | 0.1 ± 0.1% | 0.6 ± 0.3% | 0.6 ± 0.5% | 1.2 ± 0.4% |
| 139 | 0.0 ± 0.0% | 0.0 ± 0.0% | 0.0 ± 0.0% | 0.0 ± 0.1% | 0.1 ± 0.1% | 0.1 ± 0.0% | 1.1 ± 0.7% | 1.8 ± 0.9% | 0.8 ± 0.5% |
| 130 | 0.1 ± 0.0% | 0.2 ± 0.0% | 0.2 ± 0.1% | 0.6 ± 0.4% | 0.4 ± 0.4% | 0.5 ± 0.3% | 1.9 ± 0.5% | 2.0 ± 0.4% | 1.5 ± 0.3% |
| 128 | 0.0 ± 0.0% | 0.0 ± 0.0% | 0.1 ± 0.1% | 0.2 ± 0.1% | 0.1 ± 0.1% | 0.2 ± 0.2% | 1.7 ± 0.6% | 1.4 ± 0.6% | 1.9 ± 0.8% |
| 115 | 0.0 ± 0.0% | 0.0 ± 0.0% | 0.1 ± 0.1% | 0.1 ± 0.1% | 0.1 ± 0.1% | 0.1 ± 0.1% | 1.2 ± 0.7% | 1.5 ± 0.7% | 0.9 ± 0.3% |
| 106 | 1.6 ± 0.3% | 9.2 ± 1.5% | 7.0 ± 1.4% | 1.1 ± 0.2% | 4.4 ± 2.0% | 3.8 ± 0.4% | 0.9 ± 0.1% | 4.2 ± 0.6% | 2.5 ± 0.6% |
| 89 | 0.0 ± 0.0% | 0.0 ± 0.0% | 0.0 ± 0.1% | 0.0 ± 0.0% | 0.0 ± 0.0% | 0.0 ± 0.0% | 0.2 ± 0.1% | 0.2 ± 0.2% | 0.2 ± 0.1% |
| 77 | 0.1 ± 0.0% | 0.3 ± 0.1% | 0.3 ± 0.1% | 0.1 ± 0.0% | 0.1 ± 0.1% | 0.2 ± 0.1% | 0.2 ± 0.1% | 0.3 ± 0.1% | 0.2 ± 0.1% |

Table C.7. Total percent ion current for the three 2,2'-MDA ion species.

Table C.8. Total percent ion current for the three 2,4'-MDA ion species.

| Fragment Ion | 0-10 CE | | | 15-30 CE | | | 35-50 CE | | |
|--------------|--------------------|------------------|--------------------|--------------------|------------------|--------------------|--------------------|------------------|--------------------|
| | [M-H] ⁻ | [M] ⁻ | [M+H] ⁺ | [M-H] ⁻ | [M] ⁻ | [M+H] ⁺ | [M-H] ⁻ | [M] ⁻ | [M+H] ⁺ |
| 198 | | | 59.7 ± 2.8% | | | 43.1 ± 17.5% | | | 4.1 ± 3.3% |
| 197 | | 50.2 ± 2.0% | 2.0 ± 1.1% | | 33.9 ± 13.6% | 3.9 ± 2.5% | | 2.9 ± 2.2% | 4.9 ± 1.5% |
| 196 | 5.9 ± 0.4% | 0.7 ± 0.2% | 0.2 ± 0.1% | 5.5 ± 1.3% | 4.5 ± 2.6% | 1.6 ± 1.5% | 1.5 ± 0.7% | 7.0 ± 1.9% | 7.5 ± 2.0% |
| 195 | 7.4 ± 0.9% | 0.2 ± 0.1% | 0.0 ± 0.0% | 14.2 ± 5.0% | 1.4 ± 1.2% | 0.1 ± 0.1% | 17.7 ± 3.3% | 6.2 ± 0.8% | 0.5 ± 0.2% |
| 183 | 1.5 ± 0.3% | 6.3 ± 0.7% | 15.1 ± 1.1% | 0.6 ± 0.3% | 4.6 ± 1.4% | 10.6 ± 3.4% | 0.1 ± 0.1% | 1.0 ± 0.5% | 3.8 ± 1.4% |
| 182 | 5.9 ± 0.3% | 14.8 ± 0.8% | 9.1 ± 1.2% | 7.5 ± 0.9% | 10.7 ± 3.2% | 15.1 ± 3.8% | 2.6 ± 1.0% | 4.4 ± 0.8% | 10.2 ± 2.9% |
| 181 | 10.1 ± 0.4% | 11.7 ± 1.3% | 6.5 ± 0.6% | 9.5 ± 1.9% | 18.6 ± 3.1% | 17.0 ± 10.3% | 5.9 ± 0.7% | 14.5 ± 3.2% | 31.0 ± 2.9% |
| 180 | 61.5 ± 2.7% | 6.5 ± 0.3% | 0.5 ± 0.3% | 52.8 ± 6.4% | 16.2 ± 7.9% | 1.3 ± 0.9% | 30.8 ± 5.2% | 25.4 ± 3.2% | 4.7 ± 0.8% |
| 170 | 0.9 ± 0.2% | 0.1 ± 0.0% | 0.3 ± 0.1% | 0.6 ± 0.2% | 0.3 ± 0.1% | 0.4 ± 0.1% | 0.5 ± 0.2% | 0.8 ± 0.3% | 1.2 ± 0.4% |
| 169 | 0.3 ± 0.1% | 0.3 ± 0.1% | 0.2 ± 0.1% | 0.3 ± 0.1% | 0.5 ± 0.1% | 0.6 ± 0.3% | 2.1 ± 1.2% | 1.2 ± 0.3% | 2.3 ± 0.7% |
| 168 | 1.2 ± 0.1% | 0.2 ± 0.1% | 0.2 ± 0.3% | 1.2 ± 0.1% | 0.5 ± 0.3% | 1.0 ± 0.8% | 2.9 ± 0.7% | 2.7 ± 0.9% | 3.5 ± 0.7% |
| 165 | 0.2 ± 0.1% | 0.3 ± 0.1% | 0.1 ± 0.1% | 0.3 ± 0.2% | 2.1 ± 1.6% | 0.5 ± 0.3% | 0.9 ± 0.1% | 4.6 ± 0.4% | 2.0 ± 0.5% |
| 153 | 1.0 ± 0.2% | 0.1 ± 0.0% | 0.1 ± 0.1% | 2.4 ± 1.3% | 1.3 ± 1.3% | 1.0 ± 1.0% | 4.3 ± 0.1% | 8.6 ± 2.1% | 12.5 ± 4.2% |
| 152 | 0.9 ± 0.2% | 0.1 ± 0.0% | 0.0 ± 0.0% | 3.1 ± 3.0% | 0.8 ± 0.9% | 0.3 ± 0.3% | 22.5 ± 6.2% | 11.5 ± 4.9% | 3.5 ± 1.6% |
| 141 | 0.0 ± 0.0% | 0.0 ± 0.0% | 0.0 ± 0.0% | 0.1 ± 0.0% | 0.1 ± 0.1% | 0.1 ± 0.1% | 0.4 ± 0.2% | 0.5 ± 0.1% | 0.8 ± 0.5% |
| 139 | 0.0 ± 0.0% | 0.0 ± 0.0% | 0.0 ± 0.0% | 0.0 ± 0.0% | 0.1 ± 0.1% | 0.0 ± 0.0% | 1.0 ± 0.7% | 1.0 ± 0.6% | 0.6 ± 0.4% |
| 130 | 0.6 ± 0.1% | 0.1 ± 0.0% | 0.2 ± 0.1% | 0.9 ± 0.4% | 0.4 ± 0.3% | 0.4 ± 0.3% | 2.7 ± 0.5% | 1.6 ± 0.3% | 1.3 ± 0.2% |
| 128 | 0.2 ± 0.1% | 0.1 ± 0.0% | 0.1 ± 0.1% | 0.3 ± 0.2% | 0.1 ± 0.1% | 0.2 ± 0.2% | 1.7 ± 0.6% | 1.5 ± 0.7% | 1.9 ± 0.7% |
| 115 | 0.1 ± 0.1% | 0.0 ± 0.0% | 0.0 ± 0.0% | 0.1 ± 0.1% | 0.1 ± 0.1% | 0.1 ± 0.1% | 1.5 ± 0.8% | 1.2 ± 0.6% | 1.0 ± 0.5% |
| 106 | 2.2 ± 0.7% | 7.9 ± 1.3% | 5.2 ± 0.9% | 0.4 ± 0.2% | 3.6 ± 0.6% | 2.7 ± 0.3% | 0.6 ± 0.1% | 3.0 ± 0.3% | 2.5 ± 0.5% |
| 89 | 0.0 ± 0.1% | 0.0 ± 0.0% | 0.0 ± 0.0% | 0.0 ± 0.0% | 0.0 ± 0.0% | 0.0 ± 0.0% | 0.2 ± 0.1% | 0.2 ± 0.1% | 0.2 ± 0.1% |
| 77 | 0.1 ± 0.0% | 0.2 ± 0.2% | 0.2 ± 0.1% | 0.0 ± 0.0% | 0.1 ± 0.0% | 0.1 ± 0.0% | 0.0 ± 0.0% | 0.1 ± 0.0% | 0.2 ± 0.1% |

Table C.8. Total percent ion current for the three 2,4'-MDA ion species.

Table C.9. Total percent ion current for the three 4,4'-MDA ion species.

| Fragment Ion | 0-10 CE | | | 15-30 CE | | | 35-50 CE | | |
|--------------|--------------------|------------------|--------------------|--------------------|------------------|--------------------|--------------------|------------------|--------------------|
| | [M-H] ⁺ | [M] ⁺ | [M+H] ⁺ | [M-H] ⁺ | [M] ⁺ | [M+H] ⁺ | [M-H] ⁺ | [M] ⁺ | [M+H] ⁺ |
| 198 | | | 40.6 ± 3.1% | | | 34.5 ± 13.6% | | | 2.9 ± 2.5% |
| 197 | | 28.3 ± 2.1% | 1.4 ± 1.0% | | 22.0 ± 14.4% | 2.2 ± 1.3% | | 2.6 ±1.7% | 2.3 ± 0.7% |
| 196 | 1.3 ± 0.7% | 0.2 ± 0.1% | 0.2 ± 0.1% | 5.9 ± 3.1% | 4.4 ± 5.9% | 1.4 ± 1.2% | 3.1 ± 1.3% | 2.2 ± 0.3% | 5.9 ± 0.6% |
| 195 | 0.6 ± 0.2% | 0.1 ± 0.1% | 0.0 ± 0.0% | 3.6 ± 2.2% | 1.0 ± 1.2% | 0.1 ± 0.0% | 7.7 ± 0.8% | 5.3 ± 0.5% | 0.4 ± 0.2% |
| 183 | 1.8 ± 0.7% | 13.7 ± 1.7% | 10.2 ± 3.6% | 2.1 ± 1.1% | 25.5 ± 26.9% | 10.7 ± 1.7% | 0.3 ± 0.2% | 1.4 ± 0.7% | 6.1 ± 1.6% |
| 182 | 1.5 ± 0.2% | 9.3 ± 0.4% | 15.9 ± 1.3% | 5.1 ± 1.6% | 7.6 ± 3.7% | 10.4 ± 1.1% | 3.6 ± 1.3% | 6.6 ± 1.5% | 8.0 ± 0.8% |
| 181 | 4.3 ± 1.1% | 20.1 ± 2.2% | 21.3 ± 2.5% | 7.5 ± 1.1% | 11.2 ± 5.9% | 29.2 ± 8.0% | 8.0 ± 0.7% | 10.4 ± 0.9% | 32.5 ± 6.0% |
| 180 | 87.9 ± 1.9% | 17.2 ± 1.0% | 1.3 ± 0.6% | 68.0 ± 11.1% | 19.1 ± 11.0% | 1.6 ± 0.8% | 36.1 ± 10.0% | 31.8 ± 3.9% | 6.4 ± 1.4% |
| 170 | 0.2 ± 0.2% | 0.2 ± 0.1% | 0.6 ± 0.1% | 0.4 ± 0.1% | 0.3 ± 0.2% | 0.7 ± 0.1% | 0.8 ± 0.4% | 0.5 ± 0.1% | 1.2 ± 0.4% |
| 169 | 0.1 ± 0.0% | 0.6 ± 0.1% | 0.3 ± 0.2% | 0.6 ± 0.4% | 0.6 ± 0.3% | 0.6 ± 0.3% | 2.7 ± 1.2% | 1.4 ± 0.5% | 1.7 ± 0.4% |
| 168 | 0.2 ± 0.1% | 0.1 ± 0.1% | 0.4 ± 0.1% | 1.0 ± 0.6% | 0.4 ± 0.4% | 2.0 ± 1.6% | 3.9 ± 0.9% | 2.8 ± 1.6% | 5.5 ± 0.8% |
| 165 | 0.0 ± 0.0% | 0.2 ± 0.0% | 0.1 ± 0.1% | 0.3 ± 0.3% | 1.2 ± 1.3% | 0.3 ± 0.2% | 1.1 ± 0.2% | 4.3 ± 0.4% | 1.4 ± 0.5% |
| 153 | 0.1 ± 0.1% | 0.1 ± 0.0% | 0.1 ± 0.1% | 1.3 ± 0.9% | 0.8 ± 1.0% | 0.9 ± 0.9% | 4.5 ± 0.9% | 5.0 ± 1.7% | 12.7 ± 5.0% |
| 152 | 0.1 ± 0.1% | 0.0 ± 0.0% | 0.1 ± 0.1% | 2.2 ± 2.2% | 0.6 ± 0.9% | 0.3 ± 0.3% | 20.3 ± 6.2% | 13.6 ± 6.0% | 4.0 ± 1.7% |
| 141 | 0.0 ± 0.0% | 0.0 ± 0.1% | 0.1 ± 0.1% | 0.1 ± 0.0% | 0.1 ± 0.1% | 0.1 ± 0.1% | 0.6 ± 0.3% | 0.6 ± 0.5% | 1.2 ± 0.4% |
| 139 | 0.0 ± 0.0% | 0.0 ± 0.0% | 0.0 ± 0.0% | 0.0 ± 0.1% | 0.1 ± 0.1% | 0.1 ± 0.0% | 1.1 ± 0.7% | 1.8 ± 0.9% | 0.8 ± 0.5% |
| 130 | 0.1 ± 0.0% | 0.2 ± 0.0% | 0.2 ± 0.1% | 0.6 ± 0.4% | 0.4 ± 0.4% | 0.5 ± 0.3% | 1.9 ± 0.5% | 2.0 ± 0.4% | 1.5 ± 0.3% |
| 128 | 0.0 ± 0.0% | 0.0 ± 0.0% | 0.1 ± 0.1% | 0.2 ± 0.1% | 0.1 ± 0.1% | 0.2 ± 0.2% | 1.7 ± 0.6% | 1.4 ± 0.6% | 1.9 ± 0.8% |
| 115 | 0.0 ± 0.0% | 0.0 ± 0.0% | 0.1 ± 0.1% | 0.1 ± 0.1% | 0.1 ± 0.1% | 0.1 ± 0.1% | 1.2 ± 0.7% | 1.5 ± 0.7% | 0.9 ± 0.3% |
| 106 | 1.6 ± 0.3% | 9.2 ± 1.5% | 7.0 ± 1.4% | 1.1 ± 0.2% | 4.4 ± 2.0% | 3.8 ± 0.4% | 0.9 ± 0.1% | 4.2 ± 0.6% | 2.5 ± 0.6% |
| 89 | 0.0 ± 0.0% | 0.0 ± 0.0% | 0.0 ± 0.1% | 0.0 ± 0.0% | 0.0 ± 0.0% | 0.0 ± 0.0% | 0.2 ± 0.1% | 0.2 ± 0.2% | 0.2 ± 0.1% |
| 77 | 0.1 ± 0.0% | 0.3 ± 0.1% | 0.3 ± 0.1% | 0.1 ± 0.0% | 0.1 ± 0.1% | 0.2 ± 0.1% | 0.2 ± 0.1% | 0.3 ± 0.1% | 0.2 ± 0.1% |

Table C.9. Total percent ion current for the three 4,4'-MDA ion species.

Table C.10. Total percent ion current for the two 2,7-DAF ion species.

| Fragment Ion | 0-10 CE | | 15-30 CE | | 35-50 CE | |
|--------------|------------------|--------------------|------------------|--------------------|------------------|--------------------|
| | [M] ⁻ | [M+H] ⁻ | [M] ⁻ | [M+H] ⁻ | [M] ⁻ | [M+H] ⁻ |
| 198 | | | | | | |
| 197 | | 57.5 ± 9.0% | | 51.6 ± 4.0% | | 24.8 ± 9.7% |
| 196 | | 2.8 ± 2.2% | | 2.0 ± 0.4% | | 4.1 ± 0.5% |
| 195 | 67.5 ± 3.6% | 0.1 ± 0.2% | 61.3 ± 14.5% | 0.0 ± 0.0% | 37.6 ± 13.8% | 0.0 ± 0.0% |
| 183 | 0.1 ± 0.1% | 1.2 ± 1.5% | 0.1 ± 0.0% | 0.9 ± 0.3% | 0.0 ± 0.0% | 0.4 ± 0.2% |
| 182 | 0.3 ± 0.5% | 16.8 ± 5.1% | 0.0 ± 0.0% | 20.7 ± 1.6% | 0.0 ± 0.0% | 11.0 ± 3.3% |
| 181 | 0.9 ± 0.8% | 16.1 ± 6.4% | 0.2 ± 0.1% | 16.6 ± 4.8% | 0.2 ± 0.0% | 7.3 ± 2.4% |
| 180 | 26.3 ± 4.0% | 0.5 ± 0.7% | 33.4 ± 14.0% | 1.9 ± 1.4% | 17.2 ± 6.3% | 9.1 ± 1.4% |
| 170 | 0.0 ± 0.1% | 0.4 ± 0.4% | 0.0 ± 0.0% | 0.5 ± 0.2% | 0.7 ± 0.3% | 3.2 ± 1.2% |
| 169 | 0.9 ± 0.3% | 1.6 ± 2.1% | 0.6 ± 0.2% | 1.6 ± 1.3% | 6.1 ± 2.8% | 5.5 ± 0.5% |
| 168 | 1.3 ± 0.4% | 1.1 ± 1.3% | 2.5 ± 2.0% | 1.0 ± 0.6% | 11.0 ± 1.1% | 10.1 ± 3.6% |
| 165 | 0.2 ± 0.4% | 0.1 ± 0.5% | 0.0 ± 0.0% | 0.1 ± 0.1% | 0.1 ± 0.1% | 0.3 ± 0.1% |
| 153 | 0.6 ± 0.5% | 0.7 ± 1.2% | 0.5 ± 0.4% | 1.5 ± 0.9% | 4.1 ± 0.7% | 9.6 ± 3.4% |
| 152 | 0.9 ± 0.6% | 0.7 ± 0.9% | 1.0 ± 0.7% | 1.3 ± 1.0% | 14.4 ± 6.8% | 11.6 ± 4.1% |
| 141 | 0.0 ± 0.1% | 0.1 ± 0.2% | 0.2 ± 0.1% | 0.1 ± 0.1% | 2.3 ± 0.8% | 0.7 ± 0.4% |
| 139 | 0.3 ± 0.5% | 0.0 ± 0.0% | 0.1 ± 0.0% | 0.0 ± 0.0% | 3.0 ± 2.5% | 0.6 ± 0.4% |
| 130 | 0.1 ± 0.2% | 0.0 ± 0.0% | 0.1 ± 0.0% | 0.2 ± 0.1% | 0.3 ± 0.1% | 0.3 ± 0.1% |
| 128 | 0.0 ± 0.1% | 0.1 ± 0.2% | 0.0 ± 0.0% | 0.1 ± 0.1% | 0.7 ± 0.3% | 0.8 ± 0.4% |
| 115 | 0.4 ± 0.7% | 0.1 ± 0.2% | 0.1 ± 0.0% | 0.0 ± 0.0% | 2.1 ± 1.4% | 0.7 ± 0.4% |
| 106 | 0.0 ± 0.0% | 0.0 ± 0.0% | 0.0 ± 0.0% | 0.0 ± 0.0% | 0.0 ± 0.0% | 0.0 ± 0.0% |
| 89 | 0.0 ± 0.0% | 0.0 ± 0.0% | 0.0 ± 0.0% | 0.0 ± 0.0% | 0.0 ± 0.0% | 0.0 ± 0.0% |
| 77 | 0.0 ± 0.0% | 0.0 ± 0.0% | 0.0 ± 0.0% | 0.0 ± 0.0% | 0.0 ± 0.0% | 0.0 ± 0.0% |

Table C.10. Total percent ion current for the two 2,7-DAF ion species.

Figure C.11. Percent Total Ion Current for Fragment Ions

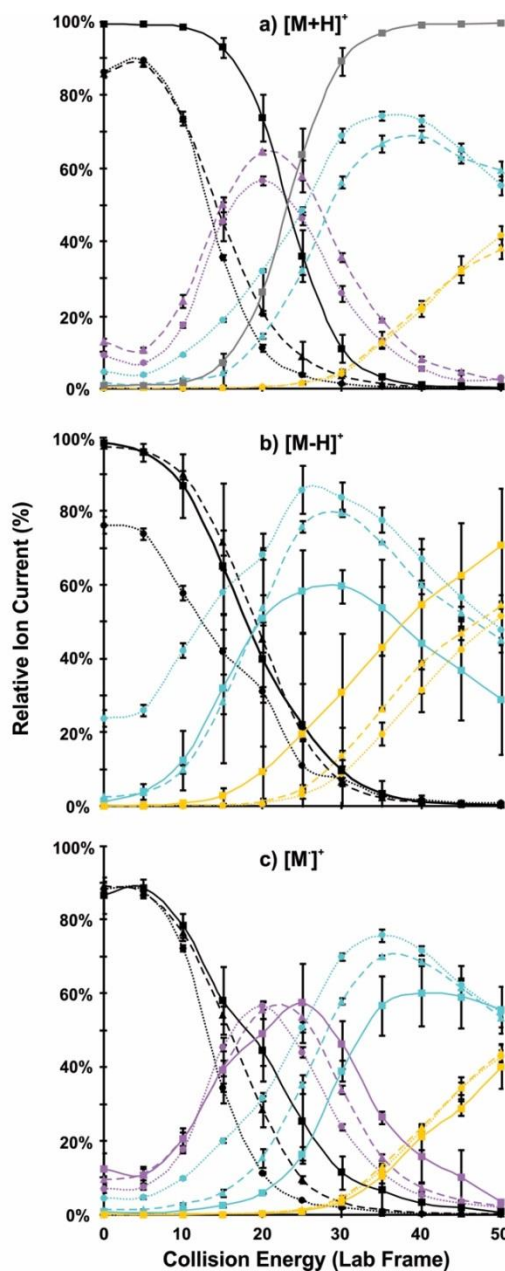


Figure C.11. Titration curves depicted in **Figure 3.4** in the manuscript. Instead of averaging the three isomers together, they are shown separately here as a solid line for 4,4'-MDA, a dashed line for 2,4'-MDA and a dotted line for 2,2'-MDA. The precursor ion is represented with black lines, M-1 with purple lines, M-17,18 with teal, M-45,46 with yellow, and M-93 with grey.

Figure C.12. Percent Total Ion Current for Fragment Ions

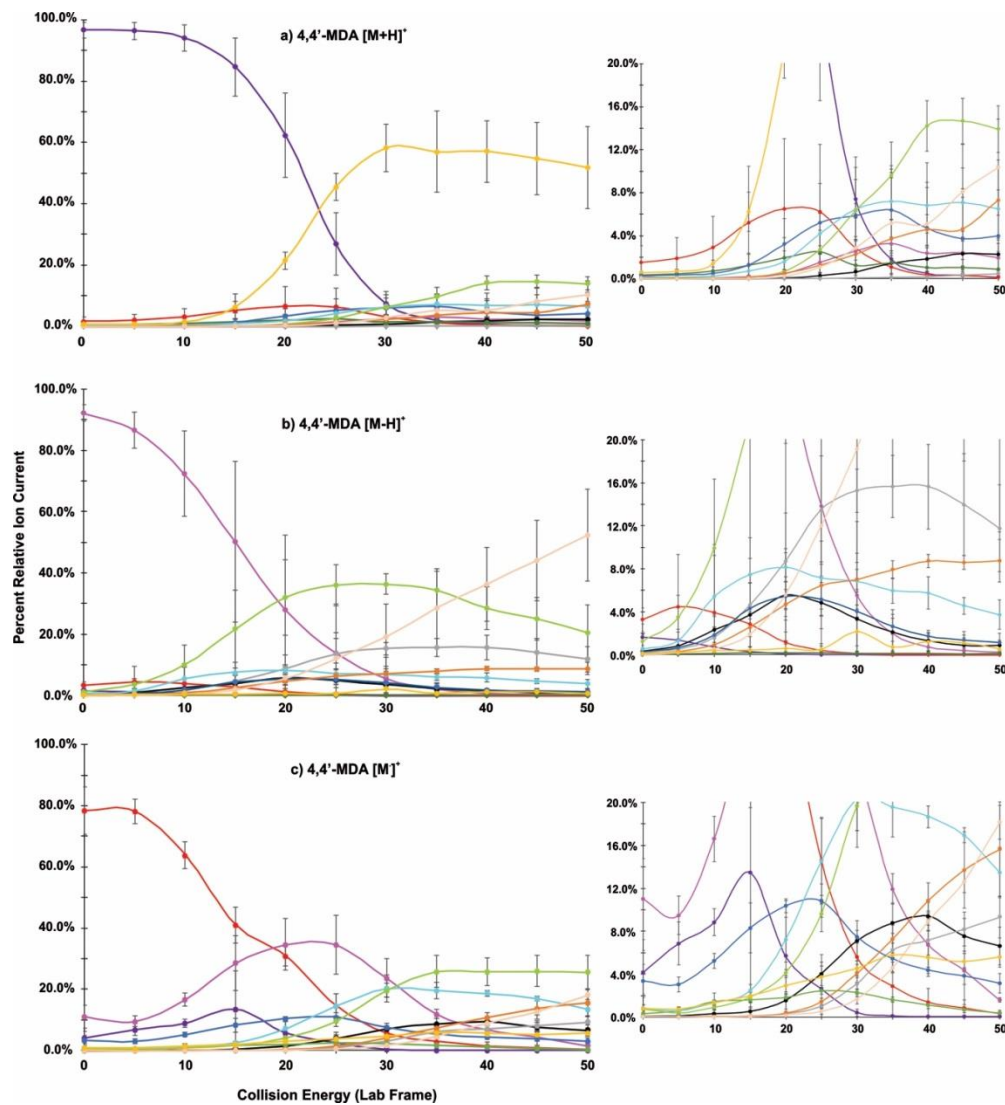


Figure C.12. Collision energy curves for a larger number of fragment ions for the $[M+H]^+$ species. Only results higher than 20% were adjusted to 100% for clarity for Figure 3.3 in the manuscript.

Figure C.13. Percent Total Ion Current for Fragment Ions

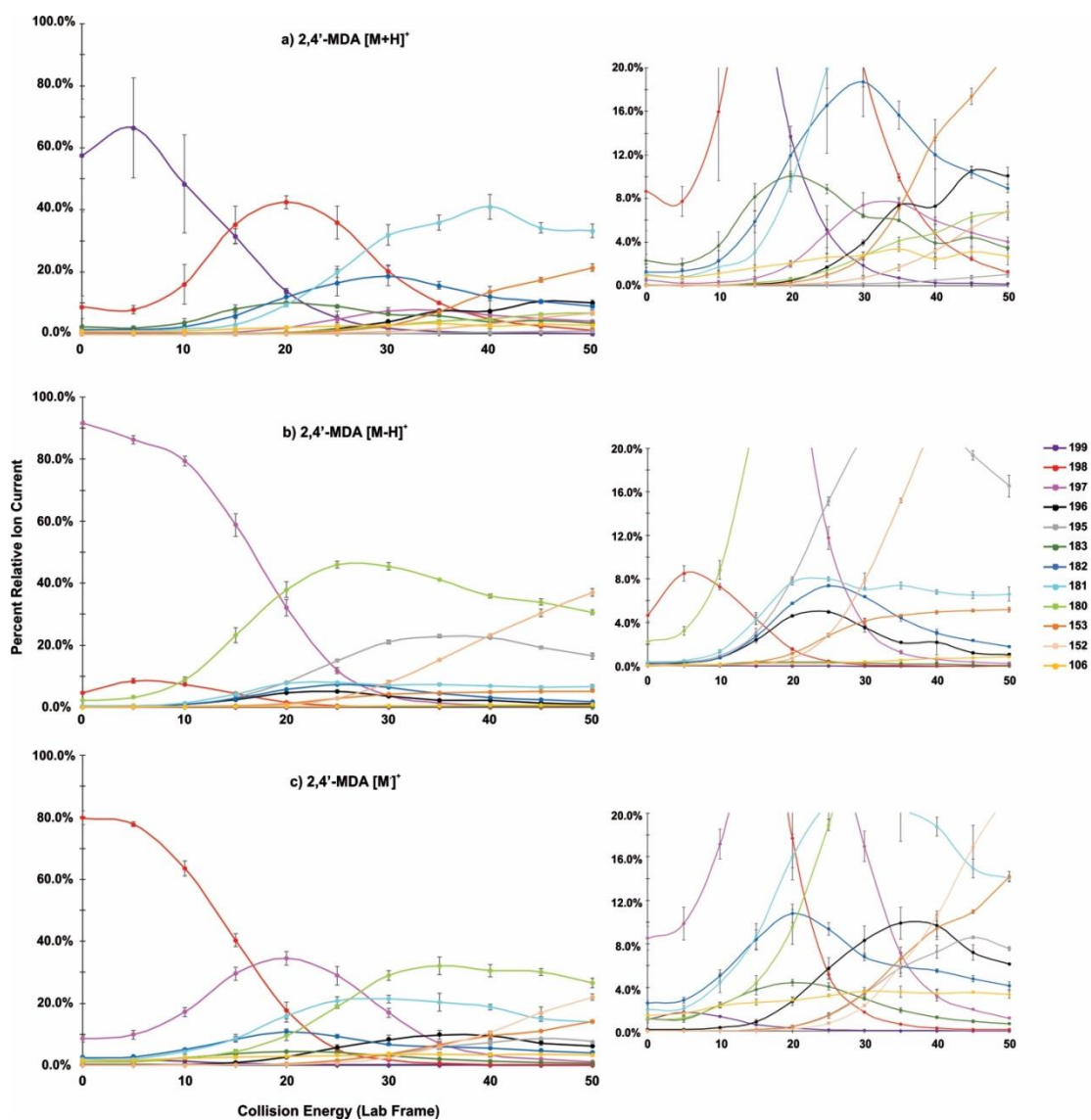


Figure C.13. Collision energy curves for a larger number of fragment ions for the $[M-H]^+$ species. Only results higher than 25% were adjusted to 100% for clarity for **Figure 3.3** in the manuscript.

Figure C.14. Percent Total Ion Current for Fragment Ions

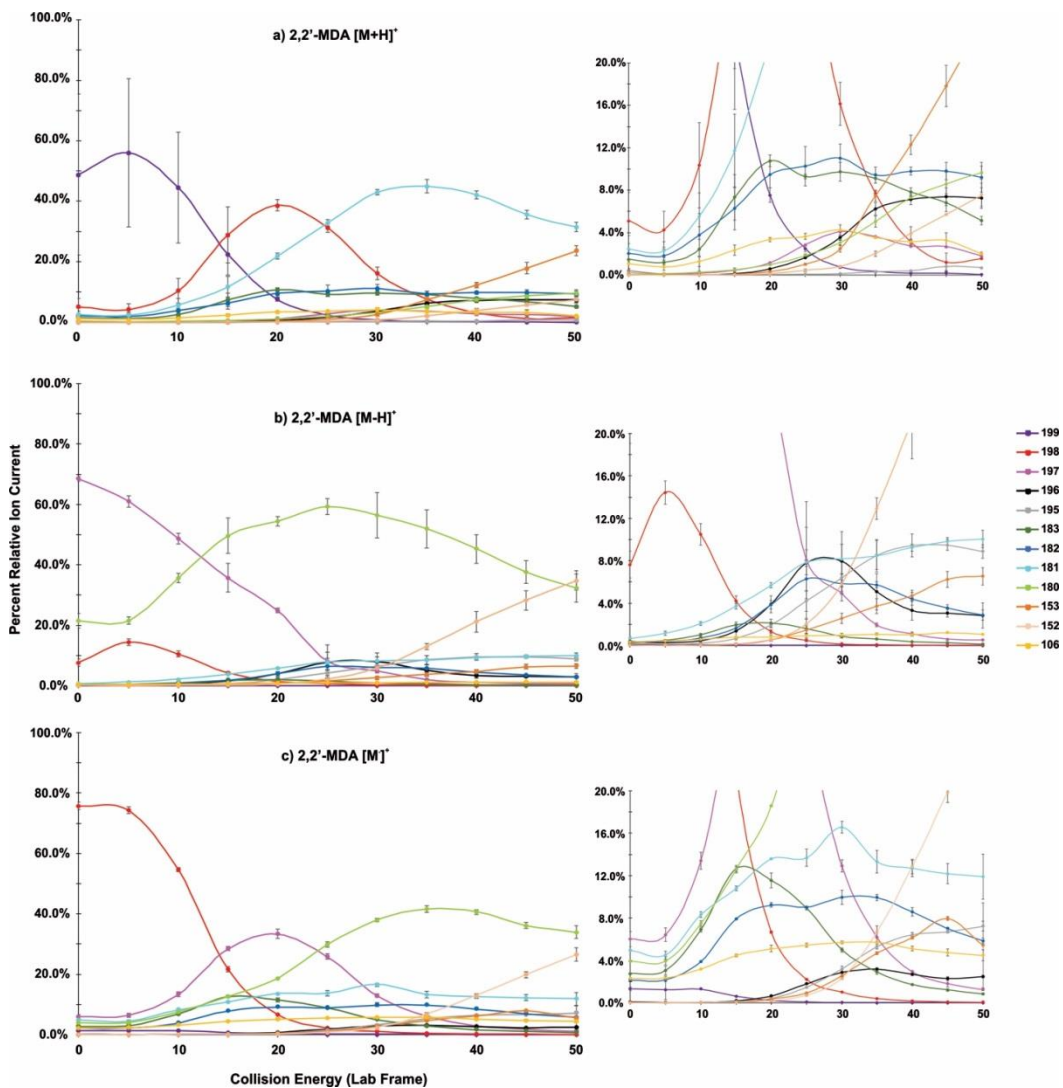


Figure C.14. Collision energy curves for a larger number of fragment ions for the $[M]^+$ species. Only results higher than 20% were adjusted to 100% for clarity for **Figure 3.3** in the manuscript.

Figure C.15. Percent Total Ion Current for Fragment Ions

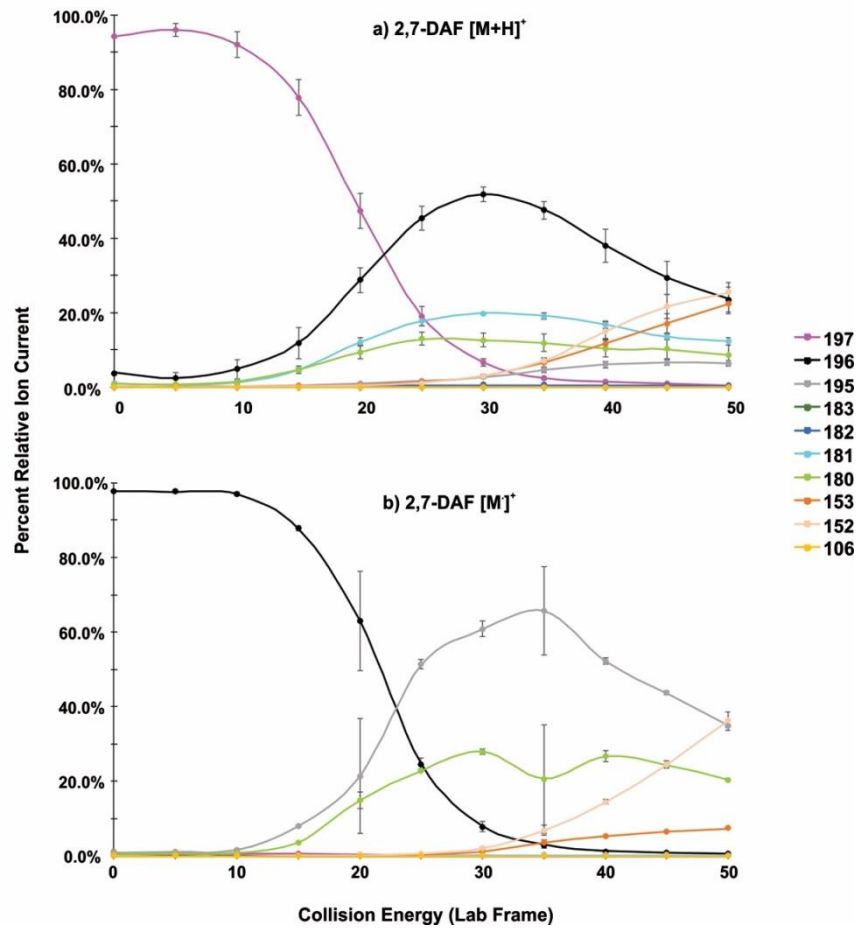


Figure C.15. Titration curves for 2,7-DAF for both (a) the [M+H]⁺ species and (b) the [M]⁺ species.

Figure C.16. MALDI and ESI MS Spectra

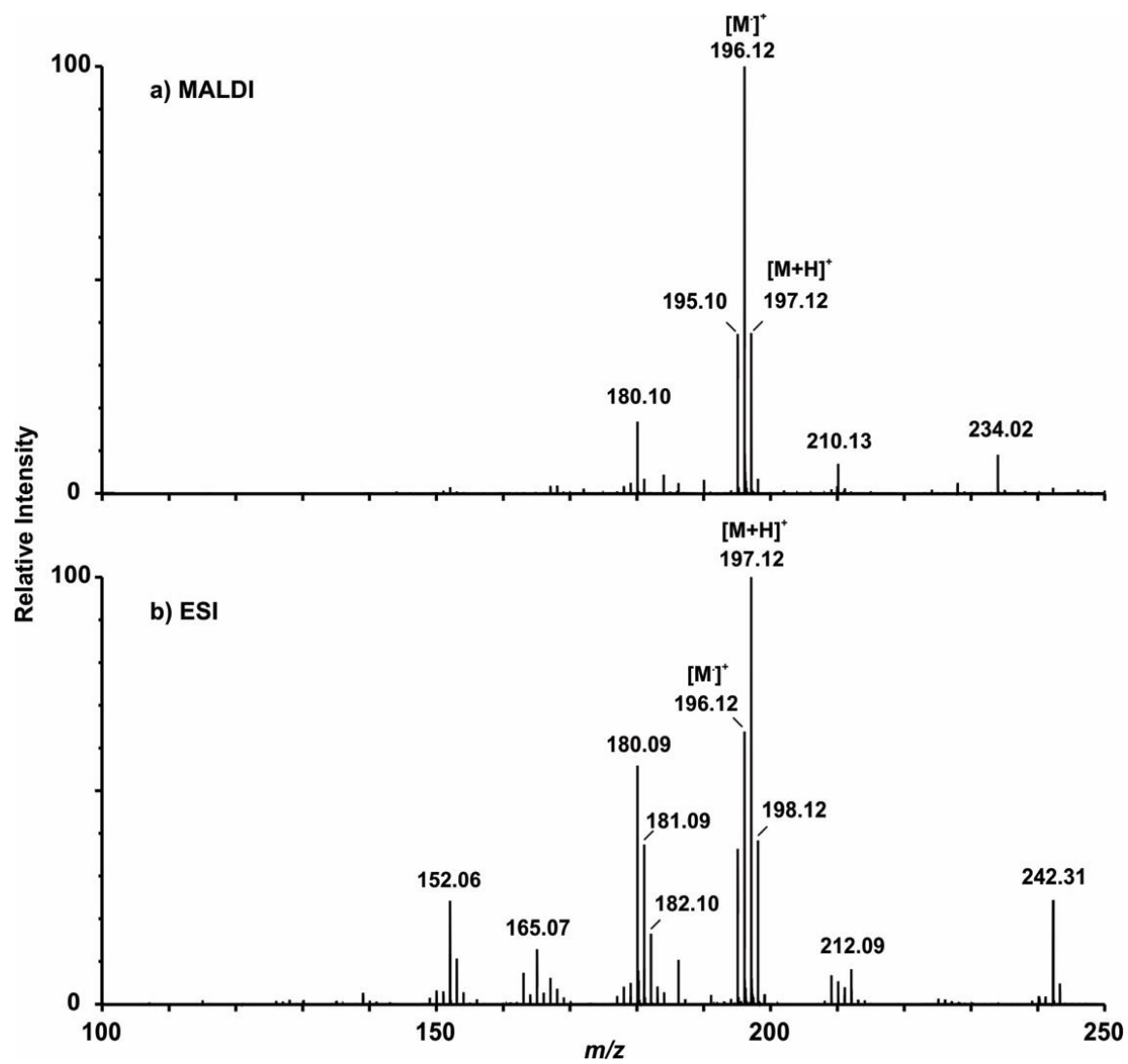


Figure C.16. Mass spectra for 2,7-DAF for both (a) MALDI and (b) ESI. Similar to the MDA isomers, 2,7-DAF preferably forms the $[M+H]^+$ in ESI and $[M]^+$ and $[M-H]^+$ in MALDI.

Figure C.17. 2,7-DAF IM-MS Traces

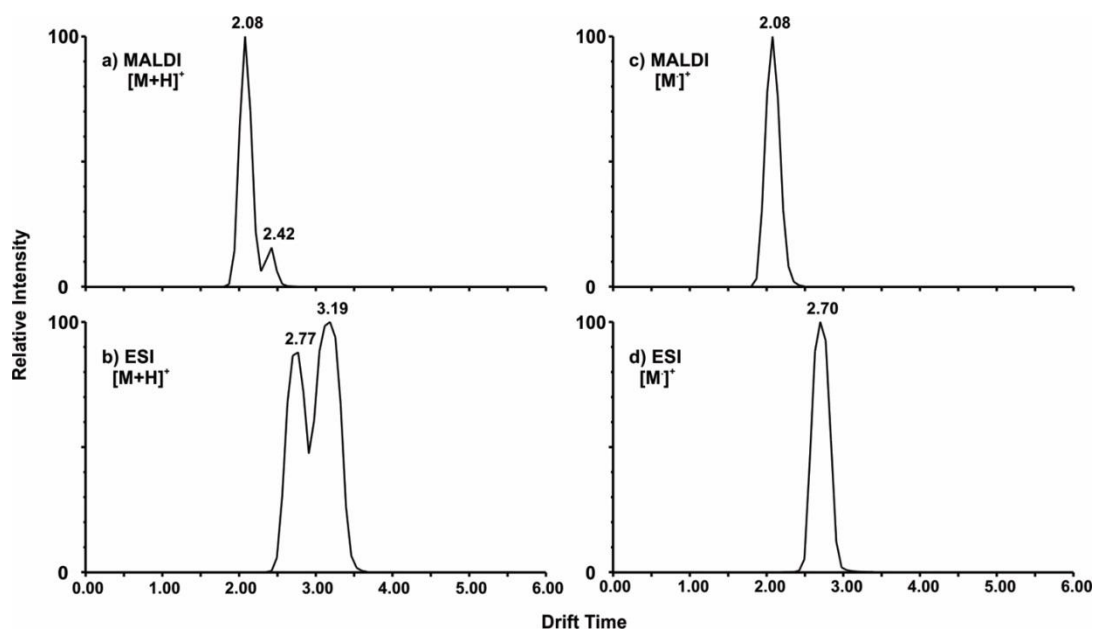


Figure C.17. Ion mobility traces for 2,7-DAF are shown for the $[M+H]^+$ species in (a) and (b) and for the $[M]^+$ species in (c) and (d). Results for MALDI are shown in (a) and (c) and for ESI in (b) and (d). Two conformations for the $[M+H]^+$ species are observed as we saw in **Figure 3.5** in the manuscript, but the preference switches in ESI.

Computational Details (Figures C.18-C.23)

Conformational Sampling with Molecular Dynamics

In order to gain more detailed structural insight from ion mobility – mass spectrometry (IM-MS) experiments, computational calculations are often performed. These calculations involve both a sampling of the conformational landscape of the molecule of interest and then a theoretical CCS calculation for each conformation generated. In this study, the $[M+H]^+$ and $[M-H]^+$ forms of all three 2-ring MDA isomers, as well as the 2,7-DAF standard were first geometry optimized in Gaussian09 at the Hartree Fock level of theory. All possible protonation sites for each species were modeled including both para and *ortho* amine protonation as well as ring protonation (i.e. 3 for 2,4'-MDA, 2 for 2,2'-MDA, and 1 for 4,4'-MDA and 2,7-DAF). The optimized structure and electrostatic potential description of the molecules were then used in AMBER to perform a molecular dynamic simulation to sample the conformational space of the molecule. Specifically, a simulated annealing protocol was used for the MD simulation as the artificial heating of the molecules allows more conformational space to be sampled than a traditional MD simulation. Each simulation resulted in 3,000 unique conformations that were then submitted to MOBCAL to determine a theoretical CCS_{He} value for each conformation. PSA was used to determine theoretical CCS_{N_2} values for a subset of conformations which were used to project the rest of the conformations from helium to nitrogen using a simple linear function. Each conformation is then represented in the scatter plots in **Figure 3.5d-f** in the main text and in **Figures C.17-18** in the supporting information.

Energy Change of the Reaction with Quantum Mechanical Calculations

Bond energies that are tabulated in **Scheme 3.1** in the main text and in **Figures C.19-22** in the supporting information are based on density function theory (DFT) calculations performed in Gaussian09. In these calculations, the parent ion is first geometry optimized and the energy is calculated for the parent ion. The bond of interest is then broken via homolytic bond cleavage, resulting in two individual pieces that are determined to be of doublet multiplicity due to the free electron on each fragment. Note that one of the fragments will be positively charged and the other neutral depending on where the charge resided on the parent ion. A geometry optimization calculation is then performed on each fragment and the resulting energy of these two calculations is summed and then subtracted from the parent ion energy. This resulting energy change of the reaction then represents the relative bond energy of the broken bond. Frequency calculations were performed to ensure that both the precursor and fragment structures were optimized to energy minimums. DFT/B3LYP/6-31G* level of theory was used for all calculations, which were performed *in vacuo* and in the ground state

Figure C.18. Ion Mobility and Theoretical Modeling

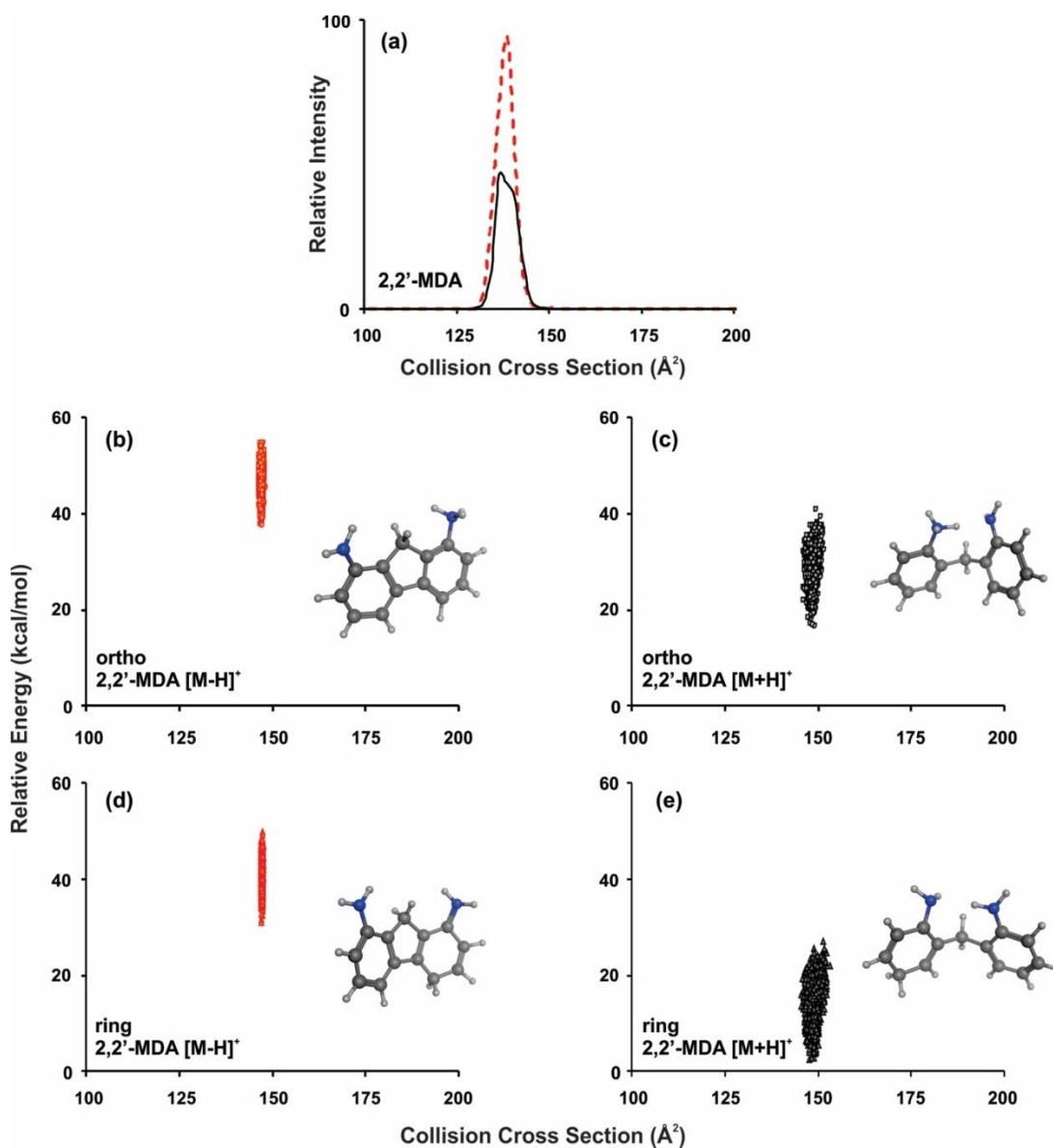


Figure C.18. Ion mobility and theoretical modeling results for 2,2'-MDA. IM traces for both $[\text{M}-\text{H}]^+$ (red, dashed line) and $[\text{M}+\text{H}]^+$ (black, solid line) are shown in (a). Conformation space plots are shown for *ortho* protonation in (b) for $[\text{M}-\text{H}]^+$ (yellow circles with red outlines) and in (c) for $[\text{M}+\text{H}]^+$ (light grey circles with black outlines). Conformational space plots for ring protonation are shown in (d) for $[\text{M}-\text{H}]^+$ (orange triangles with red outlines) and (e) for $[\text{M}+\text{H}]^+$ (dark grey triangles with black outlines). These plots are shown separately here for clarity as opposed to overlapping as is shown in the manuscript.

Figure C.19. Ion Mobility and Theoretical Modeling

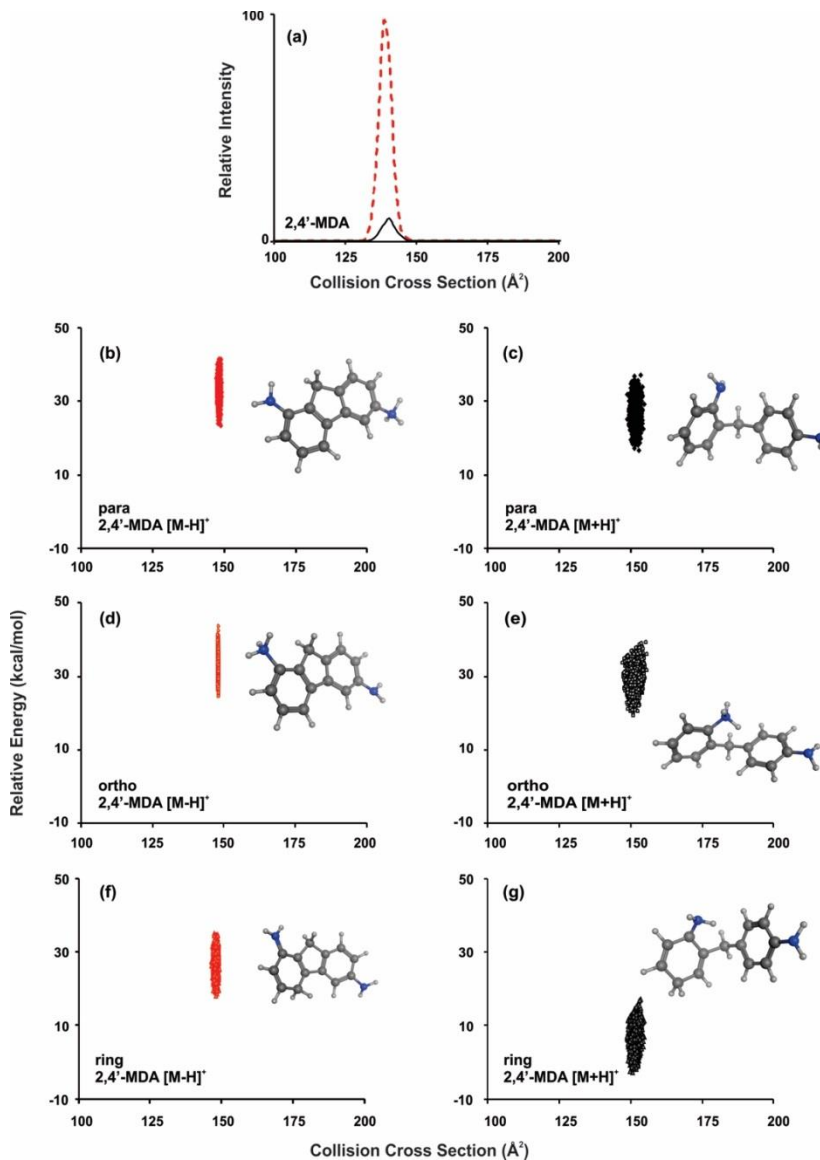
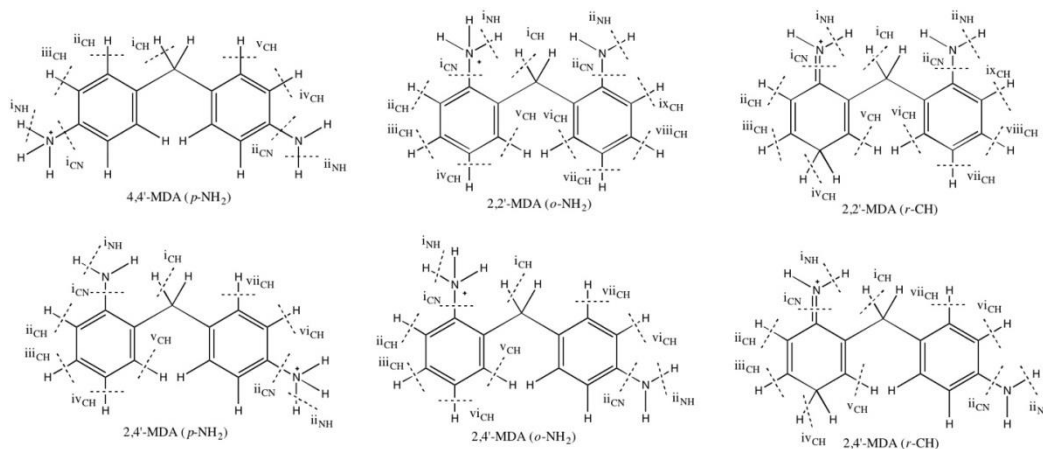


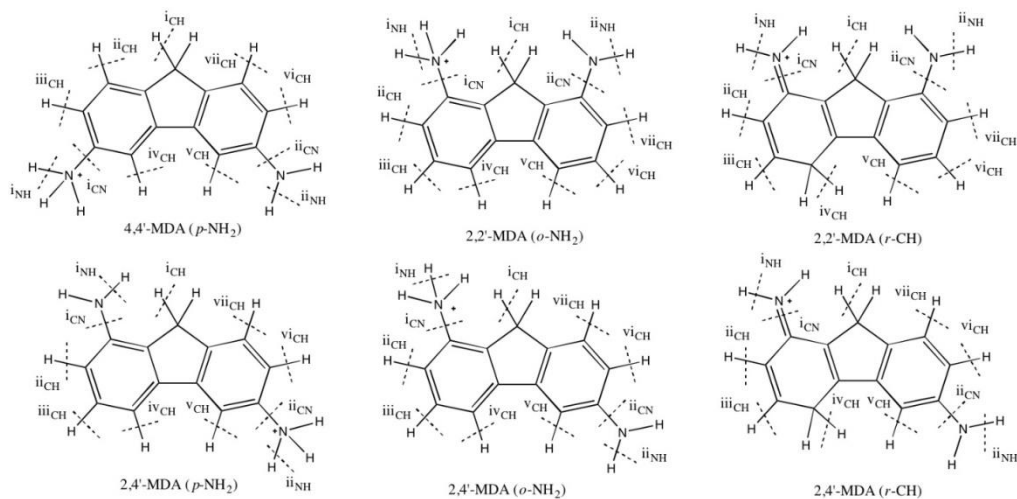
Figure C.19. Ion mobility and theoretical modeling results for 2,4'-MDA. IM traces for both [M-H]⁺ (red, dashed line) and [M+H]⁺ (black, solid line) are shown in (a). Conformational space plots are shown for *para* protonation for (b) [M-H]⁺ (red diamonds) and (c) [M+H]⁺ (black diamonds). Plots for *ortho* protonation for (d) [M-H]⁺ (yellow circles with red outlines) and (e) [M+H]⁺ (light grey circles with black outlines). Plots for ring protonation for (f) [M-H]⁺ (orange triangles with red outlines) and (g) [M+H]⁺ (dark grey triangles with black outlines). The plots are shown separately here for clarity of the different protonation sites and precursor species.

Figure C.20. Bond energies for $[M+H]^+$ isomers.



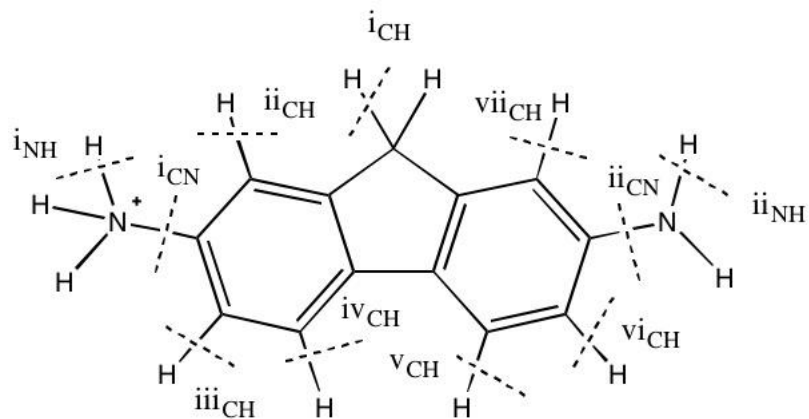
| 4,4'-MDA (<i>p</i> -NH ₂) | | 2,2'-MDA (<i>o</i> -NH ₂) | | 2,2'-MDA (<i>r</i> -CH) | |
|--|------------------------|--|------------------------|--------------------------|------------------------|
| Bond | Bond Energy (kcal/mol) | Bond | Bond Energy (kcal/mol) | Bond | Bond Energy (kcal/mol) |
| i _{CN} | 137.3 | i _{CN} | 151.0 | i _{CN} | 257.6 |
| ii _{CN} | 108.4 | ii _{CN} | 113.4 | ii _{CN} | 112.7 |
| i _{NH} | 59.2 | i _{NH} | 77.1 | i _{NH} | 91.8 |
| ii _{NH} | 96.5 | ii _{NH} | 77.1 | ii _{NH} | 89.1 |
| i _{CH} | 80.2 | i _{CH} | 86.8 | i _{CH} | 94.5 |
| ii _{CH} | 119.0 | ii _{CH} | 118.2 | ii _{CH} | 119.2 |
| iii _{CH} | 117.7 | iii _{CH} | 120.0 | iii _{CH} | 118.5 |
| iv _{CH} | 118.3 | iv _{CH} | 119.5 | iv _{CH} | 73.7 |
| v _{CH} | 116.9 | v _{CH} | 118.5 | v _{CH} | 117.2 |
| | | vi _{CH} | 118.1 | vi _{CH} | 117.3 |
| | | vii _{CH} | 119.3 | vii _{CH} | 119.1 |
| | | viii _{CH} | 119.1 | viii _{CH} | 118.9 |
| | | ix _{CH} | 118.3 | ix _{CH} | 118.3 |
| 2,4'-MDA (<i>p</i> -NH ₂) | | 2,4'-MDA (<i>o</i> -NH ₂) | | 2,4'-MDA (<i>r</i> -CH) | |
| Bond | Bond Energy (kcal/mol) | Bond | Bond Energy (kcal/mol) | Bond | Bond Energy (kcal/mol) |
| i _{CN} | 105.7 | i _{CN} | 145.8 | i _{CN} | 252.2 |
| ii _{CN} | 136.4 | ii _{CN} | 111.5 | ii _{CN} | 110.4 |
| i _{NH} | 89.4 | i _{NH} | 72.8 | i _{NH} | 102.5 |
| ii _{NH} | 62.6 | ii _{NH} | 100.4 | ii _{NH} | 99.1 |
| i _{CH} | 84.7 | i _{CH} | 85.6 | i _{CH} | 86.2 |
| ii _{CH} | | ii _{CH} | 119.4 | ii _{CH} | 119.6 |
| iii _{CH} | | iii _{CH} | 120.1 | iii _{CH} | 118.7 |
| iv _{CH} | 119.1 | iv _{CH} | 119.5 | iv _{CH} | 70.2 |
| v _{CH} | 117.0 | v _{CH} | 119.0 | v _{CH} | 117.7 |
| vi _{CH} | 119.0 | vi _{CH} | 116.5 | vi _{CH} | 116.6 |
| vii _{CH} | 118.3 | vii _{CH} | 120.2 | vii _{CH} | 118.9 |

Figure C.21. Bond energies for $[M-H]^+$ isomers.



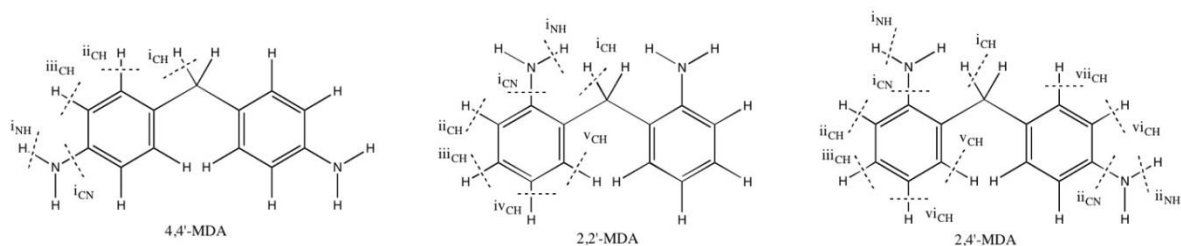
| 4,4'-MDA (<i>p</i> -NH ₂) | | 2,2'-MDA (<i>o</i> -NH ₂) | | 2,2'-MDA (<i>r</i> -CH) | |
|--|------------------------|--|------------------------|--------------------------|------------------------|
| Bond | Bond Energy (kcal/mol) | Bond | Bond Energy (kcal/mol) | Bond | Bond Energy (kcal/mol) |
| i _{CN} | 137.9 | i _{CN} | 135.8 | i _{CN} | 251.4 |
| ii _{CN} | 108.2 | ii _{CN} | 107.7 | ii _{CN} | 109.2 |
| i _{NH} | 62.1 | i _{NH} | 65.7 | i _{NH} | 103.9 |
| ii _{NH} | 97.3 | ii _{NH} | 97.7 | ii _{NH} | 95.8 |
| i _{CH} | 80.0 | i _{CH} | 79.7 | i _{CH} | 79.1 |
| ii _{CH} | 119.3 | ii _{CH} | 119.3 | ii _{CH} | 119.6 |
| iii _{CH} | 119.1 | iii _{CH} | 119.7 | iii _{CH} | 118.6 |
| iv _{CH} | 118.5 | iv _{CH} | 119.7 | iv _{CH} | 75.2 |
| v _{CH} | 118.2 | v _{CH} | 119.5 | v _{CH} | 119.7 |
| vi _{CH} | 118.7 | vi _{CH} | 118.5 | vi _{CH} | 118.9 |
| vii _{CH} | 118.2 | vii _{CH} | 118.9 | vii _{CH} | 118.9 |
| 2,4'-MDA (<i>p</i> -NH ₂) | | 2,4'-MDA (<i>o</i> -NH ₂) | | 2,4'-MDA (<i>r</i> -CH) | |
| Bond | Bond Energy (kcal/mol) | Bond | Bond Energy (kcal/mol) | Bond | Bond Energy (kcal/mol) |
| i _{CN} | 108.3 | i _{CN} | 137.3 | i _{CN} | 252.4 |
| ii _{CN} | 137.7 | ii _{CN} | 109.1 | ii _{CN} | 110.2 |
| i _{NH} | 97.9 | i _{NH} | 63.8 | i _{NH} | 100.4 |
| ii _{NH} | 64.5 | ii _{NH} | 97.6 | ii _{NH} | 99.8 |
| i _{CH} | 80.5 | i _{CH} | 78.2 | i _{CH} | 79.2 |
| ii _{CH} | 118.8 | ii _{CH} | 119.3 | ii _{CH} | 119.5 |
| iii _{CH} | 118.3 | iii _{CH} | 119.6 | iii _{CH} | 118.5 |
| iv _{CH} | 118.8 | iv _{CH} | 119.5 | iv _{CH} | 73.2 |
| v _{CH} | 118.7 | v _{CH} | 118.9 | v _{CH} | 119.1 |
| vi _{CH} | 119.2 | vi _{CH} | 119.0 | vi _{CH} | 118.9 |
| vii _{CH} | 119.3 | vii _{CH} | 118.0 | vii _{CH} | 118.7 |

Figure C.22. Bond energies for 2,7-DAF



| Bond | Bond Energy (kcal/mol) |
|-------------------------|------------------------|
| i_{CN} | 140.3 |
| ii_{CN} | 110.6 |
| i_{NH} | 51.0 |
| ii_{NH} | 98.0 |
| i_{CH} | 85.5 |
| ii_{CH} | 118.0 |
| iii_{CH} | 118.3 |
| iv_{CH} | 119.4 |
| v_{CH} | 117.7 |
| vi_{CH} | 119.1 |
| vii_{CH} | 118.9 |

Figure C.23. Bond energies for $[M]^+$ isomers.



Triplet - Modelling the two pieces as a neutral doublet and a singly charged triplet assumes that the radical on the system was nowhere near where the bond is broken.

Singlet - Modelling the two pieces as a neutral doublet and a singly charged singlet assumes that the radical on the system was on the atom where the bond is broken.

Triplet

| 4,4'-MDA | | 2,2'-MDA | | 2,4'-MDA | |
|-------------------|------------------------|-------------------|------------------------|-------------------|------------------------|
| Bond | Bond Energy (kcal/mol) | Bond | Bond Energy (kcal/mol) | Bond | Bond Energy (kcal/mol) |
| i _{CN} | 117.8 | i _{CN} | 113.5 | i _{CN} | 111.1 |
| i _{NH} | | i _{NH} | 89.1 | ii _{CN} | 117.9 |
| i _{CH} | 86.9 | i _{CH} | 98.4 | i _{NH} | 93.2 |
| ii _{CH} | 117.8 | ii _{CH} | 118.4 | ii _{NH} | 107.1 |
| iii _{CH} | 118.8 | iii _{CH} | 120.7 | i _{CH} | 86.3 |
| | | iv _{CH} | 117.9 | ii _{CH} | 119.1 |
| | | v _{CH} | 119.6 | iii _{CH} | 119.0 |
| | | | | iv _{CH} | 119.0 |
| | | | | v _{CH} | 118.2 |
| | | | | vi _{CH} | 118.9 |
| | | | | vii _{CH} | 118.5 |

Singlet

| 4,4'-MDA | | 2,2'-MDA | | 2,4'-MDA | |
|-----------------|------------------------|-----------------|------------------------|------------------|------------------------|
| Bond | Bond Energy (kcal/mol) | Bond | Bond Energy (kcal/mol) | Bond | Bond Energy (kcal/mol) |
| i _{CN} | 132.2 | i _{CN} | 48.4 | i _{CN} | 119.6 |
| i _{NH} | 98.1 | i _{NH} | 92.4 | ii _{CN} | 127.8 |
| | | | | i _{NH} | 93.5 |
| | | | | ii _{NH} | 99.3 |

APPENDIX D

SUPPORTING INFORMATION FOR CHAPTER IV

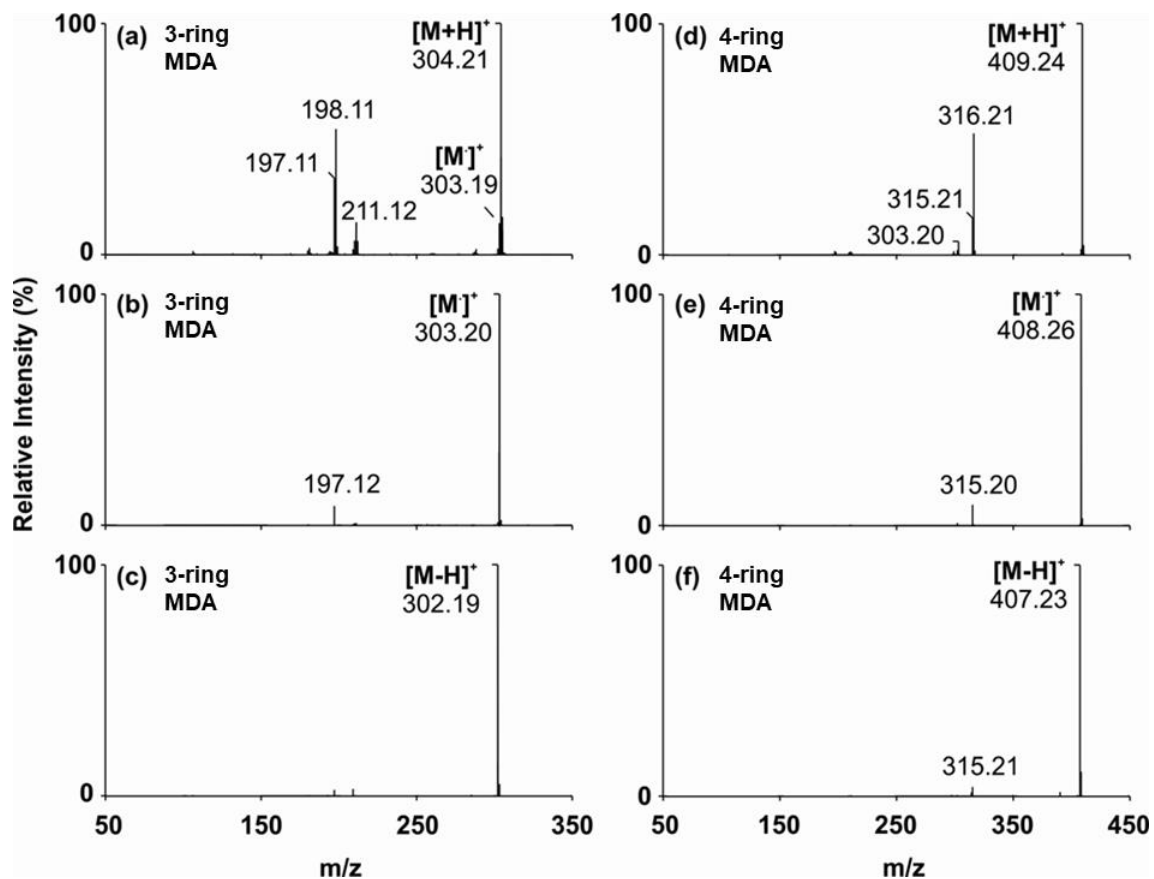
D.1. MALDI MS/MS 10 eV

Figure D.1. MALDI tandem mass spectra (MS/MS) of the 3-ring MDA (a) $[M+H]^+ = 304$ Da, (b) $[M]^+ = 303$ Da, and (c) $[M-H]^+ = 302$ Da and 4-ring MDA (d) $[M+H]^+ = 409$ Da, (e) $[M]^+ = 408$ Da, and (f) $[M-H]^+ = 407$ Da at 10 eV.

D.2. MALDI MS/MS 15 eV

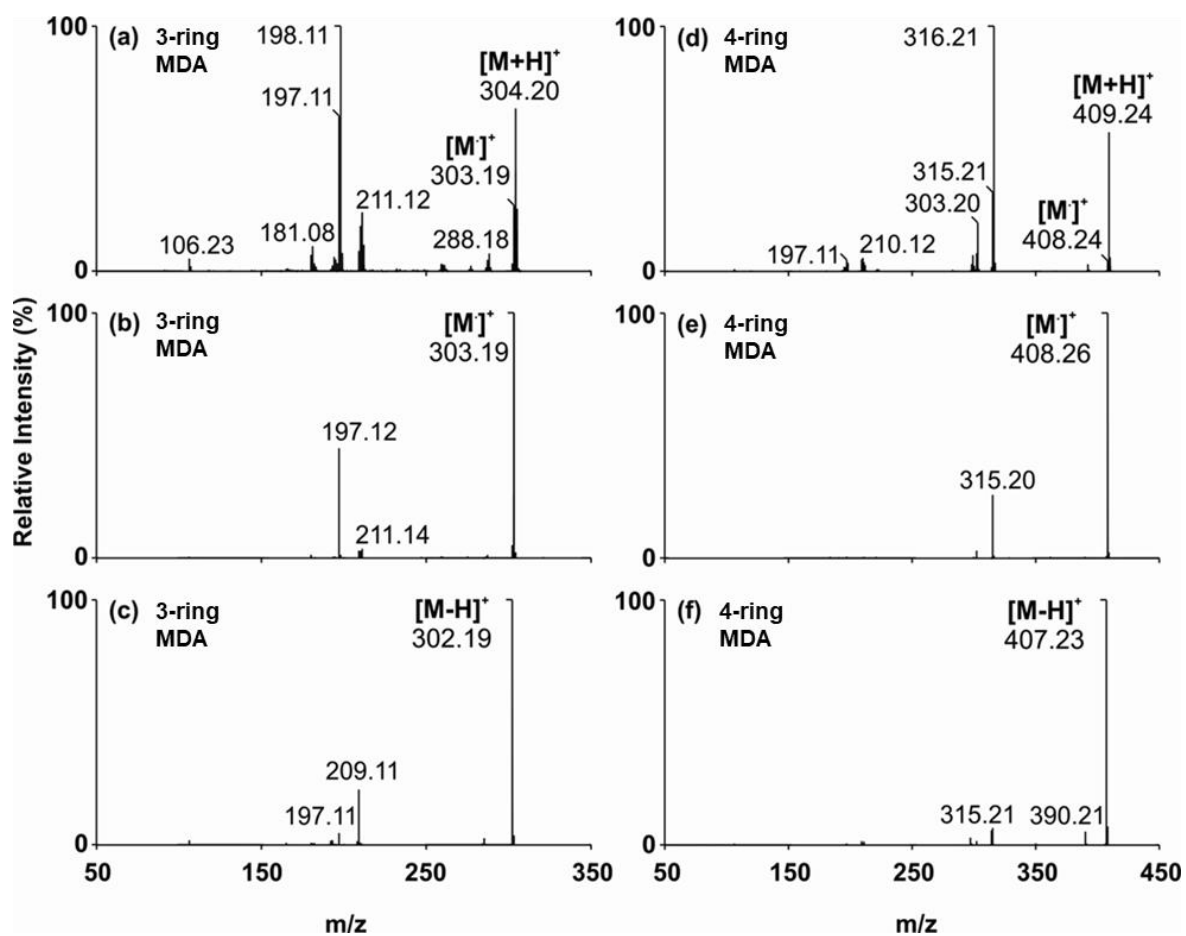


Figure D.2. MALDI tandem mass spectra (MS/MS) of the 3-ring MDA (a) $[M+H]^+$ = 304 Da, (b) $[M]^+$ = 303 Da, and (c) $[M-H]^+$ = 302 Da and 4-ring MDA (d) $[M+H]^+$ = 409 Da, (e) $[M]^+$ = 408 Da, and (f) $[M-H]^+$ = 407 Da at 15 eV.

D.3. MALDI MS/MS 20 eV

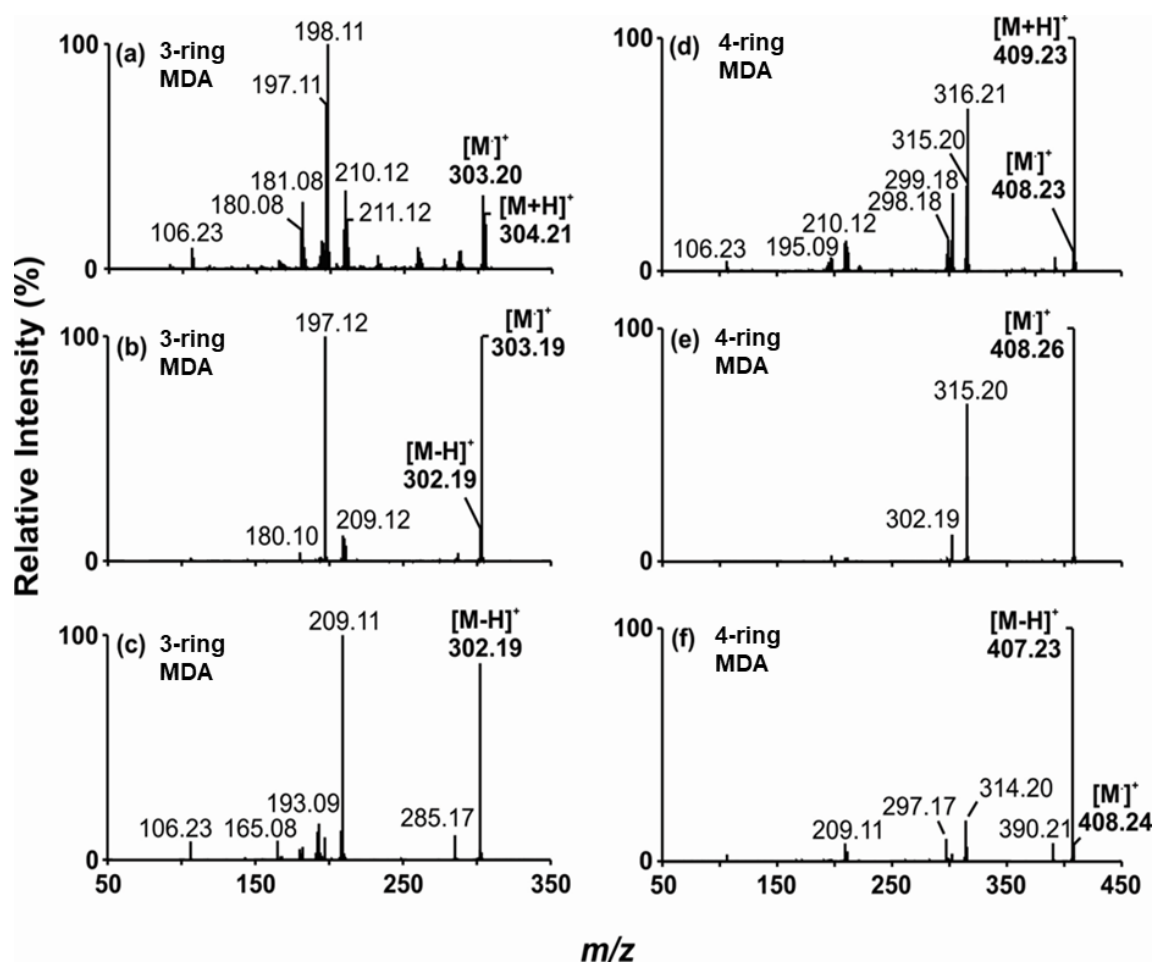


Figure D.3. MALDI tandem mass spectra (MS/MS) of the 3-ring MDA (a) [M+H]⁺ = 304 Da, (b) [M]⁺ = 303 Da, and (c) [M-H]⁺ = 302 Da and 4-ring MDA (d) [M+H]⁺ = 409 Da, (e) [M]⁺ = 408 Da, and (f) [M-H]⁺ = 407 Da at 20 eV.

D.4. MALDI MS/MS 30 eV

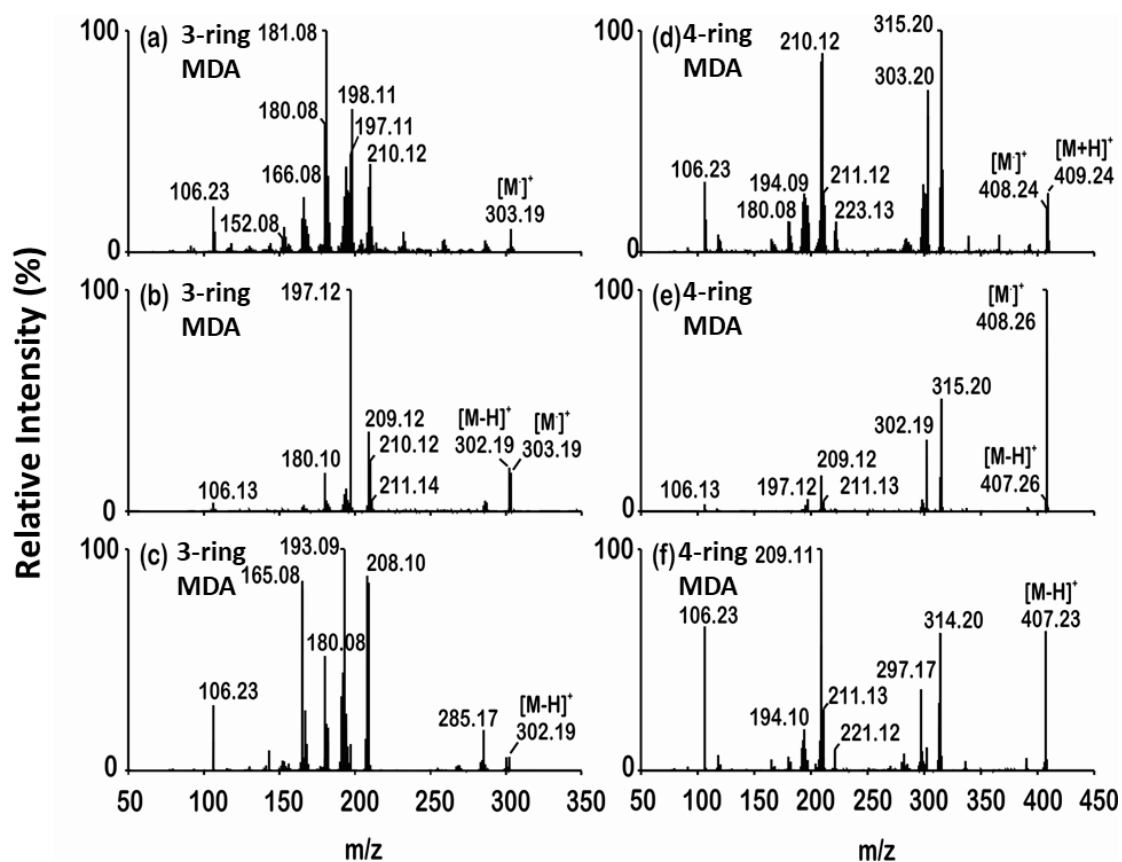


Figure D.4. MALDI tandem mass spectra (MS/MS) of the 3-ring MDA (a) $[M+H]^+$ = 304 Da, (b) $[M]^+$ = 303 Da, and (c) $[M-H]^+$ = 302 Da and 4-ring MDA (d) $[M+H]^+$ = 409 Da, (e) $[M]^+$ = 408 Da, and (f) $[M-H]^+$ = 407 Da at 30 eV.

D.5. 3-Ring MALDI MS³

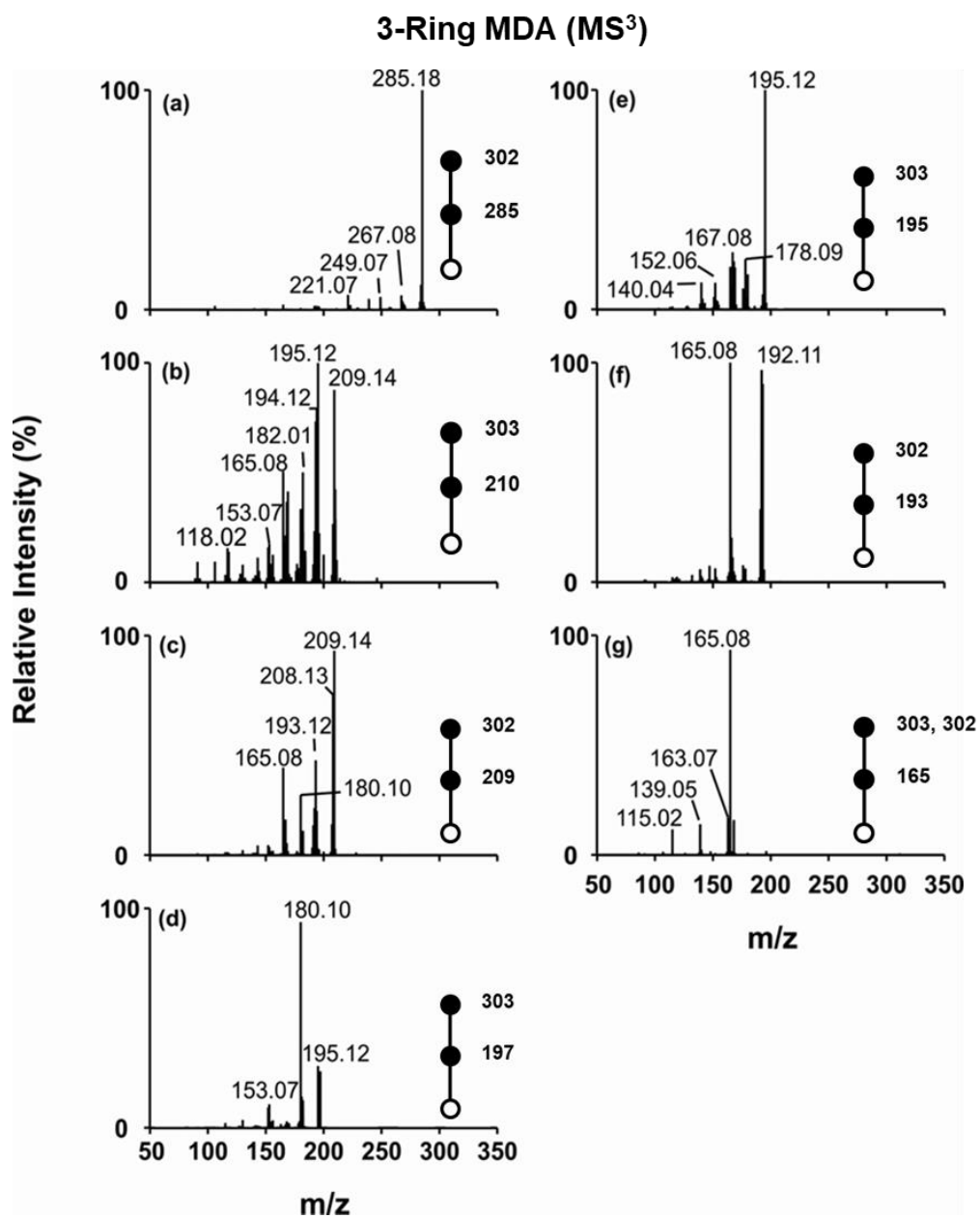


Figure D.5. Multi-stage MS³ tandem IM-MS mass spectra (MS/IM/MS) of 3-ring MDA. The 3-ring [M+H]⁺ = 304 Da parent ion was mass selected then additional major fragment ions were mass selected to acquire MS³ data. (a) 285 Da, (b) 210 Da, (c) 209 Da, (d) 197 Da, (e) 195 Da, (f) 193 Da, and (g) 165 Da. Proposed structures of observed fragment ions in spectra can be found in **Figures D.11-D.13**.

D.6. 4-Ring MALDI MS³

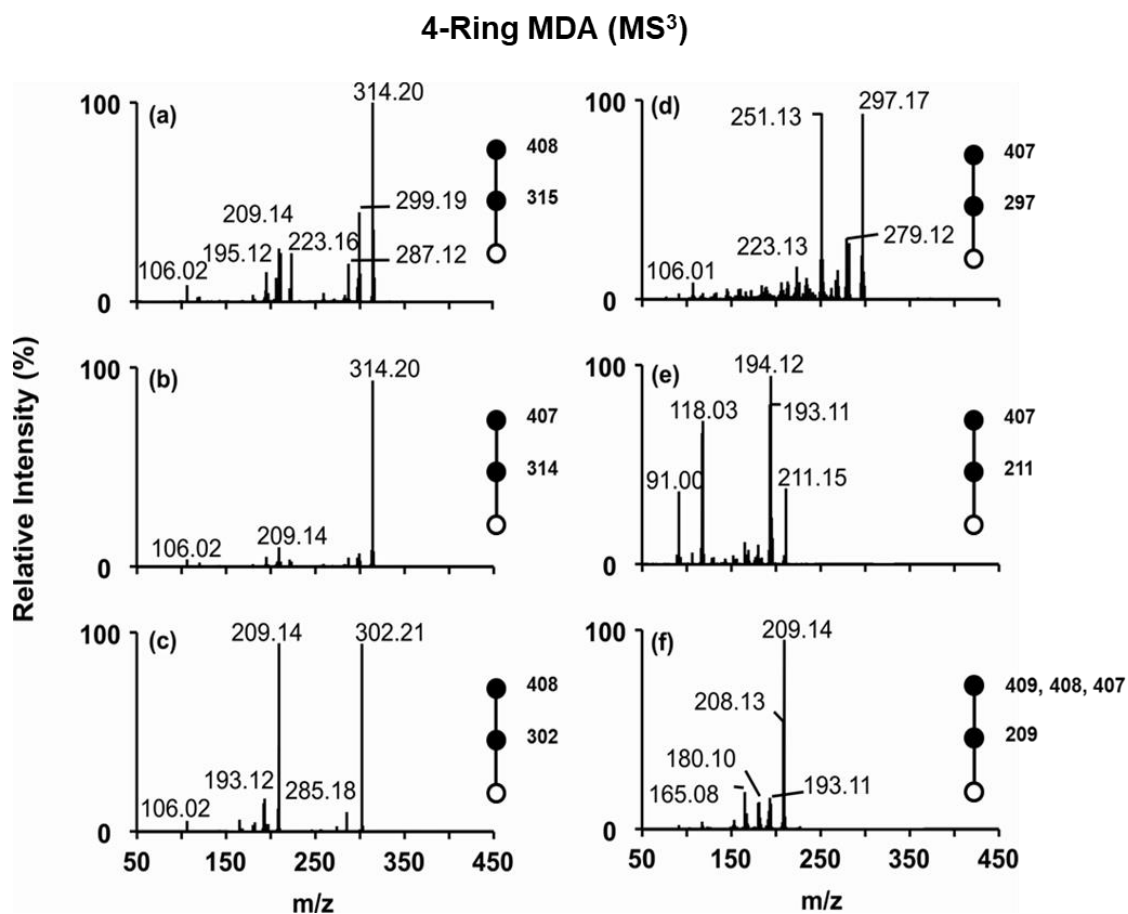


Figure D.6. Multi-stage MS³ tandem IM-MS mass spectra (MS/IM/MS) of 4-ring MDA. The 4-ring [M+H]⁺ = 409 Da parent ion was mass selected then additional major fragment ions were mass selected to acquire MS³ data. (a) 315 Da, (b) 314 Da, (c) 302 Da, (d) 297 Da, (e) 211 Da, and (f) 209 Da.

D.7. Multiple Protonation Example: Part 1

Because of multiple protonation sites in the 3-ring and 4-ring MDAs, it is possible to have multiple structures for both parent and fragment ions. The nature of this problem will be illustrated here for the mass 302 MDA 3-ring parent ions and some of their fragments, but it is common to all 3-ring and 4-ring species. The three isomeric 302 parent ions are shown **below** and are labeled “L”, “C”, and “R”, consistent with the location of the protonated amino group. The gas-phase basicities of the L and R amino groups are essentially the same, group C is somewhat less basic. Thus, protonation will form a mixture of the three parent ions.

The major fragment of the mass 302 parent is an ion at mass 209, formally M-93 corresponding to loss of aniline. Assuming charge-remote fragmentation, structures L and C will produce two different ions as shown **below**. Allowing for proton transfer, structure R can produce either the L or C fragment. The important point being that fragmentation can produce two chemically different ions.

D.7.1. Mass 302 3-Ring Ion Structures

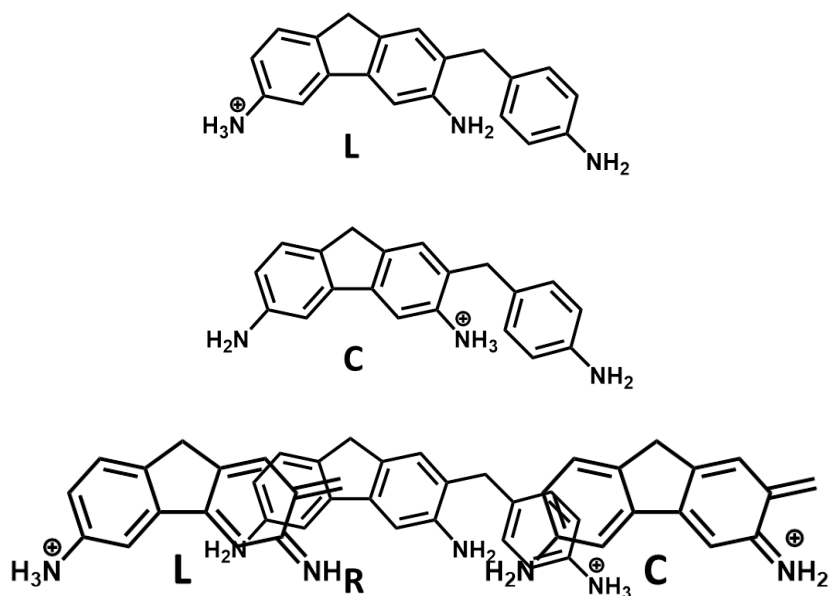


Figure D.7. Multiple Protonation Example (Part 1).

D.8. Multiple Protonation Example: Part 2

Also, these ions can be considered as a hybrid of two extreme structures, as shown **below**. The fragmentation reactions observed for the mass 302 parent indicate behavior consistent with both structures. Tautomers or resonance hybrid structures, take your pick. An extreme example is the mass 285 fragment ion from the M-H⁺ parent at mass 302. This corresponds to M-17, loss of ammonia. It is not one of the more intense fragment ions for the mass 302 parent, but loss of ammonia figures very prominently in the MALDI spectra of the 2-ring MDA M-H⁺ ions, accounting for 51-89% total intensity. Six fragment ions are possible, depending on which amine group is lost and on which the residual charge remains. These are shown **below** in the order of loss of L, C and R amine groups. Needless to say, the problem of multiple possible fragment ions will only be greater for the 4-ring isomers.

D.8.1. Multiple Protonation Example: Part 2

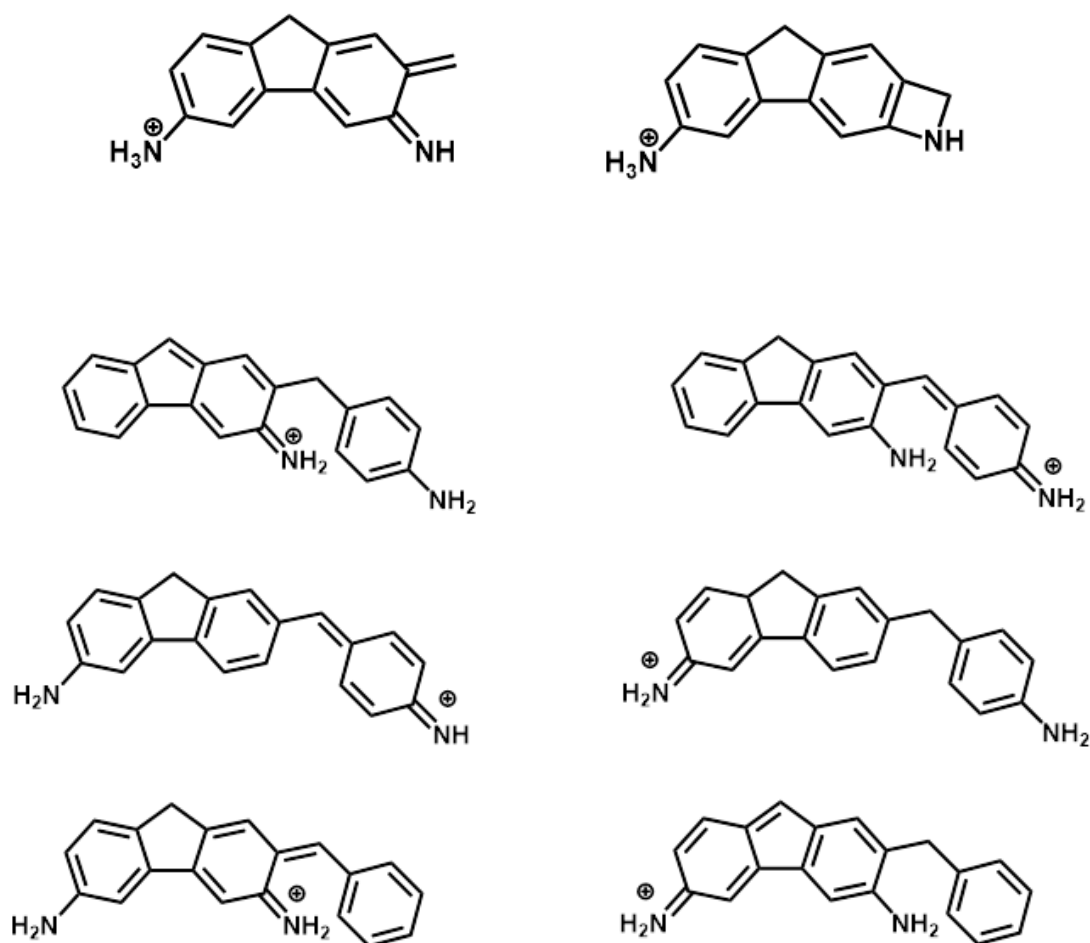


Figure D.8. Multiple Protonation Example (Part 2).

D.9. IM-MS Curve Resolution

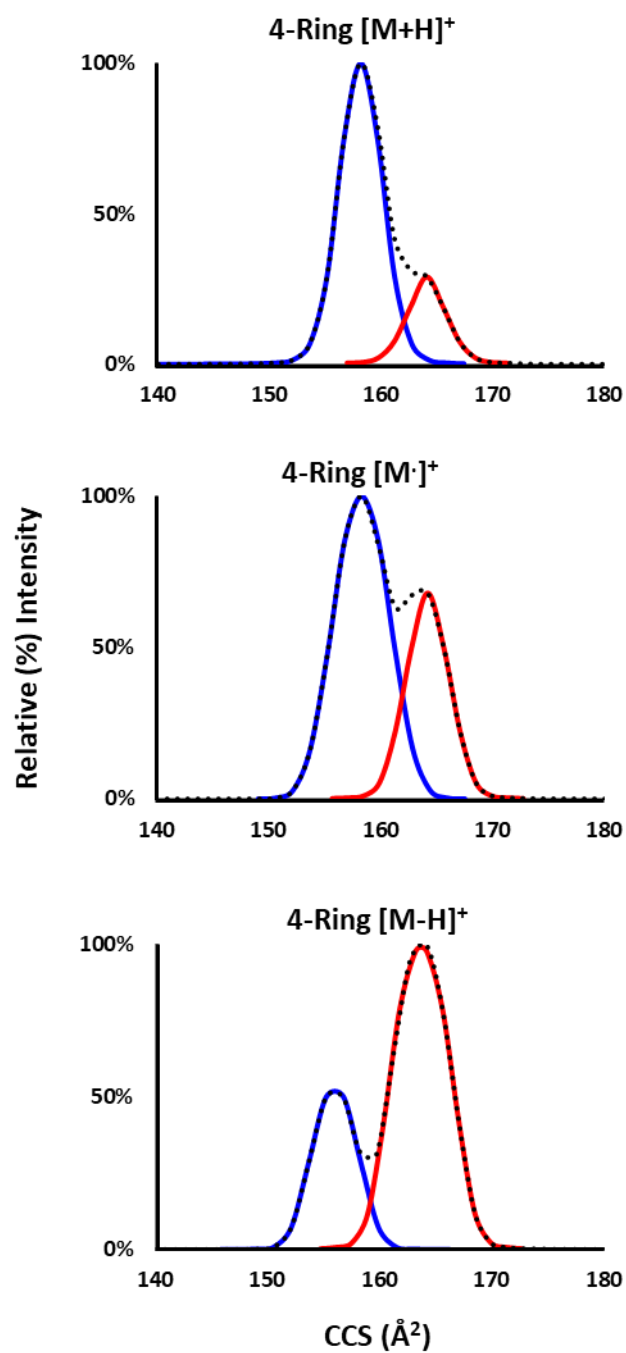


Figure D.9. Estimated Gaussian curve resolution distribution of 4-ring MDA precursor species.

Table D.1. IM-MS 3-Ring Raw Data

| 3-Ring [M+H] ⁺ | | | 3-Ring [M] ⁺ | | | 3-Ring [M-H] ⁺ | | |
|---------------------------|---------------|-----------------------|-------------------------|---------------|-----------------------|---------------------------|---------------|-----------------------|
| dt (ms) | Intensity (%) | CCS (Å ²) | dt (ms) | Intensity (%) | CCS (Å ²) | dt (ms) | Intensity (%) | CCS (Å ²) |
| 2.36 | 0.00% | 114.95 | 2.36 | 0.00% | 114.97 | 2.36 | 0.00% | 114.98 |
| 2.42 | 0.00% | 116.96 | 2.42 | 0.00% | 116.97 | 2.42 | 0.00% | 116.99 |
| 2.49 | 0.00% | 118.93 | 2.49 | 0.00% | 118.95 | 2.49 | 0.00% | 118.97 |
| 2.56 | 0.00% | 120.88 | 2.56 | 0.00% | 120.90 | 2.56 | 0.00% | 120.92 |
| 2.63 | 0.00% | 122.83 | 2.63 | 0.00% | 122.85 | 2.63 | 0.00% | 122.87 |
| 2.70 | 0.00% | 124.73 | 2.70 | 0.00% | 124.75 | 2.70 | 0.00% | 124.77 |
| 2.77 | 0.01% | 126.60 | 2.77 | 0.00% | 126.62 | 2.77 | 0.01% | 126.64 |
| 2.84 | 0.03% | 128.45 | 2.84 | 0.01% | 128.47 | 2.84 | 0.01% | 128.49 |
| 2.91 | 0.17% | 130.30 | 2.91 | 0.08% | 130.32 | 2.91 | 0.10% | 130.34 |
| 2.98 | 1.01% | 132.10 | 2.98 | 0.47% | 132.12 | 2.98 | 1.12% | 132.14 |
| 3.05 | 5.09% | 133.88 | 3.05 | 4.22% | 133.90 | 3.05 | 10.99% | 133.92 |
| 3.12 | 14.36% | 135.64 | 3.12 | 22.79% | 135.66 | 3.12 | 42.69% | 135.68 |
| 3.19 | 39.90% | 137.41 | 3.19 | 60.92% | 137.43 | 3.19 | 80.79% | 137.45 |
| 3.26 | 85.16% | 139.13 | 3.26 | 97.14% | 139.15 | 3.26 | 100.00% | 139.17 |
| 3.32 | 100.00% | 140.83 | 3.32 | 100.00% | 140.85 | 3.32 | 80.98% | 140.87 |
| 3.39 | 57.43% | 142.52 | 3.39 | 62.19% | 142.54 | 3.39 | 36.37% | 142.56 |
| 3.46 | 14.25% | 144.21 | 3.46 | 18.18% | 144.23 | 3.46 | 8.69% | 144.25 |
| 3.53 | 2.52% | 145.86 | 3.53 | 3.32% | 145.88 | 3.53 | 1.65% | 145.90 |
| 3.60 | 0.64% | 147.49 | 3.60 | 0.64% | 147.52 | 3.60 | 0.34% | 147.54 |
| 3.67 | 0.11% | 149.11 | 3.67 | 0.14% | 149.14 | 3.67 | 0.13% | 149.16 |
| 3.74 | 0.05% | 150.74 | 3.74 | 0.08% | 150.76 | 3.74 | 0.18% | 150.78 |
| 3.81 | 0.04% | 152.33 | 3.81 | 0.08% | 152.35 | 3.81 | 0.25% | 152.37 |
| 3.88 | 0.02% | 153.90 | 3.88 | 0.06% | 153.93 | 3.88 | 0.18% | 153.95 |
| 3.95 | 0.01% | 155.46 | 3.95 | 0.02% | 155.49 | 3.95 | 0.07% | 155.51 |
| 4.02 | 0.00% | 157.03 | 4.02 | 0.01% | 157.06 | 4.02 | 0.01% | 157.08 |
| 4.09 | 0.00% | 158.57 | 4.09 | 0.00% | 158.59 | 4.09 | 0.00% | 158.61 |
| 4.16 | 0.00% | 160.09 | 4.16 | 0.00% | 160.11 | 4.16 | 0.00% | 160.14 |
| 4.22 | 0.00% | 161.60 | 4.22 | 0.00% | 161.62 | 4.22 | 0.00% | 161.64 |
| 4.29 | 0.00% | 163.11 | 4.29 | 0.00% | 163.14 | 4.29 | 0.00% | 163.16 |

Table D.1. IM-MS data for each 3-ring MDA precursor trace.

Table D.2. IM-MS 4-Ring Raw Data

| 4-Ring [M+H] ⁺ | | | 4-Ring [M] ⁺ | | | 4-Ring [M-H] ⁺ | | |
|---------------------------|---------------|-----------------------|-------------------------|---------------|-----------------------|---------------------------|---------------|-----------------------|
| dt (ms) | Intensity (%) | CCS (Å ²) | dt (ms) | Intensity (%) | CCS (Å ²) | dt (ms) | Intensity (%) | CCS (Å ²) |
| 3.32 | 0.00% | 139.20 | 3.32 | 0.00% | 139.21 | 2.98 | 0.00% | 130.58 |
| 3.39 | 0.00% | 140.87 | 3.39 | 0.00% | 140.88 | 3.05 | 0.00% | 132.35 |
| 3.46 | 0.00% | 142.54 | 3.46 | 0.00% | 142.56 | 3.12 | 0.00% | 134.09 |
| 3.53 | 0.00% | 144.18 | 3.53 | 0.00% | 144.19 | 3.19 | 0.00% | 135.84 |
| 3.60 | 0.00% | 145.80 | 3.60 | 0.00% | 145.81 | 3.26 | 0.00% | 137.54 |
| 3.67 | 0.04% | 147.40 | 3.67 | 0.01% | 147.41 | 3.32 | 0.00% | 139.23 |
| 3.74 | 0.15% | 149.01 | 3.74 | 0.05% | 149.02 | 3.39 | 0.00% | 140.89 |
| 3.81 | 0.38% | 150.58 | 3.81 | 0.30% | 150.59 | 3.46 | 0.00% | 142.57 |
| 3.88 | 1.46% | 152.14 | 3.88 | 3.30% | 152.15 | 3.53 | 0.00% | 144.20 |
| 3.95 | 7.92% | 153.68 | 3.95 | 18.48% | 153.70 | 3.60 | 0.01% | 145.82 |
| 4.02 | 33.31% | 155.24 | 4.02 | 50.62% | 155.25 | 3.67 | 0.02% | 147.42 |
| 4.09 | 79.46% | 156.75 | 4.09 | 87.21% | 156.77 | 3.74 | 0.07% | 149.03 |
| 4.16 | 100.00% | 158.26 | 4.16 | 100.00% | 158.27 | 3.81 | 0.67% | 150.61 |
| 4.22 | 69.66% | 159.75 | 4.22 | 77.43% | 159.77 | 3.88 | 6.79% | 152.17 |
| 4.29 | 37.69% | 161.25 | 4.29 | 62.72% | 161.27 | 3.95 | 26.27% | 153.71 |
| 4.36 | 34.57% | 162.72 | 4.36 | 74.65% | 162.74 | 4.02 | 45.64% | 155.26 |
| 4.43 | 33.71% | 164.18 | 4.43 | 75.67% | 164.19 | 4.09 | 43.65% | 156.78 |
| 4.50 | 21.37% | 165.63 | 4.50 | 53.32% | 165.64 | 4.16 | 26.36% | 158.29 |
| 4.57 | 7.96% | 167.08 | 4.57 | 22.00% | 167.10 | 4.22 | 30.19% | 159.78 |
| 4.64 | 1.92% | 168.51 | 4.64 | 4.84% | 168.52 | 4.29 | 64.21% | 161.28 |
| 4.71 | 0.57% | 169.92 | 4.71 | 0.94% | 169.93 | 4.36 | 95.45% | 162.75 |
| 4.78 | 0.43% | 171.32 | 4.78 | 0.30% | 171.34 | 4.43 | 100.00% | 164.21 |
| 4.85 | 0.12% | 172.74 | 4.85 | 0.12% | 172.75 | 4.50 | 75.39% | 165.65 |
| 4.92 | 0.03% | 174.12 | 4.92 | 0.05% | 174.13 | 4.57 | 36.65% | 167.11 |
| 4.99 | 0.03% | 175.49 | 4.99 | 0.04% | 175.51 | 4.64 | 9.57% | 168.53 |
| 5.06 | 0.01% | 176.86 | 5.06 | 0.01% | 176.87 | 4.71 | 1.76% | 169.95 |
| 5.13 | 0.00% | 178.23 | 5.13 | 0.01% | 178.25 | 4.78 | 0.56% | 171.35 |
| 5.19 | 0.00% | 179.58 | 5.19 | 0.00% | 179.60 | 4.85 | 0.21% | 172.77 |
| 5.26 | 0.00% | 180.92 | 5.26 | 0.00% | 180.93 | 4.92 | 0.10% | 174.15 |
| 5.33 | 0.01% | 182.25 | 5.33 | 0.00% | 182.26 | 4.99 | 0.04% | 175.52 |

Table D.2. IM-MS data for each 4-ring MDA precursor trace.

D.10. CID Curves 3-Ring

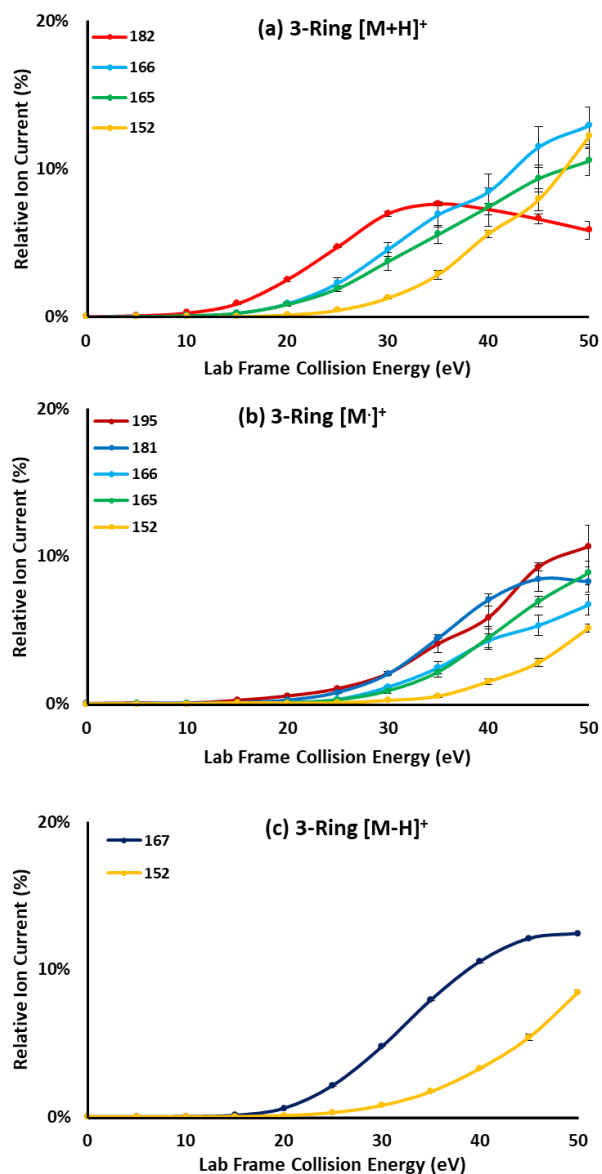


Figure D.10. CID curves monitoring the transition of 3-ring MDA precursors (a) $[M+H]^+$, (b) $[M]^+$, and (c) $[M-H]^+$ to fragment ions. These fragment ions are generated in low abundance and at relatively high lab frame energies.

Table D.3. Total RIC% 304 Da

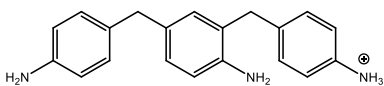
| 3-Ring [M+H] ⁺ | | | | | | | | | | | |
|---------------------------|--------------|--------------|--------------|--------------|--------------|--------------|--------------|--------------|--------------|--------------|--------------|
| Fragment Ion | 0 CE | 5 CE | 10 CE | 15 CE | 20 CE | 25 CE | 30 CE | 35 CE | 40 CE | 45 CE | 50 CE |
| 304 | 87.5% ± 0.5% | 76.2% ± 0.5% | 43.7% ± 0.6% | 18.5% ± 2.1% | 6.7% ± 0.9% | 1.3% ± 0.8% | 0.4% ± 0.1% | 0.2% ± 0.0% | 0.1% ± 0.0% | 0.1% ± 0.0% | 0.0% ± 0.0% |
| 303 | 5.1% ± 0.2% | 4.8% ± 0.2% | 5.7% ± 0.3% | 8.0% ± 0.1% | 7.8% ± 0.5% | 5.0% ± 0.1% | 2.0% ± 0.1% | 0.7% ± 0.1% | 0.2% ± 0.1% | 0.1% ± 0.1% | 0.1% ± 0.1% |
| 211 | 2.3% ± 0.3% | 4.1% ± 0.6% | 6.1% ± 0.7% | 7.0% ± 0.2% | 6.2% ± 0.8% | 4.1% ± 0.7% | 2.2% ± 0.1% | 0.9% ± 0.1% | 0.5% ± 0.2% | 0.2% ± 0.0% | 0.1% ± 0.0% |
| 210 | 0.3% ± 0.0% | 0.8% ± 0.0% | 2.6% ± 0.0% | 5.8% ± 0.6% | 8.8% ± 0.2% | 10.1% ± 0.3% | 8.4% ± 0.3% | 5.0% ± 0.2% | 3.0% ± 0.2% | 1.8% ± 0.2% | 1.2% ± 0.0% |
| 209 | 0.1% ± 0.0% | 0.3% ± 0.0% | 1.0% ± 0.1% | 2.4% ± 0.0% | 4.4% ± 0.1% | 5.6% ± 0.2% | 5.8% ± 0.3% | 5.6% ± 0.5% | 4.8% ± 0.7% | 4.1% ± 0.4% | 3.0% ± 0.2% |
| 198 | 2.4% ± 0.2% | 7.7% ± 0.2% | 22.4% ± 1.1% | 29.3% ± 1.1% | 26.7% ± 0.7% | 19.8% ± 1.4% | 12.1% ± 0.9% | 6.1% ± 0.2% | 2.7% ± 0.3% | 1.0% ± 0.1% | 0.4% ± 0.0% |
| 197 | 1.7% ± 0.1% | 5.1% ± 0.5% | 14.9% ± 0.6% | 19.7% ± 1.1% | 18.1% ± 0.9% | 14.1% ± 1.2% | 9.7% ± 0.6% | 6.0% ± 0.3% | 3.4% ± 0.1% | 2.0% ± 0.3% | 1.1% ± 0.2% |
| 182 | 0.1% ± 0.0% | 0.1% ± 0.0% | 0.3% ± 0.0% | 0.9% ± 0.1% | 2.5% ± 0.1% | 4.7% ± 0.0% | 7.0% ± 0.2% | 7.7% ± 0.2% | 7.3% ± 0.4% | 6.6% ± 0.3% | 5.9% ± 0.6% |
| 181 | 0.2% ± 0.1% | 0.3% ± 0.0% | 1.3% ± 0.1% | 3.2% ± 0.3% | 7.3% ± 0.5% | 13.8% ± 0.6% | 19.4% ± 0.8% | 24.3% ± 0.5% | 25.3% ± 0.7% | 25.0% ± 0.5% | 23.5% ± 0.4% |
| 180 | 0.1% ± 0.0% | 0.2% ± 0.1% | 0.7% ± 0.1% | 2.0% ± 0.1% | 4.4% ± 0.2% | 8.1% ± 0.3% | 12.3% ± 0.6% | 14.8% ± 0.3% | 16.4% ± 0.8% | 16.0% ± 0.9% | 15.2% ± 0.5% |
| 166 | 0.0% ± 0.0% | 0.0% ± 0.1% | 0.1% ± 0.0% | 0.3% ± 0.0% | 0.9% ± 0.1% | 2.3% ± 0.4% | 4.6% ± 0.5% | 6.9% ± 0.8% | 8.5% ± 1.2% | 11.5% ± 1.4% | 12.9% ± 1.3% |
| 165 | 0.0% ± 0.0% | 0.0% ± 0.0% | 0.1% ± 0.0% | 0.3% ± 0.0% | 0.9% ± 0.1% | 1.9% ± 0.2% | 3.8% ± 0.6% | 5.6% ± 0.6% | 7.5% ± 1.3% | 9.4% ± 0.9% | 10.6% ± 1.0% |
| 152 | 0.0% ± 0.0% | 0.0% ± 0.0% | 0.0% ± 0.0% | 0.0% ± 0.0% | 0.2% ± 0.0% | 0.5% ± 0.1% | 1.3% ± 0.1% | 2.9% ± 0.3% | 5.6% ± 0.2% | 8.0% ± 0.7% | 12.2% ± 0.8% |

Table D.3. Total percent ion currents observed for 3-ring 304 [M+H]⁺ and all associated product ion species.

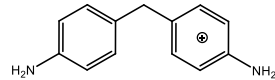
D.11. 304 Da Structures

3-Ring 304 Da

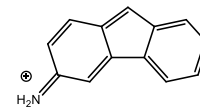
304



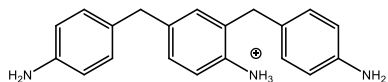
198



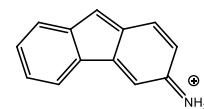
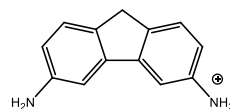
180



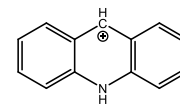
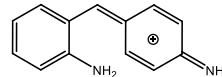
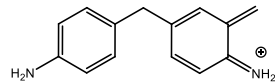
303



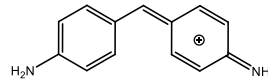
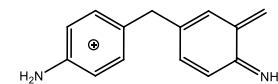
197



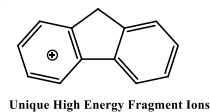
211



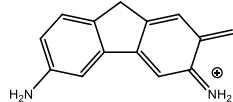
210



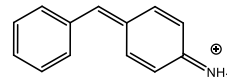
166



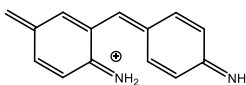
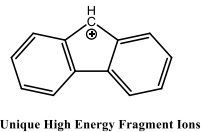
209



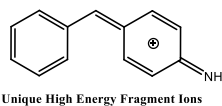
182



165



181



152

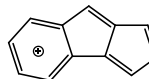


Figure D.11. Possible 3-ring fragment ion structures derived from the 304 Da = [M+H]⁺ species.

Table D.4. Total RIC% 303 Da

| 3-Ring [M] ⁺ | | | | | | | | | | | |
|-------------------------|-----------------|-----------------|-----------------|-----------------|-----------------|-----------------|-----------------|-----------------|-----------------|-----------------|-----------------|
| Fragment Ion | 0 CE | 5 CE | 10 CE | 15 CE | 20 CE | 25 CE | 30 CE | 35 CE | 40 CE | 45 CE | 50 CE |
| 303 | 95.0% ± 0.7% | 93.2% ± 0.6% | 87.2% ± 0.3% | 65.2% ± 3.9% | 38.7% ± 3.5% | 20.5% ± 1.8% | 7.4% ± 0.7% | 1.9% ± 0.0% | 0.5% ± 0.1% | 0.1% ± 0.1% | 0.1% ± 0.1% |
| 302 | 1.2% ± 0.2% | 0.7% ± 0.0% | 1.1% ± 0.1% | 3.1% ± 0.1% | 6.2% ± 0.4% | 9.3% ± 0.5% | 8.1% ± 0.2% | 4.7% ± 0.4% | 2.0% ± 0.5% | 0.6% ± 0.3% | 0.1% ± 0.0% |
| 210 | 0.6% ± 0.1% | 0.4% ± 0.1% | 0.6% ± 0.1% | 1.7% ± 0.0% | 3.7% ± 0.3% | 7.0% ± 0.2% | 10.2% ± 2.1% | 6.9% ± 0.3% | 4.0% ± 0.6% | 1.5% ± 0.2% | 0.8% ± 0.2% |
| 209 | 0.3% ± 0.1% | 0.2% ± 0.0% | 0.4% ± 0.2% | 1.5% ± 0.3% | 4.2% ± 0.3% | 8.6% ± 0.2% | 14.6% ± 1.3% | 16.0% ± 0.9% | 14.9% ± 0.9% | 10.3% ± 0.7% | 6.2% ± 0.6% |
| 197 | 3.0% ± 0.2% | 2.7% ± 0.5% | 7.2% ± 0.1% | 23.2% ± 3.6% | 39.7% ± 3.2% | 42.4% ± 1.0% | 37.7% ± 4.4% | 30.0% ± 1.3% | 20.0% ± 1.5% | 10.5% ± 0.3% | 5.1% ± 0.6% |
| 181 | 0.0% ± 0.0% | 0.0% ± 0.0% | 0.0% ± 0.0% | 0.1% ± 0.0% | 0.3% ± 0.0% | 0.8% ± 0.1% | 2.0% ± 0.1% | 4.5% ± 0.1% | 7.0% ± 0.4% | 8.5% ± 0.9% | 8.3% ± 0.7% |
| 180 | 0.1% ± 0.1% | 0.1% ± 0.0% | 0.2% ± 0.1% | 0.7% ± 0.2% | 1.8% ± 0.2% | 3.7% ± 0.5% | 7.8% ± 0.8% | 15.2% ± 1.2% | 22.1% ± 1.2% | 27.8% ± 2.1% | 30.6% ± 0.8% |
| 166 | 0.0% ± 0.0% | 0.0% ± 0.0% | 0.0% ± 0.0% | 0.0% ± 0.0% | 0.1% ± 0.0% | 0.3% ± 0.1% | 1.1% ± 0.1% | 2.4% ± 0.4% | 4.3% ± 0.5% | 5.3% ± 0.7% | 6.7% ± 0.7% |
| 165 | 0.0% ± 0.0% | 0.0% ± 0.0% | 0.0% ± 0.0% | 0.0% ± 0.0% | 0.1% ± 0.0% | 0.3% ± 0.0% | 0.9% ± 0.2% | 2.2% ± 0.4% | 4.5% ± 0.8% | 6.9% ± 0.4% | 8.9% ± 0.8% |
| 152 | 0.0% ± 0.0% | 0.0% ± 0.0% | 0.0% ± 0.0% | 0.1% ± 0.1% | 0.1% ± 0.0% | 0.1% ± 0.0% | 0.2% ± 0.0% | 0.5% ± 0.1% | 1.5% ± 0.2% | 2.8% ± 0.3% | 5.1% ± 0.3% |

Table D.4. Total percent ion currents observed for 3-ring 303 [M]⁺ and all associated product ion species.

D.12. 303 Da Structures

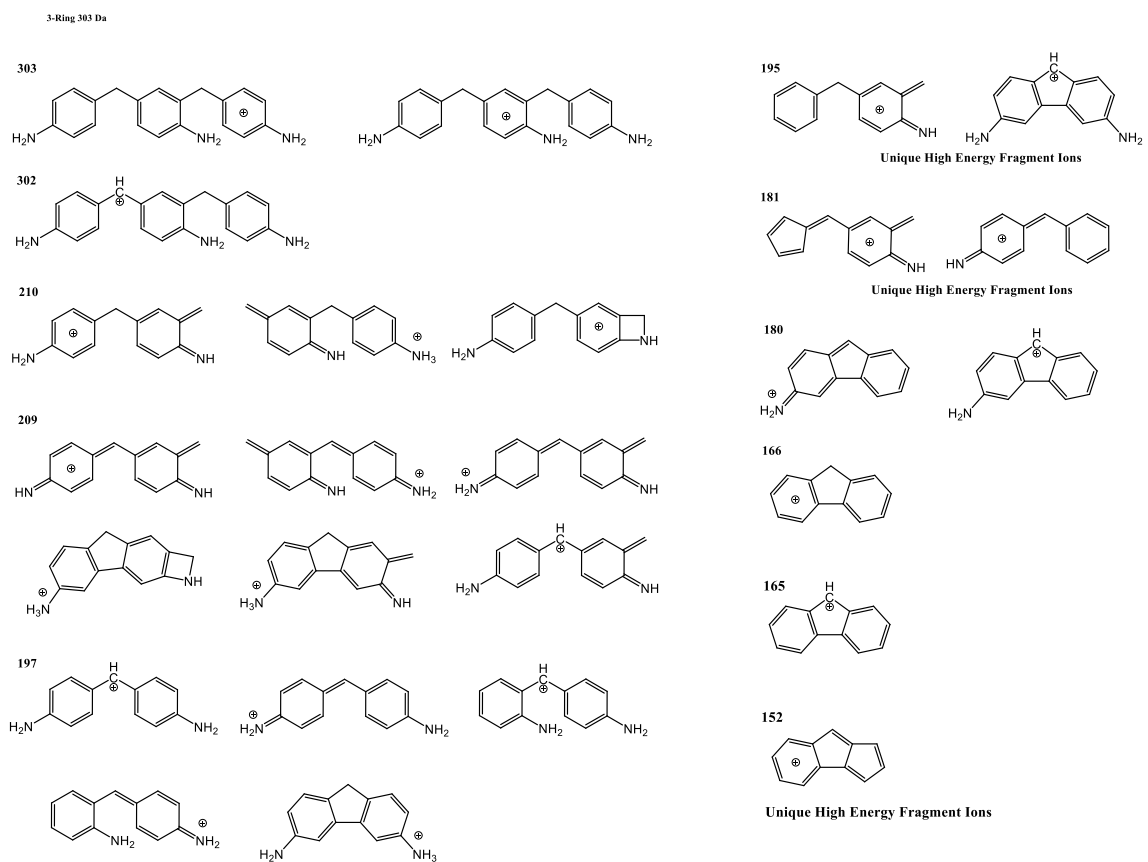


Figure D.12. Possible 3-ring fragment ion structures derived from the 303 Da = $[M]^+$ species.

Table D.5. Total RIC% 302 Da

| 3-Ring [M-H] ⁺ | | | | | | | | | | | |
|---------------------------|-----------------|-----------------|-----------------|-----------------|-----------------|-----------------|-----------------|-----------------|-----------------|-----------------|-----------------|
| Fragment Ion | 0 CE | 5 CE | 10 CE | 15 CE | 20 CE | 25 CE | 30 CE | 35 CE | 40 CE | 45 CE | 50 CE |
| 302 | 99.4% ± 0.1% | 98.2% ± 0.2% | 92.7% ± 0.6% | 71.8% ± 0.2% | 31.2% ± 0.2% | 6.7% ± 0.4% | 1.1% ± 0.0% | 0.2% ± 0.0% | 0.0% ± 0.0% | 0.0% ± 0.0% | 0.0% ± 0.0% |
| 285 | 0.0% ± 0.0% | 0.1% ± 0.0% | 0.5% ± 0.0% | 1.9% ± 0.0% | 3.9% ± 0.1% | 4.3% ± 0.1% | 3.2% ± 0.1% | 1.9% ± 0.1% | 1.0% ± 0.0% | 0.5% ± 0.0% | 0.2% ± 0.0% |
| 209 | 0.2% ± 0.0% | 0.4% ± 0.0% | 2.8% ± 0.1% | 16.0% ± 0.2% | 36.0% ± 0.2% | 30.9% ± 0.2% | 15.0% ± 0.3% | 5.5% ± 0.1% | 2.0% ± 0.1% | 0.9% ± 0.0% | 0.4% ± 0.0% |
| 208 | 0.0% ± 0.0% | 0.0% ± 0.0% | 0.2% ± 0.0% | 1.0% ± 0.0% | 4.7% ± 0.1% | 10.8% ± 0.1% | 15.6% ± 0.2% | 15.8% ± 0.1% | 12.1% ± 0.0% | 7.9% ± 0.1% | 4.7% ± 0.2% |
| 193 | 0.0% ± 0.0% | 0.1% ± 0.0% | 0.2% ± 0.0% | 1.3% ± 0.0% | 5.8% ± 0.1% | 13.0% ± 0.2% | 17.8% ± 0.2% | 17.2% ± 0.1% | 13.3% ± 0.1% | 9.2% ± 0.2% | 6.1% ± 0.1% |
| 192 | 0.0% ± 0.0% | 0.0% ± 0.0% | 0.2% ± 0.0% | 1.2% ± 0.0% | 4.6% ± 0.1% | 7.6% ± 0.0% | 7.9% ± 0.1% | 7.3% ± 0.0% | 7.3% ± 0.1% | 7.1% ± 0.0% | 6.6% ± 0.1% |
| 180 | 0.0% ± 0.0% | 0.0% ± 0.0% | 0.2% ± 0.0% | 0.6% ± 0.0% | 1.8% ± 0.1% | 4.8% ± 0.1% | 8.8% ± 0.3% | 13.4% ± 0.1% | 18.5% ± 0.3% | 22.9% ± 0.2% | 26.0% ± 0.3% |
| 167 | 0.0% ± 0.0% | 0.0% ± 0.0% | 0.0% ± 0.0% | 0.1% ± 0.0% | 0.6% ± 0.0% | 2.1% ± 0.1% | 4.8% ± 0.0% | 7.9% ± 0.1% | 10.6% ± 0.1% | 12.1% ± 0.1% | 12.4% ± 0.0% |
| 165 | 0.0% ± 0.0% | 0.0% ± 0.0% | 0.1% ± 0.0% | 0.6% ± 0.0% | 3.1% ± 0.0% | 8.7% ± 0.1% | 15.0% ± 0.1% | 20.7% ± 0.3% | 25.0% ± 0.3% | 28.0% ± 0.6% | 29.7% ± 0.2% |
| 152 | 0.0% ± 0.0% | 0.0% ± 0.0% | 0.0% ± 0.0% | 0.0% ± 0.0% | 0.1% ± 0.0% | 0.3% ± 0.0% | 0.8% ± 0.0% | 1.7% ± 0.0% | 3.3% ± 0.0% | 5.4% ± 0.2% | 8.5% ± 0.1% |
| 106 | 0.0% ± 0.0% | 0.1% ± 0.0% | 0.4% ± 0.0% | 1.3% ± 0.0% | 2.9% ± 0.0% | 4.3% ± 0.1% | 5.0% ± 0.1% | 5.2% ± 0.3% | 5.2% ± 0.2% | 4.8% ± 0.3% | 4.5% ± 0.2% |

Table D.5. Total percent ion currents observed for 3-ring 302 [M-H]⁺ and all associated product ion species.

D.13. 302 Da Structures

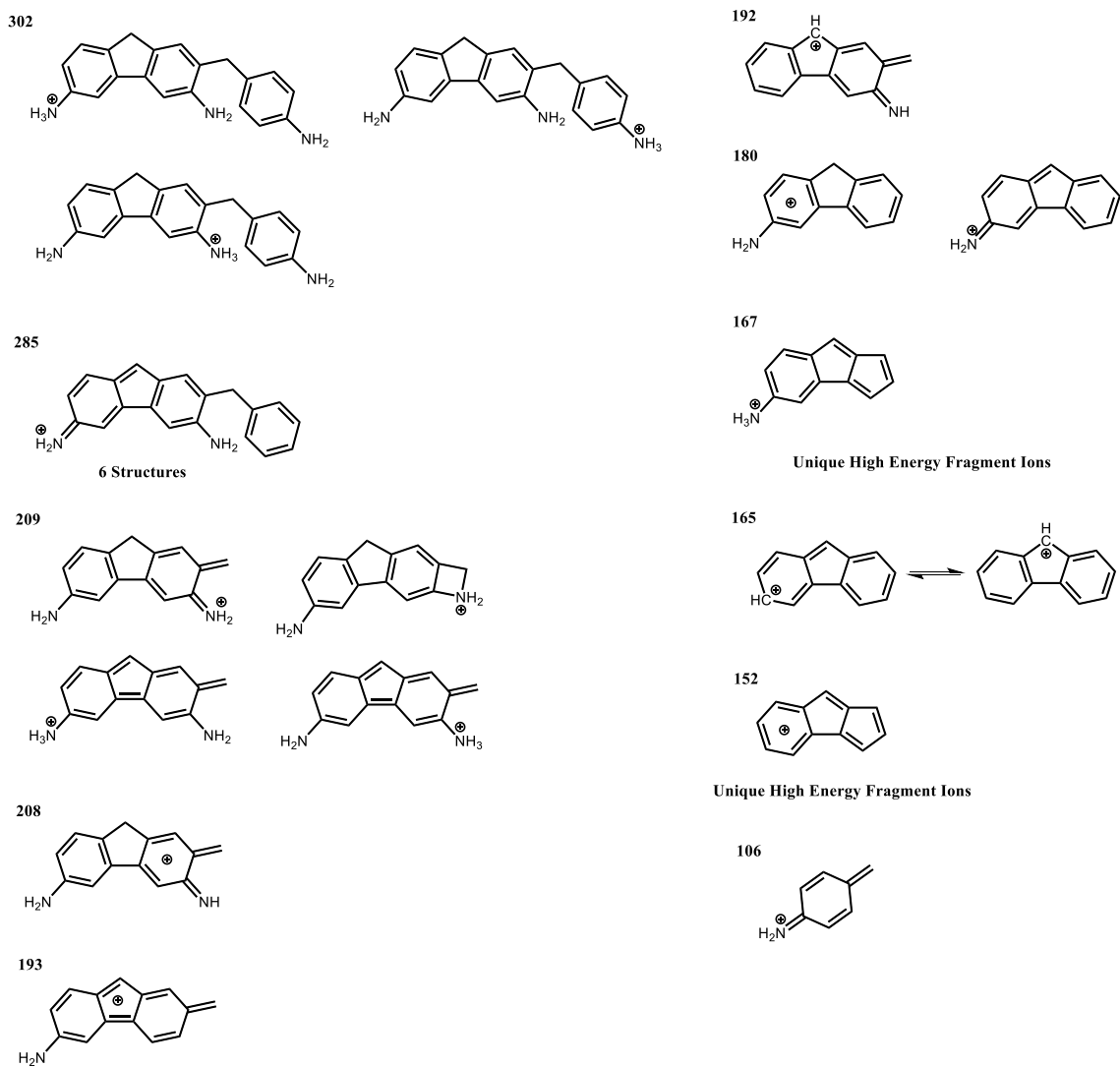


Figure D.13. Possible 3-ring fragment ion structures derived from the 302 Da = [M-H]⁺ species.

D.14. CID Curves 4-Ring

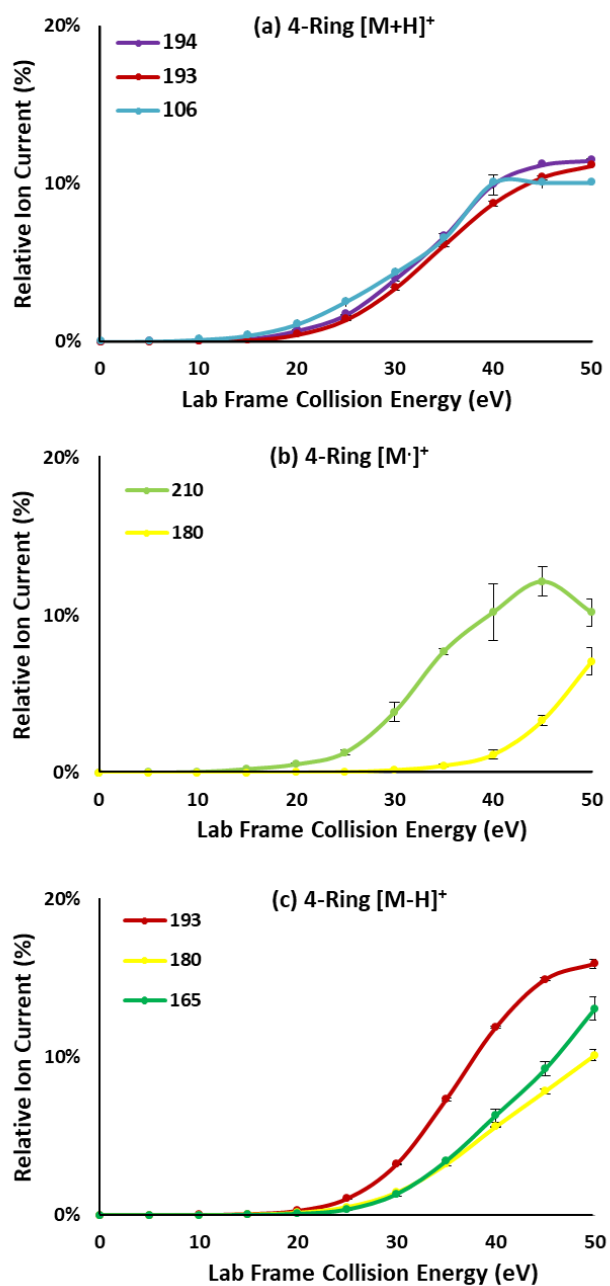


Figure D.14. CID curves monitoring the transition of 4-ring MDA precursors (a) $[M+H]^+$, (b) $[M]^+$, and (c) $[M-H]^+$ to fragment ions. These fragment ions are generated in low abundance and at relatively high lab frame energies.

Table D.6. Total RIC% 409 Da

| 4-Ring [M+H] ⁺ | | | | | | | | | | | |
|---------------------------|-----------------|-----------------|-----------------|-----------------|-----------------|-----------------|-----------------|-----------------|-----------------|-----------------|-----------------|
| Fragment Ion | 0 CE | 5 CE | 10 CE | 15 CE | 20 CE | 25 CE | 30 CE | 35 CE | 40 CE | 45 CE | 50 CE |
| 409 | 93.7% ± 0.2% | 85.3% ± 0.6% | 56.2% ± 3.5% | 27.6% ± 6.6% | 17.4% ± 4.4% | 9.9% ± 2.2% | 3.4% ± 0.7% | 0.7% ± 0.1% | 0.2% ± 0.0% | 0.0% ± 0.0% | 0.0% ± 0.0% |
| 316 | 2.3% ± 0.1% | 8.4% ± 0.9% | 26.3% ± 2.7% | 37.3% ± 4.5% | 27.5% ± 2.8% | 13.9% ± 0.7% | 5.3% ± 0.2% | 1.8% ± 0.2% | 0.7% ± 0.2% | 0.3% ± 0.0% | 0.1% ± 0.0% |
| 315 | 0.7% ± 0.1% | 2.5% ± 0.1% | 8.0% ± 0.7% | 12.2% ± 1.2% | 13.0% ± 0.9% | 13.8% ± 0.4% | 14.9% ± 0.2% | 12.6% ± 0.5% | 7.8% ± 0.9% | 3.9% ± 0.2% | 1.5% ± 0.1% |
| 303 | 0.2% ± 0.0% | 0.7% ± 0.1% | 3.0% ± 0.2% | 7.5% ± 0.6% | 12.6% ± 0.9% | 14.4% ± 1.1% | 10.8% ± 0.1% | 5.5% ± 0.1% | 1.8% ± 0.3% | 0.5% ± 0.0% | 0.1% ± 0.0% |
| 210 | 0.1% ± 0.0% | 0.1% ± 0.1% | 0.7% ± 0.1% | 2.0% ± 0.2% | 5.2% ± 0.1% | 9.4% ± 0.0% | 13.1% ± 0.1% | 13.8% ± 0.0% | 10.9% ± 0.7% | 7.5% ± 0.7% | 4.5% ± 0.4% |
| 209 | 0.1% ± 0.0% | 0.1% ± 0.0% | 0.5% ± 0.0% | 1.9% ± 0.2% | 4.6% ± 0.2% | 8.8% ± 0.3% | 12.9% ± 0.3% | 14.8% ± 0.1% | 12.7% ± 1.7% | 11.2% ± 1.2% | 8.9% ± 0.7% |
| 194 | 0.0% ± 0.0% | 0.0% ± 0.0% | 0.1% ± 0.0% | 0.2% ± 0.0% | 0.7% ± 0.1% | 1.7% ± 0.0% | 4.0% ± 0.1% | 6.7% ± 0.2% | 10.0% ± 0.6% | 11.2% ± 0.0% | 11.5% ± 0.2% |
| 193 | 0.0% ± 0.0% | 0.0% ± 0.0% | 0.0% ± 0.0% | 0.1% ± 0.0% | 0.5% ± 0.0% | 1.4% ± 0.0% | 3.4% ± 0.1% | 6.2% ± 0.2% | 8.8% ± 0.2% | 10.4% ± 0.1% | 11.2% ± 0.0% |
| 106 | 0.0% ± 0.0% | 0.1% ± 0.0% | 0.1% ± 0.0% | 0.4% ± 0.1% | 1.1% ± 0.2% | 2.6% ± 0.3% | 4.4% ± 0.4% | 6.6% ± 0.3% | 10.1% ± 3.1% | 10.1% ± 2.1% | 10.1% ± 1.6% |

Table D.6. Total percent ion currents observed for 4-ring 409 [M+H]⁺ and all associated product ion species.

Table D.7. Total RIC% 408 Da

| 4-Ring [M] ⁺ | | | | | | | | | | | |
|-------------------------|-----------------|-----------------|-----------------|-----------------|-----------------|-----------------|-----------------|-----------------|-----------------|-----------------|-----------------|
| Fragment Ion | 0 CE | 5 CE | 10 CE | 15 CE | 20 CE | 25 CE | 30 CE | 35 CE | 40 CE | 45 CE | 50 CE |
| 408 | 98.1% ± 0.4% | 96.4% ± 0.3% | 91.9% ± 4.3% | 76.4% ± 1.5% | 66.1% ± 2.0% | 58.2% ± 2.6% | 44.5% ± 2.2% | 31.4% ± 2.6% | 16.6% ± 2.6% | 5.7% ± 0.5% | 1.0% ± 0.1% |
| 315 | 1.6% ± 0.3% | 3.1% ± 0.2% | 6.4% ± 4.7% | 17.7% ± 0.7% | 20.9% ± 0.2% | 22.5% ± 0.7% | 21.8% ± 0.7% | 17.8% ± 0.8% | 10.6% ± 2.3% | 6.4% ± 0.1% | 3.1% ± 0.1% |
| 314 | 0.0% ± 0.0% | 0.0% ± 0.0% | 0.1% ± 0.0% | 0.4% ± 0.0% | 1.4% ± 0.2% | 3.9% ± 0.5% | 8.6% ± 2.2% | 12.2% ± 1.0% | 13.4% ± 2.9% | 16.2% ± 1.7% | 13.6% ± 2.2% |
| 302 | 0.2% ± 0.1% | 0.3% ± 0.0% | 1.1% ± 0.3% | 4.0% ± 0.5% | 8.2% ± 1.2% | 9.4% ± 0.7% | 10.5% ± 1.6% | 10.1% ± 0.6% | 8.1% ± 1.5% | 6.3% ± 0.9% | 2.9% ± 0.5% |
| 210 | 0.0% ± 0.0% | 0.0% ± 0.0% | 0.1% ± 0.1% | 0.3% ± 0.0% | 0.6% ± 0.1% | 1.3% ± 0.2% | 3.9% ± 0.6% | 7.7% ± 0.2% | 10.2% ± 1.8% | 12.2% ± 0.9% | 10.2% ± 0.9% |
| 209 | 0.0% ± 0.0% | 0.0% ± 0.0% | 0.1% ± 0.0% | 0.4% ± 0.1% | 1.2% ± 0.2% | 2.8% ± 0.4% | 7.1% ± 1.2% | 12.9% ± 0.1% | 18.1% ± 2.9% | 26.5% ± 0.1% | 29.9% ± 0.7% |
| 180 | 0.0% ± 0.0% | 0.0% ± 0.0% | 0.0% ± 0.0% | 0.0% ± 0.0% | 0.1% ± 0.0% | 0.1% ± 0.0% | 0.2% ± 0.1% | 0.5% ± 0.1% | 1.2% ± 0.3% | 3.3% ± 0.3% | 7.1% ± 0.9% |
| 106 | 0.0% ± 0.0% | 0.0% ± 0.0% | 0.0% ± 0.0% | 0.1% ± 0.0% | 0.2% ± 0.0% | 0.5% ± 0.0% | 2.1% ± 0.3% | 5.9% ± 0.2% | 20.1% ± 0.4% | 21.0% ± 0.8% | 29.6% ± 2.1% |

Table D.7. Total percent ion currents observed for 4-ring 408 [M]⁺ and all associated product ion species.

Table D.8. Total RIC% 407 Da

| 4-Ring [M-H] ⁺ | | | | | | | | | | | |
|---------------------------|-----------------|-----------------|-----------------|-----------------|-----------------|-----------------|-----------------|-----------------|-----------------|-----------------|-----------------|
| Fragment Ion | 0 CE | 5 CE | 10 CE | 15 CE | 20 CE | 25 CE | 30 CE | 35 CE | 40 CE | 45 CE | 50 CE |
| 407 | 85.8% ± 0.5% | 85.8% ± 1.0% | 84.0% ± 1.3% | 78.0% ± 0.8% | 61.8% ± 0.4% | 37.5% ± 0.7% | 15.3% ± 0.4% | 3.5% ± 0.0% | 0.6% ± 0.0% | 0.1% ± 0.0% | 0.0% ± 0.0% |
| 314 | 0.2% ± 0.0% | 0.4% ± 0.0% | 1.4% ± 0.0% | 4.5% ± 0.1% | 10.9% ± 0.2% | 16.3% ± 0.2% | 14.7% ± 0.0% | 8.4% ± 0.2% | 3.8% ± 0.1% | 1.5% ± 0.1% | 0.5% ± 0.1% |
| 297 | 0.1% ± 0.0% | 0.1% ± 0.0% | 0.5% ± 0.0% | 2.3% ± 0.1% | 6.0% ± 0.1% | 8.6% ± 0.2% | 8.4% ± 0.3% | 7.1% ± 0.0% | 5.7% ± 0.0% | 4.3% ± 0.1% | 3.5% ± 0.1% |
| 211 | 0.0% ± 0.0% | 0.1% ± 0.0% | 0.3% ± 0.0% | 1.0% ± 0.1% | 2.7% ± 0.0% | 5.1% ± 0.1% | 6.4% ± 0.1% | 5.5% ± 0.2% | 3.2% ± 0.0% | 1.6% ± 0.1% | 0.7% ± 0.0% |
| 209 | 0.1% ± 0.0% | 0.1% ± 0.0% | 0.3% ± 0.0% | 1.2% ± 0.1% | 4.8% ± 0.1% | 13.9% ± 0.1% | 23.7% ± 0.4% | 24.1% ± 0.3% | 17.2% ± 0.0% | 10.5% ± 0.3% | 6.0% ± 0.2% |
| 193 | 0.0% ± 0.0% | 0.0% ± 0.0% | 0.0% ± 0.0% | 0.1% ± 0.0% | 0.3% ± 0.0% | 1.1% ± 0.0% | 3.2% ± 0.0% | 7.4% ± 0.1% | 11.9% ± 0.0% | 15.0% ± 0.1% | 16.0% ± 0.3% |
| 180 | 0.0% ± 0.0% | 0.0% ± 0.0% | 0.0% ± 0.0% | 0.1% ± 0.0% | 0.2% ± 0.0% | 0.5% ± 0.0% | 1.5% ± 0.0% | 3.2% ± 0.1% | 5.6% ± 0.0% | 7.9% ± 0.2% | 10.2% ± 0.3% |
| 165 | 0.0% ± 0.0% | 0.0% ± 0.0% | 0.0% ± 0.0% | 0.0% ± 0.0% | 0.1% ± 0.0% | 0.4% ± 0.0% | 1.3% ± 0.1% | 3.5% ± 0.1% | 6.3% ± 0.4% | 9.3% ± 0.5% | 13.1% ± 0.7% |
| 106 | 0.0% ± 0.0% | 0.1% ± 0.0% | 0.1% ± 0.0% | 0.4% ± 0.0% | 1.8% ± 0.0% | 6.5% ± 0.1% | 15.8% ± 0.5% | 26.3% ± 0.7% | 33.3% ± 0.3% | 37.0% ± 0.5% | 37.1% ± 0.9% |

Table D.8. Total percent ion currents observed for 4-ring 407 [M-H]⁺ and all associated product ion species.

APPENDIX E

SUPPORTING INFORMATION FOR CHAPTER V

E.1. MS Characterization of PBA

The full ESI-MS spectra of the investigated telechelic PBA ($M_n = 2250 \text{ g mol}^{-1}$) are illustrated in **Figure E.1**. Using ESI of PBA species, we observe characteristic peaks associated with the multiply charged species detected. For **Figure E.1**, the PBA sample was dissolved in ACN that contained 0.1% formic acid to aid in ionization. Here we identified adventitious Na and K metal ion adducts derived from the solution which subsequently cationize with PBA oligomers. Despite the fact that the spray solution containing formic acid is evaporated to yield an abundant source of protons, virtually no protonated $[M+H]^+$ species were observed. As expected from scavenged alkali metal cations, Na adducted oligomers were found to be in greater abundance than the K adducted oligomers. The majority of the species contained in this polymer sample were telechelic PBA oligomers; therefore ion series annotated in **Figure E.1** is attributed to oligomers with $-OH$ end groups. Only small low MW cyclics were observed in the PBA sample: (pentagon) $[M+Na]^+$ species observed at 423 (DP = 2), 623 (DP = 3), and 823 Da (DP = 4) (**Figure E.1a**). In **Figure E.1b**, singly and doubly charged PBA oligomers are observed, cationized by both Na and K, and a low abundance $[M+K]^+$ adducted species is observed at 639 Da (DP = 3).

In **Figure E.1**, linear PBA oligomers with differing charge-states are illustrated by shapes: singly charged (square), doubly charged (circle), and triply charged (star). The nature of the polyester backbone of PBA increases the ability for cationized multiply charged species. The unique cation adducted oligomers observed for singly charged species include: $[M+Na]^+$ and $[M+K]^+$. The doubly charged adducted oligomers observed included: $[M+2Na]^{2+}$, $[M+Na+K]^{2+}$, and $[M+2K]^{2+}$. The triply charged adducted oligomers observed included: $[M+3Na]^{3+}$, $[M+2Na+K]^{3+}$, $[M+Na+2K]^{3+}$, and $[M+3K]^{3+}$. In **Figure E.1b**, singly and doubly charged PBA oligomers are observed to cationize with both Na and K ions. In **Figure E.1c**, an example of DP = 14 doubly charged adducts $[M+2Na]^{2+}$, $[M+Na+K]^{2+}$, and $[M+2K]^{2+}$ are observed. These adducts are also observed for each doubly charged PBA oligomer throughout the mass spectra. From steric and coulombic shielding considerations, it is expected that longer oligomer chains can accommodate more cations than shorter chains. Singly charged oligomers are first observed for DP = 1, doubly charged species are observed to start at DP = 4, and triply charged species form starting at DP = 7.

E.1. MS Characterization of PBA (continued)

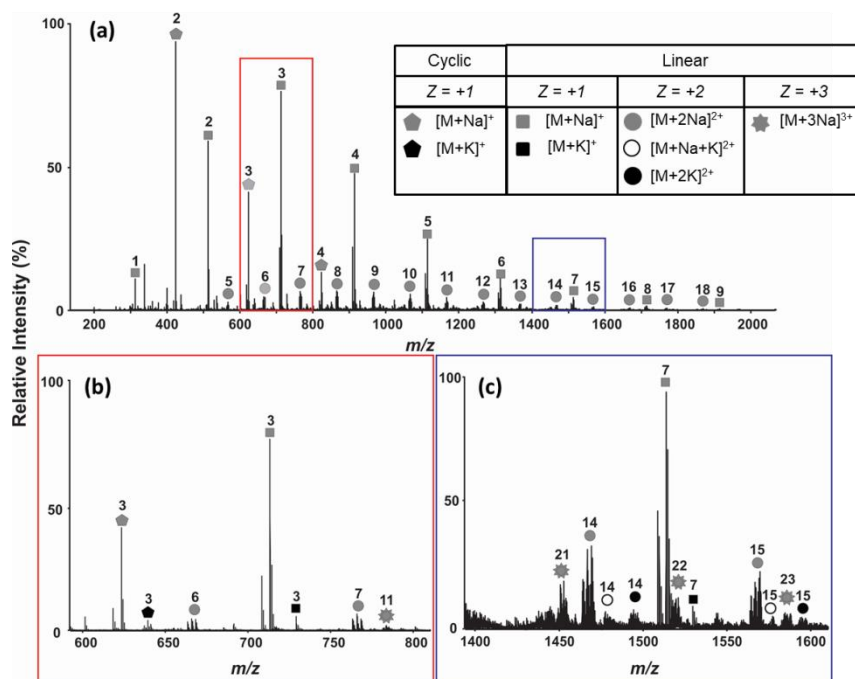


Figure E.1. (a) Full ESI mass spectrum of polybutylene adipate ($M_n = 2200$). Oligomer units are notated by a number value located on top of mass spectrum peaks. The shape symbols located above mass spectrum peaks highlight charge-state trends observed for $z = +1$ cyclic (pentagon) species and linear $z = +1$ (square), $z = +2$ (circle), and $z = +3$ (star) species. ESI spectra of (b) doubly and (c) triply charged PBA adducts.

E.2. MS Spectra of Cationized PBA (Li, Na, K, Rb, and Cs)

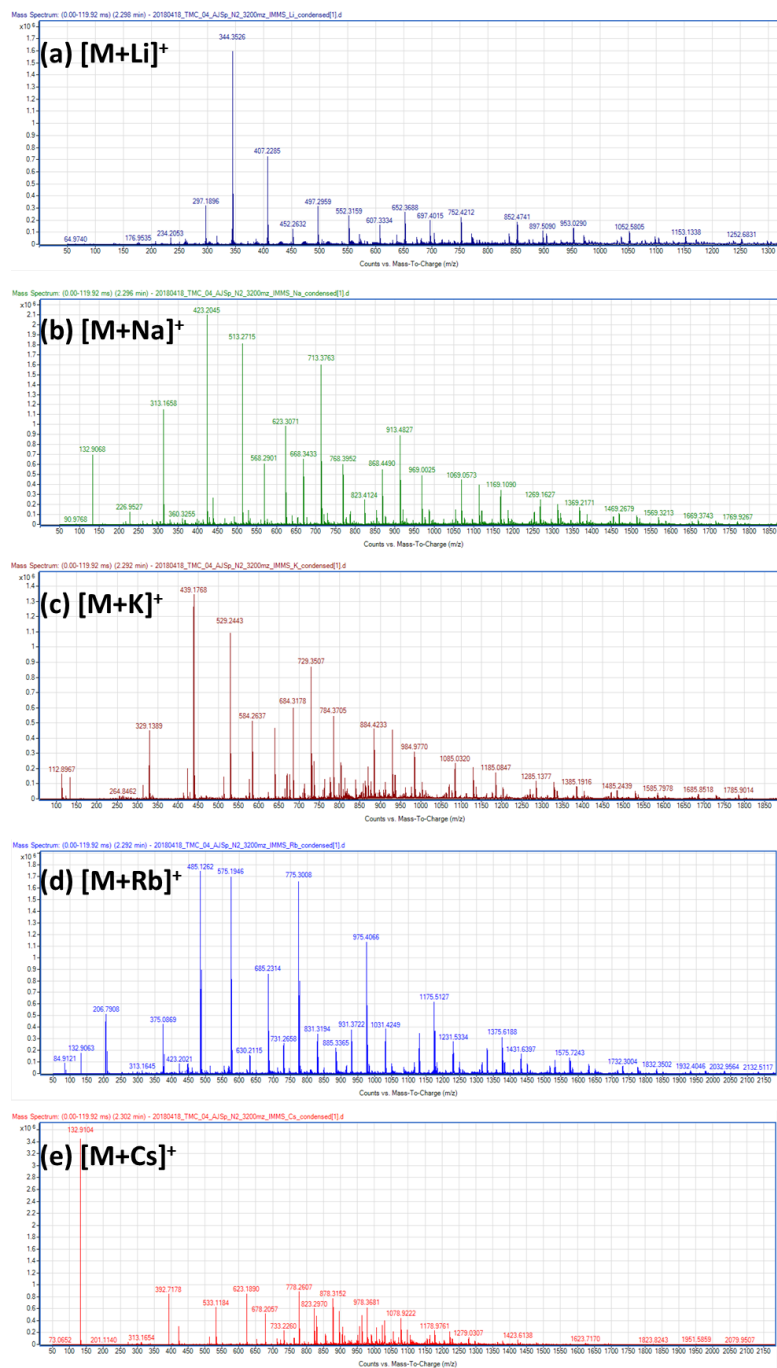


Figure E.2. ESI-MS spectra of cationized polybutylene adipate ($M_n = 2200$): (a) $[M+Li]^+$, (b) $[M+Na]^+$, (c) $[M+K]^+$, (d) $[M+Rb]^+$ and (e) $[M+Cs]^+$.

E.3. IM-MS Trap Voltage

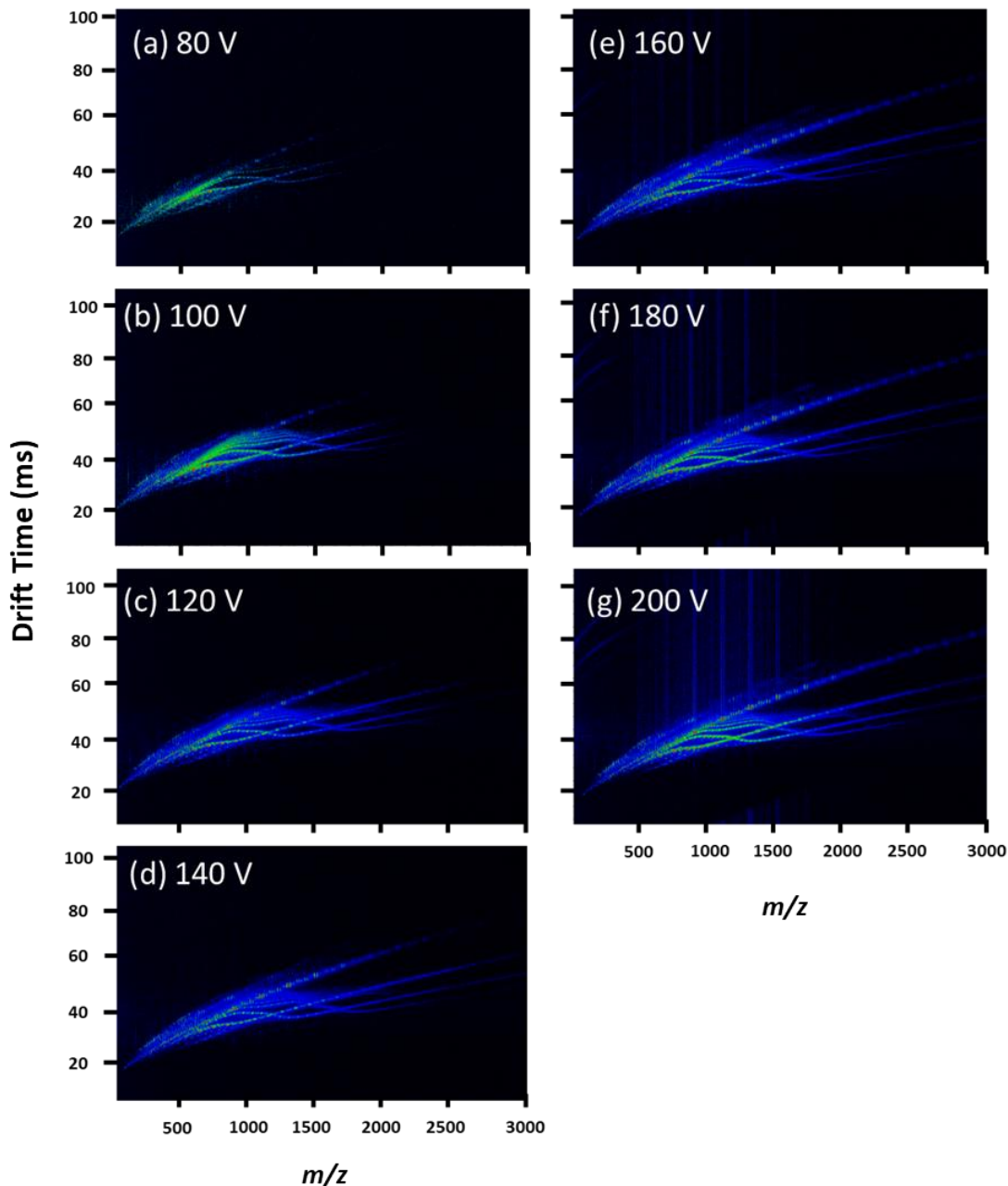


Figure E.3. A stepped ion funnel trap RF voltage experiment was performed using 20 V increments: **(a)** 80 V_{pp} , **(b)** 100 V_{pp} , **(c)** 120 V_{pp} , **(d)** 140 V_{pp} , **(e)** 160 V_{pp} , **(f)** 180 V_{pp} , and **(g)** 200 V_{pp} . While signal intensity changes, the trap RF voltages do not affect the IM distributions and by proxy the measured CCS values. This observation indicates that the observed gas-phase structures are stable and resistant to collision-induced unfolding.

E.4. IM-MS Spectra of Cationized PBA (Li, Na, K, Rb, and Cs)

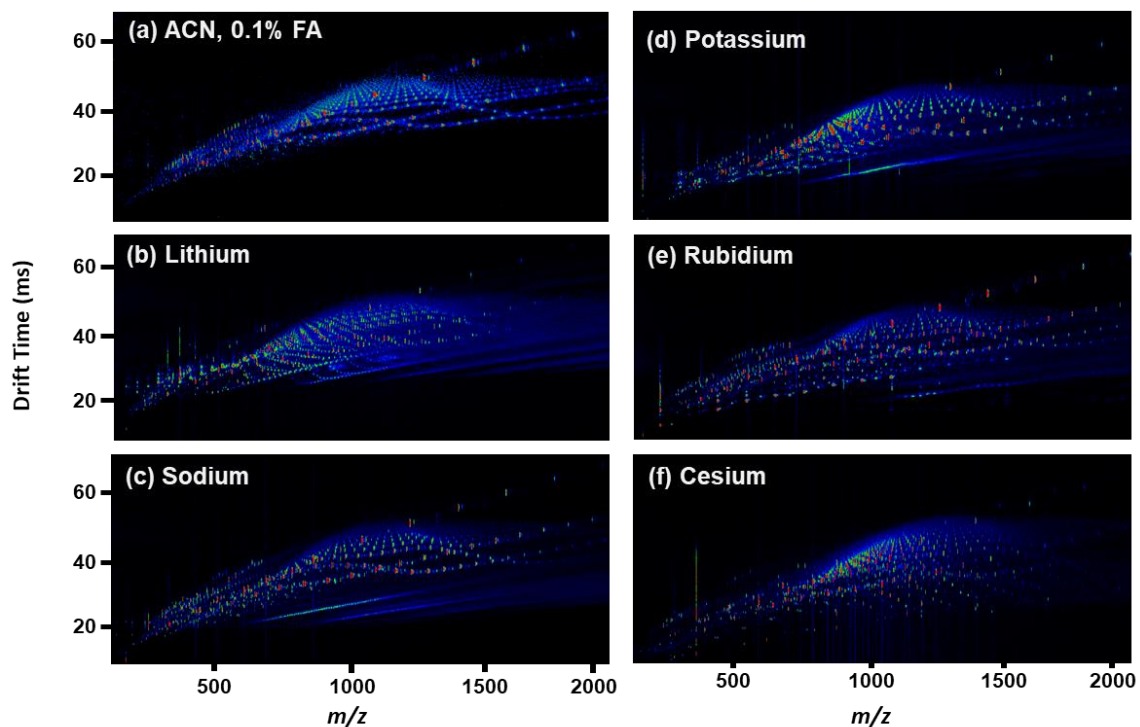


Figure E.4. Ion mobility spectra of PBA ($M_n = 2200$) ionized by alkali monovalent cations. PBA samples were independently spiked with either formic acid or one cation of interest: (a) PBA dissolved in ACN and ionized with 0.1% formic acid, (b) lithium chloride, (c) sodium chloride, (d) potassium chloride, (e) rubidium chloride, and (f) cesium chloride.

E.5. ANOVA Statistical Analysis (Example)

Single-factor analysis of variance (ANOVA) was used in the present study to quantitatively compare the differences in CCS values obtained for each PBA-cationized oligomer. Experiments were done in triplicate and compared for five groups of data: PBA-Li, PBA-Na, PBA-K, PBA-Rb, and PBA-Cs. The difference between an entire group's CCS mean was compared to the mean CCS of all groups. The results of this calculation are expressed as the F ratio, which describes the variance *between* the cation groups relative to variance *within* the cation groups. If the probability value (p) from the ANOVA test is smaller than 95%, one can conclude that there are no statistically significant differences between groups. If the p value is greater than the 95% threshold, it can be concluded that the groups are significantly different. When PBA oligomers were concluded to be statistically the same, it was determined that the polymer ions must be structurally similar to one another. As seen in **Figure E.6** (DP = 5), each cation group converges to the same CCS, therefore the architectural arrangement of DP = 5 cationized with Li has a gas-phase structure that is similar to the same oligomer cationized to Na, K, Rb, or Cs at the 95% confidence level. Whereas in **Figure E.5**, each cation group shows significant differences among CCS means, which is interpreted as indicating that the molecular geometry of each PBA-cation is unique for the PBA DP = 1 oligomer ion.

Consider the example in **Figure E.5**. Here we compare the CCS values for DP = 1 obtained for five groups: PBA-Li, PBA-Na, PBA-K, PBA-Rb, and PBA-Cs for three independent trials. The CCS *Data Values* (x) for all three trails are contained within **lines 1-5**. The sums of each cation's three trials were calculated in **line 6** (S_i). The sum of **line 6** was recorded in **line 7** as $S = 2537.70$. The sums listed in **line 6** were then squared and recorded in **line 8** (S_i^2). The sum of **line 8** was then reported in **line 9**. **Line 10** (S^2) represents the sum in **line 7** squared. In this experiment, there were 15 total data values (N) (**line 11**), with 3 sets of numbers (n) within each column (**line 12**). Therefore, there are 14 degrees of freedom (DoF) for the total data set N (**line 13**) and 2 DoF within each column n (**line 14**). There are 4 DoF for comparison among the 5 cations. The CCS *Data Values* (x) reported in **lines 3-5** were squared and reported under *Data Values Squared* (x^2) (**lines 3-5**). The sum of CCS squared was reported in **line 6** under each PBA-cation column. The sum of squared data values in **line 6** were totaled in **line 7** and recorded as **429514**.

Here we will use three mathematical identities to calculate the sums of squares. To determine the *Total Sum of Squares* (**line 15**), the sum squared in **line 10** (**6439921**) divided by the total number of data values (**line 11, 15**) was subtracted from the sum of x^2 (**line 7, 429514**). In **Figure S5**, numbers are color coded to guide from where the number value is derived. To calculate the *sum of squares within* the data, the sum of S_i^2 (**line 9, 1288514**) divided by the number of participants in each group (**line 12, 3**) was subtracted from the sum of x^2 (**line 7, 429514**). To determine the *sum of squares between* the cations, the sum of S_i^2 in each group (**line 9, 1288514**) was divided by the number of independent trails (**line 12, 3**), this value was subtracted from S^2 (**line 10, 6439921**) divided by the number of data sets (**line 11, 15**). The *sum of squares between* (**line 19, 176.60**), *within* (**line 20, 9.33**), and the *total* **line 21 (185.93)** are listed in the table. The degrees of freedom *between* and *within* the data sets are listed for the cation groups and replicates of data being compared. The F(critical 4/10) value (3.11) is reported from statistical chart for 95% confidence, for the respective to DoF. The variance in **lines 19-20** divides the sum of squares by the DoF, for both *between* and *within* source of variance data. To calculate F, the variance for *between* data is divided by the variance *within* data. The F value calculated is compared to F(critical) to determine significant differences or similarities observed for the data being compared. In this case, **Figure E.5** represents DP = 1 had an F value of 47.47 which is greater than the significance value for 95% confidence. Therefore the CCS values

compared in this data set are significantly different from one another. ANOVA results for DPs observed are summarized in **Figures E.6-E.12**.

| Line (#) | Data Values (x) | | | | | Data Values Squared (x ²) | | | | | |
|----------|------------------------|--|--------|----------|---------|---------------------------------------|----------|----------|----------|----------|-------|
| | Li | Na | K | Rb | Cs | Li | Na | K | Rb | Cs | |
| 1 | | | | | | | | | | | |
| 2 | | | | | | | | | | | |
| 3 | 163.65 | 166.64 | 170.96 | 173.15 | 174.21 | 26781.32 | 27768.89 | 29227.32 | 29980.92 | 30349.12 | |
| 4 | 164.59 | 166.93 | 170.74 | 171.78 | 171.21 | 27089.87 | 27865.62 | 29152.15 | 29508.37 | 29312.86 | |
| 5 | 163.04 | 166.67 | 169.80 | 170.85 | 173.48 | 26582.04 | 27778.89 | 28832.04 | 29189.72 | 30095.31 | |
| 6 | $\sum (x_i) = (Si)$ | 491.28 | 500.24 | 511.50 | 515.78 | 518.90 | 80453 | 83413 | 87211 | 88679 | 89757 |
| 7 | S | 2537.70 | | | | | 429514 | | | | |
| 8 | S_i^2 | 241356 | 250240 | 261632 | 266029 | 269257 | | | | | |
| 9 | $\sum Si^2$ | 1288514 | | | | | | | | | |
| 10 | S^2 | 6439921 | | | | | | | | | |
| 11 | Total x values (N) | 15 | | | | | | | | | |
| 12 | Number in Column (n) | 3 | | | | | | | | | |
| 13 | DoF in N | 14 | | | | | | | | | |
| 14 | DoF in n | 2 | | | | | | | | | |
| 15 | Total sum of squares | $\sum(x^2) - \frac{S^2}{N} \rightarrow (429514) - \frac{6439921}{15} = 185.93$ | | | | | | | | | |
| 16 | Sum of Squares Within | $\sum(x^2) - \sum(\frac{Si^2}{n}) \rightarrow (429514) - \frac{1288514}{3} = 9.33$ | | | | | | | | | |
| 17 | Sum of Squares Between | $\sum(\frac{Si^2}{n}) - \frac{S^2}{N} \rightarrow \frac{1288514}{3} - \frac{6439921}{15} = 176.60$ | | | | | | | | | |
| 18 | Source of Variance | Sum of squares | DoF | Variance | F value | F critical 4/10 | | | | | |
| 19 | Between | 176.60 | 4 | 44.15 | 47.47 | 3.11 | | | | | |
| 20 | Within | 9.33 | 10 | 0.93 | | | | | | | |
| 21 | Total | 185.93 | 14 | | | | | | | | |

Figure E.5. ANOVA statistical analysis of CCS values obtained from all three experimental trials for charge state trend +1 PBA DP = 1 species.

E.6. Raw Data for Charge State +1

| Data for Charge State +1 | | | | | |
|--------------------------|--------|--------|--------|--------|--------|
| DP = 1 | Li | Na | K | Rb | Cs |
| Different | 163.65 | 166.64 | 170.96 | 173.15 | 174.21 |
| | 164.59 | 166.93 | 170.74 | 171.78 | 171.21 |
| | 163.04 | 166.67 | 169.80 | 170.85 | 173.48 |
| DP = 2 | Li | Na | K | Rb | Cs |
| Different | 208.91 | 211.10 | 215.41 | 218.66 | 220.85 |
| | 207.25 | 210.04 | 214.75 | 216.86 | 219.20 |
| | 207.08 | 210.78 | 214.78 | 216.70 | 218.38 |
| DP = 3 | Li | Na | K | Rb | Cs |
| Different | 250.11 | 247.92 | 251.17 | 253.36 | 256.61 |
| | 248.56 | 248.11 | 250.20 | 252.02 | 255.99 |
| | 248.53 | 247.30 | 249.78 | 251.83 | 253.78 |
| DP = 4 | Li | Na | K | Rb | Cs |
| Same | 288.06 | 285.87 | 286.93 | 288.06 | 288.06 |
| | 286.86 | 288.82 | 287.75 | 288.20 | 289.58 |
| | 287.76 | 286.59 | 289.92 | 287.30 | 287.33 |
| DP = 5 | Li | Na | K | Rb | Cs |
| Same | 322.76 | 320.57 | 322.76 | 322.76 | 322.76 |
| | 322.90 | 323.07 | 325.39 | 324.81 | 323.90 |
| | 323.84 | 323.09 | 327.90 | 324.37 | 324.39 |
| DP = 6 | Li | Na | K | Rb | Cs |
| Same | 354.14 | 352.02 | 354.14 | 355.27 | 355.27 |
| | 355.63 | 355.24 | 357.54 | 358.07 | 356.90 |
| | 356.09 | 355.34 | 361.38 | 357.60 | 357.81 |
| DP = 7 | Li | Na | K | Rb | Cs |
| Same | 382.34 | 382.34 | 386.12 | 383.40 | 385.59 |
| | 383.97 | 386.71 | 387.33 | 386.25 | 387.01 |
| | 385.41 | 385.14 | 390.78 | 387.15 | 387.85 |
| DP = 8 | Li | Na | K | Rb | Cs |
| Same | 410.54 | 407.29 | 411.60 | 412.73 | 411.60 |
| | 411.15 | 411.81 | 413.13 | 416.27 | 415.14 |
| | 412.86 | 413.41 | 414.45 | 415.43 | 414.72 |
| DP = 9 | Li | Na | K | Rb | Cs |
| Same | 435.48 | 434.36 | 435.48 | 437.61 | 438.73 |
| | 434.80 | 448.56 | 440.22 | 439.72 | 439.58 |
| | 439.70 | 439.89 | 440.94 | 441.49 | 440.49 |

Figure E.6. Raw CCS data and results from ANOVA statistical analysis of +1 species. CCS values of all three experimental trials for charge state trend +1 PBA species are shown above (DP = 1 – 9). Significantly different CCS values among alkali metal cations (Li, Na, K, Rb, and Cs) are shown in blue, significantly similar CCS values are illustrated in green.

E.7. Raw Data for Charge State +2

| Data for Charge State +2 | | | | | |
|--------------------------|--------|--------|--------|--------|--------|
| | Li | Na | K | Rb | Cs |
| DP = 5 | 398.82 | 398.82 | 407.71 | 414.40 | 423.29 |
| Different | 398.05 | 397.33 | 406.34 | 413.91 | 422.71 |
| | 397.46 | 398.28 | 406.17 | 413.52 | 420.59 |
| | Li | Na | K | Rb | Cs |
| DP = 6 | 427.80 | 432.31 | 434.49 | 441.19 | 447.88 |
| Different | 424.87 | 430.28 | 433.20 | 439.62 | 447.73 |
| | 425.99 | 431.78 | 434.22 | 439.82 | 445.73 |
| | Li | Na | K | Rb | Cs |
| DP = 7 | 450.21 | 459.09 | 461.28 | 463.60 | 465.79 |
| Same | 446.80 | 457.15 | 457.64 | 460.59 | 422.71 |
| | 447.06 | 458.20 | 458.39 | 460.01 | 460.74 |
| | Li | Na | K | Rb | Cs |
| DP = 8 | 463.60 | 470.30 | 476.99 | 476.99 | 479.18 |
| Same | 459.45 | 468.17 | 471.68 | 474.04 | 447.73 |
| | 459.27 | 468.31 | 471.79 | 474.01 | 473.26 |
| | Li | Na | K | Rb | Cs |
| DP = 9 | 481.37 | 483.69 | 490.39 | 492.57 | 494.76 |
| Same | 476.37 | 482.79 | 486.69 | 489.47 | 463.84 |
| | 477.17 | 481.92 | 485.42 | 488.50 | 488.25 |
| | Li | Na | K | Rb | Cs |
| DP = 10 | 501.46 | 503.78 | 508.15 | 510.47 | 514.85 |
| Same | 499.01 | 502.85 | 505.33 | 509.33 | 475.79 |
| | 499.28 | 502.80 | 505.45 | 508.13 | 508.48 |
| | Li | Na | K | Rb | Cs |
| DP = 11 | 526.05 | 526.05 | 530.56 | 532.75 | 534.94 |
| Same | 522.41 | 527.40 | 529.67 | 531.92 | 491.88 |
| | 523.60 | 525.85 | 527.90 | 530.86 | 531.74 |
| | Li | Na | K | Rb | Cs |
| DP = 12 | 548.33 | 548.33 | 552.84 | 555.03 | 557.35 |
| Same | 546.06 | 551.72 | 551.67 | 554.97 | 512.80 |
| | 547.52 | 548.05 | 551.10 | 553.55 | 554.57 |

Figure E.7. Raw CCS data and results from ANOVA statistical analysis of +2 species. CCS values of all three experimental trials for charge state trend +2 PBA species are shown above (DP = 5 – 12). Significantly different CCS values among alkali metal cations (Li, Na, K, Rb, and Cs) are shown in blue, significantly similar CCS values are illustrated in green.

E.8. Raw Data for Charge State +2

| | Li | Na | K | Rb | Cs |
|---------|--------|--------|--------|--------|--------|
| DP = 13 | 570.74 | 570.74 | 575.11 | 577.44 | 579.62 |
| Same | 567.08 | 575.00 | 575.49 | 578.59 | 534.86 |
| | 570.17 | 572.03 | 573.46 | 575.88 | 577.70 |
| | Li | Na | K | Rb | Cs |
| DP = 14 | 593.02 | 595.20 | 597.53 | 597.53 | 599.71 |
| Same | 589.39 | 595.69 | 597.96 | 600.54 | 558.26 |
| | 591.17 | 595.01 | 604.77 | 598.18 | 605.06 |
| | Li | Na | K | Rb | Cs |
| DP = 15 | 615.43 | 613.11 | 619.80 | 619.80 | 624.31 |
| Same | 611.18 | 617.30 | 619.85 | 622.63 | 579.93 |
| | 614.67 | 616.41 | 626.43 | 620.17 | 522.35 |
| | Li | Na | K | Rb | Cs |
| DP = 16 | 637.71 | 635.52 | 639.89 | 639.89 | 642.21 |
| Same | 632.59 | 639.40 | 639.82 | 642.12 | 600.58 |
| | 636.25 | 637.84 | 638.56 | 642.09 | 648.46 |
| | Li | Na | K | Rb | Cs |
| DP = 17 | 659.98 | 653.28 | 659.98 | 664.49 | 659.98 |
| Same | 655.87 | 656.52 | 662.60 | 664.34 | 622.98 |
| | 655.83 | 659.01 | 660.72 | 662.88 | 665.09 |
| | Li | Na | K | Rb | Cs |
| DP = 18 | 680.07 | 677.88 | 682.39 | 682.39 | 682.39 |
| Same | 677.22 | 677.80 | 681.52 | 684.87 | 640.03 |
| | 679.14 | 676.95 | 679.87 | 683.68 | 685.62 |
| | Li | Na | K | Rb | Cs |
| DP = 19 | 700.16 | 693.46 | 700.16 | 702.48 | 702.48 |
| Same | 696.77 | 697.63 | 700.22 | 701.67 | 661.07 |
| | 695.10 | 696.52 | 699.75 | 702.24 | 705.44 |
| | Li | Na | K | Rb | Cs |
| DP = 20 | 718.06 | 718.06 | 722.57 | 720.25 | 718.06 |
| Same | 715.30 | 718.05 | 720.49 | 720.51 | 679.62 |
| | 720.13 | 718.25 | 719.49 | 721.67 | 722.01 |
| | Li | Na | K | Rb | Cs |
| DP = 21 | 738.15 | 740.34 | 742.66 | 742.66 | 740.34 |
| Same | 734.36 | 735.11 | 739.86 | 740.45 | 701.75 |
| | 737.21 | 735.62 | 738.86 | 740.90 | 740.58 |
| | Li | Na | K | Rb | Cs |
| DP = 22 | 756.05 | 756.05 | 756.05 | 758.24 | 762.75 |
| Same | 751.00 | 754.70 | 755.19 | 757.91 | 719.14 |
| | 753.75 | 754.67 | 757.59 | 758.04 | 757.22 |
| | Li | Na | K | Rb | Cs |
| DP = 23 | 773.82 | 776.14 | 778.33 | 780.51 | 780.51 |
| Same | 771.68 | 771.98 | 775.85 | 775.25 | 734.03 |
| | 784.34 | 774.49 | 775.83 | 777.98 | 778.54 |

Figure E.8. Raw CCS data and results from ANOVA statistical analysis of +2 species. CCS values of all three experimental trials for charge state trend +2 PBA species are shown above (DP = 13 – 23). Significantly different CCS values among alkali metal cations (Li, Na, K, Rb, and Cs) are show in blue, significantly similar CCS values are illustrated in green.

E.9. Raw Data for Charge State +3

| Data for Charge State +3 | | | | | |
|--------------------------|--------|--------|--------|--------|---------|
| | Li | Na | K | Rb | Cs |
| DP = 9 | 676.14 | 665.84 | 672.78 | 681.01 | 690.013 |
| Different | 679.69 | 669.83 | 674.60 | 682.93 | 694.65 |
| | 682.12 | 673.26 | 683.07 | 683.06 | 691.42 |
| | Li | Na | K | Rb | Cs |
| DP = 10 | 717.33 | 703.67 | 710.60 | 722.60 | 727.62 |
| Different | 719.80 | 710.62 | 712.90 | 720.43 | 731.57 |
| | 720.58 | 714.26 | 716.84 | 719.61 | 727.21 |
| | Li | Na | K | Rb | Cs |
| DP = 11 | 755.15 | 748.22 | 751.79 | 758.60 | 762.09 |
| Different | 755.25 | 752.70 | 752.26 | 757.16 | 765.41 |
| | 757.34 | 756.97 | 751.77 | 755.58 | 760.63 |
| | Li | Na | K | Rb | Cs |
| DP = 12 | 782.68 | 782.68 | 786.04 | 790.8 | 792.98 |
| Different | 779.88 | 788.51 | 786.02 | 788.73 | 793.58 |
| | 782.58 | 789.88 | 784.18 | 787.58 | 789.06 |
| | Li | Na | K | Rb | Cs |
| DP = 13 | 789.40 | 806.64 | 813.57 | 813.80 | 813.57 |
| Different | 788.55 | 812.62 | 811.43 | 813.04 | 814.66 |
| | 791.65 | 807.82 | 808.10 | 812.03 | 810.12 |
| | Li | Na | K | Rb | Cs |
| DP = 14 | 789.40 | 810.00 | 820.30 | 823.20 | 823.87 |
| Different | 786.30 | 814.62 | 818.12 | 821.95 | 824.28 |
| | 788.45 | 808.37 | 816.56 | 820.35 | 819.81 |
| | Li | Na | K | Rb | Cs |
| DP = 15 | 792.98 | 806.64 | 820.30 | 821.50 | 823.87 |
| Different | 788.98 | 810.38 | 815.14 | 821.72 | 823.55 |
| | 790.06 | 806.72 | 811.76 | 819.63 | 819.32 |
| | Li | Na | K | Rb | Cs |
| DP = 16 | 792.98 | 806.64 | 816.93 | 818.10 | 823.87 |
| Different | 787.13 | 809.92 | 810.79 | 817.87 | 819.20 |
| | 789.36 | 804.35 | 809.42 | 814.90 | 815.45 |

Figure E.9. Raw CCS data and results from ANOVA statistical analysis of +3 species. CCS values of all three experimental trials for charge state trend +3 PBA species are shown above (DP = 9 – 16). Significantly different CCS values among alkali metal cations (Li, Na, K, Rb, and Cs) are shown in blue, significantly similar CCS values are illustrated in green.

E.10. Raw Data for Charge State +3

| | | | | | |
|-----------|--------|--------|---------|--------|--------|
| | Li | Na | K | Rb | Cs |
| DP = 17 | 782.68 | 799.70 | 803.27 | 803.30 | 810.00 |
| Different | 771.41 | 796.10 | 797.19 | 802.92 | 801.49 |
| | 776.47 | 792.24 | 795.63 | 799.89 | 799.66 |
| | Li | Na | K | Rb | Cs |
| DP = 18 | 765.45 | 779.11 | 786.04 | 781.40 | 786.04 |
| Different | 754.62 | 776.06 | 776.32 | 779.61 | 778.23 |
| | 759.37 | 772.24 | 773.49 | 777.54 | 776.00 |
| | Li | Na | K | Rb | Cs |
| DP = 19 | 765.45 | 768.81 | 775.75 | 774.30 | 779.11 |
| Different | 754.51 | 770.63 | 765.98 | 771.51 | 772.95 |
| | 759.40 | 765.53 | 766.40 | 770.15 | 769.83 |
| | Li | Na | K | Rb | Cs |
| DP = 20 | 772.38 | 775.75 | 782.68 | 781.20 | 786.04 |
| Different | 761.93 | 779.63 | 775.22 | 780.41 | 784.21 |
| | 767.74 | 773.06 | 772.41 | 777.99 | 778.19 |
| | Li | Na | K | Rb | Cs |
| DP = 21 | 786.04 | 792.98 | 796.34 | 793.80 | 803.27 |
| Different | 777.86 | 795.28 | 789.68 | 793.25 | 796.03 |
| | 783.97 | 786.40 | 786.87 | 791.53 | 800.57 |
| | Li | Na | K | Rb | Cs |
| DP = 22 | 803.27 | 803.27 | 810.00 | 809.80 | 810.00 |
| Different | 799.26 | 808.16 | 805.46 | 810.55 | 815.31 |
| | 799.31 | 802.75 | 817.72 | 807.89 | 816.42 |
| | Li | Na | K | Rb | Cs |
| DP = 23 | 816.93 | 820.30 | 820.30 | 827.30 | 830.59 |
| Different | 806.07 | 825.27 | 822.97 | 825.98 | 830.62 |
| | 817.81 | 818.97 | 827.90 | 824.88 | 826.55 |
| | Li | Na | K | Rb | Cs |
| n=24 | 837.53 | 834.16 | 844.46 | 845.00 | 840.89 |
| Different | 828.46 | 842.63 | 839.865 | 843.37 | 840.89 |
| | 835.16 | 836.02 | 837.46 | 842.35 | 840.89 |
| | Li | Na | K | Rb | Cs |
| DP = 25 | 854.76 | 854.76 | 861.48 | 862.80 | 861.48 |
| Different | 845.36 | 858.25 | 857.70 | 861.71 | 861.48 |
| | 853.91 | 853.07 | 856.77 | 859.72 | 861.48 |

Figure E.10. Raw CCS data and results from ANOVA statistical analysis of +3 species. CCS values of all three experimental trials for charge state trend +3 PBA species are shown above (DP = 17 – 25). Significantly different CCS values among alkali metal cations (Li, Na, K, Rb, and Cs) are shown in blue, significantly similar CCS values are illustrated in green.

E.11. Raw Data for Charge State +3 (without Li)

| | | | | |
|-----------|---------|--------|--------|--------|
| | Na | K | Rb | Cs |
| DP = 10 | 703.67 | 710.60 | 722.60 | 727.62 |
| Different | 710.62 | 712.90 | 720.43 | 731.57 |
| | 714.26 | 716.84 | 719.61 | 727.21 |
| | Na | K | Rb | Cs |
| DP = 11 | 748.22 | 751.79 | 758.60 | 762.09 |
| Different | 752.70 | 752.26 | 757.16 | 765.41 |
| | 756.97 | 751.77 | 755.58 | 760.63 |
| | Na | K | Rb | Cs |
| DP = 12 | 782.68 | 786.04 | 790.80 | 792.98 |
| Same | 788.51 | 786.02 | 788.73 | 793.58 |
| | 789.88 | 784.18 | 787.58 | 789.06 |
| | Na | K | Rb | Cs |
| DP = 13 | 806.64 | 813.57 | 813.80 | 813.57 |
| Same | 812.62 | 811.43 | 813.04 | 814.66 |
| | 807.82 | 808.10 | 812.03 | 810.12 |
| | Na | K | Rb | Cs |
| DP= 14 | 810.00 | 820.30 | 823.20 | 823.87 |
| Different | 814.62 | 818.12 | 821.95 | 824.28 |
| | 808.37 | 816.56 | 820.35 | 819.81 |
| | Na | K | Rb | Cs |
| DP = 15 | 806.64 | 820.30 | 821.50 | 823.87 |
| Different | 810.38 | 815.14 | 821.72 | 823.55 |
| | 806.72 | 811.76 | 819.63 | 819.32 |
| | Na | K | Rb | Cs |
| DP = 16 | 806.64 | 816.93 | 818.10 | 823.87 |
| Different | 809.92 | 810.79 | 817.87 | 819.20 |
| | 804.35 | 809.42 | 814.90 | 815.45 |
| | Na | K | Rb | Cs |
| DP = 17 | 799.70 | 803.27 | 803.30 | 810.00 |
| Same | 796.10 | 797.19 | 802.92 | 801.49 |
| | 792.245 | 795.63 | 799.89 | 799.66 |

Figure E.11. Raw CCS data and results from ANOVA statistical analysis of +3 species (without Lithium). CCS values of all three experimental trials for charge state trend +3 PBA species are shown above (DP = 9 – 16). Significantly different CCS values among alkali metal cations (Na, K, Rb, and Cs) are shown in blue, significantly similar CCS values are illustrated in green.

E.12. Raw Data for Charge State +3 (without Li)

| | | | | |
|-----------|--------|--------|--------|--------|
| | Na | K | Rb | Cs |
| n=18 | 779.11 | 786.04 | 781.40 | 786.04 |
| Same | 776.06 | 776.32 | 779.61 | 778.23 |
| | 772.24 | 773.49 | 777.54 | 776.00 |
| | Na | K | Rb | Cs |
| n=19 | 768.81 | 775.75 | 774.30 | 779.11 |
| Same | 770.63 | 765.98 | 771.51 | 772.95 |
| | 765.53 | 766.40 | 770.15 | 769.83 |
| | Na | K | Rb | Cs |
| n=20 | 775.75 | 782.68 | 781.20 | 786.04 |
| Same | 779.63 | 775.22 | 780.41 | 784.21 |
| | 773.06 | 772.41 | 777.99 | 778.19 |
| | Na | K | Rb | Cs |
| n=21 | 792.98 | 796.34 | 793.80 | 803.27 |
| Same | 795.28 | 789.68 | 793.25 | 796.03 |
| | 786.40 | 786.87 | 791.53 | 800.57 |
| | Na | K | Rb | Cs |
| n=22 | 803.27 | 810.00 | 809.80 | 810.00 |
| Same | 808.16 | 805.46 | 810.55 | 815.31 |
| | 802.75 | 817.72 | 807.89 | 816.42 |
| | Na | K | Rb | Cs |
| n=23 | 820.30 | 820.30 | 827.30 | 830.59 |
| Same | 825.27 | 822.97 | 825.98 | 830.62 |
| | 818.97 | 827.90 | 824.88 | 826.55 |
| | Na | K | Rb | Cs |
| n=24 | 834.16 | 844.46 | 845.00 | 840.89 |
| Same | 842.63 | 839.86 | 843.37 | 840.89 |
| | 836.02 | 837.46 | 842.35 | 840.89 |
| | Na | K | Rb | Cs |
| n=25 | 854.76 | 861.48 | 862.80 | 861.48 |
| Different | 858.25 | 857.70 | 861.71 | 861.48 |
| | 853.07 | 856.77 | 859.72 | 861.48 |

Figure E.12. Raw CCS data and results from ANOVA statistical analysis of +3 species. CCS values of all three experimental trials for charge state trend +3 PBA species are shown above (DP = 17 – 25). Significantly different CCS values among alkali metal cations (Na, K, Rb, and Cs) are shown in blue, significantly similar CCS values are illustrated in green.

E.13. IM-MS Plot of DP = 1

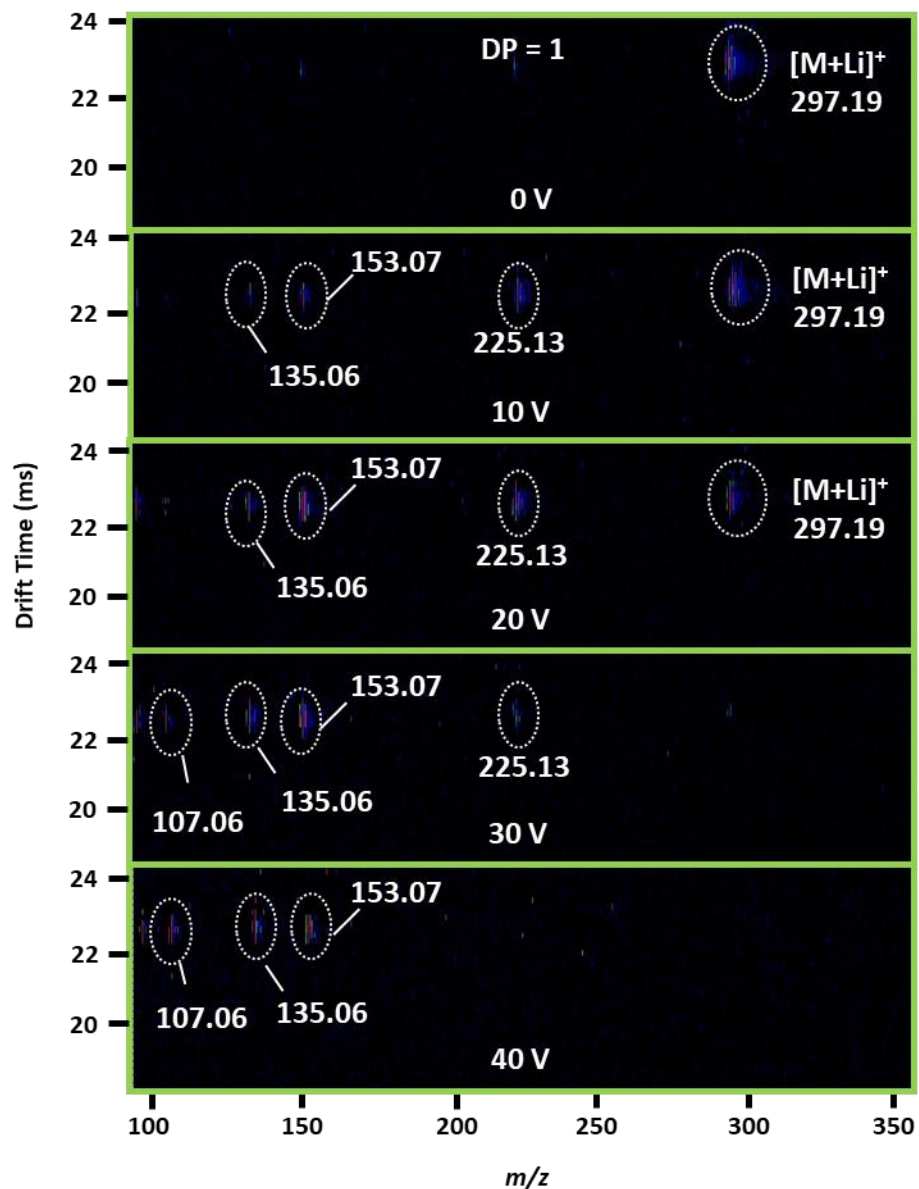


Figure E.13. IM-MS spectra from tandem MS experiments conducted on DP = 1 [M+Li]⁺ species. Each spectrum represents results observed from different CID collision energies from 0 V (top panel) to 40 V (bottom panel).

E.14. Fragment Ion Structures for DP = 1

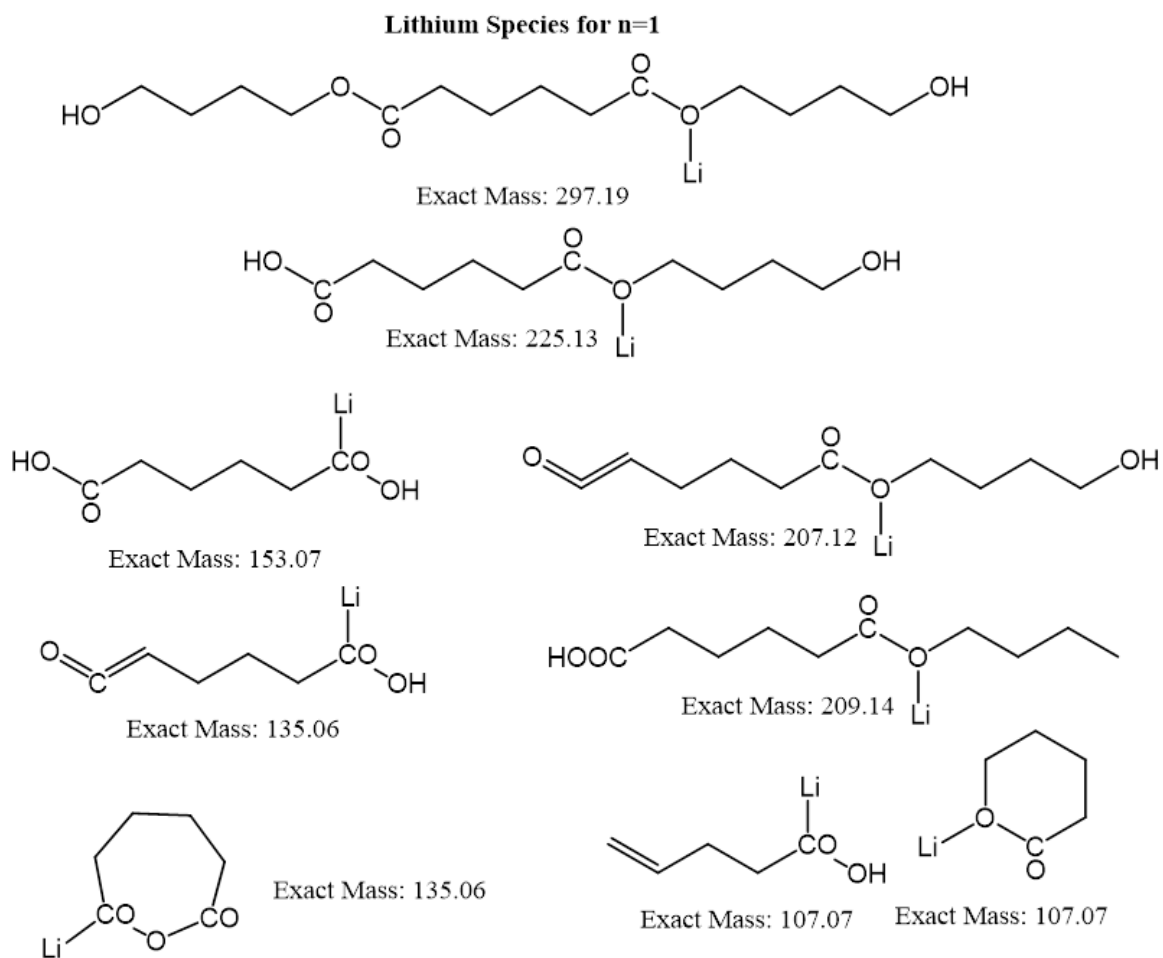


Figure E.14. Possible fragment ion structures for DP = 1 $[M+Li]^+$ species. In the above example, it is not implied that Li is covalently bonded to the “O or CO” groups. This illustration proposed the bonding of the Li cation to the fragment ion to allow the exact mass to be calculated. The exact mass represents the $[M+Li]^+$ species, illustrated above.

E.15. IM-MS Plot of DP = 1

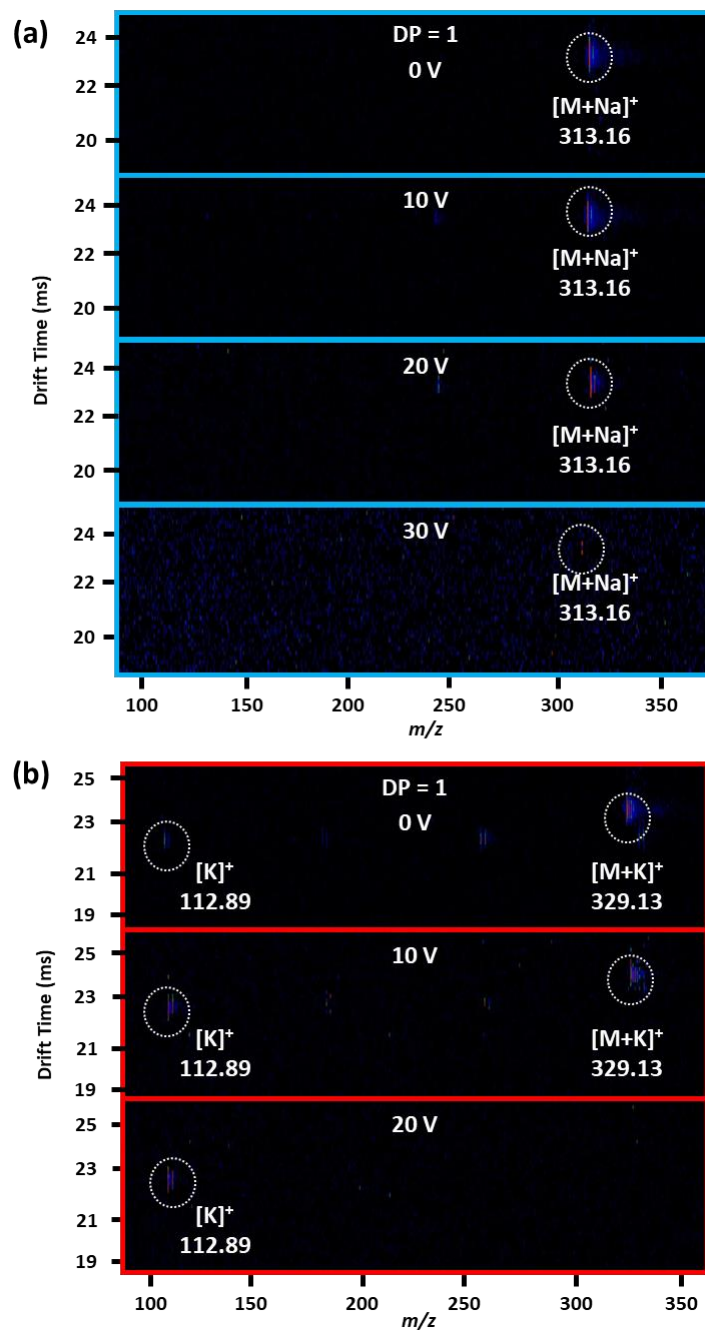


Figure E.15. IM-MS spectra from tandem MS experiments conducted on DP = 1 (a) [M+Na]⁺ and (b) [M+K]⁺ species. Each spectrum represents results observed from different CID collision energies from (a) 0 V – 30 V and (b) 0 V – 20 V.

E.16. IM-MS Plot of DP = 1

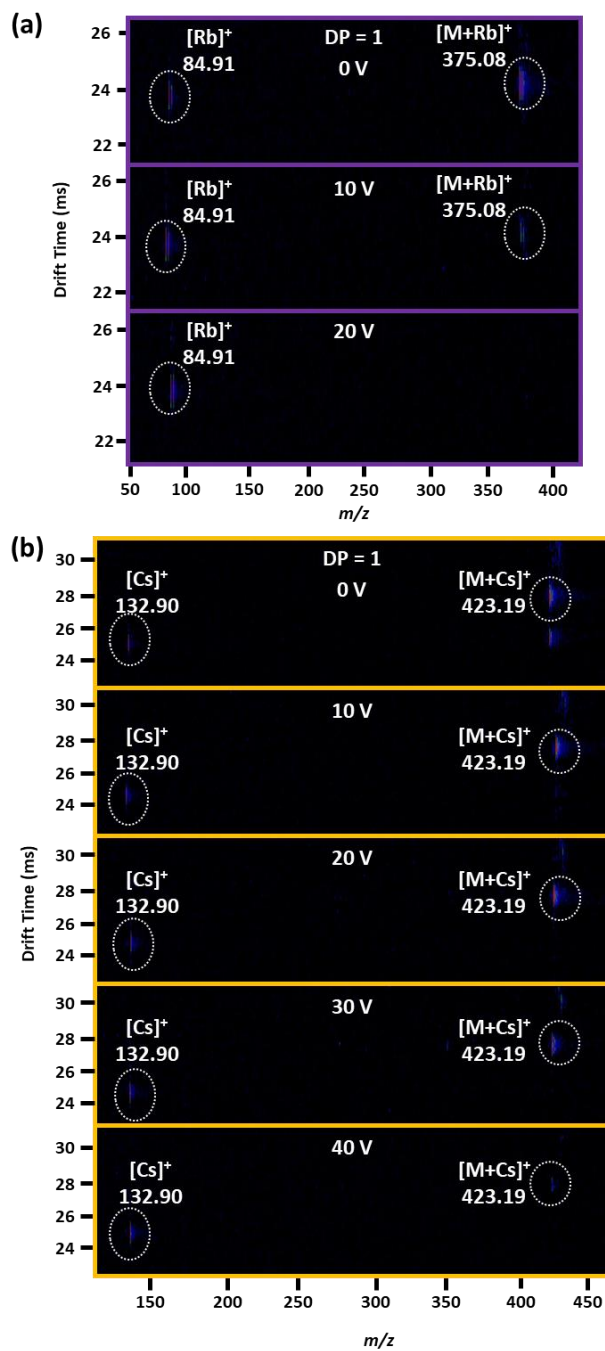
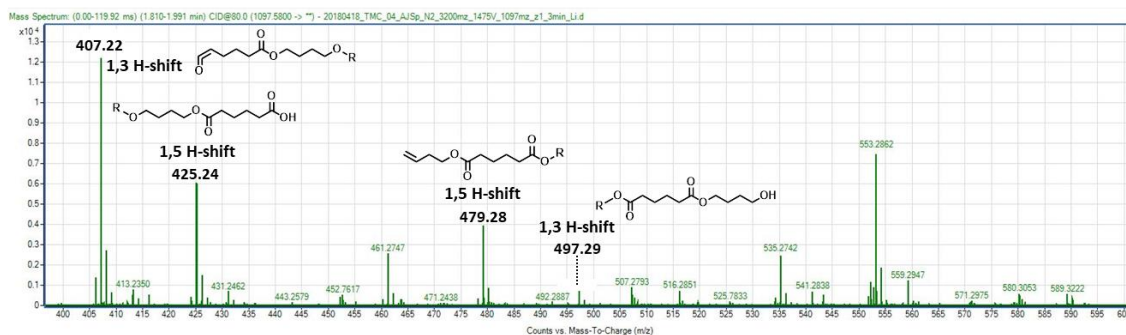


Figure E.16. IM-MS spectra from tandem MS experiments conducted on DP = 1 **(a)** [M+Rb]⁺ and **(b)** [M+Cs]⁺ species. Each spectrum represents results observed from different CID collision energies from **(a)** 0 V – 20 V and **(b)** 0 V – 40 V.

E.17. MS/MS Example of 1,5 H-shift and 1,3 H-shift

(a) DP = 5, [M+Li]⁺



(b) DP = 5, [M+Na]⁺

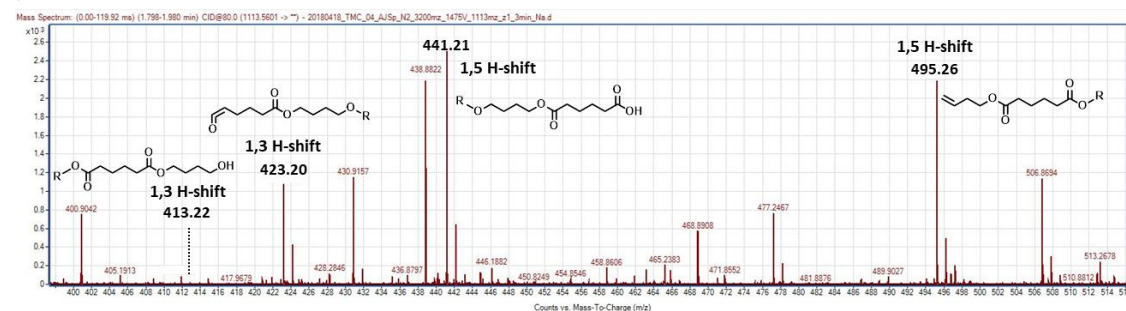


Figure E.17. Tandem MS data of DP = 5 for (a) [M+Li]⁺ and (b) [M+Na]⁺ species at 80 V_{pp}. An example of fragment ions that were observed to result from 1,5 H-shift and 1,3 H-shift are outlined.

E.18. Fragment Ion Table

| PBA-Li | | PBA-Na | |
|------------------------|-------------------------|------------------------|-------------------------|
| Fragment Ions (m/z) | Fragmentation Mechanism | Fragment Ions (m/z) | Fragmentation Mechanism |
| 1025 | 1,5 H-shift | 1041 | 1,5 H-shift |
| 897 | 1,3 H-shift | 895 | 1,5 H-shift |
| 879 | 1,5 H-shift | 841 | 1,5 H-shift |
| 825 | 1,5 H-shift | 823 | 1,3 H-shift |
| 807 | 1,3 H-shift | 813 | 1,3 H-shift |
| 697 | 1,3 H-shift | 695 | 1,5 H-shift |
| 679 | 1,5 H-shift | 641 | 1,5 H-shift |
| 625 | 1,5 H-shift | 623 | 1,3 H-shift |
| 607 | 1,3 H-shift | 613 | 1,3 H-shift |
| 497 | 1,3 H-shift | 495 | 1,5 H-shift |
| 479 | 1,5 H-shift | 441 | 1,5 H-shift |
| 425 | 1,5 H-shift | 423 | 1,3 H-shift |
| 407 | 1,3 H-shift | 413 | 1,3 H-shift |
| 297 | 1,3 H-shift | 295 | 1,5 H-shift |
| 279 | 1,5 H-shift | 241 | 1,5 H-shift |
| 225 | 1,5 H-shift | 223 | 1,3 H-shift |
| 207 | 1,3 H-shift | 213 | 1,3 H-shift |

Figure E.18. Fragment ions (m/z) and their mechanistic pathways observed for both PBA-Li and PBA-Na are listed.

E.19. IM-MS Plot of DP = 5

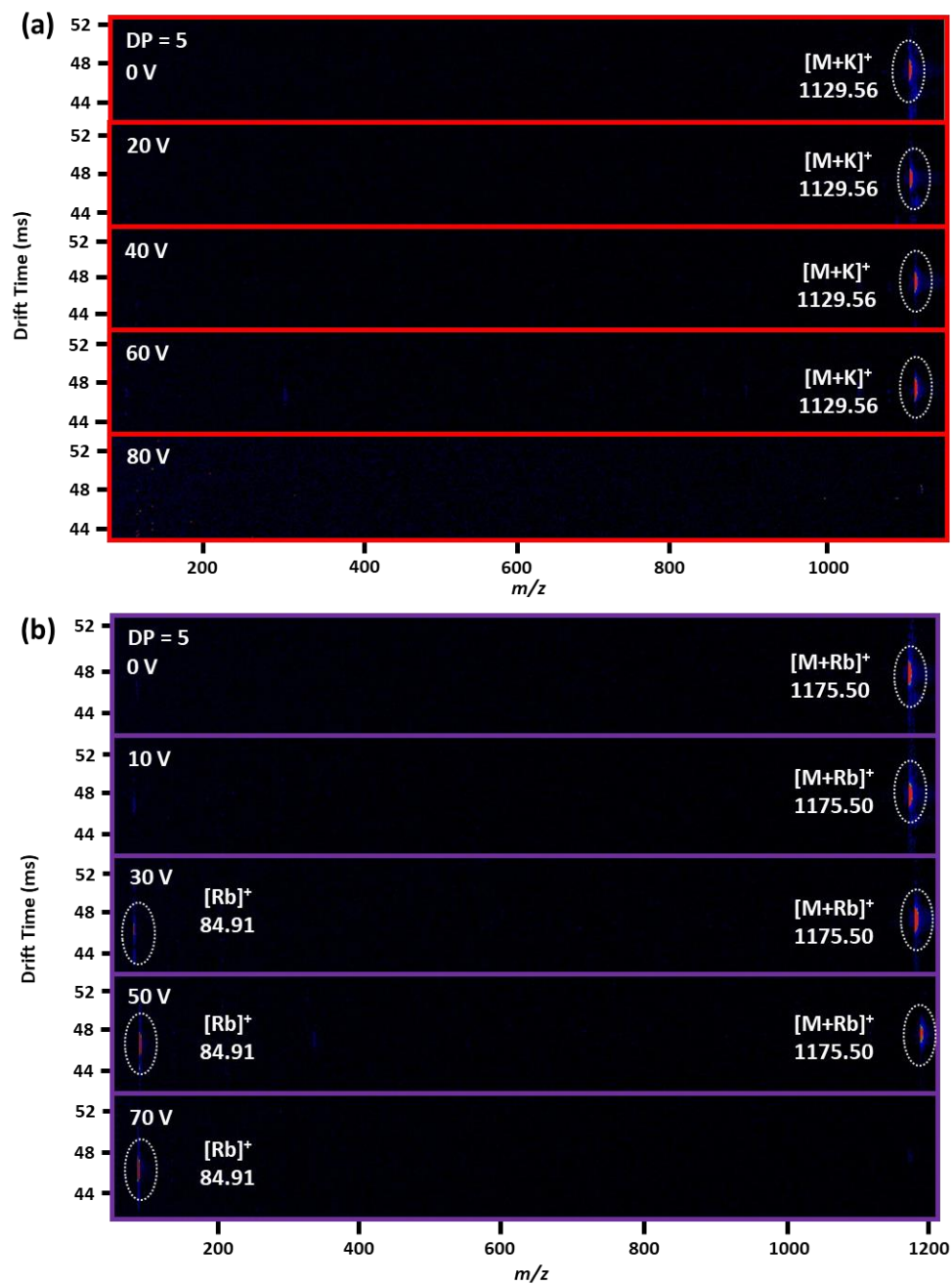


Figure E.19. IM-MS spectra from tandem MS experiments conducted on DP = 5 (a) [M+K]⁺ and (b) [M+Rb]⁺ species. Each spectrum represents results observed from different CID collision energies from (a) 0 V – 80 V and (b) 0 V – 70 V.

E.20. IM-MS Plot of DP = 5

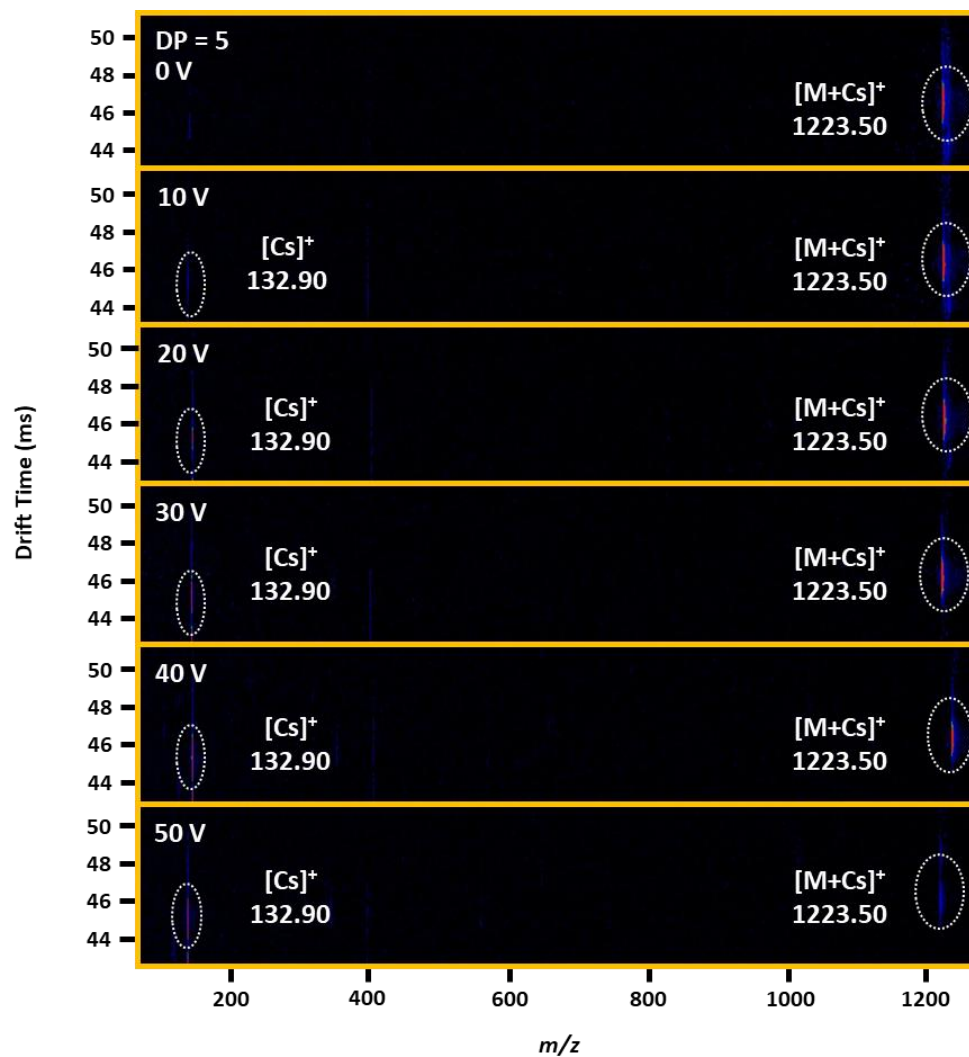


Figure E.20. IM-MS spectra from tandem MS experiments conducted on DP = 5 [M+Cs]⁺ species. Each spectrum represents results observed from different CID collision energies from 0 V – 50 V.

CURRICULUM VITAE

Tiffany M. Crescentini

EDUCATION

Vanderbilt University (2014-2019), Nashville TN

Doctorate of Philosophy, Chemistry

Cumulative GPA 3.02/4.00

Chemistry GPA 3.13/4.00

Waynesburg University (2010-2014), Waynesburg PA

B.S. Pre-Medical Chemistry, GPA 3.38/4.00

SUMMARY

I am a business woman in a chemists body – self-motivating, a problem-solver, proficient at leading in-and-out of laboratory settings, a passionate teacher, I embrace and encourage tailoring communication to the listener, team player, and driven to help others succeed to reach their goals.

RELEVANT EXPERIENCE

Department of Chemistry – Vanderbilt University, Nashville TN

Graduate Research Assistant (2014-Present)

- Synthesis – protecting group stepwise synthesis for assembling specific polyester (polybutylene adipate) oligomers. Urethane synthesis experience with 4,4-MDI and short chain polyols.
- Analytical Characterization – development of analytical methods for characterizing hard and soft segment PU starting material and short chain PU oligomers. MS techniques are used to investigate bond formation and fragmentation pathways.

SyBBURE – Vanderbilt University, Nashville TN

Summer Internship and Beyond (2013-2015)

- Developed microfluidic systems that desalt samples for online MS characterization.
- Characterized PDMS devices (organ-on-a-chip) for leaching of unreactive starting materials using various solvent systems.
- Tested absorption parameters of drug compounds with varying chemical properties.
- Experience with AutoCAD, COMSOL, microfabrication, photolithography

Technical Skills

- MS, IM-MS, IM-MS/MS ESI, MALDI, HPLC, GC, NMR (1D and 2D), FT-IR, UV-VIS, sample preparation, analytical method development, chromatography method development.
- Mass spectrometer training – Thermo Q Exactive hybrid Quadrupole-Orbitrap MS, Agilent 6560 IM-QTOF, Waters G2 Synapt

Teaching Experience

- General Chemistry I and II (2014-2015, 2018), Organic Chemistry I (2018), Analytical Chemistry (2016), Senior Capstone Independent Research Course (2017)

LEADERSHIP EXPERIENCE

- Salud Cooking School, Whole Foods, Prep-Team Lead Volunteer, 2014-Present
- Rocky Mountain Independent Gymnastic Trampoline Camp, Assistant Coach 2015-2016
- Cross Country and Track and Field Varsity Athlete 2010-2013, Waynesburg University, Team Captain 2012 (Cross Country)
- NCAA DIII Regional Qualifier, Cross Country, Waynesburg University 2010-2012
- Nike XC Midwest Regionals Woodridge High School 2009

AWARDS AND FELLOWSHIPS

- ASPIRE Module: Technology Commercialization, Technology Transfer - Vanderbilt University, 2017
- ASPIRE Module: Entrepreneurship and Intellectual Property - Vanderbilt University, 2017
- CIRTL Evidence Based Teaching Workshop - Vanderbilt University, 2017
- Certificate in College Teaching - Vanderbilt University, 2016
- GAANN Fellowship - Vanderbilt University, 2014-2016
- TELOS Leadership Conference - Waynesburg University, 2012
- Leadership Scholar - Waynesburg University, 2010-2014

JOURNAL PUBLICATION

Crescentini T.M., May J.C., McLean J.M. and Hercules D.M., Polyurethane Hard and Soft Segments – Mass Spectrometry Review. **2019**. (Manuscript in Preparation.)

Crescentini T.M., May J.C., McLean J.M. and Hercules D.M., Alkali Metal Cation Adduct Effect on Polybutylene Adipate Oligomers: Ion Mobility-Mass Spectrometry. (Submitted *Elsevier Polymer* **2019**).

Tomlinson, I.D., Kovtun O., **Crescentini T.M.** and Rosenthal S.J. Biotinylated-Spiperone Ligands for Quantum Dot Labeling of the Dopamine D2 Receptor in Live Cell Cultures. (Submitted to *Bioorganic & Medicinal Chemistry Letters*, **2018**).

Crescentini, T.M.*, Stow, S.M.*, Forsythe, J.G., May, J.C., McLean, J.A. and Hercules, D.M. Structural Characterization of Methylenedianiline Regioisomers by Ion Mobility-Mass Spectrometry and Tandem Mass Spectrometry: IV. 3-Ring and 4-Ring Isomers. *Analytical Chemistry*, **2018**. *Authors contributed equally.

Stow, S.M.*, **Crescentini, T.M.***, Forsythe, J.G., May, J.C., McLean, J.A. and Hercules, D.M. Structural Characterization of Methylenedianiline Regioisomers by Ion Mobility-Mass Spectrometry, Tandem Mass Spectrometry, and Computational Strategies. 3. MALDI Spectra of 2-Ring Isomers. *Analytical Chemistry*, **2017**, 18, 9900-9910. *Authors contributed equally.

Stow, S.M.*, **Onifer, T.M.***, Forsythe, J.G.*, Nefzger, H., Kwiecien, N.W., May, J.C., McLean, J.A. and Hercules, D.M. Structural Characterization of Methylenedianiline Regioisomers by Ion Mobility-Mass Spectrometry, Tandem Mass Spectrometry, and Computational Strategies. 2. Electrospray Spectra of 3-Ring and 4-Ring Isomers. *Analytical Chemistry*, **2015**, 12, 6288-6296. *Authors contributed equally.

CONFERENCE PRESENTATIONS

Tiffany M. Crescentini; Jody C. May; John A. McLean; David M. Hercules, Group I Metal Cation Adduct Effects on Polyester Oligomers: Ion Mobility – Mass Spectrometry, ASMS Conference San Diego CA (May **2018**). POSTER

Tiffany M. Crescentini, Multifaceted Approach to Characterizing Polyurethane Block Co-Polymers, Vanderbilt University Chemistry Forum Series Nashville, TN (March **2017**). ORAL PRESENTATION

Tiffany M. Crescentini; Sarah M. Stow; Robert W. Davis; Gary Sulikowski; David M. Hercules; John A. McLean, Single Oligomer Polyurethane Synthesis: Characterization by Ion Mobility-Mass Spectrometry and Computational Strategies, ASMS Conference San Antonio, TX (June **2016**). POSTER

Tiffany M. Crescentini; Sarah M. Stow; Jay Forsythe; David M. Hercules; John A. McLean, Structural Characterization of Isomeric Polymer Precursors by Electrospray Ion Mobility-Mass Spectrometry and Computational Strategies, ASMS Conference St Louis, MO (June **2015**). POSTER

Tiffany Onifer; Sarah Stow; Jay Forsythe; David Hercules; and John McLean, Structural Characterization of Polyurethane Precursors: Methylenedianiline Trimer and Tetramers, PITTCON Conference Chicago, IL (August **2014**). POSTER

AFFILIATIONS

American Society for Mass Spectrometry (ASMS) – member since 2014 – present

American Chemical Society (ACS) – member since 2010 – present

Society of Analytical Chemists of Pittsburgh (SACP) – member since 2010 – present